Transactions of the ASME®

FLUIDS ENGINEERING DIVISION
Technical Editor
DEMETRI P. TELIONIS (1999)
Executive Secretary
PAT WHITE (1999)
Assistants to the Editor
N. W. SCHAEFFLER
J. E. POWELL
Calendar Editor
M. F. ACKERSON

Associate Technical Editors
P. R. BANDYOPADHYAY (1997)
S. BANERJEE (1999)
P. W. BEARMAN (1998)
M. DHAUBHADEL (1999)
J. EATON (1999)
F. GIRALT (1997)
J. A. C. HUMPHREY (1997)
F. HUSSAIN (1998)
J. KATZ (1998)
B. SCHIAVELLO (1999)
O. SIMONIN (1998)
P. M. SOCKOL (1998)
M. W. SINDIR (1997)
M. SOMMERFELD (1999)
M. S. TRIANTAFYLLOU (1998)

BOARD ON COMMUNICATIONS
Chairman and Vice-President
R. MATES

OFFICERS OF THE ASME
President, **R. J. GOLDSTEIN**
Exec. Director
D. L. BELDEN
Treasurer
J. A. MASON

PUBLISHING STAFF
Managing Director, Engineering
CHARLES W. BEARDSLEY
Director, Technical Publishing
PHILIP DI VIETRO
Managing Editor, Technical Publishing
CYNTHIA B. CLARK
Managing Editor, Transactions
CORNELIA MONAHAN
Production Assistant
MARISOL ANDINO

Transactions of the ASME, Journal of Fluids Engineering (ISSN 0098-2202) is published quarterly (Mar., June, Sept., Dec.) for $185.00 per year by The American Society of Mechanical Engineers, 345 East 47th Street, New York, NY 10017. Periodicals postage paid at New York, NY and additional mailing offices. POSTMASTER: Send address changes to Transactions of the ASME, Journal of Fluids Engineering, c/o THE AMERICAN SOCIETY OF MECHANICAL ENGINEERS, 22 Law Drive, Box 2300, Fairfield, NJ 07007-2300.
CHANGES OF ADDRESS must be received at Society headquarters seven weeks before they are to be effective. Please send old label and new address.
PRICES: To members, $40.00, annually: to nonmembers, $185.00. Add $30.00 for postage to countries outside the United States and Canada.
STATEMENT from By-Laws. The Society shall not be responsible for statements or opinions advanced in papers or . . . printed in its publications (B7.1, Par. 3).

INDEXED by Applied Mechanics Reviews and Engineering Information, Inc. Canadian Goods & Services Tax Registration #126148048.

Journal of Fluids Engineering

Published Quarterly by The American Society of Mechanical Engineers

VOLUME 119 • NUMBER 1 • MARCH 1997

(Contents continued on p. 102)

(Contents continued)

Technical Briefs

Announcements and Special Notices

Journal of Fluids Engineering

Editorial

This is the annual report of the Technical Editor on the operation of this Journal. This report appears in every March issue and contains information on our efforts to disseminate more efficiently the archival material submitted by the authors and make it more accessible to our readership. This issue also contains a list of the papers published in different categories in the previous year and a list of all the reviewers who supported our efforts. Authors' indices appear in a cumulative form. The last author index, a ten-year index, was published in September 1992. The author index for issues that appear after 1992 is available in the electronic JFE and is updated annually. A cumulative index will appear again in print in 2002.

This Editorial Board has strived to reach a broader audience. The editors continue to advise and urge the authors on how to address themselves to audiences other than the specialists on the topic of their paper. To attract the attention of the readers and in particular, the practitioners, new approaches were adopted in the past year. Papers of particular significance are highlighted by introductions in the form of short editorials that appear in the Technical Forum. These editorials are prepared by the associate editor who has overseen the review process of a particular article.

Another type of introductory note was launched in the December issue. For articles of particular significance to practicing engineers, industrial experts are invited to prepare discussions. These too are published at the beginning of an issue. This idea was formulated by a group of associate editors (Ghoniem, Humphrey, Nelik, and Sindir) and was elaborated upon in an editorial that appeared in the March issue of 1996. The first issue in which discussions prepared by industrial experts appeared was the December issue of 1996.

To highlight the significance of certain areas in fluids engineering, we identify them as the theme of an issue of the journal. These issues are not dedicated exclusively to specific topics. Rather, a topic of current interest is discussed by an editorial, one or more review articles and some contributed papers are grouped together and lead the other articles of the issue. The June issue of 1996 had turbulence modeling as its theme, while the themes of the September and December issues were microfluid dynamics and industrial problems in fluid mechanics.

The number of submitted papers has been increasing monotonically for the past seven years, but it appears that in the last year this trend has leveled off. The backlog has been reduced and now papers appear six months after they are accepted. The authors should note that the printer requires manuscripts at least four months before the publication of an issue. The space limitation has also been somewhat relaxed, but it is again recommended to the authors to make use of the availability of electronic space. This space is virtually unlimited and can be used to present more figures in color, lengthy derivations, detailed descriptions of experimental rigs and computer codes and now video. The authors are also invited to deposit their data in the JFE Data Bank.

This year we did not make progress in reducing further the review time. This time depends on the response of the reviewers and the efforts the editors make to remind and urge the reviewers to return their comments. Very much related with our success to speed up the review process is the selection of reviewers. Some of the concepts that are presented below were proposed by Dr. Owen C. Jones, one of our associate editors, and were recently discussed by the Editorial Board. In fact, some of the passages that follow were removed, verbatim, from his private communication with other members of the Editorial Board.

An editor covering a certain area must solicit reviews for numerous papers on a continuous basis. As a basic rule, we try not to burden a reviewer of JFE more than once a year. Exceptions of course exist, since more than one editor covers the same area. Two careful and detailed reviews are usually sufficient to accept a paper if both are positive. But quite often they are not both positive. Such a situation is more often the rule than the exception, so that three good reviews is generally our aim. We try to complete the first phase of the review process in two months, but it very rarely happens that all three individuals who were requested to provide a review actually respond within this period of time. Here is where early on in his tenure, this editor decided to adopt a somewhat controversial policy: to request reviews for each paper from five individuals. In this way we usually collect an acceptable number of good reviews within a reasonable period of time. We then write a polite letter to the reviewers whose comments are delayed and advise them that their services are no longer necessary. We understand that this may inconvenience some reviewers who may have started reviewing a paper, but we found that this is the only method for providing authors with timely and thorough reviews. Besides, if a review does arrive late, it is shipped to the author anyway and helps improve a paper even further.

This procedure has increased our need for reviewers. The perception that most authors have of journal editors is generally one of a person with broad knowledge of the field and unlimited resources when it comes to selection of potential referees for a particular paper. This may be true only in some cases. Each editor is chosen because of his or her knowledge of a particular field of fluid mechanics. While any given editor may have a degree of expertise in one of these areas, he or she usually specializes in yet another subset of the area, which limits somewhat his or her circle of potential reviewers. So how do editors select reviewers? They draw on their professional acquaintances and the names listed in the biographical citations of the paper under consideration. Some may take the time to carry out a literature review themselves. Considering the fact that an editor may be handling twenty to thirty papers at a time, one can understand that the sources of good reviewers can quickly be exhausted.

The authors themselves are generally in an excellent, perhaps even better position to know who has the best expertise and currency to do a competent and thorough evaluation of a paper. In the directions to the authors we encourage them to suggest

the names of five or six reviewers. Editors, of course, do not necessarily turn to all or sometimes even any of the suggested reviewers. However, to preserve anonymity and give the editor more freedom of choice, it is desirable to have ten or twelve reviewers to choose from. This should hardly be a burden on the authors who generally know or should know all the active and knowledgeable people in the field of the paper. This practice has worked well in the past for some of the editors of JFE. In fact some authors have expressed gratitude for this request, because in this way they can be sure their papers would be reviewed by competent people who are current in the particular area which is the topic of the paper. It is, of course, the responsibility of the editors to evaluate submitted papers and no author will be required to provide lists of reviewers. But authors should recognize that the quality of the review of their work could be enhanced and the review process expedited by a prompt response to an editors request to suggest names and addresses of reviewers.

Authors and reviewers should know that the ultimate responsibility for acceptance of a paper lies with the editors. Reviews serve only to bring to the attention of the editors certain facts. The reviews should never be thought of as "votes" in favor or against acceptance. In fact it is not unusual to see a paper rejected, even if the majority of the reviewers were in favor of publication. The opposite, a paper accepted with the majority of reviews against publication, is possible but it is a rarity.

Finally, we should acknowledge the valuable contributions of six associate editors whose tenure has expired. These are Hiroyuki Hashimoto and Lev Nelik in the area of fluid applications and systems; David Stock in the area of fluid measurements; Pratap Vanka in the area of computational fluid mechanics; Owen Jones and Jong Kim in the area of multi-phase flow. We sincerely appreciate their hard work. We should also acknowledge the contributions of the individuals who reviewed papers for JFE this past year. Their names are listed in the last pages of this issue.

Five new associate editors have been nominated by the Executive Committee and their nominations have been approved by the ASME Board on Communications. These and the areas they will be working on are the following: Bruno Schiavello (Ingersoll-Dresser Pump Co.) and Mano Dhaubhadel (Ford Motor Co.) in fluid applications and systems; Sanjoy Banerjee (University of California—Santa Barbara) in fluid measurements; John Eaton (Stanford University) and Martin Sommerfeld (Martin—Luther—Universitat Halle—Wittenburg, Germany) in multiphase flow.

The Technical Editor

Perspective: Measurements and Analyses of Nonlinear Wave Interactions With Higher-Order Spectral Moments

M. R. Hajj
Department of Engineering Science and Mechanics, Virginia Polytechnic Institute and State University, Blacksburg, VA 24061-0219

R. W. Miksad
School of Engineering and Applied Science, University of Virginia, Charlottesville, VA 22903

E. J. Powers
Department of Electrical and Computer Engineering, University of Texas at Austin, Austin, TX 78712

In fluid flows, fluid-structure interactions and other fluids-related problem, nonlinear dynamics play an important role in determining the development, response or output. Understanding these dynamics is essential for development of analytical models and prediction and control purposes. Higher-order statistical analysis has been shown to be an effective tool that can be applied to identify nonlinear couplings and measure energy transfer rates. These techniques have been applied by our group and others to investigate transition of shear flows, energy cascading in turbulence, oceanographic and geophysical flows, and fluid-structure interactions. The results of these investigations revealed important nonlinear characteristics regarding these problems. In this paper, we review these techniques and explain their usefulness in identification and quantification of nonlinear dynamics.

1 Introduction

In a variety of physical problems related to fluid flows and fluid structure interactions, waves or modes could become unstable, grow and nonlinearly interact to transfer energy to other modes. These problems include flow instability and transition, turbulence, ocean waves, geophysical flows, dynamic response of structures such as bridges, tall buildings, offshore platforms, and ships, etc. Understanding the nonlinear dynamics of such problems is necessary for the development of ananlytical models and for prediction and control purposes. Because of the presence of many waves or modes and because of their interactions, the measured waveform often takes on a random character. Consequently, to gain any insight into the dynamics of the physical situation, one needs to perform data processing and analysis. Over the past fifteen years, we have been, independently and/or as a group, involved in the analysis of nonlinear dynamics in several problems. These include transition to turbulence of shear flows, wave-induced motions of ships, moored vessels and offshore structures, and plasma turbulence. In particular, we have applied higher-order statistical analysis to detect nonlinear couplings and measure nonlinear transfer of energy among spectral modes in all of these problems. Consequently, we have developed a better understanding of nonlinear dynamics in these problems. In this paper, we review these techniques and explain their usefulness using the transition problem as an example. We also summarize other applications of higher-order spectra.

In our work on the transition to turbulence of shear flows, the major emphasis has been to detect nonlinearly coupled modes and quantify energy cascading mechanisms that lead to breakdown to turbulence. It is well established that a common element of the transition of these flows is the evolution of the velocity fluctuations field from a broad spectrum of weak random background noise in the initial laminar state to a broad intense but nearly featureless spectrum in the final turbulence state. The transition between these two states has been described as a sequence of instabilities that corresponds to restructuring of vorticity. The primary instability results in the growth of small disturbances present in the environment of the shear flow, within a certain frequency range, into a band of instability modes around the most amplified mode, usually referred to as the fundamental mode. The growth rates and dispersion characteristics can be adequately described by linear stability theory which solves linearized Navier-Stokes equations. As the instability modes grow, the nonlinear terms in the governing equations which represent the nonlinear interaction mechanisms become significant. These interactions result in energy transfer to sum and difference components of the linearly most unstable modes and thus play a very critical role in setting up the sequence of instabilities and final breakdown to turbulence. To date, analytical treatment of transitioning flows has been limited to the early stages of the transition. The linearized and weakly nonlinear theories have been successful, to a certain extent, in revealing the characteristics of the initial stages of the transition. However, the understanding of the subsequent nonlinear behavior and the breakdown to turbulence is at best not complete. Experimental characterization of the nonlinear stages of the transition are necessary to compare with existing (and often competing) theories. Such characterization has been the main goal of our work on the transition problem.

The objectives of this paper are three-fold. The first is to review the subject of higher-order statistical analysis. The second is to show how these techniques can be used to process a finite set of data (from one or more sensors) and extract important information that is "hidden" in experimental or numerical data. The third is to summarize new insights gained by applying these techniques to transitioning shear flows. Both time and frequency domain analyses were used to study the linear and nonlinear physics of the transition. The discussion on the application of higher-order statistics in this paper is mainly concerned with the analysis of the transition of two basically different flows, namely plane wakes, see Fig. 1(a) and mixing layers, see Fig. 1(b). The wake flow was chosen because it is one of the most dynamically simple, yet physically meaningful shear flow that spatially evolves to turbulence. The mixing layer was chosen because the transition involves a sequence of subharmonic instabilities. In the case of the transitioning plane wake, it is shown how the role of low-frequency components in the spectral broadening and energy redistribution

Contributed by the Fluids Engineering Division for publication in the JOURNAL OF FLUIDS ENGINEERING. Manuscript received by the Fluids Engineering Division December 29, 1994; revised manuscript received March 7, 1996. Associate Technical Editor: D. P. Telionis.

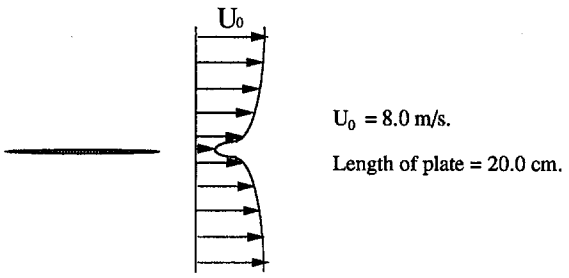

Frequency of dominant instability mode = 580 Hz.

Wavelength of dominant instability mode = 0.7 cm.

Fig. 1(*a*) Schematic and parameters of the transitioning plane wake

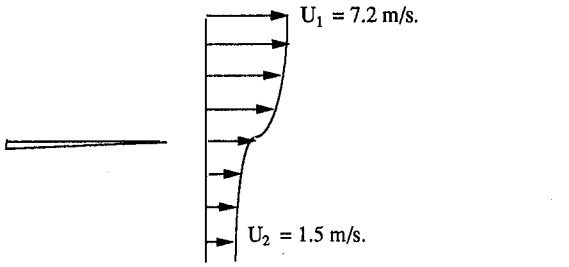

Initial momentum thickness on high speed side = 0.63 mm.

Frequency of dominant instability mode = 215 Hz.

Wavelength of dominant instability mode = 2.0 cm.

Fig. 1(*b*) Schematic and parameters of the transitioning mixing layer

processes can be quantified by measurements of the levels of amplitude and phase modulations obtained with "complex demodulation techniques." It is also shown how characterization and quantification of energy cascading processes can be obtained with estimates of higher-order spectral moments. In the case of the transitioning mixing layer, the focus is on the mechanisms that govern the generation and growth of subharmonic mode. It is demonstrated how the "auto-bispectrum" can be used to measure the phase relation, i.e., phase difference, as well as coupling level, between interacting fundamental and subharmonic modes.

2 Complex Demodulation Techniques for Analysis of Wave Modulation

In the linear stability theory of shear flows, the velocity fluctuations field is represented by a superposition of eigenmodes of the form

$$\psi = ae^{i(kx-wt)} \tag{1}$$

where a represents the amplitude of the eigenmode and where the wavenumber, k, and the frequency, w, are related by a linear dispersion relation

$$w = w(k) \tag{2}$$

As these modes gain energy, the nonlinear terms of the governing equations become more important. One significant consequence of the nonlinearity is the appearance of other parameters, apart from k, in the dispersion relation (Whitham, 1974). The dispersion relation becomes nonlinear and may take the form

$$w = w(k, a^2). \tag{3}$$

This relation introduces frequency deviation of the instability mode. Because of this deviation, amplitude modulation of the instability mode will result in phase modulation and vice-versa. These modulations result in energy transfer to the sidebands of spectral peaks and are thus involved in the broadening of the spectrum. A modulated wave is characterized by its carrier frequency, its wavenumber, and amplitude and phase modulation levels.

Estimates of the level of amplitude and phase modulations of a carrier wave can be obtained by applying complex demodulation techniques. These techniques can best be explained by considering a modulated time series $u(t)$ that can be expressed as

$$u(t) = a(t) \cos \{-2\pi f_o t + p(t)\} \tag{4}$$

where $a(t)$ and $p(t)$ are, respectively, the slowly varying amplitude and phase modulations of the carrier mode with frequency f_o. By multiplying the time series in Eq. (2) by 2 exp $[i2\pi f_d t]$, one obtains

$$2u(t) \exp[i2\pi f_d t] = a(t)\{\exp[-i2\pi(f_o - f_d)t + ip(t)] + \exp[i2\pi(f_o + f_d)t - ip(t)\}]. \tag{5}$$

The first term includes a difference frequency component and the second term includes a sum frequency component. If a low-pass filter is applied, the sum component is eliminated. If f_d is made equal to f_o, the resulting time series, $c(t)$, contains the amplitude and phase modulations in Eq. (4) and is given by

$$c(t) = a(t) \exp[ip(t)] \tag{6}$$

From the amplitude and phase modulations, $a(t)$ and $p(t)$, one can determine parameters that are related to the physics of nonlinear wave modulations and thus to spectral broadening. These parameters include the rms amplitude and phase modulation indices defined, respectively, as

$$\hat{\alpha} = \frac{(E[a(t)^2])^{1/2}}{a_o} \tag{7a}$$

and

$$\hat{\beta} = (E[p(t)])^{1/2} \tag{7b}$$

where $E[\ldots]$ denotes a time average and a_o is the mean value of $a(t)$. These indices can be used to quantify the separate roles of amplitude and phase modulations in the spectral broadening of transitioning flows. A computational procedure for the complex demodulation technique was given by Khadra (1981) and is summarized in appendix A.

In order to show the physical insights that can be gained from measurements of amplitude and phase modulations, complex demodulation techniques have been applied to velocity fluctuations in a transitioning plane wake. Waveforms of the streamwise velocity fluctuations at three downstream locations in the transition of a plane wake are shown in Fig. 2. The amplitude and phase modulations of the fundamental instability mode are plotted next to the waveforms. At $x = 1.0$ cm, before any strong nonlinear mechanisms develop, the modulations are basically sinusoidal. At $x = 3.0$ cm, the amplitude modulations show increasing amounts of harmonic and non-harmonic distortions. In contrast, the phase modulations retain a strongly periodic character. By $x = 40.0$ cm, both modulation mechanisms lost their sinusoidal characteristics. Downstream changes in the modulation indices, $\hat{\alpha}$ and $\hat{\beta}$, and their ratio $\hat{\alpha}/\hat{\beta}$ are shown in Fig. 3. The main characteristic of this figure is the increasing dominance of phase modulation over amplitude modulation as transition progresses. In the region 1.0 cm $\leq x \leq$ 5.0 cm, $\hat{\beta}$ increases dramatically, while $\hat{\alpha}$ remains nearly constant. Up to $x = 20.0$ cm, $\hat{\alpha}$ and $\hat{\beta}$ remain essentially constant, when $\hat{\beta}$ increases again. The ratio $\hat{\alpha}/\hat{\beta}$ shows the rapid initial shift in emphasis to phase modulation, and in fact $\hat{\alpha}/\hat{\beta}$ stays relatively small throughout the nonlinear region of the wake.

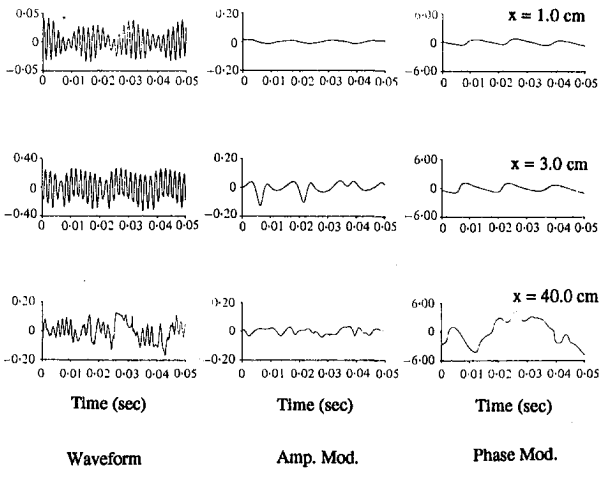

Fig. 2 Time variations of (*a*) the waveforms of longitudinal velocity fluctuations $u'(t)/U_o$; (*b*) the instantaneous amplitude modulations $a_m(t)/U_o$; and (*c*) the instantaneous phase modulations $p_m(t)$ in radians at x = 1.0, 3.0 and 40.0 cm (from Miksad et al., 1982).

One important characteristic of the transition can be obtained from these estimates of amplitude and phase modulation indices. As discussed by Miksad et al. (1982), the physical importance of the rapid growth in the intensity of phase modulation in the early nonlinear stages of the transition can best be understood in terms of spectral broadening. In amplitude modulation, sideband energy comes from the modulating (low-frequency) wave. In phase modulation, sideband energy comes from the carrier wave (instability mode). Since, in the transitioning wake, energy is pumped from the mean flow into the fluctuation field primarily at the most unstable frequencies, phase modulations provide the effective means to pass mean flow energy through the carrier wave into the surrounding sidebands. These low-frequency phase modulations play an important role in turbulence generation and randomization processes. Such results motivate the question for the possibility of "controlling" or "predicting" some basic features of turbulent flows, by controlling or predicting these generating events.

3 Bispectral Analysis and Detection of Quadratically Coupled Modes

In nonlinear systems, frequency components can interact to form new components at their sum or difference frequency. Of particular practical importance in detecting evidence of nonlinear interactions in raw fluctuation data is the fact that the phase of the new component is related to the phases of the primary interacting modes. This reality constitutes the basis of many techniques that aim at investigating nonlinear dynamics. For instance, in dynamical systems analysis, nonlinearities in time series have been characterized by measurements of phase retaining quantities such as, the fractal dimension, phase space portraits, Poincare sections, and Lyapunov exponents. These analyses have been shown to be very useful in characterizing nonlinearities in many systems (Nayfeh and Balachandran, 1995). On the other hand, in many experimental situations, the applications of these techniques is not suitable. For instance, open flows such as mixing layers, jets and boundary layers are convectively unstable, which renders any pure temporal dynamical description inappropriate. Furthermore, quantification of the effects of nonlinearities and phase couplings may be desired for modeling and control purposes. In these situations, higher-order statistical analysis techniques can be applied to provide valuable information about the dynamics of nonlinear systems. In particular, in many fields, bispectral analysis has been established as the main tool to quantify the level of phase coupling between triads of Fourier modes in quadratically nonlinear systems.

Because of the nonlinearities present in the governing equations of fluid flows and their applications, it is expected that higher-order spectral analysis can provide valuable information about many phenomena in fluid dynamics. As a matter of fact, bispectral analysis has been applied to study turbulent flows (Lii et al., 1976; Herring, 1980; Lumley and Takeuchi, 1976; and Herring and Metais, 1992), fluid-structure interactions (Choi et al., 1985; Elgar et al., 1990; Miles et al., 1992; and Dalzell 1975, 1976) and oceanographic (Hasselman et al., 1963; Elgar and Guza, 1985, and Herbers et al. 1992) and geophysical flows (Haubrich, 1965 and Hinich and Clay, 1968). Bispectral analysis has also been applied to examine nonlinear couplings in other applied fields, such as plasma, acoustics, biology and economics. In our work, we have either individually or as a group, applied bispectral analysis to examine wave-induced motions of ships, moored vessels and offshore structures, plasma turbulence and transition to turbulence of free shear flows. The latter application, being the most relevant to our work as a group will be used to show the gains obtained from the application of bispectral analysis. As will be discussed, this analysis provided a nice method for capturing nonlinear couplings among various modes of the transitioning flow as it departs the linear stage and moves into nonlinear stages. We will show how, by polyspectral analysis, one can identify the way in which modes interact and establish a measure of the strength of these interactions.

3.1 Definition and Interpretation of the Bispectrum.

From a statistical and mathematical point of view, higher-order spectra are derived by Fourier transforming the various order cumulant functions. Because this paper is directed towards researchers, scientists and practicing engineers, who are more familiar with second-order correlation and power spectral density functions, higher-order spectra are introduced by analogy with these functions. For a real-valued zero-mean stationary time series, $x(t)$, that represents a random velocity or pressure waveform, the following hierarchy of higher-order correlation functions can be defined

$$m_{xx}(\tau) = E[x(t)x(t+\tau)] \tag{8a}$$

and

$$m_{xxx}(\tau_i, \tau_j) = E[x(t)x(t+\tau_i)x(t+\tau_j)] \tag{8b}$$

One of the most useful tools in characterizing a process such as a velocity or pressure fluctuations field has been the power spectral density function or simply the power spectrum. The power spectrum gives an estimate of the distribution of power

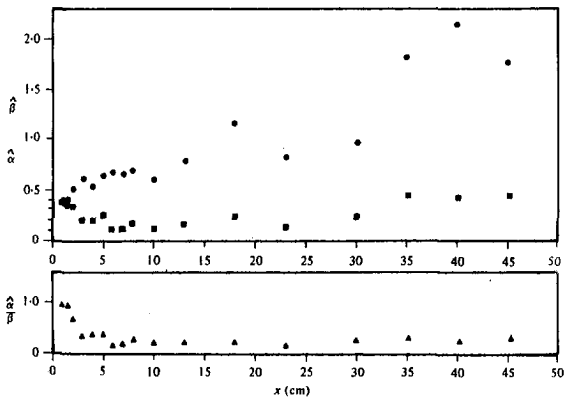

Fig. 3 Downstream variations in the amplitude modulation index $\hat{\alpha}$, ■ the phase modulation index $\hat{\beta}$, ● and their ratio $\hat{\alpha}/\hat{\beta}$ ▲ following maximum u'_{rms} (from Miksad et al., 1982)

among frequency components of the fluctuations. The power spectral density function, $P_{xx}(f)$, is obtained by Fourier transforming the second-order moment function, $m_{xx}(\tau)$. Alternatively, if $X(f)$ is used to denote the Fourier transform of a finite record of $x(t)$ duration T, the power spectrum can be expressed as

$$P_{xx}(f) = \lim_{T\to\infty} \frac{1}{T} E[X(f)X^*(f)] \tag{9}$$

By performing two-dimensional Fourier transformation on the third-order moment function, $m_{xxx}(\tau_j, \tau_k)$, the next higher-order spectrum in the polyspectra hierarchy, namely, the auto-bispectrum, $B_{xxx}(f_j, f_k)$, is obtained. Alternatively, the auto-bispectrum can be expressed as

$$B_{xxx}(f_i, f_j) = \lim_{T\to\infty} \frac{1}{T} E[X(f_i + f_j)X^*(f_i)X^*(f_j)] \tag{10}$$

In the same sense that the area under $P_{xx}(f)$ corresponds to the mean square value of $x(t)$, the volume under $B_{xxx}(f_i, f_j)$ represents the contributions to the mean cube value, i.e.,

$$\int\int_{-\infty}^{\infty} B_{xxx}(f_i, f_j)df_i\,df_j = E[x^3(t)]. \tag{11}$$

When the time series $x(t)$, is real, the complex Fourier amplitude $X(-f)$ is equal to $X^*(f)$ and thus $B(f_i, f_j) = B^*(-f_i, -f_j)$. Under these conditions, only the real part of the auto-bispectrum contributes to the mean cube value.

Another important aspect of the auto-bispectrum lies in its phase. If the three modes present at f_i, f_j and $f_i + f_j$ are independent, each mode is characterized by a statistically independent random phase which will result in a near zero value for the bispectrum when the statistical averaging (equation (10)) is carried out. On the other hand, if the three modes present at f_i, f_j and $f_i + f_j$ are coupled through a nonlinear interaction mechanism, a phase coherence will exist among them. Under these conditions, the averaging will lead to a large value of the bispectrum. The auto-bispectrum, thus, preserves the phase information between coupled modes in the form of a phase difference. Such information is not preserved by the auto-power spectrum. Another property of the auto-bispectrum is its insensitivity to any additive Gaussian noise whose both third moment $m_{xxx}(\tau_i, \tau_j)$ and the corresponding auto-bispectrum $B_{xxx}(f_i, f_j)$ are zero.

In order to remove the dependence of the auto-bispectrum on the amplitudes of the three spectral components under consideration, the auto-bispectrum is normalized by these amplitudes to obtain the auto-bicoherence which is defined as:

$$b^2(f_i, f_j) = \frac{|B_{xxx}(f_i, f_j)|^2}{E[|X(f_i)X(f_j)|^2]E[X(f_i + f_j)|^2]} \tag{12}$$

It can be shown by Schwartz inequality that the auto-bicoherence, $b^2(f_i, f_j)$ is bounded by zero and one. Thus, the triplet of waves with frequencies f_i, f_j and $f_i + f_j$ are quadratically coupled if $b^2(f_i, f_j) = 1.0$, not quadratically coupled if $b^2(f_i, f_j) = 0.0$, and partially coupled if $0.0 < b^2(f_i, f_j) < 1.0$. The auto-bispectrum and its normalized value, the auto-bicoherence, are thus triple correlation functions in the frequency domain that test for coupling between a triplet of spectral components. A digital procedure for computing the bicoherence for a time series has been given by Kim and Powers (1979) and is summarized in Appendix B.

In cases where a measure of quadratic coupling between a pair of spectral components, f_i and f_j in a time series $x(t)$, and their algebraic sum, $f_i + f_j$ in another related time series $y(t)$, is desired, the cross-bispectrum and its normalized value the cross-bicoherence should be used. The cross-bispectrum is defined as

$$B_{yxx}(f_i, f_j) = \lim_{T\to\infty} \frac{1}{T} E[X^*(f_i)X^*(f_j)Y(f_i + f_j)] \tag{13}$$

and could be thought of as the next higher order to the cross-power spectrum $P_{yx}(f)$.

The auto-bispectrum possesses important symmetry properties (Kim and Power, 1979) that follow from its definition and would reduce the necessity of its computation significantly. For a real time series, $x(t)$, these properties include the following

$$\begin{aligned} B_{xxx}(f_i, f_j) &= B_{xxx}(f_j, f_i) \\ &= B^*_{xxx}(-f_i, -f_j) = B^*_{xxx}(-f_j, -f_i) \\ &= B_{xxx}(-f_i - f_j, f_j) = B_{xxx}(f_i, -f_i - f_j) \\ &= B_{xxx}(-f_i - f_j, f_i) = B_{xxx}(f_j, -f_i - f_j) \end{aligned} \tag{14}$$

where B^* denotes complex conjugate of B. Based on these properties, the regions where the bispectrum needs to be calculated are shown in Fig. 4. The upper triangle is labeled S because the (f_i, f_j) coordinates within the triangle are positive, and thus, represent sum frequency interactions. The lower triangle, D, represents difference interactions in the sense that f_i is positive and f_j is negative. Note that it is only necessary to compute the auto-bispectrum in the region S in Fig. 4. The cross-bispectrum does not possess as many symmetry properties as the auto-bispectrum and thus must be computed in both region S and D Fig. 4.

3.2 Use of the Auto-Bispectrum to Detect Nonlinear Couplings. In the transitioning stages of shear flows, the power spectra of the velocity fluctuations are characterized by the presence of well defined peaks that represent coherent (wave-like) modes. Presented in Fig. 5 is a sequence of auto-power spectra, taken from Miksad et al. (1982), of velocity fluctuations measured at three different downstream stations in the transition of a plane wake that was excited acoustically at the frequency of the most unstable mode, $f_0 = 579$ Hz and its sideband $f_1 = 615$ Hz. These locations were chosen because they represent different stages in the transitioning flow. At $x = 1.0$ cm, the spectrum shows weak instabilities at the excited modes f_o and f_1. Evidence of significant wave-wave interactions can also be seen from the enhanced energy at the difference frequency $f_\nu = f_1 - f_0$ and at the first harmonics of the excited modes. At $x = 4.0$ cm, the spectrum displays pronounced multiple sideband structures surrounding the fundamental f_o, and the harmonic frequencies, nf_o. At the same time, we note a significant increase in energy at very low frequencies ($f < 100$ Hz). By $x = 35.0$ cm, the bands have broadened considerably with the energy spreading into the sidebands.

The utility of bispectral measurements to characterize the interaction dynamics is illustrated in Fig. 6 which shows contour

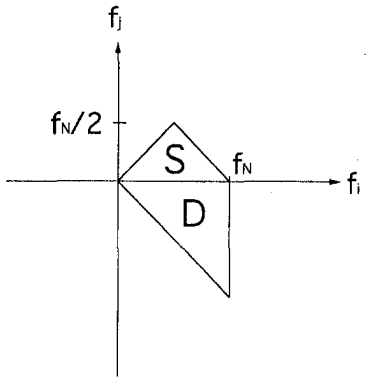

Fig. 4 Symmetry properties of the bispectrum (f_N: Nyquist frequency)

plots of the auto-bicoherence of the streamwise velocity fluctuations at $x = 1.0$, 4.0 and 35.0 cm. In viewing these plots, the reader may find it helpful to refer to the corresponding power spectra in the previous figure. At $x = 1.0$ cm, the bicoherence peaks are centered at (f_o, f_o) and at $(2f_o, f_o)$ which indicates the forcing of the first and second harmonics band, which is clearly visible in the power spectra. The other peaks at (f_o, f_ν) suggests that adjacent instability modes interact to produce low-frequency fluctuations. The high bicoherence values at $(2f_o, f_\nu)$ and $(4f_o, f_\nu)$ indicate that the sum modes are also coupled with the difference fluctuations.

The strong phase coherence of the entire harmonic band structure can be seen in the bicoherence plots at $x = 4.0$ cm. The plots show that the peaks surrounding (nf_o, mf_o) have begun to broaden and elongate and that the difference mode f_ν is now coupled with all bands. These results indicate sideband generation as a result of coupling between the low-frequency difference components and high-frequency bands. Bicoherence values at $x = 35.0$ cm show that the flow is utilizing pockets of interacting waves to complete the breakdown. These and other measurements of the auto-bicoherence in natural and controlled transition of the wake have shown important physical processes that take place in the transition to turbulence. The intriguing aspect of these results is that they provide information on the energy cascading in transitioning flows. Beyond the initial linear stage, nonlinear interactions between the unstable modes cause energy transfer to sum (harmonic bands) and difference (low-frequency) modes. These low-frequency modes play an important role throughout the rest of the transition. They interact with the unstable modes to transfer energy to the sidebands. Further downstream, they interact with a wide range of modes and play an important role in filling the spectrum. These results suggest that low-frequency modes play an important role in turbulence generation, in agreement with the conclusions of the complex demodulation studies discussed in Section 2.

3.3 Use of Auto-Bispectrum to Determine Phase Difference Between Interacting Modes. The auto-bispectrum has also been used to measure the phase difference between the fundamental and subharmonic modes in the transition of a mixing layer. Many analytical and numerical studies have shown that the growth of the subharmonic can be either amplified or depressed by varying the phase difference between the two modes. Experimentally, this has been verified by showing that the subharmonic development can be varied by exciting the fundamental and subharmonic modes with different phases. Despite the success of these experiments in showing the importance of the phase difference, they did not provide a quantitative measure of the role of the phase difference at the onset of fundamental-subharmonic interaction. The fundamental and subharmonic modes have different phase speeds in the linear stage of the transition, and thus the phase difference between them can be different from the difference imposed at the excitation source. Hajj et al. (1993) showed that the auto-bispectrum can be used to obtain local measurements of the phase difference and coupling level between the two modes as they interact.

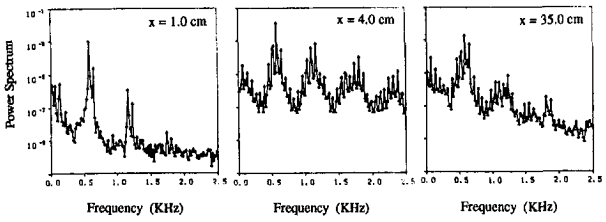

Fig. 5 Power spectra of the streamwise velocity fluctuations at $x = 1.0$, 4.0 and 35.0 cm following maximum u'_{rms} (from Miksad et al., 1982).

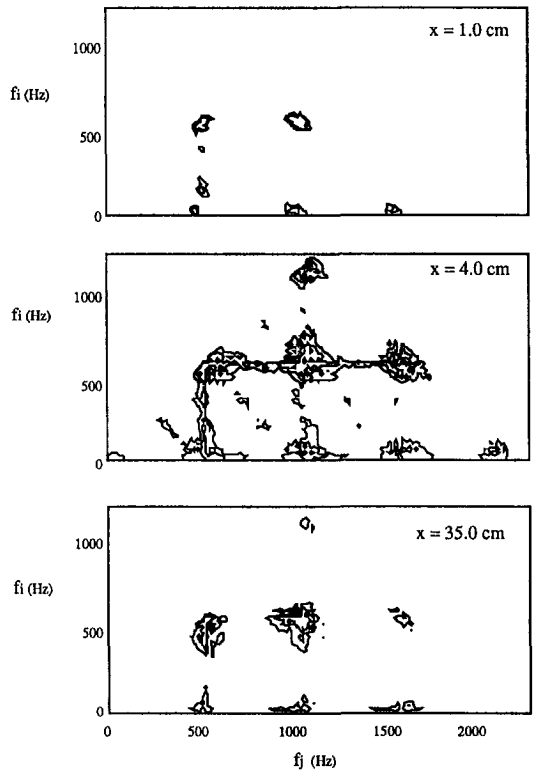

Fig. 6 Auto-bicoherence spectra of the streamwise velocity fluctuations at $x = 1.0$, 4.0 and 35.0 cm following maximum u'_{rms}. Contour levels are set at 0.3, 0.6 and 0.9

In general, because the fundamental and subharmonic modes have different frequencies, the instantaneous phase difference in a time series will vary from one instant to another. Consequently, we specify the phase difference, $\Delta\phi_o$, by setting the phase of the subharmonic to zero at $t = 0$. Hajj et al. (1993) showed that, because the frequency of the fundamental is twice that of the subharmonic, the quantity Ω defined by $\phi(f_o) - 2\phi(f_o/2)$ will at all times be equal to $\Delta\phi_o$ if the two modes are coupled. In the case where the coupling between the two modes is only partial, the quantity given by Ω in any given record will vary. This is expected as the phase difference should vary when the two modes are not coupled. Therefore, a statistical average of Ω over successively measured records can be used as a meaningful measure of the phase difference $\Delta\phi_o$. Such an average can be obtained from the phase of the auto-bispectrum of the fundamental and subharmonic modes, i.e., the phase of $E[X(f_o)X^*(f_o/2)X^*(f_o/2)]$ (based on Eq. (10)). Hajj et al. (1993) also showed that the level of confidence that can be placed in the estimate of Ω is a function of the coupling level between the two modes and thus of the auto-bicoherence. A value of auto-bicoherence near zero indicates a random phase relation between poorly-coupled modes and an irregular Ω, i.e., phase difference. A value of auto-bicoherence near one indicates that the two modes are highly coupled and that the measured Ω remains nearly constant and is equal to the phase difference $\Delta\phi_o$. Any value in between indicates a degree of partial coupling and determines the degree of variance of Ω and hence of the estimate of $\Delta\phi_o$.

Figures 7(a) and 7(b) show the downstream development of the fundamental and subharmonic modes in the transition of a mixing layer along the maximum u'_{rms} under two different excitation conditions. In each case, both modes were exited to the same level but with different phase difference. Figure 7(a) shows that the development of the fundamental is not significantly affected by the forcing conditions. In contrast, Fig. 7(b) shows that the subharmonic growth is affected by its relative

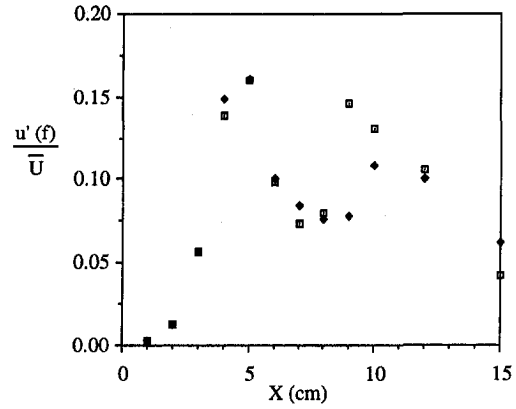

Fig. 7(*a*) Downstream variations of the normalized amplitude of the fundamental mode under two different forcing conditions

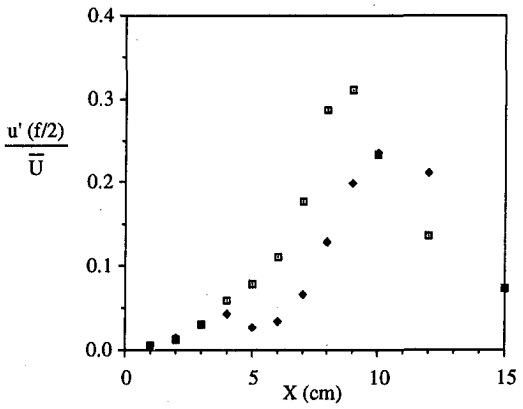

Fig. 7(*b*) Downstream variations of the normalized amplitude of the subharmonic mode under two different forcing conditions

phase with the fundamental. Both Figs. 7(*a*) and 7(*b*) show that, up to $x = 4.0$ cm, both fundamental and subharmonic components grow at rates that are close to those predicted by the linear theory (Monkewitz and Huerre, 1982). Between $x = 4.0$ and 5.0 cm, the growth of the subharmonic is different under the two forcing conditions.

As explained above, the phase and normalized magnitude of the auto-bispectrum, i.e., the auto-bicoherence, can be used to obtain an average measure of the phase difference between the two-components and its variance. Figure 8 shows the downstream variations of the measured phase difference, $\Delta\phi_o$, under the excitation forcing conditions as in Fig. 7. In the linear region, between $x = 1.0$ and 4.0 cm, the phase difference varies in each

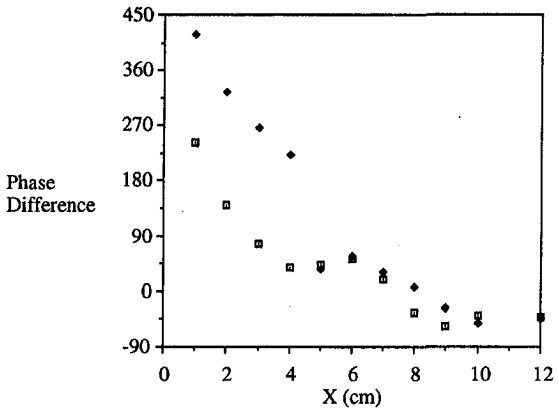

Fig. 8 Downstream variations of the phase difference between the fundamental and subharmonic modes under two different forcing conditions

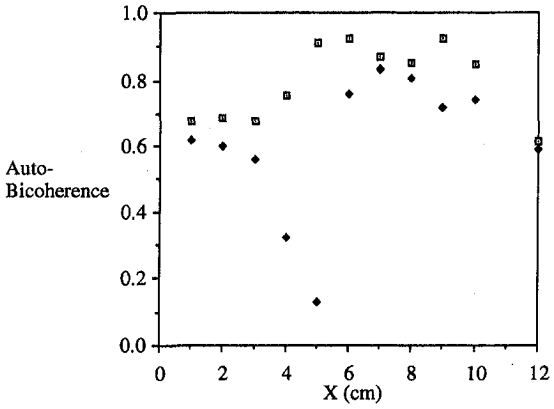

Fig. 9 Downstream variations of the auto-bicoherence (coupling level) between the fundamental and subharmonic modes under two different forcing conditions

case in the downstream direction. At $x = 5.0$ cm, the value of the phase difference starts to converge to zero in both cases. Between $x = 6.0$ and 15.0 cm, slight variations of the phase difference are complemented by measurements of the level of phase coupling which are shown in figure 9 for both forcing conditions. These measurements show that the level of phase coupling between the two modes in the linear stage of the transition vary around 0.6. Between $x = 4.0$ cm and 5.0 cm, the coupling level in one case increases. This case corresponds to the case where the subharmonic growth is enhanced, see Fig. 7(*b*). In the other case, the coupling level decreases which explains the suppression of the subharmonic mode as seen in Fig. 7(*b*). Further downstream, the coupling level in both cases is high which is related to the continuous growth of the subharmonic as seen in Fig. 7(*b*). Hajj et al. (1993) presented detailed measurements of the phase difference and its variance under different initial excitation conditions. These results showed that when the phase coupling between the fundamental and subharmonic modes is high and when the phase difference between the two modes is near zero, the subharmonic growth is enhanced.

3.4 Bispectral Analysis of Other Transitioning Flow Fields. Besides the above work on transitioning mixing layers and plane wakes, bispectral analysis has been applied to study resonant interactions in transitioning jets and boundary layers. Corke (1987) applied cross-bicoherence to study the relation between the pressure field at the tip of a jet and downstream developing instability modes. Those results demonstrated important characteristics of phase locking and resonant feedback in the instability of jets. Bispectral measurements in the transition of boundary layers (Corke, 1987) showed the importance of interactions between the initial TS waves at the fundamental frequency and the oblique subharmonic waves. The results of Corke showed also that upon its saturation, the subharmonic loses its phase coherence with the higher modes. This loss of phase coupling was accompanied by new interactions which resulted in the filling of the spectrum on both sides of the fundamental frequency component.

4 Linear and Nonlinear Modeling of Energy Cascading Mechanisms

4.1 Spectral Energy Exchange in Transitioning Flows. The transfer of energy between the spectral modes of all components of the velocity field in fluid flows occurs via the nonlinear terms $(\vec{u}\cdot\nabla)\vec{u}$ in the governing Navier-Stokes equations which are written as

$$\frac{\partial \vec{u}}{\partial t} + (\vec{u}\cdot\nabla)\vec{u} = -\rho^{-1}\nabla p + \nu\nabla^2\vec{u} \qquad (15)$$

where $\vec{u}$ is the fluid velocity vector, p is the fluid-pressure, ρ is

the density and ν is the kinematic viscosity. In order to obtain quantitative measurements of energy transfer mechanisms in fluid flows, frequency-domain analysis is required. The transformation of Eq. (15) to the Fourier domain has two basic advantages. First, the differential operators are converted into multipliers. Second, the nonlinear term, which involves the product of two velocities, give rise to the convolution of their respective transforms in the Fourier domain. These advantages lead to a relatively simple picture of the physics of linear and nonlinear energy transfer among spectral components of fluid flows. Fourier-transformed Navier-Stokes equations has been given in several forms (coordinates) for various fluid flows. The level of difficulty and technicalities of Fourier transforming these equations will depend on the assumptions that can be satisfied. Energy cascading processes in homogeneous turbulence have been described by a Fourier-transformed equation (Townsend, 1967). This equation leads to the equation for the energy spectrum. Incidently, bispectrum has been one of the main tools used to verify closure approximations of this equation, such as the direct interaction approximation (DIA) and test field model (TFM).

Unfortunately, an explicit reduction of the Navier-Stokes equations to a wave coupling equation for strongly nonparallel transitioning flows has not been given. However, developing a wave-coupling equation to study the nonlinear stages transition has been presented for several shear flows, e.g., boundary layers (Nayfeh and Bozatli, 1980), plane wakes (Jones 1983) and mixing layers (Itoh, 1977). The wave coupling equation has the following general form

$$\frac{\partial X(f_m)}{\partial x} = \Lambda_L(f_m)X(f_m) + \sum_{f_m=f_i+f_j} \Lambda_Q(f_i,f_j)X(f_i)X(f_j). \quad (16)$$

Equation (16) describes the rate of change of the complex Fourier amplitude with frequency f_m due to linear and quadratically nonlinear mechanisms. The first term on the RHS is equal to the product of the complex amplitude of the mode with frequency f_m, $X(f_m)$ and the linear coupling coefficient, $\Lambda_L(f_m)$. This product denotes the linear growth of $X(f_m)$. The real part of the linear coupling coefficient is the growth rate, $\gamma(f_m)$, and the imaginary part, $k(f_m)$, gives the dispersion relation. Because of the quadratically nonlinear terms in governing equations, pairs of frequency components can mix to contribute to sum and difference frequency components. In a transitioning or turbulent flow where the spectrum is broadband, there are many possible pairs that could affect the component with frequency f_m. The contributions of all of these modes, which satisfy the selection rule $f_i + f_j = f_m$, are represented in the second term on the RHS which gives the product of the complex amplitudes of the contributing components f_i and f_j, $X(f_i)X(f_j)$, and the quadratic coupling coefficient $\Lambda_Q(f_i, f_j)$.

The amplitude variation due to nonlinear coupling may also be expressed in terms of the power spectrum and the bispectrum. Following Ritz et al. (1989), one can derive from Eq. (16) an expression for the spatial variation of the auto-power spectrum. This equation is given by:

$$\frac{\partial P(f_m)}{\partial x} = 2\gamma(f_m)P(f_m) + \sum_{f_m=f_i+f_j} 2\,\mathrm{Re}\{\Lambda_Q(f_i,f_j)B(f_i,f_j)\} \quad (17)$$

where $P(f_m)$ is the auto-power spectrum and $B(f_i, f_j)$ is the auto-bispectrum. The first term on the right hand side represents the linear energy transfer into the wave with frequency f_m. The second term represents the power flow into the wave with frequency f_m from waves with frequencies f_i and f_j due to nonlinear interaction. In this sense it is referred to as the nonlinear energy transfer rate $T(f_i, f_j)$ and may also be written as

$$T(f_i,f_j) = |\Lambda_Q(f_i,f_j)||B(f_i,f_j)|\cos[\alpha] \quad (18)$$

where α is the phase difference between the auto-bispectrum and the coupling coefficient. The direction of energy flow is determined by the sign of $T(f_i, f_j)$ and thus depends on the sign of $\cos[\alpha]$. The characteristics of these quantities along with experimental measurements and interpretations will be given in the following sections.

4.2 Estimation of Linear and Quadratic Coupling Coefficients. As pointed out above, the energy cascading processes in transitioning and turbulent flows can be described by a wave coupling equation that describes the spectral change of the complex amplitude of a frequency component f_m due to linear and quadratically nonlinear mechanisms. The wave coupling Eq. (16) shows that this change is dependent on the frequency content of the interacting components and on the linear and quadratic coupling coefficients. The frequency content of these elements is measured from the time series. The coupling coefficients are determined by expressing the wave coupling equation as a model where the input and output are related by linear and quadratic functions. This can be achieved by transforming the wave coupling equation into an equation that relates the complex amplitude of the component with frequency f_m at a location $x + \Delta x$ linearly to the complex amplitude of f_m and quadratically to the complex amplitudes of the interacting modes f_i and f_j that algebraically add to f_m, at a location x. Such a relation is established by expressing the wave-coupling equation as

$$Y(f_m) = L(f_m)X(f_m) + \sum\sum_{f_i+f_j=f_m} Q(f_i,f_j)X(f_i)X(f_j) \quad (19)$$

where $Y(f)$ and $X(f)$ are the complex amplitude of the component with frequency f at $x + \Delta x$ and x, respectively. This input-output model is known as the second-order Volterra model. Because of its simplicity, equation 19 has been used to model many fluids-related problems such as ship dynamics (Dalzell, 1975), response of offshore structures (Choi et al., 1985) and ocean wave interactions (Hasselman, 1962).

The relationship between the wave coupling coefficients and transfer functions can be determined by introducing a finite-difference scheme into the wave-coupling equation (Ritz et al., 1989). The relation between the linear transfer function and the linear coupling coefficient is then given by

$$L(f_m) = \frac{\Lambda_L(f_m)\Delta x + 1 - i[X(f_m, x+\Delta x) - X(f_m,x)]}{e^{-i\{\phi(f_m,x+\Delta x)-\phi(f_m,x)\}}} \quad (20a)$$

where $\phi(f_m, x + \Delta x) - \phi(f_m, x)$ is the phase difference of the mode with frequency f_m over the distance Δx. The relation between the quadratic transfer function and quadratic coupling coefficient is given by

$$Q(f_i,f_j) = \frac{1}{2}\sum \frac{\Lambda_Q(f_i,f_j)\Delta x}{e^{-i\{\phi(f_m,x+\Delta x)-\phi(f_m,x)\}}} \quad (20b)$$

The remaining challenge is to estimate the linear and quadratic transfer functions of experimentally measured input and output time series data. Notice that for small Δx, $e^{-i\{\phi(f_m,x+\Delta x)-\phi(f_m,x)\}}$ approaches unity and the ratio of the quadratic transfer function to the quadratic coupling coefficient is nearly equal to Δx.

Ritz and Powers (1986) used an iterative approach to estimate the linear and quadratic transfer functions given in Eq. (19). However, their approach may not lead to a converging solution, especially when the level of the background noise is high. A more general approach was presented by Kim, Powers et al. (1988) in which the transfer functions are determined by

solving two moments equations. In this approach, the transfer function Eq. (19) is multiplied once by $X^*(f_m)$ and once by $(X^*(f_l)X^*(f_k))$ which results in the following equations.

$$E[Y(f_m)X^*(f_m)] = L(f_m)E[X(f_m)X^*(f_m)] + \sum\sum_{f_l+f_j=f_m} Q(f_l, f_j)E[X(f_l)X(f_j)X^*(f_m)] \quad (21a)$$

and

$$E[Y(f_m)X^*(f_l)X^*(f_k)] = L(f_m)E[X(f_m)X^*(f_l)X^*(f_k)] + \sum_{f_l+f_k=f_m}\sum_{f_m f_l+f_j=f_m} Q(f_l,f_j)E[X(f_l)X(f_j)X^*(f_l)X^*(f_k)] \quad (21b)$$

Note that in Eq. (21*a*), the left-hand side is the classical cross-power spectrum and is thus a measure of the linear correlation between $X(f_m)$ and $Y(f_m)$. The right-hand side includes discrete measures of the auto-power spectrum and auto-bispectrum of the input. Equation (21*b*) is one order higher than the first and the left-hand side is a measure of the quadratic correlation between the spectral components $X(f_k)X(f_l)$ and $Y(f_m)$. The right-hand side is a fourth order moment that must be evaluated in order to close the set of moment equations.

Both of the above approaches lead to a mixed linear-quadratic term in the energy equation when the input has a non-Gaussian nature. Kim, Powers et al. (1991) presented a minimum mean square error estimation technique to solve for the linear and quadratic transfer functions. This technique eliminates the contribution of the linear-quadratic interference term to the total energy transfer.

4.3 Interpretation of Linear and Quadratic Coupling Coefficients. In this section, we will show how estimating the linear and quadratic coupling coefficients enhanced our understanding of the linear and nonlinear physics of transitioning flows. Figure 10 shows the measured linear growth rates, as obtained from Eq. (16), for the instability modes in the initial region of the transition of the plane wake. The results show that spectral modes within a certain frequency range, between 500 and 620 Hz have the highest growth rates that vary around those obtained with linear stability theory. The modes with frequencies between 450 and 500 Hz and between 620 and 700 Hz have significantly lower growth rates. The other modes are damped, especially those above 700 Hz. Contour plots at three downstream locations of the quadratic coupling coefficients are

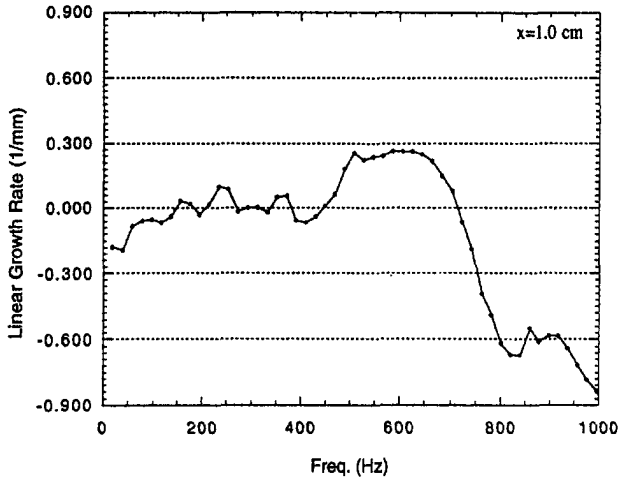

Fig. 10 Linear growth rates and dispersion relation of instability modes at x = 1.0 cm

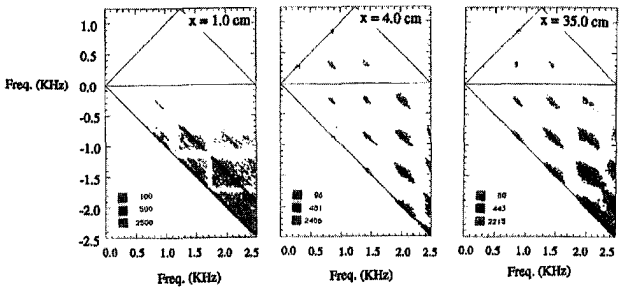

Fig. 11 Contour plots of the magnitudes of the quadratic coupling coefficients at x = 1.0, 4.0, and 35.0 cm following maximum u'_{rms}

shown in Fig. 11. This figure should be read similarly to figure 4. Note that the overall details of the magnitudes of the quadratic coupling coefficients vary in the downstream direction. Note also that when these plots are viewed in conjunction with the power spectra plots, see Fig. 5, it appears that measured values of $|\Lambda_Q(f_i, f_j)|^2$ are relatively large for pairs of interacting frequency components that have low input energy (in the valleys and at the high end of the spectrum). This can be explained by examining equation 19 which suggests that estimated values of the quadratic coupling coefficients are inversely proportional to the amplitudes of the input modes, $X(f_i)$ and $X(f_j)$. Thus, any physical interpretation of the measured values of $|\Lambda_Q(f_i, f_j)|^2$ must be viewed with caution, since these values will be high when the product $X(f_i)X(f_j)$ is small.

To eliminate this dependency, Ritz et al. (1988) extended the linear coherency idea to determine the fraction of the output power that is due to linear and nonlinear mechanisms. Specifically, they defined linear, quadratic and mixed linear-quadratic coherencies as measures of the fractions of linear, quadratic and linear-quadratic energy transfer mechanisms. The linear-quadratic coherency is an "interference" term that basically results from a nonzero auto-bispectrum in the input signal. The presence of this interference term greatly hinders the interpretation of the role of linear and nonlinear mechanisms. Depending on the relative phases of the linear and quadratic components of the model, it may result in a positive or negative contribution to the power spectrum predicted by the model. Later, Hajj et al. (1992) put forward the concept of an "interaction potential" given by the magnitude of the input interaction pair, $E|X(f_i)X(f_j)|^2$, as one way to address the amplitude dependence of the quadratic transfer function or coupling coefficient. The interaction potential is a measure of the amount of energy that two interacting modes potentially have available for nonlinear energy transfer to a third mode. Simply put, low-energy frequency modes would have less energy to transfer to a third mode than high-energy frequency modes.

While estimates of the linear and quadratic coupling coefficients and the associated quantities such as interaction potential, nondimensional transfer functions, and local coherencies have enhanced our understanding of the physics of transitioning flows, it must be stressed that none of these quantities lead to estimates of energy transfer rates or quantify the cascading processes and mechanisms. As discussed in section 3, quadratic energy transfer rates are dependent on both the amplitudes and phases of both the auto-bispectrum and coupling coefficients. Because our objective is to show how energy transfer rates can be estimated, we will not present any further measurements of transfer functions, interaction potential, nondimensional quadratic transfer functions and local coherencies. Measurements of these quantities and their interpretations have been given by Ritz et al. (1988) for the plane wake and Hajj et al. (1992) for the mixing layer.

4.4 Measurements and Analysis of Energy Transfer Rates. As discussed above, the level of energy transfer between a triad of modes is dependent on the energy content of

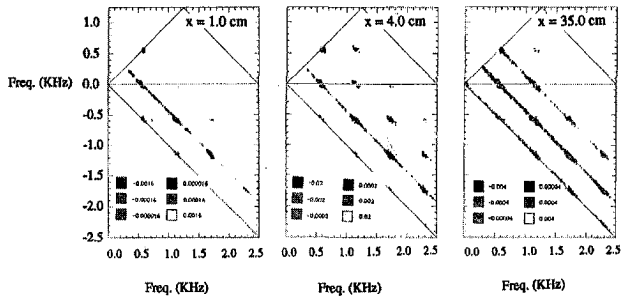

Fig. 12 Contour plots of the nonlinear energy transfer rates at x = 1.0, 4.0 and 35.0 cm following maximum u'_{rms}

these modes as well as the phase coupling between them. It is thus expected that these levels will vary in the downstream direction. Figure 12 shows contour plots of the energy transfer rates between all spectral components. All plots show three different levels of energy-transfer rates. At x = 1.0 cm, the highest energy-transfer rate is from the excited modes, f_o and f_1, to their first harmonics. Lower energy-transfer rates are measured from the excited modes into the low frequency difference mode and from the fundamental (580 Hz) and low-frequency (35 Hz) into the sideband (615 Hz). At x = 4.0 cm, the level of energy-transfer rates increased significantly. The highest level is one-order of magnitude larger than that measured at x = 1.0 cm. It is noted also that while the contours of energy transfer rates continue to show the largest values at the excited modes and their first harmonics, new contours appear between the second, third and fourth harmonics and between the low-frequency and higher harmonics modes. At x = 35.0 cm, the maximum level of energy transfer decreased. However, it can be noticed that the energy transfer rate is stressing interactions between the fundamental and all spectral components. Of particular importance is the low-frequency/high-frequency energy transfer rates. This is shown in the high contours between the peaks (excited modes and their harmonics) and the low-frequency.

The above results show that measurements of energy-transfer rates enabled us to quantify and determine the energy transfer rates mechanisms at different downstream locations. Ritz et al. (1989) tested the accuracy of the above procedure in the estimation of the quadratic energy transfer by applying the procedure to simulated numerical data in which the coupling coefficients were defined. The results showed that the modeled energy transfer differed by less than 10 percent over the entire wavenumber region. The results from the simulation experiment also showed that it is possible to compute the coefficients for the growth rate, coupling coefficients and energy transfer rates using the above procedure provided that (a) the system is stationary, (b) it can be described by a wave coupling equation and (c) a sufficient number of averages is taken to reduce the error in the estimate of the higher-order spectral moments.

5 Space/Time Statistics of Waves in Fluid Flows

While measurements of temporal Fourier components can be obtained from a time series, measurement of spatial Fourier components requires instantaneous sampling at many downstream locations. This is not practical in fluid flows since upstream probes could distort the fluctuations field measured by downstream probes. Beall et al. (1982) presented a technique for obtaining local estimates of the wavenumber-frequency spectrum, $S(k,f)$, in a stochastic medium using samples of the velocity fluctuation field measured at two closely spaced points. This technique is based on the recognition that the relation between frequency and wavenumber is stochastic. This relation is then determined by performing the following analysis. First, from either of the two signals, obtained at the two measuring

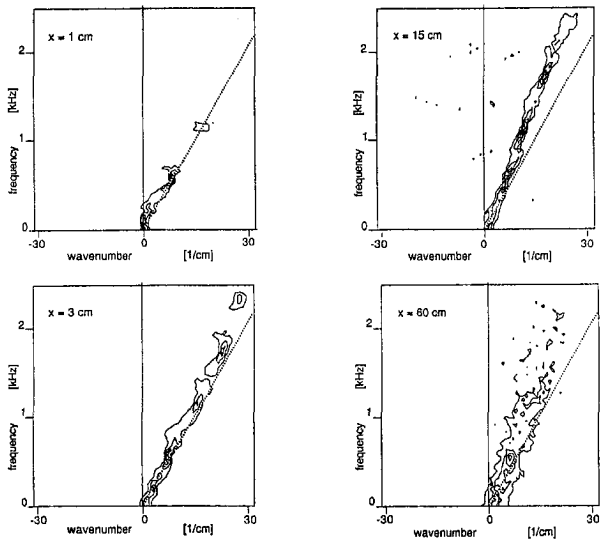

Fig. 13 Wavenumber-frequency spectra at x = 1.0, 3.0, 15.0 and 60.0 cm (from Jones et al., 1988)

points, the auto-power spectrum, $P(f_i)$, is computed, which provides a measure of the power associated with a frequency interval f_i and $f_i \Delta f$. Second, from the phase of the cross-power spectrum, $\theta(f_i)$, the local wavenumber is determined as $k_i(f_i) = \theta(f_i)/\Delta x$. Third, in the $f - k$ plane, the amount of power $P(f_i)$ is recorded at the coordinate point (f_i, k_i). Because of the stochastic nature of the velocity fluctuation field, different intervals of data will yield different estimates of the power $P(f_i)$ and wavenumber $k_i(f_i)$. These different estimates are entered at new coordinates points consisting of f_i and the new value of k_i. This process is carried out for all frequencies and is repeated for all different data intervals. The average power associated with a given frequency and local wavenumber is then defined as the local wavenumber is then defined as the local wavenumber-frequency spectrum.

Jones et al. (1988) used the above technique to measure the wavenumber spectrum and dispersion relation in a transitioning

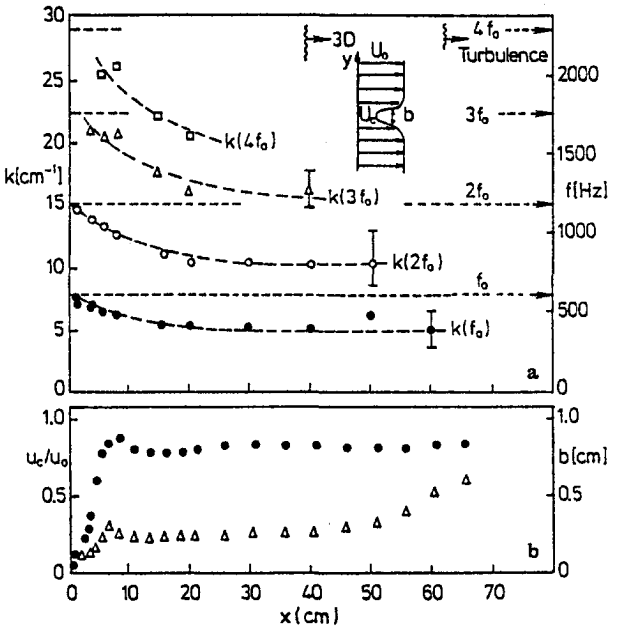

Fig. 14 Downstream variations in the wavenumber of the dominant instability and harmonic modes, in the wake centerline velocity and wake half width (from Jones et al., 1988)

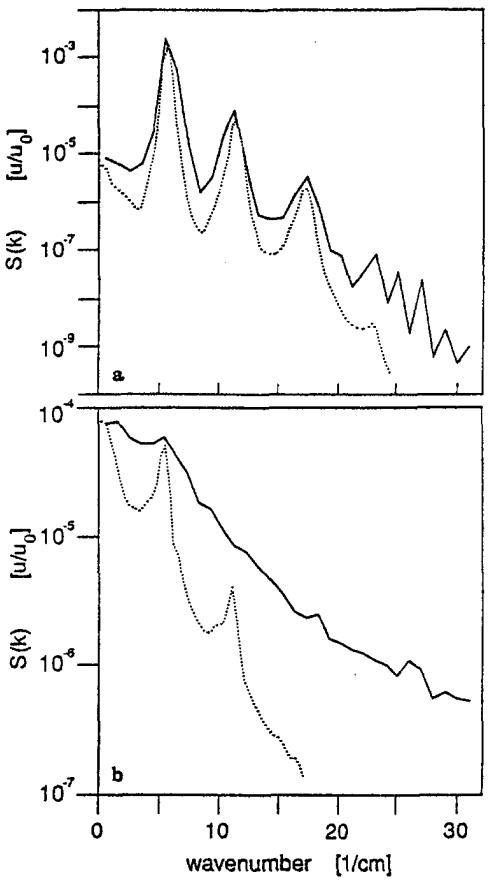

Fig. 15 Wavenumber spectra from $S(k, f)$ (solid line) and from frozen flow assumption (dotted line) at x = 15.0 and 60.0 cm (from Jones et al., 1988)

plane wake. The results are reproduced in Figs. 13, 14, and 15. Those results show several important characteristics of the transitioning flow. First, Fig. 13 shows that the fluctuations that fall between spectral peaks are not confined to a narrow range of wavenumbers. Second, Fig. 14 shows that the local wavenumbers adjust in response to the spreading of the mean flow. Third, Fig. 15 shows that while the Taylor's hypothesis (represented by the dashed line) may be an acceptable approximation in the initial stages of the transition, it breaks down at the later stages even though the spectral components could still be propagating along a linear dispersion relation. Hajj et al. (1992) used local wavenumber-frequency measurements to show that matching conditions exist between the fundamental and subharmonic modes in the region where the subharmonic gains its energy by parametric resonance.

6 Summary

In many problems involving fluid flows and fluid-structure interactions, nonlinear dynamics play an important role in energy transfer to spectral modes. Often these problems must be studied in terms of their strongly nonlinear and time-varying characteristics to complete the understanding of those dynamics. Such understanding is important for development of analytical models and for prediction and control. Higher-order statistical analysis has been shown to provide effective analysis of nonlinear dynamics that can capture couplings and quantify energy transfer among various modes. Using polyspectral analysis, one can identify the way in which modes interact and establish a measure of the energy transfer rates. In our work, polyspectral analysis allowed us to obtain quantitative measures of the space-time statistics of the nonlinear dynamics of transitioning flows. The most intriguing result of this work is the identification of the significance of the role played by low-frequency components in the transition process. This result suggests that turbulence generation and randomization process are related to the low-frequency modulations and to the nonlinear interactions between the low-frequency components and all spectral components. It seems that this mechanism is a basic feature of transition and possibly turbulent burst generation and the presence of large-scale structures. Given these results, it remains to be verified whether one could predict or control some basic features of turbulent flows. Another aspect of our work is quantifying the role of the phase relation between the fundamental and its subharmonic in affecting the subharmonic growth of the transition of mixing layer. These results can be used to quantify parameters in nonlinear systems that model transitioning flows.

It must be emphasized also that application of higher-order statistics to fluid flows has not been limited to the above work. These techniques have also been used by Solis (1987) and Hajj (1990) to study other characteristics of the transition of unsteady plane wakes and mixing layers and by Davila (1990) to examine wavenumber mismatch among interacting waves. The results of these investigations have not been discussed here. Also, it must be stressed, that we could only alude to other important applications of higher-order spectra to other fluid flows. Yet, these applications have provided important results regarding these flows. In particular, we mention the work of Corke (1987) on the use of bispectra to examine nonlinear interactions in boundary layers and jets and Herring's work (1980, 1992) on the use of bispectra to verify closure approximations for energy cascading in isotropic turbulence. The references provide a list of other important applications of higher-order statistical analysis of fluid flows and fluid-structure interactions.

References

Beall, J. M., Kim, Y. C., and Powers, E. J., 1982 "Estimation of Wave Number and Frequency Spectra Using Fixed Probe Pairs," *J. Appl. Phys.,* Vol. 53, pp. 3933–3940.

Choi, D., Miksad, R., W. and Powers, E. J., 1985 "Application of Digital Cross-Bispectral Analysis Techniques to Model the Nonlinear Response of a Moored Vessel System in Random Seas," *J. Sound and Vibration,* Vol. 99, pp. 309–326.

Corke, T. C. 1987, "Measurements of resonant phase locking in unstable axisymmetric jets and boundary layers." *Nonlinear Wave Interactions in Fluids* R. W. Miksad, T. R. Akylas and T. Herbert, eds., Winter Annual Meeting of ASME/AMD, Vol. 87, pp. 37–65.

Dalzell, J. F. 1975 "The Applicability of the Functional Input-Output Model to Ship Resistence in Waves," Report SIT-DL-75-1794, Stevens Institute of Technology.

Dalzell, J. F. 1976, "The Application of the Functional Polynomial Mode to the Ship Added Resistance Problem," *Proc. 11th Symposium on Naval Hydrodynamics.*

Davila, J. B., 1990, "Wavenumber Resonance in Nonlinear Wave Interactions in the Wake of a Flat Plate," Ph.D. dissertation, The University of Texas at Austin.

Elgar, S., and Guza, R. T., 1985, "Observations of bispectra of shoaling surface gravity waves," *J. Fluid Mechanics,* 161, pp. 425–448.

Elgar, S. Van Atta, C. W. and Gharib, M. 1990, "Cross-Bispectral Analysis of the Coupling Between a Vibrating Cylinder and its Wake in Low Reynolds Number Flow," *J. Fluids and Structures,* Vol. 4, pp. 59–71.

Hajj, M. R., 1990. An Experimental Investigation of Nonlinear Interactions Associated With the Subharmonic Growth in a Plane Mixing Layer. Ph.D. dissertation, the University of Texas at Austin.

Hajj, M. R., Miksad, R. W., and Powers, E. J., 1992, "Subharmonic Growth by Parametric Resonance," *J. Fluid Mech.* Vol. 236, pp. 385–413.

Hajj, M. R., Miksad, R. W., & Powers, E. J., 1993, "Fundamental-subharmonic interaction: effect of phase relation," *J. Fluid Mech.* Vol. 256, pp. 403–426.

Hasselmann, K., Munk, W., and MacDonald, G. 1963 "Bispectra of Ocean Waves," *Times Series Analysis,* M. Rosenblatt, ed., Wiley, New York, pp. 125–139.

Hasselman, K., 1962, "On the Nonlinear Energy Transfer in a Gravity-Wave Spectrum," Part 1, General Theory," *J. Fluid Mech.,* 12, pp. 481–500.

Haubrich, R. A., 1965, "Earth Noises, 5 to 500 Millicycles per Second," *J. Geophysical Research,* Vol. 70, pp. 1415–1427.

Herbers, T. H. C., Lowe, R. L., and Guza, R. T., 1992, "Field Observations of Orbital Velocities and Pressure in Weakly Nonlinear Surface Gravity Waves," *J. Fluid Mech.* Vol. 245, pp. 413–435.

Herring, J. R., 1980, "Theoretical Calculations on Turbulent Bispectra," *J. Fluid Mech.*, Vol. 97, pp. 205–213.

Herring, J. R., and Metais, O., 1992, "Spectral Transfer and Bispectra for Turbulence With Passive Scalars," *J. Fluid Mech*, Vol. 235, 103–122.

Hinich, M. J. & Clay, C. S., 1968, "The Application of the Discrete Fourier Transform in the Estimation of Power Spectra, Coherence, and Bispectra of Geophysical Data," *Reviews of Geophysics*, Vol. 6, pp. 347–363.

Jones, F. L., 1983, "Experimental Study of Nonlinear Wave Interactions and Modulations During Transition of a Symmetric Wake," Ph.D. dissertation, the University of Texas at Austin.

Jones, F. L., Ritz, Ch. P., Miksad, R. W., Powers, E. J., and Solis, R. S., 1988, "Measurement of the Local Wavenumber and Frequency Spectrum in a Plane Wake," *Exp. Fluids* 6, pp. 365–372.

Kim, K. I., and Powers, E. J., 1988, "A digital method of modeling quadratically nonlinear systems with a general random input," *IEEE Trans. Acoustics, Speech, Signal Processing*, Vol. 36, pp. 1758–1769.

Kim, S. B., Powers, E. J., Miksad, R. W., and Fischer, F. J., 1991, "Quantification of nonlinear energy transfer to sum and difference frequency responses of TLP's," *Proc. First Intl. Offshore and Polar Engng Conf. Edinburgh*, U.K.

Kim, Y. C., and Powers, E. J. 1979, "Digital Bispectral Analysis and Its Application to Nonlinear Wave Interactions," *IEEE Trans. Plasma Sci.*, PS-7, pp. 120–131.

Lii, K. S., Rosenblatt, M., and Van Atta, C., 1976, "Bispectral Measurements in Turbulence," *J. Fluid Mech*, Vol. 77, pp. 45–62.

Lumley, J. L., and Takeuchi, K., 1976, "Application of Central-Limit Theorems to Turbulence and Higher-Order Spectra," *J. Fluid Mech*, Vol. 74, pp. 433–468.

Miksad, R. W., Jones, F. L., Powers, E. J., Kim, Y. C., and Khadra, L. 1982, "Experiments on the Role of Amplitude and Phase Modulations During the Transition to Turbulence," *J. Fluid Mech.*, 123, pp. 1–29.

Miksad, R. W., Jones, F. L., Ritz, C. P., and Powers, E. J., 1987, "The Role of Nonlinear Wave Interactions in Laminar-Turbulent Transition," *Arch. Mech*, Vol. 39, 3, pp. 177–205.

Miles, W. H., Pezeshki, C. and Elgar, S., 1992, "Bispectral analysis of a fluid elastic system; the cantilevered pipe," *J. Fluids and Structures*, Vol. 6, pp. 633–640.

Monkewitz, P. A., and Huerre, P. 1982 "The Influence of the Velocity Ratio on the Spatial Stability of Mixing Layers," *Phys. Fluids* 25, pp. 1137–1143.

Nayfeh, A. H., and Balachandra, B., 1995, *Applied Nonlinear Dynamics*, Wiley, New York.

Nayfeh, A. H. and Bozatli, A. N., 1980, "Nonlinear Interaction of Two Waves in Boundary-Layer Flows," *Phys. Fluids*, Vol. 23(3), pp. 448–458.

Ritz, Ch. P. and Powers, E. J., 1986 "Estimation of Nonlinear Transfer Functions for Fully Developed Turbulence," *Physica* D 20D, pp. 320–334.

Ritz, Ch. P., Powers, E. J., Miksad, R. W., and Solis, R. S¿ 1988, "Nonlinear Spectral Dynamics of a Transitioning Flow," *Phys. Fluids*, Vol. 31, pp. 3577–3588.

Ritz, Ch. P., Powers, E. J., and Bengtson, R. D., 1989, "Experimental Measurement of Three-Wave Coupling and Energy Cascading," *Phys. Fluids*, Vol. B1, pp. 153–163.

Solis, R. S., 1987 "Experiments on the Effects of Mean Flow Unsteadiness on the Transition to turbulence," Ph.D. dissertation, The University of Texas at Austin.

Townsend, A. A., 1976, *The Structure of Turbulent Shear Flow*, Cambridge, U.K., Chapter 3.

Whitham, G. B., 1974, *Linear and Nonlinear Waves*, Wiley, New York.

APPENDIX A

Digital implementation of the complex demodulation analysis as explained in Section 2 consists of shifting the frequency as implied in equation 3 and applying the filter coefficients by direct convolution with the shifted time series. The basic steps in this implementation are:

- Compute the power spectrum and select a carrier wave. The power spectrum must yield well defined peaks in order to identify a carrier wave. If the spectrum yields very close peaks or broad regions, the results of complex demodulation might be misleading.
- Multiply the time series by $2 \exp(-2\pi f_o n \Delta t)$ where f_o is the frequency of the carrier wave, Δt is sampling interval and $n = 0, 1, \ldots, N-1, N$ being the number of samples. Such multiplication will cause a frequency shift.
- Convolve the low-pass filters coefficients with the shifted time series.
- Compute the amplitude and phase of the complex demoulate as given in (4).
- The amplitude modulation index, $\hat{\alpha}$, is computed as

$$\hat{\alpha} = \frac{A_{\max} - A_{\min}}{A_{\max} + A_{\min}} \tag{A1}$$

where $A_{\max}$ and $A_{\min}$ are the maximum and minimum values of the amplitude modulation. The phase modulation index, $\hat{\beta}$, is computed by equation (5*b*)

- The nonlinear frequency deviation which is caused by the phase modulation is given by

$$\delta\omega = \frac{\partial p(t)}{\partial t} \tag{A2}$$

for $p(t) = \hat{\beta} \sin(\nu t)$

$$\delta\omega = -\hat{\beta}\nu \cos \nu t$$

or

$$|\delta\omega_{\max}| = \hat{\beta}\nu \tag{A3}$$

thus the phase modulation index can also be obtained from the ratio of the frequency shift to the modulation frequency.

APPENDIX B

The auto-bispectra can be estimated directly from the Fourier transform of M segments of a signal $x(t)$. The basic steps of digital implementation are:

- Compute and subtract the mean value for each segment, m, in order to obtain zero-mean series, $x^{(m)}[n]$, where $n = 0, 1, \ldots, N$, where N is the number of samples in each segment.
- Compute the Fourier transform for each segment, $X^{(m)}[l]$ where

$$X^{(m)}[l] = \frac{1}{N} \sum_{n=0}^{N-1} x^{(m)}[n] e^{-2\pi kn/N} \tag{B1}$$

- Compute the auto-bispectrum for each segment

$$B^{(m)}[l_1, l_2] = X^{(m)}[l_1 + l_2] X^{(m)*}[l_1] X^{(m)*}[l_2] \tag{B2}$$

- Find the estimate of the auto-bispectrum by averaging over all segments M

$$\hat{B}[l_1, l_2] = \frac{1}{M} \sum_{m=1}^{M} B^{(m)}[l_1, l_2] \tag{B3}$$

- Compute the auto-bicoherence

$$b^2[l_1, l_2] = \frac{|\hat{B}[l_1, l_2]|^2}{\frac{1}{M}\sum_{m=1}^{M} |X^{(m)}[l_1 + l_2]|^2 \frac{1}{M}\sum_{m=1}^{M} |X^{(m)}[l_1] X^{(m)}[l_2]|^2} \tag{B4}$$

P. C. Stainback
Distinguished Research Associate,
NASA Langley Research Center,
Hampton, VA 23681

K. A. Nagabushana[1]
Research Associate,
Old Dominion University Research
Foundation,
Norfolk, VA 23508

Review: Hot-Wire Anemometry in Transonic and Subsonic Slip Flows

(Data Bank Contribution)*

In the past, only a relatively small number of investigations were conducted using hot-wire anemometry in transonic and subsonic slip flows. This was due to the complexity of the applicable equations. Now it appears that the developments in electronics and computational methods have made it practical to reconsider this problem. A review of past work performed in these flow regimes using hot-wire anemometry will be made along with a description of recent efforts made to develop methods which might be used to make measurements in these flow regimes. A detailed version of this review article is available through the electronic JFE.

Introduction

During the 1950's, Kovasznay (1950, 1953) and Morkovin (1956) presented theories for the application of Constant Current Anemometry (CCA) to compressible flows. For general compressible flows, where the sensitivities of a heated wire were assumed to be unequal, it was found that the mean square equation was a single equation with six unknowns. Because of the complexity of this equation, no known acceptable results were obtained. In supersonic flow it was found that the velocity and density sensitivities were equal. This resulted in a significant reduction in the complexity of the mean square equation and techniques were developed to obtain suitable measurements in supersonic flows.

Rose and McDaid (1976) conducted tests to extend the application of Constant Temperature Anemometry (CTA) to transonic flows. Under their flow conditions the velocity and density sensitivities were equal, therefore, they could use the more simple mean square equation applicable to supersonic flows.

Jones et al. (1989, 1992) considered the application of CTA to transonic flows under the condition where the velocity and density sensitivities were different. They considered the unsquared hot-wire equation which is a single equation with three unknowns. A probe having three wires was used and the instantaneous voltages from the three wires were digitized and three equations solved for instantaneous values of velocity, density and total temperature. Then statistical techniques were used to obtain results of interest.

This paper will be limited to a review of past and recently reported results obtained in transonic and subsonic slip flows. This will consider both mean flow and fluctuating results. A more complete review of hot-wire anemometry over all flow regimes is given in Stainback and Nagabushana (1993) (ASME FED-Vol. 167). An updated version of the above reference is also available through electronic JFE.

* Data have been deposited to the JFE Data Bank. To access the file for this paper, see instructions on p. 227 of this issue.

[1] Currently Engineer at Computer Science Corporation, Laurel, MD 20707; Also, Consulting Research Engineer at Advanced Engineering, Yorktown, VA 23693.

Contributed by the Fluids Engineering Division for publication in the JOURNAL OF FLUIDS ENGINEERING. Manuscript received by the Fluids Engineering Division January 3, 1996; revised manuscript received April 15, 1996. Associate Technical Editor: D. P. Telionis.

Mean Flow Results

Theoretical Considerations. The transonic and slip flow regimes will be treated together, since the theoretical and experimental results are similar. Kovasznay (1953) extended hot-wire anemometry results to compressible flows and showed that there was a significant difference between the heat transfer in compressible and incompressible flows. Several experimenters obtained heat transfer measurements at low speeds and found an apparent compressibility or Mach number effect (Baldwin, 1958; Lowell, 1950; Laurence and Landes, 1952) at Mach numbers as low as 0.1. Spangenberg (1955) conducted extensive tests over a wide range of variables and determined that the apparent compressible flow effects at Mach number as low as 0.05 was really due to gas rarefaction effects (e.g., slip flow).

In these flow regime, the heat transfer from the heated wire is generally given as:

$$Q = P = \pi l k_t (T_w - \eta T_o)\,\mathrm{Nu}_t \tag{1}$$

In transonic flow and subsonic slip flows the Nusselt number is no longer only a function of Reynolds number and Kings' law is no longer applicable. The most common functional relationship for the Nusselt number in these flow regimes is (Morkovin):

$$\mathrm{Nu}_t = f(\mathrm{M}, \mathrm{Re}_t, \theta) \tag{2}$$

since it was found that Nu_t is also a function of a temperature parameter. Another functional relationship used to analyze gas rarefaction effects is (Baldwin):

$$\mathrm{Nu}_t = f(\mathrm{M}, \mathrm{Kn}, \tau_w) \tag{3}$$

In subsonic compressible flows the recovery temperature of the wire can change and functional relationships for η are:

$$\eta = f(\mathrm{M}, \mathrm{Re}_t) \quad \text{or} \quad \eta = f(\mathrm{M}, \mathrm{Kn}) \tag{4}$$

A temperature-resistance relationship for wires is requires to compute the heat transfer rate from the heated wires. It is generally recommended that the following equation, which is a second degree equation in ΔT, be used:

$$\frac{R}{R_{\mathrm{ref}}} = 1 + \alpha_1 (T_w - T_{\mathrm{ref}}) + \beta_1 (T_w - T_{\mathrm{ref}})^2 \tag{5}$$

In general, the recovery temperature ratio is a function of

Mach and Reynolds numbers or Mach and Knudsen numbers. However, for Mach number greater than about 1.4, the recovery temperature ratio is not a function of Mach number for continuum flow. A "universal" curve presented by Vrebalovich (1962) correlated the temperature recovery ratio with Knudsen number for all Mach numbers. Using this result and the temperature recovery ratio for continuum flow and free molecular flow, curves of η versus M and Kn were calculated and presented by Stainback and Nagabushana (1993).

Examples of Data. Baldwin and Spangenberg investigated the heat transfer from wires over a wide range of Re_t, M, and T_w in the slip flow and transonic flow regimes. Spangenberg's results showed that $Nu_t = f(Re_t, M)$ for Mach numbers ranging from 0.05 to 0.90 and Reynolds numbers ranging from 1 to about 100. The effects of wire overheat on the values of Nu_t were determined. The values of Nu_t can increase or decrease with increased overheat depending on the Mach number and Knudsen number.

Results from theoretical calculations made for the effects of slip flow on heat transfer from wires were reported by Sauer and Drake (1953). The levels of the calculated Nusselt number do not agree with measured results, however, the trends seem to agree with the experimental trends.

Fluctuations

Theoretical Considerations. In compressible flows the heat transfer from a wire is described by Eq. (1). Differentiating Eq. (1) for the case where $Q = P$ gives:

$$d \log P - \frac{\theta}{\tau_w} d \log \tau_w = d \log Nu_t - \frac{\eta}{\tau_w} d \log \eta - \frac{\eta}{\tau_w} d \log T_o + d \log k_t \quad (6)$$

The terms on the right hand side of the above equation depend only on the functional forms assumed for Nu_t and η and the chosen independent variables. Ultimately these terms depend on the variation of Nu_t and η with the flow variables along with the aerodynamic and thermodynamic properties of the flow. The final form for the left-hand side of the equation depends on the type of anemometer used.

Morkovin related Nu_t and η to the nondimensional variables Re_t, M_∞, and θ whereas Baldwin used Kn, M_∞, and τ_w. However, recent results presented by Barre et al. (1992) suggested advantages from using the following variables: $E = f(m, M_\infty, T_o, T_w)$ and $E = f(p, m, T_o, T_w)$.

(a) Constant Current Anemometer (CCA). Using the heat transfer Eq. (1) and the functional relationship from equation (2) and (4), the change in voltage across a wire can be related to the changes in u, ρ, and T_o. The set of equations obtained for a constant current anemometer was given by Morkovin as:

$$\frac{e'}{E} = -S_u \frac{u'}{u} - S_\rho \frac{\rho'}{\rho} + S_{T_o} \frac{T_o'}{T_o} \quad (7)$$

where

$$S_u = \frac{E' A_w'}{\tau_{wr}} \left[\tau_{wr} \left(\frac{\partial \log Nu_t}{\partial \log Re_t} + \frac{1}{\alpha} \frac{\partial \log Nu_t}{\partial \log M} \right) - \left(\frac{1}{\alpha} \frac{\partial \log \eta}{\partial \log M} + \frac{\partial \log \eta}{\partial \log Re_t} \right) \right] \quad (8)$$

$$S_\rho = \frac{E' A_w'}{\tau_{wr}} \left[\tau_{wr} \frac{\partial \log Nu_t}{\partial \log Re_t} - \frac{\partial \log \eta}{\partial \log Re_t} \right] \quad (9)$$

Nomenclature

a_1–a_4 = constants in Eq. (16)
a = speed of sound
A_w' = overheat parameter, $\frac{1}{2}(\partial \log R_w / \partial \log I)_h$
c_p = specific heat at constant pressure
c_v = specific heat at constant volume
e' = instantaneous voltage across the wire
E = mean voltage across the wire
E' = finite-circuit parameter, $(1 - \epsilon)/(1 + 2A_w'\epsilon)$
I = current
k = thermal conductivity of air evaluated at subscript temperature
$K = \partial \log R_w / \partial \log T_w$
Kn = Knudsen number
l = characteristic length
m = mean mass flow
$m_t = \partial \log \mu_t / \partial \log T_o$
M = Mach number
$n_t = \partial \log k_t / \partial \log T_o$
Nu = Nusselt number evaluated at subscript temperature
p = mean static pressure
P = electrical power to the hot-wire
q = sensitivity ratio, S_u / S_{T_o}
Q = forced convective heat transfer
R = resistance
Re = Reynolds number based on viscosity evaluated at subscript temperature and wire diameter
R_{mT_o} = mass flow—total temperature correlation coefficient, $\overline{m'T_o'}/\tilde{m}\tilde{T}_o$
R_{uT_o} = velocity—total temperature correlation coefficient, $\overline{u'T_o'}/\tilde{u}\tilde{T}_o$
$R_{\rho T_o}$ = density—total temperature correlation coefficient, $\overline{\rho'T_o'}/\tilde{\rho}\tilde{T}_o$
$R_{u\rho}$ = velocity—density correlation coefficient, $\overline{u'\rho'}/\tilde{u}\tilde{\rho}$
s = sensitivity ratio, S_ρ / S_{T_o}
S = sensitivity of hot-wire to the subscript variable
T = temperature
u = velocity in the flow direction
$\alpha = (1 + \gamma - 1/2\, M^2)^{-1}$
α_1 = linear temperature—resistance coefficient of wire
β_1 = second degree temperature—resistance coefficient of wire
ϵ = finite circuit factor, $-(\partial \log I_w / \partial \log R_w)_s$
η = recovery temperature ratio, T_{adw}/T_o
θ = temperature parameter, T_w/T_o
θ_1 = angle between plane sound wave and axis of probe
μ = absolute viscosity
γ = specific heat ratio, c_p/c_v
ρ = density
τ_w = temperature loading parameter, $(T_w - T_{adw})/T_o$
τ_{wr} = temperature parameter, $(T_w - T_{adw})/T_{adw}$
ϕ' = normalized fluctuation voltage ratio, $(e'/E)/S_{T_o}$

Subscript

adw = adiabatic wall condition
h = M and Re_t are constant as Q varied
o = total condition
ref = reference condition
s = electrical system untouched as M and Re_t varied
so = sound source
t = evaluated at total temperature
w = wire condition
∞ = free stream or static condition

Superscript

$'$ = instantaneous
$\tilde{}$ = RMS
$\bar{}$ = mean

$$S_{T_o} = \frac{E' A'_w}{\tau_{wr}} \left[k_t \tau_{wr}(1 + A'_w) + A'_w \tau_{wr} \left(-1 - n_t + m_t \frac{\partial \log \mathrm{Nu}_t}{\partial \log \mathrm{Re}_t} + \frac{1}{2\alpha} \frac{\partial \log \mathrm{Nu}_t}{\partial \log \mathrm{M}} \right) - A'_w \left(\frac{1}{2\alpha} \frac{\partial \log \eta}{\partial \log \mathrm{M}} + m_t \frac{\partial \log \eta}{\partial \log \mathrm{Re}_t} \right) \right] \quad (10)$$

For a large range of Reynolds numbers and Mach numbers, S_u and S_ρ in Eq. (7) are unequal (Baldwin). Following Kovasznay's technique for supersonic flow, dividing Eq. (7) by S_{T_o}, squaring and forming the mean gives:

$$\overline{\phi'^2} = q^2 \overline{\left(\frac{u'}{u}\right)^2} + s^2 \overline{\left(\frac{\rho'}{\rho}\right)^2} + \overline{\left(\frac{T'_o}{T_o}\right)^2} + 2qsR_{u\rho} \frac{\tilde{u}\tilde{\rho}}{u\rho} - 2qR_{uT_o} \frac{\tilde{u}\tilde{T}_o}{uT_o} - 2sR_{\rho T_o} \frac{\tilde{\rho}\tilde{T}_o}{\rho T_o} \quad (11)$$

This is a general equation for a wire mounted normal to the flow in compressible flows where $S_u \neq S_\rho$.

(b) Constant Temperature Anemometer (CTA). The hot-wire equation for a CTA that corresponds to Eq. (7) for a CCA is:

$$\frac{e'}{E} = S_u \frac{u'}{u} + S_\rho \frac{\rho'}{\rho} + S_{T_o} \frac{T'_o}{T_o} \quad (12)$$

where

$$S_\rho = \frac{1}{2} \left[\frac{\partial \log \mathrm{Nu}_t}{\partial \log \mathrm{Re}_t} - \frac{1}{\tau_{wr}} \frac{\partial \log \eta}{\partial \log \mathrm{Re}_t} \right] \quad (13)$$

$$S_u = S_\rho + \frac{1}{2\alpha} \left[\frac{\partial \log \mathrm{Nu}_t}{\partial \log \mathrm{M}} - \frac{1}{\tau_{wr}} \frac{\partial \log \eta}{\partial \log \mathrm{M}} \right] \quad (14)$$

$$S_{T_o} = \frac{K}{2A'_w} + \frac{1}{2}(K - 1 - n_t) + m_t S_\rho + \frac{1}{2}(S_u - S_\rho) \quad (15)$$

and for $S_u \neq S_\rho$ is a single equation with three unknowns. Hinze (1975) indicated that a CTA cannot be used to obtain fluctuations using the mode diagram technique since the frequency response of the anemometer approaches the frequency response of the wire at low overheats. Because of these problems, it was suggested that a three wire probe be used and the voltage from the anemometer digitized at a suitable rate (Stainback and Johnson, 1983). Then three equations are obtained that can be solved for u', ρ', T'_o as a function of time. Statistical techniques can then be used to obtain statistical quantities of interest.

To insure that the solution to the three equations are sufficiently accurate, the three wires are operated at different and high overheats to make S_u and S_ρ as different as possible. This will insure that the condition number for the solution matrix is reasonably low. A complete description of this technique is given by Jones et al. (1989) and Stainback and Johnson.

The functional relationship for the voltage across a wire for subsonic slip flows is identical to the functional relationship for transonic flow. Therefore, the three wire probe technique under development for transonic flows should be applicable for both regimes. Since slip flows are identified by the Knudsen number, the possibility of obtaining useful measurements using a three wire probe might be improved by using different diameter wires in addition to using different overheats.

Examples of Data

(a) Freestream. Mean flow measurements were made in the transonic and slip flow regime in the 1950's (Baldwin; Spangenberg). It was only during the 1970's and 1980's that attempts were made to measure (Otten et al., 1981; Rose and McDaid; Stainback and Johnson, 1983; Jones et al., 1989; Horstman and Rose, 1977) fluctuations in these regimes because of the complexity of the response of the heated wire to velocity, density and total temperature.

In order to evaluate the effect of freestream fluctuations on boundary layer transition, hot-wire measurements were made in the Langley Research Center 8′ Transonic Pressure Tunnel during the Laminar Flow Control experiments (Jones et al., 1989). For these flow conditions $S_u \neq S_\rho$ with $S_\rho > S_u$. Because of this situation a three wire probe was used with CTA to measure $\tilde{u}/u$, $\tilde{\rho}/\rho$, $\tilde{T}_o/T_o$ and $\tilde{m}/m$.

(b) Boundary Layer. Horstman and Rose made measurements at transonic speeds where, for their flow condition, it was found that $S_u \approx S_\rho$. For this condition, the transonic hot-wire problem degenerated to the supersonic flow problem where only $\tilde{m}/m$, $\tilde{T}_o/T_o$ and R_{mT_o} could be measured. From their measurement of $\tilde{m}/m$, the velocity and density fluctuations were computed by assuming that $\tilde{T}_o/T_o$ and $\tilde{\rho}/p$ were zero. Horstman and Rose's hot-wire results agreed well with the thin film results obtained by Mikulla.

Barre et al. (1992) conducted hot-wire tests in a supersonic boundary layer where transonic effects were accounted for by using a transformation of Eqs. (7)–(10) from u, ρ, T_o to p, m, T_o. Using the assumption that $E = f(p, m, T_o)$ and $\tilde{p}/p \approx 0$, reduced their equation to $E = f(m, T_o)$. Under these condition the fluctuation diagram developed by Kovasznay was used to obtain $\tilde{m}/m$, $\tilde{T}_o/T_o$, and R_{mT_o} without the assumption that $S_u = S_\rho$. Their results show that the quantity $\sqrt{\rho u'^2/\tau_w}$ is greatly underestimated if the assumption is made that $S_u = S_\rho$ when the velocity in the boundary is transonic and $S_u \neq S_\rho$. The expected value for R_{uT_o} in the boundary layer is -0.85 and the data obtained for $S_u \neq S_\rho$ agree well with this value. However, data evaluated where S_u were assumed to be equal to S_ρ were substantially higher at the lower transonic Mach numbers.

(c) Flight in Atmosphere. Any attempts to extrapolate the effect of wind tunnel disturbances on laminar boundary layer transition to flight conditions requires some knowledge of the disturbance levels in the atmosphere. There is a limited amount of data obtained in the atmosphere using hot-wire anemometry on flight vehicles (Otten et al., 1981; MacCready, 1953). Otten et al., expanded the methods devised by Rose and McDaid by using a two-wire probe. One wire was operated by a CCA at a low overheat to measure $\tilde{T}_o$. The other wire was operated with a CTA that was sensitive to $\tilde{m}$ and $\tilde{T}_o$. The results from these two wires were used to measure $\tilde{m}$ and $\tilde{T}_o$ in the atmosphere. Spectral data obtained in the atmosphere revealed the expected $-\frac{5}{3}$ slope, for $\tilde{m}$ and $\tilde{T}_o$.

(d) Subsonic Slip Flow. For this regime $Nu_t = f(M_\infty, Re_t, \tau_w)$ and $S_u \neq S_\rho$. These results are identical to those in the transonic flow regime and attempts have been made to apply the three wire technique developed for transonic flows to sub-

sonic slip flows (Stainback and Nagabushana, 1991). For tests in subsonic slip flows, the three wires were of different diameters in addition to being operated at different overheats. Some very preliminary data obtained using this technique in the Langley LTPT tunnel indicated higher values for $\tilde{u}/u$ and $\tilde{\rho}/\rho$ than the values for $\tilde{m}/m$ obtained using King's equation.

CCA in Transonic Flow

Now reconsider the CCA in transonic and subsonic slip flow. Equation (11) is a single equation with six unknowns. In principle, this equation can be solved by operating a single wire at six overheats and solving six equations to obtain the three fluctuating quantities and their correlations. In the past, it was generally stated that the calibration of the wire cannot be made sufficiently accurate or the velocity and density sensitivities cannot be made sufficiently different to obtain a suitable solution using this technique. Demetriades (1978) noted that the coefficient in Eq. (11) must occur to at least the fifth degree polynomial. This constraint, however, appears to be too restrictive. Since s and q are function of the overheat of the wire, it can be assumed that s is a function of q as follows:

$$s = a_1 + a_2 q^{b_1} + a_3 q^{b_2} + a_4 q^{b_3} \tag{16}$$

It can be shown that b_1, b_2, and b_3 can have any value provided that the variation of s with q is properly described and the substitution of the relationship for s into Eq. (11) results in an equation having six terms. An analysis of data obtained at transonic Mach number by Spangenberg indicates that s can be non-linearly related to q and suggest that a solution to Eq. (11) is possible. However, the use of Spangenberg's data indicated that the 6×6 sensitivity matrix obtained using the least square technique applied to Eq. (11) was very ill conditioned and the condition numbers ranging from 10^6 to 10^7. This indicated that almost perfect data would be required to obtain suitable fluctuation and their correlations. A more detailed discussion of this is given by Stainback and Nagabushana (1995).

The mean square equation is the general equation for an elliptic hyperboloid, a surface which is not symmetric with respect to the $\tilde{\phi}$-axis. The very high condition number noted above indicated that there is a very high probability that data from a hot-wire, which exist in a "single quadrant", cannot adequately define the hyperboloid. Can the geometry of the problem be used to obtain more accurate solution to Eq. (11)? In reference Stainback and Nagabushana (1993), it was suggested that the elliptic hyperboloid can be transformed into a hyperboloid of revolution, symmetric with respect to the vertical axis $\bar{\phi}$ using the fluctuations and their correlation obtained from the original hot-wire data. Then the transformed values for q and s on the hyperboloid of revolution can be rotated around the surface to obtain additional points. These additional points can be inversely transformed back into the original coordinate system to give additional values for q and s to better define the elliptic hyperboloid which is required to obtain better values for the fluctuations and their correlations. This method, however, requires a trial and error solution.

If solutions to Eq. (11) are possible, what is the form of the fluctuation diagram? In Eq. (11), $\tilde{\phi}$ is a function of q and s, therefore, the fluctuation diagram exists on a three-dimensional surface, a hyperboloid, rather than a plane as for the case when $S_u = S_\rho$. The locus of points on the surface of the hyperboloid will depend on the relative changes in q and s as the overheat of the wire is changed. However, the important information, fluctuation quantities, are indicated in the $\tilde{\phi}$–q and $\tilde{\phi}$–s planes. For example when $s = 0$, Eq. (11) reduces to an equation for a hyperbola in the $\tilde{\phi} - q$ plane, where the asymptote gives the velocity fluctuations. If $q = 0$, Eq. (11) reduces to an equation for a hyperbola in the $\tilde{\phi} - s$ plane and the asymptote represents the density fluctuations. When q and s both are zero, the intercept on the $\tilde{\phi}$ axis gives the total temperature fluctuation.

Although the fluctuation diagram exists on the surface of a hyperboloid, the fluctuations can be determined from the intersection of the hyperboloid with the $\tilde{\phi} - q$ and $\tilde{\phi} - s$ planes. Because of this, the fluctuation and mode diagrams were defined as the traces of these intersections in the noted planes (Stainback, et al., 1992; Stainback and Nagabushana, 1991).

Even though there is much evidence that $S_u \neq S_\rho$ over a large range of Re_t and M_∞ in subsonic compressible flow, some experimenters have conducted tests (Zinov'ev and Lebiga, 1988; Lebiga and Zinov'ev, 1989, 1991) under the condition where $S_u = S_\rho$. When $S_u = S_\rho$ for subsonic compressible flow, the fluctuation and mode diagram technique developed by Kovasznay can be used to obtain the mass flow and total temperature fluctuations. The general fluctuation diagram is identical to the one for supersonic flow, namely, a hyperbola. Also, the mode diagrams for entropy and vorticity modes are identical. The sound mode is, however, different. For supersonic flow the angle that plane sound waves makes with respect to the axis of a probe can have only two values. If the sound source is fixed then $\cos\theta_1 = -1/M$. If the sound source has a finite velocity then $\cos\theta_1 = -1/((u/a) - (u_{so}/a))$. However, for subsonic flows the values of θ_1 can range from 0° to 360°.

Contribution to the Electronic JFE

The present paper is the shortened version of a conference paper. It was presented as an invited paper at Third International Symposium on Thermal Anemometry in Washington DC, conducted by ASME Fluids Engineering Division Summer Meeting (FED-Vol. 167, pp. 93–134). An updated version of this paper is available through the Electronic Journal of Fluids Engineering. It consists of 230 references and 68 figures which represents data obtained using hot-wire anemometry over the various flow regimes and many different types of flow fields, including both the mean and fluctuating flow measurements. Comments are made concerning the constant current and constant temperature anemometers generally in use and the recently developed constant voltage anemometer. Examples of hot-wire data obtained to substantiate theoretical results are presented. Some results are presented to compare hot-wire data with results obtained using other techniques. However, the review was limited to wires mounted normal to the flow in nonmixing gases.

Concluding Remarks

A review of hot-wire anemometry was made for the transonic and subsonic slip flow regimes. From this study the following concluding remarks can be made:

The review of the mean flow data revealed that the Nusselt number was a function of Mach and Reynolds numbers or Mach and Knudsen numbers for much of the data. This resulted in the mean voltage measured across the heated wire being a function of velocity, density and total temperature.

Measurements of fluctuations were presented for the cases where the wire was sensitive to mass flow and total temperature or velocity, density and total temperature. These latter measurements were made using CTA and multi-wire probes.

A method was described which might be used to obtain fluctuating measurements in transonic flows using the mean square equation for the CCA.

References

Barre, S., Quine, C., and Dussauge, J. P., 1992, "Compressibility Effects on the Structure of Supersonic Mixing Layers: Experimental Results," Institut de Mécanique de Marseilles, Institut de Mécanique Statistique de la Turbulence, U.M. CNRS-Université Aix-Marseille II n° 380033, 12 avenue du Général Leclerc, 13003, Marseilles, France.

Baldwin, L. V., 1958, "Slip-Flow Heat Transfer From Cylinders in Subsonic Airstreams," NACA-TN-4369.

Demetriades, A., 1978, "Probes for Multivariant Flow Characteristics," *Proceedings of the Dynamic Flow Conference on Dynamic Measurements in Unsteady Flows,* IMST, Marseille, France, pp. 13–44.

Hinze, J. O., 1975, *Turbulence,* McGraw-Hill, New York.

Horstman, C. C., and Rose, W. C., 1977, "Hot-Wire Anemometry in Transonic Flow," *AIAA Journal,* Vol. 15, No. 3, pp. 395–401.

Jones, G. S., Stainback, P. C., Harris, C. D., Brooks, C. W., and Clukey, S. J., 1989, "Flow Quality Measurements for the Langley 8-Foot Transonic Pressure Tunnel LFC Experiment," AIAA-89-0150.

Jones, G. S., Stainback, P. C., and Nagabushana, K. A., 1992, "A Comparison of Calibration Techniques for Hot-Wires Operated in Transonic Slip Flows," AIAA-92-4007.

Kovasznay, L. S. G., 1950, "The Hot-Wire Anemometer in Supersonic Flows," *Journal of the Aeronautical Sciences,* Vol. 17, No. 9, pp. 565–584.

Kovasznay, L. S. G., 1953, "Turbulence in Supersonic Flow," *Journal of the Aeronautical Sciences,* Vol. 20, No. 10, pp. 657–674.

Laurence, J. C., and Landes, L. G., 1952, "Auxiliary Equipment and Techniques for Adapting the Constant-Temperature Hot-Wire Anemometer to Specific Problems in Air-Flow Measurements," NACA-TN-2843.

Lebiga, V. A., and Zinoviev, V. N., 1989, "Hot-Wire Measurements in Compressible Flow," ICIASF'89 Record, IEEE-89CH2762-3., The 13th International Congress on Instrumentation in Aerospace Simulation Facilities, DFVLR Research Center Göttingen.

Lebiga, V. A., and Zinovyev, V. N., 1991, "Acoustic Measurements with a Hot-Wire Anemometer at High Subsonic Velocities," Dantec Information No. 10, 14–16.

Lowell, H. H., 1950, "Design and Application of Hot-Wire Anemometers for Steady-State Measurements at Transonic and Supersonic Airspeeds," NACA-TN-2117.

MacCready, P. B., 1953, "Atmospheric Turbulence Measurements," *Journal of Meteor,* Vol. 10, No. 5, pp. 325–337.

Morkovin, M. V., 1956, "Fluctuations and Hot-Wire Anemometry in Compressible Flows," AGARDograph 24.

Otten, L. J., Pavel, A. L., Finley, W. E., and Rose, W. C., 1981, "A Survey of Recent Atmospheric Turbulence Measurements from a Subsonic Aircraft," AIAA-81-0298.

Rose, W. C., and McDaid, E. P., 1976, "Turbulence Measurement in Transonic Flow," *Proceedings of the AIAA 9th Aerodynamic Testing Conference,* Arlington, Texas.

Sauer, F. M., and Drake, Jr., R. M., 1953, "Forced Convection Heat Transfer from Horizontal Cylinders in a Rarefied Gas," *Journal of the Aeronautical Sciences,* Vol. 20, pp. 175–180, 209.

Spangenberg, W. G., 1955, "Heat Loss Characteristics of Hot-Wire Anemometers at Various Densities in Transonic and Supersonic Flows," NACA-TN-3381.

Stainback, P. C., and Johnson, C. B., 1983, "Preliminary Measurements of Velocity, Density and Total Temperature Fluctuations in Compressible Subsonic Flow," AIAA-83-0384.

Stainback, P. C., and Nagabushana, K. A., 1991, "Fluctuation Diagrams for Hot Wire Anemometry in Subsonic Compressible Flows," NASA-CR-189580.

Stainback, P. C., and Nagabushana, K. A., 1993, "*Invited Paper:* Review of Hot-wire Anemometry and the Range of their Applicability," FED-Vol. 167, pp. 93–134, *Third International Symposium on Thermal Anemometry,* ASME Fluids Engineering Division Summer Meeting, Washington, DC.

Stainback, P. C., and Nagabushana, K. A., 1995, "Reinvestigation of Hot-Wire Anemometry Applicable to Subsonic Compressible Flows Using Fluctuation Diagrams," ASME JOURNAL OF FLUIDS ENGINEERING, Vol. 117, pp. 263–269.

Stainback, P. C., Nagabushana, K. A., and Bushnell, D. M., 1992, "Mode Diagrams for Hot Wire Anemometry in Subsonic Flows," International Conference on Methods of Aerophysical Research, organized by Institute of Theoretical and Applied Mechanics (ITAM) of the Siberian Division of the Russian Academy of Sciences, Novosibirsk, RUSSIA.

Vrebalovich, T., 1962, "Heat Loss From Hot-Wires in Transonic Flow," Research Summary No. 36-14, Jet Propulsion Lab., Pasadena, California.

Zinov'ev, V. N., and Lebiga, V. A., 1988, *Measurements of Fluctuations For High Subsonic Velocities Using a Hot-Wire Anemometer,* Plenum Publishing Corp. Novosibirsk, Translated from Zhurnal Prikladoni Mekhanikii Teckhnicheskoi Fiziki, No. 3, pp. 80–84.

Turbulent Near Wake Behind a Partially Grooved Circular Cylinder

K. W. Lo
Graduate Student.

N. W. M. Ko
Professor.
Mem. ASME

Department of Mechanical Engineering,
The University of Hong Kong,
Hong Kong

The near wake of a partially V-grooved circular cylinder is investigated. The flow over the smooth half is within the high subcritical regime, while that over the grooved half is within the transcritical regime. Secondary and Strouhal vortices are found in the near wakes of both halves. The formation of the secondary vortices, due to the separated shear layers, is coupled to the formation of the Strouhal vortices. These secondary vortices of the two halves are of the horse shoe type. On the grooved half, another type of secondary vortices is found to be caused by the flow over the triangular blunt end of the V grooves.

Introduction

The near wake of smooth circular cylinder had been investigated extensively, for example, Roshko (1954), Hama (1957), Bloor (1964), Gerrard (1978), Cantwell and Coles (1983), Wei and Smith (1986), Kourta et al. (1987), Hayakawa and Hussain (1989), and Bays-Muchmore and Ahmed (1993). Based on flow visualization and hot wire measurements, the transition from laminar regime and development of turbulence in the near wake of the cylinder within the subcritical regime of smooth cylinder ($Re_d < 6 \times 10^4$) were studied. Further, Kourta et al. (1987) established two Reynolds number flow regimes of $2 \times 10^3 < Re_d \leq 1.6 \times 10^4$ and $1.6 \times 10^4 \leq Re_d < 6 \times 10^4$. In the former regime, laminar wake was identified and transition to turbulence occurred downstream of the cylinder. Within the laminar and transitional wakes there are small scale structures, transition waves or secondary or streamwise vortices, within the two shear layers, in addition to the Karman or Strouhal vortices formed further downstream (Bloor, 1964; Wei and Smith, 1986; Kourta et al., 1987; and Bays-Muchmore and Ahmed, 1993). For the streamwise vortices, two types were found: those formed between successive Kelvin-Helmholtz vortices in the separated shear layers just upstream of the Karman vortex formation region and those formed in the braid region between successive Karman vortices (Bays-Muchmore and Ahmed, 1993). At $Re_d \approx 1 \times 10^3$, Bloor (1964) found that the Kelvin-Helmholtz vortices first appeared in the separated shear layers. With increasing Reynolds number, their streamwise spacing decreases and streamwise vortices appear between them (Bloor, 1964 and Wei and Smith, 1986). The frequency ratio of the secondary vortices to Karman vortices is a function of Reynolds number and was demonstrated by Wei and Smith (1986) to have a 0.87 power-law relationship. Streamwise vortices or ribs located in the braid region between successive Karman vortices in the intermediate region are in pairs or loops (Hama, 1957; Gerrard, 1978; Cantwell and Coles, 1983; Hayakawa and Hussain, 1989; Wu et al., 1994a and Wu et al., 1994b). Three-dimensionality in the spanwise direction plays an important role in the interaction between the small scale secondary vortices or ribs with the large scale Karman vortices or rolls, resulting in the distortion of the latter (Hayakawa and Hussain, 1989). Williamson (1988) demonstrated that there were two stages in the transition to three-dimensionality in the wake. From the flow visualization, Williamson (1988) observed that for $178 < Re_d < 260$, the primary rolled up and deformed into the vortex loop. The spanwise wavelength was roughly three diameters of the cylinder. For $Re_d > 260$, finer scale streamwise vortices were formed. The primary vortices were also deformed but with the spanwise wavelength of approximately one diameter. Williamson (1988) also concluded that in the separated wake, the streamwise vorticity originated mainly from the deformation of the primary vortices.

In high Reynolds number regime of $1.6 \times 10^4 < Re_d < 6 \times 10^4$, the large scale Karman vortices are formed directly at the back of the cylinder and the small scale secondary vortices merge into the former and are carried downstream (Kourta et al., 1987). At $Re_d = 2.1 \times 10^4$, pairs of counter-rotating streamwise vortices interact and distort the Karman vortices only on their upstream-facing sides (Bay-Muchmore and Ahmed, 1993). Also, in this flow regime, the frequency ranges are disconnected and no strong interaction between the two different scaled vortices occurs (Kourta et al., 1987). This is different from the strong interaction between them within the lower Reynolds number regime, in which the frequencies are of the same order.

In the investigation of flow over a partially grooved circular cylinder of Leung et al. (1992), one surface was partially grooved with groove subtend angle $\theta_g = +75$ deg and the other surface smooth ($\theta_g = -0$ deg). The Reynolds number was 9.4×10^4, within the subcritical flow regime of smooth cylinder. Because of different surface configurations, the flow over the smooth half was basically within the subcritical regime and separated at 75 deg $< |\theta| <$ 90 deg. The flow over the grooved half, because of the junction of the groove and smooth surfaces at $\theta = +75$ deg, was perturbed from laminar, became turbulent at $\theta = +90$ deg and separated at $\theta = +112.5$ deg. Based also on the boundary layer measurements, these differences in the flow characteristics resulted in asymmetric mean and fluctuating velocity profiles of the near wake. However, the effect of these two different boundary layers on the generation of the secondary vortices within the near wake was not studied.

Owing to the lack of information on the near wake behind circular cylinder at $Re_d > 6 \times 10^4$, the present investigation was initiated. The purpose of the present study was to understand the flow characteristics of the near wakes, with respect to the presence of the small scale or other vortices and of the large scale Strouhal vortices within the turbulent wake regime of $Re_d = 1.26 \times 10^5$. The use of the term "Strouhal" for the large-scale vortices (Wei and Smith, 1986) was adopted for the turbulent wake of the present case. Because of the presence of the grooves, the flow over the grooved half behaves as at higher Reynolds number, within the transcritical regime of smooth cylinder in which the drag coefficient is nearly constant

Contributed by the Fluids Engineering Division for publication in the JOURNAL OF FLUIDS ENGINEERING. Manuscript received by the Fluids Engineering Division October 22, 1995; revised manuscript received April 2, 1996. Associate Technical Editor: M. Gharib.

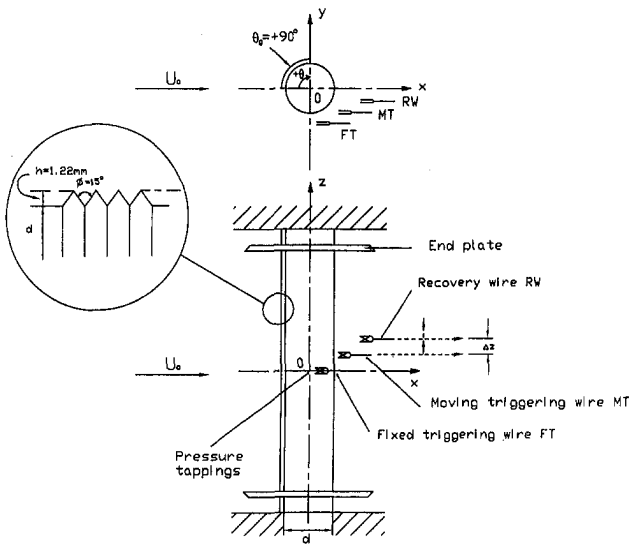

Fig. 1 Experimental setup

(Schewe, 1983 and Niemann and Hölscler, 1990), while that over the smooth half is within the subcritical regime (Lo and Ko, 1995).

Apparatus and Measurement Technique

The experiments were carried out in a wind tunnel with a test section measuring 56 cm × 56 cm. The freestream turbulence intensity was about 0.4 percent at the freestream mean velocity U_o of 22 m/s. The diameter of the cylinder, d, was 88.5 mm. The blockage ratio for the cylinder was 16 percent. End plates were used to eliminate the effect of the tunnel boundary layers. The aspect ratio l/d for the cylinder was 4.3. The present aspect ratio, blockage ratio and local turbulence intensity were within the ranges of past workers (Achenbach, 1968 and Guven et al., 1980).

The surface configurations studied are shown in Fig. 1. V-groove of height of 1.22 mm and angle ϕ of 15 deg, giving h/d of 13.8×10^{-3}, was adopted. The adoption of this V-groove configuration was due to its near lowest drag coefficient (Leung and Ko, 1991) and the shift to lower Reynolds number such that flow characteristics in higher flow regime could be studied. The subtend angle of the grooves from the front stagnation point $\theta_g = {}^{+90°}_{-0°}$, that is, grooves only from 0 to +90 deg but smooth on the rest of the cylinder. The diameter of the bottom of the grooves was the same as that of the smooth portion. Because of the small dimensions involved, it was difficult to obtain identical configurations of the V-grooves across the span of the cylinder. The dimensions were the average results of a few samples of the V-grooves. The adoption of $\theta_g = {}^{+90°}_{-0°}$ was based on the findings of Leung et al. (1992) that for $\theta_g = {}^{+75°}_{-0°}$, because of the effect of the discontinuity at $\theta_g = +75$ deg on the flow and its subsequent separation at $\theta \approx 90$ deg, this effect was minimized by extending the grooves to +90 deg.

The Reynolds number Re_d, based on the cylinder diameter, was 1.26×10^5 and was within the subcritical regime of smooth cylinder. As had been discussed above, the present Reynolds number was beyond the laminar wake regime and the wake was turbulent. The large scale Strouhal vortices were formed directly at the back of the cylinder. At this Reynolds number, Lo and Ko (1995) has found that the mean static pressure coefficients C_p indicate some differences in the mean pressure on the two halves of the cylinder but not as large as those of lower Reynolds numbers. This means that at this Reynolds number the flow on the grooved half, by itself, is within the transcritical regime, while that on the smooth half within the subcritical regime. Thus, the effect of surface configuration was minor.

Single and cross-wires were used in the present investigation. The hot wire had a diameter of 5×10^{-6} m and a working length of 2 mm. The signals from the constant temperature anemometers were acquired at a rate of 30 k samples per second per channel and digitally analyzed by a Workstation DEC 5000/200 PXG and a PC 486. The hot wire was mounted on a computer controlled table.

Because the aim of the present study was to investigate the turbulent wakes formed soon after the separation of the two different boundary layers, the regime of investigation was confined within the near wake, $0 \le x/d \le 1$, $-2 \le y/d \le 2$. Besides the statistical technique, conditional sampling was also adopted to recover the secondary vortices. Basically, two cross-wires were used to trigger the recovery signals from the recovery cross-wire. The first triggering cross-wire was located at a fixed position, at which the signals from the secondary vortices were dominant (Fig. 1). The second moving triggering cross-wire was located at different streamwise positions on the estimated loci, as obtained from spectral results, of the secondary vortices as they convected downstream. On the smooth half, the fixed triggering wire was located at $x/d = 0.03$, $y/d = -0.544$, $z/d = 0$ and the moving triggering wire at different streamwise position and $y/d = -0.544$ and $z/d = 0.03$. On the grooved half, the fixed triggering wire was at $x/d = 0$, $y/d = 0.555$, $z/d = 0$ and the moving triggering wire at different streamwise position and $y/d = 0.555$ and $z/d = 0.03$. The recovery wire was moved in the spanwise direction (z) for each set of a particular location of the moving triggering wire. In this respect, there were sets of recovered signals at different locations along the loci of the secondary vortices.

By assuming the shape of the horse-shoe vortex at high Reynolds number following the form as suggested by Head and

Nomenclature

C_d = drag coefficient
C_l = lift coefficient
C_p = mean static pressure coefficient
d = diameter of cylinder
f = frequency
f_i = frequency of secondary vortices
f_v = frequency of Strouhal vortices
h = height of V grooves
l = length of cylinder
Re_d = Reynolds number based on cylinder diameter
St_d = Strouhal number based on cylinder diameter
St_θ = Strouhal number based on momentum thickness
t = time
x, y, z = streamwise, transverse and spanwise coordinates
U_c = convection velocity
U_o = free-stream mean velocity
δ = boundary layer thickness
λ = wavelength
λ_s = spanwise wavelength of secondary vortices
λ_{sm} = mean spanwise wavelength
θ = angle from front stagnation point
θ_w = wake angle
θ_g = subtend angle of grooves
θ_{sg} = momentum thickness at separation on grooved half
σ = r.m.s. value of triggering level
u, v, w = streamwise, transverse, and spanwise fluctuating velocities
$\omega_x, \omega_y, \omega_z$ = fluctuating vorticity in streamwise, transverse and spanwise directions

Bandyopadhyay (1981) and based on the Taylor hypothesis of Zaman and Hussain (1981) that

$$\frac{\partial}{\partial x} = \frac{1}{U_c}\frac{\partial}{\partial t},$$

where U_c is the convection velocity of the vortex, the conditions at the head and two legs (left and right) of the vortex are (Hinze, 1975):

$$\text{Head: } \frac{\partial w}{\partial x} = \frac{\partial w}{\partial t} = 0,$$

$$\text{Left leg: } \frac{\partial w}{\partial x} < 0, \quad \frac{\partial w}{\partial t} > 0, \quad \text{clockwise}$$

and

$$\text{Right leg: } \frac{\partial w}{\partial x} > 0, \quad \frac{\partial w}{\partial t} < 0, \quad \text{anticlockwise.}$$

Based on the velocity distribution of the vortex filament of Tietjens and Qustav (1957), transverse and spanwise components of the vorticity are (Hayakawa and Hussain, 1989):

$$\omega_y = \frac{\partial u}{\partial z} - \frac{\partial w}{\partial x} \approx \frac{\Delta u}{\Delta z} + \frac{1}{U_c}\frac{\Delta w}{\Delta t}$$

and

$$\omega_z = \frac{\partial v}{\partial x} - \frac{\partial u}{\partial y} \approx -\frac{1}{U_c}\frac{\Delta v}{\partial t} - \frac{\Delta u}{\Delta y}.$$

At the region very close to the separation points of the two boundary layers, horseshoe or developed vortex is still not yet formed. Thus, for the conditional sampling of the signals at 3.6 kHz on the smooth half and 2.5 kHz on the grooved half, the streamwise velocity fluctuations, u, were used for triggering. For other frequency signals, as the vortices have already been formed, the signals of $\partial w/\partial t$ from both triggering wires were used.

Because of the unstable nature of the secondary vortices, signals from the two triggering wires were octave bandpass filtered at the center frequency of the vortices. The threshold levels for both triggering wires were the peak levels exceeding 1.5 σ, where σ was the filtered r.m.s. value of the triggering signal. Thus, the development of these secondary vortices convecting along the most frequent path was studied. However, for spanwise distribution, it was found that because of the near random nature, as indicated by the very broad spectral peak of these secondary vortices, the recovered ensemble averages $\langle uw \rangle$ might contain contributions from vortices in both directions of rotation at the same spanwise position. This suggested a certain amount of cancellation. Thus, additional condition for ensemble averaging was introduced, involving separate ensemble averaging of only the positive or negative recovered signals. The determination of the positive or negative recovered signals was based on the nearest peak of the recovered signal to the signal from the moving triggering wire. The number of ensembles of each recovered trace was more than 1000.

The experimental uncertainty of the data was as follows: the mean velocity ±3 percent, fluctuating velocity ±5 percent and linear dimensions ±0.1 mm. The uncertainty of the nondimensional groups, such as distance ratio is ±1 percent and that of pressure coefficient is ±0.1.

Results and Discussion

Because of the difference in the mean pressure distributions on the two halves, there is lift on the cylinder. The lift coefficient C_l is +0.09 and drag coefficient C_d is 0.96. The wake angle θ_w, as defined by Guven et al. (1980), on the smooth half is −81 deg, while that on the grooved half is 95 deg, suggesting earlier separation of the boundary layer on the smooth half. The grooved half boundary layer separates soon after the end of the grooves at $\theta = +90$ deg.

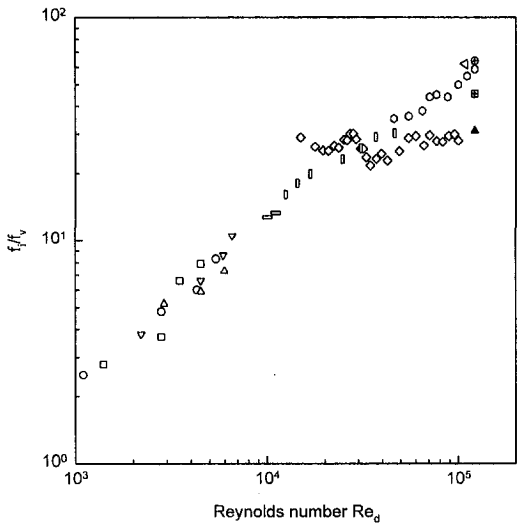

Fig. 2 Variation of frequency ratio f_i/f_v, ○, Bloor (1964); ◁, Maekawa and Mizuno (1967); □, Peterka and Richardson (1969); Wei and Smith (1986): □, d = 2.54 mm, ▽, d = 3.8 mm, △, d = 4.8 mm; ▯, Norberg (1987); present study: ○, smooth half; ◇, grooved half; ⊕, smooth half, f_i = 3.6 kHz; ⊞, grooved half, f_i = 2.5 kHz; ⏢, grooved half, f_i = 1.8 kHz. Uncertainty: f_i/f_v, ±5 percent.

On the smooth half, based on the transverse distributions of the cross-spectra Guv of the streamwise u and transverse velocity v fluctuations very near the separation point at $x/d = 0.01$ (not shown here), besides the Strouhal vortex peak at f_v of 55 Hz ($St_d = f_v d/U_o = 0.22$), spectral peaks at about 3.6 kHz and 1.8 kHz are found at $y/d > -0.556$, very near the cylinder surface. Their peak power seems to be highest just next to the surface. The ratio of the peak frequency f_i of 3.6 kHz with that of the Strouhal vortices f_v is 66 and agrees with that of Maekawa and Mizuno (1967) at $Re_d = 1.2 \times 10^5$. This ratio and those at other Reynolds numbers (Lo and Ko, 1995) of this cylinder, as shown in Fig. 2, follow the trend of those of the secondary vortices of smooth cylinders at different Reynolds numbers (Bloor, 1964; Maekawa and Mizuno, 1967; Peterka and Richardson, 1969; Wei and Smith, 1986; and Noberg, 1987).

On the grooved half, the transverse distributions of the cross-spectra Guv (not shown here), very near the separation point at $x/d = 0$, indicate the Strouhal vortices have the same shedding frequency of about 55 Hz. Very near the cylinder surface, at $y/d = 0.535$, there is a broad spectral peak at 2.5 kHz, giving f_i/f_v of 46 (Fig. 2). Further toward the freestream, at $y/d > 0.569$, there is another broad peak at about 1.8 kHz, giving f_i/f_v of 33. From the distribution of f_i/f_v, the latter ratio of 33 is in the same trend as those of the secondary vortices at other Reynolds numbers. As observed by Lo and Ko (1995), at this Reynolds number of 1.26×10^5 the flow over the grooved half is within the transcritical regime, at which transition of the laminar boundary layer to turbulent occurs before the end of the grooves. Thus, secondary vortices are formed from the separated turbulent boundary layer, resulting in the significant difference in the shedding frequency from the "laminar" secondary vortices of the smooth half and less periodic (or broader spectral peak) of these "turbulent" secondary vortices on the grooved half. The broad spectral peak, as the initial vortices and coherent structures of unexcited air jet (Ko and Davies, 1971 and Moore, 1977), suggests these secondary vortices occur not at fixed quasi-period and space. On the other hand, the f_i/f_v of 46 of the 2.5 kHz peak seems not to be related to the separated boundary layer.

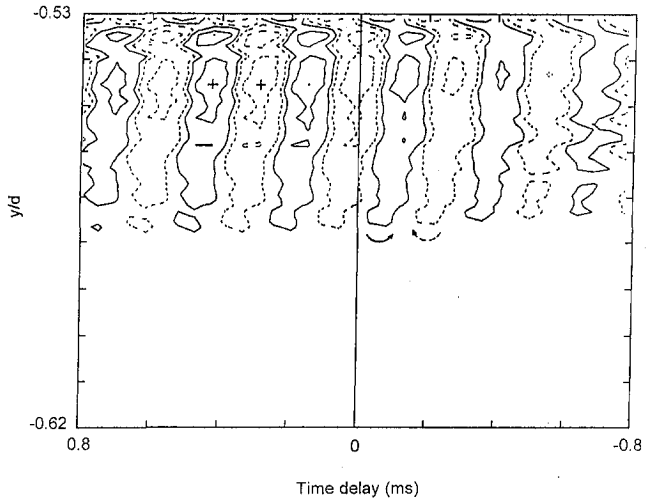

Fig. 3 Recovered spanwise component of fluctuating vorticity $\langle\omega_z\rangle$ of secondary vortices at 3.6 kHz on smooth half. $x/d = 0.175$. $\langle\omega_z\rangle/f_i$: maximum, +0.204; minimum, −0.2. $\langle\omega_z\rangle/f_i = \pm0.02, \pm0.10, \pm0.20, \pm0.30$. Uncertainty: fluctuating vorticity $\langle\omega_z\rangle/f_i$: ±5 percent.

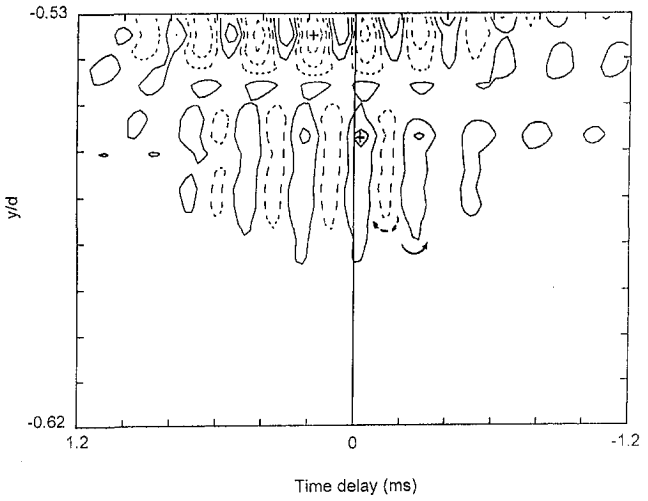

Fig. 5 Recovered Reynolds stresses $\langle uv\rangle$ of secondary vortices at 1.8 kHz on smooth half. $x/d = 0.175$. $\langle uv\rangle/U_o^2$: maximum, $+2.1 \times 10^{-4}$; minimum, -2.54×10^{-4}. $\langle uv\rangle/U_o^2$: $\pm3.0 \times 10^{-5}$, $\pm1.0 \times 10^{4}$, $\pm2.0 \times 10^{-4}$, $\pm3.0 \times 10^{-4}$, $\pm4.0 \times 10^{-4}$. Uncertainty: Reynolds stresses $\langle uv\rangle/U_o^2$, ±5 percent.

As there are differences in the secondary vortices on the two halves of the cylinder, the following sections will present the conditional sampling results of these "laminar" and "turbulent" vortices.

On the smooth half, the isocontours of the recovered spanwise component of the fluctuating vorticity $\langle\omega_z\rangle/f_i$ at 3.6 kHz for $x/d = 0.175$ are shown in Fig. 3. The fluctuating Reynolds stress $\langle uv\rangle$ (not shown here) also recovered secondary vortices with positive vorticity, indicating anticlockwise direction of rotation, very near the cylinder surface at $y/d \approx -0.535$ and further away from the surface (Fig. 3). Their loci indicate that they are shifted away from the cylinder surface as they convect downstream. These vortices are in-phased even up to $x/d = 0.175$. Based on the recovered fluctuating vorticity and Reynolds stress, within this streamwise distance of $0.08 \leq x/d \leq 0.175$ the secondary vortices convect at an angle of about 15 deg from the streamwise axis. At $\mathrm{Re}_d = 2900$, the secondary vortices convect downstream from $x/d \approx 0.8$ at an angle of about 10 deg (Wei and Smith, 1986). This is slightly lower than that of the present study. At higher Reynolds number of $2150 \leq \mathrm{Re}_d \leq 2 \times 10^4$, the instability of the shear layer makes an angle of 13 to 16 deg and is independent of Reynolds number (Kourta et al., 1987). These angles agree with that of the present study.

The different transverse locations of the recovered secondary vortices, with a mean transverse separation of about 0.01 d (Fig. 3), may suggest the flapping of the separated shear layer (Kourta et al., 1987), which wake angle θ_w on this smooth surface is −81 deg.

The streamwise variations of the maximum recovered Reynold stress $\langle uv\rangle_{\max}/U_o^2$ of two better recovered secondary vortex trains at 3.6 kHz are shown in Fig. 4. The secondary vortices develop very rapidly, within a streamwise distance of $0.1d$, before their rapid decay. Their formation length is of the order of $0.1d$.

The recovered fluctuating Reynolds stresses $\langle uv\rangle/U_o^2$ of the secondary vortices at 1.8 kHz for $x/d = 0.175$ are shown in Fig. 5. At $x/d = 0.08$ basically one train of these larger scale vortices are found at $y/d \approx -0.54$ (not shown here). Further downstream, vortices at other transverse locations are observed (Fig. 5). In addition, there are phase difference between those

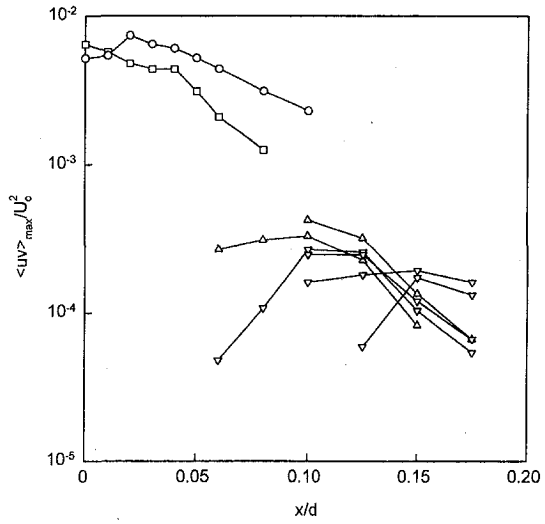

Fig. 4 Streamwise variation of maximum recovered Reynolds stresses $\langle uv\rangle_{\max}$. Smooth half: △, f_i = 3.6 kHz; ▽, f_i = 1.8 kHz; Grooved half: □, f_i = 2.5 kHz; ○, f_i = 1.8 kHz. Uncertainty: $\langle uv\rangle_{\max}$, ±5 percent.

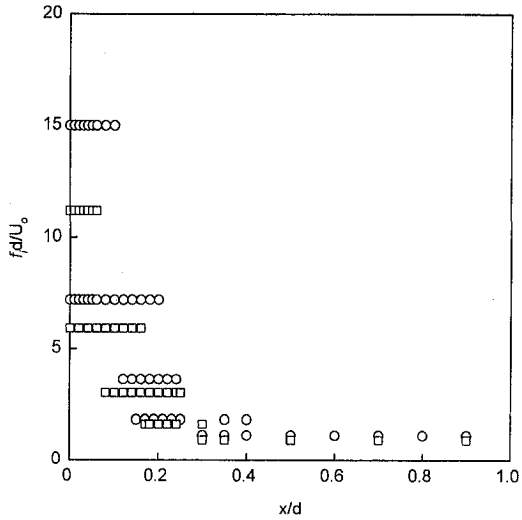

Fig. 6 Streamwise variations of peak frequencies of secondary vortices. ○, smooth half; □, grooved half. Uncertainty: frequency, ±1 percent.

very near the cylinder surface, $y/d \geq -0.54$, from those further away. The phase shift may partly be due to the mean velocity profile. The lower frequency vortices at 1.8 kHz also have a mean transverse separation of about 0.1 d and the formation length of about 0.14 d. These vortices are found to convect downstream at an angle of about 17 deg away from the streamwise axis, suggesting nearly the same as those of 3.6 kHz. However, the maximum recovered Reynolds stresses $\langle uv \rangle_{\max}/U_o^2$ of the 1.8 kHz vortices indicate that these vortices develop further downstream (Fig. 4).

The streamwise distributions of the peak frequencies show the halving of the peak frequencies not only of the 3.6 kHz and 1.8 kHz peaks, but also of another stage further downstream (Fig. 6). This suggests pairing of these secondary vortices (Winant and Browand, 1974; Kibens, 1980; Ho and Huang, 1982; and Kourta et al., 1987). However, the very broad spectral peaks suggest the occurrence of these secondary vortices is not steady in time and space. The pairing phenomenon may only be one of the causes. Also shown in Fig. 6, the halving of the peak frequency of 3.6 kHz occurs at $x/d \lesssim 0.1$, suggesting rigorous nonlinear interaction takes place within such short distance after their formation. It is also within this distance that these vortices build up their strength and experience rapid decay at $x/d > 0.1$ (Fig. 4). Further halving occurs till $x/d = 0.24$, suggesting further that rigorous interaction of these secondary vortices are found soon after their formation. As the Reynolds number of this investigation is beyond the lower Reynolds number range of $2 \times 10^3 < \mathrm{Re}_d < 1.6 \times 10^4$ of Kourta et al. (1987), in which strong interaction between the separated shear layer and the Strouhal vortex shedding occurs, one would not expect the successive occurrences of $(f_v \pm nf_i)$. At $1.6 \times 10^4 < \mathrm{Re}_d < 6.0 \times 10^4$ Kourta et al. (1987) has found the two frequency ranges are disconnected and the small secondary vortices seem to act independently. The flow is, thus, found to be intermittent. At the higher Reynolds number range of the present study the shear layer experiences flapping motion and large-amplitude oscillations at the vortex shedding frequencies, suggesting the shear layer is subjected to the effect of the large Strouhal vortices.

The above triggering criteria were based on the signal induced by the roll of the secondary vortices. The above isocontours do not explicitly indicate the pairing phenomenon. As the present study is within the higher part of the subcritical regime, it is expected that these secondary vortices of the shear layer are located closer to the separation point and that their motions are rapidly disorganised or experience decay (Fig. 4). These phonemona agree with those of Kourta et al. (1987) of lower Reynolds numbers. Thus, the flapping of the shear layer, the occasional pairings, the rapid transition to turbulence and the rapid build up and decay of these small scale vortices may be responsible for the phenomena observed.

The time histories of the streamwise fluctuating velocities of 3.6 kHz, 1.8 kHz, and 55 Hz at $x/d = 0.05$ and 0.175 are shown in Fig. 7(a) and 7(b), respectively. At $x/d = 0.05$, soon after their formation, the secondary vortices at 3.6 kHz, even those at 1.8 kHz, are mainly found at or near the troughs of 55 Hz (Strouhal vortices) time traces (Fig. 7(a)). Basically, a group of these secondary vortices is found at each trough. The amplitude and time span of these small scale vortices vary, suggesting that they are not as periodic. Further, the 55 Hz signals associated with the Strouhal vortices also have modulation in the velocity. Irrespective of the modulation, these secondary vortices are found at and near the saddle point of two successive Strouhal vortices during their formation.

Further downstream at $x/d = 0.175$ the secondary vortices are no longer confined to the troughs but also on or near the crests of the velocity time traces (Fig. 7(b)). This appearance of the secondary vortices on the crests of velocity time traces agrees with the flow visualization results in the wake of circular cylinder (Wei and Smith, 1986). At $\mathrm{Re}_d = 4530$, Wei and Smith (1986) has found the secondary vortices, though more irregular, catch up and merge with the rolls of the Strouhal vortices. This visualization further suggests that the secondary vortices convect at a higher velocity than that of the Strouhal vortices. Based on the above recovered fluctuating properties, the secondary vortices at 3.6 kHz and 1.8 kHz have significantly higher convection velocities of $1.1U_o$, in compared with that of the Strouhal vortices of $0.77U_o$. The convection velocities of the lower frequencies (results not shown here) are nearly the same as that of the Strouhal vortices.

In plane free shear layer Brown and Roshko (1974), Dimotakis and Brown (1976), and Lasheras and Choi (1988) observed the large-scale spanwise vortices are the result of Kevin-Helmholtz instability, with well-organized array of streamwise vortices superimposed on them. The studies of Hussain and Hayakawa (1987), Lasheras and Choi (1988), and Zhou and Antonia (1994) observed that the saddle point and braid region associated with the spanwise vortices behind circular cylinder provide the dominant contribution to the Reynolds shear stress and normal stress. Thus, the occurrence of these secondary vortices at and near the saddle point would have an influence on the three dimensionality of the Strouhal vortices. This effect can also be seen in Fig. 7(a) that at $x/d = 0.05$, where the secondary vortices are mainly confined at and near the saddle point, the modulation of the signals associated with the Strouhal vortices seems to be less than those further downstream (Fig. 7(b)). Nevertheless, at the downstream positions the flapping and the bigger variation in the vortex strength and convection path would also contribute to the modulation observed.

In the model of Hussain and Hayakawa (1987) it was proposed that the saddle point is formed at the mid distance between two successive spanwise vortices of the same strength. In the present study of the near wake of the circular cylinder, the Kelvin-Helmhotz instability or the developing Strouhal vortices may not be of the same strength. Based on the potential theory (not shown here) for two vortices of the same sense of circulation but different strength, the saddle point is found nearer to the vortex of smaller strength. This shift of the secondary vortices very near the separation point may partly be the reason for the occurrences of the newly formed secondary vortices not exactly at the troughs of the velocities associated with the Strouhal vortices (Fig. 7(a)).

The spanwise variations of the recovered Reynolds stress $\langle uw \rangle/U_o^2$ at the secondary vortex frequency 3.6 kHz at $x/d = 0.08$ are shown in Fig. 8. The Reynolds stresses were ensemble-averaged according to its sense of rotation and only those with positive sense of rotation are presented. At $x/d = 0.08$ Reynolds stresses of opposite senses are recovered at the same spanwise location, such as those at $z/d \approx 0.06$ and 0.14, suggesting that soon after their formation, the secondary vortices of opposite direction of rotation are found (Fig. 8). This phenomenon is also observed further downstream at $x/d = 0.16$. Further, at $x/d = 0.08$ there are pairs of counter-rotating vortices (Fig. 8). They can be nearly in-phased, such as those at $z/d \approx 0.06$ or out-of-phased, such as those at $z/d \approx 0.04$ and 0.05. The spanwise wavelength λ_s/d between two adjacent vortices varies from 0.004 to 0.010 at this streamwise position of $x/d = 0.08$. Further downstream at $x/d = 0.10$ this spanwise wavelength increases slightly to $0.006d$ to $0.014d$, with a mean of $\lambda_{sm} = 0.011d$. Downstream of this streamwise position, there is no significant change in λ_{sm}. In addition, from the recovered $\langle uw \rangle$ at 1.8 kHz, the λ_{sm} is also $0.011\ d$ (not shown here), the same as that of 3.6 kHz.

The mean spanwise wavelength λ_{sm}/d of the secondary vortices, based on the recovered Reynolds stresses, is shown in Fig. 9. The flow visualization result at $\mathrm{Re}_d = 7.7 \times 10^3$ of the present study (not shown here) is also included. The mean spanwise wavelengths of the counter-rotating secondary vortices immedi-

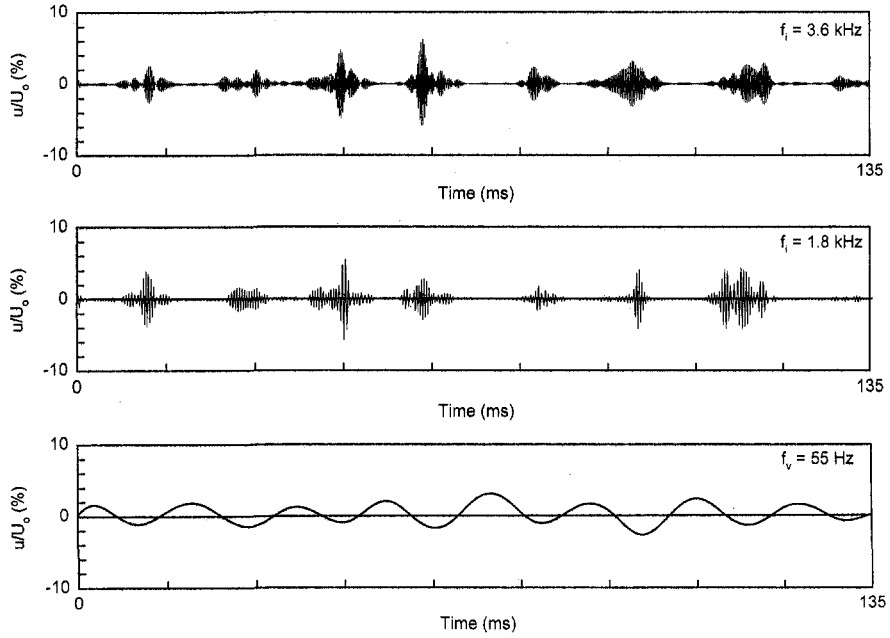

Fig. 7(*a*)

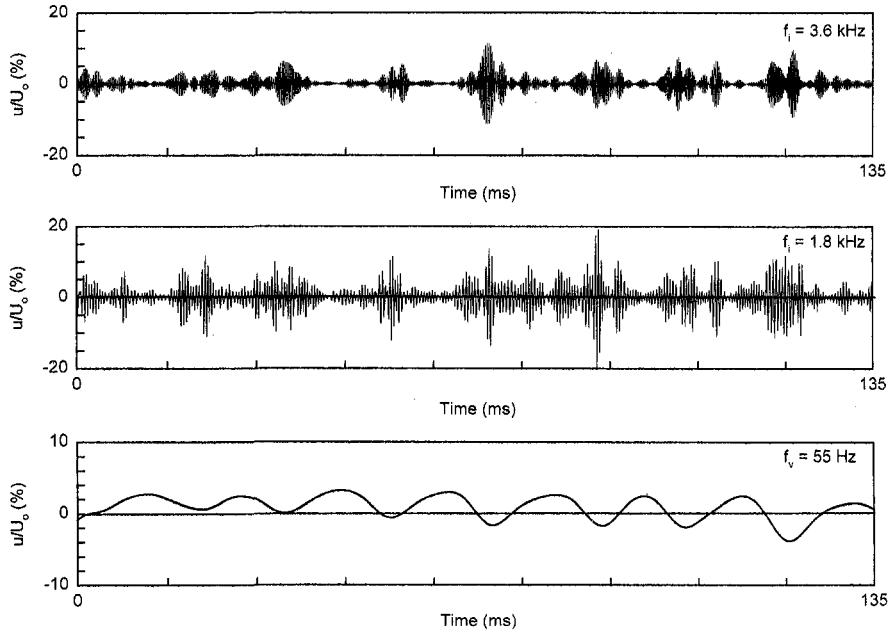

Fig. 7(*b*)

Fig. 7 Time traces of streamwise velocity fluctuations on the smooth half. (*a*) x/d = 0.05, y/d = −0.53; (*b*) x/d = 0.175, y/d = −0.555.

ately after the separation of the boundary layer of Wei and Smith (1986), Taneda (1987), and Yokoi and Kamemoto (1992) are also shown. The mean spanwise wavelength of those downstream at $x/d \approx 3$, after the appearance of the Strouhal vortices of Williamson (1988), Bays-Muchmore and Ahmed (1993), Wu et al. (1994), and Mansy et al. (1994) are also included. The wavelength of those much further downstream at x/d = 20 of Hayakawa and Hussain (1989) and at x/d = 10 of Mansy et al. (1994) are also included. It is interesting to find that those of the initially formed counter-rotating vortices, immediately after the separation of the boundary layer, depend on Reynolds number (Fig. 9). This includes that at high Reynolds number of the present study. The wavelengths of the vortices further downstream also follow the same trend. Thus, within the subcritical regime the mean spanwise wavelength of the initially formed counter-rotating vortex pair has the following relationship: $\lambda_{sm}/d = 1400/\mathrm{Re}_d$ (correlation coefficient = 0.98). For all the data at $x/d \approx 3$, $\lambda_{sm}/d = 8.1/\mathrm{Re}_d^{0.34}$ (correlation coefficient = 0.60). For those at x/d = 10 and 20, $\lambda_{sm}/d = 5.3/\mathrm{Re}_d^{0.23}$ (correlation coefficient = 0.99). In the recent study of Williamson et al. (1995), two distinct systems of streamwise vortices in the separating shear layers and in the vortex street wakes are isolated. In the vortex street wake, the length scale of the streamwise vortices is independent of Reynolds number (Williamson et al., 1995) and the nearly independent results at x/d = 10 and 20, as shown in Fig. 9, support the findings. At $x/d \approx 3$, including the results used in the correlation of Williamson et al. (1995), Fig. 9 suggests $\lambda_{sm}/d = 8.1/\mathrm{Re}_d^{0.34}$, nearly following the relationship of the length scale of the streamwise vortices in the shear layer of $1/\mathrm{Re}_d^{0.5}$ of Williamson et al.

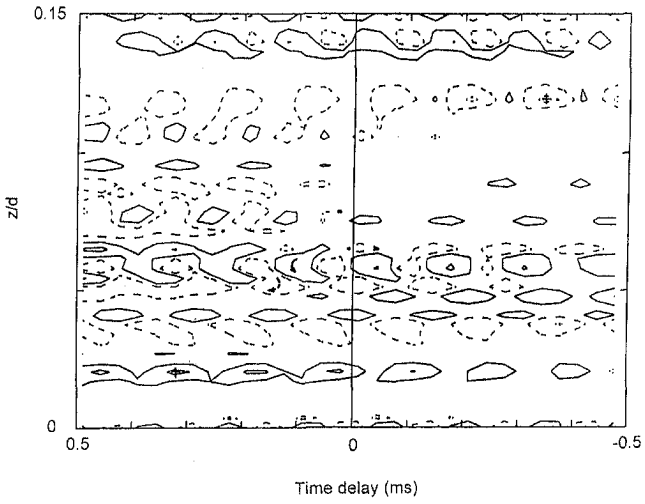

Fig. 8 Spanwise variation of recovered Reynolds stress $\langle uw \rangle$ of secondary vortices at 3.6 kHz on smooth half. $x/d = 0.08$. $\langle uw \rangle / U_o^2$: maximum, 2.07×10^{-5}; minimum, -1.45×10^{-5}. $\langle uw \rangle / U_o^2$: $\pm 2.0 \times 10^{-6}$, $\pm 1.0 \times 10^{-5}$, $\pm 2.0 \times 10^{-5}$, $\pm 3.0 \times 10^{-5}$, $\pm 4.0 \times 10^{-5}$. Uncertainty: Reynolds stress $\langle uw \rangle / U_o^2$, ±5 percent.

(1995). For the initially formed vortices, however, another relationship of the length scale of $\lambda_{sm}/d = 1400/\mathrm{Re}_d$ is shown in Fig. 9. This implies that these newly formed secondary vortices from the separated shear layers behave differently from the secondary vortices further downstream at $x/d \approx 3$. This different behavior is not surprising as in Fig. 6 these secondary vortices undergo pairing and nonlinear rigorous interaction within the streamwise distance $0 < x/d < 0.3$. Thus, at $x/d \approx 3$, one would expect the secondary vortices would have different behavior from those further upstream. As established by the above workers, these counter-rotating pairs constitute the two legs of the horseshoe vortices. The above phenomenon suggests that even at the high Reynolds number of the present study, the

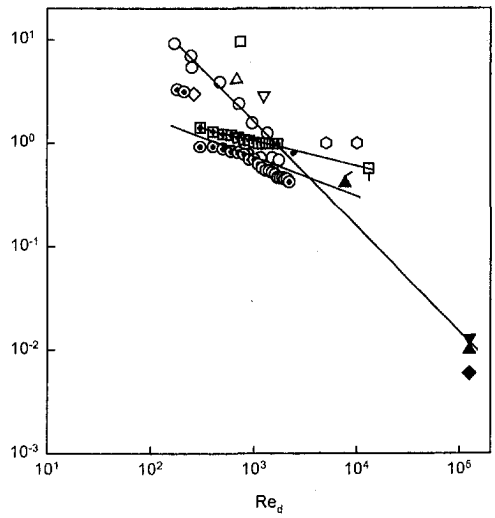

Fig. 9 Variation of mean spanwise wavelengths with Reynolds number. ▽, Roshko (1954); □, Hama (1957); +, $x/d = 0.6$, Wei and Smith (1986); △, $x/d = 1.4$, Taneda (1987); ◇, $x/d \approx 1.55$, Williamson (1988); ⊡, $x/d = 20$, Hayakawa and Hussain (1989); ○, $x/d \approx 1.5$, Yokoi and Kamemoto (1992); ○, $x/d = 3$, Bays-Muchmore and Ahmed (1993); ○, $3.0 < x/d < 3.3$, Wu et al. (1994); ⊕, $x/d = 3$, Mansy et al. (1994); ⊞, $x/d = 10$, Mansy et al. (1994); present study: ▲, smooth half; ▼, grooved half, $f_i = 1.8$ kHz; ◆, grooved half, $f_i = 2.5$ kHz; ▲, smooth half, flow visualization. Uncertainty: wavelength, ±5 percent.

recovered Reynolds stresses also indicate the presence of these counter-rotating vortex pairs and their development into horseshoe vortices.

On the grooved half, the streamwise distributions of the peak frequencies show the halving of the peak of 1.8 kHz to about 230 Hz in three stages (Fig. 6). As those on the smooth half, these 1.8 kHz secondary vortices undergo certain amount pairing as they convect downstream. For the 2.5 kHz vortices no pairing is found.

On the grooved half the time histories of the secondary vortices at $f_i = 2.5$ kHz, 1.8 kHz and 55 Hz associated with the Strouhal vortices at $x/d = 0.02$, $y/d = 0.565$ are shown in Fig. 10. The velocity associated with the Strouhal vortices also has modulation and seems to be larger than that of the smooth half, suggesting more unsteady nature of the Strouhal vortices (Fig. 10(c)). The signals of the secondary vortices of 1.8 kHz are mainly found between those associated with the Strouhal vortices (Fig. 10(a)). This suggests that the secondary vortices of 1.8 kHz are initiated from the separation of the boundary layer and their occurrences at and near the saddle point of the Strouhal vortices. However, the occurrence of the vortices of 2.5 kHz is more random and is not as specific as those of 1.8 kHz (Fig. 10(b)). The most likely cause for these 2.5 kHz vortices is due to the formation of the wake at the blunt end of the grooves at $\theta_g = +90$ deg. In the studies of flow over inclined circular and square discs, Marshall and Stanton (1931) and Calvert (1967) found that the Strouhal number of the vortex wake, based on the equivalent diameter, is 0.136. For the present investigation, as the velocity gradient inside the groove passage is not known, based on the assumption of linear gradient and equivalent diameter, the estimated Strouhal number of this 2.5 kHz peak is 0.12. This agrees reasonably well with that of 0.136 of the above workers, suggesting these 2.5 kHz vortices are due to those associated with the wake of the triangular blunt ends of the grooves. Their outward shift is estimated to be about 23 deg as they convect downstream.

Based on the momentum thickness θ_{sg} at the separation and the freestream velocity, the Strouhal number St_θ ($=f\theta_{sg}/U_o$) of the 2.5 kHz peak is 0.05. This is significantly different from the Strouhal number of about 0.016, at which the excitation frequency matches the instability frequency of the separated shear layer (Zaman, 1992 and Lo and Ko, 1995). This indicates that the disturbances associated with these 2.5 kHz wake vortices do not excite the separated shear layer of the grooves and the formation of the 1.8 kHz secondary vortices. As also shown in Fig. 4, the peak recovered Reynolds stress $\langle uv \rangle_{\max}$ of these 2.5 kHz vortices on the grooved half decreases at $x/d > 0$, suggesting the decay of these vortices soon after their formation, while the $\langle uv \rangle_{\max}$ of 1.8 kHz vortices builds up to its maximum at $x/d = 0.02$ before its decay.

For the 1.8 kHz secondary vortices, the isocontours of the recovered fluctuating vorticity $\langle \omega_p \rangle / f_i$ at $x/d = 0.12$ are shown in Fig. 11. As shown in the last section, the former position of $x/d = 0.02$ is where the peak of $\langle uv \rangle_{\max}$ is found, giving a formation length of about 0.02 d. The negative values of the recovered $\langle uv \rangle_{\max}$ and $\langle \omega_p \rangle$ suggest the vortices have clockwise direction of rotation. Although three trains of vortices are recovered at $x/d = 0.02$, only a dominant train is recovered at $x/d = 0$ (not shown here). Further downstream at $x/d = 0.12$, about 8 trains of different vorticity are recovered (Fig. 11). This phenomenon indicates the flapping of the separated shear layer and the corresponding unsteady nature of the secondary vortices formed both in time and space. Further, their loci imply the outward convection of these secondary vortices of about 23 deg. These vortices are in-phased even up to $x/d = 0.16$.

The convection velocity of these 1.8 kHz secondary vortices is found to be 0.96 U_o. This is the same as that of the groove wake vortices of 2.5 kHz. The slightly lower convection velocity, in compared with those of the smooth half, may be due to the high turbulence action from the turbulent boundary layer of

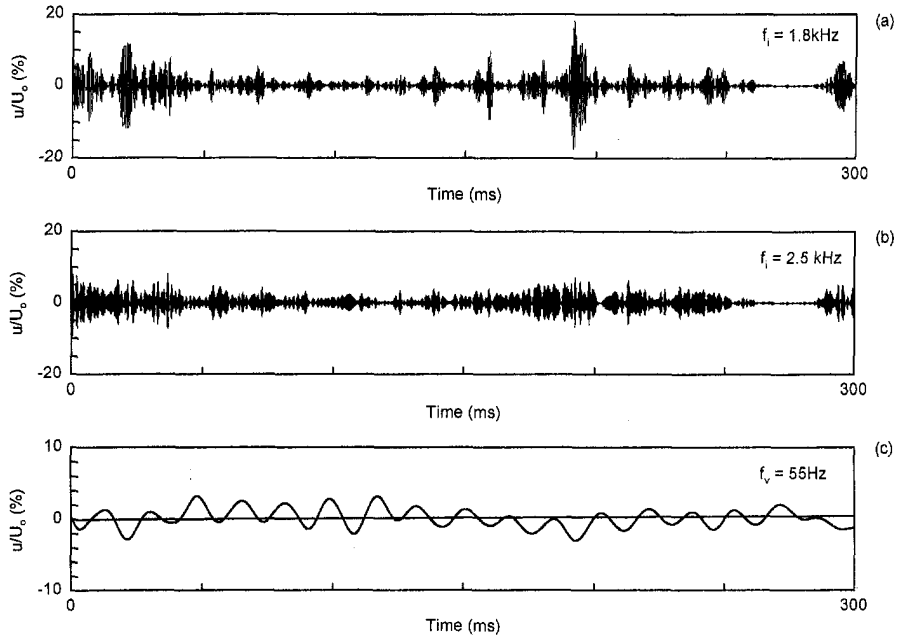

Fig. 10 Time traces of streamwise velocity fluctuations on the grooved half. $x/d = 0.02$, $y/d = 0.565$.

the grooved half and to the effect of turbulent action in the rapid widening of the vortex street (Papailliou and Lykoudis, 1974).

The spanwise variations of the recovered Reynolds stress $\langle uw \rangle / U_o^2$ at the secondary vortex frequency 1.8 kHz at $x/d = 0.08$ are shown in Fig. 12. Only those with positive sense of rotation are presented. At both locations Reynolds stresses of opposite senses are recovered at and near the same spanwise location, suggesting that there are pairs of counter-rotating vortices. The mean spanwise wavelength λ_{sm} of these secondary vortices on the grooved half is $0.013d$ and is slightly higher than those of the smooth half secondary vortices (Fig. 9). These counter-rotating vortices may also suggest that, as those on the smooth half, they are of the horseshoe type. This further implies that at the transcritical regime secondary vortices of horse-shoe shape are also observed within the separated turbulent boundary layer.

For the wake vortices of 2.5 kHz from the blunt end of the grooves, the spanwise distribution of the recovered Reynolds stress $\langle uw \rangle / U_o^2$ of negative sense of rotation at $x/d = 0$ is shown in Fig. 13. At this streamwise location of $x/d = 0$, soon after their formation from the blunt end of the grooves, the wake vortices are mainly of clockwise direction of rotation. Thus, they are different from the secondary vortices at 1.8 kHz, which have counter-rotating vortices. The mean wavelength of these wake vortices is about $0.006d$, lower than those of the other secondary vortices (Fig. 9). This mean wavelength is of the same order as that of the maximum width at the bottom of the grooves of $0.004d$.

Conclusions

At the Reynolds number, based on the cylinder diameter, of 1.26×10^5 the flow over the smooth half of the V grooved

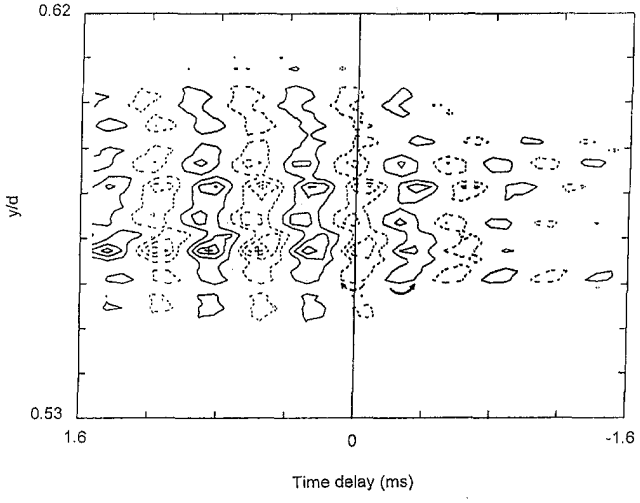

Fig. 11 Recovered spanwise components of fluctuating vorticity $\langle \omega_z \rangle$ of secondary vortices at 1.8 kHz on grooved half. $x/d = 0.12$. $\langle \omega_z \rangle / f_i$: maximum, +1.26; minimum, −1.66. $\langle \omega_z \rangle / f_i = \pm 0.2, \pm 1.0, \pm 2.0, \pm 3.0$. Uncertainty: vorticity $\langle \omega_z \rangle / f_i$, ±5 percent.

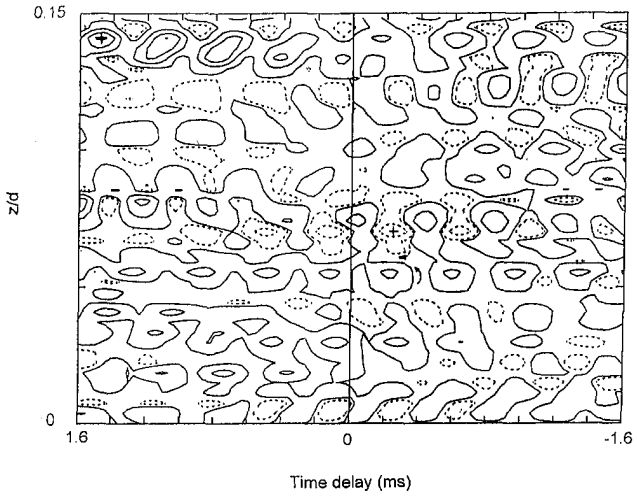

Fig. 12 Spanwise variation of recovered Reynolds stress $\langle uw \rangle$ of secondary vortices at 1.8 kHz on grooved half. $x/d = 0.08$. $\langle uw \rangle / U_o^2$: maximum, $+4.6 \times 10^{-5}$; minimum, -2.86×10^{-5}. $\langle uw \rangle / U_o^2$: $\pm 2.0 \times 10^{-6}$, $\pm 1.5 \times 10^{-5}$, $\pm 3.0 \times 10^{-5}$, $\pm 4.5 \times 10^{-5}$. Uncertainty: Reynolds stress $\langle uw \rangle / U_o^2$, ±5 percent.

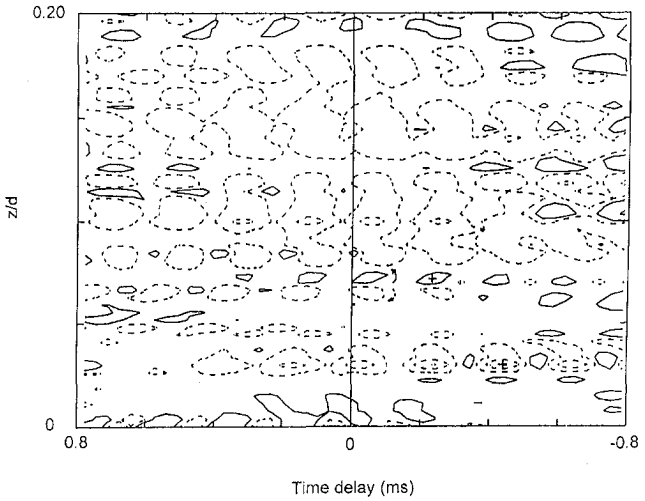

Fig. 13 Spanwise variation of recovered Reynolds stress $\langle uw \rangle$ of secondary vortices at 2.5 kHz on grooved half. $x/d = 0$. $\langle uw \rangle / U_o^2$: maximum, $+1.23 \times 10^{-4}$; minimum, -3.72×10^{-4}. $\langle uw \rangle / U_o^2$: $\pm 2.0 \times 10^{-5}$, $\pm 1.5 \times 10^{-4}$, $\pm 3.0 \times 10^{-4}$, $\pm 4.5 \times 10^{-4}$. Uncertainty: Reynolds stress $\langle uw \rangle / U_o^2$, ± 5 percent.

circular cylinder is within the high subcritical regime and that over the grooved half is within the transcritical regime. Based on the spectral and conditional sampling results, on the smooth half the near wake has the presence of the secondary and Strouhal vortices. The secondary vortices are mainly found at and near the saddle point of Strouhal vortices. Halving of the peak frequency of these secondary vortices suggests certain amount of pairing as they convect downstream and their development into horse shoe vortices.

On the grooved half the near turbulent wake also contains the secondary vortices and Strouhal vortices. Two types of secondary vortices are found. The first type with a Strouhal number, based on the equivalent diameter, of 0.12 is due to the wake vortices associated with the triangular bodies of the V-grooves and the other is associated with the separated turbulent boundary layer. The latter occurs at and near the saddle point of Strouhal vortices. Halving of the peak frequency of the latter secondary vortices also suggests certain amount of pairing, as they convect downstream and their development into horse shoe vortices.

This study gives an insight on the characteristics of the secondary vortices in the subcritical and transcritical flow regimes of smooth cylinder and their relationship with the Strouhal vortices. The present study and the quantitative results of the secondary vortices of the separated turbulent shear layer establish their existance within the transcritical flow regime, in which turbulence and three dimensionality play important role. The conditional sampling technique with the present specific criteria offers an important tool in the recovery and better understanding of these highly unsteady secondary vortices, especially those in the transcritical regime.

References

Achenbach, E., 1968, "Distribution of Local Pressure and Skin Friction Around a Circular Cylinder in Cross-flow Up to Re = 5×10^6," *Journal of Fluid Mechanics,* Vol. 34, pp. 625–639.

Batchelor, G. K., 1977, *An Introduction to Fluid Dynamics,* Cambridge University Press, Cambridge.

Bays-Muchmore, B., and Ahmed, A., 1993, "On Streamwise Vortices in Turbulent Wakes of Cylinders," *Physics of Fluids,* Vol. A5, pp. 387–392.

Bearman, P. W., 1967, "On Vortex Street Wake," *Journal of Fluid Mechanics,* Vol. 28, pp. 625–641.

Bloor, M. S., 1964, "The Transition to Turbulence in the Wake of a Circular Cylinder," *Journal of Fluid Mechanics,* Vol. 19, pp. 290–304.

Brown, G. L., and Roshko, A., 1974, "On Density Effects and Large Structure in Turbulent Mixing Layer," *Journal of Fluid Mechanics,* Vol. 64, pp. 775–816.

Calvert, J. R., 1967, "Experiments on the Flow Past an Inclined Disk," *Journal of Fluid Mechanics,* Vol. 29, pp. 691–703.

Cantwell, B., and Coles, D., 1983, "An Experimental Study of Entrainment and Transport in the Turbulent Near Wake of a Circular Cylinder," *Journal of Fluid Mechanics,* Vol. 136, pp. 321–374.

Chandrsuda, C., Mehta, R. D., Weir, A. D., and Bradshaw, P., 1978, "Effect of Free-Stream Turbulence on Large Structure in Turbulent Mixing Layer," *Journal of Fluid Mechanics,* Vol. 85, pp. 693–704.

Chang, P. K., 1970, *Separation of Flow,* Pergamon Press.

Dimotakis, P. E., and Brown, G. L., 1976, "The Mixing Layer at High Reynolds Number: Large Structure Dynamics and Entrainment," *Journal of Fluid Mechanics,* Vol. 78, pp. 535–560.

Gerrard, J. H., 1978, "The Wakes of Cylindrical Bluff Bodies at Low Reynolds Number," *Proceedings of Royal Society London,* Vol. A288, pp. 351–382.

Guven, O., Farell, C., and Patel, V. C., 1980, "Surface-roughness Effects on the Mean Flow Past Circular Cylinders," *Journal of Fluid Mechanics,* Vol. 98, pp. 673–701.

Hama, F. R., 1957, "Three-dimensional Vortex Pattern Behind a Circular Cylinder," *Journal of Aeronautical Science,* Vol. 24, pp. 156–158.

Hayakawa, M., and Hussain, F., 1989, "Three-Dimensionality of Organized Structures in a Plane Turbulent Wake," *Journal of Fluid Mechanics,* Vol. 206, pp. 375–404.

Head, M. R., and Bandyopadhyay, P., 1981, "New Aspects of Turbulent Boundary Layer Structure," *Journal of Fluid Mechanics,* Vol. 107, pp. 297–338.

Hinze, J. O., 1975, *Turbulence,* McGraw-Hill, New York.

Ho, C. M., and Huang, L. S., 1982, "Subharmonics and Vortex Merging in Mixing Layers," *Journal of Fluid Mechanics,* Vol. 119, pp. 443–473.

Hussain, A. K. M. F., and Hayakawa, M., 1987, "Eduction of Large-Scale Organized Structures in a Turbulent Plane Wake," *Journal of Fluid Mechanics,* Vol. 180, pp. 193–229.

Kibens, V., 1980, "Discrete Noise Spectrum Generated by an Acoustically Excited Jet," *AIAA Journal,* Vol. 18, pp. 434–441.

Ko, N. W. M., and Davies, P. O. A. L., 1971, "The Near Field within the Potential Core of Subsonic Cold Jets," *Journal of Fluid Mechanics,* Vol. 50, pp. 49–78.

Kourta, K., Boisson, H. C., Chassaing, P., and Ha Minh, H., 1987, "Nonlinear Interaction and the Transition to Turbulence in the Wake of a Circular Cylinder," *Journal of Fluid Mechanics,* Vol. 181, pp. 141–161.

Lasheras, J. C., and Choi, H., 1988, "Three-Dimensional Instability of a Plane Free Shear Layer: An Experimental Study of the Formation and Evolution of Streamwise Vortices," *Journal of Fluid Mechanics,* Vol. 189, pp. 53–86.

Leung, Y. C., Ko, N. W. M., and Tang, K. M., 1992, "Flow Past Circular Cylinder with Different Surface Configurations," ASME JOURNAL OF FLUIDS ENGINEERING, Vol. 114, pp. 170–177.

Lo, K. W., and Ko, N. W. M., 1995, "Effect of Acoustic Excitation on Flow over a Partially Grooved Circular Cylinder," *Experiments in Fluids,* Vol. 19, pp. 194–202.

Maekawa, T., and Mizuno, S., 1967, "Flow Around the Separation Point and in the Near-wake of a Circular Cylinder," *Physics of Fluids Supplement,* pp. S184–S186.

Mansy, H., Yang, P. M., and Williams, D. R., 1994, "Quantitative Measurement of Spanwise Periodic Three-dimensional Structures in the Wakes of a Circular Cylinder," *Journal of Fluid Mechanics,* Vol. 270, pp. 277–296.

Marshall, D., and Stanton, T. E., 1931, "On the Eddy System in the Wake of Flat Circular Plates in Three Dimensional Flow," *Proceedings of Royal Society,* London, Series A, Vol. 130, pp. 295–301.

Moore, C. J., 1977, "The Role of Shear Layer Instability Waves in Jet Exhaust Noise," *Journal of Fluid Mechanics,* Vol. 80, pp. 321–367.

Niemann, H. J., and Hölscler, N., 1990, "A Review of Recent Experiments on the Flow Past Circular Cylinders," *Bluff Body Aerodynamics and Its Application,* Amsterdam, Elsevier, pp. 197–209.

Noberg, C., 1987, "Effects of Reynolds Number and Low-intensity Freestream Turbulence on the Flow Around a Circular Cylinder," Ph.D. thesis, Chalmers University of Technology, Sweden.

Nygaad, K. J., and Glezer, A., 1991, "Evolution of Streamwise Vortices and Generation of Small-Scale Motion in a Plane Mixing Layer," *Journal of Fluid Mechanics,* Vol. 231, pp. 257–301.

Papailiou, D. D., and Lykoudis, P. S., 1974, "Turbulent Vortex Streets and the Entrainment Mechanism of the Turbulent Wake," *Journal of Fluid Mechanics,* Vol. 62, pp. 11–31.

Peterka, J. A., and Richardson, P. D., 1969, "Effects of Sound on Separated Flows," *Journal of Fluid Mechanics,* Vol. 37, pp. 265–287.

Roshko, A., 1954, "On the Drag and Shedding Frequency of Two-dimensional Bluff Bodies," NACA Tech. Note 3169.

Rockwell, D., 1990, "Active Control of Globally-Unstable Separated Flow," *Proceedings of International Symposium on Nonsteady Fluid Dynamics,* ASME, pp. 379–394.

Schewe, G., "On the Force Fluctuations Acting on a Circular Cylinder in a Crossflow from Subcritical up to Transcritical Reynolds Number," *Journal of Fluid Mechanics,* Vol. 133, pp. 265–285.

Schumm, M., Berger, E., and Monkewitz, P. A., 1994, "Self-Excited Oscillations in the Wake of Two Dimensional Bluff Bodies and their Control," *Journal of Fluid Mechanics,* Vol. 271, pp. 17–53.

Taneda, S., 1987, "Some Problems in Flow Visualization," *Journal of Visualization Society of Japan* (in Japanese), Vol. 7, pp. 379–387.

Unal, M. F., and Rockwell, D., 1988, "On Vortex Formation from a Cylinder. Part 1. The Initial Instability," *Journal of Fluid Mechanics,* Vol. 190, pp. 491–512.

Wei, T., and Smith, C. R., 1986, "Secondary Vortices in the Wake of Circular Cylinder," *Journal of Fluid Mechanics,* Vol. 169, pp. 513–533.

Williamson, C. H. K., 1988, "The Existence of Two Stages in the Transition to the Three-Dimensionality of a Cylinder Wake," *Physics of Fluids,* Vol. 31, pp. 3165–3168.

Williamson, C. H. K., Wu, J., and Sheridan, J., 1995, "Scaling of Streamwise Vortices in Wakes," *Physics of Fluids,* Vol. 10, pp. 2307–2309.

Winant, C. D., and Browand, F. K., 1974, "Vortex Pairing: The Mechanism of Turbulent Mixing Layer Growth at Moderate Reynolds Number," *Journal of Fluid Mechanics,* Vol. 63, pp. 237–255.

Wu, J., Sheridan, J., Welsh, M. C., Hourigan, K., and Thompson, M., 1994a, "Longitudinal Vortex Structures in a Cylinder Wake," *Physics of Fluids,* Vol. 6, pp. 2883–2885.

Wu, J., Sheridan, J., Soria, J., and Welsh, M. C., 1994b, "An Experimental Investigation of Streamwise Vortices in the Wake of a Bluff Body," *Journal of Fluids and Structures,* Vol. 8, pp. 621–625.

Yokoi, Y., and Kamemto, K., 1992, "Initial Stage of a Three Dimensional Vortex Structure Existing in a 2-D Boundary Layer Separation Flow," *J.S.M.E. Series II,* Vol. 35, pp. 189–195.

Zaman, K. B. M. Q., 1992, "Effect of Acoustic Excitation on Stalled Flows Over an Airfoil," *AIAA Journal,* Vol. 30, pp. 1492–1586.

Zdravkovich, M. M., 1990, "Conceptual Overview of Laminar and Turbulent Flows Past Smooth and Rough Circular Cylinders," *Journal of Wind Engineering and Industrial Aerodynamics,* Vol. 33, pp. 53–62.

Zhou, Y., and Antonia, R. A., 1994, "Critical Points in a Turbulent Near Wake," *Journal of Fluid Mechanics,* Vol. 275, pp. 59–81.

Oscillatory Momentum Transport Mechanisms in Transitional Complex Geometry Flows

D. Majumdar[1]
Graduate Student

C. H. Amon
Associate Professor,
Mem. ASME

Department of Mechanical Engineering,
Carnegie Mellon University,
Pittsburgh, PA 15213

This work reports direct numerical simulations of transitional flows in communicating channels. Above a critical Reynolds number, the flow becomes fluctuating and self-sustained with vortical motions temporally synchronized with channel traveling waves. The energy transfer mechanism between the mean and the fluctuating flow is investigated along with the distributions of oscillatory shear stress and transitional viscosity. The kinetic energy equation for the fluctuating velocity is solved from DNS data to evaluate the contributions of the production term, viscous dissipation, work of dynamic pressure and work of viscous shear stresses.

I Introduction

Until recently, numerical calculations of turbulent flows employed some form of modeling in order to evaluate the contributions of the fluctuating quantities in the Reynolds transport equations or in the time-averaged higher moment equations. However, with recent advances in memory and speed of large-scale computers, Direct Numerical Simulations (hereafter referred to as DNS) of turbulent flows at moderate Reynolds numbers are now possible. In DNS, all temporal and spatial scales of motion are resolved without using any closure model. Simulation results are useful for engineering turbulence modeling, since they can provide extensive quantitative data in any region of the domain of interest which may be very difficult to obtain experimentally owing to difficulties in measuring fluctuating turbulent quantities, especially near a wall. DNS must be performed with accurate time-discretization algorithms and on a computational grid that is fine enough to resolve all significant spatial and temporal scales arising in a turbulent flow. Consequently, this endeavor requires a large number of grid points and computer memory. Thus, even with modern supercomputers, DNS is currently possible for simple geometries, and the most comprehensive work in bounded shear flows has been in fully-developed plane channel-flow simulations at moderate Reynolds numbers (e.g., Kim and Moin, 1989; Lyons and Hanratty, 1991; Kasagi et al., 1992).

The development of accurate numerical algorithms for high-performance computing has also enabled DNS of transitional flows in complex geometries that undergo temporal transition through a series of bifurcations. These flows present time-dependent, self-sustained oscillations that increase in complexity with the Reynolds number before becoming turbulent (Ghaddar et al., 1986; Greiner et al., 1991; Nigen and Amon, 1994; Wang and Vanka, 1995; Guzmán and Amon, 1996). In our present investigation, we analyze self-sustained oscillatory flows in the communicating channels shown in Fig. 1, composed of a pair of channels separated by a thick wall with open slots. This particular geometry is encountered in many engineering devices such as plate-finned compact heat exchangers with perforated fins or slotted channels. The open slots enable the interaction of the two fluid streams, resulting in recirculating-flow regions known as communicating regions. The periodic geometric inhomogeneities of these open slots induce flow bifurcations above a critical Reynolds number (Re_c). The temporal transition occurs through a series of supercritical Hopf bifurcations and the first flow bifurcation is at $190 < Re_c < 200$ (Majumdar and Amon, 1992), where Re is defined based on one channel half-height and the centerline velocity. Traveling waves are observed, even at moderately low Reynolds numbers, inducing self-sustained oscillations that result in very well-mixed flows leading to convective heat transfer augmentation. A general discussion of the characteristics of self-sustained oscillatory flows in communicating channels is presented in Majumdar and Amon (1992). Other self-sustained oscillatory flows have been investigated experimentally in triangular grooved channels (Greiner et al., 1991) and computationally in rectangular grooved channels (Ghaddar et al., 1986; Nigen and Amon, 1994) and in converging-diverging channels (Guzmán and Amon, 1994, 1996; Wang and Vanka, 1995). Secondary instabilities in grooved-channel flows were found to induce bifurcations from two-dimensional, self-sustained oscillatory flows to stable, non-turbulent, three-dimensional flows (Amon and Patera, 1989). Experiments performed by Schatz and Swinney (1992) in a spatially-perturbed plane channel also identified bifurcations from flows with two-dimensional traveling waves to three-dimensional spanwise standing waves.

Extensive experimental work has been done in louvered fin heat exchangers (Manglik and Bergles, 1989; Webb, 1990) of which the communicating-channels geometry is a subset. Suzuki et al. (1994) studied numerically the mechanism of heat transfer enhancement due to self-sustained oscillations in an in-line fin array. They identified two mechanisms of heat transfer enhancement by looking at the vortical and fluctuating flow structures along with Nusselt and Stanton number distributions. Dissimilarities between the momentum and heat transfer processes were also observed, but the contribution of the fluctuating components of the velocity and pressure on the momentum transport has not been analyzed in these previous works.

Our primary objective in this work is to understand the physics of momentum transport in transitional, self-sustained oscillatory flows through the evaluation of the kinetic energy associated with the fluctuating flow field obtained by DNS. Researchers have looked at the production terms of the transport equations of Reynolds stresses in the context of discussing turbulent flows in non-circular ducts with a rough wall (e.g., Humphrey and Whitelaw, 1980). The mean and fluctuating kinetic energy have been investigated in turbulent flows over a step by Goel and Amano (1986) and in turbulent plane channel flows by Lyons and Hanratty (1991). However, the kinetic energy budget has been discussed only at particular streamwise loca-

[1] Current address: Delphi Harrison Thermal Systems, Lockport, NY.

Contributed by the Fluids Engineering Division for publication in the JOURNAL OF FLUIDS ENGINEERING. Manuscript received by the Fluids Engineering Division November 27, 1995; revised manuscript received August 12, 1996. Associate Technical Editor: J. A. C. Humphrey.

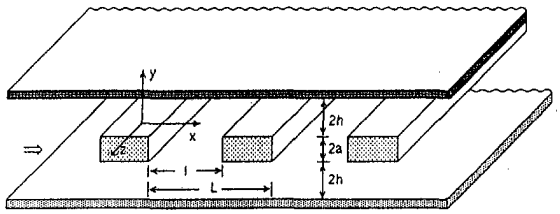

Fig. 1 Communicating-channels geometry characterized by L = periodicity length, l = separation between the interrupted plates, $2a$ = separation between the channels and $2h$ = height of each channel. Nondimensional lengths, $L/h = 8$, $l/h = 3$ and $2a/h = 1$.

tions as a function of the transverse direction in simple geometry flows.

In this work, we consider the kinetic energy equation for the fluctuating components of the velocity and pressure in self-sustained oscillatory flows with vortical structures in complex geometries. We analyze the effect of the fluctuating flowfield on the momentum transport and oscillatory shear stresses, presenting transitional flow results as energy budget plots at streamwise locations and field contour plots of all the terms in the fluctuating kinetic energy equation. We discuss the differences in energy transfer mechanisms between transitional and turbulent flows and we calculate the transitional viscosity to determine the relative contribution of momentum transfer due to the fluctuating flow over the molecular momentum transfer.

II Description of the Problem

The flow in the communicating channels (Fig. 1) is simulated numerically by solving the unsteady, incompressible two-dimensional Navier-Stokes equations. The assumption of two dimensionality is based on the experimentally-obtained flow visualizations and frequency values (Amon et al., 1992, 1993) which closely match those obtained numerically. The experimental results indicate that the onset of three-dimensional flow is above a Reynolds number of 493 (Amon et al., 1992). The simulations reported in this paper are for Re = 400, and similar qualitative results were obtained for Re = 300 and Re = 500. The velocity boundary conditions are Dirichlet on rigid walls and periodic, fully developed in the streamwise x-direction. The numerical approach followed here is that of direct simulation, in which time-dependent and asymptotic states are computed using initial value solvers. The discretization in time is done using a three-step splitting scheme (Orszag and Kells, 1980) in which three fractional steps are introduced within one time step. For two-dimensional simulations, the spatial discretization proceeds using the spectral element method proposed by Patera (1984), where the computational domain is broken up into general quadrangular elements. The geometry, pressure and velocity in each element are represented as a tensor product of high-order Lagrangian interpolants through Chebyshev-Gauss-Lobatto collocation points. The convective terms are evaluated using explicit collocation operators, while the elliptic contributions are handled with variational projection operators.

The validation of the spectral-element code has been performed by computing decay rates and oscillatory frequencies of the evolution of small disturbances in plane Poiseuille flow and by comparing them with predictions of the linear theory obtained by solving the Orr-Sommerfeld equations with a second independent code that uses eigenvalue solvers. In addition, for the communicating-channels geometry presented in this work, we have compared the experimentally- and numerically-obtained frequencies with the least stable Tollmien-Schlichting frequency (Amon et al., 1993). A Fourier-spectrum analysis for a flow at the near critical Reynolds number of 200 yields a nondimensional frequency of 0.821 compared to 0.832, which is the value of the least stable Tollmien-Schlichting frequency obtained from the solutions of the Orr-Sommerfeld equations.

The numerical calculations are performed on a mesh with 51 spectral elements using a Chebyshev collocation grid of 49 nodes per element. We consider this computational resolution to be adequate since computations performed on a refined mesh with 81 nodes per element revealed no differences on the oscillatory velocities and their time evolution up to the fifth significant digit, and the difference in the spatial spectral derivatives of the fluctuating velocity components is less than 1 percent. Further details of the mathematical formulation, numerical algorithm and DNS accuracy are reported in Amon et al. (1992) and (Majumdar, 1993). A typical run of 10000 time steps of 8.4×10^{-3} units of nondimensional time takes about 2600 CPU seconds on the Cray Y-MP/832.

III Analysis of the Fluctuating Kinetic Energy Equation

We consider the time-averaged kinetic energy equation for the fluctuating, self-sustained oscillatory components of the velocity:

$$\underbrace{\frac{D}{Dt}\overline{\frac{q^2}{2}}}_{\text{I}} = \underbrace{-\frac{\partial}{\partial x_i}\overline{u_i\left(\frac{p}{\rho}+\frac{q^2}{2}\right)}}_{\text{II}} \underbrace{-\overline{u_iu_j}\frac{\partial U_i}{\partial x_j}}_{\text{III}} + \underbrace{\upsilon\frac{\partial}{\partial x_i}\overline{u_j\left(\frac{\partial u_i}{\partial x_j}+\frac{\partial u_j}{\partial x_i}\right)}}_{\text{IV}} \underbrace{-\upsilon\overline{\left(\frac{\partial u_i}{\partial x_j}+\frac{\partial u_j}{\partial x_i}\right)\frac{\partial u_j}{\partial x_i}}}_{\text{V}} \quad (1)$$

where $q^2/2$ is the fluctuating kinetic energy, u_i is the fluctuating component of the velocity, p is the pressure fluctuation, $-\overline{u_iu_j}$ is the oscillatory shear stress, U_i is the time-averaged velocity, and ν is the kinematic viscosity. Term I corresponds to the rate of change in kinetic energy of the fluctuating components of the velocity including the convective transport by the mean motion; term II is the work due to the total dynamic pressure of the fluctuating flow which is the sum of transport of fluctuating motion by the pressure fluctuation and transport of kinetic energy by the velocity fluctuations; term III is the work of deformation of the mean motion performed by the oscillatory stresses, i.e., the production of kinetic energy of the fluctuating velocity components; term IV is the work done by the viscous shear stresses of the fluctuating motion, i.e., molecular diffusion of kinetic energy; and term V is the viscous dissipation of the fluctuating velocities—all per unit mass and time.

The derivatives in each term of the above equation are computed spectrally (Amon, 1993). Chebyshev collocation derivatives are obtained through matrix multiplication, namely,

$$(B_Nu)(x_1) = \sum_{j=0}^{N}(D_N)_{ij}u(x_j) \quad 1 = 0, \ldots N \quad (2)$$

where u is expanded in Chebyshev polynomials and N is the number of collocation points. The function B_Nu is the Chebyshev collocation derivative of u. The entries $(D_N)_{ij}$ can be computed by differentiating the Lagrangian interpolants, h_j, which at the Chebyshev-Gauss-Lobatto points, $x_j = \cos \pi j/N$, can be expressed as,

$$h_j(x) = \frac{2}{N}\sum_{n=0}^{N}\frac{1}{\bar{c}_j\,\bar{c}_n}T_n(x_j)T_n(x) \quad (3)$$

where $h_j(x_i) = \delta_{ji}$ and T_n are the Chebyshev polynomials defined as $T_n(\cos\theta) = \cos n\theta$ with $\bar{c}_j = 2$ if $j = 0, N$ and 1 if $1 \le j \le N-1$.

$$h_j'(x) = \frac{(-1)^{j+1}(1-x^2)T_N'(x)}{\bar{c}_jN^2(x-x_j)} \quad (4)$$

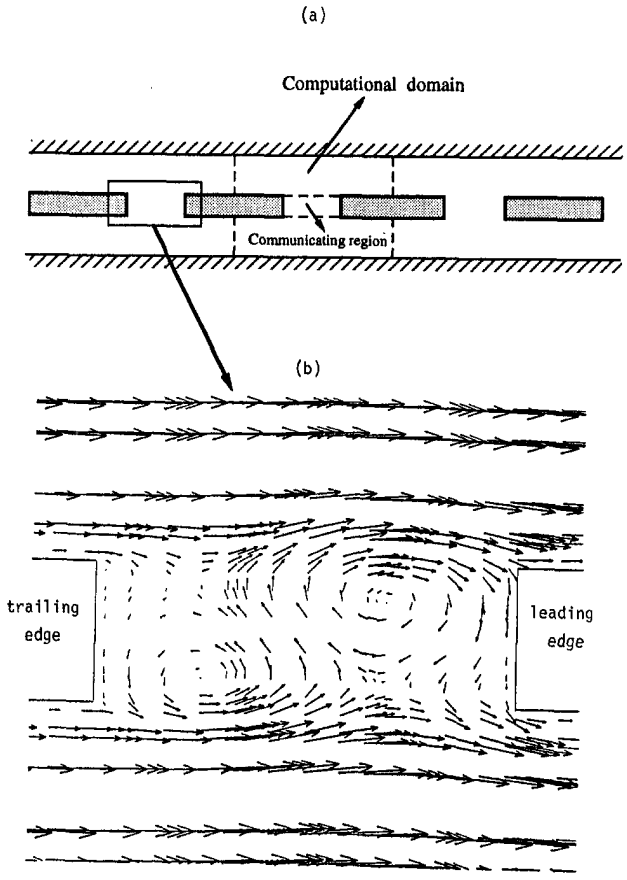

Fig. 2 *(a)* **Computational domain and** *(b)* **magnified instantaneous velocity-vector field in the communicating region**

$$(D_N)_{lj} = \begin{cases} \dfrac{\overline{c_l}}{\overline{c_j}} \dfrac{(-1)^{l+j}}{x_l - x_j} & l \neq j \\ \dfrac{-x_j}{2(1-x_j^2)} & 1 \leq l = j \leq N-1 \\ \dfrac{2N^2+1}{6} & l = j = 0 \\ -\dfrac{2N^2+1}{6} & l = j = N \end{cases} \tag{5}$$

To illustrate the calculation procedure of a typical term in Eq. (1), let us consider the production term $-\overline{u_i u_j}\partial U_i/\partial x_j$. The derivative of the time-averaged velocity $\partial U_i/\partial x_j$ at a particular location x_k for $i = j = 1$ is given by $\partial U/\partial x)_{x_k} = \sum_{j=0}^{N} (D_N)_{kj} U(x_j)$ where $(D_N)_{kj}$ is obtained from Eq. (5).

To evaluate $-\overline{u_i u_j}$, we first compute the fluctuating components of the velocity by subtracting the respective mean values from the instantaneous velocities obtained from DNS of the Navier-Stokes equations. The fluctuating velocity components are then multiplied at the collocation points and averaged over a time cycle.

IV Results

The computational domain is shown in Fig. 2(*a*) and an enlargement of an instantaneous velocity-vector field in the communicating region is shown in Fig. 2(*b*). Notice the presence of the vortical structures, trailing edge and leading edge to which we will frequently refer in the ensuing discussion.

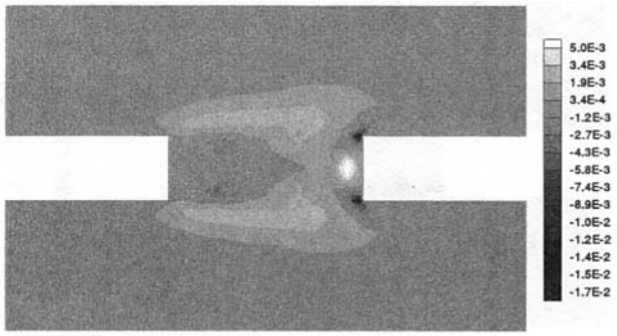

Fig. 3 Contour plot of the production of fluctuating kinetic energy

A Contour Plots of the Terms in the Fluctuating Kinetic Energy Equation. The contour plot of the production of kinetic energy of the fluctuating velocity components, i.e., term III in Eq. (1), is shown in Fig. 3, where the contour level magnitudes are indicated by the gray-scale bar. The presence of high positive values in the interfacial zone between the channels and the communicating region indicate that most of the fluctuating energy production is taking place here. Energy is extracted from the mean flow and passed on to the fluctuating components of the flow in this zone, which is comprised of the shear layer between the channels and the communicating region. Therefore, this zone supplies energy for the sustainment of the fluctuating flow. The vortical flow in the communicating region interacts with the nearly parallel flow in the main channel, generating and sustaining the oscillatory velocity components. In the communicating region, there are two distinctly different zones—the one near the leading edge which is a fluctuating kinetic energy producing zone (strong positive values) and the other near the trailing edge which exhibits negative values, causing a transfer of energy from the fluctuating to the mean flow. At the upper- and lower-right corners of the communicating region in Fig. 3, the production of fluctuating kinetic energy attains strong negative values. Therefore, oscillatory flow components transfer energy to the mean flow where the flow has to turn at the corners of the leading edge.

The contour plot of the pressure fluctuation part of term II (henceforth referred to as the pressure fluctuation term) is depicted in Fig. 4. The velocity fluctuation part of term II is at least one order of magnitude smaller than the pressure fluctuation part and hence does not contribute significantly to the energy transfer. Near the center of the leading edge vertical wall and in areas of the communicating region, the pressure fluctuation term is positive whereas in other areas of the domain, particularly in the two channels, there exist negative values. The positive zones in the communicating region are where most of the kinetic energy of the fluctuating flow is sustained due to pressure fluctuations.

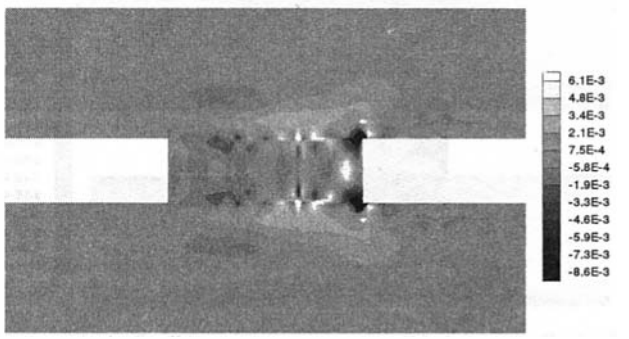

Fig. 4 Contour plot of the work done by the pressure fluctuation

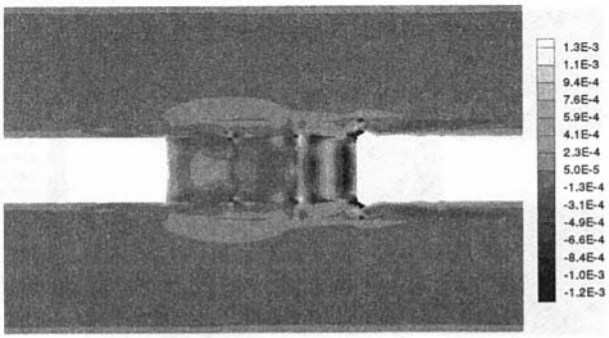

Fig. 5 Contour plot of the work done by the viscous shear stresses of the fluctuating motion

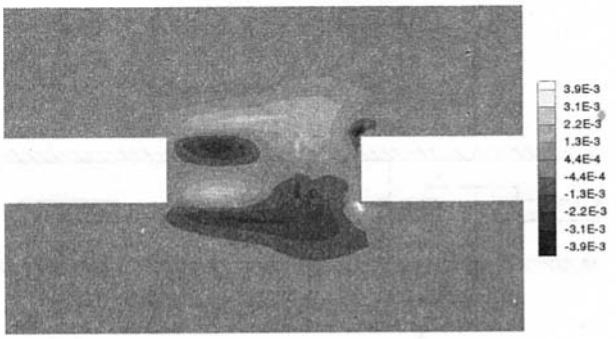

Fig. 7 Contour plot of the oscillatory shear stress, $-\overline{uv}$

Figures 5 and 6 depict the contour diagrams of the diffusion and dissipation contributions, i.e., terms IV and V, respectively. Near the leading and trailing edges in the communicating region, these terms are very high in magnitude as both are functions of gradients of the fluctuating velocity. Strong velocity gradients are indeed present near the walls and the velocity gradients at the leading edge are higher than those at the trailing edge because of the sudden contraction, so that both diffusion and dissipation near the right wall are higher. Similar boundary-layer-type behavior is noticed near the upper and lower continuous walls of the domain as well. The gradient-free central regions of the channels exhibit an almost constant and lower-valued field, whereas the shear layers between the channels and the communicating regions indicate substantial dissipation and diffusion.

These contour diagrams share two major characteristics. First, all of them show a marked bulge in the interfacial zone between the communicating region and the channels. This is attributed to the ejection of the vortices from the communicating region into the main channels, which primarily occurs by disrupting the shear layer between the communicating region and the channels (Fig. 2(*b*)). Second, the communicating regions of all the diagrams indicate the presence of strong gradients of the respective quantities and, in some instances, even zones of alternating signs which are reflective of strong mixing and vigorous energy exchange between the mean and the oscillatory motions.

B Oscillatory Shear Stress and Transitional Viscosity. Following an approach similar to that used in turbulent flows (Hinze, 1975), we define the transitional viscosity, υ_{tr}, by

$$-\overline{u_i u_j} = (\upsilon_{tr})_{ik}\left(\frac{\partial U_j}{\partial x_k} + \frac{\partial U_k}{\partial x_j}\right) \tag{6}$$

where $-\overline{u_i u_j}$ is the oscillatory shear stress corresponding to the fluctuating components of the velocity. We assume a second-order tensor for υ_{tr} and expand Eq. (6) to obtain:

$$-\overline{u^2} = (\upsilon_{tr})_{11}\left(\frac{\partial U}{\partial x} + \frac{\partial U}{\partial x}\right) + (\upsilon_{tr})_{12}\left(\frac{\partial U}{\partial y} + \frac{\partial V}{\partial x}\right) \tag{7a}$$

$$-\overline{v^2} = (\upsilon_{tr})_{21}\left(\frac{\partial U}{\partial y} + \frac{\partial V}{\partial x}\right) + (\upsilon_{tr})_{22}\left(\frac{\partial V}{\partial y} + \frac{\partial V}{\partial y}\right) \tag{7b}$$

$$-\overline{uv} = (\upsilon_{tr})_{11}\left(\frac{\partial U}{\partial y} + \frac{\partial V}{\partial x}\right) + (\upsilon_{tr})_{12}\left(\frac{\partial V}{\partial y} + \frac{\partial V}{\partial y}\right) \tag{7c}$$

$$-\overline{uv} = (\upsilon_{tr})_{21}\left(\frac{\partial U}{\partial x} + \frac{\partial U}{\partial x}\right) + (\upsilon_{tr})_{22}\left(\frac{\partial U}{\partial y} + \frac{\partial V}{\partial x}\right) \tag{7d}$$

If we assume a scalar value for $(\upsilon_{tr})_{ik}$, Eq. (6) would become:

$$-\overline{uv} = (\upsilon_{tr})\left(\frac{\partial U}{\partial y} + \frac{\partial V}{\partial x}\right) \tag{8}$$

The contour diagram of $-\overline{uv}$ is depicted in Fig. 7 where the asymmetry about the horizontal mid-plane of the domain is a result of the asymmetric nature of the y-velocity component. Near the walls, $-\overline{uv}$ exhibits extremely small values which reflect the dominance of molecular momentum transport in these regions. We also notice the presence of adjacent regions with opposite signs, e.g., in the upper channel. The shear layer between the channel and the communicating region is a predominantly positive zone which borders with two strongly negative zones in the communicating channels, one near the left vertical wall and the other near the upper-right corner. The nearly-parallel flow in the main channel suddenly encounters the vortical motions of the communicating region that cause the oscillatory shear stress to change signs. Peak absolute values of $-\overline{uv}$ also occur in these regions signifying strong momentum transport due to the oscillatory flow and the strong interactions between the vortical motions and the channel flow.

The contributions to the oscillatory shear stress $-\overline{uv}$ from the two components of υ_{tr} in Eq. (7*c*), i.e., $(\upsilon_{tr})_{11}$ and $(\upsilon_{tr})_{12}$ multiplied by the associated velocity gradient term, are shown in Fig. 8. The contour plot of $(\upsilon_{tr})_{11}$ closely resembles that of $-\overline{uv}$ in Fig. 7. In fact, a comparison of Figs. 8(*a*) and (*b*) (more apparent from the enlarged channel plots) reveals that in the channel regions, the contribution from $(\upsilon_{tr})_{11}$ is larger than the contribution from $(\upsilon_{tr})_{12}$ by about two orders of magnitude. This implies that the flowfield is nearly isotropic in the channels and the scalar representation of υ_{tr} given by Eq. (8) can be used without inducing much error. However, in the recirculating flow regions, the contributions from $(\upsilon_{tr})_{11}$ and $(\upsilon_{tr})_{12}$ are approximately of the same order of magnitude due to the presence of streamline curvatures in the large-scale vortical

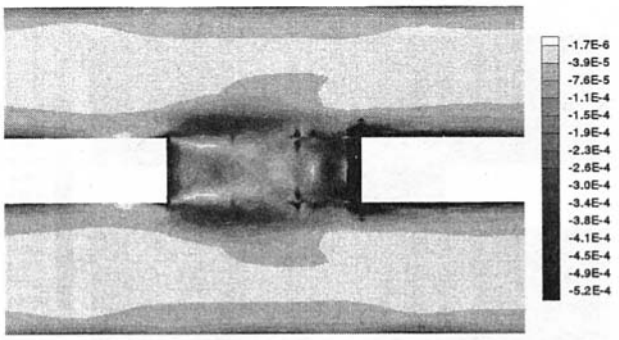

Fig. 6 Contour plot of the viscous dissipation of the fluctuating velocities

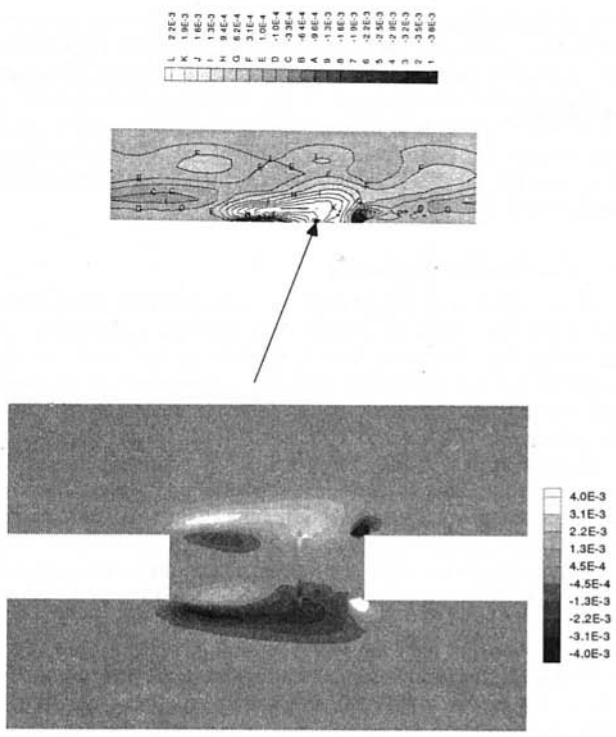

Fig. 8(*a*)

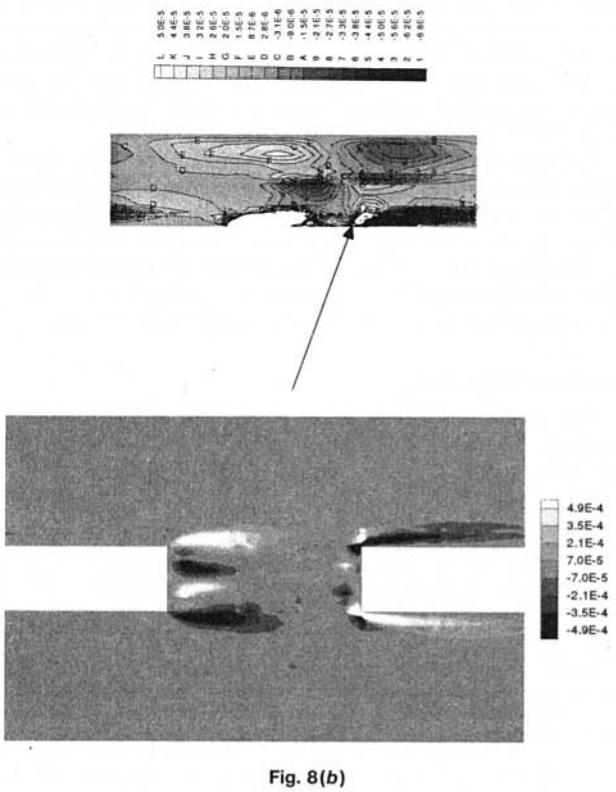

Fig. 8(*b*)

Fig. 8 Contour plot of contributions to $-\overline{uv}$ in Eq. (7*c*) from (*a*) $(\upsilon_{tr})_{11}$ and (*b*) $(\upsilon_{tr})_{12}$

structures and therefore the tensor equation must be used to accurately evaluate the transitional viscosity. The contour diagram of $(\upsilon_{tr})_{11}$ shown in Fig. 9, depicts a pattern that is strikingly similar to the plot of υ_{tr} obtained from the scalar Eq. (8). We notice the presence of negative values in several regions of the domain. Negative values of the transitional viscosity as defined in Eq. (8) may occur if there is a change in the sign of the

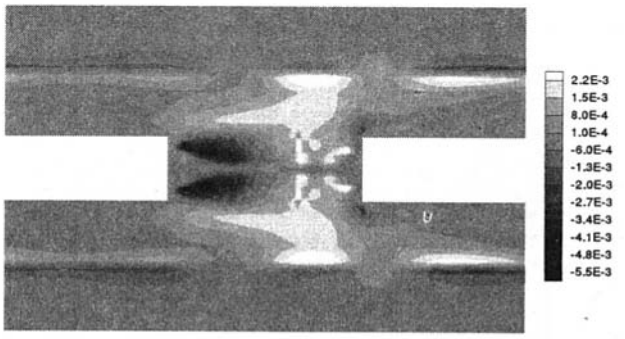

Fig. 9 Contour plot of the transitional viscosity, $(\upsilon_{tr})_{11}$, defined by Eq. (7*c*)

velocity gradients or the velocity fluctuations, so that the signs of the shear stress and the velocity gradients are no longer the same. This can be appreciated from Fig. 10 where the distributions of $-\overline{uv}$ and υ_{tr} are plotted along the transverse direction at a particular streamwise location in the upper channel. Figure 10(*b*) shows that υ_{tr} is negative in the channel's upper half for y/h values between 0.0 and 1.0. In this region, the velocity gradient $\partial U/\partial y$ is negative and $\partial V/\partial x$ is at least three orders of magnitude smaller, so the negative sign of υ_{tr} is determined

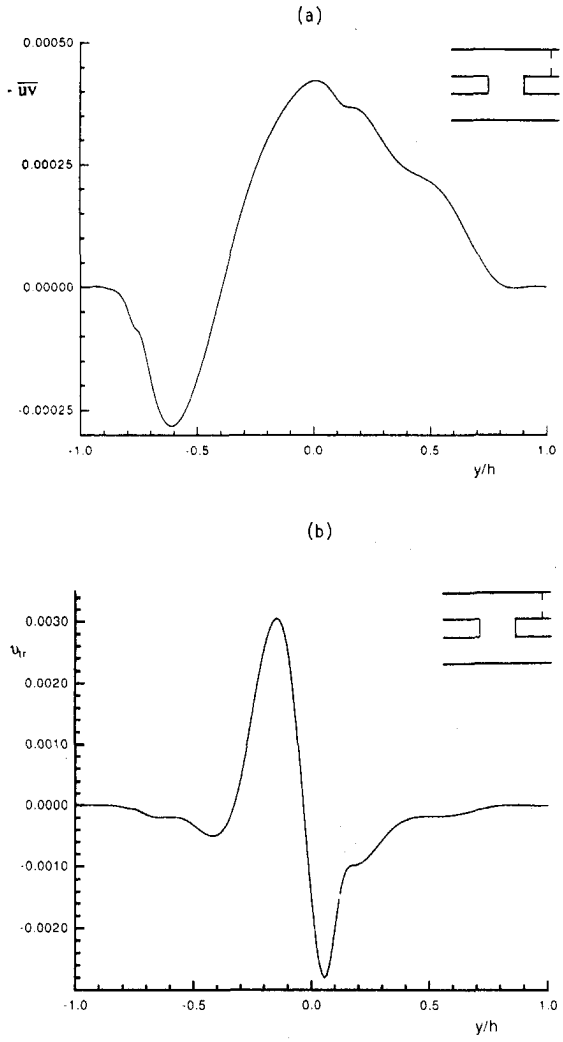

Fig. 10 Distribution of (*a*) oscillatory shear stress, $-\overline{uv}$, and (*b*) transitional viscosity, υ_{tr}, across the transverse direction at $x/h = 7.375$

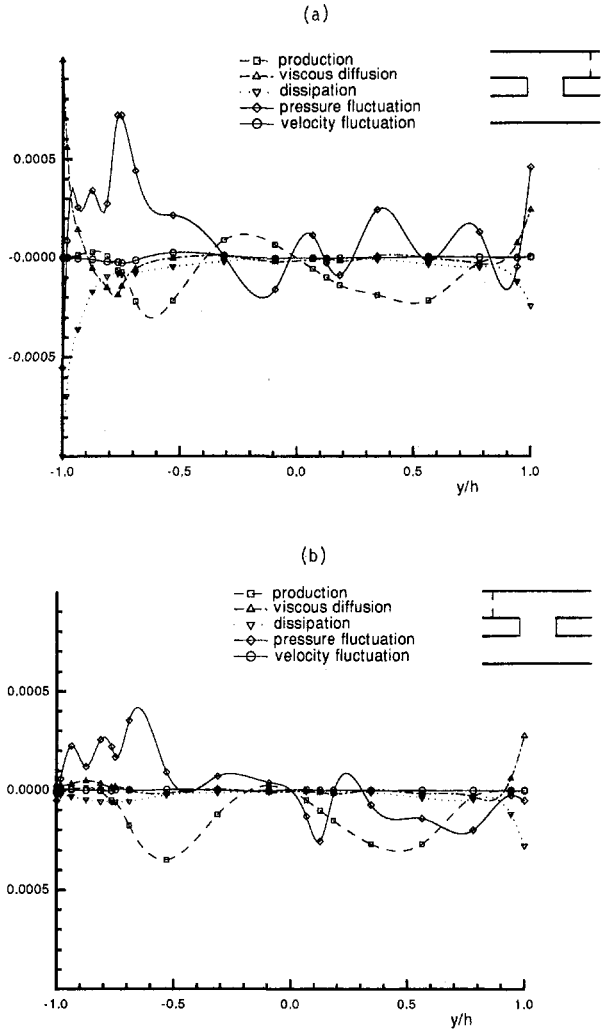

Fig. 11 Fluctuating kinetic energy budget profiles at a streamwise location (*a*) near and (*b*) far downstream of the leading edge

by the positive sign of the oscillatory shear stress, $-\overline{uv}$ (Fig. 10(a)) and $\partial U/\partial y$ in Eq. (8).

C Kinetic Energy Budget. The fluctuating kinetic energy budget profiles are shown in Figs. 11(a) and (b) at two different streamwise locations near the leading edge and downstream of the leading edge, respectively. In addition to the terms in Eq. (1), we expand the dynamic pressure contribution (term II) into its two components to investigate the contribution of the transport of fluctuating motion due to static pressure fluctuations and transport of kinetic energy due to velocity fluctuations. The alternating signs of the terms in Fig. 11 represent the continuous exchange of energy between the mean and oscillatory motions. In general, the pressure fluctuation term and the production term are the dominant terms and, for the most part, balance each other except near the walls. The component responsible for transport of kinetic energy due to the velocity fluctuations in term II is negligible. The dissipation and the diffusion terms are also relatively insignificant. This is in contrast to the corresponding turbulent kinetic energy budgets in fully-developed plane channel flow where production balances dissipation of turbulent kinetic energy in the region just outside the near wall, and the turbulent transport term due to velocity fluctuations balances dissipation in the core region (Lyons and Hanratty, 1991). Although Figs. 11(a) and (b) depict similar scenarios on an overall basis, there is one important difference due to the streamwise location. At both walls in Fig. 11(a) and at the continuous upper wall in Fig. 11(b), the pressure fluctuation, diffusion and dissipation terms attain high values because of the presence of strong velocity gradients. However, in Fig. 11(b), all the terms at the interrupted wall ($y/h = -1.0$) are close to zero because this streamwise location is far downstream the boundary layer restarting at the leading edge. Consequently, near-wall gradients are smaller and so are all the terms in the fluctuating kinetic energy equation.

V Concluding Remarks

Direct numerical simulations of self-sustained transitional flows are performed to identify mechanisms responsible for sustaining the fluctuating flow by evaluating the kinetic energy equation for the fluctuating velocity components. It is found that the pressure fluctuation contributes to sustaining the flow fluctuations in the vortical communicating region whereas the production term is mainly responsible for sustaining the fluctuating kinetic energy in the near-parallel channel flow. Most of the fluctuating energy production takes place at shear layers between the channel and the communicating region flows. Near the upper- and lower-right corners of the communicating region, fluctuating velocity components transfer energy to the mean motion. The viscous contributions of the diffusion and dissipation are dominant near the walls, attaining higher values at the leading edge due to the sudden contraction in the flow geometry. The bulge in the interfacial zones between the channels and the communicating region is synchronized with the ejection of vortices into the main flow. The distributions of the oscillatory shear stress and transitional viscosity due to the fluctuating velocity components exhibit negative values due to the presence of recirculation zones in the communicating region. The values of the transitional viscosity are particularly high near the communicating region walls, promoting a local augmentation of momentum transport.

The kinetic energy budget of the fluctuating velocity components reveals that the pressure fluctuation and the production terms are mainly responsible for the exchange of energy between the mean and fluctuating flow. The peak values of the pressure fluctuation are larger than those of the production term, unlike turbulent flow in fully-developed plane channels where the contribution of the pressure fluctuation is negligible.

Acknowledgments

The authors gratefully acknowledge the support from the National Science Foundation grants CTS-9311072 and CTS-9630801.

References

Amon, C. H., Guzmán, A. M., and Morel, B., 1996, "Lagrangian Chaos, Eulerian Chaos and Mixing Enhancement in Converging-Diverging Channel Flows," *Physics of Fluids,* Vol. 8, No. 5, pp. 1192–1206.

Amon, C. H., 1993, "Spectral Element-Fourier Method for Transitional Flows in Complex Geometries," *AIAA Journal,* Vol. 31, No. 1, pp. 42–48.

Amon, C. H., Majumdar, D., Herman, C. V., and Mikic, B. B., 1993, "Numerical and Experimental Visualization of Fast-Evolving Heat Transfer Phenomena in Self-Sustained Oscillatory Flows," *Experimental and Numerical Flow Visualization,* ASME-Fluids Engineering Division, Vol. 172, pp. 351–358.

Amon, C. H., Herman, C. V., Majumdar, D., Mayinger, F., Mikic, B. B., and Sekulic, D., 1992, "Numerical and Experimental Studies of Oscillatory Flows in Communicating Channels," *International Journal of Heat and Mass Transfer,* Vol. 35, pp. 3115–3129.

Amon, C. H., and Patera, A. T., 1989, "Numerical Calculation of Stable Three-Dimensional Tertiary States in Grooved-channel Flows," *Physics of Fluids A,* Vol. 1, No. 12, pp. 2005–2009.

Ghaddar, N. K., Korczak, K. Z., Mikic, B. B., and Patera, A. T., 1986, "Numerical Investigation of Incompressible Flow in Grooved Channels. Part 2. Resonance and Oscillatory Heat-Transfer Enhancement," *Journal of Fluid Mechanics,* Vol. 168, pp. 541–567.

Goel, P., and Amano, R. S., 1986, "Turbulence Energy and Diffusion Transport in a Separating and Reattaching Flow," *AIAA Journal,* Vol. 86, p. 1724.

Greiner, M., Chen, R. F., and Wirtz, R. A., 1991, "Enhanced Heat Transfer/Pressure Drop Measured from a Flat Surface in a Grooved Channel," ASME *Journal of Heat Transfer,* Vol. 113, pp. 498–501.

Guzmán, A. M., and Amon, C. H., 1994, "Transition to Chaos in Converging-Diverging Channel Flows: Ruelle-Takens-Newhouse Scenario," *Physics of Fluids,* Vol. 6, pp. 1994–2002.

Guzmán, A. M., and Amon, C. H., 1996, "Dynamical Flow Characterization of Transitional and Chaotic Regimes in Converging-Diverging Channels," *Journal of Fluid Mechanics,* Vol. 321, pp. 25–57.

Hinze, J. O., 1975, *Turbulence,* 2nd ed., McGraw-Hill, New York.

Humphrey, J. A. C., and Whitelaw, J. H., 1980, "Turbulent Flow in a Duct with Roughness," *Turbulent Shear Flows II,* J. S. Bradbury et al., eds., Springer-Verlag, Berlin, pp. 174–188.

Kasagi, N., Tomita, Y., and Kuroda, A., 1992, "Direct Numerical Simulation of Passive Scalar Field in a Turbulent Channel Flow," ASME *Journal of Heat Transfer,* Vol. 114, pp. 598–606.

Kim, J., and Moin, P., 1989, "Transport of Passive Scalars in a Turbulent Channel Flow," *Turbulent Shear Flows VI,* J.-C. Andre et al., eds., Springer-Verlag, Berlin, pp. 85–96.

Kurosaki, Y., Kashiwagi, T., Kobayashi, H., and Uzuhashi, H., 1988, "Experimental Study on Heat Transfer from Parallel Louvered Fins by Laser Holographic Interferometry," *Experimental Thermal Fluid Science,* Vol. 1, pp. 59–67.

Lyons, S. L., and Hanratty, T. J., 1991, "Direct Numerical Simulation of Passive Heat Transfer in a Turbulent Channel Flow," *International Journal of Heat and Mass Transfer,* Vol. 34, pp. 1149–1161.

Majumdar, D., and Amon, C. H., 1992, "Heat and Momentum Transfer in Oscillatory Viscous Flows," ASME *Journal of Heat Transfer,* Vol. 114, pp. 866–875.

Majumdar, D., 1993, "Fluid Flow and Heat Transfer Mechanisms of Self-Sustained Oscillations in Communicating Channels," Ph.D. thesis, Carnegie Mellon University, Pittsburgh, PA.

Manglik, R. M., and Bergles, A. E., 1989, "The Thermal-hydraulic Design of Rectangular Offset-strip-fin Compact Heat Exchanger," *A. L. London Symposium on Compact Heat Exchangers,* Stanford.

Nigen, J. S., and Amon, C. H., 1994, "Time-Dependent Conjugate Heat Transfer Characteristics of Self-Sustained Oscillatory Flows in a Grooved Channel," ASME JOURNAL OF FLUIDS ENGINEERING, Vol. 116, pp. 499–507.

Orszag, S. A., and Kells, L. C., 1980, "Transition to Turbulence in Plane Poiseuille and Plane Couette Flows," *Journal of Fluid Mechanics,* Vol. 96, pp. 159–205.

Patera, A. T., 1984, "A Spectral Element Method for Fluid Dynamics: Laminar Flow in a Channel Expansion," *Journal of Computational Physics,* Vol. 54, pp. 468–477.

Schatz, M. F., and Swinney, H. L., 1992, "Secondary Instability in Plane Channel Flow with Spatially Periodic Perturbations," *Physics Review Letter,* Vol. 69, p. 434.

Suzuki, K., Xi, G. N., Inaoka, K., and Hagiwara, Y., 1994, "Mechanism of Heat Transfer Enhancement Due to Self-sustained Oscillation for an In-line Fin Array," *International Journal of Heat and Mass Transfer,* Vol. 37, pp. 83–96.

Wang, G., and Vanka, S. P., 1995, "Self-Sustained Unsteady Flow in Periodic Wavy Passages," *Unsteady Flows,* ASME-Fluids Engineering Division, Vol. 216, pp. 37–42.

Webb, R. L., 1990, "The Flow Structure in the Louvered Fin Heat Exchanger Geometry," SAE #900722, International Congress & Exposition, Detroit, MI.

The Effect of Pressure Gradients on Transition Zone Length in Hypersonic Boundary Layers

R. L. Kimmel
Aerospace Engineer,
Aeromechanics Division,
2645 Fifth St Ste 7,
Wright Laboratory,
Wright Patterson Air Force Base, OH
45433-7913

Boundary layer transition was measured in zero, favorable, and adverse pressure gradients at Mach 8 using heat transfer. Models consisted of 7° half angle forecones 0.4826 m long, followed by flared or ogive aft bodies 0.5334 m long. The flares and ogives produced constant pressure gradients. For the cases examined, favorable pressure gradients delay transition and adverse pressure gradients promote transition, but transition zone lengths are shorter in favorable pressure gradient. Results of the effect of adverse pressure gradient on transition zone lengths were inconclusive.

Introduction

Transition zone phenomena, even in zero pressure gradient flow, are less clearly defined at hypersonic speeds than at lower speeds. The hypersonic transition zone length in zero pressure gradient is often assumed to be equal to the laminar length. Data obtained by Owen et al. (1974), Richards and Stollery (1966), Cary (1968), McCauley et al. (1966), and Sanator et al. (1965) on cones and flat plates show a range of transition zone lengths, x_e/x_b, from 1.6 to 2.4. These experiments used surface hot film, heat transfer, and recovery temperature measurements for transition detection. The wall-to-stagnation temperature ratio was varied by Cary (1968) and Sanator et al. (1965), but had little effect on the transition zone length. All of these experiments were done in conventional hypersonic facilities. Recovery temperature measurements in the NASA Langley $M = 3.5$ low disturbance pilot facility (Chen, 1993) showed transition zone length ratios of 1.1 to 1.2 under low disturbance conditions, and ratios of approximately 2.0 under elevated disturbance conditions.

Jack (1958) examined the effect of favorable pressure gradient on transition on bodies of revolution at Mach 3.12. Published recovery temperature data from this test do not show a clear trend. Jack tested configurations which produced constant favorable pressure gradients $d(p/p_\infty)/dx$ of 0, −0.002, and −0.004 per mm, which produced transition lengths, x_e/x_b, of 2.6, 1.7, and 3.6, respectively. The transition phenomena are expected to be sufficiently different at higher Mach number that Jack's results cannot reliably be extrapolated to higher Mach.

Experiment

Tests were conducted at Arnold Engineering Development Center (AEDC) tunnel B at a nominal freestream Mach number of 7.93. Models with nondimensional pressure gradients of −2, −1, 0, 1, and 4 were tested at a variety of unit Reynolds numbers. The test matrix is summarized in Table 1.

The baseline model (configuration 0) consisted of a 7° half angle, sharp-nosed cone. The pressure gradient models consisted of a single conical forebody, 0.4826 m long, and interchangeable power-law flared or ogive aft-bodies 0.5334 m long (configurations −2, −1, 1, and 4). A quintic fillet between the end of the cone at $x/L = 0.475$ and the beginning of the power law aft-body at $x/L = 0.550$ was chosen to match radius, first, and second derivatives between the cone and the flare. The design of the models is described in Shope (1991) and Spinetti and Shope (1991). The flare and ogive contours were calculated to provide constant pressure gradients. Configuration 1, for example, is so named because it's gradient would produce a 100 percent rise above the cone pressure coefficient, c_p, over the model reference length L. Since the flare length was 50 percent of the model length, the pressure coefficient rose 50% above the cone level by the end of the model. All models were constructed of stainless steel, with approximately 6.4 mm wall thickness. The nose radius was nominally 0.05 mm. The complete equations for the flare geometries are given in Table 2.

The models were instrumented with pressure taps and Schmidt-Boelter heat transfer gauges. Model surface temperature was measured directly from the Schmidt-Boelter gauges. Pressure taps and heat transfer gauges were installed at 50.8 mm intervals from $x/L = 0.300$ to $x/L = 0.450$, inclusive, on the cone, and at 25.4 mm intervals between $x/L = 0.550$ and $x/L = 0.925$, inclusive, on the power-law aft-body. Pressure taps and heat transfer gauges were installed on the 180 and 90° meridians, respectively. Heat transfer measurements were made by injecting the model, measuring heat transfer, and removing the model after several seconds before significant heating occurred. Between measurements, the model was cooled to nominal room temperature. The nominal wall-to-stagnation temperature ratio for all transition measurements was 0.42, ± five percent.

Caveats regarding the data are necessary. Transition Reynolds numbers obtained in the experiment are expected to be lower than free flight transition Reynolds numbers (Beckwith, 1975). However, hot wire measurements obtained in this facil-

Table 1 Test matrix

	Configuration				
Re_∞ m^{-1}	−2	−1	0	+1	+4
1.6×10^6 m^{-1}	*XX*	*	*XX*	*B*	*B*
3.3×10^6 m^{-1}	*	*B*	B_c	*B*	*B*
3.9×10^6 m^{-1}	*XX*	*XX*	B_c	*XX*	*XX*
4.9×10^6 m^{-1}	B_c, *E*	B_c, *E*	*XX*	B_c, *E*	*B*, *E*
6.6×10^6 m^{-1}	B_c, *E*	B_c, *E*	B_c, *E*	B_c, *E*	B_c, *E*
8.2×10^6 m^{-1}	*XX*	*XX*	B_c, *E*	*XX*	*XX*

$M_\infty = 7.93$
$T_0 = 722$ K
$T_w/T_0 = 0.42$
XX—Not tested
*—Completely laminar
B—Beginning of transition on model
B_c—Transition beginning on cone
E—End of transition on model

Contributed by the Fluids Engineering Division for publication in the JOURNAL OF FLUIDS ENGINEERING. Manuscript received by the Fluids Engineering Division July 1, 1996; revised manuscript received July 22, 1996. Associate Technical Editor: D. P. Telionis.

Table 2 Model geometry coefficients

Coefficient	Configuration −2	−1	+1	+4
B	−1.9	−1.0	1.0	4.0
m	1.595	1.5	1.5	1.43
a_0	−1.760775	-7.747701×10^{-1}	7.584605×10^{-1}	2.502281
a_1	1.779659×10^{1}	7.901532	−7.498973	-2.505959×10^{1}
a_2	-7.074643×10^{1}	-3.114571×10^{1}	3.054475×10^{1}	1.010698×10^{2}
a_3	1.411183×10^{2}	6.214336×10^{1}	-6.100083×10^{1}	-2.021491×10^{2}
a_4	-1.402110×10^{2}	-6.176131×10^{1}	6.068375×10^{1}	2.014049×10^{2}
a_5	5.548435×10^{1}	2.444745×10^{1}	-2.404474×10^{1}	-7.992703×10^{1}

$$\frac{r(x/L)}{L} = \frac{x}{L}\tan(\theta) \qquad \frac{x}{L} \le 0.475$$

$$\frac{r(x/L)}{L} = a_0 + a_1\left(\frac{x}{L}\right) + a_2\left(\frac{x}{L}\right)^2 + a_3\left(\frac{x}{L}\right)^3 + a_4\left(\frac{x}{L}\right)^4 + a_5\left(\frac{x}{L}\right)^5 \qquad 0.475 \le \frac{x}{L} \le 0.55$$

$$\frac{r(x/L)}{L} = \frac{x_c}{L}\tan(\theta) + \frac{\tan(\theta)}{Bm}\left\{\left[B\left(\frac{x}{L} - \frac{x_c}{L}\right) + 1\right]^m - 1\right\} \qquad \frac{x}{L} \ge 0.55$$

ity on these and other conical configurations show that the dominant instability is second mode (Stetson et al., 1983). Experimental wall cooling, nose bluntness, and Mach number transition trends measured in this facility have been shown to be described qualitatively by linear theory (Stetson and Kimmel, 1992). Thus, the instability processes leading up to the beginning of transition are not noise dominated.

Another warning regarding the experiment is that it was designed to obtain hot wire data on second mode instabilities, and was not optimized for transition experiments. In particular, the instrumentation is sparse, especially at the cone-power-law juncture. This leads to uncertainty in the transition location, as discussed below. The cone-power-law configuration was chosen so that the pressure gradient would be imposed on second mode waves which had been well-developed on the cone. Because of this, transition begins at various points either on the cone or the flare, depending on the unit Reynolds number, and thus the transitional region shows varying degrees of influence from the pressure gradient.

The primary sources of inaccuracy in the transition measurements are the accuracy of the heat transfer gauges and the uncertainty in the location of maxima and minima in heat transfer due to gauge spacing. Donaldson and Hatcher (1988) ascribe an accuracy of ± five percent to the gauges. Measurements show good run-to-run precision, with variations of less than one percent. This accuracy estimate may be assessed by fairing a ± five percent band about the predicted heat transfer estimate for a cone, and comparing it to the measurements. Most of the gauges fall within ± five percent of theoretical, although some gauges fall outside of this band. A more conservative estimate of transducer accuracy would be ± ten percent.

Uncertainty in the transition beginning and end locations is difficult to assess. The minimum error in transition onset is ±50.8 mm, which is the heat transfer gauge spacing on the pressure gradient model forecones. In practice, the primary source of uncertainty is scatter in the heat transfer values, which makes determination of the maximum and minimum heat transfer locations somewhat subjective. This source of error is also the most difficult to quantify.

Results

Surface static pressure results in Fig. 1 show that the flares produced nearly constant pressure gradients. The slope of the pressure rises shown in the figure are measured values obtained by linear regression of the data.

Pressure data for roll orientations of 0 and 180° for configuration 1 showed that this model was inadvertently installed at angle of attack AEDC angle of attack correlations for a 7° cone (Donaldson and Hatcher, 1988) show that the angle of attack of configuration 1 was approximately 0.4 to 0.8°. All heat transfer measurements were made on the leeward side of the model. Calculations of heat transfer and momentum thickness described below assumed zero angle of attack.

Edge unit Reynolds numbers obtained from boundary layer surveys on the adverse pressure gradient models at a freestream unit Reynolds number of 3.3×10^6 m^{-1} are shown in Fig. 2. The boundary layer surveys were obtained after the models had

Nomenclature

a_i = coefficients for 5th-order polynomial fillet (Table 2)
B = pressure gradient parameter (Table 2)
C_p = pressure coefficient, $(p - p_\infty)/q_\infty$
h = specific enthalpy of air, kJ/kg
L = model reference length, 1.016 m
M = Mach number
m = coefficient in power-law body description (Table 2)
p = pressure, kPa
q = dynamic pressure, $1/2\rho U^2$
$\dot{q}$ = heat transfer rate per unit area, W/m^2
Re = Reynolds number
Re_u = Unit Reynolds number, m^{-1}
r = model cross-sectional radius, m
s = arc length along model surface, m
St = Stanton number, $\dot{q}/(\rho_\infty U_\infty(h(T_0) - h(T_w)))$
T = temperature, K
U = velocity, m/s
x = distance along model longitudinal axis, m
x_c = reference length, 0.508 m
ρ = density, kg/m^3
θ = cone half angle, 7°

Subscripts

b = beginning of transition
c = conical forebody
e = end of transition, boundary layer edge
tr = transition
w = wall
∞ = freestream conditions upstream of model bow shock
0 = stagnation conditions

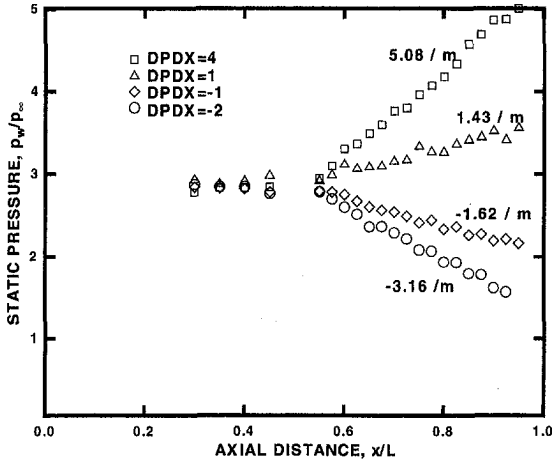

Fig. 1 Static Pressure

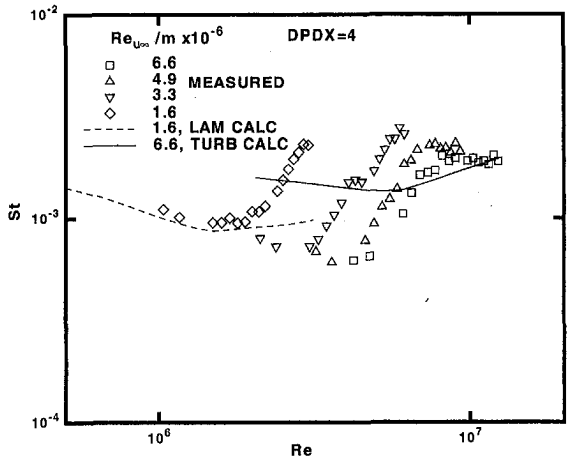

Fig. 3 Heat transfer, DPDX = 4 configuration

heated to adiabatic conditions, but adiabatic wall edge conditions are essentially identical to cooled wall edge conditions. Although velocity decreases and viscosity increases through the adverse pressure gradient, static density increases faster, so the local unit Reynolds number increases through the pressure gradient. The effect is pronounced on configuration 4, but relatively small on configuration 1.

Since only limited flow field surveys were available for the favorable pressure gradient models, their edge unit Reynolds numbers were calculated using the BLIMP (Boundary Layer Integral Matrix Procedure) program (Murray, 1987 and Kendall, 1968). Comparison of the BLIMP calculations to the experiment (Fig. 2) for the adverse pressure gradient configurations lend confidence to the favorable pressure gradient computations. The discrepancy between the configuration 1 measured and calculated values are due to the model angle of attack.

Laminar boundary layer momentum thicknesses for a freestream unit Reynolds number of 1.6×10^6 m^{-1} were calculated using the BLIMP program and used along with the model radii of curvature to calculate Görtler number. Transition began on the flare at this Reynolds number only. The Görtler numbers at transition were less than 2.3. Given the calculated Görtler number and the significant second mode component measured using hot wire anemometry (Kimmel, 1993), Görtler instability may have been present but probably was not dominant.

The heat transfer data in their entirety are plotted in Figs. 3 to 7. Laminar heating at the lowest unit Reynolds number tested for each configuration and turbulent heating at the highest unit Reynolds number tested for each configuration, as calculated with the BLIMP program, are shown for comparison. For all calculations, the origin of the turbulent boundary layer was taken at the cone apex. This produces some error in the magnitude of predicted heat transfer in the turbulent region. However, the goal of the computations was only to provide trends of heat transfer versus x to aid in transition location determination,

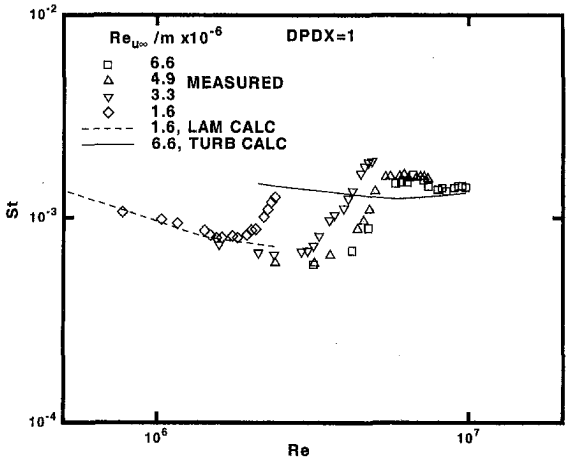

Fig. 4 Heat transfer, DPDX = 1 configuration

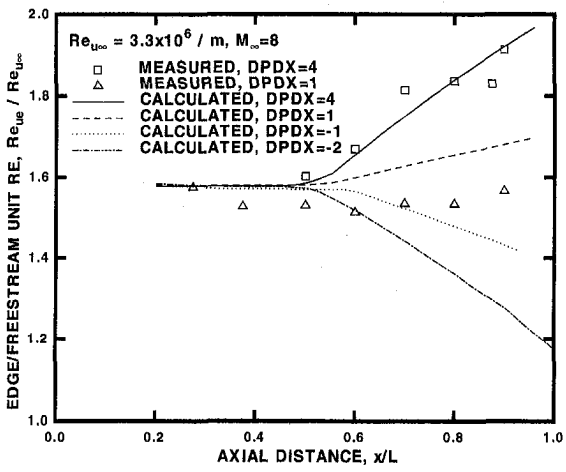

Fig. 2 Boundary layer edge unit Reynolds numbers

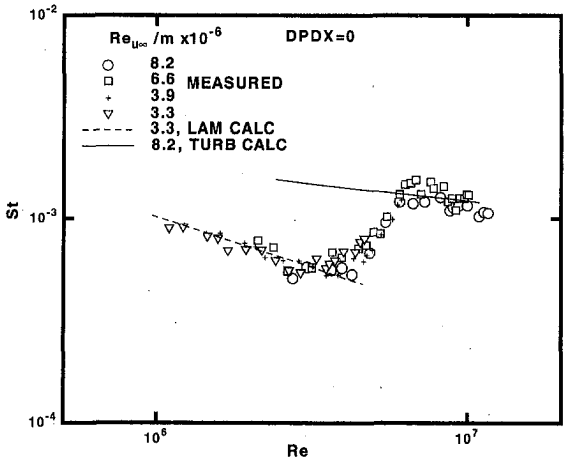

Fig. 5 Heat transfer, DPDX = 0 configuration

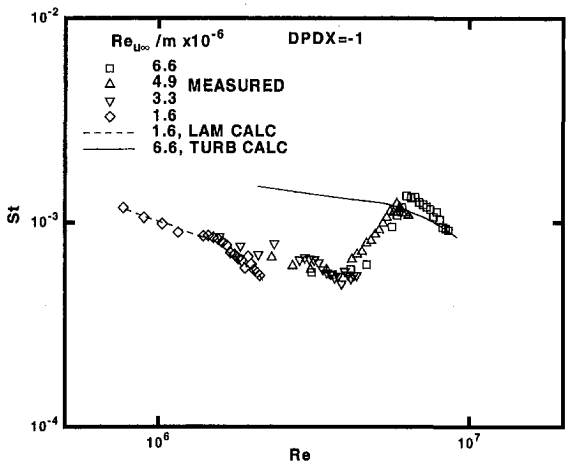

Fig. 6 Heat transfer, DPDX = −1 configuration

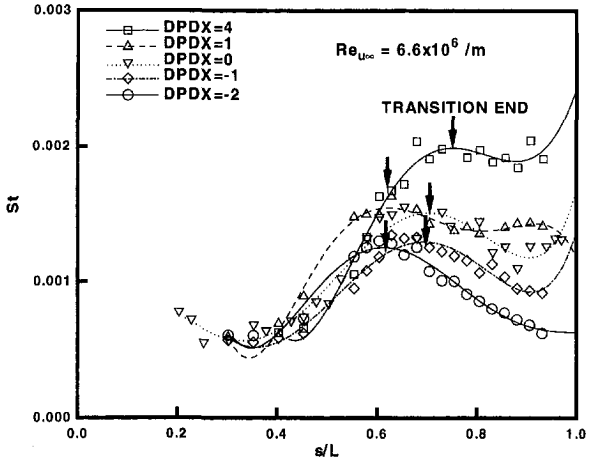

Fig. 8 Heat transfer, $Re_{u\infty} = 6.6 \times 10^6$ m^{-1}

not to provide accurate heat transfer magnitudes. Laminar heat transfer in zero pressure gradient is proportional to the $-1/2$ power of x, as expected. Turbulent data show more scatter, but have roughly a $-1/5$ power dependence for zero pressure gradient.

Heat transfer trends in the presence of pressure gradient are more complex. An adverse pressure gradient in incompressible flow causes boundary layer thickness to increase and heat transfer to decrease compared to zero-pressure gradient values, but the opposite trends occur in compressible flow. This is primarily because of streamtube compression and expansion and Mach number changes due to pressure gradients in compressible flow. Consequently, wall shear and heat transfer decrease more slowly with x in an adverse pressure gradient than in zero pressure gradient. A strong enough adverse gradient causes heat transfer and wall shear to increase in the x-direction. The opposite trends occur in a favorable pressure gradient.

Transition beginning will be defined as the minimum in heat transfer, and transition end will be defined as the maximum overshoot in heat transfer above the turbulent values. In the adverse pressure gradient cases, these may only be local minima or maxima. Because of the scatter in the heat transfer data, it is difficult to determine where the heat transfer is at a true minimum or maximum. Minima and maxima were thus determined using fifth-order, least squares polynomial curvefits of the data. Although the precise beginning and end of transition are still open to some interpretation, the curve fitting technique provided a more consistent interpretation of the data. Note that both the transition measurement technique and the definition of beginning and end affect the transition zone length.

Beginning of transition occurs on configurations 0, 1, and 4 at the lowest unit Reynolds numbers tested for these cases, 3.3 $\times 10^6$ m^{-1} for configuration 0 and 1.6 $\times 10^6$ m^{-1} for configurations 1 and 4. Configurations -1 and -2 were entirely laminar at the lowest unit Reynolds numbers at which they were tested, 1.6 and 3.3 $\times 10^6$ m^{-1}, respectively. End of transition occurs on configuration 0 at unit Reynolds numbers of 6.6 $\times 10^6$ m^{-1} and above. End of transition occurs on the pressure gradient configurations at unit Reynolds numbers of 4.9 and 6.6 $\times 10^6$ m^{-1}. At these Reynolds numbers, transition begins on the forecone, so the initial instability growth and at least part of the transition process occurs in zero pressure gradient. Heat transfer overshoots the predicted turbulent values and then relaxes to the turbulent trend in all of the pressure gradients.

Heat transfer data for freestream unit Reynolds numbers of 6.6 and 4.9 $\times 10^6$ m^{-1} are plotted in Figs. 8 and 9 with pressure gradient as a parameter. The line fairings through the data in these figures are the polynomial fits. The beginning and end of transition for configuration 1 are biased upstream compared to the other configurations. These effects are probably due to the model angle of attack. The beginning and end of transition move forward on the leeward side of a sharp cone at angle of attack (Stetson, 1982; Stetson et al., 1985), and the amount of forward movement on configuration 1 in Figs. 8 and 9 is consistent with the model being at 0.4 to 0.8° angle of attack, based on data in Stetson et al. (1985). Transition beginning and end

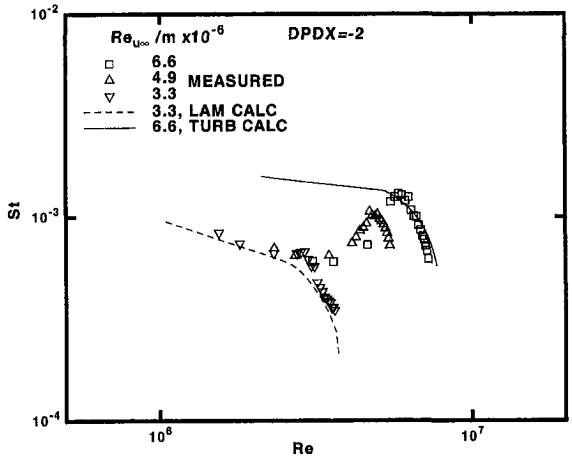

Fig. 7 Heat transfer, DPDX = −2 configuration

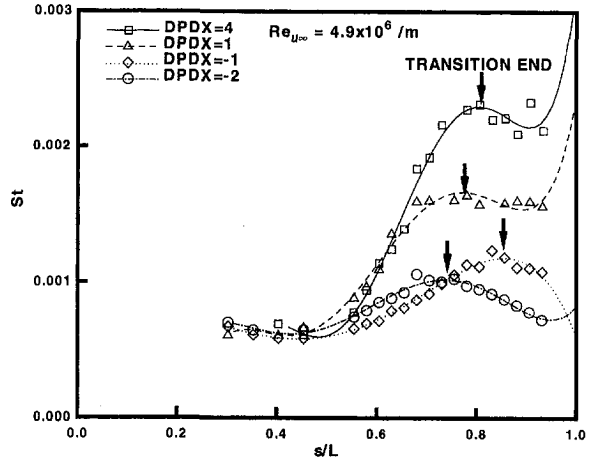

Fig. 9 Heat transfer, $Re_{u\infty} \times 10^6$ m^{-1}

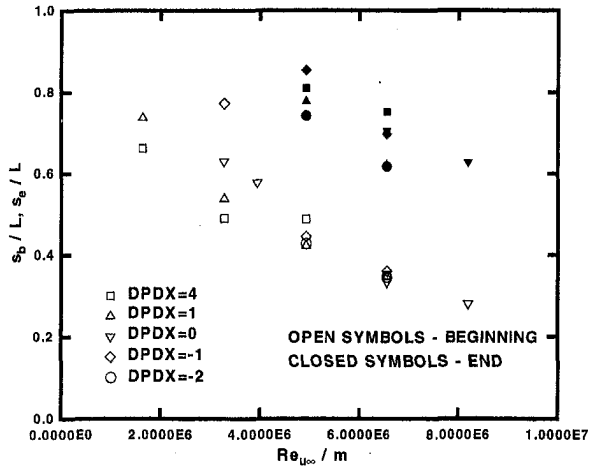

Fig. 10 Transition beginning and end

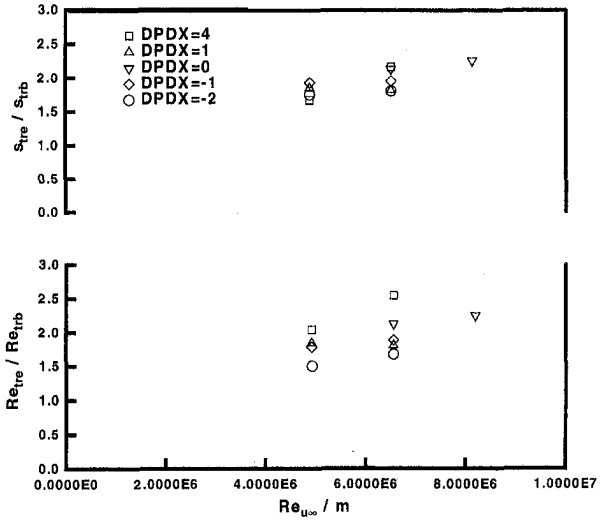

Fig. 12 Transition zone length

data taken on a sharp 8° cone at Mach 6 (Stetson, 1982) show no effect on transition zone length at 1° angle of attack and below.

Since transition begins at approximately the same location on the forecone for all the other pressure gradient models at these Reynolds numbers, the end-of-transition marker provides a direct measure of transition zone length. In all cases, increasing favorable pressure gradient decreases transition zone length. Results for the adverse pressure gradients do not show such a clear trend. For a unit Reynolds number of 6.6×10^6 m^{-1}, configuration 4 has a longer transition length than the zero pressure gradient case. No heat transfer data were available for the zero pressure gradient case at a unit Reynolds number of 4.9×10^6 m^{-1}, but interpolation indicates that end-of-transition would be at approximately $x/L = 1$. The adverse pressure gradient thus decreases transition zone length for this case.

Transition beginning and end are plotted in terms of arc length along the model in Fig. 10 and Reynolds number in Fig. 11. When the unit Reynolds numbers were low enough for transition to begin on the curved surface of the model, the favorable gradients delayed transition, and the adverse gradients promoted it, as expected.

Transition zone length is plotted in terms of length and Reynolds number in Fig. 12. The cone transition end is consistently 2.2 times the laminar length. The favorable pressure gradient transition zone length is shorter, from approximately 1.7 for configuration −2 to 2.0 for configuration −1. When the data

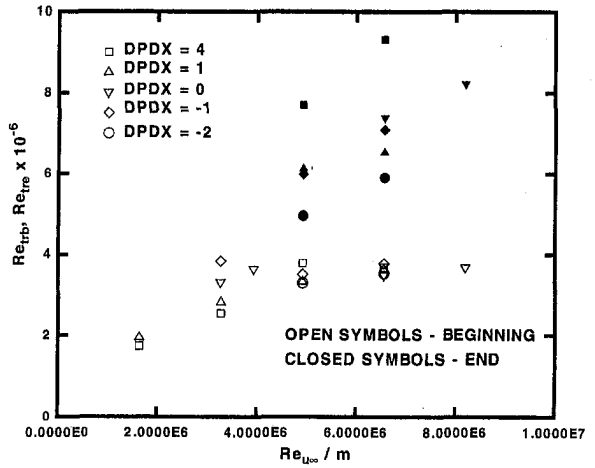

Fig. 11 Transition Reynolds number beginning and end

are plotted in terms of Reynolds number, this trend is exaggerated due to the drop in unit Reynolds number with x. Data for the adverse gradients are inconclusive in terms of transition length, but transition end Reynolds numbers generally seem higher than in zero pressure gradient, due to the increase in local unit Reynolds number. The comparison in terms of Reynolds number is somewhat misleading, due to history effects. Although the Reynolds number at the end of configuration 4 at a freestream unit Reynolds number of 6.6×10^6 m^{-1} is 12×10^6, the boundary layer is not representative of a boundary layer which has evolved to this Reynolds number at constant edge conditions, but instead probably retains characteristics of a boundary layer at lower Reynolds number.

The observed trends of shorter transition length with favorable pressure gradient are opposite to what would be expected based on subsonic results, and two factors may contribute. The first factor is that turbulent heat transfer for favorable pressure gradients is lower than zero pressure gradient heat transfer, and adverse pressure gradient heat transfer is higher. For cases where transition began on the forecone, pressure gradient had little effect on the rate of increase in transitional heat transfer with x. This means that heat transfer reaches turbulent values more quickly in favorable pressure gradient, and more slowly in adverse pressure gradient. In cases where transition begins on or near the flare, however, pressure gradient does have some influence on the rate of increase in transitional heat transfer, with adverse pressure gradient causing a faster rate of increase, and vice versa. In these cases, the net result depends on whether the rate of increase in heat transfer is great enough to overcome the effect of higher turbulent values. With these competing effects, there is no compelling reason to expect simple trends in transition zone length with pressure gradient.

A second factor which may explain trends in transition length is body curvature effects, if one postulates that transition in these hypersonic cases is due to turbulent spot spreading. Limited evidence in supersonic transition on cones (Braslow et al., 1959) and subsonic transition (Gregory, 1960) on swept wings indicates that turbulent spots spread at a constant angle with respect to the streamline passing through their origin, not with respect to local streamlines. This would encourage shorter transition lengths on the favorable pressure gradient models, since their surface area is growing at a slower rate in the x-direction compared to the cone, which means that their surface would be covered by a spot more quickly. The converse is true of the adverse pressure gradients. This argument will remain purely speculative until more detailed measurements of the transition process are made, but it does indicate that the results of this

paper may not be directly relevant to planar geometries. Quiet wind tunnel results at Mach 3.5, however, show little difference between cone and flat plate transition extent (Chen, 1993).

Conclusions

End-of-transition on a zero pressure gradient cone at Mach 8 in the AEDC VKF Tunnel B was approximately 2.2 times the laminar length. Although favorable pressure gradient delayed the beginning of transition, the favorable pressure gradient cases tested produced shorter transition lengths than the zero pressure gradient case, about 1.7 to 2.0 times the laminar length. The adverse pressure gradient cases promoted earlier transition beginning, but transition zone length results for these were inconclusive. The end-of-transition Reynolds number in adverse pressure gradient was somewhat higher than the zero pressure gradient case, primarily due to the increase in edge unit Reynolds number through the compression. In all of these cases, transition began in the zero pressure gradient regions of the models, and ended in the pressure gradient regions.

The transition zone length trends are opposite to subsonic trends. One possible cause is that in hypersonic flow, turbulent heat transfer in favorable pressure gradient is lower than zero pressure gradient heat transfer, thus the transitional boundary layer equilibrates to turbulent values more quickly in favorable pressure gradient, and vice versa in adverse pressure gradient. Another possible factor is that the body surface area is growing at a slower rate in the x-direction for the favorable pressure gradient models, thus any turbulent spot would cover the surface more quickly in favorable pressure gradient, and vice versa in adverse pressure gradient.

The present results elucidate to a certain extent the effect of pressure gradients on transition in hypersonic flow, and provide data for comparison to computation. However, the detailed mechanisms of the transition process remain unexplored, and the precise cause of the above-cited results are not certain. Detailed time-resolved and spatial measurements, especially intermittency measurements, are required for a fuller understanding of these phenomena.

References

Beckwith, I. E., 1975, "Development of a High Reynolds Number Quiet Tunnel for Transition Research," *AIAA-Journal,* Vol. 13, No. 3, Mar., pp. 300–306.

Braslow, A. L., Knox, E. C., and Horton, E. A., 1959, "Effect of Distributed Three-Dimensional Roughness and Surface Cooling on Boundary-Layer Transition and Lateral Spread of Turbulence at Supersonic Speeds," NASA TN D-53.

Cary, A. M., 1968, "Turbulent Boundary-Layer Heat Transfer and Transition Measurements for Cold-Wall Conditions at Mach 6," *AIAA Journal,* Vol. 6, No. 5, May, pp. 958–959.

Chen, F. J., 1993, "Boundary Layer Transition Extent Measurements on a Cone and Flat Plate at Mach 3.5," AIAA-93-0342, Jan.

Donaldson, J. C., and Hatcher, M. G., 1988, "Investigation of the Development of Laminar Boundary-Layer Instabilities Along a Cooled-Wall Cone in Hypersonic Flows," AEDC-TSR-88-V32, Sept.

Gregory, N., 1960, "Transition and Spread of Turbulence on a 60 deg Swept-Back Wing," *Journal of the Royal Aeronautical Society,* Vol. 64, pp. 562–564.

Jack, J. R., 1958, "Effect of Favorable Pressure Gradients on Transition for Several Bodies of Revolution at Mach 3.12," NACA TN 4313, July.

Kendall, R. M., Bartlett, E. P., 1968, "Nonsimilar Solution of the Multicomponent Laminar Boundary Layer by an Integral-Matrix Method," *AIAA Journal,* Vol. 6, No. 6, June, pp. 1089–1097.

Kimmel, R. L., 1993, "The Effect of Pressure Gradients on Transition Zone Length in Hypersonic Boundary Layers," Wright Laboratory Technical Report WL-TR-94-3012, Dec.

McCauley, W. D., Saydah, A. R., and Bueche, J. F., 1966, "Effect of Spherical Roughness on Hypersonic Boundary-Layer Transition," *AIAA Journal,* Vol. 4, No. 12, Dec. pp. 2142–2148.

Murray, A. L., 1987, "Facilitation of the BLIMP Computer Code and User's Guide," AFWAL-TR-86-3101, Jan.

Owen, F. K., Horstman, C. C., Stainback, P. C., and R. D. Wagner, 1974, "Comparison of Transition and Freestream Disturbance Measurements Obtained in Two Wind Tunnel Facilities," AIAA-74-131, Jan.

Richards, B. E., and Stollery, J. L., 1966, "Further Experiments on Transition Reversal at Hypersonic Speeds," *AIAA Journal,* Vol. 4, No. 12, pp. 2224–2226, Dec.

Sanator, 1965, "Hypersonic Boundary-Layer Transition Data for a Cold-Wall Slender Cone," *AIAA Journal* Vol. 3, No. 4, Apr., pp. 758–760.

Shope, F. L., 1991, "Aerodynamic Design of a Hypersonic Body with a Constant Adverse Pressure Gradient," AIAA-91-3319, Sept.

Spinetti, R. L., and Shope, F. L., 1991, "Aerodynamic Design of a Hypersonic Body with a Constant Favorable Pressure Gradient," AEDC-TMR-91-P15, Oct.

Stetson, K. F., 1982, "Mach 6 Experiments of Transition on a Cone at Angle of Attack," *Journal of Spacecraft and Rockets,* Vol. 19, No. 5, Sept.-Oct., pp. 397–403.

Stetson, K. F., Thompson, E. R., Donaldson, J. C., and Siler, L. G., 1983, "Laminar Boundary Layer Stability Experiments on a Cone at Mach 8, Part 1: Sharp Cone," AIAA-83-1761.

Stetson, K. F., Thompson, E. R., Donaldson, J. C., and Siler, L. G., 1985, "Laminar Boundary Layer Stability Experiments on a Cone at Mach 8, Part 3: Sharp Cone at Angle of Attack," AIAA-85-0492, Jan.

Stetson, K. F., and Kimmel, R. L., 1992, "On Hypersonic Boundary-Layer Stability," AIAA-92-0737, Jan.

Maged A. I. El-Shaarawi
Professor.

Abdulghani Al-Farayedhi
Assistant Professor.

Mohamed A. Antar[1]
Graduate Student.

Mechanical Engineering Department,
King Fahd University of Petroleum
and Minerals,
Dhahran 31261,
Saudi Arabia

Boundary Layer Flow About and Inside a Liquid Sphere

A finite-difference scheme has been developed to solve the boundary-layer equations governing laminar flows around and inside a spherical fluid droplet moving steadily in another immiscible fluid. Using this scheme, results not available in the literature have been obtained for circulating droplets at intermediate and high interior-to-exterior viscosity ratios (μ^*) and large values of the external flow Reynolds number (Re). Detailed results over the range $1.01 \leq \mu^* \leq \infty$ (solid sphere) and $100 \leq Re \leq 10000$ are presented for the velocity profiles outside and inside the droplet, the interface shear stress, the external flow separation angle, the droplet surface velocity and the drag coefficient.

Introduction

Gas flow past a liquid sphere is of interest in many engineering applications. The knowledge acquired from investigating such flows is essential to the understanding and the prediction of the performance of a liquid spray and hence the improvement of systems utilizing spray injection. Extensive work has been done to investigate the two limiting cases of flow over solid spheres (i.e., infinite inside-to-outside viscosity ratio) and gas bubbles (i.e., zero viscosity ratio). In the case of gas bubbles, the motion inside the bubble has negligible effect on the external flow (hence it is unimportant) and in the case of solid spheres such an internal motion is absent. Examples of papers on flow over solid spheres are those by Dennis and Walker (1964), Hamielec et al. (1967a), LeClair et al. (1970), Nakamura (1976), and El-Shaarawi et al. (1985). Typical investigations on gas bubbles moving in another fluid of higher viscosity are by Moore (1959 and 1963), Chao (1962), Winnikow and Chao (1966), Hamielec et al. (1967b), Brabston and Keller (1975), Ryskin, and Leal (1984a, b, c) and Pozrikidis (1989). Harper (1972) indicated that both papers by Chao (1962) and Winnikow and Chao (1966) contain technical errors.

The motion of a liquid sphere in a low-viscosity environment differs from that of a solid sphere due to the circulation of liquid and the consequent complication arising from the necessity of solving for both internal and external flows. Hadamard (1911) and Rybzynski (1911) solved independently the creeping flow ($Re \to 0$) fourth-order partial differential equation in the biharmonic stream function for the fluids inside and outside the fluid sphere. This equation was solved under the four boundary conditions of uniform stream flow at large distances from the sphere, no flow across the spherical interface (zero radial velocity), continuity (equality) of the tangential velocity component across the interface, and continuity (equality) of the tangential shear stress across the interface. The obtained closed form solutions for internal and external stream functions may be found in a number of standard texts, e.g., Batchelor (1967). The obtained solutions for the internal motion is that of Hill's spherical vortex.

If the surface tension forces are sufficiently strong (i.e., Weber number is sufficiently low) drops and bubbles can remain spherical without significant deformation up to moderate values of the external Reynolds number (e.g., Re = 600). At high internal-to-external viscosity ratio, internal circulation is negligible and the external flow around a fluid sphere is indistinguishable from that around a solid sphere at the same Reynolds number. On the other hand, internal circulation in fluid spheres other than gas bubbles affects the external flow field. Four theoretical approaches have been considered in the literature to investigate the problem of flow inside and outside such fluid spheres. These include semi-analytical series-truncation method, approximate techniques based on Galerkin's method, numerical solutions of the complete Navier-Stokes equations, and boundary-layer solutions. The semi-analytical series-truncation method is suitable for small Reynolds numbers and was used in conjunction with finite difference approximation by Oliver and Chung (1985) over a Reynolds number range $0.1 \leq Re \leq 1$ and then was extended in conjunction with a cubic finite-element scheme by Oliver and Chung (1987) up to a Reynolds number of 50. In Galerkin's (or error distribution) methods, a polynomial for the stream function has to be chosen satisfying all the boundary conditions together with an integral form of the Navier-Stokes equation. Similar to all momentum integral techniques, the success of Galerkin's method depends strongly on the form of the polynomial chosen. Neglecting inertia terms for the internal fluid, Hamielec and Johnson (1962) and Hamielec et al. (1963) applied Galerkin's method to fluid spheres up to Re = 500 and obtained polynomial solutions corresponding to ratios of inside to outside viscosity from 0 to 10^5. Another paper using Galerkin's method is that by Nakano and Tien (1963) who did not neglect inertia terms for the internal fluid. Even though the approximate techniques based on Galerkin's method have the advantage of giving analytical expressions, they usually have limited success when compared with the numerical methods. The available Galerkin solutions in the literature neither contain enough terms to accurately describe the flow field at moderate Reynolds numbers nor the correct trial functions to converge at low Reynolds number to the available creeping flow solution by Hadamard and Rybzynski.

LeClair et al. (1972) were the first to use a finite-difference method to investigate the steady motion of water drops in air (an example of high internal-to-external viscosity ratio of a typical value 55). Abdel-Alim and Hamielec (1975) presented numerical solutions of the complete Navier-Stokes equations for steady flow around circulating liquid spheres in liquid media in the Reynolds number range 1–50. Rivkind and Ryskin (1976) and Rivkind et al. (1976) used finite-difference techniques to solve the complete Navier-Stokes equation for a limited number of viscosity ratios with external Reynolds number ranging from 0.5 to 200. They correlated the obtained results of the drag coefficient for a fluid sphere in terms of the viscosity ratio, the drag coefficient of a solid sphere, and the drag coeffi-

[1] On leave from Tanta University, Egypt.

Contributed by the Fluids Engineering Division for publication in the JOURNAL OF FLUIDS ENGINEERING. Manuscript received by the Fluids Engineering Division October 30, 1995; revised manuscript received April 23, 1996. Associate Technical Editor: G. Em Karniadakis.

cient of a gas bubble. Moreover, they concluded that, for exterior Reynolds numbers ranging between 5 and 100, the interior Reynolds number has an insignificant effect on the drag coefficient. However, Oliver and Chung (1987) demonstrated that differences of up to 20 percent may occur between the values of the drag coefficient (at Re $\leq$ 20) as calculated by Abdel-Alim and Hamielec (1975) and Rivkind and Ryskin (1976). Dandy and Leal (1989) used finite-difference techniques and obtained numerical solutions for a deformable axisymmetric drop which moves steadily in a quiescent liquid over a range of Reynolds numbers from 0.005 to 250 and Weber numbers from 0.005 to 14.

Boundary layers developing on fluid spheres with internal circulation are thinner and remain attached to the surface longer than those developing on rigid spheres. A thorough review of boundary-layer solutions for circulating spheres has been given by Harper (1972). On the basis of boundary-layer theory, a first approximation for the drag on a spherical bubble was obtained by Levich (1949) as $C_D = 48/\mathrm{Re}$. Assuming a thin boundary layer at the bubble surface, using the viscous stresses and overlooking the contribution of the pressure to the drag on the bubble, Moore (1959) obtained a value of the C_D which is only two-thirds that obtained by Levich (1949). However, Moore (1963) corrected his previous result for the drag on a bubble by solving the boundary-layer equations using a perturbation technique. Other early boundary-layer treatments are in the papers by Chao (1962) and Winnikow and Chao (1966). To the best of the authors knowledge, the only available results in the literature for liquid drops (circulating spheres) for values of Re up to 1000 are those obtained by Harper and Moore (1968), on the basis of boundary-layer treatment. Harper and Moore (1968) used the unperturbed inviscid flow, described by Hill's spherical vortex inside the sphere coupled with potential external flow, to obtain a first estimate of drag. Then they used the boundary layer to perturb the velocity field only slightly at high Reynolds numbers, obtained linear equations for the boundary-layer flows and used them to find improvements to the drag coefficient and the rate of internal circulation.

A thorough survey of the literature has revealed that, other than the results of Harper and Moore (1968) for the drag-coefficient, there is a lack of results in the high-Reynolds-number range ($200 \leq \mathrm{Re} \leq 1000$) for circulating spheres at intermediate interior to exterior viscosity ratios (i.e., with a strong coupling between the internal and external flows). Moreover, there is a lack of information on the fluid mechanics inside and around circulating spheres in high-Reynolds-number range. This motivated the present work of which the objective is two-fold. First, a noniterative finite-difference scheme has been developed to solve the boundary-layer equations governing the laminar flows inside and around a fluid sphere moving steadily in another immiscible fluid. Advantages of the developed numerical scheme are simplicity, low required computer core storage, and less computational time. Second, additional data to those available in the literature and detailed fluid mechanics results are given to develop a better understanding of the problem under consideration.

Governing Equations and Boundary Conditions

This investigation is aimed at the theoretical study of flow patterns, both inside and outside of a spherical droplet moving steadily in an immiscible fluid at relatively large Reynolds numbers. A schematic of these flow patterns is shown in Fig. 1(*a*) where the liquid droplet is experiencing an internal motion engendered by the external flow. The equations describing these flows include the conservation equations of mass and momen-

Nomenclature

a = sphere radius
A = vortex strength inside the droplet, $3U_\infty/(2a^2)$ for inviscid fluids, or $3CU_\infty/(2a^2)$ for viscous fluids
C = a factor less than unity which equals the ratio between the vortex strength inside the droplet for viscous and inviscid fluids
C_D = dimensionless drag coefficient, $2D/\pi\rho U_\infty^2 a^2$
D = frictional drag, $\int_o^{x_s} 2\pi r\tau' d\bar{x}$
m = number of steps of the numerical mesh network in the x-direction
n = number of steps of the numerical mesh network in the z-direction
r = radial coordinate measured from the sphere's center
Re = Reynolds number, $2U_\infty a/\nu$
t_x = shear stress in meridional direction at the droplet surface, $(\mu\partial u/\partial z)_0$
T_x = dimensionless shear stress in the meridional direction at the droplet surface, $t_x(\mathrm{Re}/2)^{0.5}/\rho U_\infty^2$
u^* = meridional (x-direction) component of velocity
U = dimensionless meridional component of velocity, u/U_∞
u_H = velocity component in x-direction for potential flow inside the drop (Hill's spherical vortex), $-(\partial\psi_H/\partial r)/(r\sin\theta) = -A\sin\theta[a^2 - 2(1 - z)^2]$
u = velocity component in x-direction for the potential flow outside the external boundary layer, $-(\partial\psi/\partial r)/(r\sin\theta) = U_\infty \sin\theta[1 + a^3/(2r^3)]$
U_H = dimensionless potential velocity component in the x-direction for the internal flow (Hill's spherical vortex), $u_H/U_\infty = -(3/2)C\sin\theta[1 - 2(1 - Z)^2]$
U^* = dimensionless potential velocity component in the x-direction for external flow, u^*/U_∞
U_∞ = freestream velocity in the exterior flow
w = radial (z-direction) velocity component
w_H = radial (z-direction) velocity component for potential flow inside the internal boundary layer (Hill's spherical vortex), $(\partial\psi_H/\partial\theta)/(r^2\sin\theta)$
w^* = radial (z-direction) velocity component for potential flow outside the external boundary layer, $(\partial\psi/\partial\theta)/(r^2\sin\theta) = -U_\infty\cos\theta[1 - a^3/r^3]$
W = dimensionless radial velocity component, w/U_∞
W^* = dimensionless radial velocity component for the external potential flow, w^*/U_∞
W_H = dimensionless radial velocity component for the internal potential flow, w_H/U_∞
x = meridional distance (along the circular generator of the sphere's surface) measured from the stagnation point
$\bar{x}$ = the projection of the meridional coordinate x on the axis of symmetry (sphere diameter coincident with the stagnation line)
X = dimensionless meridional distance along the surface measured from the stagnation point, $2x/\mathrm{Re}a$
z = distance from the sphere's surface measured along the normal to the surface in the radial direction, being positive for the external flow and negative inside the spherical drop
Z = dimensionless distance perpendicular to the surface in the radial direction, z/a
θ = center angle measured from the frontal stagnation line.
μ = dynamic fluid viscosity
μ^* = interior-to-exterior (liquid-to-gas) dynamic viscosity ratio
ν = kinematic fluid viscosity
ν^* = interior-to-exterior (liquid-to-gas) kinematic viscosity ratio

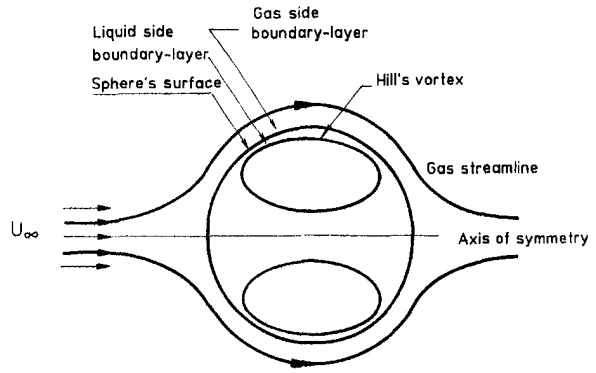

Fig. 1(a) A schematic of flow patterns inside and outside the droplet

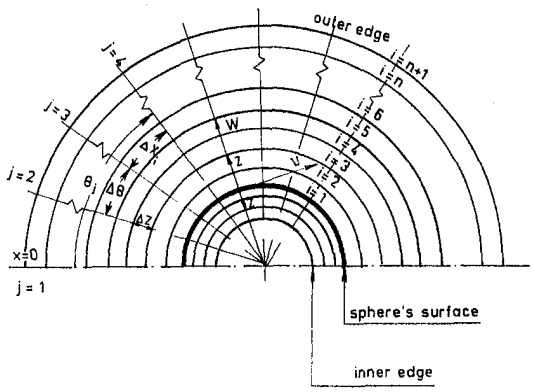

Fig. 1(b) Numerical grid

tum for both the liquid droplet and the surrounding fluid. The effects of gravity, chemical reactions, compressibility, surface active impurities, turbulence and heat transfer are absent. The flow field is assumed axisymmetric ($\partial/\partial\phi = 0$) and both fluids have constant physical properties. Both inside and outside the spherical drop, the Reynolds number is assumed to be large enough for boundary-layer theory to be applied, but small enough for surface tension to keep the drop spherical (i.e., small Weber number). The flow outside the boundary-layer developing on the external surface of the spherical drop is the potential flow which has the following classical solution.

$$\psi = -(\tfrac{1}{2})U_\infty r^2 \sin^2\theta(1 - a^3/r^3) \tag{1}$$

In the above equation U_∞ is the uniform stream velocity at infinity. The flow inside the spherical drop but outside the boundary layer which is developing on its internal surface is the potential flow given by Hill's spherical vortex, for which

$$\psi_H = (\tfrac{1}{2})Ar^2 \sin^2\theta(a^2 - r^2) \tag{2}$$

where A is the vortex strength which is dependent on the surface velocity of the drop and hence the external Reynolds number. For inviscid forced flow A equals $3U_\infty/(2a^2)$ while the presence of the boundary layers (due to viscosity) reduces the value of A to a fraction of its full inviscid value.

Under the above assumptions and using the dimensionless parameters given in the nomenclature, the nondimensional continuity and boundary-layer equations which govern the problem under consideration are as follows.

For the external gas flow,

$$\frac{\partial U}{\partial X} + \frac{\mathrm{Re}}{2}\frac{\partial W}{\partial Z} + \mathrm{Re}\,\frac{W}{1+Z} + \frac{U\,\mathrm{Re}}{2}\frac{\cot\theta}{1+Z} = 0 \tag{3}$$

$$U\frac{\partial U}{\partial X} + \frac{\mathrm{Re}W}{2}\frac{\partial U}{\partial Z} = U^*\frac{\partial U^*}{\partial X} + \frac{\partial^2 U}{\partial Z^2} \tag{4}$$

For the internal liquid flow,

$$\frac{\partial U_l}{\partial X_l} - \frac{\mathrm{Re}}{2}\frac{\partial W_l}{\partial Z_l} + \mathrm{Re}\,\frac{W_l}{1-Z_l} + \frac{\mathrm{Re}U_l}{2}\frac{\cot\theta}{1-Z_l} = 0 \tag{5}$$

$$U_l\frac{\partial U_l}{\partial X_l} - \frac{\mathrm{Re}W_l}{2}\frac{\partial U_l}{\partial Z_l} = U_H\frac{\partial U_H}{\partial X_l} + \nu^*\frac{\partial^2 U_l}{\partial Z_l^2} \tag{6}$$

The above equations are subject to the following boundary conditions.

for $X = 0$, $Z \geq 0$ (stagnation line in the external region):

$$U = 0,$$

for $Z = \infty$, $X \geq 0$ (far away from the droplet):

$$U = U^* \text{ and } W = W^* \text{ (i.e., potential flow)}, \tag{7}$$

for $Z = 0$, $X > 0$ (on the droplet surface):

$$U = U_l \text{ (equality of gas and liquid velocities)}$$

$$\frac{\partial U}{\partial Z} = -\mu^*\frac{\partial U_l}{\partial Z_l} \text{ (equality of shear stress)},$$

for $Z_l \gg \delta_l$ (inside the droplet and far away from its surface):

$$U_l = U_H$$

It is worth mentioning that the strength of the vortex inside the droplet (A) is not known a priori. Therefore, the ratio between the actual vortex strength, in the presence of the external and internal boundary layers due to fluid viscosities, and the ideal (inviscid or Hill's) spherical vortex strength has to be determined in the course of solution of the problem. In the present work, such a ratio between the actual and ideal vortex strengths has been taken equal to the ratio between the actual meridional surface velocity obtained from the external flow solution to the meridional component of the potential vortex (Hill's spherical vortex) calculated at the sphere's (droplet's) surface.

It might be noteworthy that solutions of the complete Navier-Stokes equations (e.g., Dandy and Leal, 1989) fully account for the droplet wake which cannot be resolved using the present

Nomenclature (cont.)

τ' = meridional shear stress at the droplet surface, $\mu(\partial U/\partial Z)|_o$
τ = dimensionless shear stress, $\tau'\sqrt{\mathrm{Re}/2}/(\rho U_\infty^2)$
ζ' = vorticity at the droplet surface, $\zeta = (u/r) + (\partial u/\partial r) - (1/r)(\partial w/\partial\theta)$
ζ = dimensionless vorticity, $\zeta'/(U_\infty/a)$
ρ = fluid density
ρ^* = interior-to-exterior (liquid-to-gas) density ratio
ϕ = third spherical polar coordinate
ψ = stream function of external potential flow far away from the droplet, given by Eq. (1)
ψ_H = stream function of Hill's spherical vortex inside the droplet, given by Eq. (2)

Subscripts

H = Hill's spherical vortex flow inside the sphere
i = initial (at time, $t = 0$)
l = inside the liquid sphere (droplet)
o = on the sphere surface
s = at separation point

boundary-layer approach. Also, the boundary-layer approach cannot account for the contribution of pressure drag on overall coefficient. However, the solutions of the complete Navier-Stokes equations which have been reported in the literature are for only Reynolds numbers lower than the range examined in this paper.

Numerical Method of Solution

Figure 1(*b*) shows the numerical grid where (i, j) is a typical mesh point. In either outside or inside the droplet, mesh points are numbered consecutively with the i progressing in the radial direction starting from $i = 1$ on the spherical droplet's surface till $i = n + 1$ in the external flow or $i = n_l + 1$ inside the droplet. The j progresses in the meridional direction with $j = 1, 2, 3, \ldots, m + 1$ from the front stagnation point. At each meridional station (j) the numbers of external and internal radial increments n and n_l, respectively, should be chosen so that the uppermost and innermost points ($i = n + 1$ and $n_l + 1$, respectively) lie in essentially undisturbed fluid (potential flow).

Replacing the derivatives by appropriate finite-difference representations and taking into consideration that $U_H(\partial U_H/\partial X) = \frac{9}{4}C[1 - 2(1 - Z)^2]^2[\sin^2\theta(\partial C/\partial X) + (\mathrm{Re}C)/4(1 - Z) \times \sin 2\theta]$, the governing Eqs. (3–6) and the boundary conditions (7) can be written in the following forms.

$$\frac{U_{i+1,j+1} + U_{i,j+1} - U_{i+1,j} - U_{i,j}}{2\Delta X_{i+1/2}} + \frac{\mathrm{Re}}{2}\frac{W_{i+1,j+1} - W_{i,j+1}}{\Delta Z} + \frac{\mathrm{Re}(W_{i+1,j+1} + W_{i,j+1})}{2(1 + Z_{i+1/2})} + \frac{(U_{i+1,j+1} + U_{i,j+1})\,\mathrm{Re}\cot(j\Delta\theta)}{4(1 + Z_{i+1/2})} = 0 \quad (8)$$

$$U_{i,j}\frac{U_{i,j+1} - U_{i,j}}{\Delta X_i} + \frac{\mathrm{Re}}{2}W_{i,j}\frac{U_{i+1,j+1} - U_{i-1,j+1}}{2\Delta Z} = \frac{3}{2}\sin(j\cdot\Delta\theta)\cdot\frac{3}{4}\mathrm{Re}\cos(j\cdot\Delta\theta) + \frac{U_{i+1,j+1} - 2U_{i,j+1} + U_{i-1,j+1}}{\Delta Z^2} \quad (9)$$

$$\frac{U_{li+1,j+1} + U_{li,j+1} - U_{li+1,j} - U_{li,j}}{2\Delta X_{li+1/2}} + \frac{\mathrm{Re}}{2}\frac{W_{li+1,j+1} - W_{li,j+1}}{\Delta Z_l} + \frac{\mathrm{Re}(W_{li+1,j+1} + W_{li,j+1})}{2(1 - Z_{li+1/2})} + \frac{(U_{li+1,j+1} + U_{li,j+1})\,\mathrm{Re}\cot(j\Delta\theta)}{4(1 - Z_{li+1/2})} = 0 \quad (10)$$

$$U_{li,j}\frac{U_{li,j+1} - U_{li,j}}{\Delta X_{li}} - \frac{\mathrm{Re}}{2}W_{li,j}\frac{U_{li+1,j+1} - U_{li-1,j+1}}{2\Delta Z_l} = \frac{9}{4}C[1 - 2(1 - (i - 1)\Delta Z_l)^2]^2 \times (\sin^2((j - 1)\Delta\theta_j) \times \frac{C_{j+1} - C_j}{\Delta X_{li}} + \frac{\mathrm{Re}C_j}{4(1 - (i - 1)\Delta Z_l)}\sin(2(j - 1)\Delta\theta_j) + \nu^*\frac{U_{li+1,j+1} - 2U_{li,j+1} + U_{li-1,j+1}}{\Delta Z_l^2} \quad (11)$$

for $X = 0$, i.e., $j = 1$, and $Z \geq 0$:

$$U_{i,1} = 0 \text{ and } W_{i,1} = -1 + \frac{1}{[1 + (i - 1)\Delta Z]^3}$$

for $Z = \infty$, i.e., $i = n + 1$, and $X > 0$:

$$U_{n+1,j} = \left[1 + \frac{1}{2(1 + n\Delta Z)^3}\right]\sin[(j - 1)\Delta\theta]$$

for $Z = 0$, i.e., $i = 1$, and $X > 0$:

$$U_{1,j} = U_{l1,j},\ W_{1,j} = W_{l1,j} = 0 \text{ and}$$

$$\frac{U_{2,j} - U_{1,j}}{\Delta Z} = \frac{\mu^*}{\Delta Z_l}(U_{l2,j} - U_{l1,j}) \quad (12)$$

In the finite-difference Eqs. (8)–(11), the variables with subscript $j + 1$ represent the unknowns and those with subscript j are knowns. Moreover, these finite-difference equations are linearized by assuming that, where the product of two unknowns (with subscript $j + 1$) occurs, one of them is given approximately by its value at the previous meridional step (with subscript j). The numerical solution is obtained by first selecting values of the hydrodynamic similarity parameters Re, μ^* and ν^*. Then starting with $j = 1$ (stagnation line) and applying (9) with $i = 1, 2, 3, \ldots, n$, taking into consideration that $U_{0,2} = U_{l2,2} = (\Delta Z_l/\Delta Z)[(U_{2,2} - U_{1,2})/\mu^*] + U_{1,2}$ (as a result of the application of the boundary conditions at the droplet surface), we obtain n simultaneous linear algebraic equations in n unknowns at the second meridional station ($U_{1,2}, U_{2,2}, U_{3,2}, \ldots U_{n,2}$). The matrix of coefficients of this system of equations is a tridiagonal matrix and hence Thomas method can be used to obtain the unknown values of U's at all points of the second meridional station. Now, using the computed values of U and applying (8) with $i = 1, 2, 3, \ldots, n$, the values of W at the grid points of the second meridional station are obtained in a step-by-step manner. Knowing the surface velocity $U_{1,2}$, the value of C_2 can be computed by dividing $U_{1,2}$ over the corresponding value of U for the inviscid Hill's spherical vortex at $r = a$. Equation (11) can now be used with $C_1 = 0$ and $i = 1, 2, 3, \ldots n_l$ to obtain $(n_l - 1)$ linear algebraic equations of a tridiagonal matrix of coefficients which can be solved by Thomas method to obtain $(n_l - 1)$ values of $U_l(U_{l2,2}, U_{l3,2}, \ldots U_{ln+1,2})$. Using these values of the meridional velocity inside the spherical droplet and applying Eq. (10) with $i = 1, 2, \ldots, n_l$, the values of W at the grid points of the second meridional station ($j = 2$) are obtained in a step-by-step fashion. Repeating the whole previous procedure with $j = 2, 3, \ldots m$, one can advance, step by step, along the sphere surface until the separation point in the external gas flow (at which $\partial U/\partial Z|_0 = 0$) is reached.

For the selection of n and n_l at each meridional station (j) an iterative type method is used. In this method the values of n and n_l should be large enough so that the computed meridional velocity distributions U and U_l are close in tangents at the uppermost and innermost points ($i = n + 1$ and $n_l + 1$, respectively), within an arbitrarily chosen accuracy, to the corresponding potential distribution U^* and the modified potential spherical vortex distribution U_H, respectively. For given j and a value of n, once the computations have been carried out for U and the aforesaid matching was not attained, the value of n was increased, the computations again performed and the computed values of U accepted if the aforesaid matching criterion is satisfied. Then, a similar iterative procedure is done for the selection of the number of radial increments inside the droplet (n_l).

Following procedures as those given by El-Shaarawi and El-Bedeawi (1987) it can be shown that the finite-difference Eqs. (8)–(11) are consistent with the boundary-layer equations (3)–(6) and are stable as long as the meridional velocity components (U and U_l) are non-negative. Thus, until the separation point, the numerical solution of eqs. (8–11) is guaranteed to be convergent. On the other hand, suitable mesh sizes were usually chosen such that a numerical solution of the finite-difference equations is practically independent of the increment

sizes in X and Z. Near the front stagnation and the separation points, where large gradients exist, the mesh sizes in the meridional direction were chosen to give $\Delta\theta = 0.1$ deg. However, downstream of the stagnation point and upstream of the separation point, the step size in the meridional direction was chosen to give $\Delta\theta$ not more than 1 deg, while that in the radial direction (ΔZ) was 0.001.

Results and Discussion

It is worthy of note that the external flow is governed by only two hydrodynamic similarity parameters, viz. Reynolds number (Re) and the dynamic viscosity ratio (μ^*). On the other hand, a third similarity parameter (ν^*, the kinematic viscosity ratio, or ρ^*, the density ratio) is needed to describe the flow inside the droplet. The numerical computations were carried out over a wide range of Reynolds number ($100 \leq \mathrm{Re} \leq 10{,}000$), dynamic viscosity ratio ($1.01 \leq \mu^* \leq 100$) and density ratio ($15 \leq \rho^* \leq 2000$, i.e., for $\mu^* = 1.5$, $0.007 \leq \nu^* \leq 0.1$). The obtained results clarify the effect of each of these hydrodynamic similarity parameters on the velocity profiles outside and inside the droplet, the surface velocity distribution, separation angle in the external flow, the shear stress at the droplet surface, and the drag coefficient.

For Re = 10,000, Fig. 2(a) shows the effect of the viscosity ratio μ^* on the developing meridional velocity profiles U against the radial coordinate Z at some meridional stations corresponding to some selected values of the central angle θ measured from the front stagnation point. This figure shows that the meridional velocity profiles developing outside the droplet surface indicate

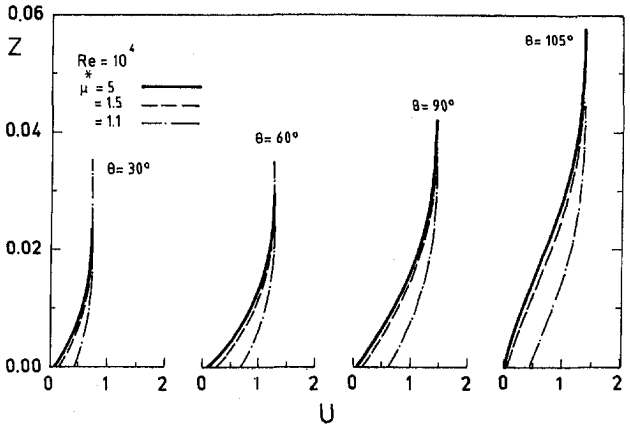

Fig. 2(a) Meridional velocity Profiles versus radial distance for different viscosity ratios at different meridional locations

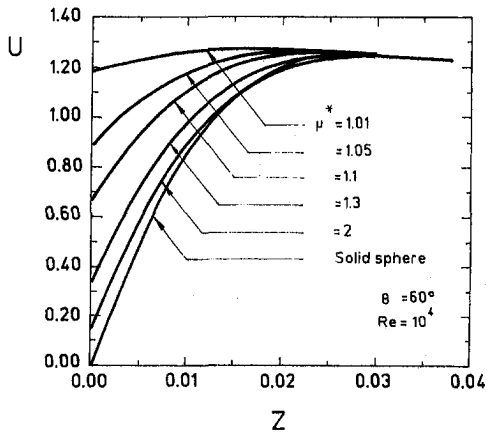

Fig. 2(b) Meridional velocity distribution for different viscosity ratios including solid sphere results of El-Shaarawi et al.

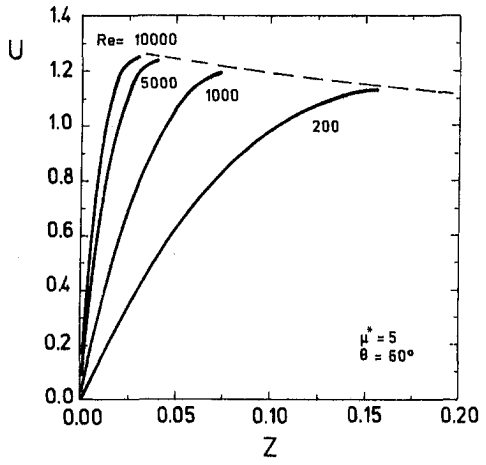

Fig. 3(a) Effect of Reynolds number on meridional velocity profiles

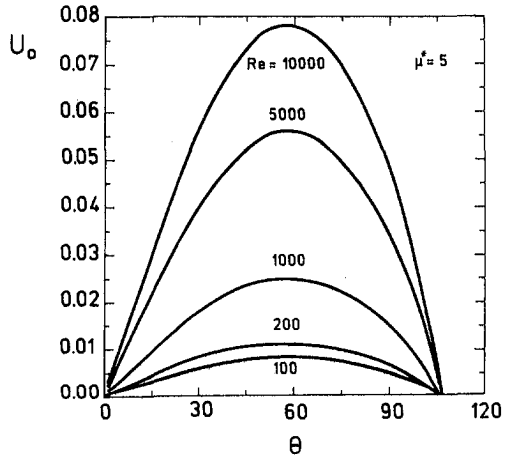

Fig. 3(b) Effect of Reynolds number on the surface velocity versus the polar angle

an increasing boundary-layer thickness as θ increases. Moreover, these profiles are greatly influenced by the viscosity ratio μ^*. For a given θ, each of these profiles has its own surface velocity value U_0 (at $Z = 0$) but all profiles asymptotically approach the potential flow at large values of Z (far away from the droplet surface). As the value of the viscosity ratio μ^* increases the velocity profiles approach the corresponding profiles for flows over rigid (solid) spheres where the surface velocity is zero. To augment the clarification concerning the effect of μ^* on the meridional velocity profiles, Fig. 2(b) presents, for given Re and θ, such profiles for some selected values of μ^*. This figure shows that the higher the viscosity ratio (μ^*) the smaller the value of the surface velocity (at $Z = 0$). Indeed, at considerably large values of μ^* the velocity profile becomes identical to that of a flow over a solid sphere ($\mu^* = \infty$). The latter case was investigated by many workers (e.g., El-Shaarawi et al., 1985) and its corresponding velocity profile is also drawn in Fig. 2(b). The present computations proved that the obtained meridional velocity profiles at considerably large values of μ^* ($\mu^* > 100$) almost coincide with the corresponding profiles of El-Shaarawi et al. (1985); this provided a check on the adequacy of the present model and computer code.

Figure 3(a) focuses on the effect of Reynolds number on the meridional velocity component. For a given μ^* ($\mu^* = 5$), this figure presents meridional velocity profiles at a given angle ($\theta = 60$ deg) for some selected values of Re. As anticipated, the higher the value of Re, the thinner the external boundary layer which develops on the outer surface of the droplet. On the other hand, the droplet surface velocity is an important

parameter which has been obtained from the solution of the external flow equations under the boundary conditions of equality of shear stress and velocity for the liquid and the gas at the droplet surface. For a given viscosity ratio (μ^*), Fig. 3(b) presents the droplet surface velocity up to the point of flow separation against the angle θ (i.e., the meridional distance) for the selected values of Re. For a given Re, the distribution of the surface velocity starts from zero at the front stagnation point and ends again with zero at the separation point in the external flow. As might be expected, the figure shows that the surface velocity, and consequently the internal circulation of the liquid within the droplet, increases with Re. The effect of the viscosity ratio (μ^*) on the variation of the droplet surface velocity with θ is shown in Figs. 4(a–b) for a given value of Re (Re = 10^4). It is clear from these figures that increasing the liquid-to-gas viscosity ratio (μ^*) decreases the engendered velocity. Moreover, it is interesting to notice that for $\mu^* = 1.05$ the maximum of the surface velocity attains a value of about 0.95 U_∞ ($U_o \sim 0.95$) while for $\mu^* = 5$ such a maximum is only about 8 percent of U_∞.

It is important to know the effect of each of the two parameters of similitude for the external flow (Re and μ^*) on the position of the point of laminar separation (point at which $\partial U/\partial Z|_o = 0$, Schlichting, 1979). Figure 5 gives the position of the separation point (θ_s) against the Reynolds number for various values of μ^*. This figure shows that, for a given μ^*, increasing the Reynolds number delays the separation, i.e., separation occurs at a larger meridional distance. This is attributed to the thinning of the boundary layer developing on the droplet's surface as Re increases. On the other hand, for a given Re, the separation point shifts forward downstream as the value of μ^* decreases. This is attributable to the higher meridional surface velocities, in the same direction of the meridional-component of the external flow, as the viscosity ratio decreases. Again, such higher surface velocities reduce the relative velocity between the external flow and the droplet surface and hence delays the separation. The curve corresponding to the case of a solid sphere ($\mu^* = \infty$) practically lies on top of that for $\mu^* > 5$ which is shown in this figure. The present θ_s-results have been found to approach the corresponding solid-sphere results at considerably large values of μ^* ($\mu^* > 100$); this finding provided a check on the adequacy of the present computer code. For example, for Re = 10^4, θ_s for a solid sphere is 107° (El-Shaarawi et al., 1985) while the corresponding θ_s for $\mu^* = 100$ is 106.4, i.e., the difference is only 0.56 percent.

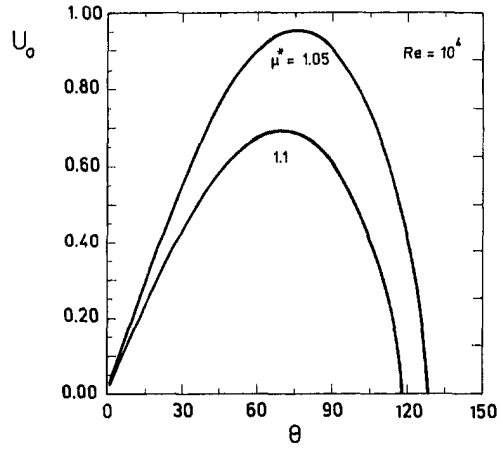

Fig. 4(a) Effect of viscosity ratio on the surface velocity versus the polar angle

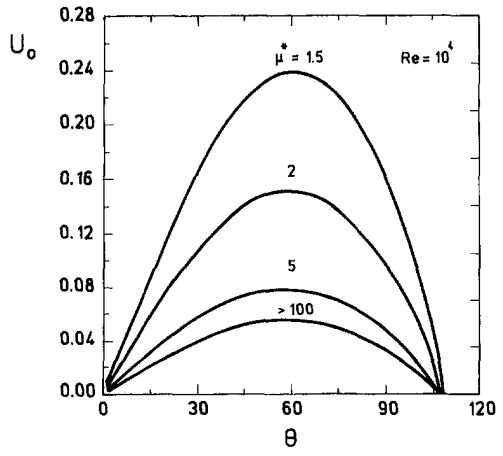

Fig. 4(b) Effect of viscosity ratio on the surface velocity versus the polar angle

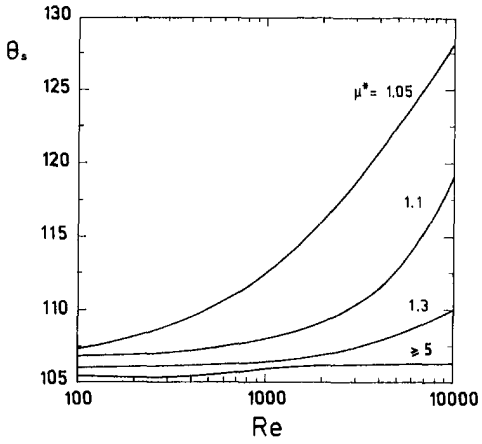

Fig. 5 Effect of viscosity ratio on the variation of the angle of separation with Reynolds number

Over the investigated range $1.05 \leq \mu^* \leq \infty$, Fig. 6($a$) gives the variation of the dimensionless meridional shear stress (τ) with the meridional distance (i.e., θ) for various selected values of μ^* and a given Re = 10^4. Each of the curves presented in this figure (for a given μ^*) starts with a zero value at the front stagnation point ($\theta = 0$) and ends again with zero at the point of external flow separation ($\theta = \theta_s$) which varies according to the value of μ^*. As can be seen from this figure, the higher the viscosity ratio (μ^*) the larger the value of the interface shear stress (τ). This is attributed to the increase in the value of the droplet's surface velocity and hence the decrease in the value of meridional velocity gradient at the interface ($\partial U/\partial Z|_o$) as the value of μ^* decreases. On the other hand, Fig. 6(b) presents the effect of Re on τ for two given values of μ^*. This figure indicates that the larger the value of μ^*, the less pronounced the effect of Re on τ. Indeed for $\mu^* = \infty$ (solid sphere) it is known (El-Shaarawi et al., 1987) that increasing the Reynolds number decreases slightly the value of τ even though the U-profiles become steeper with increasing Re. However, increasing the Reynolds number at low values of μ^* decreases significantly the values of τ since the value of the gradient $\partial U/\partial Z|_o$ decreases due to the simultaneous effects of Re and the higher droplet surface velocity.

Knowing the shear stress at the interface, the dimensionless drag coefficient has been computed and is given as a function of μ^* and Re in Table 1. As might be expected the value of C_D increases with μ^* and decreases with Re. It is also worthy of note that the value of C_D at $\mu^* = 100$ and Re = 10^4 differs by only some 3 percent than that of a solid sphere ($\mu^* = \infty$) for the same value of Re = 10^4; the latter was given by El-Shaarawi et al. (1985) to be 0.06716.

It is worth mentioning that the authors of this paper have not found detailed velocity profile, θ_s, C_D or τ results in the litera-

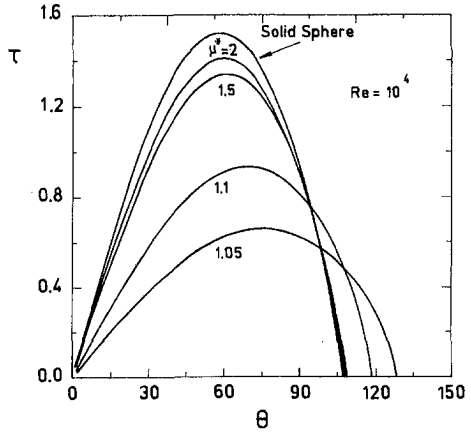

Fig. 6(*a*) Effect of viscosity ratio on interface shear stress at a given value of Reynolds number

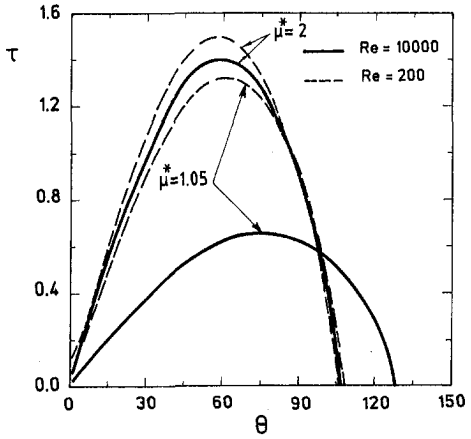

Fig. 6(*b*) Effect of Reynolds number on the interface shear stress at a given value of Reynolds number

ture for values of μ^* other than infinity (the solid sphere). Therefore, Fig. 7 compares the surface vorticity as computed from the present results at Re = 100 with that presented by Hamielec et al. (1967). This figure indicates a close agreement and hence it provides another validation of the present work.

The meridional velocity profiles for the liquid inside the droplet with different values of the viscosity ratio (μ^*) are presented in Fig. 8(a) for a polar angle of θ = 60 deg, Reynolds number (Re) = 500 and a kinematic viscosity ratio (ν^*) of 0.04. As can be seen from this figure, as μ^* increases, U_l at a given Z_l decreases due to the associated lower surface velocity as was presented before. For a given μ^*, the velocity starts with its surface value at the interface and decreases as one moves inside the droplet until the flow matches with the internal potential vortex. The matching occurs at large values of Z_l as μ^* increases, i.e., a thicker internal boundary layer. On the other hand, the effect of Re on the internal meridional velocity profiles is shown in Fig. 8(b) which gives these profiles at three different values of Re for given values of μ^*, ν^* and θ. For a given Z_l, the meridional velocity U_l increases with Re due to the associated increase in the surface velocity. Finally, Figs. 8(a) and 8(b) indicate that the meridional velocity profiles inside the droplet have very slight curvature; therefore, $\partial^2 U_l/\partial Z_l^2$ is

Table 1 Variation of C_D with μ^* for various values of Re

	C_D			
μ	Re = 100	Re = 500	Re = 1000	Re = 10000
1.01	0.55586	0.17586	0.10224	0.01351
1.05	0.64023	0.26210	0.17785	0.04087
1.10	0.65415	0.27470	0.19040	0.05175
1.30	0.66414	0.28460	0.19979	0.06020
1.50	0.66589	0.28670	0.20190	0.06199
2.00	0.66811	0.28847	0.20354	0.06339
5.00	0.66825	0.28955	0.20457	0.06459
10.0	0.66870	0.28975	0.20513	0.06482
100.	0.66902	0.28990	0.20533	0.06499

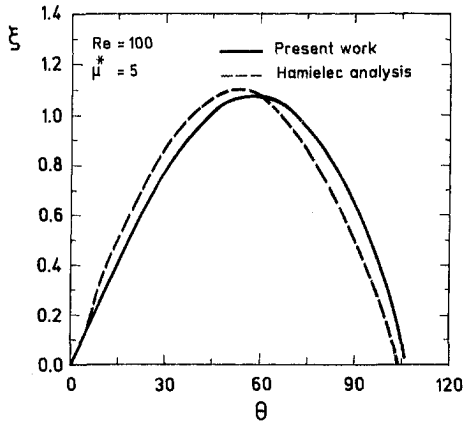

Fig. 7 Surface vorticity compared with boundary layer solution of Hamielec et al.

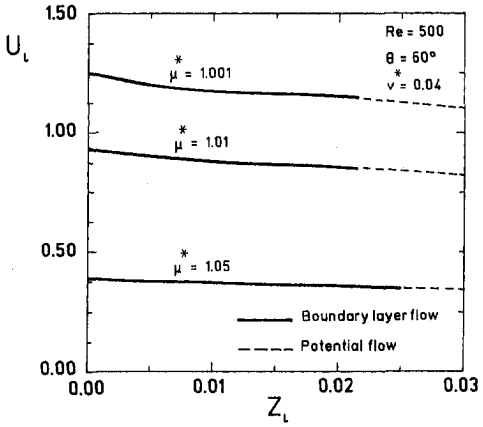

Fig. 8(*a*) Effect of viscosity ratio on the meridional velocity distribution inside the sphere

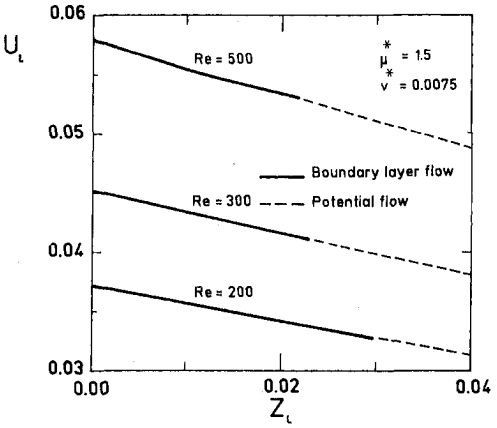

Fig. 8(*b*) Effect of Reynolds number on the meridional velocity distribution inside the sphere

negligible. Accordingly, unpresented results show that the effect of ν^* on these internal velocity profiles is insignificant.

Conclusions

A simple, linearized and non-iterative finite-difference scheme has been developed and successfully used to solve the boundary-layer equations governing the laminar flows around and inside a spherical fluid droplet moving steadily in another immiscible fluid. Two hydrodynamic similarity parameters are needed to describe the external flow around the droplet; these are the Reynolds number (Re) and the interior-to-exterior viscosity ratio (μ^*). An additional parameter of similitude, ν^* (the kinematic viscosity ratio), is needed for the description of the flow inside the droplet. Results not available in the literature have been obtained for circulating droplets at intermediate and high viscosity ratios (i.e., with a strong coupling between the internal and external flows) and large values of the external flow Reynolds number (Re). The obtained results clarify that each of μ^* and Re has significant effects on the flow characteristics both inside and outside the droplet while the third parameter (ν^*) has negligible effects on the flow inside the droplet. Over the ranges $1.01 \leq \mu^* \leq \infty$ (solid sphere) and $100 \leq \mathrm{Re} \leq 10000$ results are presented for the meridional velocity profiles inside and outside the spherical droplet, the interface shear stress, the external flow point of separation, the droplet surface velocity and the drag coefficient.

Acknowledgment

The support of King Fahd University of Petroleum and Minerals (KFUPM) to carry out this investigation is gratefully acknowledged.

References

Abdel-Alim, A. H., and Hamielec, A. E., 1975, "A Theoretical and Experimental Investigation of the Effect of Internal Circulation on the Drag of Spherical Droplets Falling at Terminal Velocity in Liquid Media," *Industrial and Engineering Chemistry Fundamentals,* Vol. 14, No. 4, pp. 308–312.

Batchelor, G. K., 1967, *An Introduction to Fluid Dynamics,* Cambridge Univ. Press, London and New York.

Brabston, D. C., and Keller, H. B., 1975, "Viscous Flows Past Spherical Gas Bubbles," *Journal of Fluid Mechanics,* Vol. 69, No. 1, pp. 179–189.

Chao, B. T., 1962, "Motion of Spherical Gas Bubbles in a Viscous Liquid at Large Reynolds Number," *The Physics of Fluids,* Vol. 5, No. 1, pp. 69–79.

Dandy, D. S., and Leal, L. G., 1989, "Buoyancy-driven Motion of a Deformable Drop Through a Quiescent Liquid at Intermediate Reynolds Numbers," *Journal of Fluid Mechanics,* Vol. 208, pp. 161–192.

Dennis, S. C. R., and Walker, J. D. A., 1971, "Calculation of the Steady Flow Past a Sphere at Low and Moderate Reynolds Numbers," *Journal of Fluid Mechanics,* Vol. 48, pp. 771–789.

El-Shaarawi, M. A. I., El-Refaie, M. F., and El-Bedeawi, S. A., 1985, "Numerical Solution of Laminar Boundary Layer Flow About a Rotating Sphere in an Axial Stream," ASME JOURNAL OF FLUIDS ENGINEERING, Vol. 107, pp. 97–104.

El-Shaarawi, M. A. I., and El-Bedeawi, S. A., 1987, "Consistency, Stability and Convergence of the Finite-Difference Equations for Flow About a Rotating Sphere in an Axial Stream," *Journal of Numerical Methods in Fluids,* Vol. 7, pp. 825–831.

El-Shaarawi, M. A. I., Kemry, M. M., and El-Bedeawi, S. A., 1987, "Further Studies on Laminar Flow About a Rotating Sphere in an Axial Stream," ASME JOURNAL OF FLUIDS ENGINEERING, Vol. 109, pp. 75–77.

Hadamard, M., 1911, "Mouvement Permenant lent d'une Sphere Liquide et Riqueuse dans un Liquide Risqueux," *Comptes Rendus, Academie des Sciences,* Vol. 152, pp. 1735–1739.

Hamielec, A. E., Hoffman, T. W., and Ross, L. L., 1967a, "Numerical Solution of The Navier-Stokes Equation for Flow Past Spheres: Part I. Viscous Flow Around Spheres with and Without Radial Mass Efflux," *AIChE Journal,* Vol. 13, No. 2, pp. 212–219.

Hamielec, A. E., Johnson, A. I., and Houghton, W. T., 1967b, "Viscous Flow Around Circulating Spheres of Low Viscosity," *AIChE Journal,* Vol. 13, No. 2, pp. 220–224.

Hamielec, A. E., and Johnson, A. I., 1962, "Viscous Flow Around Fluid Spheres at Intermediate Reynolds Numbers," *Canadian Journal of Chemical Engineering,* Vol. 40, pp. 41–45.

Hamielec, A. E., Storey, A. E., and Whitehead, J. M., 1963, "Viscous Flow Around Fluid Spheres at Intermediate Reynolds Numbers (II)," *Canadian Journal of Chemical Engineering,* Vol. 41, pp. 246–251.

Harper, J. F., and Moore, D. W., 1968, "The Motion of a Spherical Liquid Drop at High Reynolds Number," *Journal of Fluid Mechanics,* Vol. 32, part 2, pp. 367–391.

Harper, J. F., 1972, "The Motion of a Spherical Drop at High Reynolds Number," *Advanced Applied Mechanics,* Vol. 32, pp. 59–129.

LeClair, B. P., Hamielec, A. E., Pruppacher, H. R., and Hall, W. D., 1972, "A Theoretical and Experimental Study of the Induced Circulation in Water Drops Falling at Terminal Velocity in Air," *Journal of the Atmospheric Science,* Vol. 29.

Levich, V. G., 1962, *Physicochemical Hydrodynamics,* Printice Hall.

Moore, D. W., 1959, "The Rise of a Gas Bubble in a Viscous Liquid," *Journal of Fluid Mechanics,* Vol. 6, pp. 113–130.

Moore, D. W., 1963, "The Boundary Layer on Spherical Gas Bubble," *Journal of Fluid Mechanics,* Vol. 16, pp. 161–177.

Nakamura, I., 1976, "Steady Wake Behind a Sphere," *Physics of Fluids,* Vol. 19, pp. 5–8.

Nakano, Y., and Tien, C., 1967, "Approximate Solution of Viscous Incompressible Flow Around Fluid Spheres at Intermediate Reynolds Numbers," *Canadian Journal of Chemical Engineering,* Vol. 45, pp. 135–140.

Oliver, D. L., and Chung, J. N., 1985, "Steady Flows Inside and Around a Fluid Sphere at Low Reynolds Numbers," *Journal of Fluid Mechanics,* Vol. 54, pp. 215–230.

Oliver, D. L., and Chung, J. N., 1987, "Flow About a Fluid Sphere at Low to Moderate Reynolds Numbers," *Journal of Fluid Mechanics,* Vol. 177, pp. 1–18.

Pozrikidis, C., 1989, "Inviscid Drops with Internal Circulation," *Journal of Fluid Mechanics,* Vol. 209, pp. 77–92.

Rivkind, V., Ryskin, G. M., and Fishbein, G. A., 1976, "Flow Around a Spherical Drop at Intermediate Reynolds Numbers," *Applied Mathematics and Mechanics,* Vol. 40, pp. 687–691.

Rivkind, V. Y., and Ryskin, G. M., 1976, "Flow Structure in Motion of a Spherical Drop in a Fluid Medium at Intermediate Reynolds Numbers," Translated from *Russian Fluid Dynamics,* Vol. 11, No. 1, pp. 5–12.

Rybzynski, W., 1911, "Uber die Fortschreitende Bewegung einer Flussiger in einem Zaben Medium," *Bulletin of International Academic Science Cracovia,* Ser. A, No. 1A, pp. 44–46.

Ryskin, G., and Leal, L. G., 1984, "Numerical Solution of Free-Boundary Problems in Fluid Mechanics: Part 1. The Finite-Difference Technique," *Journal of Fluid Mechanics,* Vol. 148, pp. 1–17.

Ryskin, G., and Leal, L. G., 1984, "Numerical Solution of Free-Boundary Problems in Fluid Mechanics: Part 2. Buoyancy-Driven Motion of a Gas Bubble Through a Quiescent Liquid," *Journal of Fluid Mechanics,* Vol. 148, pp. 19–35.

Ryskin, G., and Leal, L. G., 1984, "Numerical Solution of Free-Boundary Problems in Fluid Mechanics: Part 3. Bubble Deformation in an Axisymmetric Straining Flow," *Journal of Fluid Mechanics,* Vol. 148, pp. 37–43.

Schlichting, H., *Boundary Layer Theory,* Seventh edition, McGraw-Hill, 1979.

Winnikow, S., and Chao, B. T., 1966, "Droplet Motion in Purified Systems," *Physics of Fluids,* Vol. 9, No. 1, pp. 50–61.

Effects of Convection and Decay of Turbulence on the Wall Pressure Wavenumber-Frequency Spectrum

W. L. Keith
Mechanical Engineer.
Mem. ASME

B. M. Abraham
Mechanical Engineer.
Mem. ASME

Submarine Sonar Department,
Naval Undersea Warfare Center Detachment,
New London, CT 06320

Cross-spectral and cross-correlation data from experiments and numerical simulations have shown the turbulent wall pressure convection velocity to vary with the streamwise sensor spatial separation. This variation is due to the spatial decay rates of turbulent structures in the inner and outer regions of the boundary layer. Its effect is shown to have a significant impact on the distribution of energy in the wavenumber-frequency spectrum $\Phi(k_1, \omega)$. The standard Corcos model is known to overpredict the wavenumber-frequency spectrum at low wavenumbers. This is shown to result from its constant convection velocity assumption. The spectral levels at subconvective and lower wavenumbers are shown to be directly influenced by the spatial variation in convection velocity. Convection velocity measurements from past investigations that cover the range $285 \leq R_\theta \leq 29{,}000$ are compared, and an outer variable scaling is shown to effectively collapse the data.

Introduction

The energy content of the turbulent wall pressure wavenumber-frequency spectrum is of interest in problems of flow-induced vibration and noise. Estimates of $\Phi(k_1, \omega)$ are often derived from measurements of the cross spectrum made with a relatively small number of sensors. However, uncertainties result from the limited number of spatial separations as well as from the size of the pressure sensors which limits the smallest separations that are possible. In addition, many ensemble averages (500 or more), are required to minimize the random errors in the measured cross-spectrum.

A convection or phase velocity, u_c, may be determined from the streamwise cross-spectrum phase $\phi(\xi, \omega)$ by using the relationship $\phi(\xi, \omega) = \omega\xi/u_c$. It is commonly assumed in estimating the wavenumber-frequency spectrum that u_c is independent of separation ξ. In fact, u_c depends on ξ due to the variation in convection velocities and spatial decay rates of the pressure-producing turbulent structures in the inner and outer regions of a turbulent boundary layer. The focus of this paper is to determine the effect of this variation in u_c on the wavenumber-frequency spectrum.

Modeling the Wall Pressure Cross-Spectrum

The streamwise wall pressure cross-spectrum may be expressed as

$$G(\xi, \omega) = |G(\xi, \omega)| e^{-i\phi(\xi,\omega)}. \quad (1)$$

For a fixed frequency ω_o, if we were to assume u_c is independent of ξ and $|G(\xi, \omega_o)|$ decays exponentially with ξ, Eq. (1) becomes

$$G(\xi, \omega_o) = \Phi(\omega_o) e^{(\alpha|\xi| - i\omega_o\xi/u_c(\omega_o))}, \quad (2)$$

where α is a decay parameter of negative sign. The spectrum $\Phi(k_1, \omega_o)$ is then

$$\Phi(k_1, \omega_o) = \Phi(\omega_o)/2\pi \int_{-\infty}^{\infty} e^{(\alpha|\xi| - i(k_1 + \omega_o/u_c(\omega_o))\xi)} d\xi. \quad (3)$$

Using MACSYMA (Rand, 1984), we obtain the closed-form solution to Eq. (3) as

$$\Phi(k_1, \omega_o) = (\Phi(\omega_o)/2\pi)(-2\alpha/(\alpha^2 + (k_1 + k_c)^2)). \quad (4)$$

We now define $\alpha = \gamma\omega_o/u_c(\omega_o)$, and express Eq. (2) in terms of the similar variable $\xi^* = \omega_o\xi/u_c(\omega_o)$, such that

$$G(\xi^*, \omega_o) = \Phi(\omega_o) e^{(\gamma|\xi^*| - i\xi^*)}. \quad (5)$$

Note that if we allowed u_c to vary with ξ as well as with ω_o in Eq. (3), a spatial modulation of the phase term results, and, in general, the integral cannot be evaluated in closed form.

Equation (5) is the streamwise component of the separable cross-spectrum model proposed by Corcos (1963). (As we are only concerned with the streamwise component, the issue of separability is irrelevant here.) Recently Farabee and Casarella (1991) and Keith and Barclay (1993) have shown that the similarity scaling holds over a limited frequency range. Although Corcos did not transform his model to the wavenumber domain, Eq. (4) with α replaced by γk_c is commonly referred to as the Corcos model of $\Phi(k_1, \omega_o)$. Corcos defined a convection velocity in terms of the phase of the cross spectrum, and stated that "u_c is found to be a function of ω and to be almost independent of ξ and η." This conclusion was based upon the limited amount of convection velocity data available at that time.

Farabee and Casarella (1991) showed that the similarity scaling proposed by Corcos was effective for collapsing their cross-spectral data, taking into account the variation of u_c with ξ. However, the influence of the variation of u_c with ξ on the wavenumber-frequency spectrum has not been investigated to date. A criticism of the model for $\Phi(k_1, \omega_o)$ given by Eq. (4) is its apparent overprediction of spectral levels at subconvective and lower wavenumbers. In this paper, higher spectral levels in these regions will be shown to result from constraining u_c to be constant when we transform the cross-spectrum. Taking into account the variation of u_c with ξ will be shown to lead to improved estimates of $\Phi(k_1, \omega_o)$.

Comparison of Wall Pressure Convection Velocities

The dominant trend in the convection velocity data from previous investigations shows an increase in $u_c(\xi, \omega)$ as ξ in-

Contributed by the Fluids Engineering Division for publication in the JOURNAL OF FLUIDS ENGINEERING. Manuscript received by the Fluids Engineering Division July 7, 1995; revised manuscript received May 13, 1996. Associate Technical Editor: F. Giralt.

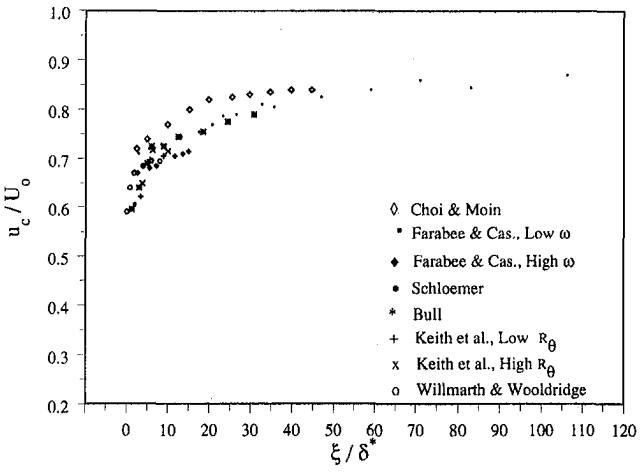

Fig. 1 Comparison of convection velocities scaled with outer variables

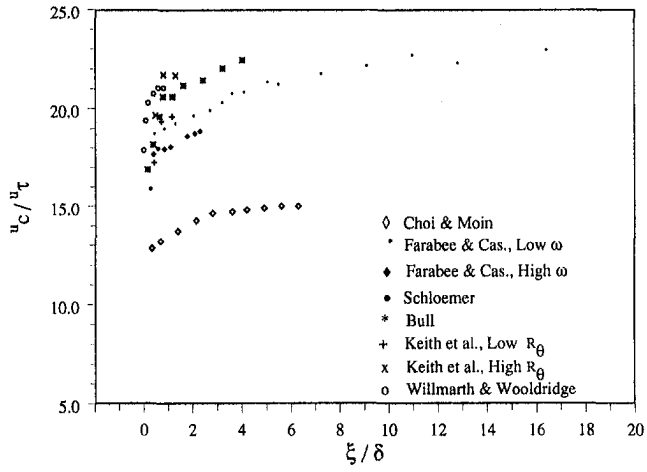

Fig. 2 Comparison of convection velocities scaled with mixed variables

creases and ω decreases. This is caused by the spatial decay rates of the pressure-producing turbulent structures, which are directly proportional to the distance of the structures from the wall. The larger structures at locations farther from the wall convect faster and are coherent over larger distances than those near the wall. For larger separations, the contributions from the larger structures therefore dominate $u_c(\xi, \omega)$. At smaller separations, the additional contributions from the smaller near-wall structures coherent over those distances cause a reduction in $u_c(\xi, \omega)$. The increase in $u_c(\xi, \omega)$ with decreasing ω also results from these dynamics.

In comparing convection velocity data, we must consider the spatial variation of u_c measured in discrete, narrowband, and broadband frequency ranges. We compare data from the six investigations of Table 1, which cover two orders of magnitude in R_θ. For comparisons of the data using the outer scaling u_c/U_o versus ξ/δ^*, the frequency bands are scaled as $\omega\delta^*/U_o$.

The higher discrete frequency of Farabee and Casarella falls at the center of the narrow bandwidth of Keith et al. (1991) (at both R_θ values). Both data sets display a reasonable collapse, as shown in Fig. 1. Although the narrow bandwidth of Willmarth and Wooldridge (1962) lies above the higher discrete frequency of Farabee and Casarella, these data sets collapse well. The numerical simulation of Choi and Moin (1990) covers approximately the same broad band as Bull's (1967). Choi and Moin's data are above those of Bull at the lower separations, but converge at the higher. The broadband data of Schloemer (1967) and Bull agree well. We note that Schloemer's data covers a slightly higher frequency range than Bull's. The low discrete frequency of Farabee and Casarella lies within the broad band of Bull. The two data sets agree well for the larger separations. This agreement between broad band and discrete low-frequency data reflects the inherent filtering of the higher frequency contributions in the broad band data resulting from the sensor separations.

The outer scaling effectively collapses the discrete, narrowband, and broadband data sets. The dominant trend of increasing convection velocity with increasing separation is apparent. The use of δ rather than δ^* as an outer length scale produces no significant effect. At low values of ξ/δ^*, the data sets at higher R_θ tend to display a sharper roll-off than the Farabee and Casarella low-frequency data.

For the mixed scaling (u_c/u_τ versus ξ/δ) of Fig. 2, the frequency bands are scaled as $\omega\delta/u_\tau$. Although the higher discrete frequency data of Farabee and Casarella fall at the center of the narrow bands of Keith et al. at both R_θ, these data sets do not collapse well. In addition, the collapse of the data of Keith et al., which covers the same narrow band at both R_θ, is poor, with the lower R_θ data lying below the higher. Bull and Schloemer's broad bands are comparable, and the two data sets collapse fairly well, with Schloemer's data slightly below Bull's. Although Choi and Moin's broad band covers the lower half of Bull's, it also lies significantly below. The use of u_τ as a velocity scale combined with an outer length scale (δ or δ^*), therefore, does not effectively collapse these data over a wide range of R_θ. Data at lower R_θ are mapped below the higher R_θ

Nomenclature

$G(\xi, \omega)$ = cross-spectrum (Pa^2/(rad/sec))
$K_1 = -k_1\delta^*$ = streamwise wavenumber
$K_c = \Omega/U_c$
$= (\omega/u_c)\delta^*$ = convective wavenumber
$R_\tau = u_\tau\delta/\nu$ = ratio of the outer to inner length scale
$R_\theta = U_o\theta/\nu$ = momentum thickness Reynolds number
$U_c = u_c/U_o$ = convection velocity
U_o = freestream velocity (m/s)
$u_\tau = (\tau/\rho)^{1/2}$ = friction velocity (m/sec)
$X = \xi/\delta^*$ = streamwise separation
δ = boundary layer thickness (m)
δ^* = boundary layer displacement thickness (m)
λ = wavelength (m)
ν = kinematic viscosity (m^2/s)
ρ = density (kg/m^3)
θ = boundary layer momentum thickness (m)
τ = mean wall shear stress (N/m^2)
$\Phi(\omega)$ = autospectrum (Pa^2/(rad/sec))
$\phi(\xi, \omega)$ = cross-spectrum phase (rad)
$\Phi^*(\Omega) = \Phi(\omega)/(\rho^2\delta^*U_o^3)$ = autospectrum (nondimensional)
$\Phi^*(K_1, \Omega) = \Phi(k_1,\omega)2\pi/(\Phi(\omega)\delta^*)$ = wavenumber-frequency spectrum (nondimensional and normalized)
$1/2\pi \int_{-\infty}^{\infty} \Phi^*(K_1, \Omega)dK_1 = 1$
$\Omega = \omega\delta^*/U_o$ = nondimensional frequency

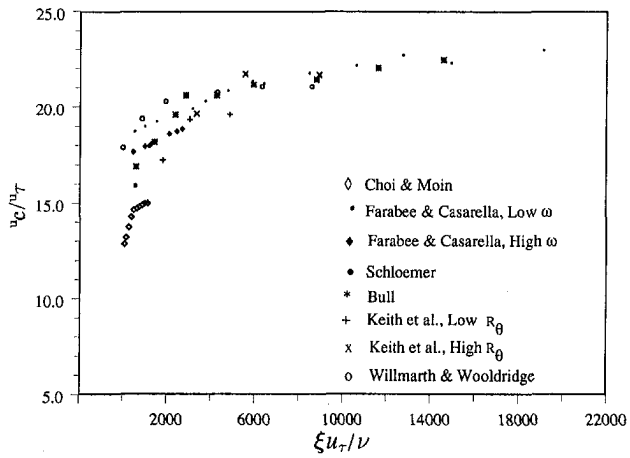

Fig. 3 Comparison of convection velocities scaled with inner variables

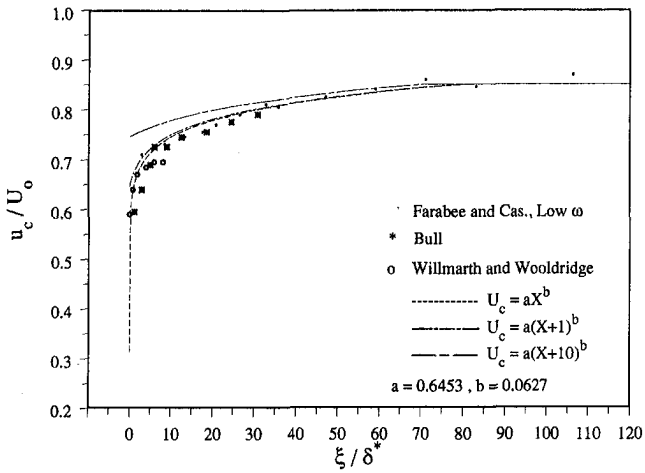

Fig. 4 Curve fits to convection velocity data

data, resulting in the trend of increasing levels with increasing R_θ.

The use of u_τ as a velocity scale with the inner length scale ν/u_τ leads to an improved collapse of the data of Fig. 2, as shown in Fig. 3. Here, the frequency bands are scaled as $\omega\nu/u_\tau^2$. The low discrete frequency data of Farabee and Casarella fall at the center of the narrow band of Keith et al. at the higher R_θ. These data collapse well. The high discrete frequency data of Farabee and Casarella fall at the center of the narrow band of Willmarth and Wooldridge. The Willmarth and Wooldridge data lie above those of Farabee and Casarella. Choi and Moin's broadband data extend to significantly higher frequencies ($\omega\nu/u_\tau^2$) than the other data sets and lie significantly below the other three investigations. Although Schloemer's data covers a somewhat higher frequency range than Bull's, both data sets collapse fairly well. The data of Farabee and Casarella (low ω), Bull, Keith et al. (high R_θ), and Willmarth and Wooldridge collapse well at larger values of $\xi u_\tau/\nu$.

The outer variable scaling of Fig. 1 collapses all the data sets over two orders of magnitude in R_θ slightly more effectively than the inner variable scaling. Based upon the analysis of Farabee and Casarella (1991), and in view of the frequency bands as given in Table 1, contributions to the wall pressure autospectra are from a significant or entire portion of the log-law region. The effectiveness of outer and inner variables for collapsing the convection velocity data is consistent with the pressure-producing sources existing in the log-law region.

Estimated Wavenumber-Frequency Spectrum

If we define nondimensional outer variables as $X = \xi/\delta^*$, $K_1 = -k_1\delta^*$, $U_c = u_c(\omega_o, \xi)/U_o$, $\Omega = \omega_o\delta^*/U_o$, and $K_c = \Omega/U_c$, a nondimensional normalized form of the Corcos model is given by

$$\Phi^*(K_1, \Omega) = (-2\gamma/K_c)(1/(\gamma^2 + (1 - K_1/K_c)^2)). \quad (6)$$

The sign of K_1 was chosen as negative to place the convective ridge at positive K_1. If the dependence of U_c on X is taken into account, the spectrum may be evaluated as

$$\Phi^*(K_1, \Omega) = \int_{-\infty}^{\infty} e^{(\gamma|\Omega X/U_c(X)| - i(-K_1 + \Omega/U_c(X))X)} dX. \quad (7)$$

A value for γ of -0.145 provided an accurate exponential curve fit to Farabee and Casarella's (1991) cross spectrum for $\Omega = 0.24$. A function of the form $U_c(X) = aX^b$ was fit to the low frequency data of Farabee and Casarella, resulting in a standard deviation of 0.04. For $X > 81$, $U_c(X)$ was taken as constant at 0.85. This curve fit results in a sharper roll-off near the origin than supported by the Farabee and Casarella data, and more accurately models the broadband data of Bull (1967) and the higher frequency data of Willmarth and Wooldridge (1962), as shown in Fig. 4. The function $U_c(X) = a(X + 1)^b$ resulted in the same standard deviation of 0.04 for Farabee and Casarella's low-frequency data, and gives a value for $U_c(0)$ of 0.645, which agrees with that estimated by Farabee and Casarella.

Equation (7) was evaluated numerically with $U_c(X) = aX^b$. In comparison to the Corcos model given by Eq. (6) with a constant value of 0.85 for U_c, the spectrum of Fig. 5 exhibits significantly lower spectral levels at subconvective and lower wavenumbers and increased levels at higher wavenumbers. The function $U_c(X) = a(X + 1)^b$ leads to the same trends in the spectrum as $U_c(X) = aX^b$, with the effects slightly diminished. For comparison, we also considered the function $a(X + 10)^b$ with less of a roll-off near the origin. This function produced the same trends in the spectrum, but the effects were further diminished. A fifth-order polynomial (not shown here) was also fit to the data of Farabee and Casarella, and resulted in a spec-

Table 1 Parameters for comparison of convection velocity data

Investigation	R_θ	R_τ	$\omega\delta^*/U_o\|1$	$\omega\delta^*/U_o\|2$	$\omega\delta/u_\tau\|1$	$\omega\delta/u_\tau\|2$	$\omega\nu/u_\tau^2\|1$	$\omega\nu/u_\tau^2\|2$	Region
Choi and Moin (1990), $R(\xi, \tau)$, broad band	285 (DNS)	180	0.08	3.55	10.00	450.00	0.055	2.484	mid-high
Farabee and Casarella (1991),			0.24	—	40.8	—	0.035	—	mid
$\Phi(\xi, \omega)$ narrow band	3,400 (air)	1,165	0.96	—	163.0	—	0.140	—	log-law
Schloemer (1967), $R(\xi, \tau)$ broad band	5,800 (air)	2,043	0.115	7.655	20.772	1,384.83	0.010	0.678	mid-high
Bull (1967), $R(\xi, \tau)$ broad band	10,000 (air)	3,614	0.038	4.08	8.24	884.30	0.002	0.245	mid-log law
Keith et al. (1991), $R(\xi, \tau)$	11,700	4,182	0.47	1.41	100.09	300.28	0.024	0.072	log-law
narrow band	21,700 (water)	6,778	0.46	1.42	106.29	328.11	0.016	0.048	log-law
Willmarth and Woolridge (1962), $R(\xi, \tau)$, narrow band	29,000 (air)	10,560	4.10	6.80	1,222.80	2,028.10	0.116	0.193	log-law

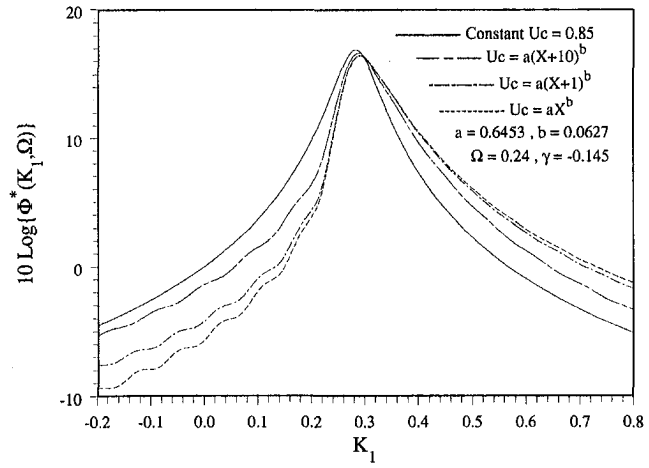

Fig. 5 Effects of the roll-off of $U_c(X)$ for small X on the wavenumber-frequency spectrum $\Phi^*(K_1, \Omega)$

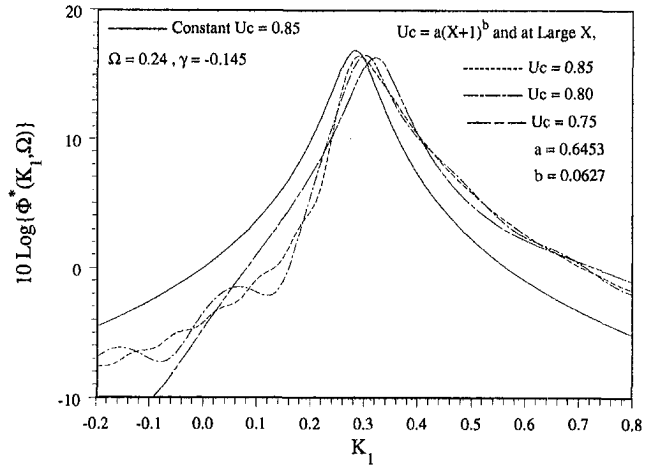

Fig. 6 Effects of the value of $U_c(X)$ for large X on the wavenumber-frequency spectrum $\Phi^*(K_1, \Omega)$

trum which agreed quite well with that obtained using the function $a(X + 1)^b$. The function $a(X + 1)^b$ was found to most accurately model the convection velocity data and therefore leads to a more accurate wavenumber-frequency spectrum.

Comparison of the cases aX^b and $a(X + 1)^b$ shows the sensitivity of the spectrum to small-scale turbulence. The roll-off of $U_c(X)$ near the origin results from small-scale turbulence with lower convection velocities and rapid spatial decay. For $X \geq 1$, the values for $U_c(X)$ given by aX^b and $a(X + 1)^b$ agree to within 5 percent. The differences in the roll-off of $U_c(X)$ for $0 < X < 1$, therefore, lead to the differences in the spectra at low wavenumbers, with the sharper roll-off leading to lower spectral levels. For the boundary layer of Farabee and Casarella, $X = 1$ corresponds to $\xi = 188\nu/u_\tau$. A decay constant of -0.145 implies that a turbulent pressure-producing structure loses 84 percent of its coherence as it convects and decays over 2λ. An approximate cut off may then be defined as $\lambda < 100\nu/u_\tau$ for turbulence, which influences $U_c(X)$ only over this particular spatial range.

At the low frequency $\omega\delta^*/U_o = 0.24$, the primary energy in $\Phi(\omega)$ results from turbulence activity in the outer region of the boundary layer since wavelengths associated with the convective ridge are of the order of δ. However, the spectral levels at wavenumbers above and below the convective ridge are directly influenced by the small-scale turbulence. The primary energy in small-scale turbulence, with wavelengths of approximately $100\ \nu/u_\tau$ or less, exists at high convective wavenumbers ($k_c\nu/u_\tau > 0.06$) and their corresponding high frequencies ($\omega\nu/u_\tau^2 > 1.0$). Farabee and Casarella concluded that energy at $\omega\nu/u_\tau^2 > 0.3$ results from small-scale turbulence activity in the buffer region. This small-scale turbulence has little effect on the total energy in $\Phi(\omega)$ at low frequencies, but significantly influences the distribution of energy in wavenumber. By considering the spectral solution to the Poisson equation, Farabee (1986) concluded that contributions to $\Phi(\omega)$ at low frequencies are possible from turbulent velocity fluctuations throughout the entire boundary layer.

The effect of the convection velocities of the large-scale structures on the spectrum was also determined by varying the constant value of $U_c(X)$ at large separations. The largest value of $U_c(X)$ for Farabee and Casarella's low-frequency data was 0.87 at $X = 106$. Using the function $a(X + 1)^b$ and a constant value of 0.87 for $X > 105$ rather than 0.85 for $X > 80$ had a negligible effect on the spectrum. Using a lower value of 0.80 for $X > 29$ had a very small effect on the convective and higher wavenumbers. However, at subconvective and lower wavenumbers, the spectral levels display an apparent oscillation (Fig. 6), which clearly results from changes in $U_c(X)$ for $X > 29$. For Farabee and Casarella's boundary layer, $X = 29$ corresponds to $\xi = 5{,}460\nu/u_\tau$, or 4.7δ. Structures with $\lambda < 2{,}730\nu/u_\tau$ (or $\lambda < 2.3\ \delta$) have a negligible influence on $U_c(X)$ for $X > 29$ since they have lost more than 84 percent of their coherence. The convection velocities of turbulence with $\lambda > 2.3\delta$ in the outer region therefore also influence the spectrum at subconvective and lower wavenumbers. For comparison, we considered a constant value of 0.75 for $U_c(X)$ for $X > 9$. This leads to a shift of the convective ridge to higher wavenumbers. The shape of the spectrum agrees with the model of Eq. (6) as expected, since $U_c(X)$ is constant over a large spatial region.

The sensitivity of the spectrum to the decay constant γ (with the frequency Ω held constant) was determined for $-0.165 \leq \gamma \leq -0.110$, with $U_c(X) = a(X + 1)^b$. At the convective ridge, the levels increase as $|\gamma|$ decreases, as shown in Figure 7. At higher wavenumbers, the levels decrease slightly as $|\gamma|$ decreases. At subconvective and low wavenumbers the levels decrease significantly as $|\gamma|$ decreases, and exhibit oscillations. The value of -0.145 corresponds to the data of Farabee and Casarella at $\Omega = 0.24$, and the value of -0.125 (which is accurate at higher frequencies) is commonly used with the Corcos model when the frequency dependence of γ is not taken into account.

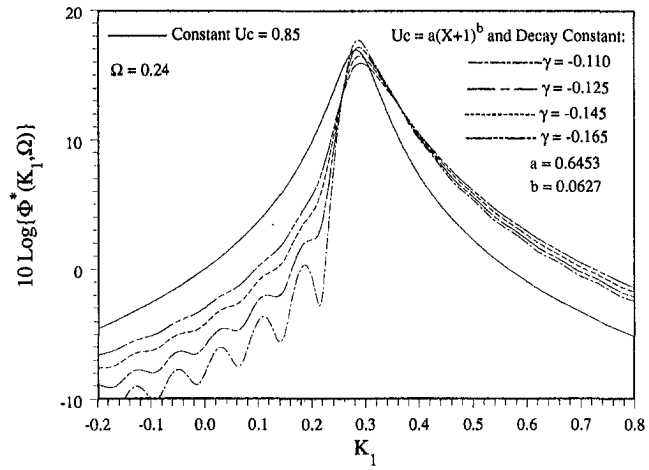

Fig. 7 Effects of the exponential decay constant on the wavenumber-frequency spectrum $\Phi^*(K_1, \Omega)$

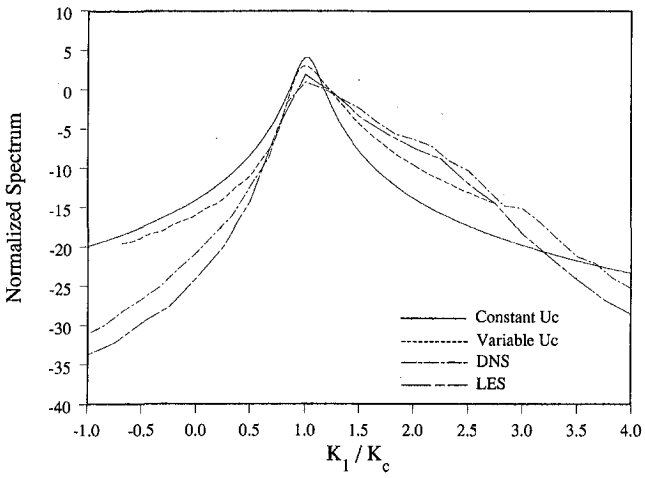

Fig. 8 Comparison with "DNS" and "LES" numerical results

Control of the small-scale turbulence may reduce flow induced vibrations and noise by lowering the low wavenumber spectral levels. A sharper roll-off for small separations was shown to result in lower spectral levels at low wavenumbers. In particular, reducing the convection velocities of the small-scale structures could lead to this effect. However, changes in the spatial decay, as well as the inherent coupling between the inner and outer regions of the boundary layer, will clearly impact the desired effects. Keith and Barclay (1993) investigated the influence of a large eddy breakup device (LEBU) on the wall pressure cross-spectra. The LEBU caused no measurable changes in the convection velocities, but led to a significant loss of coherence and greater spatial decay at low frequencies. Reductions in the autospectral levels also occurred at low frequencies. Using the model given by Eq. (4), they found the normalized wavenumber-frequency spectrum had reduced levels at the convective ridge and increased levels at lower and higher wavenumbers. The results of Fig. 7 support the same trends, although the shapes of the spectra are different due to the variation of convection velocity with separation. Keith (1989) investigated the effect of riblets on the wall pressure cross-spectra. The riblets produced no measurable change in the convection velocities or the autospectra, but led to increased coherence levels, implying reduced spatial decay at low frequencies. The results of Fig. 7 indicate that riblets may therefore lead to increased levels near the convective ridge and reduced levels at subconvective and low wavenumbers.

Recent numerical simulations of low Reynolds number, fully developed channel flow provide a detailed description of the space-time wall pressure field. The characteristics of the streamwise wavenumber-frequency spectra computed from these simulations were recently discussed by Chang et al. (1994). The direct numerical simulation "DNS3" (with $R_\tau = 180$) and large eddy simulation "LES2" (with $R_\tau = 171$) results of Chang et al. (1994) for the frequency $\Omega = 0.24$ are compared with the results of this study in Fig. 8. In the figure, the spectra are presented in normalized form using the convective wavenumber to represent the length scale. A value for the convective wavenumber was determined from the peak of the convective ridge in each case. The present results, taking into account the variation of convection velocity with spatial separation, show better agreement with both the DNS and LES results at both superconvective and subconvective wavenumbers than do the constant convection velocity (Corcos) results. The Corcos model clearly overpredicts the levels at subconvective and low wavenumbers. A value of -0.145 for the decay constant at this frequency was found to yield the best agreement with the numerical results. This is consistent with the cross-spectral measurements of Farabee and Casarella (1991) at this frequency. The differences in the numerical spectra with respect to our estimated spectra may likely result from the Reynolds number of Farabee and Casarella given by $R_\tau = 1169$, which is an order of magnitude greater than the numerical simulations.

Part of the motivation for the original work by Corcos (1963) was to determine the effect of sensor size on measured autospectra. It is therefore appropriate to determine if the changes shown to result from the variation in convection velocity have a significant effect on the attenuations due to sensor size. Corcos derived an expression for the ratio of the measured to the true autospectrum by formulating the problem in the spatial domain. As discussed earlier, in his formulation, the convection velocity did not vary with separation. Keith and Abraham (1995) investigated the effect of the spatial variation of convection velocity on the attenuations in the autospectrum due to spatial averaging, and found no significant effect. Here, the redistribution of energy with wavenumber, shown to occur, is insufficient to have a significant effect on the attenuations in the autospectrum due to the spatial averaging resulting from the sensor.

Conclusions

Comparison of convection velocities from experimental measurements and numerical simulations covering two orders of magnitude in R_θ support an outer variable scaling for collapsing the data. The early work of Corcos provided a model for the wall pressure cross spectrum in terms of a similarity scaling based upon a convection velocity assumed independent of spatial separations. Recent measurements still support this similarity scaling, if the dependence of u_c on spatial separation is taken into account. An improvement in the wavenumber-frequency spectrum $\Phi^*(K_1, \Omega)$ estimated from the cross spectrum is obtained by including the effect of u_c when the spatial Fourier transform is computed.

In view of the sensitivity of the estimated spectrum to the convection velocity and also to the decay constants, the limited cross-spectral data presently available precludes formulating a model for the wavenumber-frequency spectrum valid over a wide range of frequencies as well as Reynolds numbers. For applied problems of flow-induced vibration and noise, estimates of the wall pressure wavenumber-frequency spectrum may be determined numerically with the methods presented here, taking into account the effects that are related to the particular frequencies and Reynolds numbers of interest. Although we have used convection velocity data, the actual phase data will improve the accuracy of the estimates. The results presented here also emphasize the requirement for extremely small pressure sensors of diameter $25\nu/u_\tau$ or less to accurately measure the phase at very small spatial separations.

Acknowledgments

This research was supported by the Independent Research Program, Manager Dr. K. M. Lima, Code 102, Naval Undersea Warfare Center Division, Newport, RI.

References

Bull, M. K., 1967, "Wall-Pressure Fluctuations Associated With Subsonic Turbulent Boundary Layer Flow," *Journal of Fluid Mechanics,* Vol. 28, Part 4, pp. 719–754.

Chang, P. A., Abraham, P. M., and Piomelli, U., 1994, "Wavenumber-Frequency Characteristics of Wall Pressure Fluctuations Computed Using Turbulence Simulations," *Proceedings of the ASME Symposium on the Active Control of Vibration and Noise,* DE-Vol. 75.

Choi, H., and Moin, P., 1990, "On the Space-Time Characteristics of Wall-Pressure Fluctuations," *Physics of Fluids* (A) 2 (8), Aug., pp. 1450–146.

Corcos, G. M., 1963, "Resolution of Pressure in Turbulence," *Journal of the Acoustical Society of America,* Vol. 35, No. 2, Feb., pp. 192–199.

Farabee, T. M., 1986, "An Experimental Investigation of Wall Pressure Fluctuations Beneath Non-Equilibrium Turbulent Flows," Report No. DTNSRDC-86/047, David Taylor Naval Ship R & D Ctr., Bethesda, MD, May.

Farabee, T. M., and Casarella, M. J., 1991, "Spectral Features of Wall Pressure Fluctuations Beneath Turbulent Boundary Layers," *Physics of Fluids* A 3 (10), Oct.

Keith, W. L., 1989, "Spectral Measurements of Pressure Fluctuations on Riblets," *Journal of the AIAA* (TN), Vol. 27, No. 12, Dec., pp. 1822–1824.

Keith, W. L., and Abraham, B. M., 1995, "The Influence of Convection Velocity on the Turbulent Wall Pressure Wavenumber-Frequency Spectrum," NUWC-NPT Technical Report 10,859, 21 Apr.

Keith, W. L., Bennett, J. C., and Barclay, J. J., 1991, "Hydroacoustic Research at the Quiet Water Tunnel Facility of the Naval Underwater Systems Center," *Proceedings of the ASME Symposium on Hydroacoustic Facilities,* NCA-Vol. 10, Atlanta, Dec. 1–6.

Keith, W. L., and Barclay, J. J., 1993, "Effects of a Large Eddy Breakup Device on the Fluctuating Wall Pressure Field," ASME JOURNAL OF FLUIDS ENGINEERING, Vol. 115, No. 3, Sept., pp. 389–397.

Rand, R. H., 1984, *Computer Algebra in Applied Mathematics: An Introduction to MACSYMA,* Pitman Publishing Corporation, MA.

Schloemer, H. H., 1967, "Effects of Pressure Gradients on Turbulent-Boundary-Layer Wall-Pressure Fluctuations," *Journal of the Acoustical Society of America,* Vol. 42, No. 1, July, pp. 93–113.

Willmarth, W. W., and Wooldridge, C. E., 1962, "Measurements of the Fluctuating Pressure at the Wall Beneath a Thick Turbulent Boundary Layer," *Journal of Fluid Mechanics,* Vol. 14, No. 2, pp. 187–210.

P. M. Ligrani
Associate Professor.
Mem. ASME

R. Gong
Graduate Student.

J. M. Cuthrell
Graduate Student.

Convective Heat Transfer Laboratory,
Department of Mechanical Engineering,
University of Utah, Salt Lake City,
Utah 84112

J. S. Lee
Associate Professor,
Turbo and Power Machinery
Research Center,
Department of Mechanical Engineering,
Seoul National University,
Seoul 151-742,
Republic of Korea,
Mem. ASME

Effects of Bulk Flow Pulsations on Film-Cooled Boundary Layer Structure

Experimental results are presented which describe the effects of bulk flow pulsations on film cooled boundary layer structure. The film is produced by a single row of simple angle film cooling holes and the pulsations are in the form of sinusoidal variations of static pressure and streamwise velocity. Such pulsations are important in turbine studies because: (i) static pressure pulsations result in significant periodic variations of film cooling flow rates, coverage, and trajectories, and (ii) static pressure pulsations occur near blade surfaces in operating engines from passing shock waves and potential flow interactions between moving blade rows. Distributions of ensemble-averaged and time-averaged Reynolds stress tensor components are presented for x/d of 4.5, 9.8, 16.4, and 24.1 along with distributions of streamwise mean velocity and streamwise mean vorticity, where x is streamwise distance from the downstream edge of the holes and d is hole diameter. Important changes from the imposed bulk flow pulsations are evident in all measured quantities, especially just downstream of the holes at x/d = 4.5. Here, maximum Reynolds shear stresses $-2\overline{u'v'}/\overline{u_\infty}^2$ *are reduced by the pulsations in regions containing the largest film concentrations. This is because the shear layer produced by the injectant oscillates its position as each pulsation is imposed. This causes the shear layer to become more diffused as it is spread over a larger spatial volume.*

Introduction

Film cooling is employed to protect turbine component surfaces from the detrimental effects which result from exposure to the hot gases produced in gas turbine combustion chambers. The coolant originates in the compressor and is ejected over blade and endwall surfaces from arrays of holes. Film cooling is strongly dependent upon the geometries and orientations of these holes. It also depends upon a variety of film and freestream flow conditions including unsteadiness from passing wakes, combustor turbulence, families of passing shock waves, and potential flow interactions between moving blade rows.

Of these different sources of turbine unsteadiness, the ones having the most dramatic effect on film cooling are from potential flow interactions and shock waves. This is because: (i) both result in important variations of the *static* pressure near cooling hole exits as blade rows move relative to each other, (ii) periodically unsteady *static* pressure fields at the exits of the injection holes result in pulsating coolant flow rates, and (iii) the resulting pulsating *static* pressure and velocity fields in the boundary layer just downstream from the injection holes produce complex time variations of film trajectories, distributions, and surface coverage. Changes to film protection from passing wakes are different because they produce periodic pulsations of *total* pressure and increased turbulence. Because neither of these significantly alter the mass flow rates of the film cooling, changes to film protection from passing wakes are often far less significant than the changes produced by potential flow interactions and passing shock waves.

Of previous investigations of the effects of flow unsteadiness on film cooling, Abhari and Epstein (1994) is the first to indicate that important changes to film cooling are caused by the static pressure pulsations in the bulk flow. Other related studies are described by Takeishi et al. (1991), who consider the effects of wake flows on film cooling, and by Norton et al. (1990), Rigby et al. (1990), and Abhari and Epstein (1994), who address the influences of passing shock waves and wakes on film cooling. Additional information on wake effects without film cooling is provided by Dunn (1990), and Dunn et al. (1989, 1992).

Like Abhari and Epstein (1994), the present work is also designed to examine the effects on film cooling of bulk flow pulsations in the form of periodic variations of static pressure and streamwise velocity. Changes to the three mean velocity components and turbulence structure (i.e. Reynolds stress tensor components) measured at four different streamwise stations downstream of the holes (x/d = 4.5, 9.8, 16.4, and 24.1) are presented and discussed. Also described are the phase-averaging procedures, and the technique employed to impose the pulsations. These data and experimental details are of interest because they show important effects of imposed bulk flow static pressure (and velocity) pulsations on boundary layer film cooling. New understanding of the physical interactions between pulsations and film cooling is thus provided, thereby enabling the development of improved numerical models and design methods to account for these effects. In doing so, insight is also provided into the important changes which occur on and near blade surfaces during the passage of potential flow interactions and passing shock waves.

Experimental Apparatus and Procedures

The experiment is conducted using a large scale model facility to allow detailed probing of flow features. Low speeds, flat plate test sections, and constant property flows are used to isolate the interactions between the film cooling, imposed bulk flow pulsations, and boundary layer.

Wind Tunnel The wind tunnel is an open-circuit, subsonic facility with the blower located at the upstream inlet. It is located in the Convective Heat Transfer Laboratory of the Department of Mechanical Engineering of the University of Utah. The test section is a rectangular duct 3.05 m long, 0.61 m wide, and

Contributed by the Fluids Engineering Division for publication in the JOURNAL OF FLUIDS ENGINEERING. Manuscript received by the Fluids Engineering Division July 10, 1995; revised manuscript received June 7, 1996. Associate Technical Editor: Wing Ng.

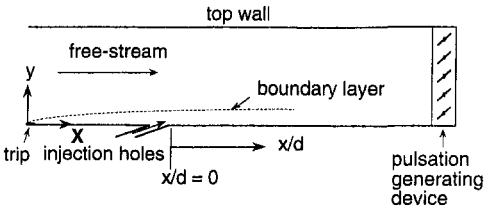

Fig. 1 Schematic of test section and coordinate system

0.203 m high at the inlet, with a zero pressure gradient set to within 0.0025 cm of water differential pressure along its length, both with and without pulsations. Flow at the test section inlet shows excellent spatial uniformity and a freestream turbulence level less than 0.1 percent at a freestream velocity of 10.7 m/s.

A schematic of the test section, including the coordinate system, is shown in Fig. 1. A boundary layer trip is located on the test plate just downstream of the nozzle exit. The downstream edge of the injection holes is then 1.050 m downstream of the trip, and measuring stations are subsequently located at x/d of 4.5, 9.8, 16.4, and 24.1. Corresponding Reynolds numbers, based on streamwise distance (from the trip) and a freestream velocity of 10.7 m/s, range from 790,000 to 1,090,000.

Film Cooling Configuration and Air Supply The film cooling holes are placed in a single row with spanwise spacing of 3 hole diameters. Each of five holes is oriented in a streamwise/normal plane (i.e., with a simple angle orientation) at a 35 degree angle from the test surface. Hole diameter is 2.22 cm, giving an l/d ratio of 4.0, and a ratio of boundary layer thickness to hole diameter of 1.23 (measured with no pulsations 0.237 m or 10.7 d upstream of $x = 0$). Ratios of displacement thickness to hole diameter, and momentum thickness to hole diameter are 0.191, and 0.136, respectively. The test section and injectant air supply are maintained isothermal at ambient temperature (about 19°C) for all tests so that minimal temperature variations are present in the test section as surveys are made with the hot-wire probes. Blowing ratio $\bar{m}$ is 0.98, momentum flux ratio is 0.96, and ratio of injectant to freestream density ρ_c/ρ_∞ is 1.0 for most all tests. Injection Reynolds number $d\overline{u_c}/\nu$ is then about 15,000.

Mean Velocity and Turbulence Structural Details Boundary layer mean velocity components and Reynolds stress tensor components are measured using hot-wire anemometry probes. A Dantec 55PO5 hot-wire probe, with gold plated leads, sensor diameter of 5 μm and sensor length of 1.25 mm, is used to measure the instantaneous longitudinal velocity. A Dantec 55P51 crossed-hot wire probe, also with gold plated leads and sensors having the same approximate diameter and sensor length, is used to simultaneously measure either u and v, or u and w. DISA 55M10 constant-temperature bridges are used to operate all of the sensors at an overheat ratio of 1.6. The hot-wire is calibrated in the potential flow of the wind tunnel with the same bridge settings employed for measurements. Hot-wire velocity calibrations are conducted with the crossed-wire probe oriented both in the uv plane and the uw plane, and yaw calibrations are conducted with the probe in the uw plane to determine the effective wire angles with respect to the streamwise flow direction. Calibrations are repeated at each new streamwise measurement location and for each new survey because effective wire angles change slightly as the probe sensors are rotated and as the probe traversing mechanism is relocated. During calibrations and measurements, the voltage signal from each hot-wire bridge is processed using a Dantec Model 56N20 signal conditioner system set with an amplifier gain of 1, a low-pass filter of 3 kHz, and no high pass filter.

Data Acquisition System Signals from the signal conditioners connected to the hot-wire anemometry bridges are acquired using a Hewlett-Packard 3852A data acquisition control unit. This unit operates with a Hewlett-Packard 44702A high speed voltmeter, Hewlett-Packard 44711A high-speed FET multiplexers, and Hewlett-Packard 44703B extended memory cards. The control unit with installed components is controlled and programmed using a Hewlett-Packard Model 9836S mainframe computer with a 10 mbyte 3.5 hard disk drive. The system is capable of acquiring up to 24 channels of data at a total rate up to 100 kHz (for all channels).

Generation of Bulk Flow Pulsations

Static pressure pulsations are produced in the test section using an array of rotating shutters driven by a system of gears and an electric motor. The shutters are located at the exit of the test section, as shown in Fig. 1. Advantages of this technique are described by Karlsson (1959) and Al-Asmi and Castro (1993), and include the ability to oscillate the static pressure without significant total pressure variations, and the ability to produce deterministic sinusoidal variations of static pressure at selected frequencies.

Here, pulsations at a frequency of 2 Hz are produced which gives a freestream Strouhal number St_∞ of 0.031, which pertains to the time required for the boundary layer to recover fully after the passing of each different type of disturbance (Doorly and Oldfield, 1985). The parameter which quantifies the influence

Nomenclature

d = injection hole diameter
l = injection hole length
$\bar{m}$ = blowing ratio, $\rho_c\overline{u_c}/\rho_\infty\overline{u_\infty}$
m = instantaneous blowing ratio, $\rho_c u_c/\rho_\infty\overline{u_\infty}$
n = pulsation frequency in Hz
St_c = coolant Strouhal number, $2\pi n l/\overline{u_c}$
St_∞ = freestream Strouhal number, $2\pi n\delta/\overline{u_\infty}$
t = time
u = streamwise velocity
$\overline{u_c}$ = time-averaged injectant velocity, spatially averaged over hole cross-section
u_c = instantaneous injectant velocity, spatially averaged over hole cross-section
$\overline{u_\tau}$ = friction velocity
v = normal velocity
w = spanwise velocity
x = streamwise distance measured from downstream edge of injection holes
X = streamwise distance measured from trip
y = distance normal to the surface
$y^+ = y\overline{u_\tau}/\nu$
z = spanwise distance from test surface centerline
δ = boundary layer thickness
ρ = density
τ = time period of one pulsation
ν = kinematic viscosity

Subscripts

c = injectant at exit plane of injection holes
∞ = freestream

Superscripts

$'$ = fluctuating component
$\bar{}$ = time average
$\tilde{}$ = periodic component
$\hat{}$ = phase-average

of disturbance passing frequency on the injectant is the coolant Strouhal number St_c. Here, $St_c = 0.11$, which gives quasi-steady film behavior, and is low enough to ensure that temporal pressure variations influence the injectant mass flow rate (Abhari and Epstein, 1994).

Phase-Averaging and Data Processing

Procedures for phase-averaging and data processing are now described. Briefly, instantaneous voltages are converted into instantaneous velocities using look-up tables which minimize the time required to compute turbulence statistical quantities. Look-up table values are computed from calibration data and account for signal digitization, amplifier gains, and all other aspects of signal processing. For each measurement location, a total of 14000 data points are acquired for each of two channels at a rate of 4 kHz per channel, giving a total sampling time of 3.5 secs. Each spanwise/normal plane survey covers a grid of 15 by 12 locations spaced 0.508 cm apart. Surveys are conducted using a computer controlled, automated two-dimensional probe traversing system. Because the set-up accounts for backlash of the threaded drive threads, each y and z location is set within about $\pm.006$ cm. Because total survey time is 19.2 hours (actually conducted in two parts), freestream air temperature is not constant, and calibration coefficients are corrected for air temperature variations as the survey is conducted using procedures described by Perry (1982). These temperature corrections are implemented in the look-up tables just prior to determination of effective velocities from the output of the analog-to-digital converter. The local freestream velocity is also determined for every 12th data location as each survey is conducted to account for any small changes in wind tunnel flow conditions which may occur.

With imposed periodic flow, instantaneous velocities u can be considered to be the sum of three components such that $u = \bar{u} + \tilde{u} + u'$, where $\bar{u}$ is the time-averaged velocity, $\tilde{u}$ is the periodic velocity, and u' is the fluctuating component (Hussein and Reynolds, 1970). In the present study, $\bar{u}$ and $\tilde{u}$ are combined as the phase-averaged velocity $\hat{u}$, such that $u = \hat{u} + u'$ following Ramaprian and Tu (1980). Thus, for a steady flow with no periodic velocity, $\hat{u}$ is then equal to $\bar{u}$. $\hat{u}$ is then determined from phase-averaging instantaneous velocity results using the equation given by

$$\hat{u}(n)\big|_{n=1}^{2000} = \frac{1}{npulse}\sum_{m=1}^{npulse} u(m, n)\big|_{n=1}^{2000}$$

where m and n correspond to the number of pulsations and to the number of locations across each phase where data are sampled, respectively, and *npulse* denotes total number of pulsations.

Phase-averaging is accomplished here using procedures developed exclusively for this study. After the velocities u, u and v, or u and w are determined at a particular probe location, $\bar{u}$, the time-averaged magnitude of the longitudinal velocity is calculated. The overall average pulsation time period and overall average frequency of the pulsations are then determined. After this is accomplished, all velocity samples are adjusted to account for the fact that the overall pulsation period does not coincide exactly with an exact integer multiple of the time period between data samples. Phase-averaged velocities ($\underline{\hat{u}}$), time-averaged Reynolds stress component magnitudes ($\overline{u'^2}$, $\overline{v'^2}$, $-\overline{u'v'}$, $\overline{u'w'}$), and time-averages of pulsating quantities ($\overline{\hat{u}^2}$) are then determined along with maximum and minimum magnitudes of $\hat{u}$. Time-averaged distributions of streamwise vorticity are also determined from surveys of $\bar{v}$ and $\bar{w}$ using $\partial\bar{v}/\partial z - \partial\bar{w}/\partial y$. Additional background on phase-averaging is provided by Dunn (1990).

For the present study, the pulsating generating device produces near-sinusoidal velocity (and static pressure) wave forms at a frequency of 2 Hz at peak-to peak amplitudes from 40 percent of $\bar{u}$ in the freestream to 125 percent of $\bar{u}$ near the wall. The pulsations propagate throughout the wind tunnel test section including all locations within the boundary layer developing along the test surface. The sinusoidal form for the wave form is easily described and deterministic allowing the effects of different parts of the wave form (i.e., high and low static pressures, high and low velocities, accelerations and decelerations) on film cooling to be clearly discerned.

An example of instantaneous velocity data is shown in the top of Fig. 2, along with the corresponding traces of phase-averaged velocity $\hat{u}$ and phase-averaged fluctuating velocity $\widehat{u'^2}$. At the bottom of the figure, a trace of $\bar{u} + u'$ is shown determined from $u - \tilde{u}$. These data illustrate the sinusoidal nature of the velocity wave form produced by the pulsation device. Another interesting feature is the destabilizing effect of decelerations and the stabilizing influence of accelerations, evident from respective increases and decreases of $u' + \bar{u}$ and $\hat{u}'^2$. The data presented in Fig. 2 were obtained from a sample of 14,000 data points acquired at 400 Hz per channel at $X = 0.191$ m, $Z = 0.0$ m, $y/d = 0.29$, and y^+ of 154 in a boundary layer with pulsations imposed at 2 Hz ($St_\infty = 0.016$) and no film cooling. A spectrum taken at $X = 0.813$ m, $Z = 0.0$ m, $y/\delta = 0.014$, y^+ of 9.4, and $St_\infty = 0.033$ is shown in Fig. 3 to illustrate the frequency components in the flow. Here, it is evident that flow energy levels are significantly lower than the energy in the local maximum due to the pulsation at 2.031 Hz. In addition, amplitudes of the harmonics are much lower than the principal amplitude, indicating a wave form close to a pure sinusoid.

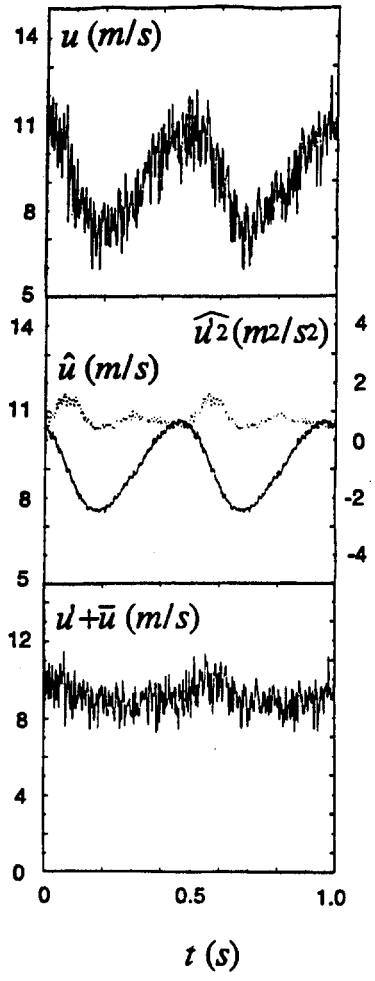

Fig. 2 Instantaneous, phase-averaged, and fluctuating streamwise velocity in a turbulent boundary layer with pulsations imposed at 2 Hz at $X = 0.191$ m, $z/d = 0$, $y/d = 0.29$, $y^+ = 154$, and $St_\infty = 0.016$

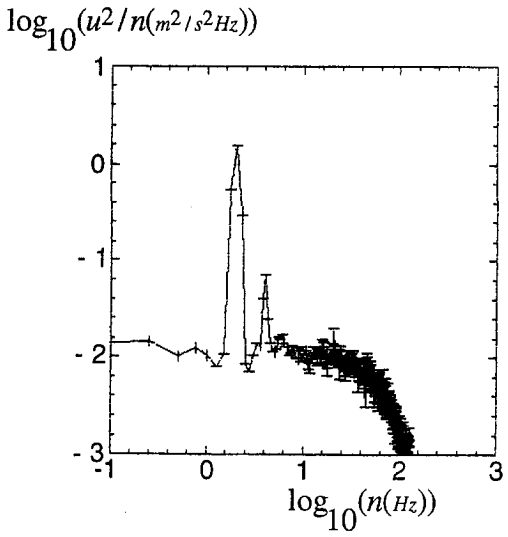

Fig. 3 Spectrum of instantaneous longitudinal velocity in a turbulent boundary layer with pulsations imposed at 2 Hz at X = 0.813 m, z/d = 0, y/δ = 0.014, y^+ = 9.4, and St_∞ = 0.033

Variations of freestream static pressure P_∞ are related to variations of freestream velocity u_∞ by the Euler equation for inviscid unsteady flow along a streamline, given by

$$\partial u_\infty/\partial t + u_\infty(\partial u_\infty/\partial x) = -1/\rho(dP_\infty/dx)$$

For the present experimental conditions, the freestream is quasi-steady, and the $\partial u_\infty/\partial t$ term is negligible. Consequently, the relationships between u_∞, instantaneous injectant velocity u_c, and freestream static pressure P_∞ are given by

$$P_{o\infty}/\rho = P_\infty/\rho + u_\infty^2/2 \quad \text{and}$$

$$u_c = C_D[2(P_{oc} - P_\infty)/\rho]^{1/2} \qquad (1, 2)$$

where C_D is the injection hole discharge coefficient. Variations of C_D with instantaneous injectant Reynolds number during each pulsation are quite small but included as u_c values are determined. Figure 4 shows traces of u_∞, P_∞, u_c, and instantaneous injectant blowing ratio m for two pulsation cycles. The freestream velocity trace is determined from hot-wire anemometry measurements such as the ones shown in Fig. 2. P_∞, u_c, and m are calculated using this u_∞ variation in Eqs. (1) and (2) with constant freestream total pressure $P_{o\infty}$ and constant injection plenum total pressure P_{oc}. $P_{o\infty}$ is assumed constant as there is no mechanism present in the wind tunnel test section to alter it (other than very small variations of the blower operating point) as each pulsation is imposed. P_{oc} is assumed constant because of the large volume of the injectant plenum. With an average freestream velocity of 10.83 m/s, Fig. 4 shows that the 2 Hz pulsating freestream ranges from 8.60 to 12.93 m/s. This results in a ±9 percent change both to the injectant velocity and blowing ratio with respect to time-averaged values ($\bar{m}$ = 0.98, $\overline{u_c}$ = 10.64 m/s), such that m varies from 0.89 to 1.07. This is confirmed by similar u_c variations measured at the exits of the film cooling holes during qualification tests using hot-wire anemometry probes. The agreement between measured and calculated u_c variations also confirms the assumption of quasi-steady freestream conditions as well as negligible $\partial u_\infty/\partial t$ in the freestream.

Uncertainty Estimates

Uncertainty estimates are based on 95 percent confidence levels, and determined using the methods described by Kline and McClintock (1953) and by Moffat (1988). The uncertainty of the phase-averaged velocity $\hat{u}$ is about 2.5 percent, and the uncertainty of $\bar{u}$ is about 1.5 percent. Uncertainty of $\overline{u'^2}$ is typically 4 percent. Uncertainties of $\overline{v'^2}$, $\overline{w'^2}$, $-\overline{u'v'}$, and $\overline{u'w'}$ are each about 10 percent.

Baseline Test Results

Three types of baseline tests were conducted: (a) no film cooling and no pulsations, (b) with film cooling and no pulsations, and (c) with bulk flow pulsations and no film cooling. The first two types of baseline tests show expected behavior. With no pulsations and no film cooling, normalized profiles of $\overline{u'^2}$, $\overline{v'^2}$, $\overline{w'^2}$, and $-\overline{u'v'}$ show behavior characteristic of turbulent boundary layers with two-dimensional mean flow fields, and excellent agreement with the measurements of Green (1989) and Klebanoff (1954), after accounting for a different freestream turbulence level in the latter case. Comparisons with the data of Klebanoff (1954) are shown in Figs. 5(a) and 5(b). Profiles of $\sqrt{\overline{u'^2}}/\overline{u_\infty}$ and $\sqrt{\overline{v'^2}}/\overline{u_\infty}$ measured both with and without pulsations and no film cooling show excellent agreement with measurements from Menendez and Ramaprian (1989) considering slightly different experimental conditions in the two studies (Cuthrell, 1995; Gong, 1996).

The agreement of all three types of baseline measurements with ones from other sources validates the experimental apparatus and procedures, and provides confidence that the results obtained with film cooling and pulsations are accurate.

Experimental Results-Mean Velocity Components

Profiles of $\bar{u}/\overline{u_\infty}$ measured at z/d = 0 and x/d of 4.5, 9.8, 16.4, and 24.1 are presented in Fig. 6. Surveys of $\bar{v}/\overline{u_\infty}$ and $\bar{w}/\overline{u_\infty}$ at x/d = 4.5 are given in Figs. 7 and 8, respectively. At each location, profiles are presented for three situations: (i) no film, no pulsations, (ii) with film, no pulsations, and (iii) with film and with pulsations.

Flow Structure With No Pulsations Considering results with no pulsations, streamwise velocities for the boundary layer with film cooling are generally less than ones measured with no film cooling at all four x/d for $\bar{m}$ = 0.98. This is a result of

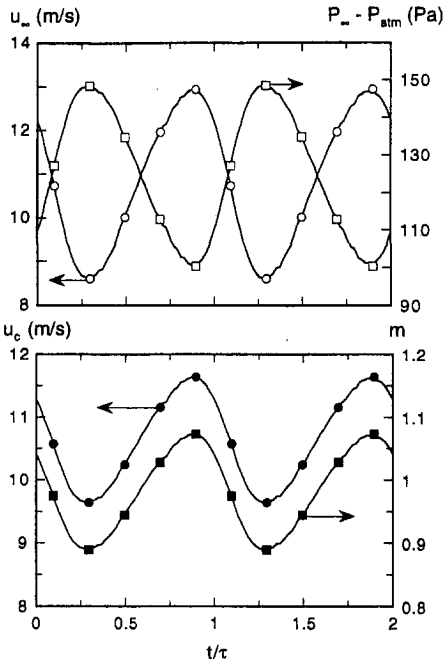

Fig. 4 Variation of freestream static pressure, freestream velocity, injectant velocity at film hole exits, and injectant blowing ratio over two pulsation cycles

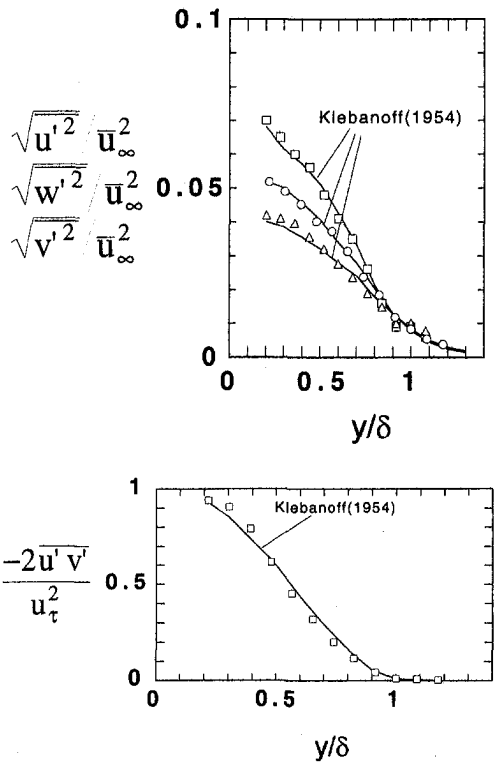

Fig. 5 Profiles of Reynolds stresses (with no pulsations) compared with Klebanoff (1954). Present data for X = 0.813 m, z/d = 0, δ = 2.63 cm, $\bar{u}_\infty$ = 10 m/s, and u_τ = 0.447 m/s. (*a*) Normalized normal Reynolds stress components. (*b*) Normalized Reynolds shear stress.

low streamwise momentum fluid which is entrained by the film and then advected away from the wall by the positive magnitudes of normal velocity $\bar{v}$. Positive magnitudes of $\bar{v}$ are characteristic of the most important injectant accumulations. Figure 7 provides evidence that these accumulations are oval in shape, and extend from the wall to y/d of about 1.6, and from z/d = −0.5 to +0.5 at x/d = 4.5. Upwash portions of the two legs of the injectant horseshoe vortex are responsible for the positive $\bar{v}$ at z/d = 0, and thus play an important role in decreasing film cooled $\bar{u}$ relative to the boundary layer with no film cooling at z/d = 0. The vortex legs are also largely responsible for the $\bar{w}/\bar{u}_\infty$ distribution shown in Fig. 8. The horseshoe vortex and its two legs are discussed in more detail in the next section.

Because of these phenomena, the gradient of $\bar{u}$ becomes significant at y/d locations from 1.0 to 1.5 (at x/d = 4.5) which correspond to the outer portion of the film concentration. The gradient evidences a shear layer developing at the interface between fluid with low streamwise momentum (below) and fluid with high streamwise momentum (above). Pietrzyk et al. (1989) observe similar behavior at the same $\bar{m}$, which at larger x/d, is located between the low speed fluid in the wake (just downstream of the film) and the lower edge of the film accumulation. Magnitudes of $\bar{v}/\bar{u}_\infty$ then decrease significantly with y/d in this shear layer. As y/d becomes greater than 1.0 at x/d = 4.5, film cooled streamwise velocities in Fig. 6 increase significantly and normal velocities in Fig. 7 then approach zero. At x/d of 9.8, 16.4, and 24.1, the $\bar{u}/\bar{u}_\infty$ increase (as well as the $\bar{v}/\bar{u}_\infty$ decrease) begin at larger y/d.

As the boundary layer advects downstream to larger x/d, Fig. 6 shows film cooled profiles of $\bar{u}/\bar{u}_\infty$ with qualitative characteristics similar to the x/d = 4.5 profile. The most important quantitative differences pertain to the location and intensity of the shear layer. In particular, the shear layer is located farther from the wall with normal gradient $\bar{u}/\bar{u}_\infty$ magnitudes which decrease as x/d increases.

At y/d > 2.3, the $\bar{u}/\bar{u}_\infty$ film cooled profile at x/d = 4.5 approaches the profile with no film cooling in Fig. 6. Similar behavior is observed at x/d of 9.8, 16.4, and 24.1, except that the approach location becomes farther from the wall as x/d increases.

Effects of Pulsations on Flow Structure Significant changes to the flow structure occur when the pulsations are present. These are evident in the $\bar{v}/\bar{u}_\infty$ and $\bar{w}/\bar{u}_\infty$ distributions shown in Figs. 7 and 8. Figure 6 shows $\bar{u}/\bar{u}_\infty$ from the pulsating boundary layer which are lower than values measured with no pulsations for y/d < 1.0–1.5 at x/d of 4.5, 9.8, and 16.4. At x/d = 4.5, $\bar{u}/\bar{u}_\infty$ magnitudes with pulsations are greater than 1 (ranging from 1.00 to 1.03) at y/d from 1.5 to 2.1, and are thus higher than the values measured with no pulsations. Thus, the same $\bar{u}/\bar{u}_\infty$ shear layer gradient is present in the film cooled boundary layer both with and without pulsations, but it extends over a larger vertical portion of the boundary layer at x/d of 4.5, 9.8, and 16.4 when the pulsations are imposed.

These characteristics are present because the imposed pulsations produce periodically unsteady static pressure fields at the exits of the injection holes which result in pulsating coolant flow rates. In addition, the pulsating static pressure and velocity fields in the boundary layer just downstream from the injection holes result in complex variations with time of the trajectories,

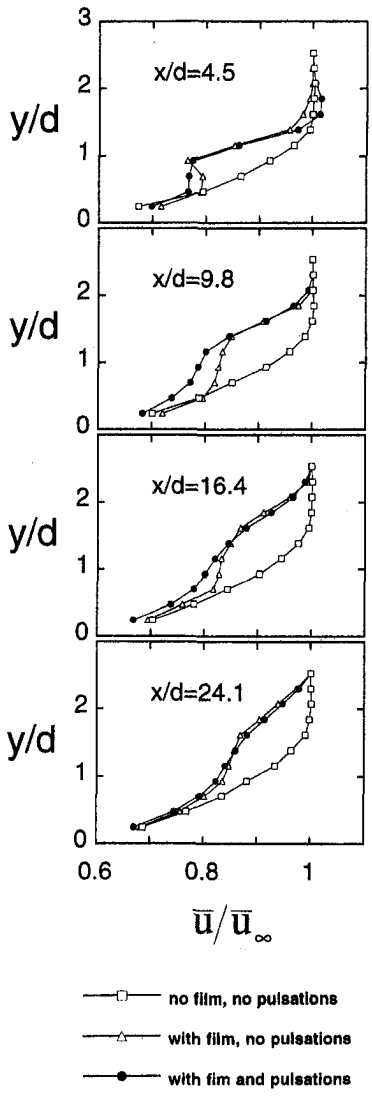

Fig. 6 Streamwise development of profiles of normalized time-averaged streamwise velocity $\bar{u}$ at z/d = 0

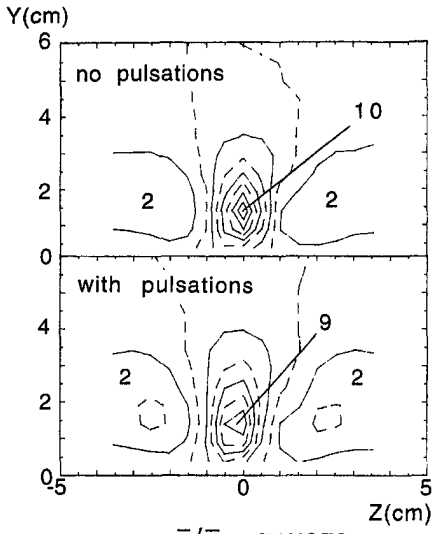

$\bar{v}/\bar{u}_\infty$ RANGES

0	< -.09	6	.06 ~ .09
1	-.09 ~ -.06	7	.09 ~ .12
2	-.06 ~ -.03	8	.12 ~ .15
3	-.03 ~ .00	9	.15 ~ .18
4	.00 ~ .03	10	.18 ~ .21
5	.03 ~ .06	11	> .21

Fig. 7 Surveys of normalized time-averaged normal velocity $\bar{v}$ at $x/d = 4.5$

distributions, as well as the coverage of the injectant along the surface. The film thus instantaneously changes its momentum and position in the boundary layer when bulk flow pulsations are imposed. The mean injectant trajectory with pulsations is also somewhat different, and the same amount of injectant is spread over a larger volume compared to nonpulsating flow.

The local streamwise velocities higher than the freestream velocity ($\bar{u}/\bar{u}_\infty > 1$) at $x/d = 4.5$ in Fig. 6 are then due to the behavior of the injectant when its momentum is highest during each pulsation cycle. During each of these intervals, Fig. 4 shows that instantaneous m reach 1.07, which give local injectant velocities as large as about $1.10\bar{u}_\infty$ at the injection hole exits. $\bar{u}/\bar{u}_\infty$ is then greater than 1 just downstream of the hole exits, and the injectant is lifted farther away from the wall than the trajectory produced with no pulsations when $\bar{m}$ is constant at 0.98. As this occurs in the outer portions of the boundary layer, streamwise velocities continue to be locally higher than the freestream velocity at x/d as large as 4.5 (Fig. 6). As x/d becomes larger and steamwise momentum is diffused, local values of $\bar{u}/\bar{u}_\infty$ greater than 1 are not apparent in Fig. 6.

As the static pressure at the hole exits increases, u_c decreases to 9.64 m/s (Fig. 4) which gives $u_c/\bar{u}_\infty = 0.89$ and the lowest injectant momentum at the injection hole exits during each pulsation cycle. The injectant is then located closer to the wall than the trajectory produced when no pulsations are imposed. As a result, streamwise velocities are locally lower than the velocities measured at the same y/d when no pulsations are imposed. As mentioned earlier, this is evident at x/d of 4.5, 9.8, and 16.4 in Fig. 6 for $y/d < 1.0-1.5$.

Also important are phase shifts between the pulsating static pressure at the exits of the film cooling holes and the pulsating freestream static pressure. Although their effects are not included in the calculated results shown in Fig. 4, they result in phase shifts between instantaneous u_c and instantaneous u_∞, which result in important variations of $\rho_c u_c/\rho_\infty u_\infty$ with time. It is these phase shifts which produce the pulsations of film cooling flow rates (confirmed by hot-wire qualification surveys mentioned earlier used to measure the instantaneous u_c at the film hole exits), since without them, $\rho_c u_c/\rho_\infty u_\infty$ would be constant and would not vary with time.

As x/d reaches 24.1 in Fig. 6, the film cooled profile measured with pulsations approaches the film cooled profile measured with no pulsations. As y/d becomes greater than 2.0–2.5, each $\bar{u}/\bar{u}_\infty$ profile in Fig. 6 approaches the baseline profile with no pulsations and no film.

Experimental Results-Streamwise Mean Vorticity

Surveys of streamwise mean vorticity measured with film cooling at x/d of 4.5, 9.8, 16.4, and 24.1 are presented in Figs. 9 and 10. The first of these figures gives results obtained with no pulsations and the second gives results obtained with pulsations.

Flow Structure With No Pulsations. As an injectant stream emerges from each film cooling hole, a horseshoe vortex forms on the upstream and lateral sides of the injectant stream. Each leg of this horseshoe vortex is then advected downstream near the wall on either side of the largest injectant concentration. The streamwise vorticity surveys in Fig. 9 evidence regions of concentrated vorticity within each leg of the horseshoe vortex. Distributions of $\bar{v}/\bar{u}_\infty$ and $\bar{w}/\bar{u}_\infty$ in Figs. 7 and 8 for $x/d = 4.5$ are consistent. In the plane of the measurements, the vortex on the right-hand side of the film concentration (i.e., with positive vorticity at larger z/d) is then rotating clockwise, and the vortex on the left-hand side of the film concentration (i.e., with negative vorticity at smaller z/d) is rotating counter-clockwise when viewed looking downstream. Peak vorticity at the centers of the vortices at all four x/d are located at $y/d = 0.6-0.7$ and $z/d = 0.3-0.4$ and at $y/d = 0.6-0.7$ and $-z/d = 0.3-0.4$.

The upwash region is located in Fig. 9 between the two concentrations of vorticity at z/d from -0.2 to $+0.2$. It is characterized by $\bar{v}/\bar{u}_\infty$ in Fig. 7 with positive magnitudes from 0.00 to 0.18, which result from the upward trajectory of the film as it moves away from the holes. Because these act to advect low momentum fluid away from the wall, local magnitudes of $\bar{u}/\bar{u}_\infty$ are lower than ones measured without film cooling, as mentioned earlier. The downwash portions of the legs of the

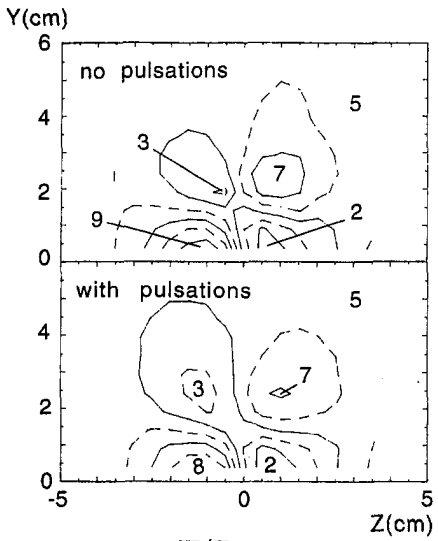

$\bar{w}/\bar{u}_\infty$ RANGES

0	< -.12	6	.03 ~ .06
1	-.12 ~ -.09	7	.06 ~ .09
2	-.09 ~ -.06	8	.09 ~ .12
3	-.06 ~ -.03	9	.12 ~ .15
4	.03 ~ .00	10	.15 ~ .18
5	.00 ~ .03	11	> .18

Fig. 8 Surveys of normalized time-averaged spanwise velocity $\bar{w}$ at $x/d = 4.5$

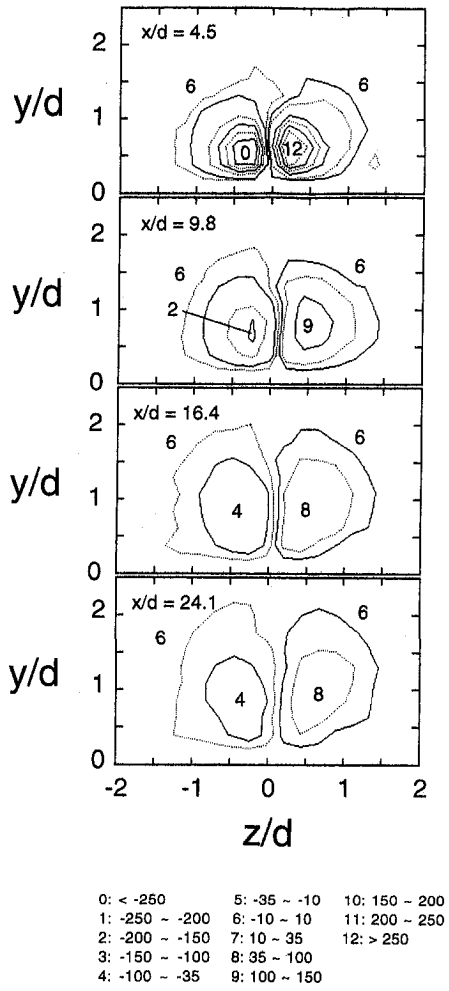

Fig. 9 Streamwise development of streamwise mean vorticity measured with no pulsations

horseshoe vortex are located to the sides of the concentrations of vorticity in Fig. 9. These are outside of the regions with the most important film accumulations at $z/d > .54$ and $z/d < -.54$. $\overline{v}/\overline{u_\infty}$ here are negative and range from 0.0 to $-.09$ indicating significant normal velocities towards the wall. $\overline{u}/\overline{u_\infty}$ at corresponding locations show values which are significantly greater than ones measured with no film cooling because of the action of the downwash regions to advect high momentum fluid from the freestream, boundary layer, and injectant towards the wall.

The highest magnitudes of streamwise vorticity, the highest local gradients of vorticity, and most concentrated distributions of vorticity are located at $x/d = 4.5$ in Fig. 9. As x/d increases, vorticity distributions become more spread out and less intense. Corresponding absolute values of peak vorticity then decrease from 382 1/s to 62 1/s and total circulation for each vortex decreases from .068 m^2/s to .029 m^2/s as x/d increases from 4.5 to 24.1. At most every x/d location examined, absolute values of circulation for the two opposite sign vortices are the same within .0015 m^2/s.

Effects of Pulsations on Flow Structure. Figure 10 shows vorticity distributions in the pulsating flow which are more spread out and less concentrated than distributions in Fig. 9 obtained without pulsations (especially for $x/d = 4.5$). Such behavior evidences lower secondary flow velocities in each vortex. With pulsations, circulation magnitudes for each vortex range from .064 m^2/s to .029 m^2/s as x/d varies from 4.5 to 24.1. At x/d from 4.5 to 16.4, circulation magnitudes are thus 2 to 7 percent lower than when no pulsations are present, and at $x/d = 24.1$, circulation magnitudes with and without pulsations are about the same. The differences are probably partially because of small alterations to vortex structure which occur from the imposed unsteadiness (i.e., from different levels of vorticity diffusion), but mostly because the results in Fig. 10 represent time-averaged distributions of structures which are changing position with time. As the each pulsation is imposed on the film cooled boundary layer, the two horseshoe vortex legs oscillate toward and away from the wall. As a result, vorticity regions associated with each vortex cover a larger volume, and each oscillating vortex appears somewhat weaker and more spread out in the time-averaged surveys.

Such behavior is further evidenced by the reductions to the absolute values of peak streamwise vorticity caused by the imposed pulsations. This is as much as 20 percent at x/d of 4.5 and 9.8. At $x/d = 16.4$, peak vorticity magnitudes then decrease by 7 to 17 percent. Somewhat smaller reductions are present at $x/d = 24.1$ probably because the unsteadiness of the vortex legs produces little change to vorticity distributions which are already quite diffused.

Experimental Results-Reynolds Shear Stresses

Profiles of $-2\overline{u'v'}/\overline{u_\infty}^2$ and $\overline{u'w'}/\overline{u_\infty}^2$ in film cooled boundary layers both with and without pulsations are presented in Figs. 11 and 12, respectively, along with baseline profiles with no pulsations and no film cooling. Data in both figures are given at $z/d = 0$ for x/d from 4.5 to 24.1.

Flow Structure With No Pulsations. The film cooled $-2\overline{u'v'}/\overline{u_\infty}^2$ distributions in Figure 11 and the film cooled $\overline{u'w'}/\overline{u_\infty}^2$ distributions in Fig. 12 (both for no pulsations) are

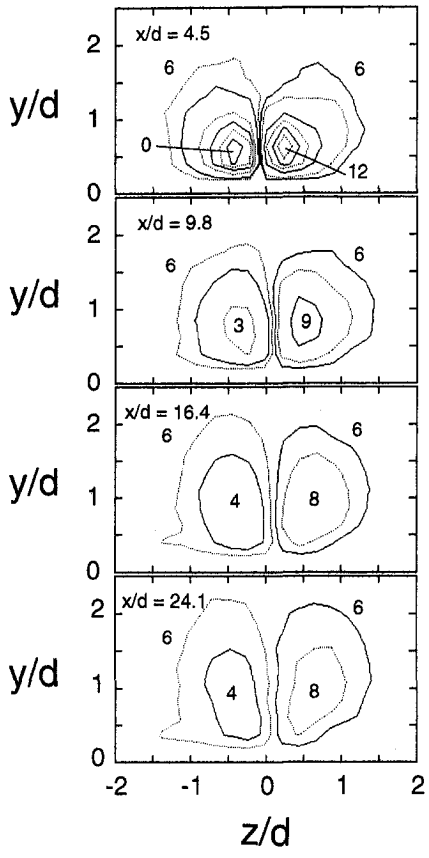

Fig. 10 Streamwise development of streamwise mean vorticity measured with pulsations. Contour labels are the same as for Fig. 9.

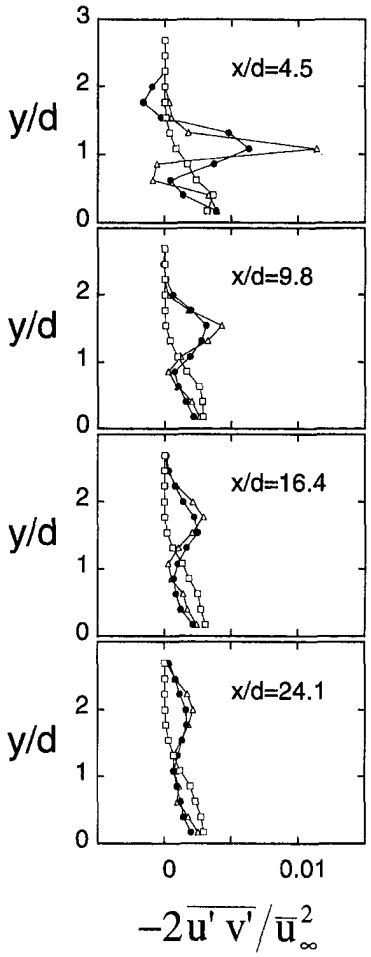

Fig. 11 Streamwise development of profiles of normalized $-2\overline{u'v'}$ Reynolds shear stress at $z/d = 0$. Symbol labels are given with Fig. 6.

significantly different from ones with no film cooling (and no pulsations).

At $x/d = 4.5$, the film cooled profile in Fig. 11 shows an important local maximum in $-2\overline{u'v'}/\overline{u_\infty}^2$ located about 1.0 d from the wall. Here, magnitudes of maximum $-2\overline{u'v'}/\overline{u_\infty}^2$ are much higher than measured at the same location with no film and no pulsations because of high production of turbulence $(-\overline{u'v'}(\partial\overline{u}/\partial y))$. The shear layer (mentioned earlier) at the interface between fluid with low streamwise momentum below and fluid with much higher streamwise momentum above is responsible. This region of high $-2\overline{u'v'}/\overline{u_\infty}^2$ is bounded by regions above and below where the normalized Reynolds shear stress is sometimes negative and significantly lower than measured in the baseline boundary layer. This behavior is due to the advection of fluid with high streamwise momentum away from the wall, as well as the streamwise advection of the film from the holes.

As x/d increases to 9.8–24.1, Fig. 11 shows that the intensity of the shear layer decreases and that magnitudes of $-2\overline{u'v'}/\overline{u_\infty}^2$ become less. Local maxima are located farther from the wall, regions of negative $-\overline{u'v'}$ are no longer present, and $-2\overline{u'v'}/\overline{u_\infty}^2$ gradients are much smaller than measured at $x/d = 4.5$. The outer portions of the film cooled boundary layers at $x/d = 9.8$–24.1 are then characterized by $-2\overline{u'v'}/\overline{u_\infty}^2$ which are greater than in the baseline boundary layer with no film cooling. The inner portions are characterized by $-2\overline{u'v'}/\overline{u_\infty}^2$ which are then lower than baseline boundary layer magnitudes. The y/d boundary between these two regions increases with streamwise development, ranging from 1.0 to 1.4.

Values of normalized three-dimensional shear stress $\overline{u'w'}/\overline{u_\infty}^2$ in Fig. 12 from the film cooled boundary layer are generally negative and significantly less than in the baseline boundary layer (with no film cooling) at $x/d = 4.5$. As x/d increases to 9.8–24.1, $\overline{u'w'}/\overline{u_\infty}^2$ magnitudes become positive and greater than values measured in the baseline boundary layer.

Effects of Pulsations on Flow Structure As for the mean velocity components, significant changes to the Reynolds shear stresses occur when the pulsations are present. The most important factors affecting these changes are periodic alterations of the y positions of the shear layer and the highest film concentrations.

Figure 11 shows that the highest measured $-2\overline{u'v'}/\overline{u_\infty}^2$ at $x/d = 4.5$ with pulsations are contained in the shear layer. As this shear layer oscillates to and from the wall, the fluid containing the highest values of $-\overline{u'v'}$ is more spread out spatially which gives lower *time-averaged* magnitudes of maximum Reynolds shear stress. Figure 11 also shows that the y/d locations of these time-averaged maxima do not change in the pulsating flow at $x/d = 4.5$ compared to the boundary layer with no pulsations. Magnitudes of $-2\overline{u'v'}/\overline{u_\infty}^2$ above and below the shear layer also change significantly when pulsations are imposed. Values at $x/d = 4.5$ are more negative (above) at $y/d = 1.6$–2.3, and less negative (below) at $y/d = 0.4$–0.8 compared to the film cooled boundary layer with no pulsations. As x/d increases to 9.8–24.1, Figure 11 shows that the $-2\overline{u'v'}/\overline{u_\infty}^2$ profiles measured with film cooling and pulsations approach the profiles measured with film cooling and no pulsations.

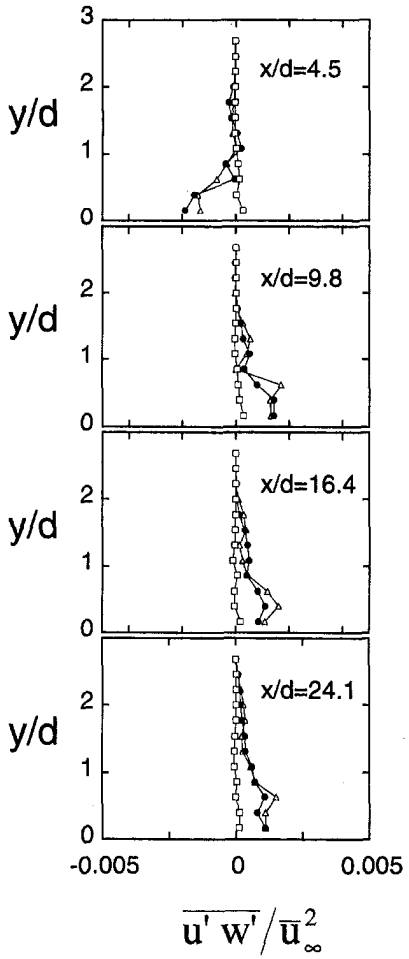

Fig. 12 Streamwise development of profiles of normalized $\overline{u'w'}$ Reynolds shear stress at $z/d = 0$. Symbol labels are given with Fig. 6.

Profiles of $\overline{u'w'}/\overline{u_\infty}^2$ show fairly complicated behavior relative to the film cooled boundary layer with no pulsations. Figure 12 shows that values from the pulsating flow at $x/d = 4.5$ and $x/d = 9.8$ are both higher and lower than in the non-pulsating flow depending upon y/d. The $\overline{u'w'}/\overline{u_\infty}^2$ profiles measured with pulsations then become more similar to the profiles measured with no pulsations as x/d increases from 9.8 to 24.1.

Experimental Results-Reynolds Normal Stresses

Profiles of $\overline{u'^2}/\overline{u_\infty}^2$ and $\overline{v'^2}/\overline{u_\infty}^2$ are presented in Figs. 13, and 14, respectively. As for the results in the previous figures, these data are obtained in film cooled boundary layers with and without pulsations, as well in a boundary layer with no pulsations and no film cooling. Because profiles of $\overline{w'^2}/\overline{u_\infty}^2$ are qualitatively similar to the $\overline{v'^2}/\overline{u_\infty}^2$ profiles, they are presented elsewhere (Cuthrell, 1995).

Flow Structure With No Pulsations The film cooled $\overline{u'^2}/\overline{u_\infty}^2$ and $\overline{v'^2}/\overline{u_\infty}^2$ profiles with no pulsations are all significantly higher than the baseline profiles (with no pulsations and no film cooling) over most of the boundary layer thickness at $x/d = 4.5$. Increases of normal stresses extend to y/d as large as 2.5, which is well outside of the turbulence field in the baseline boundary layer. Magnitudes of $\overline{u'^2}/\overline{u_\infty}^2$ and $\overline{v'^2}/\overline{u_\infty}^2$ in Figs. 13 and 14 are especially large at y/d from 1.0 to 1.5 which correspond to locations within and near the shear layer.

The shear layer is where large Reynolds shear stresses $-u'v'$ and large $\partial\overline{u}/\partial y$ result in high values of production of

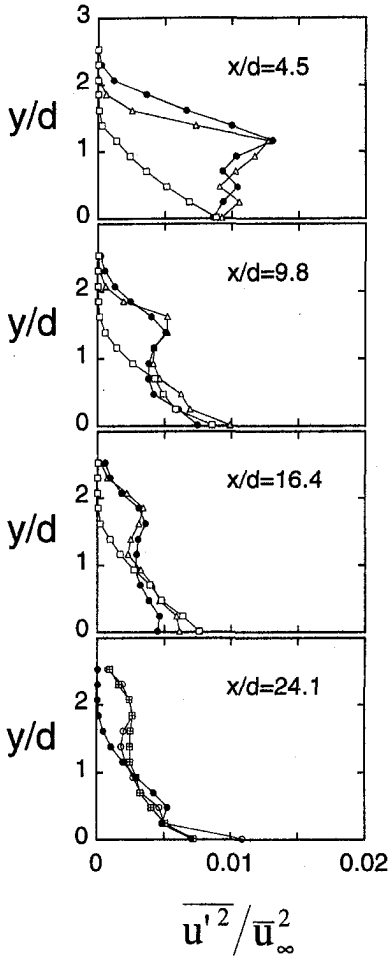

Fig. 13 Streamwise development of profiles of normalized $\overline{u'^2}$ longitudinal Reynolds normal stress at $z/d = 0$. Symbol labels are given with Fig. 6.

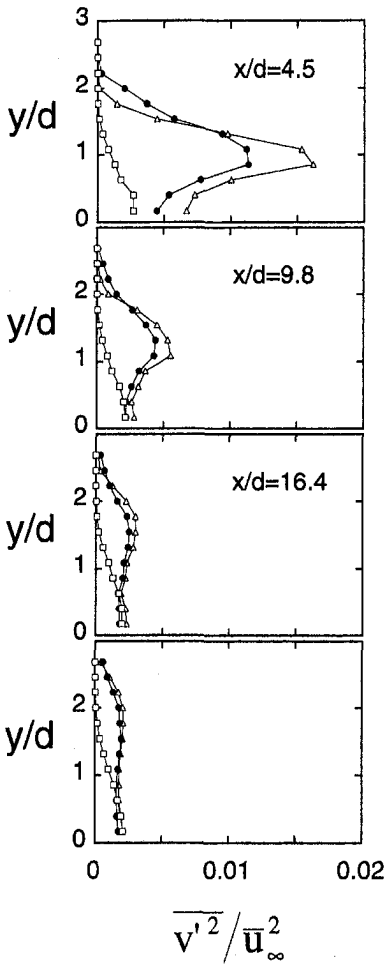

Fig. 14 Streamwise development of profiles of normalized $\overline{v'^2}$ normal Reynolds normal stress at $z/d = 0$. Symbol labels are given with Fig. 6.

$\overline{u'^2}$ and turbulence kinetic energy. The pressure redistribution components of the pressure/strain correlation are then responsible for the transport of $\overline{u'^2}$ energy into $\overline{v'^2}$ and $\overline{w'^2}$ (Ligrani, 1988). However, because magnitudes of $\overline{v'^2}/\overline{u_\infty}^2$ are significantly higher than $\overline{u'^2}/\overline{u_\infty}^2$ in Figs. 13, and 14, three-dimensional production terms also likely contributing to $\overline{v'^2}$. Similar conclusions can be drawn with respect to the profiles of $\overline{w'^2}/\overline{u_\infty}^2$ (Cuthrell, 1995) since they show qualitative and quantitative trends similar to the $\overline{v'^2}/\overline{u_\infty}^2$ profiles.

As x/d increases to 9.8–24.1, peak magnitudes of $\overline{u'^2}/\overline{u_\infty}^2$ and $\overline{v'^2}/\overline{u_\infty}^2$ decrease relative to the profiles measured at $x/d = 4.5$. However, in spite of this, film cooled values of these quantities continue to be higher than baseline values over much of the boundary layer thickness.

Effects of Pulsations on Flow Structure Figure 13 shows profiles of $\overline{u'^2}/\overline{u_\infty}^2$ from the pulsating film cooled boundary layer at $x/d = 4.5$ which are about the same as the film cooled boundary layer with no pulsations for $y/d < 1.3$. Values in the pulsating flow then become relatively higher as y/d becomes larger than 1.3. Film cooled profiles of $\overline{u'^2}/\overline{u_\infty}^2$ measured with pulsations are then about the same as film cooled profiles measured with no pulsations when $x/d = 9.8$, 16.4, and 24.1.

The $\overline{v'^2}/\overline{u_\infty}^2$ profiles with film cooling and pulsations in Fig. 14 for $x/d = 4.5$ are less than values from film cooled boundary layer with no pulsations for $y/d < 1.5$, and higher for $y/d > 1.5$. As the boundary layers advect downstream to $x/d = 9.8$, 16.4, and 24.1, the $\overline{v'^2}/\overline{u_\infty}^2$ profiles (with film cooling and pulsations) show qualitative trends similar to the $\overline{u'^2}/\overline{u_\infty}^2$ profiles

since they are about the same as film cooled profiles measured with film cooling and no pulsations.

Profiles of Time-Averaged Periodic Quantities. Profiles of $\tilde{u}^2/\overline{u_\infty}^2$ with and without film cooling are presented for $x/d = 4.5$ and $z/d = 0$ in Figure 15. Profiles of $\tilde{u}^2/\overline{u_\infty}^2$ with no film cooling are in good agreement with Menendez and Ramaprian (1989). According to them, the region of augmented $\tilde{u}^2/\overline{u_\infty}^2$ values in the boundary layer (compared to the freestream) is called a "turbulent Stokes layer," and is connected to unsteady vortical effects. The trends of the film cooled $\tilde{u}^2/\overline{u_\infty}^2$ data in Fig. 15 are interesting because of their similarity to the $-2\overline{u'v'}/\overline{u_\infty}^2$ profile at $x/d = 4.5$ in Fig. 11. Magnitudes of $\tilde{u}^2/\overline{u_\infty}^2$ are significantly lower than ones with no film cooling because of altered u and v behavior above, within, and below the shear layer located at $y/d = 0.9-1.6$.

Profiles of $\tilde{u}\tilde{v}/\overline{u_\infty}^2$, $\tilde{v}^2/\overline{u_\infty}^2$, and $\tilde{w}^2/\overline{u_\infty}^2$ are presented by Gong (1996). They are not given here since magnitudes are near zero at most all measurement locations.

Experimental Results at Other Conditions-Reynolds Shear Stresses

Profiles of $-2\overline{u'v'}/\overline{u_\infty}^2$ are given in Figs. 16 and 17 for $z/d = 0$ and x/d of 4.5, 9.8, 16.4, and 24.1 for flow conditions which are different from the ones for Figs. 6–15. The results in Fig. 16 are obtained with a turbulent external approach boundary layer, $\overline{u_\infty} = 2$ m/s, $n = 8$ Hz, and $St_c = 8.93$. The results in Fig. 17 are obtained for a laminar external approach boundary layer, $\overline{u_\infty} = 1$ m/s, $n = 8$ Hz, and $St_c = 7.57$.

The data in Figs. 16 and 17 are presented with higher frequencies of pulsations, lower freestream velocities, and in one case, a different type of external approach boundary layer compared to the data in earlier figures to illustrate the effects of these changes on one component of the Reynolds stress. Surveys of the other components of Reynolds stresses and surveys of the components of mean velocity at the new experimental conditions are given by Gong (1996).

Compared to the profiles in Fig. 11, the most important differences at x/d of 4.5 in Figs. 16 and 17 are smaller decreases of peak shear stress levels with pulsations. At x/d of 16.4 and 24.1, qualitative differences between Figs. 16 and 17 and Fig. 11 are even more substantial. Profiles of $-2\overline{u'v'}/\overline{u_\infty}^2$ with pulsations are different from the ones measured in the film cooled boundary layers with no pulsations throughout each boundary layer in the latter two figures, whereas $-2\overline{u'v'}/\overline{u_\infty}^2$ profiles for these two conditions are nearly the same in Fig. 11.

Summary and Conclusions

Experimental results are presented which describe the effects of bulk flow pulsations on film cooled boundary layer structure. Sinusoidal velocity (and static pressure) wave forms at a frequency of 2 Hz are produced using an array of rotating shutters placed at the downstream end of the wind tunnel test section.

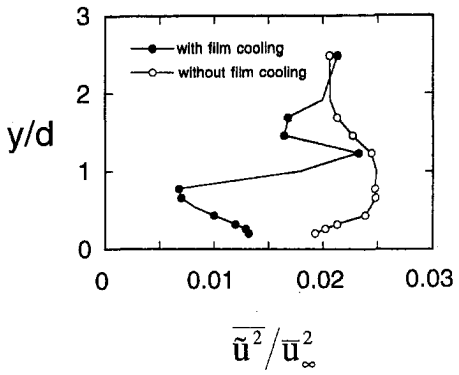

Fig. 15 Profiles of normalized $\tilde{u}^2$ at $x/d = 4.5$ and $z/d = 0$

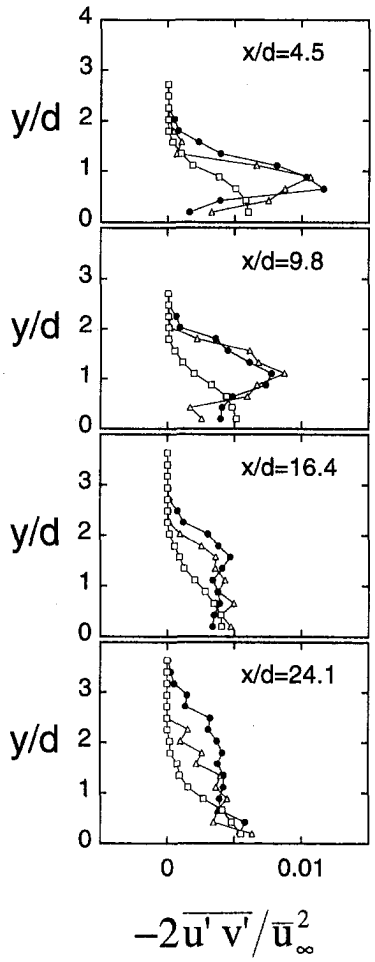

Fig. 16 Streamwise development of profiles of normalized $-2\overline{u'v'}$ Reynolds shear stress at $z/d = 0$. Flow conditions: turbulent external approach boundary layer, $\overline{u_\infty} = 2$ m/s, $n = 8$ Hz, and $St_c = 8.93$. Symbol labels are given with Fig. 6.

Because the bulk flow pulsations cause the film to instantaneously change its momentum and position in the boundary layer, important changes to film cooled boundary layer structure result. At a freestream velocity of 10 m/s, particularly significant changes are evident in time-averaged mean velocities. For example, (i) time-averaged streamwise velocities are locally lower than velocities measured when no pulsations are imposed at $y/d < 1.0-1.5$ and x/d of 4.5, 9.8, and 16.4, (ii) time-averaged streamwise velocities are locally higher than velocities measured when no pulsations are imposed at $y/d = 1.5-2.1$ and x/d of 4.5, and (iii) the $u/\overline{u_\infty}$ shear layer gradient extends over a larger vertical portion of the boundary layer at x/d of 4.5, 9.8, and 16.4 when the pulsations are imposed.

Important changes to profiles of streamwise mean vorticity, time-averaged Reynolds normal stresses $\overline{u'^2}$ and $\overline{v'^2}$, and time-averaged Reynolds shear stresses $-\overline{u'v'}$ and $\overline{u'w'}$ are also present in the film cooled boundary layers because of the pulsations at $\overline{u_\infty} = 10$ m/s. These are particularly evident at $x/d = 4.5$ where the strong shear layer located in the outer portions of the largest film accumulations at $y/d = 0.9-1.6$ oscillates its position with respect to the wall. As a result, the spatial extent of the shear layer increases, fluid with high stresses is more spread out spatially, and time-averaged magnitudes of maximum Reynolds shear stress $-2\overline{u'v'}/\overline{u_\infty}^2$ are lower. Many of the qualitative differences due to pulsations continue to be present as x/d increases to 9.8, 16.4, and 24.1. However, as the injectant be-

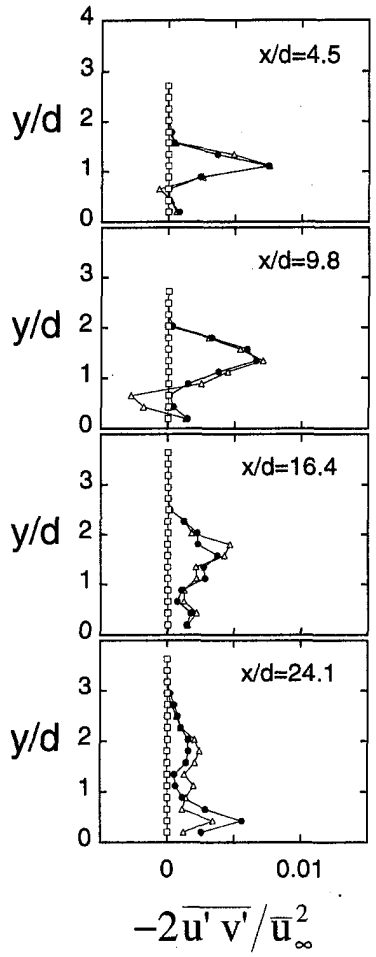

Fig. 17 Streamwise development of profiles of normalized $-2\overline{u'v'}$ Reynolds shear stress at $z/d = 0$. Flow conditions: laminar external approach boundary layer, $\overline{u}_\infty = 1$ m/s, $n = 8$ Hz, and $St_c = 7.57$. Symbol labels are given with Fig. 6.

comes more diffuse, differences between the film cooled boundary layer with pulsations and the film cooled boundary layer with no pulsations generally tend to become less significant.

The overall trends presented evidence decreased film effectiveness from pulsations, depending upon flow conditions. This will be discussed in future papers.

Acknowledgments

This study was supported, in part, by the Turbo and Power Machinery Research Center of Seoul National University, South Korea.

References

Abhari R. S., and Epstein A. H., 1994, "An Experimental Study of Film Cooling in a Rotating Transonic Turbine," ASME *Journal of Turbomachinery*, Vol. 116, No. 1, pp. 63–70.

Al-Asmi K., and Castro I. P., 1993, "Production of Oscillatory Flow in Wind Tunnels," *Experiments in Fluids*, Vol. 15, pp. 33–41.

Cuthrell J. M., 1995, "A Study of Film Cooling and Bulk Flow Pulsations," M. S. thesis, Department of Mechanical Engineering, University of Utah.

Doorly D. J., and Oldfield M. J., 1985, "Simulation of the Effects of Shock Wave Passing on a Turbine Rotor Blade," ASME *Transactions-Journal of Engineering for Gas Turbines and Power*, Vol. 107, No. 4, pp. 998–1006.

Dunn M. G., 1990, "Phase and Time-Resolved Measurements of Unsteady Heat Transfer and Pressure in a Full-Stage Rotating Turbine," ASME *Journal of Turbomachinery*, Vol. 112, No. 3, pp. 531–538.

Dunn M. G., Bennett W. A., Delaney R. A., and Rao K. V., 1992, "Investigation of Unsteady Flow Through a Transonic Turbine Stage: Data/Prediction Comparison for Time-Averaged and Phase-Resolved Pressure Data," ASME *Journal of Turbomachinery*, Vol. 114, No. 1, pp. 91–99.

Dunn M. G., Seymore P. J., Woodward S. H., George W. K., and Chupp R. E., 1989, "Phase-Resolved Heat Flux Measurements on the Blade of a Full-Stage Rotating Turbine," ASME *Journal of Turbomachinery*, Vol. 111, No. 1, pp. 8–19.

Gong R., 1996, "Structure of Film Cooled Boundary Layers Subject to Bulk Flow Pulsations," Ph.D. thesis, Department of Mechanical Engineering, University of Utah.

Green J. G., 1989, "Turbulence Structure Resulting from Interactions Between an Embedded Vortex and Wall Jet," Master of Science Thesis, Department of Mechanical Engineering, U.S. Naval Postgraduate School, Monterey, CA.

Hussain A. K. M. F., and Reynolds, W. C., 1970, "The Mechanics of an Organized Wave in Turbulent Shear Flow," *Journal of Fluid Mechanics*, Vol. 41, No. 2, pp. 241–258.

Karlsson S. K., 1959, "An Unsteady Turbulent Boundary Layer," *Journal of Fluid Mechanics*, Vol. 14, pp. 622–636.

Klebanoff P. S., 1954, "Characteristics of Turbulence in a Boundary Layer With Zero Pressure Gradient," NACA Technical Note 3178.

Kline S. J., and McClintock F. A., 1953, "Describing Uncertainties in Single-Sample Experiments," *Mechanical Engineering*, pp. 3–8.

Ligrani P. M., 1988, "Structure of Turbulent Boundary Layers," *Aerodynamic and Compressible Flows, Encyclopedia of Fluid Mechanics*, Editor; N. Cheremisinoff, Gulf Publishing, Vol. 8, pp. 111–189.

Ligrani P. M., Cuthrell J. M., and Gong R., 1995, "Bulk Flow Pulsations and Film Cooling, Flow Structure Just Downstream of the Holes," Paper 95-GT-44, ASME 40th International Gas Turbine and Aeroengine Congress and Exposition, Houston, Texas.

Menendez A. N., and Ramaprian B. R., 1989, "Experimental Study of a Periodic Turbulent Boundary Layer in Zero Mean Pressure Gradient," *Aeronautical Journal*, Vol. 93, pp. 195–206.

Moffat, R. J., 1988, "Describing the Uncertainties in Experimental Results," *Experimental Thermal and Fluid Science*, Vol. 1, No. 1, pp. 3–17.

Norton R. J. G., Forest A. E., White A. J., Henshaw D. G., Epstein A. H., Schultz D. L., and Oldfield M. L. G., 1990, "Turbine Cooling System Design, Volume I-Technical Report," Report WRDC-TR-89-2109, Aero Propulsion and Power Laboratory, Wright Research Development Center, Air Force System Command, Wright-Patterson Air Force Base, OH.

Perry A. E., 1982, *Hot-Wire Anemometry*, Clarendon Press Oxford.

Pietrzyk J. R., Bogard D. G., and Crawford M. E., 1989, "Hydrodynamic Measurements of Jets in Crossflow for Gas Turbine Film Cooling Applications," ASME *Journal of Turbomachinery*, Vol. 111, No. 2, pp. 139–145.

Ramaprian B. R., and Tu, S. W., 1980, "An Experimental Study of Oscillatory Pipe Flow At Transitional Reynolds Numbers," *Journal of Fluid Mechanics*, Vol. 100, pp. 513–544.

Rigby M. J., Johnson A. B., Oldfield M. L. G., 1990, "Gas Turbine Rotor Blade Film Cooling With and Without Simulated NGV Shock Waves and Wakes," ASME Paper 90-GT-78, ASME International Gas Turbine and Aeroengine Congress and Exhibition, Brussels, Belgium.

Takeishi K., Aoki S., Sato T., and Tsukagoshi K., 1991, "Film Cooling on a Gas Turbine Rotor Blade," ASME Paper 91-GT-279, ASME International Gas Turbine and Aeroengine Congress and Exhibition, Orlando, FL.

M. S. Cramer
Professor.

S. H. Park
Graduate Student,
Department of Engineering Science and Mechanics.

L. T. Watson
Professor,
Department of Computer Science.

Virginia Polytechnic Institute and State University,
Blacksburg, VA 24061

Numerical Verification of Scaling Laws for Shock-Boundary Layer Interactions in Arbitrary Gases

The steady, two-dimensional interaction of an oblique shock with a laminar flat-plate boundary layer has been examined through use of the Beam-Warming implicit scheme. A wide range of fluids is considered as are freestream pressures corresponding to dense gases, i.e., gases at pressures which are so large that the ideal gas law is no longer accurate. The results, when combined with the triple-deck theory of Kluwick (1994), provides strong support for the idea that the classical scaling laws can be extended to dense gases.

1 Introduction

One of the best documented viscous-inviscid interactions is that of shock-boundary layer interaction. Such interactions can give rise to separation of the boundary layer and to laminar-turbulent transition. The former phenomenon is an important loss mechanism in both aerodynamic and turbomachinery flows. Summaries of the analytical, numerical, and experimental efforts to understand and describe shock-boundary layer interaction can be found in the reviews by Delery and Marvin (1986) and Adamson and Messiter (1980). Inspection of these reviews suggests that virtually all of our intuition of the interaction process is based on the perfect gas theory. In addition, the data base also appears to be largely restricted to diatomic gases such as molecular nitrogen (N_2) or air. However, in recent years applications involving a wide range of gases and high pressure effects have become increasingly important. One such example is the use of heavy gas wind tunnels for the purposes of obtaining a better match between flight and test Mach and Reynolds numbers. In such tunnels the working fluid is one of moderately large molecular weight, e.g., SF_6 or a freon, at pressures high enough to render the ideal gas assumption invalid. A further summary of the motivations for such tunnels and the program at NASA Langley has been given by Anders (1993). A second class of applications where shock-boundary layer interactions are important is that of Rankine cycle turbomachinery which frequently employ steam at very high pressures (Reynolds and Perkins, 1977). A second type of Rankine cycle are organic Rankine cycles which employ large molecular weight fluids to take advantage of their retrograde character, i.e., their tendency to dry, rather than condense, on adiabatic expansion. As a result, condensation, droplets, and the resultant blade erosion in the turbine are avoided through use of the natural dynamics of the fluids. Such fluids range from common refrigerants to hydrocarbons such as toluene to pure fluorocarbons such as PP1 (C_6F_{14}). For a more complete review of the fluids used the reader is referred to the articles by Curran (1981), Devotta and Holland (1985), Manco and Nervegna (1985), Yan and Svedberg (1991), and Angelino and Invernizzi (1993). As in the case of steam Rankine cycles, the pressures and temperatures are on the order of those at the thermodynamic critical point so that the ideal gas law is no longer accurate and more sophisticated equations of state are required. In the remainder of this report, we will refer to such high-pressure effects as dense gas effects. Finally, we note that the design of planetary probes must account for shock-boundary layer-interactions in fluids such as CO_2 and H_2. Thus, it is felt that there is both a strong motivation for the study of viscous-inviscid interactions in fluids other than low-pressure air or nitrogen and simultaneously a scarcity of data in this area. The elimination of this discrepancy is the primary goal of the present study.

Two recent studies of more general fluids and operating conditions are due to Anderson (1991) and Kluwick (1994). In the first article Anderson examined the viscous-inviscid interaction of nearly normal shocks with a turbulent boundary layer in a transonic flow of SF_6. In the second study Kluwick extended the well-known triple-deck theory for free interactions to general, rather than perfect, gases. An important result of Kluwick's work is the conclusion that the classical scaling laws remain valid for general fluids and essentially arbitrary pressures, provided the appropriate measures of the pressure levels and wall stress are incorporated. In particular, it can be shown that the pressure variation in the interaction region can be written

$$\frac{c_p(M_1^2 - 1)^{1/4}}{\sqrt{c_{f1}}} = P(\bar{x}), \tag{1.1}$$

where c_p is the pressure coefficient

$$c_p \equiv \frac{p - p_1}{\frac{1}{2}\rho_1 U_1^2} = \left(\frac{p}{p_1} - 1\right)\frac{2p_1}{\rho_1 a_1^2 M_1^2}, \tag{1.2}$$

c_{f1} is the wall skin friction coefficient evaluated immediately before the interaction, i.e.,

$$c_{f1} \equiv \frac{\tau_{w1}}{\frac{1}{2}\rho_1 U_1^2}, \tag{1.3}$$

and M_1, U_1, ρ_1, p_1, and a_1 are the flow Mach number, particle velocity, density, pressure, and sound speed of the inviscid flow immediately upstream of the interaction. The quantity p is the local pressure in the interaction region and τ_{w1} is the wall shear stress evaluated immediately before the interaction. The variable P turns out to be the same function of the scaled streamwise variable $\bar{x}$ as in the classical triple-deck theory; in the present study the scaling on $\bar{x}$ will not need to be specified explicitly. The particular form of (1.1) is consistent with our focus on supersonic flows ($M_1 > 1$) and in particular, the interaction of oblique shocks with boundary layers.

An advantage suggested by the result (1.1) is that the well-established results of the perfect gas theory can be carried over

Contributed by the Fluids Engineering Division for publication in the JOURNAL OF FLUIDS ENGINEERING. Manuscript received by the Fluids Engineering Division August 24, 1995; revised manuscript received July 18, 1996. Associate Technical Editor: G. Em Karniadakis.

immediately to the case of dense gases. As an example of such an extension of the low-pressure results to dense gases we consider the separation criterion proposed by Katzer (1989) for the interaction of an oblique shock reflected from a laminar boundary layer. Thus, if we combine the results of Katzer (1989) and Kluwick (1994) it appears that separation in an arbitrary gas occurs if

$$\frac{c_{pT}(M_1^2 - 1)^{1/4}}{\sqrt{c_{f1}}} > P_{\text{inc}} \approx 2.6, \tag{1.4}$$

where c_{pT} is the pressure coefficient corresponding to the total pressure change across the reflection. The numerical value of P_{inc} is that suggested by Katzer's own calculations and, as Katzer points out, can vary from about 2.2 to 2.8, depending on the source and method of determination. Further universal values of $P(\bar{x})$ for separated flows given by Katzer (1989) yield the plateau pressure and the local pressure at the separation point:

$$\frac{c_{p|_p}(M_1^2 - 1)^{1/4}}{\sqrt{c_{f1}}} = P_p \approx 2.3 \tag{1.5}$$

$$\frac{c_{p|_s}(M_1^2 - 1)^{1/4}}{\sqrt{c_{f1}}} = P_s \approx 1.4, \tag{1.6}$$

where $c_{p|_p}$ and $c_{p|_s}$ are the pressure coefficients corresponding to the plateau and the separation point. Again we note that Katzer points out that the numerical values for P_p, P_s can vary from source to source.

The main objective of the present investigation is to evaluate the validity of the Kluwick's triple-deck scaling laws for the well-established benchmark problem of the reflection of an oblique shock from a laminar flat-plate boundary layer. Here we employ a form of the Beam-Warming (1978) implicit scheme which has been modified to account for dense gas effects. A wide variety of gases are considered and cases having freestream pressures corresponding to the dense gas regime will also be included. We follow Katzer (1989) in regarding the estimates of P_p and P_s as good measures of the validity of the triple deck theory. The results presented here are seen to be in complete agreement with the predictions of Kluwick (1994). On the basis of these observations it appears that the classical scaling laws can in fact be extended to dense gases as well as fairly complex gases at low pressures.

In the next section we record the general form of the Navier-Stokes equations used in the present study. The gas models for the equation of state and transport properties are given in Section 3 and the general features of the implementation of the Beam-Warming scheme are given in Section 4. Our final results are summarized in Section 5.

2 Formulation

In the present study, we restrict our attention to the steady, two-dimensional flow of a Navier-Stokes fluid. Body forces and heat sources will be neglected and the flow is regarded as being single-phase and in equilibrium. The x and y coordinate axes are depicted in Fig. 1. The origin is taken to be at some arbitrary distance x_0 upstream of the flat plate, the positive x axis is in the direction of the undisturbed flow, and the y direction is transverse to the incoming flow.

For the numerical scheme used here, the unsteady form of the Navier-Stokes equations will be required. When these equations are written in conservative form, we have

$$\frac{\partial \mathbf{Q}}{\partial t} + \frac{\partial \mathbf{F}}{\partial x} + \frac{\partial \mathbf{G}}{\partial y} = \frac{\partial \mathbf{F}_v}{\partial x} + \frac{\partial \mathbf{G}_v}{\partial y}, \tag{2.1}$$

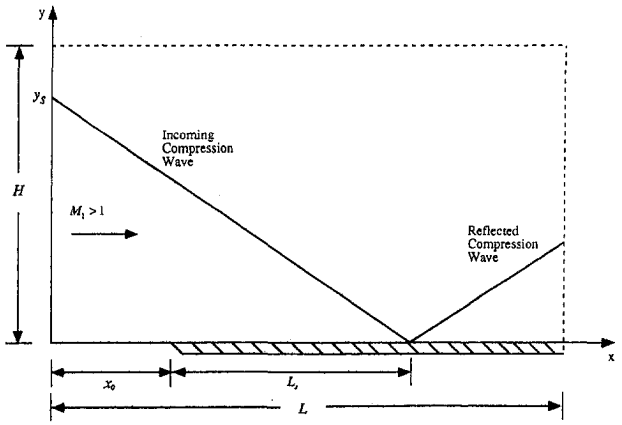

Fig. 1 Sketch of computational domain

where

$$\mathbf{Q} = \begin{Bmatrix} \rho \\ \rho u \\ \rho v \\ E \end{Bmatrix}, \quad \mathbf{F} = \begin{Bmatrix} \rho u \\ \rho u^2 + p \\ \rho uv \\ u(E + p) \end{Bmatrix},$$

$$\mathbf{G} = \begin{Bmatrix} \rho v \\ \rho uv \\ \rho v^2 + p \\ v(E + p) \end{Bmatrix}, \tag{2.2}$$

and

$$\mathbf{F}_v = \begin{Bmatrix} 0 \\ \tau_{xx} \\ \tau_{xy} \\ w_x \end{Bmatrix}, \quad \mathbf{G}_v = \begin{Bmatrix} 0 \\ \tau_{yx} \\ \tau_{yy} \\ w_y \end{Bmatrix}. \tag{2.3}$$

The quantities u and v are the x and y components of the fluid velocity, p and ρ are the fluid pressure and density, and

$$E \equiv \rho\left(e + \frac{u^2 + v^2}{2}\right). \tag{2.4}$$

Here the thermodynamic quantity e is the thermal energy; thus, (2.4) will be referred to as the total energy per unit volume. The quantities τ_{xx}, $\tau_{yx} = \tau_{xy}$, τ_{yy} are the Cartesian components of the Navier-Stokes stress tensor which can be written

$$\tau_{xx} = (\lambda + 2\mu)\frac{\partial u}{\partial x} + \lambda\frac{\partial v}{\partial y}$$

$$\tau_{xy} = \tau_{yx} = \mu\left(\frac{\partial u}{\partial y} + \frac{\partial v}{\partial x}\right)$$

$$\tau_{yy} = (\lambda + 2\mu)\frac{\partial v}{\partial y} + \lambda\frac{\partial u}{\partial x}, \tag{2.5}$$

where μ and λ are the shear and second viscosities which satisfy

$$\mu \geq 0, \quad \mu_b \equiv \lambda + \tfrac{2}{3}\mu \geq 0, \tag{2.6}$$

where μ_b is the bulk viscosity. The quantities w_x and w_y are the energy fluxes defined as

$$w_x \equiv \tau_{xx}u + \tau_{xy}v - q_x$$

$$w_y = \tau_{yx}u + \tau_{yy}v - q_y, \tag{2.7}$$

where $\mathbf{q} = -k\nabla T$ is the Fourier heat flux vector, T is the absolute temperature, and

$$k > 0 \tag{2.8}$$

is the thermal conductivity. The first two terms in each of (2.7) represent the work done per unit time by the stress tensor. The first row of (2.1) is recognized as the mass equation, the second and third rows are the two components of the momentum equation, and the fourth row is the energy equation.

The plate is taken to be adiabatic, impenetrable, and located at $y = 0$, $x > x_0$, where x_0 is the location of the leading edge of the plate. As a result, the physical boundary conditions at the plate can be written

$$u = v = \frac{\partial T}{\partial y} = 0 \quad \text{for} \quad y = 0, \quad x > x_0. \tag{2.8}$$

The flow far upstream, i.e., as $x \to -\infty$, is taken to be uniform with velocity components $u = U_1 > 0$, $v = 0$. The flow velocity U_1 is such that the incoming flow is supersonic. Here we restrict our attention to reflections which leave the flow supersonic; thus, for the present purposes, Mach reflections will be ignored.

3 Gas Models

A full specification of any single-phase gas requires a knowledge of the functions

$$p = p(\rho, T) \quad \text{and} \quad c_{v\infty} = c_{v\infty}(T), \tag{3.1}$$

and

$$\mu = \mu(\rho, T), \quad \lambda = \lambda(\rho, T), \quad k = k(\rho, T), \tag{3.2}$$

where $c_{v\infty}(T)$ is the low-pressure, i.e., the ideal gas, specific heat at constant volume. In the usual way we will refer to the first of (3.1) as the equation of state. In the present investigation we employ the equation of state developed by Martin and Hou (1955). The advantages of this model is that it is widely employed in engineering practice and it has a strong analytical basis so that only a minimum number of experimental parameters are required for its use.

The ideal gas specific heat will be modeled by a power-law of the form

$$c_{v\infty}(T) = c_{v\infty}(T_{\text{ref}})\left(\frac{T}{T_{\text{ref}}}\right)^n, \tag{3.3}$$

where T_{ref} is a reference temperature, and n is a material-dependent exponent. The advantage of (3.3) is its simplicity and accuracy over the temperature ranges of interest in the present study. The values of $c_{v\infty}(T_{\text{ref}})$ and n are typically estimated by fitting (3.3) to empirical data or more complex specific heat models. Once the temperature dependence of the ideal gas specific heat and the full form of the equation of state (3.1) are known, all other thermodynamic parameters can be determined through use of the standard identities found in most texts on thermodynamics.

In the dense gas regime, the variation of the transport properties (3.2) with both density and temperature will be important. In the present investigation we employ the dense-gas shear viscosity and thermal conductivity models developed by Chung et al. (1984, 1988). The key characteristics of these models are similar to the Martin-Hou equation. That is, they have a strong analytical basis and therefore require only a minimum amount of physical data and they reduce to standard ideal gas formulas in the low pressure limit. Furthermore, the comparisons provided by Reid et al. (1987) reveal reasonable accuracy in the dense gas regime.

Finally, the bulk viscosity (2.6) must be specified. Bulk viscosity data is exceedingly rare, even for common fluids at atmospheric conditions. Data for its variation with temperature and pressure is even more scarce and we will simply take the ratio μ_b/μ to be a numerical constant throughout the present investigation. One naturally expects that errors in the value of the bulk viscosity are not likely to have a significant effect on the results. In the lowest order approximation of the boundary layer, in the viscous-inviscid interaction region (as described by the classical triple-deck theory), and in the inviscid flow, any effects due to the bulk viscosity are seen to be negligible. The only influence of μ_b is expected to be in the description of the interior of shock waves. Numerical trials reported by Park (1994) have verified that reasonable variations in the value of μ_b have essentially no effect on the complete viscous-inviscid interaction.

In order to ensure that the flow is single-phase, the final pressures and temperatures were checked against the Riedel (1954) vapor-pressure correlation. If any point was found to be in the two-phase regime, the whole calculation was rejected.

As pointed out above, each model for the equation of state, ideal gas specific heat, transport properties, and the phase boundary require only a minimum number of physical data. The required quantities include the values of the pressure, temperature, and specific volume at the thermodynamic critical point, the boiling temperature, the molecular weight, the acentric factor and the dipole moment of the molecule. The acentric factor is a macroscopic measure of the acentricity of the molecule and is zero for spherical molecules such as those of monatomic gases. The definition of this factor can be found in Reid et al. (1987) which reveals that it may be computed directly from vapor-pressure data and the critical properties. The dipole moment is a measure of the polarity of the molecule and is zero for nonpolar substances. When polar substances such as steam, ammonia, acids, alcohols, and freons are considered, two more empirical constants are required. These are discussed below when the modeling of steam is considered.

The fluids considered in this report are air, N_2, CO_2, SF_6, steam and FC-71 ($C_{18}F_{39}N$). In the remainder of this section, we summarize the basis for the choices of the relevant physical parameters. The actual numerical values are tabulated by Park (1994).

Most of the data for air was taken from Rohsenow et al. (1985). The dipole moment was taken to be zero and the acentric factor was taken to be that of N_2, i.e., 0.039. The bulk viscosity was taken to be 0.6 μ as suggested by Truesdell (1953). Because the specific heat of air is nearly constant over a wide range of temperatures, we have taken $n = 0$ in all calculations.

The bulk of the data for the nonpolar fluids N_2, CO_2, and SF_6 were taken from Reid et al. (1987). The bulk viscosity of N_2 was taken to be the same as that of air, i.e., 0.6 μ. According to Truesdell (1953) and Emanuel and Argrow (1994), the bulk viscosities of CO_2 and SF_6 can be large compared to the shear viscosity. As pointed out in Park (1994), preliminary studies indicate that such large bulk viscosities may have a non-negligible impact on the interaction processes. However, the main point of the present investigation is to examine the validity of the scaling laws with a range of fluids and under high-pressure conditions. The effects of very large bulk viscosity on the interaction process will be reported in a comprehensive fashion at a later date. The actual value of μ_b used for SF_6 was 2μ. For CO_2 two values of μ_b were employed. The first was identically zero and the second was 100μ. The difference between the values of P_p and P_s for these two choices of μ_b were less than 1.5 percent which in turn was less than the overall scatter inherent in the calculations.

The physical data for steam is also well-established. Most of the relevant parameters were taken or estimated from those provided by Jones and Hawkins (1986) and Reid et al. (1987). Because water is a polar substance, the shear viscosity and thermal conductivity models of Chung et al. (1984, 1988) require a so-called association factor and a second parameter related to the self-diffusion coefficient of water. Both parameters were chosen to be the values given by Chung et al. (1984) in their Tables 1 and 2. No data for the bulk viscosity of water

vapor is available at either low or high pressure. Here we simply set the ratio $\mu_b/\mu = 1$. Specific tests conducted by Park (1994) show negligible variation in the resultant skin friction, wall pressure, and wall temperature values as μ_b is ranged from 0 to 5μ.

The bulk of the data for the heat transfer fluid FC-71 was taken or estimated from the manufacturers' (3-M Corporation) technical publications. A detailed discussion of the estimation procedures and results for the critical properties, boiling temperature, and specific heat data is found in the article by Cramer (1989). Private communication between the first author (MSC) with the manufacturers' representatives indicates that FC-71 is nonpolar so that the dipole moment was taken to be zero. No data for the bulk viscosity of FC-71 exists and we arbitrarily took $\mu_b/\mu = 5$ for FC-71.

4 Numerical Scheme

The Navier-Stokes Eqs. (2.1)–(2.8) were solved by the (second order) Beam-Warming implicit scheme (1978) adapted to allow for the dense gas equation of state and transport laws. The advantage of this scheme is that it is well-known and can be immediately extended to imperfect gases. Explicit second and fourth-order artificial viscosities were added to reduce oscillations at the shocks. The coefficients for the explicit damping were taken to be on the order of 10^{-2} or less depending on the fluid. The implicit coefficients were taken to be on the order of 0.2 to 0.5, again depending on the fluid and freestream thermodynamic state. Full details of its implementation in the present application and the nondimensionalization scheme employed are given by Park (1994).

To minimize the computation time without sacrificing accuracy, a grid clustered in the direction transverse to the plate was employed. The mapping between the physical and computational domain is given by

$$\xi = \frac{x}{L}, \quad \eta = 1 - \frac{\ln\left\{\dfrac{\beta + 1 - \dfrac{y}{H}}{\beta - \left(1 - \dfrac{y}{H}\right)}\right\}}{\ln\left\{\dfrac{\beta + 1}{\beta - 1}\right\}},$$

where $\xi = \xi(x)$ and $\eta = \eta(y)$ are the nondimensional computational variables, β is the clustering parameter satisfying $\beta > 1$, and L and H are the dimensions of the computation domain in the flow and transverse directions, respectively. Typical values of β were between 1.002 and 1.003. As a result, the number of points across the boundary layer at the shock impingement point was approximately 20–40.

The computational domain is depicted in Fig. 1. The shock was introduced either at the inflow boundary ($x = 0$) or at the upper boundary ($y = H$). At each of these boundaries, the flow variables were fixed at either the freestream conditions or the conditions after the incident shock; the latter conditions were computed from an iterative solution to the oblique shock relations similar to that described by Cramer (1991). At the right boundary, outflow conditions were imposed. At the lower boundary ($y = 0$), either symmetry conditions or the physical boundary conditions were applied as appropriate.

Extensive numerical checks and comparisons with known solutions have been carried out by Park (1994). These comparisons included checks with the dense gas boundary layer computations of Whitlock (1992) and Cramer et al. (1996) and with (ideal gas) shock-boundary layer experiments and computations of other authors. The result of these comparisons was that the present scheme was found to agree well with all previously published numerical results. The agreement with the experimental results was as good as that obtained with other schemes. Full details can be found in Park (1994).

Extensive tests were also made by Park (1994) to determine the grid refinement required to render the computed results independent of the grid size. It was found that ξ vs η grids in the range of 125×76 to 187×101, depending on the fluid, were adequate to ensure that the grid size no longer influenced the results, although even more refined grids were typically used in the present study. The ultimate criteria for convergence was that the values of P_s and P_p remained unchanged to the accuracy reported here.

5 Results

The numerical data for the cases run are listed in Table 1. In each case the impingement Reynolds number was taken to be 2.96×10^5. The freestream Mach number (M_1), pressure (p_1), and temperature (T_1) are given in the first three columns. Because the conventional measure of the strength of the reflection is the pressure ratio across the reflection we have recorded p_3/p_1 to indicate this strength. Here p_3 is the pressure immediately downstream of the reflection. Values of (1.1) corresponding to the separation point and the plateau pressure are listed in the last two columns and are plotted as a function of p_3/p_1 in Fig. 2. In each case the plateau pressure is defined as the central inflection point in the pressure coefficient distribution. Low pressure cases which closely approximate perfect gas conditions are denoted by open symbols and those where dense gas effects are non-negligible are denoted by solid symbols. The latter correspond to the 30.7 and 36.2 atm cases involving N_2 and the 9.0 and 34.0 atm cases involving SF_6. In the case of steam, the freestream pressure is seen to be approximately four percent of the pressure at the thermodynamic critical point. As a result this case corresponds to ideal gas conditions.

Inspection of Fig. 2 reveals that the results for P_s are roughly constant with respect to the strength of the reflection; this invariance is in complete agreement with the triple deck theory. The average value generated by our calculations is 1.39 which agrees well with the value of 1.4 given by Katzer (1989). We also note that the four cases involving dense gases fall well within the numerical scatter seen in the perfect gas cases.

As in the perfect gas cases studied by Katzer (1989), the parameter P_p corresponding to the plateau pressure is essentially constant but has more scatter than that for the separation point. However, the average value of 2.31 agrees well with the average value of $P_p = 2.3$ given by Katzer (1989). The case having the largest deviation from the average value is that of N_2 at high pressure. In this case the separation was marginal. As demonstrated later in this section, the separation region only contained five grid points in the x direction. Again our results appear to be in agreement with Katzer (1989) who also observed an increase in scatter when marginal separation occurred.

If we attempt to use intuition based on monatomic and diatomic gases in the perfect gas limit, the observation that the 36.2 atm case involving N_2 results in marginal separation may appear to be paradoxical. Afterall, a pressure ratio $p_3/p_1 = 1.43$ corresponds to a well-developed separation in low pressure nitrogen or air. To further illustrate this point we have plotted the computed skin friction and pressure coefficient distributions for the three cases involving N_2 listed in Table 1 in Figs. 3–4. The marginal separation of the 36.2 atm case is clearly illustrated as is the well-developed separation of the cases involving lower pressures. The reason that the separation is relatively weak when $p_3/p_1 = 1.43$ is clearly seen on inspection of Fig. 4, the definition (1.2), and the criterion (1.4). From the latter it is clear that it is the pressure coefficient, not just the pressure ratio, which must be considered in the prediction of separation. From (1.2) we see that the factor $p/\rho a^2$ must be considered in addition to the pressure ratio. In the perfect gas theory this ratio equals γ^{-1}, where γ is the ratio of specific heats, and therefore

Table 1 Numerical data for cases plotted in Fig. 2. The impingement Reynolds number for each case was 2.96×10^5. The expressions in parentheses associated with CO_2 denote the values of the bulk viscosity chosen for each run. The subscript 1 denotes freestream conditions and p_3 is the pressure immediately following the reflected shock.

Fluid	M_1	p_1	T_1	$\frac{p_3}{p_1}$	P_s	P_p
—	—	atm	K	—	—	—
N_2	2.0	1.0	127.5	1.4	1.44	2.24
N_2	2.0	30.7	127.5	1.4	1.36	2.34
N_2	2.0	36.2	127.5	1.43	1.42	2.01
Air	2.0	0.134	308.6	1.32	1.40	2.38
Air	2.0	0.134	308.6	1.4	1.31	2.19
Steam	2.0	8.55	646.2	1.35	1.37	2.22
CO_2 (0 μ)	2.0	1.0	304.1	1.35	1.42	2.36
CO_2 (100 μ)	2.0	1.0	304.1	1.35	1.44	2.38
SF_6	2.25	1.0	318.7	1.32	1.44	2.42
SF_6	2.25	9.0	318.7	1.3	1.42	2.45
SF_6	2.25	34.0	318.7	1.22	1.33	2.21
FC-71	2.0	1.0	646.2	1.26	1.35	2.28

does not depend on the undisturbed state. However, $p/\rho a^2$ can deviate significantly from γ^{-1} when dense gas effects are important. For example, the ratio $p_1/\rho_1 a_1^2$ for N_2 takes on values of 0.33, 0.69 and 0.71 for the 36.2 atm, 30.7 atm, and 1 atm cases listed in Table 1. As a result, the increase in c_p across the reflection for the 36.2 atm case is only about half as large as that for the low and moderate pressure cases. This difference is clearly illustrated in Fig. 4.

An interesting phenomenon also illustrated by Fig. 3 is the general decrease in the skin friction immediately upstream of the interaction zone. This decrease is completely consistent with the findings of Whitlock (1992) who generated numerical solutions with a dense-gas boundary layer code and showed that the general effect of increasing pressure was to decrease c_f. It should be noted that, when dense gas effects are important, these decreases frequently cannot be predicted by the well-known scaling

$$c_f \approx c_{fB}\sqrt{C_w}, \tag{5.1}$$

where c_{fB} is the Blasius skin friction coefficient and C_w is the Chapman-Rubesin parameter evaluated at the plate. A further discussion of this breakdown in the similarity law (5.1) is found in the thesis by Whitlock (1992) and in Cramer et al. (1996). This breakdown is of interest in the present context because many authors combine (5.1) with (1.4) to obtain an explicit expression for the effect of the Reynolds number on separation. A point revealed by the present investigation is that the factor which is really needed is the skin friction in (1.1) and (1.4) which may or may not be given by (5.1).

As a final check on the triple-deck scaling laws, we computed the values of

$$\frac{c_{pT}(M_1^2 - 1)^{1/4}}{\sqrt{c_{f1}}} \tag{5.2}$$

for each of the cases listed in Table 1. In each case, as well as many not reported here, the computed value of (5.2) for the separated cases was consistent with the separation criterion (1.4). Examples which include non-separated flows are illustrated in Fig. 5. In this figure the fluid is N_2, the freestream Mach number is 2.0, and the freestream temperature is 127.5 K. As in previous cases, the shock impingement point corresponds to a Reynolds number of 2.96×10^5. In each case, the flow deflection angle of the incident shock is 1.2 deg. According to the linear theory, the strength of the reflection, as measured by c_{pT}, should be identical for each interaction. This contrasts with the cases illustrated in Figs. 3–4 where the pressure ratio was approximately 1.4 for each case but the flow deflection angle took on values of 1.2 deg, 2.9 deg, and 3.2 deg for the 36.2 atm, 30.7 atm, and 1 atm cases, respectively.

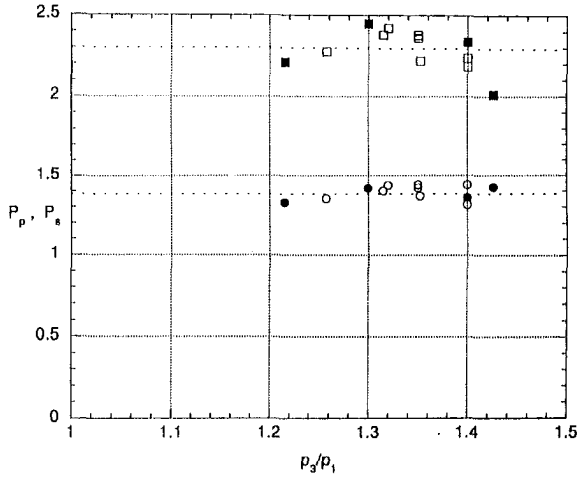

Fig. 2 Computed values of P_p (squares) and P_s (circles). The open symbols denote cases which may be regarded as perfect gases whereas the solid symbols denote freestream conditions corresponding to dense gases.

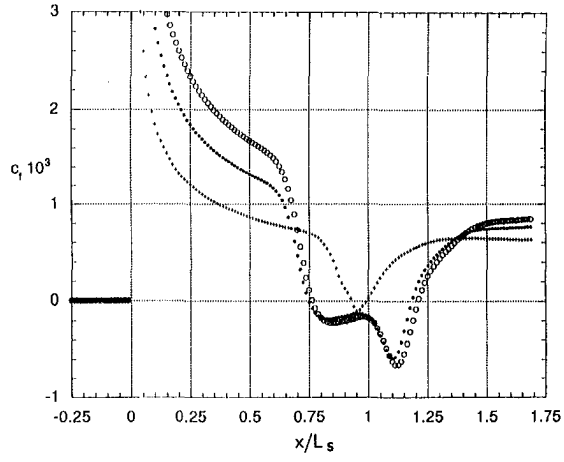

Fig. 3 Computed skin friction coefficients for three flows of N_2. The freestream conditions and reflection strengths are identical to those listed for N_2 in Table 2. The open circles denote the 1 atm case, the closed circles denote the 30.7 atm case, and the ++++ symbols denote the high pressure (36.2 atm) case.

The differences among the three cases illustrated is that the freestream pressures were taken to be 36.2 atm, 30.7 atm, and 1 atm. It turns out that the 36.2 atm case is identical to that listed in Table 1 and plotted in Figs. 3 and 4. Inspection of Fig. 5 reveals that the two lower pressure cases remain attached. This is primarily due to the differences in the skin frictions, i.e., in c_{f1}, which in turn is due to the differences in the degree of dense gas effects experienced at the different pressures. Here we note that the values of (5.2) for the 36.2 atm, 30.7 atm, and 1 atm cases were computed to be 3.2, 2.1, and 1.8, respectively. Again, these are seen to be consistent with the separation criterion (1.4).

The differences among the three cases illustrated by Fig. 5 clearly reveal the pressure dependence of the separation characteristics. These in turn may be taken to be one measure of the deviations from the classical perfect gas theory where the skin frictions would be expected to be independent of the freestream pressure.

6 Summary

The present study employs the Beam-Warming (1978) implicit scheme to study the interaction of an oblique shock with a laminar boundary layer. We believe that the present work, combined with the analytical study of Kluwick (1994), provides strong evidence for the claim that the well-known triple-deck theory, and more specifically the triple-deck scaling laws, holds for a wide range of fluids and for dense, i.e., high-pressure, gases. While it is naturally expected that the precise fluid type should not render the scaling laws invalid, the extension to dense gases is less obvious. In particular, Whitlock (1992) and Cramer, Whitlock and Tarkenton (1996) have demonstrated that many of the classical scaling laws for inviscid transonic flows and laminar boundary layers can break down when dense gas effects become important.

The appropriate generalized form of the scaling laws are those given by Kluwick (1994) and in Section 1 of the present investigation. As recognized by Kluwick, the appropriate generalized measure of the strength of the reflection is based on the pressure coefficient rather than the pressure ratio. When the scalings given by Kluwick (1994) and here are employed, it is expected that the well-known perfect gas results, determined either numerically or experimentally, can, for example, be applied directly to problems involving very high pressure steam, CO_2 in a planetary atmosphere, or high-pressure toluene in an organic Rankine cycle. In addition, comparisons between flight conditions in air and test conditions in a heavy gas wind tunnel are expected to be immediate.

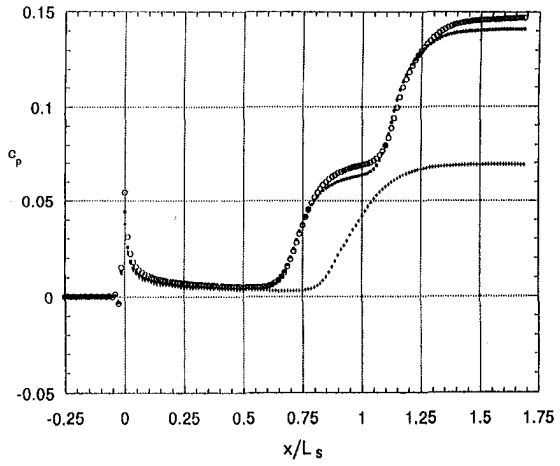

Fig. 4 Computed pressure coefficients for three flows of N_2. Each case and the notation used is identical to that of Fig. 3.

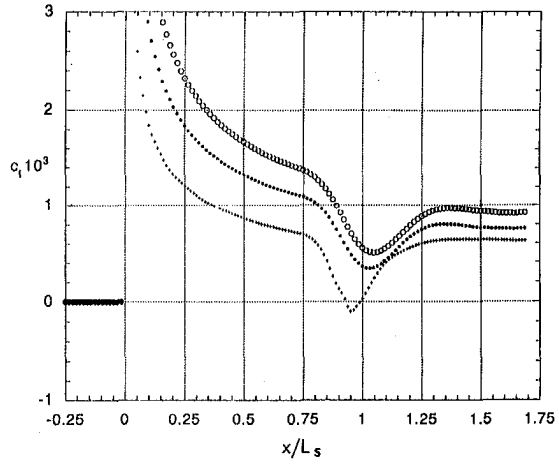

Fig. 5 Computed skin friction coefficients for three flows of N_2. The shock impingement point corresponds to a Reynolds number of 2.96×10^5 and the freestream Mach number, temperature and flow deflection angle of the incident shock were 2.0, 127.5 K and 1.2°, respectively. The symbols used correspond to exactly the same freestream pressures as in Fig. 3.

A factor not considered here is the effect of very large bulk viscosities on the interaction process. As indicated earlier in this report, preliminary studies by the first two authors indicate that the large bulk viscosities of CO_2 and, to lesser extent SF_6, may have a non-negligible impact on the shock-boundary layer interaction. Further work on this complication will be reported at a later date.

Acknowledgments

This work was supported by the National Science Foundation under Grant CTS-8913198. The authors would also like to thank Professor S. A. Ragab for his patience and many helpful suggestions during the course of this work.

References

Adamson, T. C., and Messiter, A., 1980, "Analysis of Two-Dimensional Interactions Between Shock Waves and Boundary Layers," *Annual Review of Fluid Mechanics,* Vol. 12, pp. 103–138.

Anders, J. B., 1993, "Heavy Gas Wind-Tunnel Research at Langley Research Center," ASME Paper 93-FE-5.

Anderson, W. K., 1991, "Numerical Study of the Aerodynamic Effects of Sulfur Hexafluoride (SF_6) as a Test Gas in Wind Tunnels," NASA TP-3086.

Angelino, G., and Invernizzi, C., 1993, "Cyclic Methylsiloxanes as Working Fluids for Space Power Cycles," *Journal of Solar Engineering,* Vol. 115, pp. 130–137.

Beam, R. M., and Warming, R. F., 1978, "An Implicit Factored Scheme for the Compressible Navier-Stokes Equations," AIAA *Journal,* Vol. 16, No. 4, pp. 393–402.

Chung, T. H., Ajlan, M., Lee, L. L., and Starling, K. E., 1988, "Generalized Multiparameter Correlation for Nonpolar and Polar Fluid Transport Theories," *Industrial Engineering Chemistry Research,* Vol. 27, pp. 671–679.

Chung, T. H., Lee, L. L., and Starling, K. E., 1984, "Application of Kinetic Gas Theories and Multiparameter Correlation for Prediction of Dilute Gas Viscosity and Thermal Conductivity," *Industrial Engineering Chemistry Fundamentals,* Vol. 23, No. 23, pp. 8–13.

Cramer, M. S., 1989, "Negative Nonlinearity in Selected Fluorocarbons," *Physics of Fluids* A, Vol. 1, No. 11, pp. 1984–1987.

Cramer, M. S., Whitlock, S. T., and Tarkenton, G. M., 1996, "Transonic and boundary layer similarity laws in dense gases," ASME JOURNAL OF FLUIDS ENGINEERING, Vol. 118, Sept., pp. 481–485.

Curran, H. M., 1981, "Use of Organic Working Fluids in Rankine Engines," *Journal of Energy,* Vol. 5, pp. 218–223.

Delery, J., and Marvin, J. G., 1986, "Shock-Wave Boundary Layer Interactions," AGAR-Dograph No. 280.

Devotta, S., and Holland, F. A., 1985, "Comparison of Theoretical Rankine Power Cycle Performance Data for 24 Working Fluids," *Heat Recovery Systems,* Vol. 5, No. 6, pp. 503–510.

Emanuel, G., and Argrow, B. M., 1994, "Linear Dependence of the Bulk Viscosity on Shock Wave Thickness," *Physics of Fluids,* Vol. 6, No. 9, pp. 3203–3205.

Jones, J. B., and Hawkins, G. A., 1986, *Engineering Thermodynamics,* McGraw-Hill, New York.

Katzer, E., 1989, "On the Scales of Laminar Shock/Boundary Layer Interaction," *Journal of Fluid Mechanics,* Vol. 206, pp. 477–496.

Kluwick, A., 1994, "Interacting Laminar Boundary Layers of Dense Gases," *Acta Mechanica,* Springer-Verlag, Vol. 4, pp. 335–349.

Manco, S., and Nervegna, N., 1985, "Working Fluid Selection via Computer Assisted Analysis of ORC Waste Heat Recovery Systems," SAE Paper 859432.

Martin, J. J., and Hou, Y. C., 1955, "Development of an Equation of State for Gases," *AIChE Journal,* Vol. 1, No. 2, pp. 142–151.

Park, S.-H., 1994, "Viscous-Inviscid Interactions of Dense Gases," Ph.D. dissertation, Virginia Polytechnic Institute and State University, Blacksburg, Virginia.

Reid, R. C., Prausnitz, J. M., and Poling, B. E., 1987, *The Properties of Gases & Liquids,* 4th Ed., McGraw-Hill, New York.

Reidel, L., 1954, "Eine neue Universelle Damfdruckformel-Untersuchungten über eine Erweiterung des Theorems der übereinstimmenden Zustände Teil 1," *Chemische Ingeneure Technik,* Vol. 26, pg. 83.

Reynolds, W. C., and Perkins, H. C., 1977, *Engineering Thermodynamics,* 2nd ed., McGraw-Hill, New York.

Rohsenow, W. M., Harnett, J. P., and Ganic, E. N., 1985, *Handbook of Heat Transfer Fundamentals,* 2nd ed., McGraw-Hill, New York.

Truesdell, C., 1953, "Precise Theory of the Absorption and Dispersion of Forced Plane Infinitesimal Waves According to the Navier-Stokes Equations," *Journal of Rational Mechanics and Analysis,* Vol. 2, pp. 643–741.

Whitlock, S. T., 1992, "Compressible Flows of Dense Gases in Boundary Layers," M. S. thesis, Virginia Polytechnic Institute and State University, Blacksburg, Virginia.

Yan, J., and Svedberg, G., 1991, "An Analytical Hierarchy Process (AHP) Model for Screening Working Fluids in Heat Engine Cycles," *Proc. 26th Intersociety Energy Conversion Engineering Conference.*

Energy Separation in a Jet Flow

W. S. Seol[1]
Senior Researcher.

R. J. Goldstein
Regents' Professor.

Mechanical Engineering Department,
University of Minnesota,
Minneapolis, MN, 55455

Fluids in motion can separate into regions of higher and lower energy (temperature); this is called "energy separation." The present study concerns the mechanism of energy separation in a free, circular, air jet, including the effects of acoustic excitation. Starting with the initial energy separation occurring in the boundary layer inside the nozzle, the energy separation in a jet begins to be affected by the action of vortices from an axial location, measured from the jet exit, of about 0.3D (D is the diameter of nozzle exit), becomes intensified at about 0.5D, begins to be diffused from about 1D, and there is no discernible energy separation at about 14D. The entrainment of the ambient fluid considerably affects the energy separation, and its effects appear at axial locations between about 6D and 8D. The present definition of the energy separation factor renders its distribution independent of the jet Reynolds number; except for axial locations between about 0.3D and 4D. The development of energy separation in the region close to the nozzle exit is faster when the jet Reynolds number is higher. Acoustic excitation not only enhances the energy separation, but also accelerates its diffusion. This effect is greatest for axial locations between about 1D and 4D. The fact that the acoustic excitation has a strong effect on the vortex structure and the energy separation provides good evidence that the convective movement of vortices is the cause of energy separation in jets.

1 Introduction

The boundary layer of a gas ($Pr < 1$) flow over a flat plate has an outer region with a higher energy and an inner region with a lower energy (total temperature).[2] The wake behind a cylinder separates into outer regions with a higher energy and a central region with a lower energy, when the alternate separation of vortices occurs. Evidence of such behavior, called energy separation (or "total temperature separation"), is found in other flows including the vortex tube (or Ranque-Hilsch tube), the resonance tube, the impinging jet, and the gas ejector. Previous studies established that in some cases energy separation is connected with the unsteady pressure fluctuations induced by the convective movement of vortices, and it is strongly affected by the presence of sound waves.

One form of energy separation was observed by Eckert and Drewitz (1941) in a boundary layer. They showed that the total temperature of the inner region of the boundary layer of an air flow is smaller, and that of the outer region is larger than the free-stream total temperature. Energy separation in a vortex street was found by Eckert and Weise (1940), when they measured the recovery temperature[3] distribution on a cylinder in a high speed air stream. They observed that the recovery temperature near the rear stagnation line was even lower than the static temperature of the approaching airstream.[4] Ryan (1951) observed that the recovery temperature near the rear stagnation line dropped noticeably when a strong sound was generated by the flow, indicating that the unsteady character of the flow favored the energy separation. Thomann (1959) showed that the energy separation decreased significantly when a splitter blade was attached downstream of the wedge to prevent the vortex shedding.[5] Kurosaka (1982) demonstrated that the energy separation in a vortex tube decreases as soon as the whistling sound, which several observers have noticed, is damped out by acoustic suppressors. Kurosaka et al. (1987) observed that the strength of the vortex street and the energy separation, in general, intensify when resonance occurs between the vortex shedding and the transversely standing acoustic waves in a wind tunnel. The degree of the intensification is dependent on the amplitude of the acoustic wave.

Recently, Eckert (1987) provided good insight into understanding of the mechanism of energy separation through the examination of the unsteady energy equation:

$$\rho C_p \frac{DT_t}{Dt} = \frac{\partial p}{\partial t} + \frac{\partial}{\partial x_i}\left(k \frac{\partial T}{\partial x_i}\right) + \frac{\partial}{\partial x_j}(v_i \sigma_{ij}). \qquad (1)$$

The total temperature of a fluid particle may be changed along its pathline by temporal variation of static pressure, by heat conduction, and by work of viscous stresses.

Eckert (1986) noted that the energy separation in a shear layer, including a boundary layer, is caused by the imbalance between two processes of energy transport. One is the heat conduction from a region with a higher temperature to a neighboring region with a lower temperature, and the other is the work of viscous stresses from a region with a higher velocity to a neighboring region with a lower velocity. This process depends on Pr and is a weak process for a gas flow. The energy separation in a vortex tube or in the wake of a cylinder, which is much stronger than that in a boundary layer, is caused by another mechanism.

For an unsteady flow without friction and heat conduction, the energy equation simplifies to

$$\rho C_p \frac{DT_t}{Dt} = \frac{\partial p}{\partial t}, \qquad (2)$$

which indicates that the total temperature, T_t, varies along a pathline when the pressure at a fixed location varies in time. The energy separation by this process can be more rapid and

[1] Present address: Korea Aerospace Research Institute, P.O. Box 113, Yusung, Taejon 305-600, Korea.

[2] The total temperature represents the sum of the internal energy and the kinetic energy of a fluid. It is the temperature measured when a flow is decelerated adiabatically to zero velocity and the kinetic energy is converted into internal energy. The static (or true) temperature represents the internal energy; it is the temperature measured by a sensor moving with the same velocity as the flow. The difference between the two is the dynamic temperature, which represents the kinetic energy; it is $V^2/2C_p$ for a gas with a constant specific heat.

[3] The recovery temperature is the temperature of the adiabatic surface, which is equal to the temperature of the fluid adjacent to the surface.

[4] Ryan (1951) called this "aerodynamic cooling" in contrast to "aerodynamic heating."

[5] It was found by Roshko (1955) that the vortex street was suppressed by the attachment of a splitter blade behind a wedge.

Contributed by the Fluids Engineering Division for publication in the JOURNAL OF FLUIDS ENGINEERING. Manuscript received by the Fluids Engineering Division December 4, 1995; revised manuscript received August 26, 1996. Associate Technical Editor: D. P. Telionis.

intense than the energy separation in a shear layer, and would occur even in an inviscid flow. Based on the above equation, Kurosaka et al. (1987) proposed an explanation of the mechanism of energy separation in a vortex street.

Eckert (1987) analyzed the temperature distribution across a convecting vortex. He showed that the maxima and minima of the total temperature are located close to the border of the viscous core, and that the total temperature separation is proportional to the convection velocity and the rotational velocity of the vortex. The energy separation starts with the generation of the vortices, grows during the time when the strength of vortices increases, and gradually decreases by viscous forces or turbulence as the vortices move downstream.

Another example of energy separation induced by unsteady pressure fluctuations due to moving vortices was observed in an impinging jet by Goldstein et al. (1986, 1990) and Goldstein and Seol (1991). For a jet which discharges into a still ambient, vortex rings occur at a certain distance from the nozzle exit and travel downstream. Due to the sense of rotation of vortices, a temperature maximum occurs in the central region surrounded by a minimum at a certain radial distance, opposite to the energy separation distribution in a wake behind a cylinder. For a short distance (about 2 jet diameters) between the nozzle exit and an impingement plate, the distribution of recovery temperature on the impingement plate shows a maximum at the impingement point surrounded by a minimum at a radial distance (about 1.5 jet diameters) from the impingement point. At about the same radial location, a local maximum of heat transfer coefficient exists, indicating the enhancement of heat transfer.

Recently, Fox et al. (1993) proposed that the energy separation in an impinging jet is significantly modified by secondary vortices on the impingement plate, which are induced by the approach of the primary vortices formed at the nozzle lip. They also measured energy separation in a free jet for a limited range of jet velocity and found that acoustic excitation enhances the energy separation.

In the present study, the energy separation in a free jet, including the effect of acoustic excitation, is investigated. A jet flow is formed by a smooth-contoured, bell-shaped nozzle with an exit diameter of 2 cm. When desired, the jet is excited with acoustic waves applied externally at X/D of 1. The applied excitation frequency is 4500 Hz, which corresponds to St_e of 0.96 for Re_j of 120,000.

According to Yule (1978), the above excitation frequency is close to the natural frequency of the jet at X/D of 1 where the acoustic waves are applied. He noted that the initial vortex rings generally coalesce with neighboring rings so that the scale and the separation distance of vortex rings increase with distance from the nozzle exit. Thus the natural frequency of a jet generally decreases with axial distance. According to his measurement for Re_j of 200,000, which is slightly higher than the highest Re_j (=160,000) of the present study, St_j corresponding to the natural frequency of a jet is about 1.4, 0.85, 0.5, 0.4, 0.35 at X/D of 0.5, 1, 2, 4, 5.5, respectively.

2 Experimental Apparatus and Procedure

The experimental apparatus used in the present study, indicated in Fig. 1, was designed to measure the energy separation in a jet flow with and without acoustic excitation. It has three major components: air flow system, acoustic excitation system, and automated measurement system. A brief description is given here; a more detailed description is given by Seol (1993).

Air Flow System. Air is provided by a compressor at a pressure of 830 ± 10 kPa (8.3 ± 0.1 bar). After filtration, the air is regulated to a pressure not exceeding 310 kPa (3.1 bar). The flow rate is further controlled by 3 needle valves in parallel, and metered by a sharp-edged orifice. Temperature of the air is controlled in a heater section downstream of the metering orifice. The air from the heater section is introduced into an acoustic silencer (Burgess-Manning CA-2.5) to reduce unwanted noise from upstream. It provides an attenuation of more than 20 dB over a frequency range of 300 Hz to 5000 Hz with a small pressure drop. The air then flows into a settling chamber which contains a section of aluminum chips and a section of honeycomb. The aluminum chips help provide a uniform temperature, and the honeycomb straightens the flow. The settling chamber is insulated with fiberglass.

The temperature of the settling chamber is monitored by two thermocouple probes which can traverse horizontally through the settling chamber to check the uniformity of the temperature. The temperature variation in the settling chamber is within 0.05°C. The jet total temperature is measured about 5 cm upstream from the start of the nozzle contraction. Since the velocity is very low at this location, even for the largest jet velocity

Nomenclature

C_p = specific heat at constant pressure
D = diameter of the nozzle exit, 2 cm in present study
f_e = excitation frequency, ≈ 4,500 Hz in present study
k = thermal conductivity of fluid
p = static pressure
$p_{j,t}$ = local jet total pressure
p_{j,t^e} = total pressure at the jet centerline
p_{j,t^e} = jet total pressure at the nozzle exit
Pr = Prandtl number
R = radial coordinate normal to the direction of jet flow (considered as + or − to show symmetry in a given plane of measurement)
R_b = radial location of the border (S = 0) between the region of positive S and the region of negative S
R_{in} = radial location of the inner boundary of the region affected by the energy separation
R_{max} = radial location of the maximum energy separation factor
R_{min} = radial location of the minimum energy separation factor
R_{out} = radial location of the outer boundary of the region affected by the energy separation
Re_v = jet Reynolds number, $Re_j = u_j^e D/\upsilon$ in present study
S = energy separation factor, $S = (T_{j,t} - T_{j,t^e})/T_{j,d}^e$
S_{cl} = energy separation factor at the jet centerline
S_{max} = maximum energy separation factor
S_{min} = minimum energy separation factor
St_e = excitation Strouhal number, $St_e = f_e D/u_j^{ee}$, ≈0.96
T = temperature
$T_{j,d}$ = jet dynamic temperature, $T_{j,d} = u_j^2/2C_p$
T_{j,d^e} = jet dynamic temperature at the nozzle exit, $T_{j,d}^e = (u_j^e)^2/2C_p$
$T_{j,s}$ = jet static temperature
$T_{j,t}$ = jet total temperature, $T_{j,t} = T_{j,s} + T_{j,d}$
T_{j,t^e} = jet total temperature at the nozzle exit
T_t = local total temperature
t = time
u_j = local jet velocity
u_j^e = average jet velocity at the nozzle exit
V = velocity
v_i = velocity components, Eq. (1)
x_i, x_j = length components, Eq. (1)
X = axial coordinate parallel to the direction of jet flow
ν = kinematic viscosity of fluid
ρ = density of fluid
σ_{ij} = viscous stress components, Eq. (1)

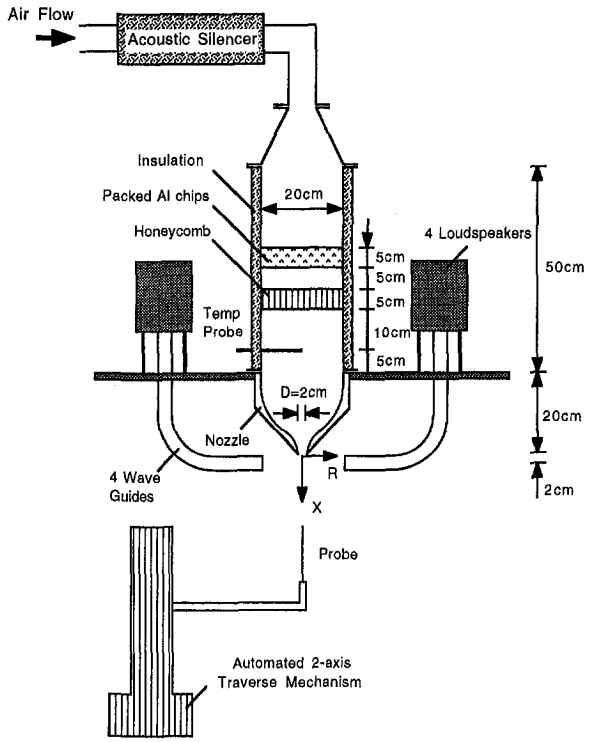

Fig. 1 Experimental apparatus

considered, the velocity error associated with the thermocouple probe is small.

The nozzle is made of aluminum and has a bell-shaped geometry. The bell-shaped nozzle is superior in providing a uniform velocity profile at the nozzle exit. A uniform velocity along with a uniform temperature is necessary to have a uniform total temperature distribution at the nozzle exit.

Acoustic Excitation System. Acoustic excitation of a jet could be accomplished either internally by a loudspeaker located in the settling chamber or externally by a series of loudspeakers distributed around the circumference of the jet. In the former case, the frequency and the amplitude of excitation is limited by the settling chamber resonance characteristics, while, in the latter case, they can be varied with more freedom. In the present study, an external excitation scheme is employed in order to strengthen the vortical structure of a relatively high speed jet.

An acoustic wave is generated by 4 compression driver loudspeakers (Altec 290-8K, 8Ω, 100W) mounted 90 deg apart around the settling chamber. A 90 deg-bent steel pipe with ID of about 3.5 cm and OD of about 4.1 cm is connected to the opening of each loudspeaker and used as a wave-guide to introduce the acoustic wave to the nozzle exit. The four wave-guides are aligned such that the center of the exit of each guide is located at $X/D = 1$ and $R/D = 5$, i.e., 2 cm downstream of the nozzle exit and 10 cm away from the jet centerline. The wave-guides are placed in a plane normal to the jet axis and are 90 deg apart. Two of them are parallel to the plane of measurement field, and the other two are vertical to it.

The four loud-speakers are driven by an Altec 9444A power amplifier. The input to the amplifier is provided with a sinusoidal signal generated by a Wavetek 110 function generator. The frequency of the input wave is measured with a Fluke 1900A frequency counter and monitored with a Hewlett-Packard 1740A oscilloscope.

Automated Measurement System. Determination of energy separation in a jet requires precise positioning of the probe and accurate measurement of the temperature. In addition, it requires a large number of data points which in turn require very frequent repositioning of the probe. To fulfill these requirements, a computer-controlled measurement system has been employed. The system consists of a temperature probe, a stepper-motor driven two-axis positioner, a unit for motor control, a digital multimeter, a switch controller, a pressure transducer, a computer, etc. Though the resolution of positioning of the probe is 0.0254 mm (about 0.0013D), the finest increment used in the present study is 0.2 mm (0.01D). The error in positioning the probe is about 0.0127 mm.

Temperatures are measured with 36 gauge iron-constantan thermocouples. Four thermocouples are used for the ambient temperature around the nozzle exit, two for the ice point, one for the plenum temperature, and one for the total temperature distribution in the jet.

The total temperature in the jet is measured by a total-temperature probe, similar to the one suggested by Hottel and Kalitinsky (1945) and Moffat (1962) as the simplest and most direct design for reducing the velocity error of a thermocouple probe. The OD and the ID of the probe are about 2.4 mm and about 1.8 mm, respectively, and the tip is tapered so that its diameter is close to ID of the probe. Inside the probe, a thermocouple junction is located at 1.8 mm from the tip and a vent hole (0.9 mm) is drilled on the probe wall at 40 mm from the tip. With this probe, the velocity error in temperature measurement could be limited within 0.1°C for the entire velocity range of the present study.

All thermocouple readings are referenced to an isothermal box, made of aluminum and well insulated with fiberglass. To measure the temperature of the isothermal box relative to the ice point, two thermocouples with their junctions in the ice bath (Model Kaye K140-4) are connected to the isothermal box. The emf between the measuring junction and the ice point is obtained by the law of intermediate temperature.

The thermocouple leads in the isothermal box are connected by copper wires to a Fluke 2205A switch controller. The switch controller is connected to a Fluke 8520A digital multimeter, with which the thermocouple emf 's are read. It has a resolution of 1 μV which corresponds to about 0.02°C for an iron-constantan thermocouple.

The total pressure of the jet is measured by a total pressure probe, the OD and the ID of which are about 1.5 mm and about 1.0 mm, respectively, and the tip is tapered so that its diameter is close to ID of the probe. The probe is connected to a port of Validyne DP15-60 variable reluctance pressure transducer which is connected to a Validyne CD15 sine wave carrier demodulator. The other port of the pressure transducer is open to the ambient. The demodulator output is read with a Fluke 8520A digital multimeter.

Measurement Procedure. The flow rate is set at the start of an experiment. The jet total temperature at the nozzle exit is controlled to be equal to the ambient temperature. After the steady state is reached, the total-temperature distribution in the jet is measured.

The output of the thermocouple in the total-temperature probe is read 10 times with a time interval of about one second, and an average is taken and stored in the computer. For each set of measurements at a given axial location, the variation of the room temperature (also the jet total temperature at the nozzle exit) is checked to determine whether the condition of the steady state is fulfilled during the measurement period. If the variation is less than 0.1°C for a period of 30 minutes, steady state is assumed. If it is larger than 0.1°C, the measurements for that axial location are discarded and redone.

In order to study the effect of acoustic excitation on the energy separation, the acoustic wave is imposed. The excitation frequency is 4,500 Hz, and the amplitude is fixed.

3 Results

In the present study, the total temperature of the jet is set equal to the ambient temperature, so that the static temperature of the jet is lower than the ambient by the jet dynamic temperature. Thus the energy transport due to heat conduction occurs in a direction from the ambient towards the center of the jet, and the energy transport due to shear work occurs in the opposite direction, with the net effect of the energy transport in a direction from the ambient to the center, generating a region of higher total temperature on the inside of the jet and a region of lower total temperature on the jet periphery. The effect is significant near the nozzle exit, where the velocity gradient as well as the (static) temperature gradient is large across the very narrow jet shear layer, and decreases as the shear layer spreads with increasing axial distance. As mentioned earlier, the energy separation by the above mechanism depends on Pr, and is a weak process for air since Pr is close to 1.

The energy separation by the action of vortices depends on the strength of the vortices, their convection velocity, and the spacing between two adjacent vortices. According to Kurosaka et al. (1987), it increases as the vortex strength and the convection velocity increase, and as the spacing between adjacent vortices decreases. In jets, the energy separation is expected to occur with the formation of vortices at a location close to the nozzle exit, increase as the vortices grow in size and strength up to a certain axial distance, and decrease as the vortices decay with further increase in axial position. The sense of rotation of the vortices is in a way that causes a region of higher total temperature toward the center of the jet and a region of lower total temperature toward the outside of the jet.

The distribution of the energy separation in the present study should be interpreted as the superposition of the energy separation in the jet, which is caused by the imbalance among heat conduction, shear work, and pressure work, and the initial energy separation in the boundary layer inside the nozzle and carried downstream along the jet shear layer.

In the present study, the nondimensional "energy separation factor" (S) is defined as

$$S = \frac{T_{j,t} - T^e_{j,t}}{T^e_{j,d}}, \tag{3}$$

where

$$T_{j,t} = T_{j,s} + T_{j,d}, \tag{4}$$

and

$$T_{j,d} = \frac{u_j^2}{2C_p}. \tag{5}$$

The experimental uncertainty of the energy separation factor, calculated using the method of Kline and McClintok (1953) is not more than 0.035 (Seol, 1993).

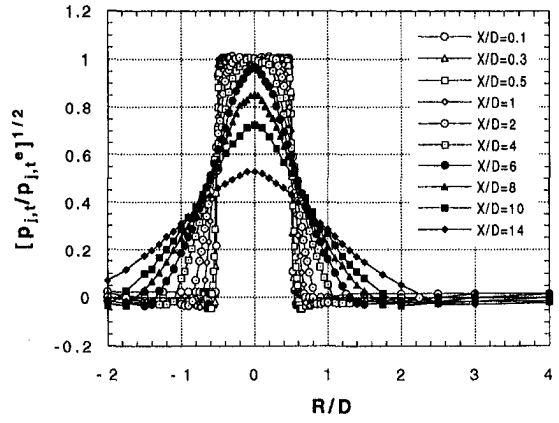

Fig. 2 Distribution of total pressure at various downstream distances. Re_j = 120,000.

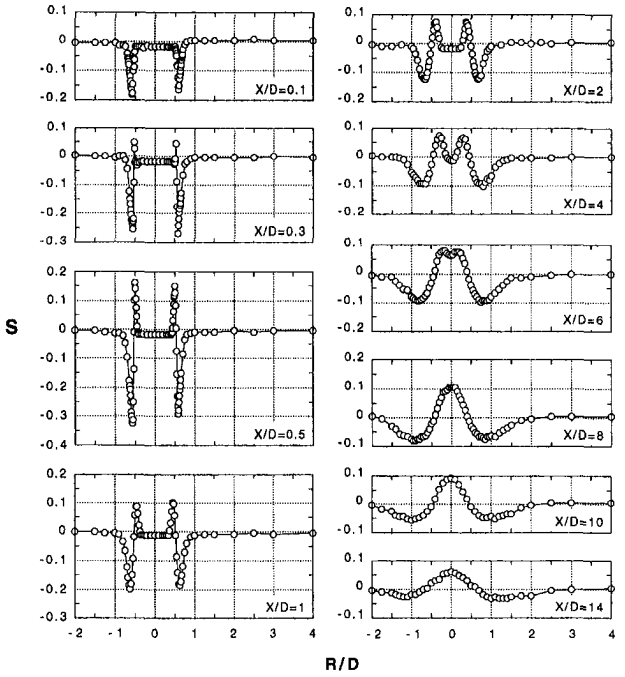

Fig. 3 Distribution of energy separation factor at various downstream distances. Re_j = 120,000.

Total Pressure Distribution. The total pressure distribution for Re_j = 120,000 is shown in Fig. 2 for X/D = 0.1, 0.3, 0.5, 1, 2, 4, 6, 8, 10, and 14 (velocity at the nozzle exit (u_j^e) of about 95 m/s). Symmetry is excellent.

At X/D = 0.1, the total pressure has a "tophat" profile, and the shear layer is very narrow. The jet core narrows with X, but exists up to an axial location between X/D = 4 and X/D = 6. From this location on downstream the total pressure profile has a "bell shape."

Note that there exists a small region of lower total pressure near the jet periphery, where the total pressure ($\approx$ the static pressure in that region) is slightly smaller than the ambient pressure. This, most evident for $0.3 \leq X/D \leq 1$, is believed to be due to the low pressure core of the small vortices.

Distribution of Energy Separation Factor. Distribution of the energy separation factor for Re_j = 120,000 is presented in Fig. 3. At this Re_j, $u_j^e \approx 94$ m/s and $T^e_{j,d} \approx 4.4$°C. Symmetry is good at all axial locations.

At X/D = 0.1, it appears that there is only a region of lower total temperature ($S < 0$) without any region of higher total temperature ($S > 0$). This may be due to the energy separation factor in the region of positive S being too small to be detected. Since the negative S is in a region of low velocity, and the positive S is in a region of high velocity, the excess in the energy separation factor in the region of positive S should be smaller than the defect in the energy separation factor in the region of negative S for the same amount of energy excess (or defect).

Energy separation at this location should primarily be due to the energy separation from the boundary layer inside the nozzle. The recovery factor at the wall within an air boundary layer is about 0.84 for a laminar boundary layer and about 0.90 for a turbulent one. The corresponding energy separation factors are −0.16 and −0.1, respectively. The measured minimum energy separation factor of −0.17 corresponds approximately to the recovery factor for a laminar boundary layer.

In addition to the energy separation in the nozzle boundary layer, there should be a certain contribution of the imbalance between heat conduction and shear work in the jet shear layer. The magnitude of energy separation by this may be comparable to that in the nozzle boundary layer.

The small offset of S from zero at $-0.5 < R/D < 0.5$, which appears in the region close to the jet exit, may be due to measurement error caused by the high velocity of the jet flow. For Re_j of 120,000 ($T^e_{j,d} \approx 4.4$°C), the maximum error in the energy separation factor due to this is about 0.023.

At $X/D = 0.3$, a region of positive S begins to appear and the magnitude of minimum energy separation factor increases, indicating an intensification of energy separation. The action of vortices, even though small in size and strength, apparently starts to affect the energy separation near this location. The distribution of S should be regarded as the superposition of the energy separation caused by vortices to the initial energy separation from the nozzle boundary layer and from the jet shear layer.

By $X/D = 0.5$, the magnitude of energy separation factor and the width of the region of energy separation have significantly increased, indicating further intensification of energy separation, which is believed due to the growth of vortices in size and strength. The energy separation here appears to be primarily due to the action of vortices.

At $X/D = 1$, the magnitudes of the maximum and the minimum energy separation factor have decreased while the width of the region of energy separation continues to increase. As the vortices grow in size and decrease in strength, and the spacing between them increases through the coalescence of vortices, there are smaller pressure fluctuations in time. This, along with the spread of the jet shear layer, provides less driving potential for energy separation. Moreover, the initial energy separation that occurs in the nozzle boundary layer should decay as the jet travels downstream. The spread and decay of the energy separation are believed to be due to the combined effects of these factors.

At $X/D = 2$, the energy separation has spread and decayed further, though the decay rate from $X/D = 1$ to $X/D = 2$ is less than that from $X/D = 0.5$ to $X/D = 1$. At $X/D = 4$, the energy separation has spread almost to the jet axis, leaving little "unaffected" region in the central part of the jet. The decay of the energy separation from $X/D = 2$ to $X/D = 4$ is small, as indicated by minimal decrease in the magnitudes of the maximum and minimum energy separation factor. By $X/D = 6$, the center of the jet is affected by the energy separation as indicated by positive energy separation factor at the center. However, the energy separation factor at the axis is slightly smaller than the maximum energy separation factor at $R/D \approx \pm 0.15$, making a small depression near the center of the distribution curve.

At $X/D = 8$, the maximum energy separation factor occurs at the jet axis, and the distribution curve of energy separation factor does not show any central depression. Note that the magnitude of the maximum energy separation factor has increased, whereas the magnitude of the minimum energy separation factor has decreased. This may be due to the entrainment of ambient air to the jet, as indicated by Fox et al. (1993). The energy separation factor in the central region of a jet increases due to the entrainment.

At $X/D = 10$, the magnitudes of both the maximum and the minimum energy separation factor have decreased, indicating that the energy separation diminishes including the effect of entrainment. At $X/D = 14$, the energy separation is small.

Effect of Re_j on the Energy Separation. In order to find the effect of Re_j on the energy separation, measurements of the energy separation factor were performed for a smaller Re_j (80,000) and a larger Re_j (160,000). The corresponding jet velocities are about 62 m/s and 124 m/s, and the corresponding dynamic temperatures are about 1.92°C and 7.66°C, respectively. The distribution curves of energy separation factor for the three Re_j's are plotted in the same graph and presented in Fig. 4. For a more detailed presentation, the curves are shown only for the region between $R/D = 0$ and $R/D = 2$.

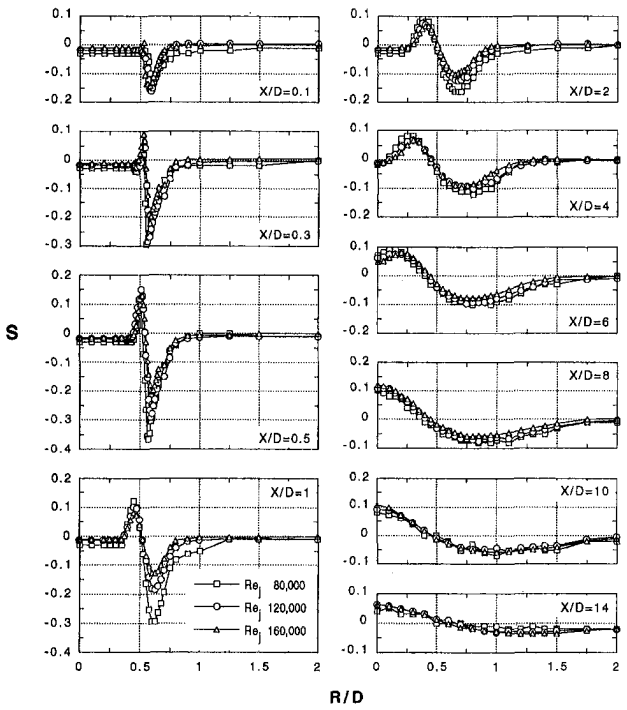

Fig. 4 Effect of Re_j on the distribution of energy separation factor

The form of the energy separation factor renders it independent of Re_j except for certain axial locations, approximately $0.3 \leq X/D \leq 4$ (most significant dependence on Re_j occurs at $X/D = 0.5$ and 1), in the range of Re_j studied. The independence (on Re_j) of the recovery factor had been proposed by Goldstein et al. (1986, 1990) and Goldstein and Seol (1991) in their experiments with impinging jets for $X/D \geq 2$.

The distributions of energy separation factor for Re_j of 80,000 and 160,000 are generally similar to that for Re_j of 120,000. However, there are some differences too. At $X/D = 0.3$, for example, the region of positive S is very small when $Re_j = 80{,}000$, but it is significantly larger when $Re_j = 160{,}000$. In the axial locations of $X/D = 0.5$ and $X/D = 1$, S_{min} is smaller for the smaller Re_j. The offset of S from zero in the central region near the nozzle exit, which is due to the velocity error of the total temperature probe, is larger for Re_j of 80,000 than for Re_j of 160,000, since a given velocity error of the total temperature probe produces a larger error in S when the dynamic temperature is smaller. The Re_j of 80,000 is close to the minimum flow rate which provides S without a significant experimental error, and the Re_j of 160,000 is close to the maximum flow rate which the flow system can provide.

Axial variations of the maximum energy separation factor (S_{max}), the minimum energy separation factor (S_{min}), and the energy separation factor at the jet centerline (S_{cl}) are presented in Fig. 5, and those of the radial locations of the minimum energy separation factor (R_{min}), the maximum energy separation factor (R_{max}), the border between the region of negative S and the region of positive S (R_b), and the inner (R_{in}) and outer (R_{out}) boundaries of the region affected by the energy separation are presented in Fig. 6 for the three Re_j's. Axial variations of S_{max} and S_{min} are generally similar regardless of Re_j except for $0.1 < X/D < 4$, and axial variations of R_{min}, R_{max}, R_b, R_{in}, and R_{out} are essentially independent of Re_j.

The axial variations of S_{max}, S_{min}, and S_{cl} show the development of energy separation. S_{min} decreases from $X/D \approx 0.1$ to

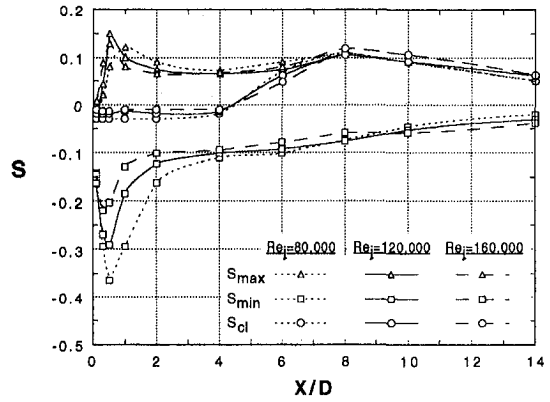

Fig. 5 Effect of Re_j on the variation of S_{max}, S_{min}, and S_{cl} with X/D

$X/D \approx 0.5$, indicating intensification of energy separation, then increases with X. The variation of S_{max} corresponds to that of S_{min} in the opposite sense. By "opposite sense" one means that S_{max} increases when S_{min} decreases, and S_{max} decreases when S_{min} increases. The relatively large value of S_{max} from $X/D \approx 4$ to $X/D \approx 8$ may be due to the entrainment of ambient air as indicated by Fox et al. (1993).

The axial variations of R_{min}, R_{max}, R_b, R_{in}, and R_{out} show the spread of the energy separation. The inner (R_{in}) and outer (R_{out}) boundaries spread in a roughly linear manner. The border between the region of negative S and the region of positive S (R_b) remains at $X/D \approx 0.5$, though it slightly approaches the center till $X/D \approx 6$ to 8 and then moves away from it for larger X.

As shown in Fig. 5, the minimum of S_{min} occurs at $X/D \approx 0.5$ for Re_j of 80,000 and 120,000 but at a shorter axial distance ($X/D \approx 0.3$) for the higher Re_j of 160,000. The maximum of S_{max} occurs at $X/D \approx 1$ for Re_j of 80,000 but at $X/D \approx 0.5$ for the higher Re_j of 120,000 and 160,000. In other words, the minimum of S_{min} and the maximum of S_{max} occur somewhat closer to the nozzle exit when Re_j is higher; the energy separation develops faster for the higher Re_j. This may be indicated by comparing the rate of variation of S_{min} and S_{max} for the three Re_j's from $X/D = 0.1$ to $X/D = 1$.

The influence of Re_j on the development of energy separation with position is closely related to the effect of Re_j on the development of the vortex structure. Yule (1978) showed that the peak of the radial component of turbulent intensity, which is closely related to the development of vortices, occurs closer to the nozzle exit for higher Re_j. According to his measurements, it occurs at $X/D \approx 0.6$ when $Re_j = 50{,}000$ and at $X/D \approx 0.3$ when $Re_j = 100{,}000$.

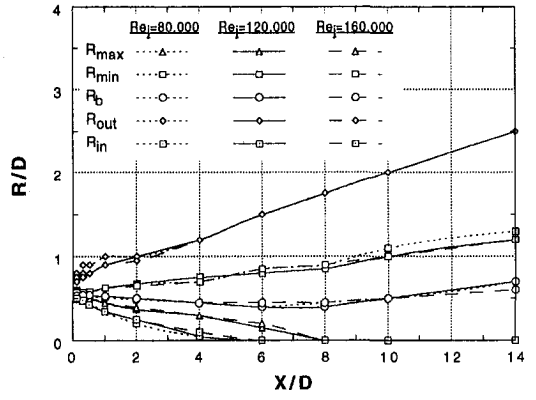

Fig. 6 Effect of Re_j on the variation of R_{max}, R_{min}, R_b, R_{out}, and R_{in} with X/D

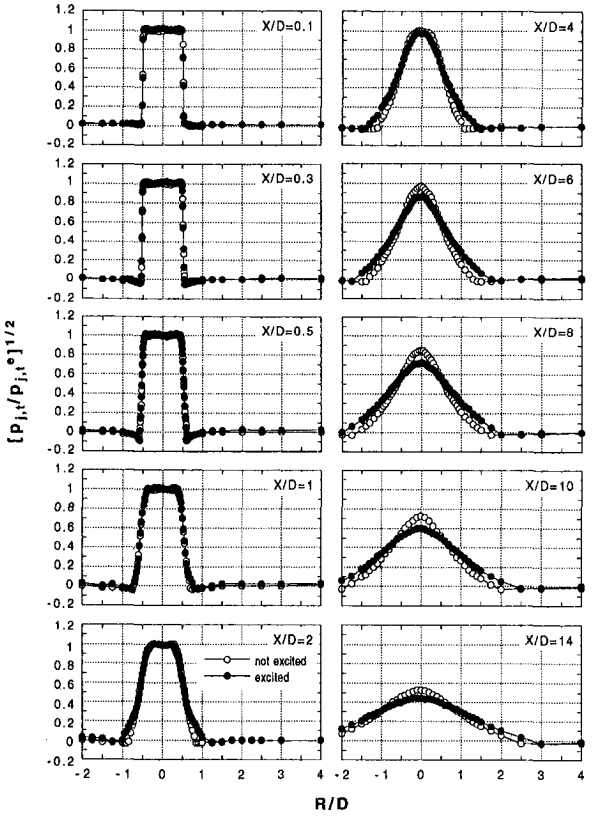

Fig. 7 Effect of acoustic excitation on the distribution of total pressure. $Re_j = 120{,}000$. Excitation is at 4,500 Hz, $St_e = 0.96$.

In addition to the similarity between the axial variations of S_{max} and S_{min}, there is an interesting difference between them. For $Re_j = 80{,}000$, the minimum of S_{min} occurs closer to the nozzle exit ($X/D \approx 0.5$) than the maximum of S_{max} ($X/D \approx 1$). For $Re_j = 160{,}000$, the minimum of S_{min} also occurs at a smaller axial position ($X/D \approx 0.3$) than the maximum of S_{max} ($X/D \approx 0.5$). For $Re_j = 120{,}000$, though both the minimum of S_{min} and the maximum of S_{max} occur at about the same axial position ($X/D \approx 0.5$), the region of the largest rate of change of S_{min} (from $X/D = 0.1$ to $X/D = 0.3$) is closer to the nozzle exit than that of S_{max} (from $X/D = 0.3$ to $X/D = 0.5$). Thus, the development of the axial variation of S_{min} leads that of S_{max}. This may be related to the formation procedure of a vortex, since S_{min} is affected by the pressure fluctuations in the front region of a moving vortex, and S_{max} is affected more by the pressure fluctuations in the back of the vortex.

Effect of Acoustic Excitation on the Distribution of Total Pressure of a Jet. A knowledge of the effect of acoustic excitation on total pressure distribution of a jet is useful in interpreting the effect of acoustic excitation on energy separation. A measurement of total pressure distribution was done for $Re_j = 120{,}000$ with acoustic excitation at $f_e = 4{,}500$ Hz, which corresponds to $St_e = 0.96$. A presentation of the effect of excitation is given in Fig. 7, where the total pressure distribution of an excited jet is compared with that of an unexcited jet.

The excitation shortens the potential core of the jet, as indicated by an early decay of the centerline total pressure (or velocity), hastens the spread of jet shear layer, and decreases the total pressure in the region of lower total pressure near the jet periphery in the near field (about $0.3 < X/D < 0.5$), indicating an increase in vortex strength.

The effect of excitation appears to be insignificant for $0.1 \leq X/D \leq 1$, except for the slight decrease of the pressure near the jet periphery at $X/D = 0.3$ and 0.5. The total pressure

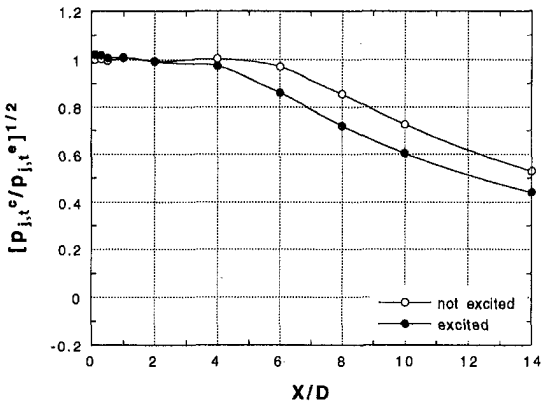

Fig. 8 Effect of acoustic excitation on the decay of centerline total pressure. Re_j = 120,000. Excitation is at 4,500 Hz, St_e = 0.96.

distribution of an excited jet starts to deviate significantly from that of an unexcited jet at $X/D \approx 2$, where the former shows a slightly larger spread near the jet periphery. At $X/D = 4$, the centerline total pressure of an excited jet becomes slightly smaller than the nozzle-exit value, while that of the unexcited jet remains at the nozzle-exit value. Moreover, the spread of the total pressure profile is further enlarged by the excitation. For X/D from 6 to 14, the effect of excitation is generally similar; the centerline total pressure is lower and the spread of the total pressure profile is larger for an excited jet than for an unexcited jet.

The effect of acoustic excitation on the decay of centerline total pressure is shown in Fig. 8. The centerline total pressure begins to deviate from the nozzle-exit value at $X/D \approx 4$ when the jet is excited, but at $X/D \approx 6$ when it is unexcited. Thus it is expected that the potential core exists till $X/D \approx 4$ when the jet is excited, but till $X/D \approx 6$ when it is unexcited. The early decay of the centerline velocity is believed to be due to the enhanced mixing and the faster spread of shear layer caused by excitation. For X/D from 6 to 14, the decay rates are much the same, so that the gap between the two curves is approximately constant. Crow and Champagne (1971) obtained similar results for the decay of centerline velocity.

Effect of Acoustic Excitation on the Energy Separation. It is known that the vortex structure of a jet is strongly affected by a controlled excitation (Heavens, 1980). Thus it is expected that the energy separation is also affected by the excitation. Distribution of the energy separation factor for Re_j of 120,000 with acoustic excitation at f_e = 4,500 Hz (St_e = 0.96) is compared with that for an unexcited jet in Fig. 9.

At $X/D = 0.1$, the excitation does not have any discernable effect on the distribution of energy separation factor. At this location, the energy separation is caused mainly by the imbalance between heat conduction and shear work from the boundary layer in the nozzle and the jet shear layer. At $X/D = 0.3$ and 0.5, the excitation hardly changes the magnitudes of the maximum energy separation factor or the minimum energy separation factor, but enlarges the region of energy separation slightly. At these locations, the acoustic excitation appears to affect the size of vortices rather than their strength.

At $X/D = 1$, the energy separation is greatly affected by acoustic excitation. The magnitudes of the maximum and the minimum energy separation factor are significantly increased; in addition the region of energy separation is enlarged. It is apparent that not only the size but also the strength of vortices is greatly affected by the excitation. The effect of excitation on the energy separation is also large at $X/D = 2$.

At $X/D = 4$, the effect of excitation on the energy separation in the central region of a jet is greater than that for $X/D = 2$. The difference in the central region indicates that the excitation not only enhances the energy separation but also accelerates its diffusion. Due to the accelerated diffusion, the center of an excited jet is considerably affected by the energy separation as indicated by a positive S, while that of the unexcited jet remains unaffected. The enhanced mixing and the faster spread of the shear layer of an excited jet were already observed with the corresponding changes in total pressure profiles.

At $X/D = 6$, the effect of excitation is significant in the region of positive S. Due to the accelerated diffusion in the excited jet, the maximum energy separation factor occurs at the center, while that of the unexcited jet occurs at R of about 0.15D. The larger value of the maximum energy separation factor is attributed to the enhanced entrainment in addition to the enhanced vortex structure by acoustic excitation.

At $X/D = 8$, the effect of excitation primarily appears in broadening the distribution curve. At $X/D = 10$, the faster decay of energy separation makes the distribution curve of the excited jet flatter than that of the unexcited jet. At $X/D = 14$, little effect of the excitation remains, though the distribution curve of the excited jet is slightly flatter.

The authors studied the effect of acoustic excitation for the wider range of excitation frequency and jet velocity, and found that the most effective frequency depends not only on the jet velocity but also on the axial location (Seol, 1993). The St_e of 0.96 is close to the natural frequency of the jet at X/D of 1, where the acoustic waves are applied, and provides the most effective excitation at this axial location. More detailed discussions will be presented in a subsequent paper by the authors.

Effect of Acoustic Excitation on the Axial Variation of Energy Separation. The effect of acoustic excitation on the axial variation of energy separation is presented in Fig. 10 and Fig. 11, where axial variations of S_{max}, S_{min}, S_{cl} and those of R_{min}, R_{max}, R_b, R_{in}, R_{out} for an excited jet are compared with those for an unexcited jet.

As shown in Fig. 10, the effect of excitation is most significant at certain axial locations. The magnitude of S_{min} for an

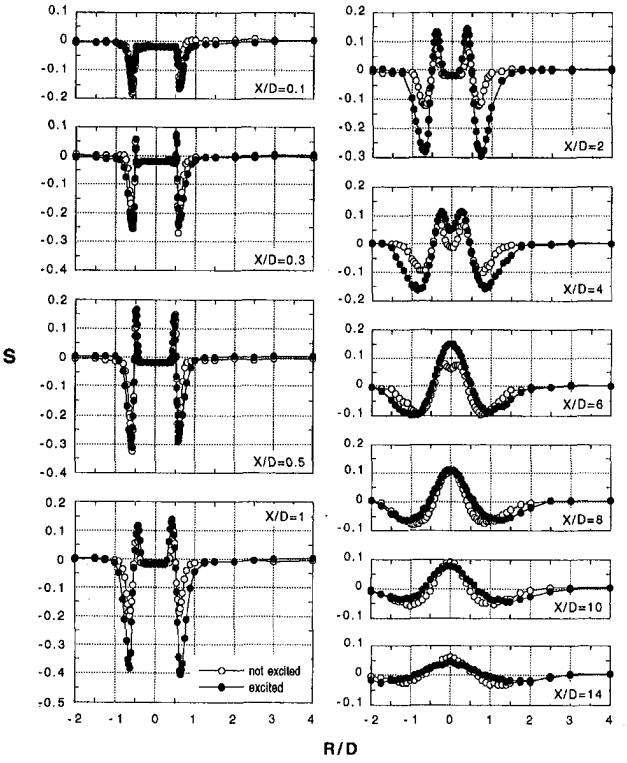

Fig. 9 Effect of acoustic excitation on the distribution of energy separation factor. Re_j = 120,000. Excitation is at 4,500 Hz, St_e = 0.96.

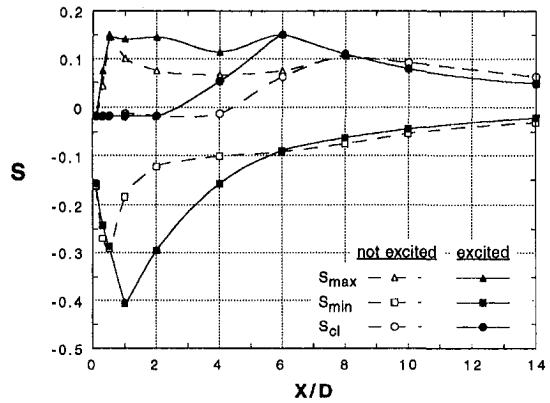

Fig. 10 Effect of acoustic excitation on the variation of S_{max}, S_{min}, and S_{cl} with X/D. Re_j = 120,000. Excitation is at 4,500 Hz, St_e = 0.96.

excited jet is considerably larger for $0.5 < X/D < 6$ but the same or even slightly smaller for $6 < X/D < 14$ than that of an unexcited jet. The magnitude of S_{max} of an excited jet is larger than that for an unexcited jet for $0.5 < X/D < 8$, but the former is the same or even slightly smaller than the latter for $8 < X/D < 14$. Due to the faster penetration of the energy separation into the center, S_{cl} of an excited jet deviates from its initial value (≈ 0) at a shorter axial distance ($X/D \approx 2$) and reaches a maximum at a shorter axial distance ($X/D \approx 6$).

When the jet is not excited, the minimum of S_{min} occurs at $X/D \approx 0.5$, and S_{min} increases sharply from $X/D \approx 0.5$ to 1. However, in the excited jet, S_{min} decreases from $X/D \approx 0.5$ to 1, and the minimum of S_{min} occurs at $X/D \approx 1$. It is believed that this follows as the strength of vortices continues to increase till $X/D \approx 1$ when the jet is excited, whereas it begins to decrease from $X/D \approx 0.5$ when the jet is not excited. The difference in S_{min} between the two jets is significant between $X/D \approx 0.5$ and 6. S_{min} of an excited jet increases at a greater rate from $X/D \approx 1$ to $X/D \approx 6$ after which the rate of increase is almost independent of excitation. According to these observations, it appears that the acoustic excitation not only increases the strength of vortices till a more downstream location, but may cause vortices to decay faster past that location.

The difference in S_{max} between an excited and an unexcited jet starts at $X/D \approx 0.5$, as for S_{min}, but extends a little further downstream, to $X/D \approx 8$. The difference between the two jets for $0.5 \leq X/D \leq 4$ is believed mainly due to the intensification of vortex strength, and that between $X/D \approx 4$ and 8 is apparently due to an increase in the entrainment of ambient air by excitation. As the excitation hastens the decay of the centerline total pressure of a jet at larger X, it also hastens the decay of energy separation. The faster decay of energy separation may be due to the faster break-up of vortical structures and the enhanced diffusion of a jet caused by the excitation.

Axial variations of R_{max}, R_{min}, R_b, R_{out}, and R_{in}, which characterize the spread of energy separation, are greatly affected by the excitation as shown in Fig. 11. Generally speaking, R_{in} and R_{max} approach the jet axis, and R_{min} and R_{out} move to larger R more rapidly when the jet is excited. R_b approaches the jet axis till $X/D \approx 4$, where it gets closest to the axis, and moves away from the axis thereafter. This location of closest approach ($X/D \approx 4$) is shorter than the corresponding location for an unexcited jet ($X/D \approx 6$ to 8). All these confirm that the diffusion of energy separation is faster both inward and outward, when the jet is excited.

5 Concluding Remarks

A study of the energy separation in a jet was performed, including the effects of acoustic excitation. The energy separation can be due to different mechanisms. One is the imbalance between the energy transport by heat conduction and the energy transport by shear work; another is the unsteady pressure fluctuations induced by convective movement of vortices with low-pressure cores (i.e., pressure work). The former effect is significant in a region where the velocity gradient and temperature gradient are large, but the latter effect occurs even in an inviscid flow, in accordance with the development and decay of vortices. The energy separation due to the latter effect is generally a much stronger process and is strongly affected by sound waves.

The total pressure distribution shows a small region of lower total pressure near the jet periphery, where the total pressure ($\approx$ the static pressure in that region) is slightly smaller than the ambient pressure, which is most evident in the region close to the nozzle exit ($0.3 \leq X/D \leq 1$). This apparently is due to the low pressure cores in the vortices. The acoustic excitation shortens the potential core of the jet and hastens the spread of the jet shear layer, indicating an enhanced diffusion or mixing. It also decreases the pressure in the region of lower total pressure near the jet periphery, indicating an increase of the vortex strength.

With an unexcited jet, the energy separation near the nozzle exit ($X/D \approx 0.1$) is mostly caused by the imbalance between heat conduction and shear work in the boundary layer inside the nozzle and in the jet shear layer. At $X/D \approx 0.3$, the action of vortices, though small in size and strength, starts to affect the energy separation. At $X/D \approx 0.5$, the energy separation is significantly intensified due to the growth of vortices in size and strength. The energy separation begins to decay from $X/D \approx 1$. As vortices grow in size and decrease in strength, and the spacing between them increases through the coalescence of vortices, there are smaller pressure variations due to vortex passage. This, along with the spread of the jet shear layer, provides less driving force for energy separation. In the region between $X/D \approx 6$ and 8, the entrainment of ambient air affects the energy separation. There is no significant energy separation at $X/D \approx 14$.

The present definition of the energy separation factor renders its distribution relatively independent of Re_j except for $0.3 \leq X/D \leq 4$, in the Re_j range studied. An effect of Re_j is that the development of energy separation in the region, $X/D < 1$, is faster for the higher Re_j. However, the spread of energy separation appears independent of Re_j.

The effect of acoustic excitation on the energy separation is closely related to the effect of acoustic excitation on the vortex structure as well as on the total pressure profile of a jet. Acoustic excitation ($St_e \approx 0.96$) has a significant impact on the energy separation for $1 < X/D < 2$, and apparently not only the size but also the strength of vortices is greatly increased by the excitation. At $X/D \approx 6$, the excitation affects the energy separation due to enhanced entrainment. Acoustic excitation hastens

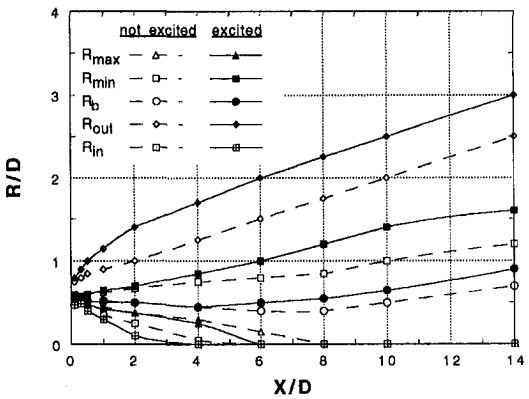

Fig. 11 Effect of acoustic excitation on the variation of R_{max}, R_{min}, R_b, R_{out}, and R_{in} with X/D. Re_j = 120,000. Excitation is at 4,500 Hz, St_e = 0.96.

the decay of energy separation which may be due to the faster break-up of vortical structures. The fact that the acoustic excitation has a strong effect on the energy separation provides good evidence that the convective movement of vortices is a key cause of energy separation.

Acknowledgment

We wish to thank the Engineering Research Program of the U.S. Department of Energy, for their support, and contract monitor, Dr. Oscar Manley, for his continued interest in our research.

References

Crow, S. C., and Champagne, F. H., 1971, "Orderly Structure in Jet Turbulence," *Journal of Fluid Mechanics,* Vol. 48, Part 3, pp. 547–591.

Eckert, E. R. G., 1986, "Energy Separation in Fluid Streams," *International Communications in Heat and Mass Transfer,* Vol. 13, No. 2, pp. 127–143.

Eckert, E. R. G., 1987, "Cross Transport of Energy in Fluid Streams," *Thermo- and Fluid Dynamics,* Vol. 21, No. 2–3, pp. 73–81.

Eckert, E. R. G., and Drewitz, O., 1941, "Die Berechnung des Temperaturfeldes in der Laminaren Grenzschichtschnell Angeströmter Unbeheizter Körper," *Luftfahrtforschung,* Vol. 19, p. 189.

Eckert, E. R. G., and Weise, W., 1982, "Messung der Temperaturverteilung auf der Oberfläche Schnell Angeströmter Unbeheizter Körper," Jahrbuch 1940 der Deutschen Luftfahrtforschung, Vol. 2, pp. 25–31, 1940, reprinted in *Forschung Ingenieur Wesen,* Vol. 13, pp. 246–254.

Fox, M., Kurosaka, M. Hedges, L., and Hirano, K., 1993, "The Influence of Vortical Structures on the Thermal Fields of Jets," *Journal of Fluid Mechanics,* Vol. 255, p. 447.

Goldstein, R. J., and Behbahani, A. I., and Heppelmann, K. K., 1986, "Streamwise Distribution of the Recovery Factor and the Local Heat Transfer Coefficient to an Impinging Circular Air Jet," *International Journal of Heat and Mass Transfer,* Vol. 29, pp. 1227–1235.

Goldstein, R. J., and Seol, W. S., 1991, "Heat Transfer to a Row of Impinging Circular Air Jets Including the Effect of Entrainment," *International Journal of Heat and Mass Transfer,* Vol. 34, pp. 2133–2147.

Goldstein, R. J., Sobolik, K. A., and Seol, W. S., 1990, "Effect of Entrainment on the Heat Transfer to a Heated Circular Air Jet Impinging on a Flat Surface," ASME *Journal of Heat Transfer,* Vol. 112, No. 3, pp. 608–611.

Heavens, S. N., 1980, "Visualization of the Acoustic Excitation of a Subsonic Jet," *Journal of Fluid Mechanics,* Vol. 100, pp. 185–192.

Hottel, H. C., and Kalitinsky A., 1945, "Temperature Measurements in High Velocity Air Streams," Trans. ASME, Vol. 67, p. A-25.

Kline, S. J., and McClintok, F. A., 1953, "Describing Uncertainties in Single Sample Experiments," *Mechanical Engineering,* Vol. 75, No. 1.

Kurosaka, M., 1982, "Acoustic Streaming in Swirling Flow and the Ranque-Hilsch (Vortex Tube) Effect," *Journal of Fluid Mechanics,* Vol. 124, pp. 139–172.

Kurosaka, M., Gertz, J. B., Graham, J. E., Goodman, J. R., Sundaram, P., Riner, W. C., Kuroda, H., and Hankey, W. L., 1987, "Energy Separation in a Vortex Street," *Journal of Fluid Mechanics,* Vol. 178, pp. 1–29.

Moffat, R. J., 1962, "Gas Temperature Measurement," *Temperature: Its Measure and Control in Science and Industry,* Rheinhold, New York, p. 553.

Ryan, L. F., 1951, "Experiments on Aerodynamic Cooling," Ph.D. thesis, Eidgen. Tech. Hochschule, Zurich.

Seol, W. S., 1993, "Energy Separation in a Jet Flow," Ph.D. thesis, University of Minnesota, Minneapolis, MN.

Thomann, H., 1959, FFA Report 84, Stockholm.

Yule, A. J., 1978, "Large-Scale Structure in the Mixing Layer of a Round Jet," *Journal of Fluid Mechanics,* Vol. 89, pp. 413–432.

P. S. Cumber
Senior Scientist/Engineer.

M. Fairweather
Resource Leader.

British Gas plc, Research and Technology,
Gas Research Centre,
Loughborough LE11 3QU, England

S. A. E. G. Falle
Professor,
Department of Applied Mathematics,
The University of Leeds,
Leeds LS2 9JT, England

J. R. Giddings
Director,
Mantis Numerics Ltd., 46 The Calls,
Leeds LS2 7EY, England

Predictions of Impacting Sonic and Supersonic Jets

A mathematical model of sonic and supersonic jets, validated previously by the present authors for the prediction of moderately and highly underexpanded free jets, is used to simulate the near field structure of jets which impact a flat surface orthogonally, and its accuracy assessed by comparing model predictions with experimental data available in the literature. For impacting, moderately underexpanded jets, results derived from the model are found to be in close agreement with data on the location of both free jet shocks, and the stand-off shock formed adjacent to the impacted surface. In addition, the model provides reasonable estimates of density within the free jet and stagnation regions of such flows, with the existence, or otherwise, of stagnation bubbles being successfully predicted. Measurements of pressure occurring on the surface of the impacted plate, produced by the impingement of both sonic and supersonic jets, are also predicted with reasonable accuracy, although the decaying amplitude of spatially periodic pressure oscillations within the wall jet region of these flows is slightly overpredicted in some cases.

Introduction

The impingement of a turbulent, circular jet normally onto a flat surface is a flow configuration that is of interest in many engineering applications. Examples include the operation of vertical take-off and landing aircraft, the launch of rockets, and many cooling, heating, and drying processes used in industry. Of particular interest in the present work, this flow situation is also encountered in assessments of the consequences of accidental gas releases on both onshore and offshore installations involving high pressure pipework and gas handling plant.

As well as being of practical interest, the impacting jet is also an important test case for the development and validation of mathematical models of turbulent flows. For the case of a subsonic jet, the impacting flow gives rise to three flow regimes; namely, a free jet region, a stagnation zone, and ultimately a radial wall jet region. These flow regimes in turn contain both free shear layer and near-wall regions, as well as zones of strong boundary-induced curvature, whose prediction represents a demanding test of any mathematical model. If the Mach number or underexpansion ratio of the jet is sufficiently large then a curved shock wave, orthogonal to the jet flow, is also produced in the stagnation region close to the surface; in addition to any shocks that may already exist in the free jet flow. This shock wave spans the width of the jet and is concave to the flat surface. Between the shock wave and the surface the flow is subsonic, but as fluid moves radially outwards along the surface its velocity increases and a sonic line occurs close to the edge of the jet. After this sonic line the fluid enters a wall jet region which is initially supersonic, although the shear layer which grows along the upper boundary of the wall jet and the boundary layer which develops on the surface ultimately merge and reduce the wall jet velocities to subsonic values.

The impaction of sonic or supersonic jets can also give rise to other complexities which do not occur in subsonic jet impingement. For sufficiently large Mach numbers, therefore, strong oblique shock waves can occur within the wall jet region, with the subsequent shock-boundary layer interaction leading to a thickening, or even separation, of the boundary layer prior to the occurrence of a reattachment shock (Carling and Hunt, 1974). The overall wall jet thickness also decreases dramatically in the vicinity of these shock waves (Carling and Hunt, 1974). In addition, regions of slowly recirculating fluid, known as stagnation bubbles, can occur in the stagnation region of the flow beneath the curved shock wave and in close proximity to the surface (Kalghatgi and Hunt, 1976). These bubbles, which are characterized by off-axis peak pressures on the impingement surface, influence heat transfer between the jet and the surface within the stagnation zone, although they do not significantly affect the subsequent development of the wall jet region (Carling and Hunt, 1974). The reasons for the occurrence of stagnation bubbles have been studied, for example, by Ginzburg et al. (1973) and by Kalghatgi and Hunt (1976).

A great deal of experimental work has been performed on the impaction of compressible jets normal to flat surfaces. Examples include the studies of Donaldson and Snedeker (1971), Hunt and co-workers (1971, 1974 and 1976), and Iwamoto (1990). For the most part, measurements in this flow configuration have been restricted to flow visualisation using schlieren photography, and surface pressure distributions in the stagnation region and near field of the wall jet. Iwamoto (1990) did, however, employ interferometry to obtain densities within the free jet and stagnation regions of an impacting flow.

Corresponding numerical work on impinging sonic and supersonic jets is less common, primarily because of the excessive computational demands associated with predicting such complex flows. This is in contrast to recently increased interest in subsonic impacting flows where the further development of second-order turbulence closures (Craft et al., 1993; Dianat et al., 1991) has enabled the accurate prediction of all three flow regimes noted above, and in particular the influence of the solid surface in damping velocity fluctuations normal to the wall. Iwamoto (1990) did, however, simulate two of the compressible jets he studied experimentally using a two-step Lax-Wendroff scheme to solve the Euler equations for inviscid, axisymmetric flow, although the use of artificial viscosity terms in the numerical solution, employed to enhance stability, did mean that shock waves within the flow were difficult to locate with any degree of accuracy. McGuirk and Page (1989) derived a more sophisticated model based on solutions of the viscous flow equations,

Contributed by the Fluids Engineering Division for publication in the JOURNAL OF FLUIDS ENGINEERING. Manuscript received by the Fluids Engineering Division October 12, 1994; revised manuscript received June 7, 1996. Associate Technical Editor: R. L. Panton.

closed using a standard k-ϵ turbulence model (Jones and Launder, 1972), that were obtained using a version of the pressure-correction scheme modified to include compressibility effects. Predictions of this model were found to reproduce faithfully the wave length of the shock structure in the free jet region of an impinging flow studied experimentally by Donaldson and Snedeker (1971), although further validation of the model's predictions was not presented.

The present paper describes the application of a model outlined by Cumber et al. (1994 and 1995) to predicting the near field regions of sonic and supersonic jets which impact a flat surface orthogonally, and validates model predictions against appropriate experimental data. In particular, predictions of the latter model are compared with the impacting flow measurements obtained by Iwamoto (1990) and by Hunt and co-workers (1971 and 1974). The work described is an extension of earlier studies by the present authors which validated the latter model for application to the prediction of moderately (Cumber et al., 1994) and highly (Cumber et al., 1995) underexpanded free jets.

Mathematical Model

In the interests of brevity, only the essential details of the mathematical model employed in the present work are reproduced below. Full details may be found in Cumber et al. (1994 and 1995).

Governing Equations. The model was based on solutions of the high Reynolds number versions of the fluid flow equations, expressed in axisymmetric form (Jones and Whitelaw, 1982). Transport equations for the conservation of mass, momentum and total energy were therefore solved, with density-weighted (Favre) averaging being used as most appropriate for the variable density flows of interest. Closure of this set of equations was achieved using a two-equation, k-ϵ turbulence model (Jones and Launder, 1972), modified in line with the recommendations of Sarkar et al. (1991) in order to account for the increase in turbulence energy dissipation rates in compressible flows caused by the formation of compression waves in the instantaneous flow field. Modeling constants employed were standard values found to give acceptable agreement between theoretical predictions and experimental data in a wide range of flows (Jones and Whitelaw, 1982). Finally, the system of equations was augmented by the ideal gas law for solution.

As noted earlier, the model described above has been found (Cumber et al., 1994 and 1995) to be capable of accurately reproducing the structure of both moderately and highly underexpanded free jets. In subsonic impinging jets, however, it is known (Craft et al., 1993) that the linear, eddy viscosity based stress-strain relationship used in the standard k-ϵ turbulence model leads to the generation of unrealistically large turbulence energies in the irrotational region close to the stagnation point of the flow. Taken together with the inability of this turbulence model to account adequately for streamline curvature effects induced by the lateral divergence of the impinging flow, this in turn causes an overprediction of normal-to-wall velocity fluctuations both close to the stagnation point and in the radial wall jet region. Mean velocities within the latter region are also not predicted accurately. These shortcomings can be rectified through the use of nonlinear k-ϵ turbulence models (e.g., Craft et al., 1995) or full second-moment closures (e.g., Craft et al., 1993; Dianat et al., 1991).

Despite these considerations, use of the standard (compressibility corrected) k-ϵ model has been retained in the present work. This is because the impinging sonic and supersonic jets considered later are, in general, devoid of viscous flow features, particularly in those regions where experimental data is available for model validation purposes, i.e., in close proximity to the stagnation point of the flow. In addition, there is a paucity of experimental data of sufficient detail to permit a systematic evaluation of the model's ability to predict viscous phenomena in impinging sonic and supersonic jets.

Computational Procedure and Boundary Conditions. The model described required the solution of six coupled partial differential equations. Solutions were obtained by expressing the equation set in cylindrical coordinates, and integrating the time dependent form of these equations numerically by time-marching to a steady state.

Integration of the equations was performed using a second-order accurate finite-volume scheme. Discretization of the descriptive equations therefore followed a conservative, control volume approach, with values of the dependent variables stored at the centres of the computational cells over which the differential equations were integrated. Diffusion and source terms in the modeled equations were approximated using central differencing, while approximations to the inviscid (advective and pressure) fluxes were derived using a second-order accurate (in space) variant of Godunov's method (see, for example, Hirsch, 1990). The latter method was derived from a conventional first-order Godunov scheme by introducing gradients within computational cells using a nonlinear, slope-limiting function which ensures monotinicity. In its fully explicit, time-accurate form the method uses a predictor-corrector procedure, where the predictor stage is spatially first-order and is used to provide an intermediate solution at the half-time between time steps. This in turn is used at the corrector stage for the calculation of second-order fluxes.

To increase the rate of convergence a diagonalized implicit scheme was also employed. This scheme first calculates the explicit rate of change to second-order space accuracy, as described above, and then applies diagonalised implicit operators in each of the space directions to make the scheme implicit for sound waves and diffusion. This allows the calculation to proceed using much larger time-steps, based on advection velocities rather than sound waves, than would be possible using the explicit scheme alone. The composite scheme is nominally second-order accurate in space and first-order in time, although since steady-state solutions are of interest in the present work the time accuracy of the scheme is unimportant.

An adaptive finite-volume grid algorithm was employed in order to avoid the normally excessive computational cost involved in capturing shock structures. This method used a two-dimensional, rectangular mesh, with local adaptation being

Nomenclature

d = diameter
k = turbulence kinetic energy
l_1, l_2 = nozzle-to-shock spacing for free jet shocks
l_3 = nozzle-to-shock spacing for stand-off shock
M = Mach number
n = power law index
P = pressure
r = coordinate parallel to surface
x = coordinate normal to surface
Δr = grid spacing in r direction
Δx = grid spacing in x direction
ϵ = dissipation rate of k
ρ = density

Subscripts

a = ambient conditions
n = nozzle
o = nozzle exit conditions
t = throat of convergent-divergent nozzle

achieved by overlaying successively refined layers of computational grid. At the start of any calculation, the first two grid layers covered the entire computational domain, with finer grids only being generated in regions which required higher resolution. Local adaption was achieved by generating estimates of the local truncation error for all transported variables by comparing solutions on adjacent grid levels. The grid was then refined if any of these errors exceeded a given tolerance, taken to be two percent. In the results presented below up to six levels of grid were used. Further details of the numerical and adaptive grid algorithms may be found in Falle (1991) and Falle and Giddings (1992).

In simulating the experiments performed by Iwamoto (1990) and Hunt and co-workers (1971 and 1974), the flow configurations used by the latter authors were approximated using a jet issuing from a circular cross-sectioned pipe placed above a flat surface. The boundary conditions applied in the computations assumed symmetry along the jet centerline, represented as the x axis at $r = 0$. On the impacted surface (at $x = 0$), and the external surface of the pipe, finite-volume solutions were patched onto fully turbulent, local equilibrium wall law profiles (see, for example, Spalding and Patankar, 1967). The remaining boundaries, at the base of the pipe ($+x$) and at $+r$, were both treated as constant pressure surfaces. In performing calculations the sensitivity of computed solutions to the positioning of the latter boundaries was investigated, and in the results presented below these surfaces were located at positions which had a negligible influence on the flow. Inlet conditions at the pipe exit were specified as sonic or supersonic, with density, pressure, and velocity being prescribed consistent with the hyperbolic nature of the flows under investigation. In the simulations of Iwamoto's (1990) jets, the pipe exit was sufficiently far from the normal surface for inlet profiles to have little influence on predicted flow fields, so that flat profiles of all dependent variables were prescribed at the inlet. This was not the case, however, for the experiments performed by Hunt and co-workers (1971 and 1974) where predictions showed some sensitivity to the distributions used for k and ϵ, and in particular required profiles for these variables to be prescribed consistent with the existence of a boundary layer attached to the nozzle wall. As a consequence, and in the absence of appropriate experimental data, profiles for the latter variables were obtained from Hinze (1977), with flat profiles being employed for all other variables. These initial conditions were then used as the basis of time dependent calculations. Typically, transient runs were started with time steps of the order of 10^{-7} s, decreasing to 10^{-9} s as finer mesh was introduced, with calculation times of the order of 10^{-2} s being required to achieve steady state.

The simulations used computational domains which ranged from $(x, r) = (5d, 3d)$ to $(10.5d, 20d)$, depending on the measured data available for comparison purposes and the sensitivity of computed solutions to the positioning of the constant pressure boundaries. For the smaller domains, and for regions close to the nozzle exit and normal surface, uniform grids were used; whereas for larger domains and regions remote from the jet source geometrically expanding grids were employed with a maximum expansion ratio of 1.05. The fineness of grid required to obtain grid independent solutions was examined for each of the jets studied. As an example, simulation of the supersonic jet considered by Hunt and co-workers (1971 and 1974), with an inlet Mach number of 2.77, required a grid spacing of $\Delta x = \Delta r = d/128$ for essentially grid independent solutions of the mean flow field. For a nonadaptive grid this corresponds to approximately 390k nodes required to cover the domain $(10.5d, 20d)$ used in the computations, whereas the adaptive simulation required approximately 39k nodes. This simulation did, however, require a particularly fine grid as at a certain grid resolution the calculated flow separated, as observed in the experiments, introducing an additional physical scale which had to be resolved. Other simulations required, typically, $\Delta x = \Delta r = d/32$ and 10k nodes for grid independence.

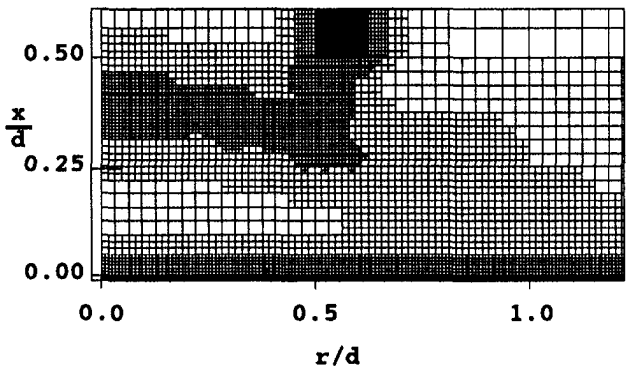

Fig. 1 A portion of the adapted grid used in the simulation of Hunt and co-workers (1971 and 1974) $M = 1.64$ jet ($d_t = 12.7$ mm, $P_o/P_a = 1$)

Figure 1 shows a portion of the adapted grid used in the simulation of one of the flows studied by Hunt and co-workers (1971 and 1974) which employed five levels of finite-volume grid, with the two coarsest levels being non-adaptive. As can be seen from this figure, in which the x axis at $r = 0$ is a symmetry boundary, the finest mesh is located adjacent to the impacted surface (shown as the lower boundary to the figure) and the pipe exit (at the center of the upper boundary), and around the stand-off shock located between the pipe exit and the surface. Figure 2 shows the sensitivity of predictions of shock layer and wall jet surface pressures to the grid resolution used in computations of the supersonic jet studied by Hunt and co-workers (1971 and 1974), with an inlet Mach number of 2.77, mentioned above. Results derived using the coarsest computational mesh are seen not to exhibit flow separation downstream of the first shock in the near field of the wall jet region (at $r/d \approx 1.3$), whilst the more refined grids do predict such a region. Results obtained using the two finer meshes are also essentially grid independent, apart from in the separated flow region itself ($1.2 \leq r/d \leq 1.6$) where the separation point moves closer to the stagnation point with increasing grid refinement. Results derived using $\Delta x = \Delta r = d/256$, not shown in the figure, were found to be identical to those obtained using a grid spacing of $d/128$. At this level of grid refinement, therefore, the influence of the finite-volume mesh used on the predicted flow field is negligible. Differences between predicted and measured quantities, considered below, can then be attributed to deficiencies in the mathematical model itself, and to experimental uncertainty.

Results and Discussion

Iwamoto (1990) studied the impaction on a flat surface of a moderately underexpanded air jet issuing from a 10 mm diameter convergent nozzle. The distance of the surface from the nozzle was varied in order to examine the location of shock waves in the free jet and stagnation regions of the flow using shadow-photography. In addition, for two particular plate-to-nozzle spacings ($x_n/d = 2.0$ and 2.5), interferometry was employed to obtain densities within these regions of the impinging flows, with transducers located within the impacted plate being used to measure surface pressures. For the latter flows, surface pressure measurements also indicated the presence of a stagnation bubble for a plate-to-nozzle spacing of 2.5 which was not apparent when the plate was placed closer to the nozzle.

Figure 3 shows the predicted Mach number field for $x_n/d = 4$. The shock diamond structure characteristic of moderately underexpanded jets is seen to exist in the free jet region of the flow, with a stand-off or bow shock occurring adjacent to the impacted surface. The nomenclature used to define the location

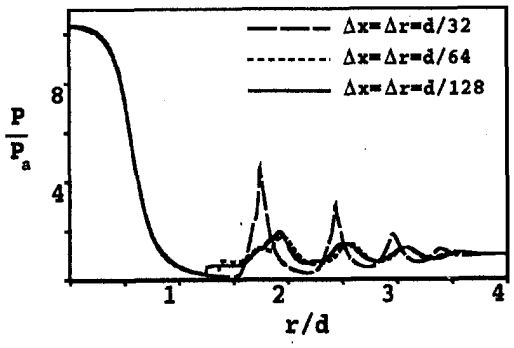

Fig. 2 Effect of grid resolution on predictions of surface pressure for Hunt and co-workers (1971 and 1974) $M = 2.77$ jet ($d_t = 12.7$ mm, $P_o/P_a = 1$)

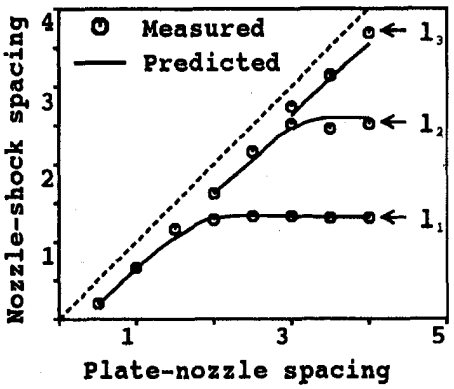

Fig. 4 Variation of shock location with plate-to-nozzle spacing for the jets studied by Iwamoto (1990) ($d = 10$ mm, $M = 1$, $P_o/P_a = 1.59$)

of the latter shocks relative to the nozzle exit, as employed by Iwamoto (1990) and in Fig. 4, is also defined in Fig. 3. For this particular release, two free jet shocks exist at distances of l_1 and l_2 from the nozzle, while the stand-off shock is at a distance l_3.

The shock capturing capabilities of the model were assessed by comparing predictions of the locations of the latter shocks with the experimental data for different plate-to-nozzle spacings obtained by Iwamoto (1990). The results are given in Fig. 4, where the dashed line indicates the location of the impacted surface. For $x_n/d \leq 1.5$, only one shock (the stand-off shock) is present, and the distance between the surface and the shock is insensitive to the plate-to-nozzle spacing. When the latter spacing is increased to values between 2 and 3 two shocks occur; a free jet shock at l_1 and a stand-off shock adjacent to the surface. Similar to results obtained at closer plate-to-nozzle spacings, the distance of the stand-off shock from the surface is almost independent of the latter spacing. Finally, at $x_n/d \geq 3$, the second shock becomes coincident with free jet shock location l_2, and a third stand-off shock is formed. Agreement between model predictions and experimental data over these different flow regimes is seen to be good, with the difference between predictions and observations being typically four percent, and a maximum of nine percent, relative to the data.

Figure 5 compares model predictions and measured densities along the stagnation line of two flows with $x_n/d = 2.0$ and 2.5. From Fig. 4, both these flows contain one free jet shock and one stand-off shock. For the larger plate-to-nozzle spacing, agreement between theory and experiment is good. The decrease in density from the nozzle up to the measured minimum at $x/d = 1.9$ is therefore predicted reasonably well, as are increases in density caused by oblique shocks crossing the jet axis (centred around $x/d = 1.2$) and the presence of the stand-off shock (at $x/d = 0.4$). The main discrepancy between theory and experiment is close to the impacted surface where the data exhibit a maximum which is not reproduced in the simulations. This trend is in agreement with the inviscid flow predictions made by Iwamoto (1990). Similar agreement is apparent between predictions and data obtained for the smaller plate-to-nozzle spacing, although the model does tend to overpredict measured densities, by approximately twelve percent, in the vicinity of the stand-off shock (at $x/d = 0.3$).

Equivalent results for radial profiles of density within the free jet and stagnation regions of the flow are given in Fig. 6 for the larger plate-to-nozzle spacing. Agreement between theory and experiment is similar to that found for the axial variation of density, except for the profile at $x/d = 0.1$, close to the plate, where predictions overpredict data by up to seventeen percent due to an underestimation by the model of the rate of decay of density with increasing radial distance. The off-axis peak in

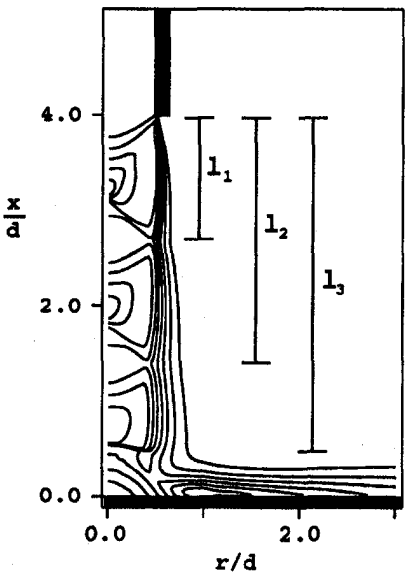

Fig. 3 Predicted Mach number contours for the $x_n/d = 4$ case studied by Iwamoto (1990) ($d = 10$ mm, $M = 1$, $P_o/P_a = 1.59$)

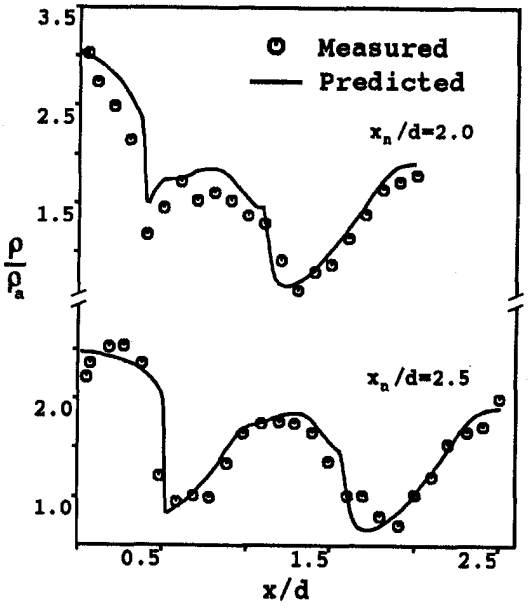

Fig. 5 Stagnation line densities for the $x_n/d = 2.0$ and 2.5 cases studied by Iwamoto (1990) ($d = 10$ mm, $M = 1$, $P_o/P_a = 1.59$)

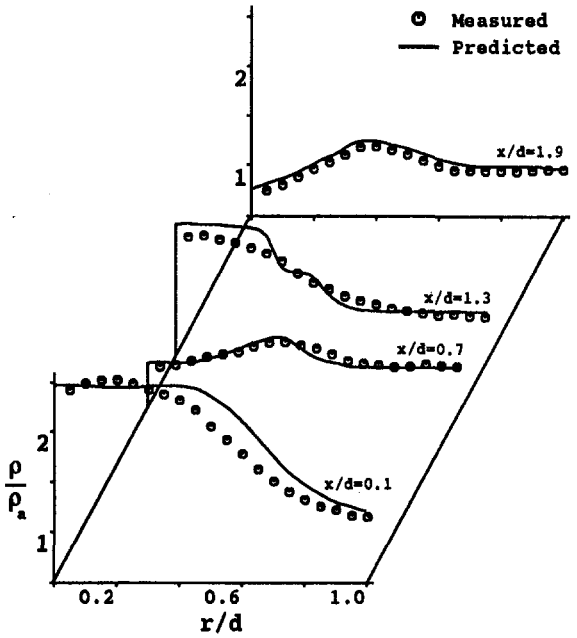

Fig. 6 Radial profiles of density for the x_n/d = 2.5 case studied by Iwamoto (1990) (d = 10 mm, M = 1, P_o/P_a = 1.59)

density exhibited by data obtained at the latter measurement station is, however, reproduced by the predictions. Although not shown, similar agreement between theory and experiment was also found for the x_n/d = 2 case, though consistent with the results of Fig. 5 agreement did deteriorate in the vicinity of the impacted surface close to the axis of the jet.

The final comparison for Iwamoto's (1990) impacting jets is given in Fig. 7, which shows results for pressure distribution on the surface of the impacted plate for the two plate-to-nozzle spacings considered above. In accord with the results of Fig. 6, both predictions and measurements for the x_n/d = 2.5 case exhibit an off-axis peak in pressure, indicating the presence of a stagnation bubble close to the surface that is not apparent for the smaller plate-to-nozzle spacing. Ginzburg et al. (1973) proposed that for this type of sonic jet stagnation bubbles occur at plate-to-nozzle spacings which give rise to a free jet shock that intersects the stand-off shock, causing the formation of two flow regions close to the plate of which the outer has the higher total pressure. Mixing then occurs along the slip-line which exists between these two regions, and the interaction of the high pressure shear layer formed with the inner boundary layer close to the plate causes separation and the formation of a bubble of recirculating fluid. For both plate-to-nozzle separations considered in Fig. 7, pressure decreases monotonically from its peak value with increasing radial distance until a minimum occurs at r/d = 1. After this minimum, the pressure undergoes a spatially periodic oscillation of decaying amplitude due to the presence of weak oblique shocks in the wall jet region of the impacted flow. Agreement between theory and experiment is on the whole good, although there is a tendency for predictions to overestimate slightly the strength of the wall jet shocks, and hence surface pressures, for the smaller plate-to-nozzle spacing.

Turning to the impaction of fully expanded supersonic jets, Gummer and Hunt (1971) examined surface pressures in the shock layer region, close to the stagnation point, formed by the impingement of air jets issuing from a convergent-divergent nozzle with a throat diameter of 12.7 mm. Various plate-to-nozzle spacings were considered. Carling and Hunt (1974) extended this work to re-examine shock layer surface pressures for a number of jets, with Mach numbers ranging from 1.64 to 2.77, and to obtain new measurements of surface pressure within the wall jet region. In the latter study, the plate-to-nozzle spacing was kept constant at approximately one jet radius. In using the results of these authors below, surface pressures close to the axis of the jet, and within the shock layer region, were taken from Gummer and Hunt (1971), while the data of Carling and Hunt (1974) were employed for the wall jet region. This approach was taken because the data of the latter authors exhibit asymmetric behaviour and off-axis pressure maxima, indicating the presence of stagnation bubbles, whilst those of Gummer and Hunt (1971) do not. Carling and Hunt (1974) and Kalghatgi and Hunt (1976) investigated this phenomena and found that its occurrence was due to the interaction of the stand-off shock with weak shocks produced by small imperfections in the walls of the nozzles employed, or slight inaccuracies in the design or manufacture of the contoured nozzles themselves. Because of this, the asymmetry of the results of Carling and Hunt (1974) must be considered to be an artefact of the experimental apparatus used, rather than representing a predictable phenomena such as stagnation bubbles which occur for the reasons advanced by Ginzburg et al. (1973) and outlined above.

One reason for Hunt and co-workers' (1971 and 1974) interest in these fully expanded supersonic jets was the influence of the nozzle Mach number on the flow produced by impingement. For low Mach numbers (M = 1.64 and 1.76) these authors found that a weak system of shocks exists that is attached to the impacted surface, whereas at higher Mach numbers (M = 2.77) shock-induced boundary layer separation occurs. Figure 8 shows predicted Mach number contours for the lowest and highest nozzle Mach numbers considered by Hunt and co-workers (1971 and 1974) which reproduce the qualitative findings of the latter authors, and indicate the different types of flow structure that are produced.

Figure 9 compares predicted and measured surface pressures for three of the jets examined by these authors. For the M = 1.64 and 1.76 jets, the surface pressure distribution is qualitatively similar to that observed by Iwamoto (1990) for the x_n/d = 2 case. Peak pressures are therefore on axis, with spatially periodic oscillations of decaying amplitude occurring in the near wall jet region. For both jets, qualitative and quantitative agreement between predicted and measured pressure distributions is good, particularly close to the axis of the jets. The major discrepancies are a tendency to overpredict the strength of the oscillating pressure field of both jets, and a slight phase error

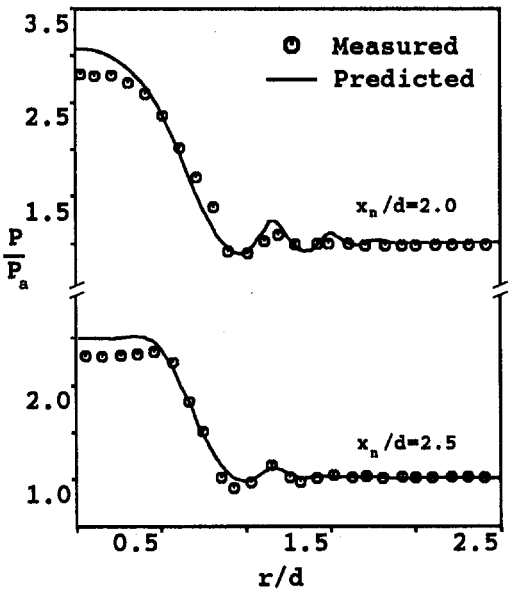

Fig. 7 Pressure distribution on the impacted surface for the x_n/d = 2.0 and 2.5 cases studied by Iwamoto (1990) (d = 10 mm, M = 1, P_o/P_a = 1.59)

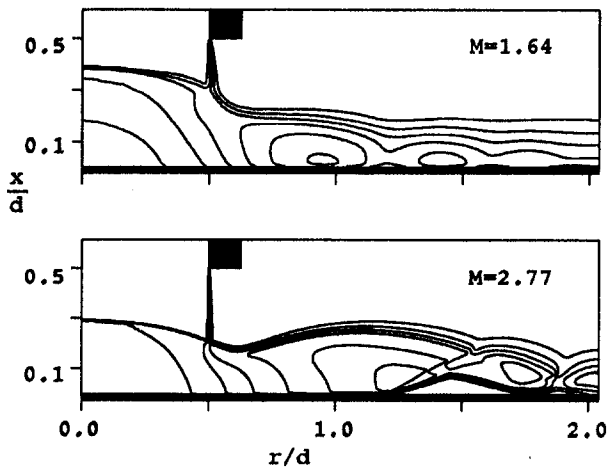

Fig. 8 Predicted Mach number contours for the M = 1.64 and 2.77 cases studied by Hunt and co-workers (1971 and 1974) (d_t = 12.7 mm, P_o/P_a = 1, contours for M = 1.64 jet range from 0.3 (outer) to 1.8 (inner) in steps of 0.3, contours for M = 2.77 jet range from 0.5 to 3.0 in steps of 0.5)

in the predictions of the M = 1.76 case. Overall, however, agreement between theory and experiment is acceptable.

Equivalent results for Hunt and co-workers' (1971 and 1974) M = 2.77 jet are also given in Fig. 9. Surface pressures in the latter flow differ qualitatively from those established by the lower Mach number jets considered above in that the first shock in the near field of the wall jet region, at $r/d \approx 1.2$, is sufficiently strong to cause boundary layer separation. This in turn establishes a small zone of recirculating subsonic fluid, as indicated by the ambient pressure region which extends from $1.2 \leq r/d \leq 1.6$. At $r/d \approx 1.6$, the flow reattaches to the plate causing the pressure to rise and again undergo a series of spatially periodic, decaying oscillations due to the system of weak oblique shocks within the wall jet region. Agreement between predictions and measurements is remarkably good over all these flow regimes, particularly in terms of the point at which separation occurs, indicating that the location of the first shock within the wall jet region is predicted accurately. One other feature of interest is that the point of reattachment is also predicted well, with the consequence that pressures downstream of this point are in phase with the experimental data. This must be to some extent considered fortuitous given the known (Simpson, 1981) deficiencies of the turbulence model used in the present work for predicting separated flows. Wilcox (1992) has, however, reported a similar level of agreement with measured surface pressures for shock induced separation in a supersonic compression corner using a two-equation turbulence model modified to include compressibility effects.

Accurate prediction of a fourth jet studied by Hunt and co-workers (1971 and 1974), with M = 2.41, was found difficult to achieve. In particular, although measured pressures in the shock layer region were accurately reproduced, those within the wall jet tended to be overpredicted despite the phase of the pressure oscillations being correct. This is not surprising, however, since for this particular release the first shock within the latter region of the flow was found to cause a very rapid thickening of the boundary layer, giving rise to an inflection in the surface pressure measurements, without actually leading to its separation. Flow within the wall jet region for this release was therefore at a transition point between one flow regime and another, making accurate prediction difficult. Some uncertainty also exists regarding the reproducibility of this particular impacting jet since Dayglo patterns obtained on the impacted surface, and used for surface flow visualisation purposes, were found to vary significantly from one test to another (Carling and Hunt, 1974).

As noted above, for some of the impacting jets considered predictions of the model do tend to overestimate the strength of the shocks contained within the wall jet region of the flows, leading to an overprediction of surface pressures within this region. This is particularly the case for the two lower Mach number releases studied by Hunt and co-workers (1971 and 1974). Because of this, a sensitivity study was performed in order to establish the possible causes of this behavior, with particular attention being paid to the M = 1.64 jet of Hunt and co-workers (1971 and 1974). Considering the experiments performed by the latter authors, the main parameters which could influence the strength of predicted wall jet shocks, and for which some uncertainty about the actual conditions used in the experiments exists, include the nozzle exit velocity profile and turbulence levels, and the plate-to-nozzle spacing. The sensitivity of computed solutions to these parameters was therefore explored for the M = 1.64 release, and it was found that only the prescribed nozzle exit velocity profile had a significant influence on predictions of surface pressure. In particular, the use of a $\frac{1}{7}$th power law profile for the latter velocity, typical of fully developed turbulent pipe flows, led to shocks within the wall jet region which were too weak and as a consequence slightly underpredicted the amplitude of the decaying pressure field, as well as having a slight phase error. This does, however, imply that for some power law index $0 < n < \frac{1}{7}$, likely to be more representative of the actual experimental profile used than the flat profile employed in the computations, the level of agreement between model predictions and data within the wall jet region could be improved over that shown in Fig. 9.

Finally, the present results could be influenced by the inadequacy of the k-ϵ turbulence model for simulating boundary layer flows at high Mach numbers (Huang et al., 1994). Work by the latter authors has therefore demonstrated that both the stan-

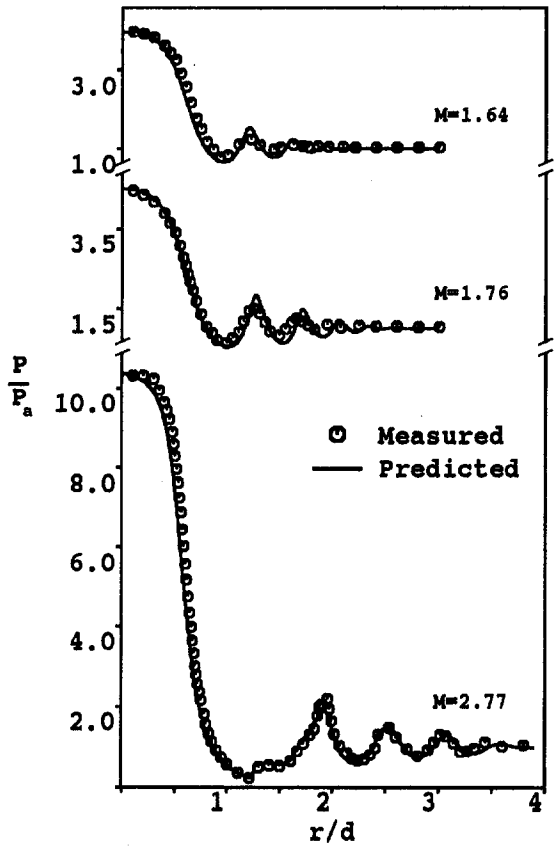

Fig. 9 Pressure distribution on the impacted surface for the M = 1.64, 1.76 and 2.77 cases studied by Hunt and co-workers (1971 and 1974) (d_t = 12.7 mm, P_o/P_a = 1)

dard and compressibility corrected (Sarkar et al., 1991) versions of this model do not satisfy the generally accepted compressible law-of-the-wall derived from the Van Driest transformation (Huang et al., 1994). In order to improve the standard k-ϵ model's performance for such flows, additional compressibility related terms are required in order to increase turbulence kinetic energy levels. Such a modification is, however, in exactly the opposite sense to the compressibility corrections used in the present work which are needed to reduce turbulence energy levels predicted by the standard k-ϵ approach in order to simulate successfully compressible mixing layers. The extent to which this inadequacy of the turbulence model affects the present results might be expected to be small since in the near wall jet regions examined the boundary layer is only at the early stages of its development, with local Mach numbers being relatively small. In addition, as has been seen from simulations of the releases studied by Hunt and co-workers (1971 and 1974), the performance of the present model actually improves with increasing Mach number; again in the opposite sense to what might be anticipated from the results of Huang et al. (1994). Further work is obviously required in order to explain these findings, although more detailed experimental data than is currently available within the wall jet region of impacting flows is needed before such work can proceed.

Conclusions

A mathematical model of sonic and supersonic jets has been applied to predicting the near field structure of jets which impact a flat surface orthogonally, and its accuracy assessed by comparing model predictions with experimental data available for such flows. For impacting, moderately underexpanded jets, predictions of the model were found to reproduce accurately the location of free jet shocks and the stand-off shock formed adjacent to the impacted surface for various plate-to-nozzle spacings. For two particular plate-to-nozzle spacings, the model was found to provide reasonable estimates of density within the free jet and stagnation regions of the flow, with the existence, or otherwise, of regions of slowly recirculating fluid, or stagnation bubbles, which occur beneath the stand-off shock being predicted successfully. Measurements of pressure occurring on the surface of the impacted plate, produced by the impingement of both sonic and supersonic jets, were also predicted with reasonable accuracy, although the decaying amplitude of spatially periodic pressure oscillations within the wall jet region of these flows was slightly overpredicted in some cases. A need for more detailed experimental data in the latter regions of impacting flows has been identified from the anomalous requirements of the standard k-ϵ turbulence model in terms of the compressibility corrections required to predict successfully compressible mixing layers and high Mach number boundary layer flows. In addition, although the model has been shown to reliably predict inviscid flow features, and some viscous features such as shock induced boundary layer separation, viscous flow features are largely absent from the experimental data sets examined. There is therefore a further requirement for experimental data which examines such features in impacting sonic and supersonic jets, and for further assessment of the model's capabilities in this respect.

Acknowledgments

The calculations reported in this paper were made using a modified version of the Mantis Numerics Ltd. code, COBRA. This paper is published by permission of British Gas plc.

References

Carling, J. C., and Hunt, B. L., 1974, "The Near Wall Jet of a Normally Impinging, Uniform, Axisymmetric, Supersonic Jet," *Journal of Fluid Mechanics,* Vol. 66, pp. 159–176.

Craft, T. J., Graham, L. J. W., and Launder, B. E., 1993, "Impinging Jet Studies for Turbulence Model Assessment-II. An Examination of the Performance of Four Turbulence Models," *International Journal of Heat and Mass Transfer,* Vol. 36, pp. 2685–2697.

Craft, T. J., Launder, B. E., and Suga, K., 1995, "A Non-Linear Eddy Viscosity Model Including Sensitivity To Stress Anisotropy," *10th Symposium on Turbulent Shear Flows,* Pennsylvania.

Cumber, P. S., Fairweather, M., Falle, S. A. E. G., and Giddings, J. R., 1994, "Predictions of the Structure of Turbulent, Moderately Underexpanded Jets," ASME JOURNAL OF FLUIDS ENGINEERING, Vol. 116, pp. 707–713.

Cumber, P. S., Fairweather, M., Falle, S. A. E. G., and Giddings, J. R., 1995, "Predictions of the Structure of Turbulent, Highly Underexpanded Jets," ASME JOURNAL OF FLUIDS ENGINEERING, Vol. 117, pp. 599–604.

Dianat, M., Fairweather, M., and Jones, W. P., 1991, "Predictions of a Turbulent Jet Impacting a Flat Surface," *8th Symposium on Turbulent Shear Flows,* Munich.

Donaldson, C. DuP., and Snedeker, R. S., 1971, "A Study of Free Jet Impingement. Part 1. Mean Properties of Free and Impinging Jets," *Journal of Fluid Mechanics,* Vol. 45, pp. 281–319.

Falle, S. A. E. G., 1991, "Self-Similar Jets," *Monthly Notices of the Royal Astronomical Society,* Vol. 250, pp. 581–596.

Falle, S. A. E. G., and Giddings, J. R., 1992, "Body Capturing Using Adaptive Cartesian Grids," *Proc. ICFD Conf. on Numerical Methods for Fluids,* 7th–10th April.

Ginzburg, I. P., Semiletenko, B. G., Terpigor'ev, V. S., and Uskov, V. N., 1973, "Some Singularities of Supersonic Underexpanded Jet Interaction with a Plane Obstacle," *Journal of Engineering Physics,* Vol. 19, pp. 1081–1084.

Gummer, J. H., and Hunt, B. L., 1971, "The Impingement of a Uniform, Axisymmetric, Supersonic Jet on a Perpendicular Flat Plate," *The Aeronautical Quarterly,* Vol. 22, pp. 403–420.

Hinze, J. O., 1977, *Turbulence,* McGraw-Hill, New York.

Hirsch, C., 1990, *Numerical Computation of Internal and External Flows,* Vol. 2, Wiley, Chichester.

Huang, P. G., Bradshaw, P., and Coakley, T. J., 1994, "Turbulence Models for Compressible Boundary Layers," *American Institute of Aeronautics and Astronautics Journal,* Vol. 32, pp. 735–740.

Iwamoto, J., 1990, "Impingement of Under-Expanded Jets on a Flat Plate," ASME JOURNAL OF FLUIDS ENGINEERING, Vol. 112, pp. 179–184.

Jones, W. P., and Launder, B. E., 1972, "The Prediction of Laminarization with a Two-Equation Model of Turbulence," *International Journal of Heat and Mass Transfer,* Vol. 15, pp. 301–314.

Jones, W. P., and Whitelaw, J. H., 1982, "Calculation Methods for Reacting Turbulent Flows: A Review," *Combustion and Flame,* Vol. 48, pp. 1–26.

Kalghatgi, G. T., and Hunt, B. L., 1976, "The Occurrence of Stagnation Bubbles in Supersonic Jet Impingement Flows," *Aeronautical Quarterly,* Vol. 27, pp. 169–185.

McGuirk, J. J., and Page, G. J., 1989, "Shock Capturing Using a Pressure-Correction Method," American Institute of Aeronautics and Astronautics Paper 89-0561.

Sarkar, S., Erlebacher, G., Hussaini, M. Y., and Kreiss, H. O., 1991, "The Analysis and Modelling of Dilatational Terms in Compressible Turbulence," *Journal of Fluid Mechanics,* Vol. 227, pp. 473–493.

Simpson, R. L., 1981, "REVIEW-A Review of Some Phenomena in Turbulent Flow Separation," ASME JOURNAL OF FLUIDS ENGINEERING, Vol. 103, pp. 520–533.

Spalding, D. B., and Patankar, S. V., 1967, *Heat and Mass Transfer in Boundary Layers,* Morgan-Grampian, London.

Wilcox, D. C., 1992, "Dilatation-Dissipation Corrections for Advanced Turbulence Models," *American Institute of Aeronautics and Astronautics Journal,* Vol. 30, pp. 2639–2646.

On the Slightly Reduced Navier-Stokes Equations

Jian-Zhong Xu
Professor.

Wen-Sheng Yu
Graduate Student.

Institute of Engineering Thermophysics,
Chinese Academy of Sciences,
P.O. Box 2706, Beijing 100080, People's
Republic of China

In this paper the so-called slightly reduced Navier-Stokes (SRNS) equations with most streamwise viscous diffusion and heat conduction terms are investigated in detail. It is proved that the SRNS equations are hyperbolic-parabolic in mathematics, which is the same as the current RNS or PNS equations. The numerical methods for solving the RNS equations are, therefore, applicable to the present SRNS equations. It is further proved that the SRNS equations have a uniformly convergent solution with accuracy of 0 (ϵ^2) or 0 (Re^{-1}) which is higher than that of the RNS equations, and for a laminar flow past a flat plate the SRNS solution is regular at the point of separation and is a precise approximation to that of the complete Navier-Stokes equations. The numerical results demonstrate that the SRNS equations may give accurate picture of the flow and are an effective tool in analyzing complex flows.

Introduction

The numerical simulation of viscous flows is attracting more attention for many years. With the development of the computer technology and the numerical methods much progress on this area has been achieved in recent years. But there are still some problems of signifigance yet to be solved. To develop an accurate, general, and simple method of solving viscous flows is one of such problems.

Reynolds average governing equations for solving viscous flows may be divided into four levels of approximation according to the orders of magnitude of viscous terms neglecting in the equations (Gao, 1988). The lowest one in the hierarchy is the classical boundary layer equations which cannot be applied to many complex flows. The highest level is the complete Navier-Stokes (CNS) equations. They are exact in theory but require the solution of a set of elliptic-parabolic equations, which severely limits their application in many problems.

The next higher level from the classical solutions is the so-called reduced Navier-Stokes (RNS) equations. In deriving the RNS equations the flow is assumed to have a dominant stream direction aligned approximately with one coordinate direction and the streamwise viscous diffusion and heat conduction terms are all considered to be ignored compared with the transverse viscous diffusion and heat conduction terms in simplifying the CNS equations. In this case, most of the equations are hyperbolic-parabolic along the streamwise direction. Since the equations are "parabolized" in that direction, the space-marching technique may be used to calculate the velocity components. This leads to a substantial reduction in the complexity, time and storage of computation. So the study on the RNS equations received much attention during the past twenty years (Anderson et al., 1984).

The higher level has an accuracy between the CNS and RNS equations. Previously it is believed that the mathematical property of these equations is the same as that of the CNS equations, consequently, they have no advantage over the other methods. However, in this paper the method of simplifying the CNS equations is reexamined in detail and it is proved that this kind of slightly reduced Navier-Stokes (SRNS) equations with most streamwise viscous diffusion and heat conduction terms may have the same mathematical character as the current RNS equations and the velocity components may be solved by a space-marching finite difference method. The theoretical analysis on their solution in a series form and the numerical experiments all demonstrate that the SRNS equations may compute complex viscous flows accurately and simply.

Theoretical Analysis

For the sake of convenience, the basic equations of a two-dimensional flow are considered in a Cartesian coordinates:

$$(\rho u)_x + (\rho v)_y = 0 \tag{1}$$

$$(\rho u^2)_x + (\rho uv)_y = -p_x + \tfrac{2}{3}[\mu(2u_x - v_y)]_x + [\mu(u_y + v_x)]_y \tag{2}$$

$$(\rho uv)_x + (\rho v^2)_y = -p_y + [\mu(u_y + v_x)]_x + \tfrac{2}{3}[\mu(2v_y - u_x)]_y \tag{3}$$

$$[(E + p)u]_x + [(E + p)v]_y = (u\tau_{xx} + v\tau_{yy} - q_x)_x + (u\tau_{xy} + v\tau_{yy} - q_y)_y \tag{4}$$

where x denotes the primary flow direction and $\tau_{xx} = 2\mu(2u_x - v_y)/3$, $\tau_{xy} = \mu(u_y + v_x)$, $\tau_{yy} = 2(2v_y - u_x)/3$, $q_x = -kT_x$, $q_y = -kT_y$.

These equations and all other equations in this paper are written for laminar flows, but they can be easily changed to a form suitable for turbulent flows.

According to analysis of the classical boundary-layer theory, the order of magnitude of the nondimensional viscous diffusion and heat conduction terms in the equations are, respectively:

$$\begin{array}{cccccccccc} u_{xx} & u_{xy} & u_{yy} & v_{xx} & v_{xy} & v_{yy} & T_{xx} & T_{yy} \\ \epsilon^2 & \epsilon^1 & \epsilon^0 & \epsilon^3 & \epsilon^2 & \epsilon^1 & \epsilon^2 & \epsilon^0 \end{array}$$

with $\epsilon = \mathrm{Re}^{-1/2}$. It is seen that if the viscous terms of the order of magnitude of ϵ^0 are retained in the equations, only one viscous term $(\mu u_y)_y$ appears in Eq. (2), and Eq. (3) becomes $\partial p/\partial y = 0$. They are the familiar boundary-layer equations.

The usual RNS equations will be obtained if all viscous terms up to the order of ϵ^1 are included. From a standpoint of fluid dynamics for the flow with a main stream direction the streamwise partial derivatives are usually much smaller than the transverse ones and may be omitted in the equations, and the simplified equations are parabolic in mathematics.

Another type of the reduced Navier-Stokes equations is of the order of ϵ^2 with respect to the viscous terms and contain most terms of the streamwise partial derivatives. In order to

Contributed by the Fluids Engineering Division for publication in the JOURNAL OF FLUIDS ENGINEERING. Manuscript received by the Fluids Engineering Division December 4, 1994; revised manuscript received August 22, 1996. Associate Technical Editor: S. P. Vanka.

investigate the mathematical property of this kind of simplified equations, it is necessary to analyze their characteristic and subcharacteristic surfaces which determine the structure of the flow governed by the equations and identify the zones of influence and dependence.

Equations (1)–(4), together with the equation of state, may be transformed into a set of first-order partial derivative equations

$$AZ_x + BZ_y = C$$

where $Z = (\zeta, u, u_x, u_y, v, v_x, v_y, T, T_x, T_y)$, A and B are the matrics of 10×10 dimensions and C is a vector.

The corresponding characteristic equation is

$$\det(\sigma_1 a_{ij} + \sigma_2 b_{ij}) = 0.$$

The characteristic analysis (Courant and Hilbert, 1962) shows that the factors of the characteristic equation for the CNS equations are

$$\sigma_1 = -v/u, \quad \sigma_{2-4} = i, \quad \sigma_{5-7} = -i,$$

and the CNS equations are elliptic in mathematics. Here factors equalling to zero are not of importance and ignored.

For the common RNS equations, the characteristic roots of the equation are

$$\sigma_1 = -v/u, \quad \sigma_{2-7} = 0.$$

It is seen that the mathematical character of the RNS equations is parabolic-hyperbolic.

The characteristic roots of the boundary-layer equations are $\sigma_{1-7} = 0$, therefore, the equations are parabolic in mathematics.

The characteristic equation of the simplified Navier-Stokes equations with the viscous terms up to the order of ϵ^2 has the following roots:

$$\sigma_1 = -v/u, \quad \sigma_{2,3} = 0, \quad \sigma_4 = i,$$

$$\sigma_5 = -i, \quad \sigma_6 = 2\sqrt{5}\, i/5, \quad \sigma_7 = -2\sqrt{5}\, i/5.$$

The mathematical characteristics of these equations is the same as the CNS equations.

Now it is noted that the continuity equation actually gives a relation between the streamwise partial derivatives and the transverse ones:

$$u_x = -[v_y + u(\ln \rho)_x + v(\ln \rho)_y]$$

Equations (2) and (3) then take the following form

$$(\rho u^2)_x + (\rho uv)_y = -\{p + \tfrac{4}{3}\mu[u(\ln \rho)_x + v(\ln \rho)_y]\}_x - 2(\mu_x v_y - \mu_y v_x) + [\mu(u_y - v_x)]_y \quad (2a)$$

$$(\rho uv)_x + (\rho v^2)_y = -p_y + \mu_x u_y - \mu_y u_x + \tfrac{1}{3}[\mu(u_x + 4v_y)]_y \quad (3a)$$

For this set of the slightly reduced Navier-Stokes (SRNS) equations the characteristic roots are

$$\sigma_1 = -v/u, \quad \sigma_{2-7} = 0.$$

It is concluded that the SRNS equations are parabolic-hyperbolic in mathematics, which is the same as the existing RNS equations.

For the three-dimensional flows it is not difficult to prove that the CNS equations and the simplified Navier-Stokes equations with the viscous diffusion and heat conduction terms up to the order of ϵ^2 are all hyperbolic-elliptic in mathematics, while the usual RNS equations are hyperbolic-parabolic.

When the continuity equation is substituted into the second set of equations the momentum equations become

$$\begin{aligned}(\rho u^2)_x + (\rho uv)_y + (\rho uw)_z &= -\{p + \tfrac{4}{3}\mu[u(\ln \rho)_x + v(\ln \rho)_y + w(\ln \rho)_z]\}_x \\ &\quad - 2(\mu_x v_y - \mu_y v_x) - 2(\mu_x w_z - \mu_z w_x) + [\mu(u_y - v_x)]_y \\ &\quad + [\mu(u_z - w_x)]_z (\rho uv)_x + (\rho v^2)_y + (\rho vw)_z \\ &= -p_y + \mu_x u_y - \mu_y u_x + 2(\mu_z w_y - \mu_y w_z) \\ &\quad + [\mu(u_x + 4v_y + 4w_z)]_y/3 + [\mu(v_z - w_y)]_z \quad (5)\end{aligned}$$

$$\begin{aligned}(\rho uw)_x + (\rho vw)_y + (\rho w^2)_z &= -p_z + \mu_x u_z - \mu_z u_x + 2(\mu_y v_z - \mu_z v_y) \\ &\quad - [\mu(v_z - w_y)]_y + [\mu(u_x + 4v_y + 4w_z)]_z/3 \quad (6)\end{aligned}$$

It is easy to show that these three-dimensional SRNS equations have the same mathematical character as the RNS equations.

The subcharacteristics or limiting characteristics of the equations may be obtained under the limiting case (Telionis, 1981) which is equivalent to $\mathrm{Re} \to \infty$ or $\mu \to 0$. In this condition all viscous diffusion and heat conduction terms are omitted in the equations, and the CNS, RNS, and SRNS equations all have the same subcharacteristics as the Euler equations. In other words, they all are hyperbolic in the region of $M > 1$ and are elliptic in the region of $M < 1$.

From above analysis it is seen that both SRNS and RNS equations have the same mathematical characteristics and subcharacteristics. This means that the elliptic character related to the high-order viscous terms is neglected in these sets of equations, and the one associated with the nonviscous effect is retained and the small disturbances are allowed to propogated upstream through the subsonic region. The numerical methods for solving the RNS equations, especially the space-marching technique, are also suitable to the SRNS equations which have a higher accuracy in principal. So the SRNS equations are valuable both in theory and in practice.

It is important to note that compared with the RNS equations, the streamwise component of the vorticity is included in the SRNS

Nomenclature

E = total energy per unit volume, $E = e + V^2/2$
J = Jacobian of coordinate transformation
k = coefficient of heat conductivity
L = reference length
p = pressure
p_w = pressure at wall
q = heat flux
Re = Reynolds number, $\mathrm{Re} = UL/\mu$
T = temperature
u, v, w = velocity components in Cartesian coordinate system
U = reference velocity
x, y, z = Cartesian coordinates
X = nondimensional length, $X = x/L$
Y = nondimensional length, $Y = y/\epsilon L$
Y' = nondimensional length, $Y' = y/L$
δ = viscous layer thickness
$\epsilon = \mathrm{Re}^{-1/2}$
σ = factor of the characteristic equation
μ = coefficient of viscosity
ζ, η = transformed coordinates
ρ = density
$\tilde{\rho}$ = reference density
τ = shear stress

Superscript

i = components of a vector

Eqns. (5) and (6). Therefore, with the SRNS equations it is possible to compute the complex flows with both streamwise and crossflow separation, which is of significance in application.

Finally, in the current RNS equations the only nonviscous effect is the pressure gradients while in the present SRNS equations the nonviscous effects are the pressure gradients and the second-order derivatives of density. The elliptic factors in the SRNS equations are more in number than those in the RNS equations, so the SRNS equations can represent the structure and the feature of the flow more precisely. It is evident that a technique for handling these terms carefully is needed in the computation.

Accuracy of the SRNS Equations

The perturbation analysis method is used to study the accuracy of the SRNS equations. The momentum equations of a 2D viscous flows are

$$\rho u u_x + \rho v u_y = -p_x + \mu(4u_{xx}/3 + u_{yy} + v_{xy}/3) \quad (7)$$

$$\rho u v_x + \rho v v_y = -p_y + \mu(u_{xy}/3 + v_{xx} + 4v_{xy}/3) \quad (8)$$

The solution of the CNS equations in the viscous layer ($0 \le y \le \delta$) may be expanded as a series of $\epsilon(=\mathrm{Re}_\infty^{-1/2})$:

$$\left.\begin{aligned} u/U &= u_{i0} + \epsilon u_{i1} + \epsilon^2 u_{i2} + \dots \\ v/\epsilon U &= v_{i0} + \epsilon v_{i1} + \epsilon^2 v_{i2} + \dots \\ \rho/\rho_\infty &= \rho_{i0} + \epsilon\rho_{i1} + \epsilon^2\rho_{i2} + \dots \\ [p(X,Y) - p_w(X)]/\epsilon\rho U^2 &= p_{i0} + \epsilon p_{i1} + \epsilon^2 p_{i2} + \dots \end{aligned}\right\} \quad (9)$$

with $X = x/L$, $Y = y/\epsilon L$, $\partial/\partial Y = 0(1)$, u_{i0}, u_{i1}, ..., $\partial u_{i0}/\partial x$, $\partial u_{i1}/\partial x' \dots = 0(1)$.

Substitution of these equations into Eqs. (7) and (8) and comparison of the same order of ϵ yield

$$O(\epsilon^0):\quad \left.\begin{aligned} &\rho_{i0}\left(u_{i0}\frac{\partial u_{i0}}{\partial X} + v_{i0}\frac{\partial u_{i0}}{\partial Y}\right) = -\frac{d\bar{p}_w}{dX} + \mu\frac{\partial^2 u_{i0}}{\partial Y^2} \\ &O = \frac{\partial p_{i0}}{\partial Y} \end{aligned}\right\} \quad (10)$$

$$O(\epsilon^1):\quad \left.\begin{aligned} &\rho_{i0}\left[\frac{\partial(u_{i0}u_{i1})}{\partial X} + v_{i0}\frac{\partial u_{i1}}{\partial Y} + v_{i1}\frac{\partial u_{i0}}{\partial Y}\right] \\ &\quad + \rho_{i1}\left(u_{i0}\frac{\partial u_{i0}}{\partial X} + v_{i0}\frac{\partial v_{i0}}{\partial Y}\right) = -\frac{\partial p_{i0}}{\partial X} + \mu\frac{\partial^2 u_{i1}}{\partial Y^2} \\ &\rho_{i0}\left(u_{i0}\frac{\partial v_{i0}}{\partial X} + v_{i0}\frac{\partial v_{i0}}{\partial Y}\right) \\ &\quad = -\frac{\partial p_{i1}}{\partial Y} + \frac{\mu}{3}\left(\frac{\partial^2 u_{i0}}{\partial X\partial Y} + 4\frac{\partial^2 v_{i0}}{\partial Y^2}\right) \end{aligned}\right\} \quad (11)$$

$$O(\epsilon^2):\quad \left.\begin{aligned} &\rho_{i0}\left[u_{i1}\frac{\partial u_{i1}}{\partial X} + \frac{\partial(u_{i0}u_{i2})}{\partial X} + v_{i0}\frac{\partial u_{i2}}{\partial Y} + v_{i1}\frac{\partial u_{i1}}{\partial Y} + v_{i2}\frac{\partial u_{i0}}{\partial Y}\right] + \rho_{i1}\left[\frac{\partial(u_{i0}u_{i1})}{\partial X} + v_{i0}\frac{\partial u_{i1}}{\partial Y} + v_{i1}\frac{\partial u_{i0}}{\partial Y}\right] \\ &\quad + \rho_{i2}\left(u_{i0}\frac{\partial u_{i0}}{\partial X} + v_{i0}\frac{\partial v_{i0}}{\partial Y}\right) = -\frac{\partial p_{i1}}{\partial X} + \mu\left(\frac{4}{3}\frac{\partial^2 u_{i0}}{\partial X^2} + \frac{\partial^2 u_{i1}}{\partial Y^2} + \frac{1}{3}\frac{\partial^2 v_{i0}}{\partial X\partial Y}\right) \\ &\rho_{i0}\left[u_{i0}\frac{\partial v_{i1}}{\partial X} + u_{i1}\frac{\partial v_{i0}}{\partial X} + \frac{\partial(v_{i0}v_{i1})}{\partial Y}\right] + \rho_{i1}\left(u_{i0}\frac{\partial v_{i0}}{\partial X} + v_{i0}\frac{\partial v_{i0}}{\partial Y}\right) = -\frac{\partial p_{i2}}{\partial Y} + \frac{\mu}{3}\left(\frac{\partial^2 u_i}{\partial X\partial Y} + 4\frac{\partial^2 v_{i1}}{\partial Y^2}\right) \end{aligned}\right\} \quad (12)$$

where $\bar{p}_w(x) = p_w(x)/\rho_\infty U^2$. The continuity equation and energy equation may be expanded similarly.

It is seen that the zero-order approximation of the CNS equation, Eq. (10), is just the boundary-layer equations and the first-order approximation, Eq. (11), is the RNS equations.

The CNS solution in the inviscid region ($y > \delta$) may be also expanded as a power series of ϵ, and substitution of them into Eqs. (7) and (8) and comparison of the same order give the similar expressions.

From these expressions in both viscous region and inviscid part and the SRNS equations it is easily proved that the solution of an arbitrary flow parameter F of the SRNS equations will satisfy the following relations:

Within $y \le \delta$, $|F - (F_{i0} + \epsilon F_{i1} + \epsilon^2 F_{i2})| \le 0(\epsilon^3 = \mathrm{Re}^{-3/2})$;

Beyond $y > \delta$, $|F - (F_{e0} + \epsilon F_{e1} + \epsilon^2 F_{e2})| \le 0(\mathrm{Re}^{-3/2})$.

In other words, the SRNS equations have a uniformly convergent solution with accuracy of $\epsilon = \mathrm{Re}^{-1}$.

Character of the SRNS Equations Near the Point of Separation

Now consider a steady, incompressiple, laminar flow past a flat plate. The SRNS equations are

$$\frac{\partial u'}{\partial x'} + \frac{\partial v'}{\partial y'} = 0 \quad (13)$$

$$u'\frac{\partial u'}{\partial x'} + v'\frac{\partial u'}{\partial y'} = -\frac{1}{\rho}\frac{\partial p}{\partial x'} + v\left(\frac{\partial^2 u'}{\partial x'^2} + \frac{\partial^2 u'}{\partial y'^2}\right) \quad (14)$$

$$u'\frac{\partial v'}{\partial x'} + v\frac{\partial v'}{\partial y'} = -\frac{1}{\rho}\frac{\partial p}{\partial y'} + v\frac{\partial^2 v'}{\partial y'^2} \quad (15)$$

These equations may be transformed to a nondimensional form

$$\frac{\partial u}{\partial x} + \frac{\partial v}{\partial y} = 0$$

$$u\frac{\partial u}{\partial x} + v\frac{\partial u}{\partial y} = -\frac{\partial p}{\partial x} + \frac{1}{\mathrm{Re}}\frac{\partial^2 u}{\partial x^2} + \frac{\partial^2 u}{\partial y^2}$$

$$u\frac{\partial v}{\partial x} + v\frac{\partial v}{\partial y} = -\mathrm{Re}\frac{\partial p}{\partial y} + \frac{\partial^2 v}{\partial y^2}$$

with $x = x'/L$, $y = \mathrm{Re}^{1/2}y'/L$, $u = u'/U$, $v = \mathrm{Re}^{1/2}v'/U$, and $p = p'/\delta U^2$ (L is the characteristic length and U is the characteristic velocity).

When the stream function ψ is introduced: $u = \partial\psi/\partial y$, $v = -\partial\psi/\partial x$, the momentum equations become

$$\frac{\partial^2}{\partial y^2}\left(\frac{\partial^2\psi}{\partial y^2} + \frac{2}{\mathrm{Re}}\frac{\partial^2\psi}{\partial x^2}\right) + \left(\frac{\partial\psi}{\partial x}\frac{\partial}{\partial x} - \frac{\partial\psi}{\partial y}\frac{\partial}{\partial x}\right)\left(\frac{\partial^2\psi}{\partial y^2} + \frac{1}{\mathrm{Re}}\frac{\partial^2\psi}{\partial x^2}\right) = 0 \quad (16)$$

According to Dean (1950), the solution of stream function is assumed to be expressed as

$$\psi(x,y) = a_2\frac{y^2}{2!} + a_3\frac{y^3}{3!} + b_3\frac{y^2}{2!}\frac{x}{1!} + a_4\frac{y^4}{4!} + b_4\frac{y^3}{3!}\frac{x}{1!} + c_4\frac{y^2}{2!}\frac{x^2}{2!} + a_5\frac{y^5}{5!} + b_5\frac{y^4}{4!}\frac{x}{1!}$$

$$+ c_5 \frac{y^3}{3!}\frac{x^2}{2!} + d_5 \frac{y^2}{2!}\frac{x^3}{3!} + a_6 \frac{y^6}{6!} + b_6 \frac{y^5}{5!}\frac{x}{1}$$

$$+ c_6 \frac{y^4}{4!}\frac{x^2}{2!} + d_6 \frac{y^3}{3!}\frac{x^3}{3!} + e_6 \frac{y^2}{2!}\frac{x^4}{4!} + \ldots \quad (17)$$

It is obvious that it meets the boundary conditions along $y = 0$: $u = v = 0$ or

$$\frac{\partial \psi}{\partial y} = \frac{\partial \psi}{\partial x} = 0 \quad \text{and} \quad \frac{\partial^2 u}{\partial x^2} = \frac{\partial^3 \psi}{\partial x^2 \partial y} = 0$$

From Eq. (14a) it is obtained that

$$\left.\frac{\partial p}{\partial x}\right|_{y=0} = \mu \left.\frac{\partial^3 \psi}{\partial y^3}\right|_{y=0} = \mu\left(a_3 + b_4 \frac{x}{1!} + c_5 \frac{x^2}{2!}\right) + \ldots$$

and from Eq. (17) a relation is defined:

$$u|_{k=0} = \left(\frac{\partial \psi}{\partial y}\right)_{k=0} = a_2 \frac{y}{1!} + a_3 \frac{y^2}{2!} + a_4 \frac{y^3}{3!} + \ldots$$

This means that from the given conditions the series a_3, b_4, c_5, . . . , and a_2, a_3, a_4, . . . are all determined uniquely.

Substitution of the expression ψ into Eq. (16) yields the following relations ($r = /\mathrm{Re}$):

$$\left.\begin{aligned} a_4 + 2rc_4 &= 0 \\ a_5 + 2rc_5 - a_2 b_3 &= 0 \\ b_5 + 2rd_5 &= 0 \end{aligned}\right\}$$

$$\left.\begin{aligned} a_6 + 2rc_6 - 2a_2 b_4 &= 0 \\ b_6 + 2rd_6 - a_2 c_4 - b_3^2 &= 0 \\ c_6 + 2rc_6 &= 0 \end{aligned}\right\}$$

$$\left.\begin{aligned} a_7 + 2rc_7 + 2a_4 b_3 - 2a_3 b_4 - 3a_2(b_3 + rd_3) + 3rb_3 c_4 &= 0 \\ b_7 + 2rd_7 - 2a_2 c_5 - 2b_3 b_4 &= 0 \\ c_7 + 2rc_7 - a_2 d_5 - 3b_3 c_4 &= 0 \\ d_7 + 2rf_7 &= 0 \end{aligned}\right\}$$

$$\left.\begin{aligned} a_8 + 2rc_8 + 5a_5 b_3 - 4a_2(b_6 + rd_6) \\ - a_3(5b_5 + 6rd_3) + 6rb_3 c_5 + 4rb_4 c_4 &= 0 \\ b_8 + 2rd_8 + 2a_4 c_4 - 3a_2(c_6 + re_6) \\ - 2a_3 c_5 - b_5 b_5 - 2b_4^2 + 3rc_4^2 &= 0 \\ c_8 + 2rc_8 - 2a_2 d_6 - 4b_3 c_5 - 2b_4 c_4 &= 0 \\ d_8 + 2rf_8 - a_2 e_6 - 4b_3 d_5 - 3c_4^2 &= 0 \\ c_8 + 2rg_8 &= 0 \end{aligned}\right\}$$

By use of the method of alternating recurrence (Dean, 1950), it is easy to demonstrate that either for the ordinary points in the flow or for the point of separation all coefficients in the expression of stream function may be determined. In other words, the SRNS equations have a series solution in the whole flow field which contains some separated flow regions, or the solution of the SRNS equations is regular at the point of separation.

Furthermore, it is worthwhile to compare the series solutions of the CNS equations, the SRNS equations, the RNS equations, and the boundary-layer equations. Denote these solutions as $\psi^{(1)}(x, y)$, $\psi^{(2)}(x, y)$, $\psi^{(3)}(x, y)$, and $\psi^{(4)}(x, y)$.

When the origin (0, 0) is not the point of separation ($a_2 \neq 0$), these solutions are

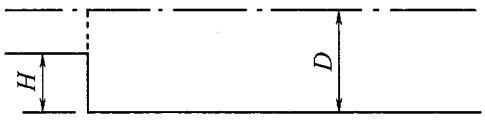

Fig. 1 Sketch of the duct with a sudden expansion

$$\psi^{(1)}(x, y) = a_2 \frac{y^2}{2!} + a_3 \frac{y^3}{3!} + \frac{a_3 + 2rc_3}{a_2}\frac{y^2}{2!}\frac{x}{1!} + a\frac{y^4}{4!}$$

$$+ b_4 \frac{y^3}{3!}\frac{x}{1!} + \frac{a_4}{2r}\frac{y^2}{2!}\frac{x^2}{2!} + \ldots$$

$$\psi^{(2)}(x, y) = a_2 \frac{y^2}{2!} + a_3 \frac{y^3}{3!} + \frac{a_5 + 2rc_3}{a_2}\frac{y^2}{2!}\frac{x}{1!} + a_4\frac{y^4}{4!}$$

$$+ b_4 \frac{y^3}{3!}\frac{x}{1!} + \frac{a_4}{2r}\frac{y^2}{2!}\frac{x^2}{2!} + \ldots$$

$$\psi^{(3)}(x, y) = a_2 \frac{y^2}{2!} + a_3 \frac{y^3}{3!} + \frac{a_3 + rc_5}{a_2}\frac{y^2}{2!}\frac{x}{1!} + a_4\frac{y^4}{4!}$$

$$+ b_4 \frac{y^3}{3!}\frac{x}{1!} - \frac{a_4}{r}\frac{y^2}{2!}\frac{x^2}{2!} + \ldots$$

$$\psi^{(4)}(x, y) = a_2 \frac{y^2}{2!} + a_3 \frac{y^3}{3!} + \frac{a_5}{a_2}\frac{y^2}{2!}\frac{x}{1!} + b_4\frac{y^3}{3!}\frac{x}{1!}$$

$$+ \frac{a_2 a_8 + a_5}{4a_2^2}\frac{y^2}{2!}\frac{x^2}{2!} + \ldots$$

It is seen that within the fourth order the solutions of the CNS equations and the SRNS equations are completely the same.

When the origin is the separation point ($a_2 = 0$ and $a_4 \neq 0$), the boundary-layer equations have no solution (Goldstein, 1948) and the other three solutions are

$$\psi^{(1)}(x, y) = a_3 \frac{y^3}{3!} + \frac{2}{5a_4}(a_7 - 3r^2 e_7 - 2a_3 b_4)\frac{y^2}{2!}\frac{x}{1!}$$

$$+ a_4 \frac{y^4}{4!} + b_4 \frac{y^3}{3!}\frac{x}{1!} - \frac{a_4}{2r}\frac{y^2}{2!}\frac{x^2}{2!} + \ldots$$

$$\psi^{(2)}(x, y) = a_3 \frac{y^3}{3!} + \frac{2}{5a_4}(a_7 - 4r^2 e_7 - 2a_3 b_4)\frac{y^2}{2!}\frac{x}{1!}$$

$$+ a_4 \frac{y^4}{4!} + b_4 \frac{y^3}{3!}\frac{x}{1!} - \frac{a_4}{2r}\frac{y^2}{2!}\frac{x^2}{2!} + \ldots$$

$$\psi^{(3)}(x, y) = a_3 \frac{y^3}{3!} + \frac{1}{4a_4}(a_7 - r^2 e_7 - 2a_3 b_4)\frac{y^2}{2!}\frac{x}{1!}$$

$$+ a_4 \frac{y^4}{4!} + b_4 \frac{y^3}{3!}\frac{x}{1!} - \frac{a_4}{r}\frac{y^2}{2!}\frac{x^2}{2!} + \ldots$$

It is seen that the solutions of the CNS equations and the SRNS equations are almost the same if Re is not very small.

From the comparison it is concluded that for the common flows the SRNS equations are a precise approximation to the CNS equations.

Numerical Examples

To test the accuracy and effectiveness of the present SRNS equations some numerical experiments on 2D incompressible flows downstream of a plate symmetric sudden expansion in ducts (Fig. 1) are conducted. In these cases, the basic governing equations of motion are

$$\frac{\partial A}{\partial x} + \frac{\partial B}{\partial y} = \frac{1}{\mathrm{Re}}\frac{\partial^2 C}{\partial y^2} - \frac{1}{\mathrm{Re}}\frac{\partial^2 D}{\partial x \partial y} \tag{18}$$

with

$$A = \begin{bmatrix} \mu \\ u^2 + ap \\ \mu v \end{bmatrix}, \quad B = \begin{bmatrix} v \\ uv \\ v^2 + p \end{bmatrix},$$

$$C = \begin{bmatrix} 0 \\ u \\ 0 \end{bmatrix}, \quad D = \begin{bmatrix} 0 \\ v \\ 0 \end{bmatrix}.$$

This equation may be solved by use of a single sweep marching method (Kirtley and Lakshminarayana, 1985). The terms with the streamwise pressure are splitted into two parts: $A = A_{im} + A_{ex}$, where

$$A_{im} = \begin{bmatrix} u \\ u^2 + ap \\ uv \end{bmatrix}, \quad A_{ex} = \begin{bmatrix} 0 \\ -ap + p \\ 0 \end{bmatrix}.$$

The governing equations of motion then may be written as

$$\frac{\partial A_{im}}{\partial x} + \frac{\partial B}{\partial y} - \frac{1}{\mathrm{Re}}\frac{\partial^2 C}{\partial y^2} + \frac{1}{\mathrm{Re}}\frac{\partial^2 D}{\partial x \partial y} = -\frac{\partial A_{ex}}{\partial x} \tag{18a}$$

It is obvious that there is some restriction on the values of a to guarentee that the character of the equation is parabolic. In fact, from the characteristic equation of Eq. (18a) it is obtained that only when $(1 + a) < 0$, the equation is hyperbolic-parabolic in mathematics. It means that it requires $a < -1$ for the SRNS equations.

In the practical calculations the following form of Eq. (18) is employed:

$$\bar{A}_1 \frac{\partial u}{\partial x} + \bar{B}\frac{\partial u}{\partial y} - \frac{\bar{C}}{\mathrm{Re}}\frac{\partial^2 u}{\partial y^2} + \frac{\bar{D}}{\mathrm{Re}}\frac{\partial^2 u}{\partial x \partial y} = -\frac{\partial \overline{A_2}}{\partial x}$$

where $U = (u, v, p)^T$,

$$\bar{A}_1 = \begin{bmatrix} 1 & 0 & 0 \\ 2f_u & 0 & 0 \\ v & u & 0 \end{bmatrix}, \quad \bar{B} = \begin{bmatrix} 0 & 1 & 0 \\ v & u & 0 \\ 0 & 2v & 1 \end{bmatrix},$$

$$\bar{C} = \begin{bmatrix} 0 & 0 & 0 \\ 1 & 0 & 0 \\ 0 & 1 & 0 \end{bmatrix}, \quad \bar{D} = \begin{bmatrix} 0 & 0 & 0 \\ 0 & 1 & 0 \\ 0 & 0 & 0 \end{bmatrix},$$

and f is the coefficient in FLARE approximation. The difference equation of Eq. (18a) may be expressed as

$$\bar{A}_1 \frac{u_{ij} - u_{i-1j}}{\Delta x} + \bar{B}\frac{u_{ij+1} - u_{ij-1}}{\Delta y} - \frac{\bar{C}}{\mathrm{Re}}\frac{u_{ij+1} - 2u_{ij} + u_{ij-1}}{(\Delta y)^2}$$
$$+ \frac{\bar{D}}{\mathrm{Re}}\frac{(u_{ij+1} - u_{ij-1}) - (u_{i-1j+1} - u_{i-1j-1})}{2\Delta x \Delta y}$$
$$= \left[0, -a\frac{p_{ij}}{\Delta x}, 0\right]^T$$

where Δx and Δy are the intervals between two neighboring grids along x and y, respectively.

The set of equations to be solved are in block-triangle form and can be calculated by a standard procedure.

After the velocity field has been solved by the single-sweep technique, if one has some interest in the pressure itself a Poisson equation of the pressure can be solved to give its correction:

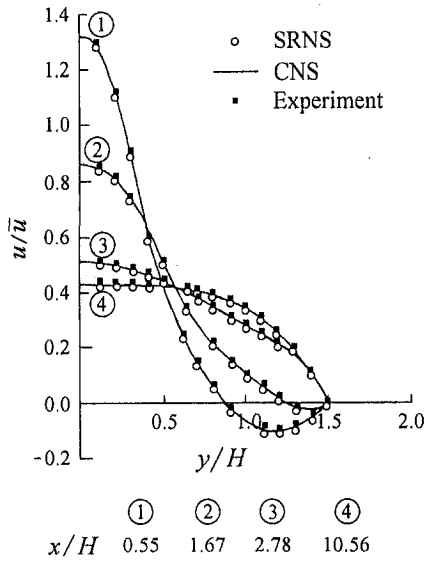

Fig. 2 Distributions of the streamwise velocity in 3:1 sudden expansion (Re = 37.33)

$$\Delta p = 2(u_x v_y - u_y v_x)$$

Example 1. The flow downstream of a plane 3:1 symmetric sudden expansion in a duct with Re = 37.333 (H is the step height).

For this symmetric flow only a half flow field is needed to solve. The inlet parabolic profile of the velocity is

$$\left.\begin{aligned} u &= -6(y-1)(y-2) \\ v &= 0 \end{aligned}\right\}$$

All quantities in this expression are dimensionless with reference to H and U (the mean inlet velocity).

A 30 × 30 grid with the same intervals is used.

The computed streamwise velocity distributions at four points are shown in Fig. 2. It is seen that a reverse flow region exists in the beginning of the duct. It is also noted that the SRNS solution is in good agreement with both experimental results and the CNS solution (Durst, 1974). The distance between the inlet section and the point of reattachment, L_r, is a very important parameter to represent the separated flow region. In this calculation, L_r/Re is 0.0670, which is close to the data, 0.066 and 0.068, computed by Macagno et al. (1967) and Agarwal (1981), respectively. All these indicate that the present SRNS equations can give accurate results and the calculation is very simple.

Example 2. The flow downstream of a plane 2:1 symmetric sudden expansion in a duct with Re = 46.6.

The inlet velocity profile now is

$$\left.\begin{aligned} u &= -1.5(y-1)(y-3) \\ v &= 0 \end{aligned}\right\}$$

The comparison of the velocity distributions between the SRNS solution and the test results (Durst, 1974) is given in Fig. 3. It is seen that they are very close. The calculated reattachment distance, L_r/Re, obtained from this method is 0.0680, which also agrees well with the results given by Macagno et al. (1967) and Agarwal (1981).

The numerical examples show that the SRNS equations are an accurate and effective tool to solve a laminar separated flow.

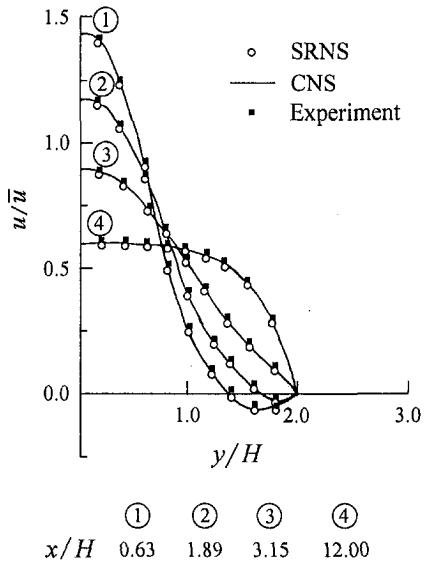

Fig. 3 Distributions of the streamwise velocity in 2:1 sudden expansion (Re = 46.6)

Concluding Remarks

Based on the investigation of the slightly reduced Navier-Stokes (SRNS) equations with mostly streamwise viscous diffusion and heat conduction terms, it is found that they have the same mathematical characteristics and subcharacteristics as the usual RNS equations. So the space-marching method may be used to solve the velocity components in the SRNS equations.

Compared with the RNS equations, the SRNS equations retain all the streamwise and transverse vorticity components and reflects more nonviscous elliptic effects. It is also shown that they have a uniformly convergent solution with the accuracy of order of $0(\epsilon^2)$ or $0(\mathrm{Re}^{-1})$ and for a laminar flow past a plate the SRNS solution is regular in mathematics at the separation point and is very close to the CNS solution. The SRNS equations are a precise approximation to the CNS equations and may be used to calculate the complex flows with separation.

The numerical examples on the incompressiple flows show that the SRNS equations are a useful tool to compute the viscous flow accurately.

References

Agarwal, R. K., 1981, "A Third-Order-Accurate Upwind Scheme for Navier-Stokes Solutions in Three Dimensions," ASME/AIAA Conference on Computers in Flow Predictions and Fluid Dynamics Experiments, pp. 73–84.

Anderson, D. A., Tannehill, J. C., and Plether, R. H., 1984, *Computational Fluid Mechanics and Heat Transfer,* Hemisphere Publishing Corporation.

Courant, R., and Hilbert, D., 1962, *Methods in Mathematical Physics,* Vol. 2, Interscience.

Dean, W. R., 1950, "Note on the Motion of Liquid near a Position of Separation," *Proceedings of Cambridge Philosophical Society,* Vol. 46.

Durst, F., Melling, A., and Writelaw, J. H., 1974, "Low Reynolds Number Flow over Plane Symmetric Sudden Expansion," *Journal of Fluid Mechanics,* Vol. 64.

Gao, Z., 1988, "On the Simplified Navier-Stokes (SNS) Equations," *Science in China* (Series A), No. 10.

Goldstein, S., 1948, "On Laminar Boundary-Layer Flow near a Position of Separation," *Quarterly Journal of Mechanics and Applied Mathematics,* Vol. 1.

Kirtley, K. B. and Lakshminarayana, B., 1985, "Computation of Internal Incompressible Separated Flows Using a Space-Marching Technique," AIAA Paper 85-1624.

Macagno, B. O., and Huang, T. K., 1967, "Computational and Experimental Study of a Captive Body," *Journal of Fluid Mechanics,* Vol. 28.

Telionis, D. P. 1981, *Unsteady Viscous Flow,* Springer-Verlag.

Numerical Analysis of Unsteady Flow in the Weis-Fogh Mechanism by the 3D Discrete Vortex Method With GRAPE3A

Kideok Ro
Professor,
Department of Marine Engineering,
Fisheries College,
Gyeongsang National University,
445 Inpyung-dong, Tongyeong,
Kyungnam 650-160, Korea

Michihisa Tsutahara
Professor,
Graduate School of Science and Technology, Kobe University,
Rokkodai-cho 1-1, Nada-ku,
Kobe 657, Japan

The three-dimensional flows in the Weis-Fogh mechanism are studied by flow visualization and numerical simulation by a discrete vortex method. In this mechanism, two wings open, touching their trailing edges (fling), and rotate in opposite directions in the horizontal plane. At the "fling" stage, the flow separates at the leading edge and the tip of each wing. Then they rotate, and the flow separates also at the trailing edges. The structure of the vortex systems shed from the wings is very complicated and their effect on the forces on the wings have not yet been clarified. Discrete vortex method, especially the vortex stick method, is employed to investigate the vortex structure in the wake of the two wings. The wings are represented by lattice vortices, and the shed vortices are expressed by discrete three-dimensional vortex sticks. In this calculation, the GRAPE3A hardware is used to calculate at high speed the induced velocity of the vortex sticks and the viscous diffusion of fluid is represented by the random walk method. The vortex distributions and the velocity field are calculated. The pressure is estimated by the Bernoulli equation, and the lift and moment on the wing are also obtained. However, the simulations, especially those for various Reynolds numbers, should be treated with caution, because there is no measurement to compare them with and the discrete vortex method is approximate due to rudimentary modeling of viscosity.

Introduction

The Weis-Fogh mechanism, discovered by analyzing the wing motion in the hovering flight of a small insect called Encarsia formosa, is an efficient mechanism of lift generation (Weis-Fogh, 1973). Lighthill (1973) has studied the two-dimensional flow in this mechanism by the potential theory. Maxworthy (1979) has experimentally investigated three-dimensional flow.

The motion of the wings in the Weis-Fogh mechanism as shown in Fig. 1 may consist of five stages. The first is the "clap" stage, in which the two wings close touching their leading edges. The second is the "fling" stage, in which the two wings open touching their trailing edges. The third is the "rotating" stage, in which the two wings rotate in the horizontal plane with the center corresponding to the insect's body. The fourth is the "flap" stage, in which the wings change the angle of attack, and the last is the "returning" stage, in which the wings return to the position of the clap stage. These stages are repeated and the lift on each wing is always generated in the upward direction. In this figure, the insect is on the hovering flight and the arrows indicate the direction of circulation around wings.

The three-dimensional flow in the Weis-Fogh mechanism has not yet been studied theoretically. In this study, the flow around the wings in the fling and the following rotating stages are investigated by both flow visualization and numerical simulation by discrete vortex method. The flow is fully three-dimensional and unsteady. The configuration of the boundary, which corresponds to the complex motion of the wings, changes rapidly with time. The separated shear layers form a very complex wake behind the wings. The finite difference method or the finite element method may not be readily applicable to this kind of flow, because the mesh must be constructed from moment to moment. The discrete vortex method is most convenient to use, because no grid is necessary, and is good for simulating the separated flows (Leonard, 1980; Sarpkaya, 1989; and Kamemoto, 1993).

The following two points have to be considered in the flowfield calculation by the discrete vortex method. One is the calculation time. In this method, many vortex sticks are shed into the flowfield in each time step. Therefore, it takes a long time to calculate the induced velocity of vortex sticks in each time step. The GRAPE(GRAvity PipE)3A (Okumura et al., 1992 and Sugimoto, 1994), which is a special purpose hardware with pipelines developed to calculate gravitational many-body simulations at high speed, is used to reduce the calculating time for the velocity of vortex sticks. In many-body simulations, almost all computational time is spent calculating the long-range forces between particles, such as gravitational and coulomb forces, since the number of interactions between particles is proportional to the square of the number of particles. The GRAPE3A calculates the forces between particles due to two-body interactions, and the host workstation, which is connected to the GRAPE3A, integrates the orbits of particles. Namely, the GRAPE3A is an accelerator which may be regarded by the host as a hardware subroutine to calculate the forces.

The other is how to express the viscous effect of fluid. The flow in the discrete vortex method is looked upon as a potential flow. Therefore, the viscous term has to be introduced in order to apply this method to an actual flowfield. Ogami and Akamatsu (1991) have proposed the method by diffusion velocity which they call, but the method has not yet been applied to three-dimensional flows. Beale and Majda (1982) have represented the viscous effect by using the so-called core spreading method, in which the core radius is enlarged with time. But the calculat-

Contributed by the Fluids Engineering Division for publication in the JOURNAL OF FLUIDS ENGINEERING. Manuscript received by the Fluids Engineering Division February 14, 1996; revised manuscript received July 22, 1996. Associate Technical Editor: P. R. Bandyopadhyay.

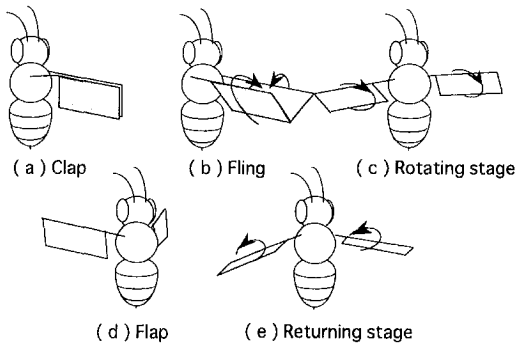

Fig. 1 Motion of the wing in the Weis-Fogh mechanism

ing time in this method increases because if the core radius changes, the calculating speed of the GRAPE3A is greatly decreased. Therefore, the viscous diffusion is represented by introducing the random walk method (Chorin, 1973) and this method is known to be statistically more accurate as the number of elements increases.

Though both methods used in this study, which are the discrete vortex method and the random walk method, are convenient in the calculation of the unsteady and complex flow, their results are strictly qualitative because those methods give approximate solutions.

Flow Visualization

Experimental Method. The flow patterns around the wings were visualized by titanium tetrachloride, which generates a thick mist of HCl. The apparatus for the experiments was as follows.

The wings were made of acryl and each had a square shape with a 70-mm chord length, a 140-mm span, and a 2-mm thickness.

The two wings were set to move symmetrically, and the motion was controlled by hand. The rods to control the wings' motion were connected to wings at their trailing edges as shown in Fig. 2, unlike Maxworthy's experiments (1979), in which they were connected with the wings at their leading edges. Therefore, the wings were rotated about their trailing edges in the fling stage, and they translated (or rotated) with their trailing edges leading. The edges and the tips of the wings were coated with $TiCl_4$ just before the wings opened. The flow patterns were recorded by a video camera.

Experimental Results and Discussion. The flow patterns in the fling stage only are shown in Fig. 3, in which (a) is the photograph of a flow visualization and (b) is a sketch of the structure of vortices under the same condition as in (a). The Reynolds number is defined by $\mathrm{Re} = \Omega c^2/\nu$, where Ω is the angular velocity of rotation in the fling, c is the chord length, and ν is the kinematic viscosity. In this figure, the eddies formed

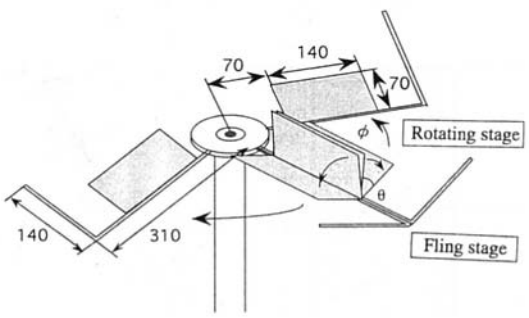

Fig. 2 Schematic diagram of experimental apparatus (unit:mm)

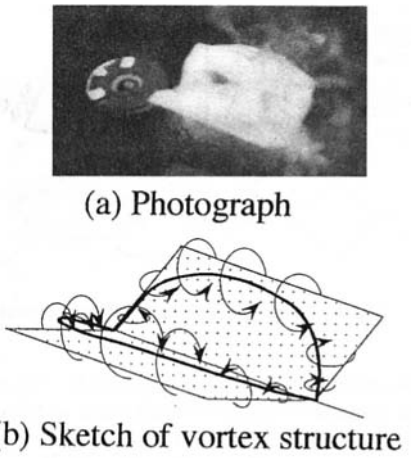

Fig. 3 Visualization of flowfield around the wings in the fling stage (Re = 400, $\theta = \pi/3$)

by the shearing layers shed from the leading edges are located near the leading edges. These eddies are known to increase the lift in the fling stage. The eddies near the leading edge of each wing take a convex shape because the eddies shed from both tips of the wings entrain the flows.

The flow pattern in the rotating stage, as shown in Fig. 4, becomes complicated owing to the interaction among the eddies from the leading edges and the tips. The strongest eddies are those from the leading edges, and the eddy from one wing is connected to the one from the other wing. The flow is formed by three-dimensional vortices, and a sketch is presented in Fig. $4(b)$.

Numerical Study

Method of Simulation. In this study, the so-called vortex stick method was employed, in which all the vortex lines are

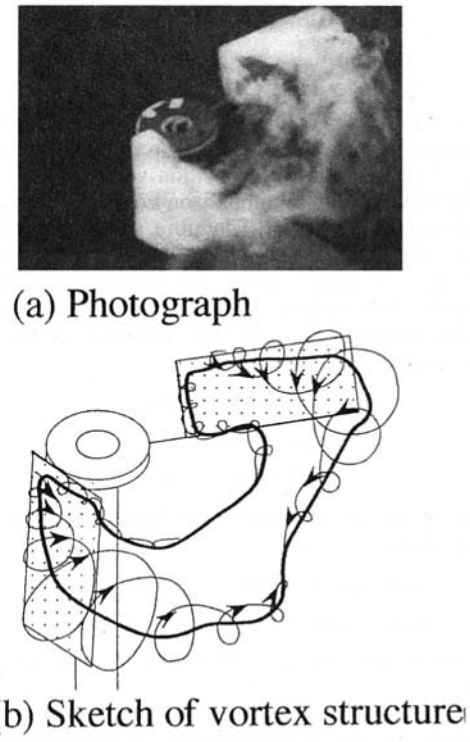

Fig. 4 Visualization of flowfield around the wings in the rotating stage (Re = 400, $\theta = \pi/3$, $\phi = \pi/3$)

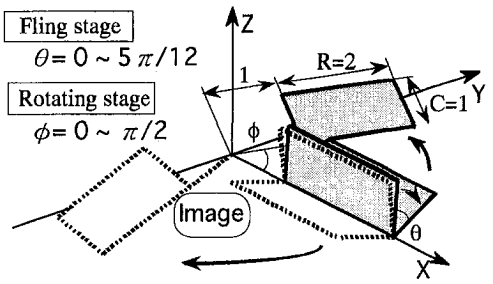

Fig. 5 Three-dimensional analytical model

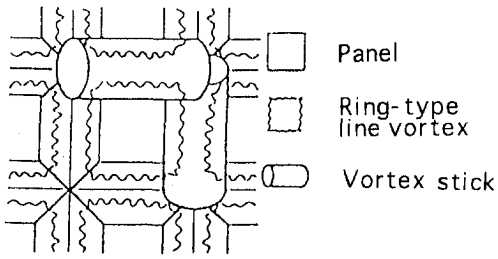

Fig. 6 An enlarged diagram of panel

divided into several cylindrical vortex sticks (Shirayama et al., 1985). The induced velocity of each stick is calculated by the Biot-Savart law using the GRAPE3A hardware as follows. The acceleration due to gravity on the ith particle $\mathbf{a}_i$ is calculated by GRAPE3A as

$$\mathbf{a}_i = -\sum_{j=1}^{N} \frac{m_j(\mathbf{r}_i - \mathbf{r}_j)}{(|\mathbf{r}_i - \mathbf{r}_j|^2 + \epsilon^2)^{3/2}} \tag{1}$$

where N is the number of all the particles, m_j is the mass of the jth particle, $\mathbf{r}_i$ and $\mathbf{r}_j$ denote the position vectors of the i and jth particles, respectively, and ϵ is the softening parameter having the dimension of length. It is introduced to avoid the divergence of solution in case the distance between particles approaches 0. It is similar to the size of mesh when the motion of fluid is calculated by the finite-difference method, the motion of less size than this can't be represented. Biot-Savart's law used to calculate the induced velocity of vortex sticks is expressed as

$$\mathbf{u} = \frac{1}{4\pi} \int \frac{\omega(\mathbf{r}') \times (\mathbf{r} - \mathbf{r}')}{|\mathbf{r} - \mathbf{r}'|^3} d\mathbf{r}' \tag{2}$$

To use the GRAPE3A hardware, Eq. (2) has to be changed to the same form as Eq. (1), which is expressed as

$$\mathbf{u}_i = -\sum_{j=1}^{N} \frac{\mathbf{q}_j \times (\mathbf{r}_i - \mathbf{r}_j)}{(|\mathbf{r}_i - \mathbf{r}_j|^2 + \epsilon^2)^{3/2}} \tag{3}$$

where

$$\mathbf{q}_j = -\frac{1}{4\pi} \omega_j V_j = -\frac{\Gamma_j(\mathbf{r}_{tj} - \mathbf{r}_{bj})}{4\pi}$$

and $\mathbf{u}_i$ is the induced velocity of the ith vortex stick; ω_j, V_j, and Γ_j denote vorticity, volume, and circulation of the jth vortex sticks; and $\mathbf{r}_{tj}$ and $\mathbf{r}_{bj}$ are the position vectors of the two ends of the jth vortex stick. In comparison Eq. (3) with Eq. (1), the only difference is the $\mathbf{q}_j$ curl. Therefore, it makes the GRAPE3A calculate three times, by giving $q_{x,j}$, $q_{y,j}$ and $q_{z,j}$, three components of vector $\mathbf{q}_j$ instead of m_j. The GRAPE3A produces nine components, for example, $K_{xx,i}$, $K_{xy,i}$, $K_{xz,i}$ against $q_{x,j}$. From these nine components, using the definition of the curl, the induced velocity $\mathbf{u}_i$ is calculated as

$$\begin{aligned} u_{x,i} &= K_{yz,i} - K_{zy,i} \\ u_{y,i} &= K_{zx,i} - K_{xz,i} \\ u_{z,i} &= K_{xy,i} - K_{yx,i} \end{aligned} \tag{4}$$

The ends of the ith shedding vortex stick are moved in every time step Δt by

$$\begin{aligned} \mathbf{r}_{ti}(t + \Delta t) &= \mathbf{r}_{ti}(t) + \mathbf{u}_{ti}(t) \cdot \Delta t + \Delta \mathbf{r} \\ \mathbf{r}_{bi}(t + \Delta t) &= \mathbf{r}_{bi}(t) + \mathbf{u}_{bi}(t) \cdot \Delta t + \Delta \mathbf{r} \end{aligned} \tag{5}$$

where $\Delta \mathbf{r}$ is the displacement vector by the random walk method.

The motions of the two wings are completely symmetrical, so that only one wing was considered, and the entire flowfield was obtained by the assumption of symmetry as shown in Fig. 5. Each wing was represented by 10 × 20 square panels. Each panel has a ring-type line vortex, represented by the wavy lines in Fig. 6, and then is finally replaced with vortex sticks as shown in Fig. 6. The circulation of each vortex stick is evaluated by the difference between the circulations of two ring-type vortices that the vortex stick contains. The middle in span direction and a quarter in chord direction of each panel was taken as the control point at which the boundary condition was applied. The boundary condition for determining the circulations of the ring-type vortices was that the normal components of the velocities of the fluid and those of the wing at the control points coincide with each other.

The vortex sticks at the edges and tips of the wing are shed into the flow in each time step, maintaining their circulations. The structure of the vortices in the flowfield is also ring-like as shown. All the vortex lines are connected and no vortices disappear.

If the vorticity of the ring-type line vortices on the surface of the wing is assumed to be concentrated on the cores, the flow on the surface, excluding the cores, can be considered as potential flow. Therefore, the pressure distribution on the wing can be evaluated by the Bernoulli equation for unsteady flows

$$\frac{\partial \phi}{\partial t} + \frac{u^2}{2} + \frac{p}{\rho} = \text{const} \tag{6}$$

where ϕ is the velocity potential, u is the local velocity, p is the pressure, and ρ is the density of the fluid. For calculating the forces on the wing, only the forces due to the pressure are considered.

The calculation method for the force on the wing is shown in Fig. 7. The wing is approximated as a flat plate without thickness, so that only the difference between the pressures on both sides of the wing should be considered. Only the first term in Eq. (6) is different, that is, this term is multi-valued, but the other terms are not different between the two sides, and those are single-valued. Therefore, the first term will be evaluated here. For example, since the difference of the velocity potential between both sides of the "a" point in Fig. 7, which is $(\Phi_{a1} - \Phi_{a2})$, corresponds to the circulation Γ_a of the ring-type line vortex, the first term of Eq. (6) on that point can be obtained by estimating the variation of the circulation with time.

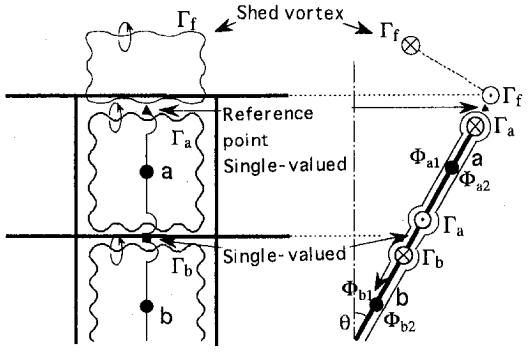

Fig. 7 The calculating method for force on the wing

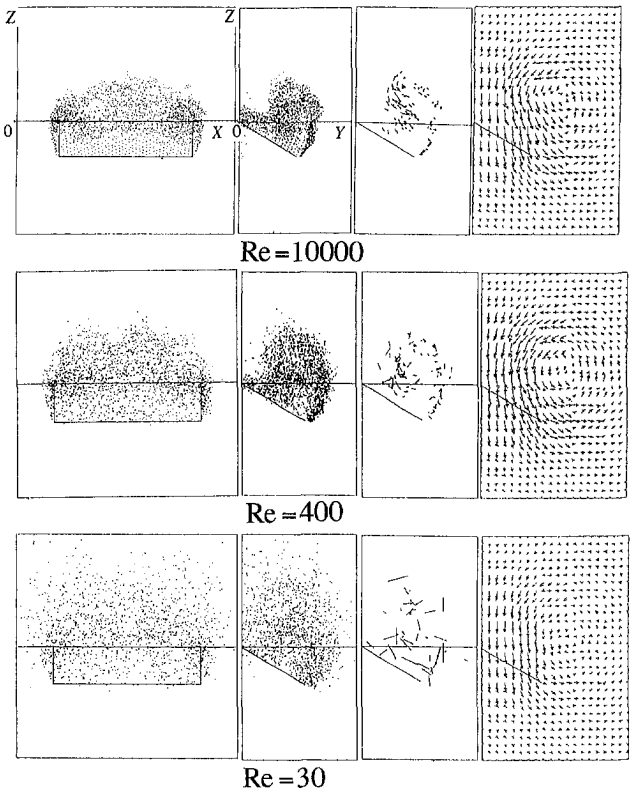

Fig. 8 Flowfield around the wing in the fling stage ($\theta = 2\pi/3$)

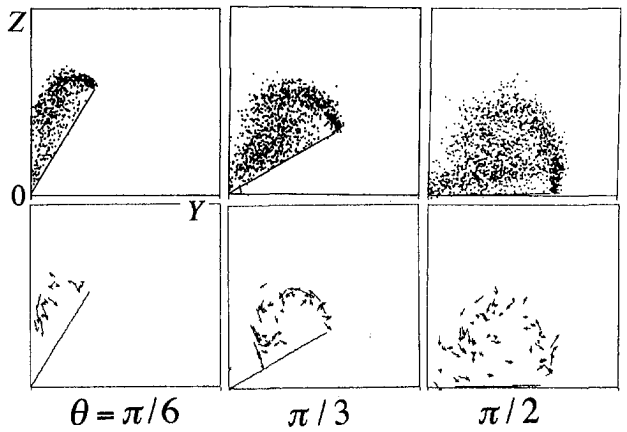

Fig. 9 Vortex sticks and stick traces around the wing in the fling stage (Re = 400)

$$\frac{\Phi_{a1}}{\partial t} - \frac{\Phi_{a2}}{\partial t} = \frac{\Gamma_a^t - \Gamma_a^{t-\Delta t}}{\Delta t} = \dot{\Gamma}_a \tag{7}$$

As the same method, that on the "b" point is expressed as

$$\frac{\Phi_{b1}}{\partial t} - \frac{\Phi_{b2}}{\partial t} = \frac{\Gamma_b^t - \Gamma_b^{t-\Delta t}}{\Delta t} = \dot{\Gamma}_b \tag{8}$$

The force on the perpendicular direction to the surface of the wing F is calculated by

$$F = \int pds = -\rho \sum_{j=1}^{n} \dot{\Gamma}_j \Delta s_j \tag{9}$$

where the term $\dot{\Gamma}_j$ represents the time-variations of the circulations in the jth panel, which is evaluated as shown in Eq. (7) and Eq. (8) and Δs_j is the area of the panel. All the Γ_j on the surface affect the force and they are ring-type. Therefore, the force remains the same whether it is calculated the spanwise or chordwise. The lift, which is the z-direction component of the force in Fig. 5, is expressed as

$$L = -\rho(\sum_{j=1}^{n} \dot{\Gamma}_j \Delta s_j) \sin\theta \tag{10}$$

where θ is the opening angle shown in Fig. 5. The moment on each axis M is expressed as

$$M = -\rho \sum_{j=1}^{n} \dot{\Gamma}_j \Delta s_j \Delta P_j \tag{11}$$

where ΔP_j is the distance from the x-axis (fling stage) or the z-axis (rotating stage) in Fig. 5 to the control point of the jth panel, but for the rotating stage, the term is multiplied by $\cos\theta$.

Numerical Results and Discussion. For easy comparison with the experimental results, the calculating conditions were made similar to the experimental conditions. The chord length c and the span R of the wing are 1.0 and 2.0, respectively; the time step Δt is 0.05; the softening parameter ϵ is 0.01; the angular velocity Ω is 1.0 both in the fling and rotating stages; and the distance from the z-axis to the middle of the wing span is 2.0. The results are represented as a function of the Reynolds number Re, the opening angle θ, and the rotating angle ϕ.

The flow patterns for various Reynolds numbers in the fling stage are shown in Fig. 8. The figures in the first and second columns represent the distributions of the vortex sticks in the z-x and z-y planes, respectively; and the third and last columns show the stick traces and the velocity fields in the z-y plane in the cross section at the middle of the wing span, respectively.

The distributions of the vortex sticks and the stick traces are scattered more at low Reynolds numbers. This explains the effect of the viscous diffusion. In the first column, the distribution of the vortex sticks is convex in structure, and this corresponds to the results obtained by flow visualization. The velocity fields show that a large circulation in the opposite direction to the opening is formed behind the leading edge of the wing.

The flow patterns for various opening angles in the fling stage are shown in Fig. 9. A large structure of the vortex shed from the leading edge is located near the leading edge as seen from the distribution of vortex sticks, and this agrees well with the results of flow visualization shown in Fig. 3. The stick traces show that the flow separates from the leading edge and reattaches to the wing with time.

The lift coefficient $C_L = L/(\frac{1}{2}\rho\Omega^2 c^2 S)$ in the fling stage is shown in Fig. 10 as a function of the opening angle. The maximum of the lift, regardless of the Reynolds number, occurs at an opening angle of about $\pi/2$. It is difficult to compare exactly these results with the experimental results by Spedding and Maxworthy (1986) because the angular velocity in their experiments changes with time. But the calculation results agree qualitatively with the experimental results because the lift is maxi-

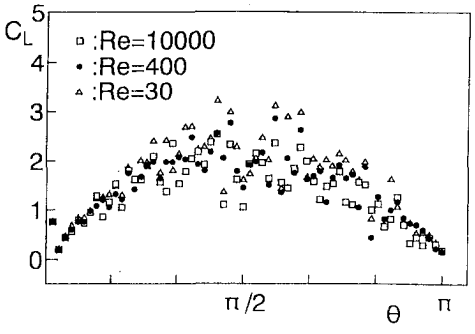

Fig. 10 Lift coefficient in the fling stage

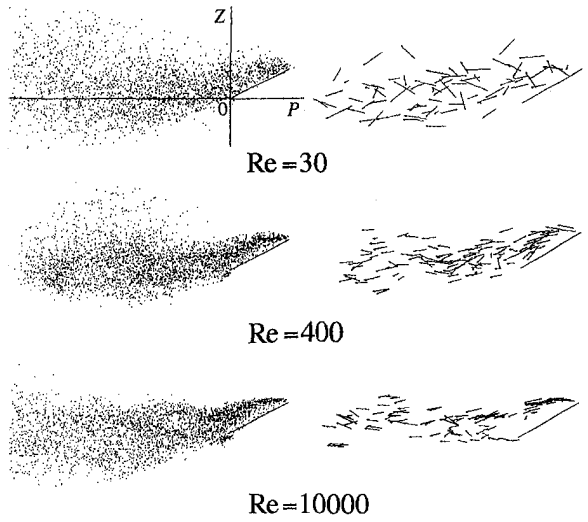

Fig. 11 Vortex sticks and stick traces around the wing in the rotating stage ($\theta = \pi/3$, $\phi = \pi/2$)

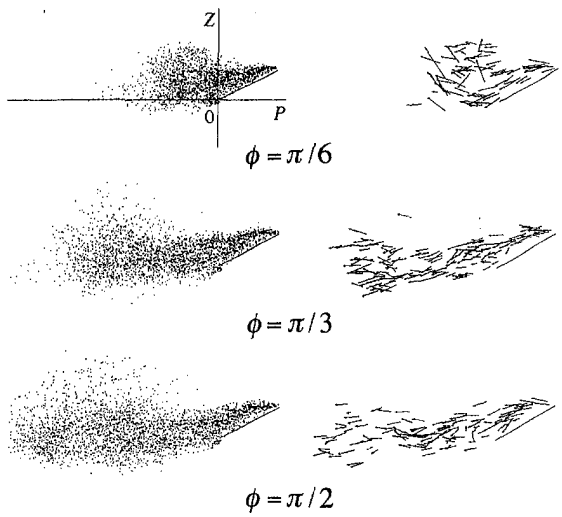

Fig. 13 Vortex sticks and stick traces around the wing in the rotating stage (Re = 400, $\theta = \pi/3$)

mum at an opening angle of $\theta = \pi/2$ and minimum at $\theta = 0$ and $\theta = \pi$.

The flow patterns for various Reynolds numbers in the rotating stage are shown in Fig. 11. In this calculation, the wing opens up to $\pi/3$ and moves to the rotating stage. In this figure P, which is fixed on the wing as shown in Fig. 11, represents an axis of coordinates in the horizontal and perpendicular plane to the span direction of the wing. At the Reynolds number Re = 10000, the region of the wake was narrower than the other two and the flow separated from the leading and trailing edges of the wing.

Under the same conditions as in Fig. 11, the flow patterns in the *Z-Q* plane are shown in Fig. 12. In this figure Q, which is also fixed on the wing in the rotating stage, represents the span direction of the wing. The velocity fields in the second column show that the flow near the center of the upper surface of the wing is accelerated by the tip vortices in the opposite direction.

The flow patterns for various rotating angles are shown in Fig. 13. Under the same conditions as in Fig. 13, the flow patterns in the *Z-Q* plane are shown in Fig. 14. The vortices of the convex type at the rotating angle $\phi = \pi/6$ flow along the trailing edge with an increase of the rotating angle ϕ because of the downwash by tip vortices. The velocity fields show that the downwash is deflected toward the outside because the outside tip vortex is stronger than the inside one.

In the first columns of Figs. 13 and 14, the vortex sticks are distributed in the direction opposite to the moving direction of the wing. This means that the vortices between the wings are connected to each other and it agrees well with the results of the flow visualization shown in Fig. 4.

The lift coefficients for various Reynolds numbers in the fling and rotating stages are shown in Fig. 15. This figure shows that the lift coefficient is almost independent of the Reynolds number in the rotating stage as well as in the fling stage. In this study,

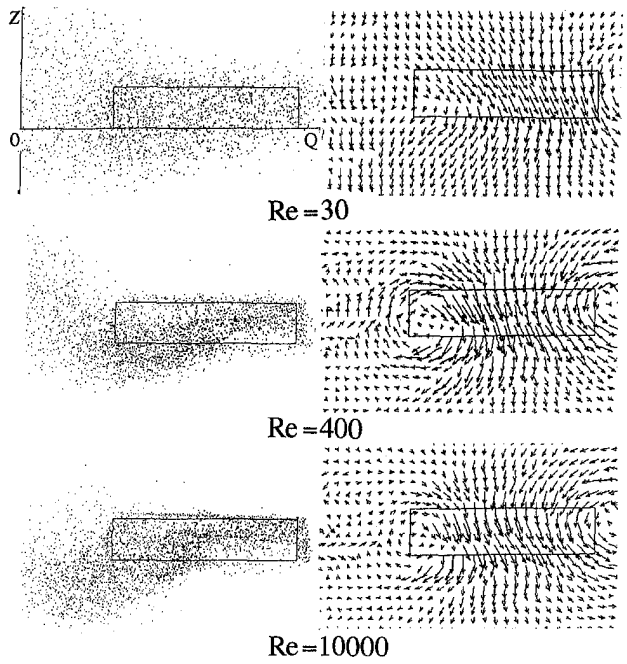

Fig. 12 Vortex sticks and velocity vectors around the wing in the rotating stage ($\theta = \pi/3$, $\phi = \pi/2$)

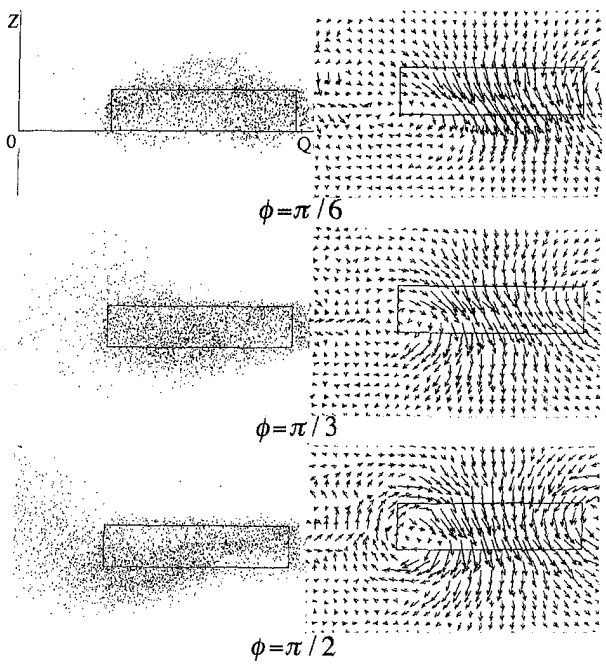

Fig. 14 Vortex sticks and velocity vectors around the wing in the rotating stage (Re = 400, $\theta = \pi/3$)

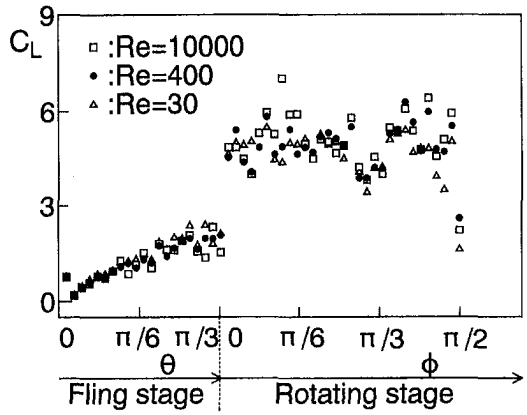

Fig. 15 Lift coefficient in the fling and rotating stages ($\theta = \pi/3$)

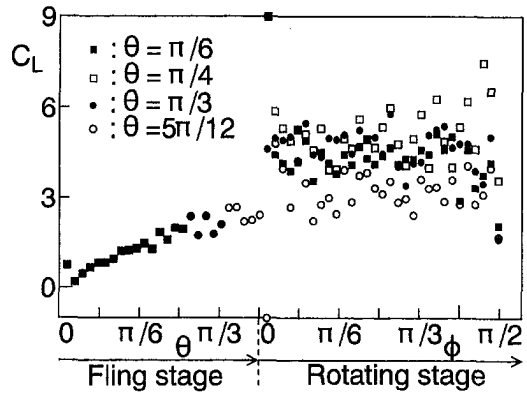

Fig. 16 Lift coefficient in the fling and rotating stages (Re = 30)

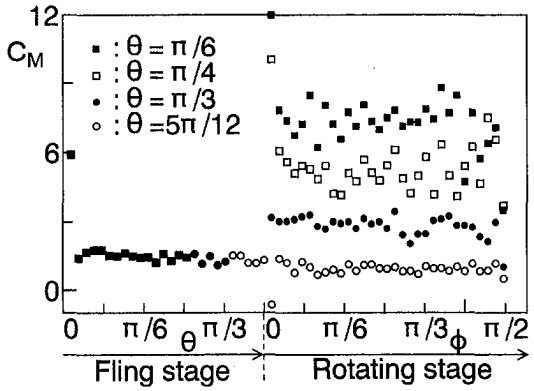

Fig. 17 Moment coefficient in the fling and rotating stages (Re = 30)

the angular velocity in the rotating stage Ω is unity as well as that in the fling stage. Therefore, the moving velocity of the edge at the middle of the span in the rotating stage is twice as large as that in the fling stage. If the lift coefficient is nondimensionalized by the middle speed of the wing span in the rotating stage, this coefficient in the rotating stage should be the quarter of the present value.

The lift coefficients for various opening angles in the fling and rotating stages are shown in Fig. 16. In the rotating stage, the lift coefficient for the opening angle of $\theta = 5\pi/12$ is about 3.0, but that for the other opening angles, which is about 5.0, represents the same value regardless of the opening angle.

Under the same conditions as in Fig. 16, the moment coefficient $C_M = M/(\frac{1}{2}\rho\Omega^2 c^2 SP)$ is shown in Fig. 17. In the rotating stage, the moment coefficient decreases monotonously as the opening angle increases. From Figs. 16 and 17, we can understand that at the opening angle of $\theta = \pi/3$ the lift coefficient is large and the moment coefficient is relatively small. At the opening angle of $\theta = 5\pi/12$ this is also small in comparison with the lift coefficient. However, in this case the lift seems not enough to support the body. This explains well the reason that small insects open their wings up to $\pi/3$ and rotate them when they are in hovering flight (Weis-Fogh, 1973).

Table 1 The Comparison of calculating speed between workstation (HP730) and GRAPE3A (unit:min)

VORTEX STICKS	10000	50000	100000
GRAPE	0.1	2.0	7.8
HP730	12.3	329.1	

A comparison of the calculating speed between a workstation (HP730) and the GRAPE3A is shown in Table 1. The workstation used for this calculation was the HP Apollo Model 730 G/CRX and had a CPU speed of 22 Mflops, while the peak speed of the GRAPE3A was 4.8 Gflops. When there are 50,000 vortex sticks in the flowfield, the calculating time for the induced velocity for one step is 329 minutes on of the workstation, but that on the GRAPE3A is 2 minutes as seen from Table 1. That is to say, the Grape3A can calculate 165 times as fast as the HP730.

Conclusions

The three-dimensional flows in the Weis-Fogh mechanism were studied by flow visualization and numerical simulation using the vortex method. In this study, the GRAPE3A hardware was used to calculate the induced velocity of the vortex sticks at high speed, and the viscosity of the fluid was represented by the random walk method.

The flow patterns by simulations agreed well with those of the flow visualization. And those around the wings, which are widely different from those in the two-dimensional flow, are strongly influenced by the tip vortices. The eddies near the leading edge of each wing in the fling stage take a convex shape because the eddies shed from both tips entrain the flows. The downwash in the rotating stage is deflected toward the outside because the outside tip vortex is stronger than the inside one.

The reason for the opening angle θ being $\pi/3$ for real insects' hovering flight was clarified by the calculation results for various opening angles,; at the opening angle the lift on the wing is large and the moment is relatively small.

By using the GRAPE3A hardware, the discrete vortex method could be calculated almost as fast as by a supercomputer, and it was proved that the GRAPE3A is a powerful tool for the vortex method.

In this study, we showed that the discrete vortex method is very effective for simulating this type of flow. However, the simulations reported in this paper, especially those for various Reynolds numbers, should be treated with caution, because there is no measurement to compare them with and the discrete vortex method is approximate due to rudimentary modeling of viscosity.

References

Beale, J. T., and Majda, A., 1982, "Vortex Methods. I: Convergence in Three Dimensions," *Mathematics of Computation,* Vol. 39, pp. 1–27.

Chorin, A. J., 1973, "Numerical Study of Slightly Viscous Flow," *Journal of Fluid Mechanics,* Vol. 57, pp. 785–796.

Kamemoto, K., 1993, "Ranryu Moderu Toshiteno Uzuhouno Hattensei," *Japan Society of Computational Fluid Dynamics,* Vol. 2, No. 1, pp. 20–29. (in Japanese)

Leonard, A., 1980, "Vortex Method for Flow Simulation," *Journal of Computational Physics.* Vol. 37, pp. 289–335.

Lighthill, M. J., 1973, "On the Weis-Fogh Mechanism of Lift Generation," *Journal of Fluid Mechanics,* Vol. 60, pp. 1–17.

Maxworthy, T., 1979, "Experiments on the Weis-Fogh Mechanism of Lift Generation by Insects in Hovering Flight," *Journal of Fluid Mechanics,* Vol. 93, pp. 47–63.

Ogami, Y., and Akamatsu, T., 1991, "Viscous Flow Simulation Using the Discrete Vortex Method—The Diffusion Velocity Method," *Computers and Fluids,* Vol. 19, Pt. 3, pp. 433–441.

Okumura, S. K., Makino, J., Ito, T., Fukushige, T., Sugimoto, D., Hashmoto, E., Tomita, K., and Miyakawa, N., 1992, "GRAPE-3: Highly parallelized Special Purpose Computer for Gravitational Many-Body Simulations," *Proceedings of the Twenty-Fifth Hawaii International Conference on System Sciences,* Vol. 1, pp. 151–160.

Sarpkaya, T., 1989, "Computational Methods with Vortices," ASME JOURNAL OF FLUIDS ENGINEERING, Vol. 111, March, pp. 5–52.

Shirayama, S., et al., 1985, "A Three-dimensional Vortex Method," AIAA Paper, 85–1488, pp. 14–24.

Spedding, G. R., and Maxworthy, T., 1986, "The Generation of Circulation and Lift in a Rigid Two-Dimensional Fling," *Journal of Fluid Mechanics,* Vol. 165, pp. 247–272.

Sugimoto, D., 1994, "Senyo Kesanki Niyoru Simulation," *Asakura Shoten* (in Japanese).

Weis-Fogh, T., 1973, "Quick Estimates of Flight Fitness in Hovering Animals, Including Novel Mechanism for Lift Production," *Journal of Experimental Biology,* Vol. 59, pp. 169–231.

B. Newling
Graduate Student.

S. J. Gibbs
Post-Doctoral Research Fellow.

J. A. Derbyshire
Graduate Student.

D. Xing
Graduate Student.

L. D. Hall
Professor of Medicinal Chemistry.

Herchel Smith Laboratory for Medicinal Chemistry, Forvie Site, Robinson Way, Cambridge, UK, CB2 2PZ

D. E. Haycock
Process Scientist.

W. J. Frith
Physical Chemist.

S. Ablett
NMR Spectroscopist.

Unilever Research Laboratory, Colworth House, Sharnbrook, Bedford, UK, MK44 1LQ

Comparisons of Magnetic Resonance Imaging Velocimetry With Computational Fluid Dynamics

The flow of Newtonian liquids through a pipe system comprising of a series of abrupt expansions and contractions has been studied using several magnetic resonance imaging (MRI) techniques, and also by computational fluid dynamics. Agreement between those results validates the assumptions inherent to the computational calculation and gives confidence to extend the work to more complex geometries and more complex fluids, wherein the advantages of MRI (utility in opaque fluids and noninvasiveness) are unique. The fluid in the expansion-contraction system exhibits a broad distribution of velocities and, therefore, presents peculiar challenges to the measurement technique. The MRI protocols employed were a two-dimensional tagging technique, for rapid flow field visualisation, and three-dimensional echo-planar and gradient-echo techniques, for flow field quantification (velocimetry). The computational work was performed using the FIDAP package to solve the Navier-Stokes equations. The particular choice of parameters for both MRI and computational fluid dynamics, which affect the results and their agreement, have been addressed.

Introduction

The use of computational fluid dynamics (CFD) is increasingly widespread across a range of industries. In common with all simulation-based methodologies, CFD analyses require that certain assumptions be made, for example with regard to flow boundary conditions and the shear and extensional properties of the fluid. Issues such as computation sensitivity to the meshing strategy (e.g., mesh density, moving meshes, etc.) also depend upon the specific flow problem to be addressed. Techniques which can be used to validate such assumptions, particularly by quantitative measurement of the flow-field, are important. One such method is magnetic resonance imaging (MRI).

The considerable potential of MRI to study industrial process-related flow phenomena is becoming increasingly recognized (Hall and Carpenter, 1992; Gladden, 1994; Sinton and Chow, 1991; Fukuda et al., 1985; Agemura et al., 1995), partly because the technique is noninvasive (in contrast to hot-wire anemometry or particle tracking measurements), but more importantly because it can be used with optically opaque systems (unlike laser doppler anemometry) and in two or three spatial dimensions (Maier et al., 1989). However, with few exceptions (Agemura et al., 1995; Derbyshire et al., 1994), the type of flow fields which have been studied bear little resemblance to those which can occur inside a complex processing plant (e.g., around manifolds or mixers). In particular, the flow fields inside a processing plant, even within the laminar regime, may be highly textured (i.e., spatially inhomogeneous) due to vessel geometry. The problems associated with MRI of complex flow fields are also prevalent in clinical MRI, where much work has been done on fluid flow in complex geometries, such as stenoses (Gatenby et al., 1993) and bifurcations (Dumoulin et al., 1987; Vu et al., 1993), to study the type of flow fields which may occur in vivo (Moore et al., 1994). A comparison of CFD and MRI results has recently been undertaken in this context (Sun et al., 1992).

As part of a general, systematic study of the capabilities of MRI for visualisation of the flow of complex materials in complex geometries, work in this laboratory has explored the combination of several different MRI methods to visualise and quantify flow fields. We have deliberately used that same combination in the present study and report the determination by MRI of the textured flow fields generated within a small axisymmetric pipe system, consisting of two expansions separated by a constriction (Fig. 2).

The flow fields associated with laminar flow of a Newtonian fluid (50 percent sucrose solution), were calculated using a commercial CFD software package and the results compared

Contributed by the Fluids Engineering Division for publication in the JOURNAL OF FLUIDS ENGINEERING. Manuscript received by the Fluids Engineering Division August 8, 1995; revised manuscript received April 15, 1996. Associate Technical Editor: J. H. C. Humphrey.

with those obtained from MRI. This pipe system exhibits a wide variation in fluid velocities, including slow recirculation in two zones, and places significant demands upon the design of the MRI measurement. A variety of MRI motion sensitisation techniques were evaluated and the associated advantages and disadvantages established. As will be seen, the MRI measurements are in very good agreement with the CFD simulation values and encourage future studies of more complex flow geometry applications (e.g., those with some time dependence) and more complex fluids (e.g., those which are optically opaque or those which exhibit extensional viscosity effects, making CFD more complicated).

Motion Encoded MRI

One of the greatest strengths of the MRI technique is the variety of physico-chemical parameters which may provide image contrast, dependent upon the MRI protocols employed. Information about fluid motion is obtained by encoding the position of a nuclear ensemble, allowing some fixed time to elapse, and observing the displacement. Position may be encoded in either the magnitude or the phase of local nuclear magnetisation in that plane transverse to the static magnetic field (Caprihan and Fukushima, 1990; Pope and Yao, 1993).

This study followed the precedent (Derbyshire et al., 1994) of using a combination of two methods to study fluid motion in the pipe system, one a magnitude and the other a phase based technique. In the magnitude *tagging* method, sample magnetization was nulled in an orthogonal grid pattern, prior to the imaging section of the procedure. A delay between the preparation and imaging sections was incremented during a series of measurements, permitting the distortion of the grid with time to be observed (Axel and Dougherty, 1989; Mosher and Smith, 1990). Alternating radiofrequency (RF) excitations and delays with accompanying magnetic field gradients (hereafter, simply *gradients*) impose the tag pattern upon the sample in an application of the DANTE technique (Morris and Freeman, 1978). The number and duration of pulses, duration of interpulse delays, and magnitude of accompanying gradients define the grid dimensions. The two-dimensional tagged images give a qualitative impression of fluid behavior in the pipe system.

The pulsed field gradient (PFG) approach (Stejskal and Tanner, 1965) has found much favor, where quantification is required, for its general applicability in the measurement of a wide range of fluid velocities (mm/s to m/s). In very fast or turbulent flows, other techniques may be more appropriate (Lee et al., 1991), but in this study PFG provides a relatively rapid MRI method for velocimetry in three-dimensions and at the same spatial resolution as the image acquisition.

The PFG approach relies upon the application of gradients to encode displacement. Consider an ensemble of nuclei at $\mathbf{r}$ as a gradient, $\mathbf{g}$, is applied for a fixed time, δ. Magnetization in that plane transverse to $\mathbf{B}_0$ (the local, static, magnetic field) evolves, for the case of negligible motion during δ, with a frequency

$$\omega = \gamma[B_0 + (\mathbf{g}\cdot\mathbf{r})], \tag{1}$$

advancing in phase $\phi = \gamma\delta(\mathbf{g}\cdot\mathbf{r})$ relative to the Larmor frequency, $\omega_0 = \gamma B_0$ (γ is the magnetogyric ratio, a constant particular to each nuclear species). Following an opposite δ-length gradient (beginning a time Δ after the start of the first) $\phi = 0$ for a stationary nuclear ensemble. A moving nuclear ensemble, undergoing a displacement $\mathbf{R}$ during Δ has a final, relative phase $\phi = -2\pi(\mathbf{q}\cdot\mathbf{R})$, where $\mathbf{q} = (1/2\pi)\gamma\delta\mathbf{g}$ (Callaghan, 1991). The signal from a nuclear ensemble in the volume element at $\mathbf{r}$ in an MR echo, image acquisition depends upon sample motion;

$$E(\mathbf{q}, \mathbf{r}, \Delta) \propto \int_V \mathcal{P}(\mathbf{R}|\Delta, \mathbf{r}) \exp[-i2\pi(\mathbf{q}\cdot\mathbf{R})]d^3\mathbf{R}, \tag{2}$$

where $\mathcal{P}(\mathbf{R}|\Delta, \mathbf{r})$ is the probability that the ensemble undergo a displacement $\mathbf{R}$ during the interval Δ. For the case of Brownian diffusion superposed on coherent flow, Eq. (3) holds (Stejskal and Tanner, 1965)

$$E(\mathbf{q}, \mathbf{r}, \Delta) \propto \exp(-4\pi^2\mathbf{q}\cdot\mathcal{D}(\mathbf{r})\cdot\mathbf{q}\Delta' + i2\pi\mathbf{q}\cdot\mathbf{v}(\mathbf{r})\Delta). \tag{3}$$

This simple model, a complex sinusoid with Gaussian attenuation, forms the basis upon which data from a complete, MRI flow measurement (several images acquired at different values of $\mathbf{q}$) are evaluated for local velocity, $\mathbf{v}(\mathbf{r})$, and diffusivity, $\mathcal{D}(\mathbf{r})$ ($\Delta' = (\Delta - \delta/3)$, correcting for motion during non-zero δ).

Analysis of the $\mathbf{q}$-space samples is a parameter estimation within the model of Eq. (3) using a Bayesian analysis (Xing et al., 1995), which yields a map of $\mathbf{v}$, $\mathcal{D}$ (assumed isotropic) and an estimate of the errors in fitting these parameters, by maximising the posterior probability density (in terms of v and $\mathcal{D}$) at each voxel. The principle advantage of this approach, over the more common Fourier transformation in the $\mathbf{q}$-space dimension, lies in the availability of an error estimate.

The PFG pair (separated by the interval Δ) can precede the imaging section of an MRI protocol (as does the DANTE tagging) or be interleaved (as Fig. 1(*b*) and (*c*)) to reduce overall measurement time.

Flow Simulation

The flow simulation was undertaken using the FIDAP (version 7.0) finite element fluid dynamics analysis package (from Fluid Dynamics International, % Applied Computing & Engineering Ltd., Science Park South, Birchwood, Warrington, Cheshire, WA3 7BH, United Kingdom), which was installed on a Silicon Graphics Iris Indigo workstation (33 MHz R3000 processor, 48 MByte main memory).

Nomenclature

$\mathbf{B}_0$ = local, static, magnetic field
CFD = computational fluid dynamics
$\mathcal{D}$ = diffusivity tensor ($=\mathcal{D}_{00} = \mathcal{D}_{11} = \mathcal{D}_{22}$)
E = peak echo signal
EPI = echo planar imaging
$\mathbf{g}$ = motion encoding gradient ($=g_0 + g_1 + g_2$)
$\mathbf{k}$ = positional wave-vector
MRI = magnetic resonance imaging
NMR = nuclear magnetic resonance
$\mathcal{P}$ = propagator function
PFG = pulsed field gradient
$\mathbf{q}$ = displacement wave-vector ($=\gamma\delta\mathbf{g}/(2\pi)$)
$\mathbf{R}$ = displacement of a nuclear ensemble during Δ
RF = radiofrequency
$\mathbf{r}$ = position of a nuclear ensemble
SNR = signal to noise ratio
TE = time between initial RF excitation and echo
TR = time between consecutive RF excitations
$\mathbf{v}$ = velocity of a nuclear ensemble ($=v_0 + v_1 + v_2$)
Δ = interval between leading edges of $\mathbf{g}$ and $-\mathbf{g}$ gradients of a PFG pair
Δ' = effective Δ, for non-zero δ ($=\Delta - \delta/3$)
α = RF pulse flip angle
δ = duration of $\mathbf{g}$
γ = magnetogyric ratio
ϕ = phase of magnetisation, in the plane transverse to $\mathbf{B}_0$, for a nuclear ensemble
ω = precession frequency of a nuclear ensemble
ω_0 = the Larmor frequency ($=\gamma B_0$)

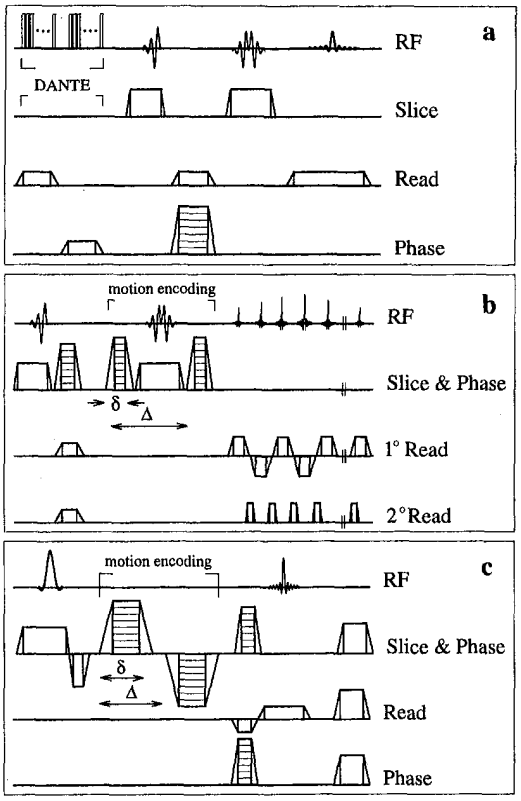

Fig. 1 MRI protocols used to obtain velocity encoded images. Each diagram shows the history of RF transmission/reception and gradient application in 3 orthogonal directions. (*a*) DANTE magnetization preparation: two trains of short, RF pulses with accompanying gradients (orthogonal to the tag plane in each case). The following Hahn spin-echo imaging sequence is made slice selective by use of two, shaped RF pulses (Roberts et al., 1990, Roberts et al., 1993). An MRI echo follows, as signal is induced in the probe by the sample. (*b*) A spin-echo EPI transient with interleaved PFG unit (δ = 1 ms, Δ = 18.125 ms). A train of gradient recalled echoes is collected under the spin-echo envelope (TE = 100 ms). (c) A gradient recalled echo transient (TE = 21.54 ms) with interleaved PFG unit (δ = 1 ms, Δ = 12 ms). The final (spoiler) gradient in each direction dephases any residual magnetization transverse to B_0, which could interfere with the subsequent transient.

The axial symmetry associated with the pipe system enabled this three dimensional flow problem to be studied with a two-dimensional analysis. A rectangular (four node) finite element mesh was utilized, with axial node spacings of 9.8×10^{-2} (inlet and outlet pipes), 3.7×10^{-2} (central contraction) and 3.3×10^{-2} cm (expansion sections, to the contraction corners). The solution, consisting of computed values of axial and radial velocity components at each node, was interpolated (a process facilitated by the use of a rectangular mesh) to provide values at each positional coordinate in the velocity maps derived from the MRI data, in which the volume element (voxel) dimensions were $(7.6 \times 10^{-2})^3$ cm. To demonstrate the independence of the solution from the mesh, the calculation was repeated with a coarser, non-rectangular, four node mesh, (node spacing between 4.9×10^{-2} cm and 1.3×10^{-1} cm)) with no discernible change.

The flow rate conditions were chosen to ensure laminar flow throughout the pipe system (a nominal Reynolds number, based upon the central, 0.59 cm diameter contraction region, is approximately 40). There was assumed to be no wall slip and flow in the inlet pipe was Newtonian and laminar. The solution, based upon the Navier-Stokes equations, was derived using a successive substitution (or successive approximation) approach (Burden and Faires, 1995) with convergence being achieved within 25 iterations (approximately 13 minutes processing time).

Experimental Procedures

MRI measurements were performed in a 1 m, horizontal bore, superconducting, 2 *T*, Oxford Magnet Technology magnet attached to a Bruker MSL 400 console, running Tomikon imaging software (version 890601, Bruker Medizin Technik GmBH., Karlsruhe, Germany). The imaging gradients were generated using Maxwell (axial) and Golay (transverse) coil windings on a 20.0 cm internal diameter former. Current was supplied to each winding set by two Tecron amplifiers (models 7560 and 7570, Crown International Inc., Elkhart, In., USA) arranged in a master/slave configuration (Carpenter et al., 1989). The pipe system ran through a home-built, 8.5 cm diameter, eight strut, quadrature, RF probe (Hayes et al., 1985), which was used to both transmit and receive RF radiation.

The flow system of Fig. 2 was oriented axially along the magnet bore. Fluid was supplied to the pipe system from a constant head reservoir and, at the outflow, fluid was pumped from an open collection vessel back to the reservoir. DANTE tagged images were obtained using a ca. 1 mM solution of copper sulphate in tap water. PFG measurements were carried out on a solution of sucrose in tap water (50 percent by mass), which had a density 1.2 times that of water and a viscosity 15.4 times that of water at 20°C (Norrish, 1967). Fluid temperature was monitored during the MRI measurement, using a thermocouple in the constant head reservoir. Volume flow rates were also recorded using a stopwatch and graduated cylinder. The several MRI protocols employed are shown in Fig. 1.

(*a*) The DANTE tagging magnetization preparation consisted of 10 short RF pulses (each 50 μs and separated by 470

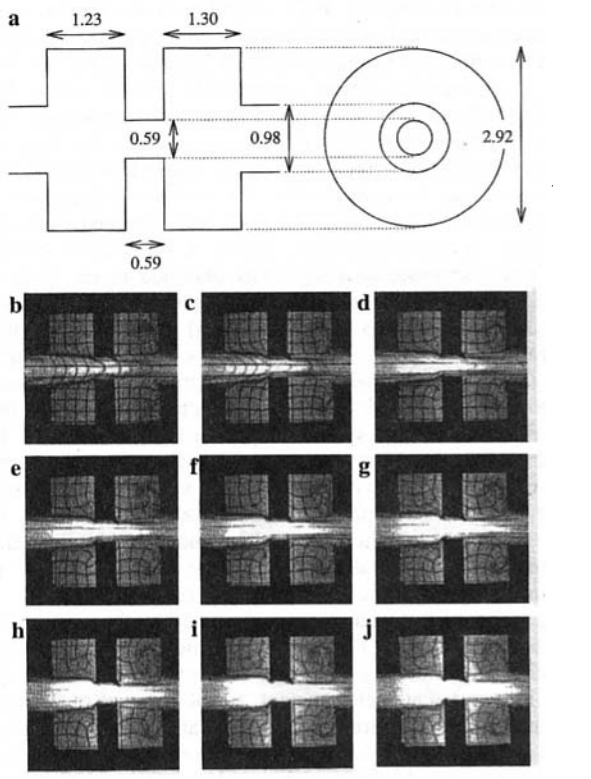

Fig. 2 (*a*) The expansion-contraction-expansion-contraction pipe system (lengths in cm). Fluid flow was horizontal and from left to right. Pipes were constructed from polymethylmethacrylate, which is both nonmetallic and transparent to RF radiation. (*b*) Planes of DANTE-nulled magnetization (dark lines) in a solution of copper sulphate in tap water, flowing at 101.3 ± 0.5 ml/min. The delay between tagging and imaging is 90 ms in (*b*) and is incremented by 120 ms in each of (*c*)–(*j*). Image brightening is due to an influx of nuclear ensembles from outside the probe in the interval between preparation and imaging sequences and, hence, increases from (*b*)–(*j*).

μs), which nulled magnetization in planes at 0.2 cm intervals, orthogonal to the accompanying gradient. The imaging sequence, which follows, is the spin-warp adaptation (Edelstein et al., 1980) of the Hahn spin-echo (Hahn, 1950) imaging sequence (Fig. 1(a)). The protocol (Fig. 1(a)) is repeated, with a different value of phase encode gradient, for each pixel required in the phase encode direction (128 in the images in Fig. 2) at 1200 ms intervals. During this time (TR), sample magnetization recovers back toward thermal equilibrium according to the time constant T_1. If TR <ca.5T_1 recovery of nuclear magnetisation between transients is incomplete (*partial saturation*) and signal is reduced as TR is decreased. T_1 for water is of the order **s** and TR (as herein) is usually kept <ca.5T_1 in order that overall measurement time is not prohibitively long. Both the 90 and 180 deg pulses are shaped RF excitations (Roberts et al., 1990; Roberts et al., 1993) and are made slice-selective by simultaneous gradient application. The 180 deg pulse reverses phase dispersion (and consequent signal attenuation) caused by $\mathbf{B}_0$ inhomogeneities and gradient application in the time between the 90 and 180 deg pulses, so as to form an echo an equivalent time after the 180 deg pulse. The time taken to apply the DANTE preparation (5.2 ms) leads to some spatial misregistration, as the fluid is in motion during this interval. The principle effect is some blurring of the dark (tagged) lines in the image (Fig. 2(b)), which leads to uncertainties in velocity measurement using this DANTE technique (q.v.), but does not detract from the qualitative impression of fluid behavior given by the method.

(b) The PFG motion encoding pair was interleaved with a spin-echo, echo-planar, ultra-fast imaging sequence (EPI) (Fig. 1(b)), which samples a boustrophodonic locus in **k**-space to obtain a complete two-dimensional image in a single ca. 100 ms transient (Mansfield, 1977; Stehling et al., 1991). A train of echoes is recalled by gradient reversal (which does not counteract the effects of $\mathbf{B}_0$ inhomogeneity like the spin-echo above) under a spin-echo envelope, generated by slice selective 90 and 180 deg pulses (see [a]). The EPI method is extremely sensitive to $\mathbf{B}_0$ inhomogeneities and inaccuracies in the very rapid gradient switching, which both cause image distortions. These distortions may be corrected by the complex subtraction of a phase template image, acquired with no secondary read gradients (Fig. 1(b)) (Derbyshire, 1995). A 64 × 64 × 64 voxel MRI three-dimensional image was obtained in ca. 5 minutes (64 repeats of the protocol of Fig. 1(b)) at each of twenty magnitudes of **g** (up to 4×10^4 Hz/cm) and, therefore, twenty different values of **q**. These **q**-space samples were acquired three times, with the motion encoding gradient applied successively in each of three orthogonal directions (one axial to the magnet bore and pipe system, the other two transverse). Each set of **q**-space samples was independently analyzed to give a three-dimensional map of v_i and $\mathcal{D}_{ii}$, the velocity and diffusivity in the direction of applied motion encoding gradient, g_i (i = 0, 1, 2). Taken together, these three maps constitute a three-dimensional representation of the flow field within the pipe system, from which the following results were extracted.

(c) The EPI sequence was compared with a gradient recalled echo sequence (Fig. 1(c)), in which only a single gradient-echo and, therefore, a single line of a Cartesian **k**-space raster is sampled at each transient. At the expense of increasing the time taken to acquire each **q**-space sample to ca. 30 minutes (for a 64 × 64 × 64 voxel image, the protocol of Fig. 1(c) is repeated (64 × 64) times at intervals of TR = 400 ms), the duration of each transient (TE) was reduced to 20 ms (in MRI velocimetry the fluid motion during a long imaging transient may lead to misregistration errors (q.v.)). The use of a gradient-echo rather than a spin-echo generally leads to shorter transients, as there is no 180 deg pulse application, but $\mathbf{B}_0$ inhomogeneities lead to a reduction in signal intensity. Careful adjustment of $\mathbf{B}_0$ and the use of a small sample relative to the size of the magnet bore (see Experimental Procedures) can minimize this problem. A gradient-echo implementation also allows for the use of an excitatory pulse of lower power (reduced flip angle, α) than an α = 90 deg pulse and the maximization of signal intensity by the choice of $\alpha = \exp(-\mathrm{TR}/T_1)$ (Ernst et al., 1987). The results in this paper were obtained with α = 90 deg. In order that the entire measurement should not be prohibitively time consuming, only seven **q**-space samples were acquired (greatest **g** again 4×10^4 Hz/cm).

Two factors govern the choice of **q**-space samples in [b] and [c]; the closest two values of **q** must satisfy the Nyquist sampling theorem (i.e., the difference in ϕ between them, for the highest fluid velocity under consideration, must not exceed 180 deg, lest aliasing occur) and the maximum applicable **g** is generally hardware limited. Given the latter, upper bound and knowing approximately the velocity sensitivity required of the PFG MRI measurement, suitable values of δ and Δ may be chosen (Eq. (3)).

Results

In Fig. 2, the general form of the velocity field inside the pipe system is clearly shown by the distortion of the (dark) tag grid. The tags are separated by 0.2 cm and are ca. 0.07 cm wide. The DANTE-nulled magnetisation recovers (according to the time constant T_1) between preparation and imaging sequences and the tags are no longer visible when this delay exceeds ca. 1.5 s. That resolution is insufficient to show the very slowest recirculant velocities and although improvements to the tagging approach have been suggested (Fischer et al., 1993) to increase its suitability for quantification, the implementation used herein is sufficient to give a qualitative impression of the velocity field in the pipe system. Fluid moving rapidly along the pipe system axis washes tagged ensembles out of the frame within ca. 500 ms, whereas the tags persist in the expansions. In both expansion sections some fluid recirculates, away from the axis at the contraction wall and then back toward the entry pipe. The 0.59 cm contraction causes the fluid to enter the second expansion at a higher velocity than that into the first, which leads to a more pronounced recirculation in the second expansion. All these features are confirmed by FIDAP calculation.

Figure 3 shows greyscale maps of axial velocity, in a plane through the centre of the pipe system, and accompanying graphs of these velocities. Those velocity maps were calculated from EPI and gradient-echo MRI data and using FIDAP, and are extracted from three-dimensional maps of axial velocity in the pipe system. The EPI derived velocity map is clearly incomplete and noisy. Zero values of velocity in the 0.59 cm contraction and the second expansion, and the velocity spike, arise from a failure to fit Eq. (3) to the MRI data at these voxels. Those inconsistencies are caused by significant fluid motion during each imaging transient. At the velocities under consideration, the fastest moving nuclear ensembles traversed several pixels during the 100 ms EPI transient. All subsequent analysis considers velocities derived from gradient-echo MRI data (22 ms transient), which are shown to be comparable with the FIDAP solution. The flow fields show sequential deceleration, acceleration and deceleration of the sucrose solution at corresponding points along the axis of the pipe system. In the FIDAP solution, the peak axial velocity inside the 0.59 cm contraction is approximately 14.5 cm/s, whereas an ideal parabolic profile would require a peak velocity of 18.8 cm/s. This contraction section is too short (0.59 cm) for a parabolic flow profile to fully develop. The peak axial velocity in the MRI map is 12.1 cm/s, which occurs within 0.1 cm of the end of the 0.59 cm contraction. MRI and FIDAP axial velocities along the centerline of the pipe system are compared in Fig. 4(a). Although FIDAP suggests a greater peak axial velocity, the form of the lines is similar; the correlation coefficient, r, between the two velocity series is 0.989 over 55 points.

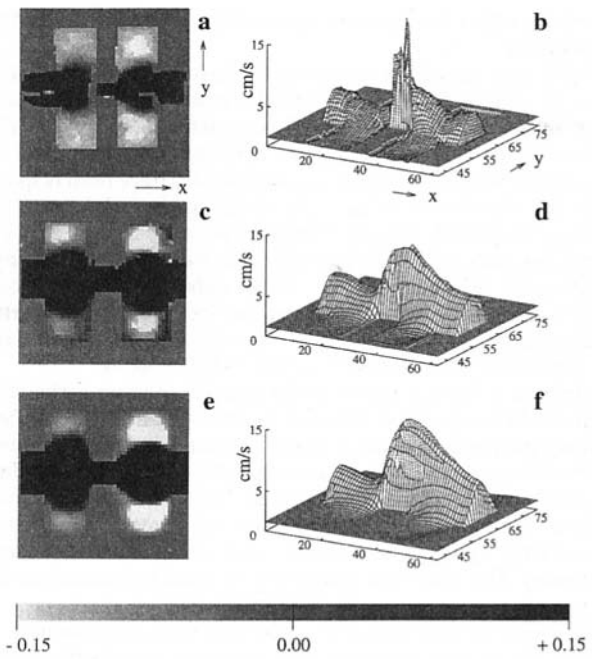

Fig. 3 *(a)* **A map of EPI derived axial (*x*-direction) velocity in a plane through the centre of the pipe system. The brightness of each pixel represents velocity: background mid-grey is zero, brighter velocities are in the $-x$-direction, darker in $+x$. The bar shows the grey scale in cm/s. Velocities outside this range appear as white ($-x$) or black ($+x$). A graph of these velocities is shown in (*b*). Equivalent maps and graphs are shown of (*c*, *d*) gradient-echo derived velocities and (*e*, *f*) the FIDAP solution.**

Half way along the first expansion section FIDAP and MRI axial velocities were extracted from the three-dimensional velocity map and subjected to a circumferential averaging procedure. The position of the pipe center was calculated from first spatial moments and velocity values at each pixel were sorted according to their radial position. These velocities were grouped into bins of a fixed size (20 samples) to give increasing radial resolution at the edges of the pipe. The mean velocity of each bin is shown, for both FIDAP (solid line) and MRI (points) velocities in Fig. 4(*b*). The error bars on the MRI velocities indicate the standard error in the mean over each radial bin. Over 53 radial points, r between MRI and FIDAP velocities is 0.999 and 0.996 in the first and second expansions, respectively. Figure 4(*c*) shows the circumferentially averaged estimate of error (and the standard error over each radial bin) in the Bayesian calculation of the fluid velocities of Fig. 4(*b*). The Bayesian error, which is calculated for every voxel in the velocity map, includes uncertainties in the fitting of equation 3 to the signal at each voxel along with uncertainties due to imaging noise. The very smallest measured velocities are of the same order as that error (the six outermost radial bins). Close to the pipe system axis (first radial bin), the error estimate corresponds to <1 percent of the measured velocity, and to 15 percent at a radial position of 1.12 cm.

Figure 4 also shows three slices extracted from the three-dimensional map of *transverse* velocity and their counterparts from the FIDAP solution. In the first expansion section fluid converges as it enters the 0.59 cm contraction. The FIDAP solution shows a peak convergent velocity of 1.91 cm/s either side of the slice centre. The MRI velocities are not perfectly symmetrical about the contraction, but the average of the peak convergent velocities either side of the center is 1.62 cm/s (standard deviation 0.25 cm/s). Within the second expansion, fluid near the centre of the pipe system diverges (as it emerges from the contraction) and fluid nearer the walls converges (as it recirculates back into the central stream). The peak convergent velocity is 0.62 cm/s in the FIDAP solution and 0.55 cm/s (s. d. 0.14 cm/s) in the MRI velocity map. Nearing the next contraction wall, the divergent fluid motion dominates. The peak divergent velocity is 0.81 cm/s from FIDAP and 0.91 cm/s (s. d. 0.03 cm/s) from MRI.

Discussion

Although the velocities from the FIDAP computation and MRI measurements are in very clear overall agreement, there are some discrepancies.

There are errors inherent to any MRI measurement of flow due to the finite duration of each transient. During the time interval between the PFG pair and the read imaging gradients, further displacement of nuclear ensembles occurs. An ensemble may, thus, have moved to a different voxel before positional encoding, which would result in spatial misregistration in the velocity map. A spin ensemble with a velocity of 15.0 cm/s traversed only one pixel between motion encoding and positional encoding during the gradient-echo acquisition of Fig. 1, and errors arising from this misregistration at the flow rate under consideration were deemed negligible. (This is in contrast to the gross misregistration observed in EPI velocity maps.) Addi-

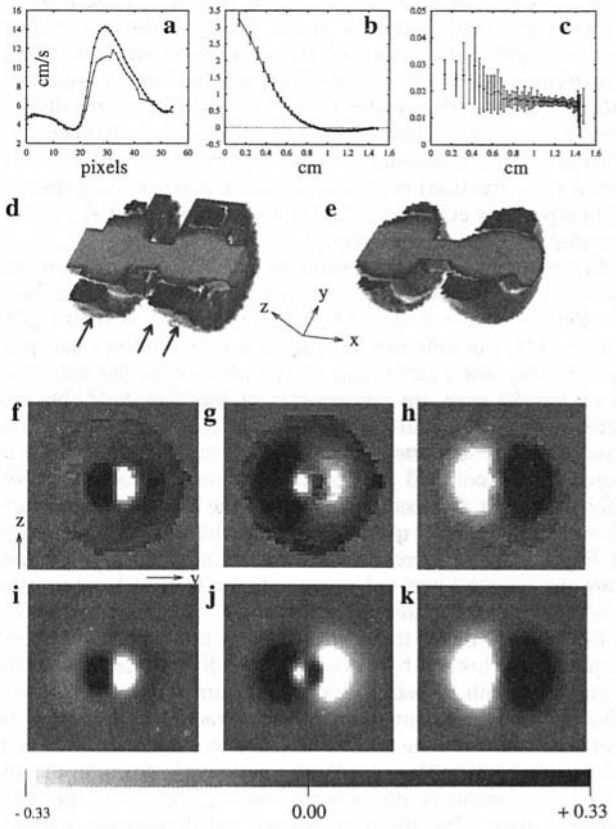

Fig. 4 *(a)* **A graph of axial velocity vs position along the centreline of the pipe system; upper curve the FIDAP solution, lower curve MRI derived velocities. (*b*) A graph of circumferentially averaged axial velocity half way through the first expansion vs radial position. The points are MRI derived velocities (error bars show the standard error in the circumferential mean), the line shows the FIDAP solution. (*c*) A graph of circumferentially averaged error estimates for the velocities of (*b*). The error includes uncertainties due to image noise and in the fitting of Eq. (3) to the *q*-space samples at each pixel. Cutaway three-dimensional maps of axial velocity calculated (*d*) from MRI data and (*e*) using FIDAP. Greater $+x$-velocities are increasingly light grey and $-x$-velocities are represented by darker shades. (*f* –*k*) are maps of a transverse (*y*-direction) velocity. Background grey is zero and the bar shows the grey scale in cm/s. Velocities outside this range appear as white ($-y$) or black ($+y$). The positions of the three slices, (*f* –*h*), in the pipe system are indicated by the arrows in (*d*) ((*f*) is leftmost). These *y*-velocity maps were calculated from MRI data. (*i*–*k*) are corresponding slices from the FIDAP solution.**

tionally, during application of the PFG pair, nuclei may experience not only displacement, but also acceleration; consequently ϕ becomes a measure of velocity averaged over this time. Higher order motion terms (including acceleration) may be responsible for some disagreement between FIDAP and MRI, especially in regions of high shear such as the entrance to the 0.59 cm contraction. The peak centerline axial acceleration, from the graph of FIDAP centerline velocities (Fig. 4(a)), is 1.4 cm/s/voxel. This acceleration is approximately constant over 3 voxels (23–25), which contain fluid with a mean velocity of 8.61 cm/s (113.3 voxel/s). During Δ a spin ensemble traverses 1.4 voxels at that mean velocity and might, thus, experience a change in velocity of up to 2.0 cm/s (a ca. 20 percent change in velocity), so that ϕ reflects some average over a velocity range of 2 cm/s.

The effect of acceleration upon the measurement might be reduced by adjusting the MRI protocol. Thus, the contribution to ϕ from velocity is proportional to the product $\delta\Delta$, whereas the contribution due to acceleration (ignored in Eq. (3)) is proportional to $\delta\Delta(\delta + \Delta)$. That acceleration contribution is minimised (for a given $\delta\Delta$ product) when $\delta = \Delta$, but a finite time must be allowed for switching of the large motion encoding gradients, which ensures $\Delta > \delta$ in practice. The proportional contributions to ϕ from higher order motion terms (including acceleration) may also be reduced by partial echo acquisition (Guo et al., 1991; Gatenby et al., 1993), reducing gradient moments about the center of the acquisition window. Phase sensitivity to all orders of motion is reduced, but the higher the order of motion, the greater the reduction in phase sensitivity. However, reconstruction errors may arise from partial echo acquisitions (where assumptions must be made about the uncollected echo fraction) or, when an entire echo is reconstructed from separately acquired partial echoes (Boesiger et al., 1992), imaging time must be increased.

In comparing the FIDAP solution and MRI velocities, it was assumed that the MRI components of velocity are precisely parallel (x) and orthogonal (y and z) to the axis of the pipe system. It is possible that the gradient coil windings and pipe system were not exactly aligned, in which case the velocities in each MRI map are components of the flow field, but not necessarily those parallel and transverse to the pipe system. The pipe system is supported by a series of coaxial rings, which fit inside the RF coil and gradient coil former and could conceivably allow a ca. 4° misalignment along the length of the former. However, in the MRI **q**-samples, from which the velocity maps of Figs. 3 and 4 were constructed, misalignment (measured from the images) was $\leq$1 voxel side ($\leq 7.6 \times 10^{-2}$ cm) over a 4.9 cm region of interest ($\leq$1°).

Consistency of the three MRI velocity components with one another was checked by calculating the divergence of velocity normalised with respect to local fluid turnover at each voxel. This figure is a measure of an apparent fractional volume accumulation over the time taken to replace the voxel contents and, where non-zero, indicates different systematic errors in the velocity components or imperfect spatial registration of the three velocity maps. The mean of normalized divergence was 2.0×10^{-3} and the distribution of the frequency of normalized divergence was sharply peaked at zero (full width at half maximum 6.0×10^{-3}). Significantly nonzero values of divergence are found at the pipe system boundaries, resulting in a broad distribution overall (standard deviation 2.9). MRI velocities were compromised by the effects of partially filled voxels and poor registration of velocity components (and, possibly, by clinging bubbles) at these boundaries.

The MRI velocities are not completely symmetrical about the pipe system axis (Figs. 3 and 4), while the FIDAP calculation assumed perfect symmetry. It is for this reason that the axial velocities are circumferentially averaged before comparison (see above). We ascribe the asymmetry, and possibly some numerical discrepancies, to several features of the MRI measurement, rather than to inherent inaccuracies of the PFG MRI velocimetry.

Particulate impurities, which might have been present in the sucrose solution (dust or microbial contamination, for example), would tend to settle out of slow, recirculant fluid in the expansion sections, breaking the symmetry. Imperfections in the construction of the pipe system might also have been responsible for asymmetry in the flow field; particularly any nonorthogonality of the pipes and roughness of the surfaces. Surface ridges not only affected the flow field, but also allowed tiny, clinging air bubbles to lodge. These bubbles were often too small to be seen with the naked eye, but induced local magnetic field gradients by their magnetic susceptibility difference with the liquid and were, therefore, clear in MR images.

There is a heating effect on the sucrose solution associated with an MRI acquisition, which is a combination of the elevated running temperature of the gradient coil windings and RF power deposition (a small effect in nonconducting fluids). Recirculating fluid in the expansion sections, spending longer in the pipe system than that in the central, fast-moving stream, might have significantly changed temperature and *density,* thus reducing symmetry. The numerical simulation assumed isothermal conditions.

Temperature gradients within the pipe system are again important when considering numerical discrepancies between the FIDAP and MRI velocities. The critical dependence on temperature of the viscosity of a sucrose solution may have led to a distribution of viscosities (cooler liquid in the central stream being more viscous), which affected the relative magnitudes of axial and recirculant flows. This may account, in part, for the disagreement in peak, axial, centerline velocities indicated in Fig. 4(a).

It is also possible that instability over the duration of the measurement affected the MRI velocities. The mean measured volume flow rate was 111.0 $\pm$ 0.5 ml/min with a fluctuation over 4.0 ml/min during the MRI measurement. A corresponding fluctuation of 0.2 cm/s in mean velocity would be expected in the 0.59 cm contraction. The fluctuating flow rate is probably explained by a variation in temperature of 0.5°C (mean 20.7 $\pm$ 0.1°C), which would alter viscosity by as much as 0.7×10^{-3} Pa s (Norrish, 1967). Stability of the MRI hardware is also critical and might be compromised by fluctuations such as temperature.

Conclusions

There is clear agreement between MRI measurements and CFD results, both in the general form of the flow field (Fig. 3) and the quantification of velocities (in three dimensions) throughout much of that field (Fig. 4). We have validated assumptions necessarily made for the FIDAP calculation and have confirmed the potential of carefully selected MRI protocols for the non-invasive, quantitative study of complex flow fields. We have addressed the causes of discrepancy, which are of significant magnitude (ca. 20 percent) in the region of the 0.59 cm contraction. The inherent inaccuracies of the MRI measurement (in this implementation), caused by the motion of nuclear ensembles during the PFG pair, are the subject of ongoing work; it is desirable to demonstrate whether these errors can be the sole cause of such disagreement and, if so, to reduce their effect at the cost of increased measurement time (see above).

The substantial variation in laminar flow velocity, which occurs over a short distance within this pipe system, is relevant to a range of industrial processing environments, such as those which can occur in mixing vessels and nozzle flows. Consequently, this flow vessel provides a test for the development of MRI protocols for studying such highly textured flow fields. Further expansion/contraction zones of varying diameters could be added to the pipe system, for example in order to achieve tailored velocity fluctuations along the phantom centreline. The

results described herein give confidence to proceed to more complex geometries and more complex fluids, with increasing relevance to industrial process flow phenomena.

Acknowledgments

The authors thank Dr. Herchel Smith, whose handsome endowment has provided support and the MRI facilities used. We would like to thank Dr. N. J. Herrod for writing much of the software used in MRI analysis and Dr. T. A. Carpenter for maintaining the laboratory facilities with the assistance of Messrs. C. Bunch and S. Smith. Dr. L. Barratt (Unilever Research) provided computing facilities and Dr. S. M. Chouikhi (Unilever Research) originally proposed the use of axisymmetric baffled flow phantoms for generation of textured flow fields.

References

Agemura, C. K., Kauten, R. J., and McCarthy, K. L., 1995, "Flow Fields in Straight and Tapered Screw Extruders Using Magnetic Resonance Imaging," *Journal of Food Engineering,* Vol. 25, pp. 55–72.

Axel, L. and Dougherty, L., 1989, "MR imaging of Motion with Spatial Modulation of Magnetisation," *Radiology,* Vol. 171, p. 841.

Boesiger, P., Maier, S. E., Kecheng, L., Scheidegger, M. B., and Meier, D., 1992, "Visualization and Quantification of the Human Blood Flow by Magnetic Resonance Imaging," *Journal of Biomechanics,* Vol. 25(1), pp. 55–67.

Burden, R. L. and Faires, J. D., 1995, *Numerical Analysis,* Prindle, Weber and Schmidt, third edition.

Callaghan, P. T., 1991, *Principles of Nuclear Magnetic Resonance Microscopy,* Chapter 6, pp. 339–340, Oxford University Press, Oxford, UK.

Caprihan, A. and Fukushima, E., 1990, "Flow Measurements by NMR," *Physics Reports,* Vol. 198(4), pp. 196–235.

Carpenter, T. A., Jezzard, P., and Hall, L. D., 1989, "Proton Magnetic Resonance Imaging of Solid Polymers using Instrumentation Designed for the Liquid-State," *Journal of Magnetic Resonance,* Vol. 84, pp. 384–387.

Derbyshire, J. A., 1995, "Echo Planar Anemometry using Conventional Magnetic Resonance Imaging Hardware," PhD thesis, University of Cambridge.

Derbyshire, J. A., Gibbs, S. J., Carpenter, T. A., and Hall, L. D., 1994, "Rapid Three-Dimensional Velocimetry by Nuclear Magnetic Resonance Imaging," *AIChE Journal,* Vol. 40(8), pp. 1404–1407.

Dumoulin, C. L., Souza, S. P., and Hart, H. R., 1987, "Rapid Scan Magnetic Resonance Angiography," *Magnetic Resonance in Medicine,* Vol. 5(3), pp. 238–245.

Edelstein, W. A., Hutchinson, J. M. S., Johnson, G., and Redpath, T., 1980, "Spin Warp NMR Imaging and Applications to Human Whole-Body Imaging," *Physics in Medicine and Biology,* Vol. 25, pp. 751–756.

Ernst, R. R., Bodenhausen, G., and Wokaun, A., 1987, *Principles of Nuclear Magnetic Resonance in One and Two Dimensions,* Chapter 4, Oxford University Press, Oxford, UK, 1 edition.

Fischer, S. E., McKinnon, G. K., Maier, S. E., and Boesiger, P., 1993, "Improved Myocardial Tagging Contrast," *Magnetic Resonance in Medicine,* Vol. 30, pp. 191–200.

Fukuda, K., Inouye, A., Kawabe, Y., and Hirai, A., 1985, "Transition from Laminar to Turbulent Flow of Water in a Pipe Measured by a Pulsed NMR Method," *Journal of the Physical Society of Japan,* Vol. 54(12), pp. 4555–4560.

Gatenby, J. C., McCauley, T. R., and Gore, J. C., 1993, "Mechanisms of Signal Loss in Magnetic Resonance Imaging of Stenoses," *Medical Physics,* Vol. 20(4), pp. 1049–1057.

Gladden, L. F., 1994, "Industrial Applications of NMR Imaging," *Process Tomography '94,* Proceedings of ECAPT '94 (Brite-Euram Conference on Process Tomography), pp. 466–477.

Guo, Q., Kashmar, G., and Nalcioglu, O., 1991, "NMR Angiography with Enhanced Quasi-Half-Echo Scanning," *Magnetic Resonance Imaging,* Vol. 9, pp. 129–139.

Hahn, E. L., 1950, "Spin Echoes," *Physical Review,* Vol. 80, pp. 580–594.

Hall, L. D. and Carpenter, T. A., 1992, "Magnetic Resonance Imaging: A New Window into Industrial Processing," *Magnetic Resonance Imaging,* Vol. 10, pp. 713–721.

Hayes, C. E., Edelstein, W. A., Schenk, J. F., Mueller, O. M., and Eash, M., 1985, "An Efficient, Highly Homogeneous Radiofrequency Coil for Whole-Body NMR Imaging at 1.5 *T*," *Journal of Magnetic Resonance,* Vol. 63, pp. 622–628.

Lee, H. K., Nalcioglu, O., and Moran, P. R., 1991, "Spatially Resolved Flow Velocity Measurements and Projection Angiography by Adiabatic Passage," *Magnetic Resonance Imaging,* Vol. 9, pp. 115–127.

Maier, S. E., Meier, D., Boesiger, P., Moser, U. T., and Vieli, A., 1989, "Human Abdominal Aorta: Comparitive Measurements of Blood Flow with MR Imaging and Multigated Doppler Ultrasound," *Radiology,* Vol. 171, pp. 487–492.

Mansfield, P., 1977, "Multi-Planar Image Formation Using NMR Spin Echoes," *Journal of Physics C,* Vol. 10, p. L55.

Moore, J. E., Maier, S. E., Ku, D. N., and Boesiger, P., 1994, "Hemodynamics in the Abdominal Aorta: a Comparison of in Vitro and in Vivo Measurements," *Journal of Applied Physiology,* Vol. 76(4), pp. 1520–1527.

Morris, G. A. and Freeman, R., 1978, "Selective excitation in Fourier Transform Nuclear Magnetic Resonance," *Journal of Magnetic Resonance,* Vol. 29, p. 433.

Mosher, T. J. and Smith, M. B., 1990, "A DANTE Tagging Sequence for the Evaluation of Translational Sample Motion," *Magnetic Resonance in Medicine,* Vol. 15, p. 334.

Norrish, R. S., 1967, "Selected Tables of Physical Properties of Sugar Solutions," Scientific and Technical Survey 51, The British Food Manufacturing Industries Research Association.

Pope, J. M. and Yao, S., 1993, "Quantitative NMR imaging of Flow," *Concepts in Magnetic Resonance,* Vol. 5, pp. 281–302.

Roberts, T. P. L., Carpenter, T. A., and Hall, L. D., 1990, "Design and Application of Prefocused Pulses by Simulated Annealing," *Journal of Magnetic Resonance,* Vol. 29(3), pp. 595–604.

Roberts, T. P. L., Carpenter, T. A., and Hall, L. D., 1993, "A Simple Method for the Construction of 180° Refocusing Radiofrequency Pulses for Use in Magnetic Resonance Imaging," *Journal of Magnetic Resonance,* Series B, Vol. 101(1), pp. 78–82.

Sinton, S. W., and Chow, A. W., 1991, "NMR Imaging of Fluids and Solid Suspensions in Poiseuille Flow," *Journal of Rheology,* Vol. 35(5), pp. 735–772.

Stehling, M. K., Turner, R., and Mansfield, P., 1991, "Echo-Planar Imaging: Magnetic Resonance Imaging in a Fraction of a Second," *Science,* Vol. 254, p. 43.

Stejskal, E. O., and Tanner, J. C., 1965, "Spin Diffusion Measurements: Spin Echoes in the Presence of a Time-Dependent Field Gradient," *Journal of Chemical Physics,* Vol. 42, p. 288.

Sun, Y., Hearshen, D. O., Rankin, G. W., and Haggar, A. M., 1992, "Comparison of Velocity-Encoded MR Imaging and Fluid Dynamic Modelling of Steady and Disturbed Flow," *Journal of Magnetic Resonance Imaging,* Vol. 2(4), pp. 443–452.

Vu, A. T., Lee, H. K., Moran, P. R., and Nalcioglu, O., 1993, "Flow Field Mapping Multi-Zone Adiabatic Passage Excitation," *Magnetic Resonance Imaging,* Vol. 11, pp. 1129–1137.

Xing, D., Gibbs, S. J., Derbyshire, J. A., Carpenter, T. A., and Hall, L. D., 1995, "Bayesian Analysis for Quantitative NMR Flow and Diffusion Imaging," *Journal of Magnetic Resonance,* Series B, Vol. 106, pp. 1–9.

C. Y. Wang
Professor,
Departments of Mathematics and Mechanical Engineering,
Michigan State University,
East Lansing, MI 48824
Mem. ASME

Stokes Flow Through a Transversely Finned Channel

The efficient method of eigenfunction expansion and point match is used to solve the Stokes flow through a channel with transverse fins. Both in-phase and staggered fins are considered. Streamlines and resistances are found in terms of fin height and fin spacing. Extrapolating to large spacings, the added resistances due to a single pair of aligned fins and that of a single fin in a channel are obtained.

Introduction

The study of minute Reynolds number viscous flow through a channel is important in predicting seepage through rock fissures (Dagan, 1989) micro heat transfer (Bergles, 1988) and fluid transport through endothelial clefts in the microvasculature (Crone and Levitt, 1984). If the channel is smooth the velocity profile is parabolic and Poiseuille's law of resistance holds. However, if the channel is rough, Poiseuille's law would invariably underestimate the resistance. Previous literature on the flow through a nonsmooth channel considered channel walls with sinusoidal corrugations. Due to the irregular boundary, two approximate analytical approaches have been used. One approach assumes the wavelength of the corrugations is long compared to the channel width (Chow and Soda, 1973; Hasegawa and Izuchi, 1984). Another approach assumes the amplitude of the corrugations are small compared to the channel width (Wang, 1976, 1979). All above sources use small perturbations about Poiseuille flow, thus the corresponding resistances are also close to Poiseuille resistance.

For large protuberances, such as fins on the channel walls, perturbation theory fails. Using numerical finite differences, Sparrow et al. (1978), Lauder and Li (1984) studied the longitudinal flow parallel to the fins and Kelkar and Patankar (1987) investigated the transverse flow across staggered fins on the channel walls. For minute Reynolds number Stokes flow considered in this paper, the governing equation becomes linear, and we can use an eigenfunction expansion and point match method which requires much less computations than direct numerical integration.

The earliest use of eigenfunction expansion and point match for parallel flow inside an irregular boundary was perhaps due to Sparrow and Loeffler (1950) although for certain geometries such a method may not be suitable (Sparrow, 1966). We shall show later that in order for point match to succeed, completeness of the eigenfunctions on the matching boundary must be shown. Using this method, Wang (1994) studied the flow in a channel in the same direction as the longitudinal ribs. Since the flow is parallel the governing equation is the Poisson equation whose eigenfunction solution is relatively simple.

In this paper we shall study the Stokes flow in a channel with thin transverse fins using the eigenfunction expansion and point match method. The governing equation is the biharmonic which has more complicated eigenfunctions. Our results would be useful not only for micro fin forced convection but also for the flow in small rough channels where the fins mimic protuberances caused by milling with a rounded bit.

Formulation

Figure 1(a) shows the cross sections of channels with in-phase or staggered fins. Let the channel width be $2H$ the fin height be bH and the period be $2aH$. We assume the Reynolds number (UH/kinematic viscosity) where $2UH$ is the flow rate (per depth), is so low that Stokes approximation is valid. Let ψ be the stream function normalized by UH (thus the difference in ψ across the channel is 2) and (x, y) be cartesian coordinates normalized by H. The governing equation is the biharmonic

$$\nabla^4\psi = 0 \tag{1}$$

Due to periodicity we can consider a single cell. Figure 1(b) shows the appropriate boundary conditions. No slip condition gives $\psi = \pm 1$ and $\psi_y = 0$ on top and bottom plates, and $\psi = \pm 1$ and $\psi_x = 0$ on top and bottom fins. Since Stokes flow is reversible, the stream function is continuous and symmetrical about the dashed cell boundaries, i.e., ψ must be even in $x - a$. Thus $\psi_x = 0$ and $\psi_{xxx} = 0$ there.

Solution for In-Phase Fins

Placing the coordinates at the center of the cell, it is clear that the stream function for in-phase fins is odd in y and even in x. We choose

$$\psi(x, y) = \frac{3y - y^3}{2} + A_0(y - y^3) + \sum_{n=1}^{\infty} A_n \cos(\alpha x) S_n(y) + \sum_{n=1}^{\infty} B_n \sin(\beta y) T_n(x) \tag{2}$$

where $\alpha = n\pi/a$ and $\beta = n\pi$. The first term on the righthand side is the Poiseuille flow in a smooth channel. To satisfy Eq. (1) the function $S_n(y)$ normally consists of a linear combination of $\cosh(\alpha y)$, $\sinh(\alpha y)$, $y\cosh(\alpha y)$, $y\sinh(\alpha y)$. Choosing the odd terms and further requiring $S_n(1) = 0$ yield

$$S_n(y) = [e^{\alpha(y-1)} - e^{-\alpha(y+1)}]K_1 - y[e^{\alpha(y-1)} + e^{-\alpha(y+1)}] \tag{3}$$

where $K_1 = (1 + e^{-2\alpha})/(1 - e^{-2\alpha})$. The exponential forms ensure S_n is of reasonable magnitude even for large n. The sets of unknown constants A_nB_n are to be determined. The term with A_0 is the degenerate case when $n = 0$.

Similarly we find

$$T_n(x) = [e^{\beta(x-a)} + e^{-\beta(x+a)}]K_2 - x[e^{\beta(x-a)} - e^{-\beta(x+a)}] \tag{4}$$

where $K_2 = 1/\beta + a(1 + e^{-2\beta a})/(1 - e^{-2\beta a})$ in order to make $T_n'(a) = 0$. Equation (2) now satisfies the partial boundary conditions $\psi(x, \pm 1) = \pm 1$ and $\psi_x(\pm a, y) = 0$. Next we set $\psi_y(x, 1) = 0$. This relates A_n to B_n:

$$-2A_0 + \sum_1 A_n \cos(\alpha x) S_n'(1) + \sum_1 B_n \beta(-1)^n T_n(x) = 0 \tag{5}$$

Equation (2) at $x = a$ then represents a complete odd Fourier series in $-1 \le y \le 1$, where any odd function in y can be prescribed on the boundary at $x = a$. This shows the representation of Eq. (2) is complete.

Contributed by the Fluids Engineering Division for publication in the JOURNAL OF FLUIDS ENGINEERING. Manuscript received by the Fluids Engineering Division October 20, 1995; revised manuscript received September 23, 1996. Associate Technical Editor: F. Giralt.

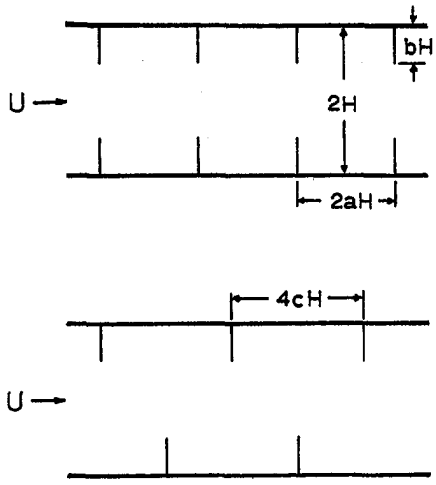

Fig. 1(a)

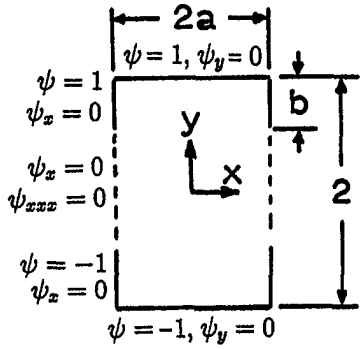

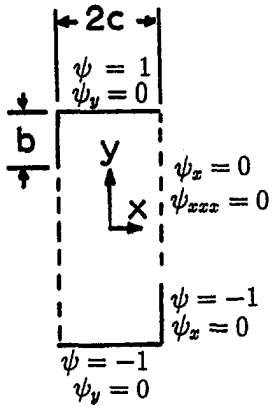

Fig. 1(b)

Fig. 1 (a) Flow through channel with transverse fins (b) cell domain

Integrating Eq. (5) with respect to x from 0 to a yields

$$A_0 = \frac{1}{2a} \sum B_n \beta (-1)^n I_n \tag{6}$$

where

$$I_n = \int_0^a T_n(x)dx = [1 - a\beta + K_2\beta - (1 + a\beta + K_2\beta)e^{-2a\beta}]/\beta^2 \tag{7}$$

Multiplying Eq. (5) by $\cos(\alpha x)$ and integrating yield

$$A_n \frac{a}{2} S_n'(1) + \sum_{m=1}^{\infty} B_m \beta_m (-1)^m J_{mn} = 0 \tag{8}$$

where

$$J_{mn} = \int_0^a T_m(x) \cos(\alpha_n x)dx = \frac{2(-1)^n \beta_m^2 (1 - e^{-2a\beta_m})}{(\beta_m^2 + \alpha^2)^2}$$

Here $\beta_m = m\pi$. Lastly we take the mixed boundary condition on $x = a$. Considering the top half, we have

$$\psi(a, y) = 1 \quad 1 - b < y \le 1 \tag{9}$$

$$\psi_{xxx}(a, y) = 0 \quad 0 \le y < 1 - b \tag{10}$$

We truncate B_n to N terms A_n to $M = \text{Int}[aN]$ terms, and choose N evenly spaced points along $x = a$, $0 < y < 1$.

$$y_j = \frac{j}{N + 1}, \quad j = 1, N \tag{11}$$

Equation (8) gives

$$A_n \frac{a}{2} S_n'(1) + \sum_{m=1}^{N} B_m \beta_m (-1)^m J_{mn} = 0 \quad n = 1, M \tag{12}$$

Set $k = \text{Int}[(1 - b)N]$. Substitute Eq. (6) into Eq. (9) to obtain

$$\sum_{n=1}^{M} A_n (-1)^n S_n(y_j) + \sum_{n=1}^{N} B_n \left[\beta (-1)^n I_n \frac{(y_j - y_j^3)}{2a} + \sin(\beta y_j) T_n(a) \right] = 1 - \frac{(3y_j - y_j^3)}{2}, \quad j = k + 1, N \tag{13}$$

Eq. (10) yields

$$\sum_{n=1}^{N} B_n \sin(\beta y_j) T_n'''(a) = 0, \quad j = 1, k \tag{14}$$

Equations (12)–(14) represent $M + N$ linear algebraic equations and $M + N$ unknowns. These are inverted by a standard numerical program. After A_n, B_n are found, A_0 is then obtained from Eq. (6). A typical result for the streamlines ($a = 1$, $b = 0.5$) is shown in Fig 2(a). There exist recirculating eddies in the almost stagnant corners. When the fin spacing is decreased (Fig 2(b) for $a = 0.5$, $b = 0.5$), these corner eddies coalesce into a single recirculation. Similar to cavity flows driven by a moving boundary, (see e.g., Pan and Acrivos, 1967), more eddies are induced when the fins become closer together (Fig

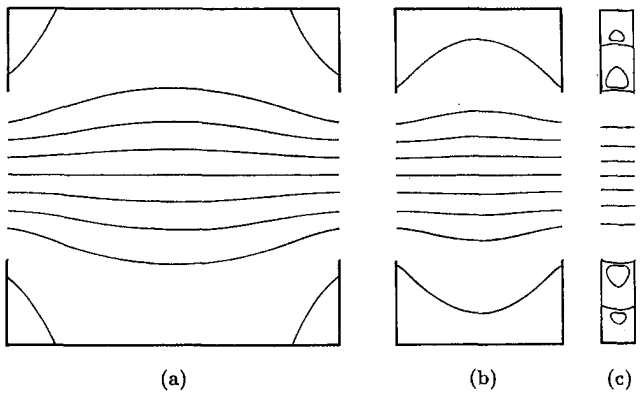

Fig. 2 Streamlines for in-phase fins (ψ values for each individual curve differ by 0.25 unless otherwise noted) (a) $a = 1$, $b = 0.5$, (b) $a = 0.25$, $b = 0.5$, (c) $a = 0.1$, $b = 0.5$

$2(c)$). The convergence for moderate a, b is fast. The error of ψ is about 0.5 percent for $N = 10$ and decreases to 0.2 percent for $N = 20$. In general, we started with $N = 30$ and confirm 3 significant digits using $N = 50$. For extreme cases $a \approx 0$, $b \approx 0$ or close to touching up to $N = 100$ are used.

Solution for Staggered Fins

The staggered case is more complicated. Let the axes be at the middle of the cell shown in Fig 1(b). We see that ψ has the property

$$\psi(x, y) = -\psi(-x, -y) \tag{15}$$

Construct similarly

$$\psi(x, y) = \frac{3y - y^3}{2} + A_0(y - y^3) + \sum_1^\infty A_n \cos(\alpha x) S_n(y) + \sum_1^\infty B_n \sin(\beta y) T_n(x) + \sum_1^\infty C_n \cos(\mu y) P_n(x) + \sum_1^\infty D_n \sin(\nu x) Q_n(y) \tag{16}$$

where $\alpha = n\pi/c$, $\beta = n\pi$, $\mu = (n - \frac{1}{2})\pi$, $\nu = (n - \frac{1}{2})\pi/c$, $c \equiv a/2$ (to simplify bookkeeping), and

$$S_n(y) = [e^{\alpha(y-1)} - e^{-\alpha(y+1)}]K_1 - y[e^{\alpha(y-1)} + e^{-\alpha(y+1)}] \tag{17}$$

$$T_n(x) = [e^{\beta(x-c)} + e^{-\beta(x+c)}]K_2 - x[e^{\beta(x-c)} - e^{-\beta(x+c)}] \tag{18}$$

$$P_n(x) = [e^{\mu(x-c)} - e^{-\mu(x+c)}]K_3 - x[e^{\mu(x-c)} + e^{-\mu(x+c)}] \tag{19}$$

$$Q_n(y) = [e^{\nu(y-1)} + e^{-\nu(y+1)}]K_4 - y[e^{\nu(y-1)} - e^{-\nu(y+1)}] \tag{20}$$

$$K_1 = (1 + e^{-2\alpha})/(1 - e^{-2\alpha}),$$
$$K_2 = 1/\beta + c(1 + e^{-2\beta c})/(1 - e^{-2\beta c})$$
$$K_3 = 1/\mu + c(1 - e^{-2\mu c})/(1 + e^{-2\mu c}),$$
$$K_4 = (1 - e^{-2\nu})/(1 + e^{-2\nu}) \tag{21}$$

Note Eq. (16) has four infinite sums, due to the much weaker polar symmetry Eq. (15), and that completeness (shown later) requires 4 independent series. $\psi(x, y)$ now satisfies the biharmonic and the boundary conditions $\psi(x, \pm 1) = \pm 1$ and $\psi_x(\pm c, y) = 0$. The condition $\psi_y(x, 1) = 0$ yields

$$-2A_0 + \sum A_n \cos(\alpha x) S_n'(1) + \sum B_n \beta(-1)^n T_n(x) + \sum C_n \mu(-1)^n P_n(x) + \sum D_n \sin(\nu x) Q_n'(1) = 0 \tag{22}$$

Integrating with respect to x, the Fourier harmonics give

$$A_0 = \frac{1}{2c} \sum B_n \beta(-1)^n I_n \tag{23}$$

$$A_n c S_n'(1) + 2 \sum_m B_m \beta_m (-1)^m J_{mn} = 0 \tag{24}$$

$$2 \sum_m C_m \mu_m (-1)^m K_{mn} + D_n c Q_n'(1) = 0 \tag{25}$$

where $\beta_m = m\pi$, $\mu_m = (m - \frac{1}{2})\pi$ and

$$I_n = \int_0^c T_n(x)dx = \frac{1}{\beta^2}[1 - \beta c + \beta K_2 - (1 + \beta c + \beta K_2)e^{-2\beta c}] \tag{26}$$

$$J_{mn} = \int_0^c T_m(x) \cos(\alpha x)dx = \frac{2\beta_m^2(1 - e^{-2\beta_m c})(-1)^n}{(\alpha^2 + \beta_m^2)^2} \tag{27}$$

$$K_{mn} = \int_0^c P_m(x) \sin(\nu x)dx = \frac{2\mu_m^2(1 + e^{-2\mu_m c})(-1)^{n+1}}{(\mu_m^2 + \nu^2)^2} \tag{28}$$

Since the A_n's are related to B_n and the D_n's are related to C_n, Eq. (16) is left with both odd and even Fourier series in y. Since $\psi(c, y)$ can describe any function of y at the vertical boundary, the solution is complete.

Lastly, the mixed boundary conditions are to be satisfied

$$\psi(c, y) = -1 \quad 0 \le y < b \tag{29}$$

$$\psi_{xxx}(c, y) = 0 \quad b < y \le 1 \tag{30}$$

We truncate B_n, C_n to N terms and A_n, D_n to $M = \text{Int}[cN]$ terms. Collocation is then applied to $2N$ points equally spaced along $y = c$:

$$y_j = \frac{2j}{2N + 1} - 1 \quad j = 1 \text{ to } 2N$$

Let $k = \text{Int}[b(N + 0.5)]$. Equations (29, 30) become

$$\sum_{n=1}^M A_n(-1)^n S_n(y_j) + \sum_{n=1}^N B_n\left[\sin(\beta y_j)T_n(e) + \frac{1}{2c}\beta(-1)^n I_n\right] + \sum_{i=1}^N C_n \cos(\mu y_j)P_n(c) + \sum_{n=1}^M D_n(-1)^{n+1}Q_n(y_j) = -1 - \tfrac{1}{2}(3y_j - y_j^3) \quad j = 1 \text{ to } k \tag{31}$$

$$\sum_{n=1}^N B_n \sin(\beta y_j)T_n^m(c) + \sum_{n=1}^n C_n \cos(\mu y_j)P^m(c) = 0 \quad j = k + 1 \text{ to } 2N \tag{32}$$

Together with Eqs. (24), (25) there are $2N + 2M$ equations and equal number of unknowns. The algebraic equations are then inverted. Streamline patterns are shown in Fig 3.

The Pressure Drop

We normalize the pressure by $\mu U/H$ where μ is the viscosity. Then

$$p_x = \nabla^2\psi_y, \quad p_y = -\nabla^2\psi_x \tag{33}$$

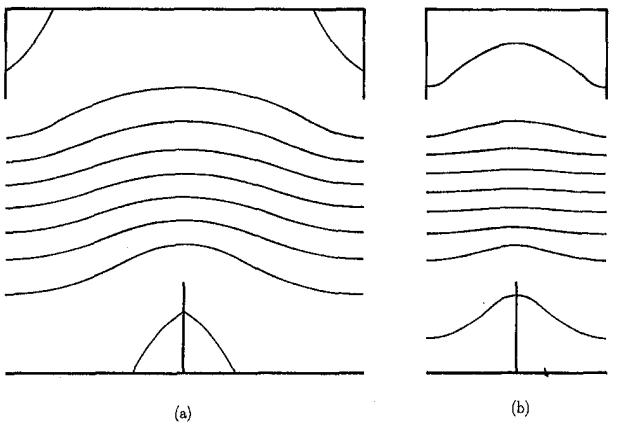

Fig. 3 Streamlines for staggered fins (ψ values for each individual curve differ by 0.25), (*a*) $c = 0.5$, $b = 0.5$, (*b*) $c = 0.25$, $b = 0.5$

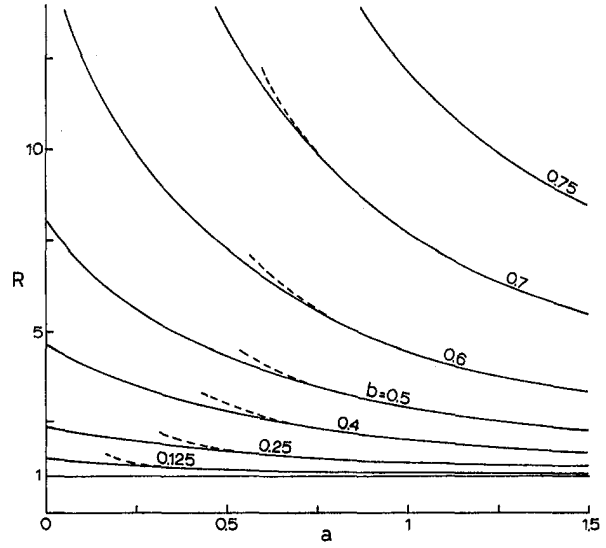

Fig. 4 Resistance ratio for in-phase fins. Dashed lines are from Eq (36).

Using Eq. (2) the pressure distribution for the case of in-phase fins is

$$p(x, y) = -3(1 + 2A_0x) - 2\sum B\beta \cos(\beta y)(e^{\beta(x-a)} - e^{-\beta(x+a)}) - 2\sum A\alpha \sin(\alpha x)(e^{\alpha(y-1)} + e^{-\alpha(y+1)}) \quad (34)$$

Here the pressure is set to zero at the origin. The pressure gradient, or pressure drop per length is $-p(a, 0)/a$. This value is 3 if the channel is smooth. We define the resistance ratio R as the pressure drop due to finned channel to that of smooth channel:

$$R = \frac{-p(a, 0)}{3a} \quad (35)$$

Due to the truncation of the Fourier series and second derivatives on ψ, the pressure at $x = a$, $|y| < 1 - b$ does not converge as fast as ψ and tends to oscillate with wave length $0(1/N)$ about some mean. Instead of increasing N further, the accuracy for $p(a, 0)$ is improved by integrating for the mean across $\frac{1}{2}$ gap width (there are pressure singularities at the sharp edges).

Figure 4 shows the ratio R as a function of a and b for in phase fins. When $a = 0$, the fins are stacked together, and effective channel width is decreased to $2(1 - b)$. The resistance ratio is thus $(1 - b)^{-3}$. For large a and constant b, we find the ratio decrease to unity through the formula

$$R = 1 + \frac{\Delta p_0}{3a} \quad (36)$$

where Δp_0 is the extrapolated normalized pressure drop due to a single pair of constrictive fins. Figure 5 shows Δp_0 as a function of fin height b. Equation (36) is then plotted in Fig. 4 for comparison. For low a, interaction between adjacent fins become quite important.

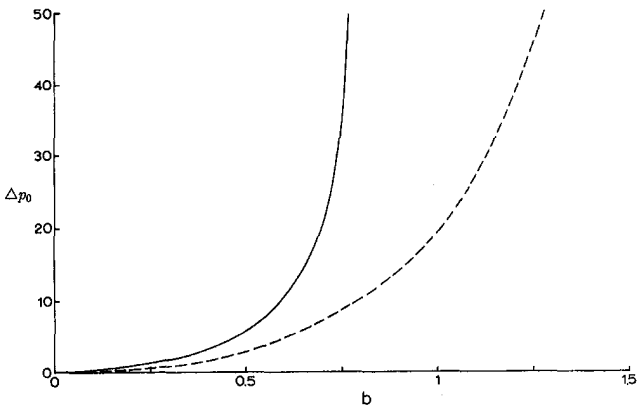

Fig. 5 Added pressure drop due to a single pair of aligned fins in a channel ——, due to a single fin in a channel – – –

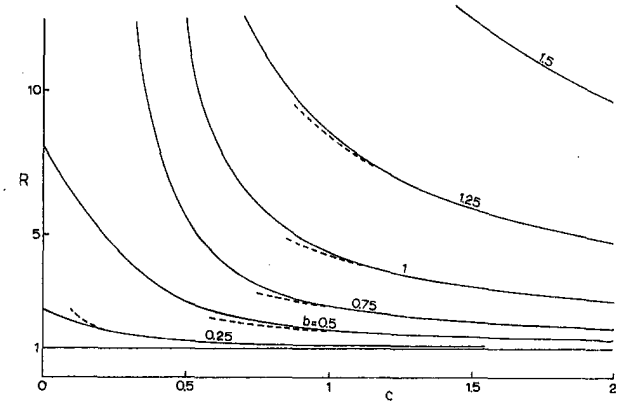

Fig. 6 Resistance ratio for staggered fins. Dashed lines are from Eq (39).

Similarly the pressure distribution for the case of staggered fins is

$$p(x, y) = -3(1 + 2A_0)x - 2\sum A\alpha \sin(\alpha x)(e^{\alpha(y-1)} + e^{-\alpha(y+1)}) - 2\sum B\beta \cos(\beta y)(e^{\beta(x-c)} - e^{-\beta(x+c)}) + 2\sum C\mu \sin(\mu y)(e^{\mu(x-c)} + e^{-\mu(x+c)}) + 2\sum D\nu \cos(\nu x)(e^{\nu(y-1)} - e^{-\nu(y+1)}) \quad (37)$$

The resistance ratio is defined as

$$R = \frac{-p(c, 1)}{3c} \quad (38)$$

Again it is advisable to average the pressure for some height to improve convergence. The results are shown in Fig. 6. Due to the staggering the resistance is smaller than that of in-phase case. When $a = 0$, the resistance ratio is $(1 - b)^{-3}$. For $b \geq 1$ the resistance tend to infinity as $a \to 0$. When a becomes large we have the asymptotic formula (shown as dashed lines)

$$R = 1 + \frac{\Delta p_0}{6c} \quad (39)$$

where Δp_0 now represents the added pressure drop due to single fin on one wall. The value of Δp_0, also shown in Fig. 5, is extrapolated from our numerical results. For the staggered case the fin height b can be larger than unity and still permit fluid flow. In constructing Figs. 4–6, the data points are computed for a, b, c at intervals of at most 0.25 supplemented by in-between values at the steeper slopes.

Discussions and Conclusion

The method of eigenfunction expansion and point match is highly efficient in comparison to direct numerical integration. The number of computations used is comparable to that of

boundary integral methods and is less than the square root of those needed in finite difference or finite element methods.

For Stokes flow there are two (no slip) boundary conditions on the channel walls. Our stream function satisfies one condition exactly and the other in an integral sense. This way the eigenvalues and Fourier inversions are very simple. On the other hand, if both conditions are to be satisfied at $y = \pm 1$ exactly, one obtains complicated complex eigenvalues (see e.g., Joseph, 1977) and a biorthogonal integral relation is needed for inversion.

We mention that completeness of the eigenfunction representation should always be shown, otherwise convergence is not assured. For example let us consider Poiseuille flow in a circular tube. If cartesian eigenfunctions are used and point match is attempted on the circular boundary, convergence can not be attained. This is perhaps because completeness cannot be shown on the boundary.

There exists a weak singularity (in pressure) at the tips of the sharp fins. However this singularity has little effect on the streamlines or the total pressure gradient. In conclusion, our Figs. 4–6 should be very useful in the prediction of the Stokes resistance through channels with fined walls.

The convective heat transfer rate can be predicted using the detailed results of the velocity distribution. Although the heat transfer problem is not solved in this paper, some qualitative recommendations can be made for micro fin enhancement based on the flow characteristics. First, the spacing of the fins should not be too close as to cause slow-moving recirculating eddies between the channel wall and the through flow, i.e., the flow of Fig. 2(a) is more convective than that of Fig. 2(c). Second, assuming each fin has similar heat transfer rates, the staggered arrangement is preferable to the in-phase arrangement. This is because the flow resistance for an in-phase pair of fins is more than twice that of a single fin (see, e.g., Fig. 5).

Another area of application is the endothelial cleft which is a major pathway for the transcapillary movement of fluids and solutes in the microcirculation. The cleft is a 2D slit of about 20 nm height with a longitudinal length of about 700 nm. The observed resistance through the cleft, however, is much higher than that computed from a smooth channel, suggesting internal obstructions. In the absence of detailed morphological data, several models are suggested (Crone and Levitt, 1984). These include a channel filled with a fiber matrix and a channel with a discrete constrictive junction. The present paper introduces another possibility—a channel with internal transverse fins. The staggered fins forces a longer, tortuous pathway through the cleft and the in-phase fins resemble constrictive junctions.

Acknowledgment

This research is partially supported by NIH grant RR 01243.

References

Bergles, A. E., 1988, "Some Perspectives on Enhanced Heat Transfer-Second-Generation Heat Transfer Technology," ASME *Journal of Heat Transfer,* Vol. 110, pp. 1082–1096.

Chow, J. C. F. and Soda, K., 1973, "Laminar Flow and Blood Oxygenation in channels with Boundary Irregularities," ASME *Journal of Applied Mechanics,* Vol. 40, pp. 843–850.

Crone, C. and Levitt, D. G., 1984, "Capillary Permeability to Small Solutes," *Handbook of Physiology,* Section 2, Vol. IV, Part 1, Microcirculation, E. M. Renkin and C. C. Michel, eds., American Physiological Society, Md, pp. 411–466.

Dagan, G., 1989, *Flow and Transport in Porous Formations,* Springer, Berlin.

Hasegawa, E., and Izuchi, H., 1984, "On Steady Flow Through a Channel Consisting of an Uneven and a Plane Wall," *Bull. JSME,* Vol. 27, pp. 1631–1636.

Joseph, D. D., 1977, "The Convergence of Biorthogonal Series for Biharmonic and Stokes Flow Edge Problems," SIAM *Journal of Applied Mathematics,* Vol. 33, pp. 337–347.

Kelkar, K. M,. and Patankar, S. V., 1987, "Numerical Prediction of Flow and Heat Transfer in a Parallel Plate Channel with Staggered Fins," ASME *Journal of Heat Transfer,* Vol. 109, pp. 25–30.

Lauder, B. E., and Li, S., 1989, "A Numerical Study of Riblet Effects on Laminar Flow through a Plane Channel," *Applied Scientific Research,* Vol. 46, pp. 271–279.

Pan, F., and Acrivos, A., 1967, "Steady Flow in Rectangular Cavities," *Journal of Fluid Mechanics,* Vol. 28, pp. 643–655.

Sparrow, E. M., 1966, Discussion of K. C. Cheng, "Analog Solution of Laminar Heat Transfer in Non Circular Ducts by Moiré and Point Matchings," ASME *Journal of Heat Transfer,* Vol. 88, p. 182.

Sparrow, E. M., Baliga, B. R., and Patankar, S. V., 1978, "Forced Convection Heat Transfer from a Shrouded Fin Array with and without Tip Clearance," ASME *Journal of Heat Transfer,* Vol. 100, pp. 572–579.

Sparrow, E. M., and Loeffler, A. L., 1959, "Longitudinal Laminar Flow Between Cylinders Arranged in Regular Array," *AIChE Journal,* Vol. 5, pp. 325–330.

Wang, C. Y., 1976, "Parallel Flow Between Corrugated Plates," ASCE *Journal of Engineering Mechanics Division,* Vol. 102, pp. 1088–1090.

Wang, C. Y., 1979, "On Stokes Flow Between Corrugated Plates," ASME *Journal of Applied Mechanics,* Vol. 46, pp. 462–464.

Wang, C. Y., 1994, "Flow in a Channel with Longitudinal Ribs," ASME JOURNAL OF FLUIDS ENGINEERING, Vol. 116, pp. 233–237.

Flow Driven by a Torsionally-Oscillating Shrouded Endwall Disk

Tae Gyu Lim
Graduate Student.

Jae Min Hyun
Professor.

Department of Mechanical Engineering,
Korea Advanced Institute of Science
and Technology,
373-1 Kusong-dong Yusong-gu,
Taejon 305-701, South Korea

A study is made of time-dependent flow of a viscous fluid driven by an oscillating shrouded disk in finite geometry. Numerical solutions to the Navier-Stokes equations are obtained for the flow in a cylindrical cavity with its upper endwall disk executing torsional oscillation at a velocity $\Omega \cos \lambda t$. Details of the three-component velocity field are examined at high Reynolds number. The value of the nondimensional amplitude of disk oscillation, $\epsilon = \Omega/\lambda$, encompasses a range up to $\epsilon \gtrsim O(1)$. The numerical results for the azimuthal flow for $\epsilon \ll 1$ are consistent with the predictions of the earlier analytical model. The azimuthal flow is largely confined to the Stokes layer thickness. The analytical predictions of the meridional flow, based on a straightforward expansion technique, display discrepancies from the numerical results. The steady meridional streaming at finite values of ϵ is exhibited. The qualitative patterns of meridional steady streaming are verified by laboratory flow visualizations. The explicit effect of Re on the overall flow character is scrutinized. The numerical data are processed to describe the behavior of the torque coefficient at the oscillating disk.

1 Introduction

Flow of a viscous fluid induced by a rotating disk constitutes a classical problem. The rudimentary configuration is flow in an infinite expanse of fluid, maintained by a steadily rotating infinite disk. The fluid at infinity is assumed to be at rest. The description of the three-component velocity field (u, v, w), under the assumption of axisymmetric, was given by von Karman (see e.g., Schlichting, 1968), in which similarity considerations were adopted. Depictions of several other fundamental flow configurations involving a rotating infinite disk have been documented in the textbooks. Subsequent authors considered the case of one (or more) rotating disk(s) of finite size. This represents an effort to move closer to realism. For many realistic systems, the rotating disk(s) is shrouded by a cylindrical sidewall, and the domain of flow is restricted to finite geometry. Numerical and experimental attempts have been reported, which illustrate the behavior of viscous fluid flow driven by rotating disk(s) at constant angular frequency in a confined apparatus (e.g., see Pao, 1971; Tomlan and Hudson, 1971; Alonso, 1975; Lang et al., 1994).

A perusal of the recent literature reveals that the majority of prior studies have been concerned with time-invariant flows, which are established by a steadily rotating disk. The problem of viscous flows caused by a disk executing a time-dependent rotation has received relatively little attention. The canonical setup in this case is when the disk performs torsional oscillations. The determination of the fluid flow is of direct relevance to practical techniques of measuring the coefficient of viscosity. Also, this presents a significant self-standing problem in fluid dynamics research. The knowledge gained from this elemental flow configuration offers baseline information. This is vital to a proper understanding of the flows about a disk, which undergoes a more complex unsteady rotational motion.

Early studies on torsional oscillations of a disk in a viscous fluid were undertaken by Rosenblat (1959). In this model, the otherwise motionless fluid domain is assumed to be unbounded in space, and flows arise due to a small-amplitude torsional oscillation of an infinite plane disk. A systematic expansion of the velocity components in powers of nondimensional oscillation amplitude was made, which resulted in a series of linear partial differential equations. One important achievement of this analysis is the identification of a second-order meridional flow, which consists of a steady term and a term of frequency twice that of the disk. An insightful interpretation of the primary (azimuthal) as well as secondary (meridional) velocity components was presented, and the inner structure of radial flow was scrutinized. Benney (1961), by means of an extended analytical methodology, discussed the applicability of higher approximations and of different geometrical conditions. The outcome of these theoretical endeavors of Benney (1961) was shown to be consistent with the essential results of Rosenblat (1959). No other comparable independent studies appear to have been reported in the literature (Singh et al., 1988).

It is noted that these previous analytical models were formulated with several restrictive assumptions. In order to yield a tractable mathematical system, the analyses were inherently limited to the cases when the dimensionless amplitude of the disk oscillation was small. Another key assumption of the analysis was that the disk was infinite in size, and that an infinite expanse of fluid was considered. It is emphasized that the issues of a finite shrouded disk executing a finite-amplitude torsional oscillation have yet to be addressed. The present paper aims to tackle these technical points. The engineering relevance of flows driven by an oscillating disk has been noted in recent technological developments. Larrousse (1987) demonstrated potential applications of a continuous process of spin-up and spin-down, which can be simulated by an oscillating disk, in growing crystals. Also, the oscillating-disk flow serves as a rudimentary model in the important topic of fluid mixing (Ottino, 1990).

In this work, numerical studies and laboratory flow visualizations have been made of more practically relevant flows of a viscous fluid in a cylinder, which are driven by a finite, shrouded, torsionally-oscillating endwall disk.

Numerical solutions to the unapproximated Navier-Stokes equations are secured for the flow in a closed cylindrical container of radius R. For definiteness, the angular velocity of the upper endwall disk at $z = H$ is $\Omega \cos \lambda t$, and the rest of the

Contributed by the Fluids Engineering Division for publication in the JOURNAL OF FLUIDS ENGINEERING. Manuscript received by the Fluids Engineering Division May 16, 1995; revised manuscript received September 4, 1996. Associate Technical Editor: M. M. Sindir.

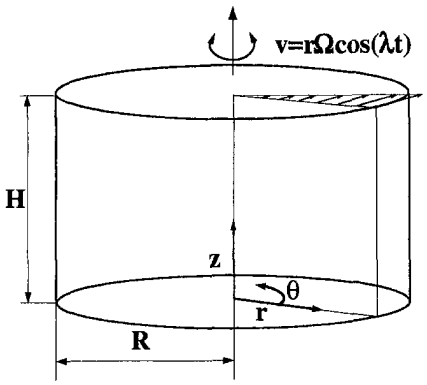

Fig. 1 Flow geometry and coordinate system

cylindrical surface walls are at rest. In accordance with the original problem statement, the rotational Reynolds number, $\mathrm{Re} = R^2\Omega/\nu$, where ν denotes the kinematic viscosity, emerges to be the major parameter. In the present paper, concern is directed to the situations in which $\mathrm{Re} \gg 1$; this is of direct relevance to industrial applications. The nondimensional amplitude of the disk oscillation, $\epsilon \equiv \Omega/\lambda$, is permitted to encompass a broad range up to $\epsilon \gtrsim O(1)$. This relaxes the restriction, $\epsilon \ll 1$, of the preceding theoretical analysis. The time-dependent numerical solutions are processed to exhibit principal features of three-dimensional flow fields. The primary interest is focused on the flow characteristics in the central portions of the cylinder interior, where the sidewall effects are minimal. The structure of the azimuthal flow, both time-averaged and fluctuating parts, is scrutinized. The presence of significant meridional flows is discussed; and, in particular, the quasi-steady periodic behavior of meridional flows is examined. In the interior region far away from the sidewall, the gross features of azimuthal flow are shown to be in accord with the analytical predictions when ϵ is small. Laboratory flow visualization experiments have been conducted to verify the qualitative patterns of the meridional streaming. The numerically-constructed flow fields are shown to be consistent with the visualizations.

The numerical flow data have been processed to evaluate the time-dependent torque experienced by the oscillating disk. The explicit effects of Re and ϵ are delineated, which will be of interest to practical techniques of measuring viscosity.

2 The Numerical Model

As shown in Fig. 1, an incompressible fluid of density ρ fills completely a cylindrical container. The aspect ratio $A(=H/R)$ is, for most computations, $O(1)$. The fluid is in contact with the upper endwall disk ($z = H$), and no free surface exists. Denoting the velocity components (u, v, w) for cylindrical coordinates (r, θ, z), the fluid motion is governed by the axisymmetric, time-dependent, Navier-Stokes equations:

$$\frac{\partial u}{\partial t} = -\frac{1}{r}\frac{\partial}{\partial r}(ruu) - \frac{\partial}{\partial z}(uw) + \frac{v^2}{r} - \frac{1}{\rho}\frac{\partial p}{\partial r} + \nu\left[\frac{\partial}{\partial r}\frac{1}{r}\frac{\partial}{\partial r}(ru) + \frac{\partial^2 u}{\partial z^2}\right] \quad (1)$$

$$\frac{\partial v}{\partial t} = -\frac{1}{r}\frac{\partial}{\partial r}(ruv) - \frac{\partial}{\partial z}(vw) + \frac{vu}{r} + \nu\left[\frac{\partial}{\partial r}\frac{1}{r}\frac{\partial}{\partial r}(rv) + \frac{\partial^2 v}{\partial z^2}\right] \quad (2)$$

$$\frac{\partial w}{\partial t} = -\frac{1}{r}\frac{\partial}{\partial r}(ruw) - \frac{\partial}{\partial z}(uw) - \frac{1}{\rho}\frac{\partial p}{\partial z} + \nu\left[\frac{1}{r}\frac{\partial}{\partial r}\left(r\frac{\partial w}{\partial r}\right) + \frac{\partial^2 w}{\partial z^2}\right] \quad (3)$$

$$\frac{1}{r}\frac{\partial}{\partial r}(ru) + \frac{\partial w}{\partial z} = 0 \quad (4)$$

At the initial state, the fluid is at rest

$$u = v = w = 0 \quad \text{at} \quad t = 0. \quad (5)$$

All computations were started from an initially motionless state, and at time zero a rotational speed is imposed on the top disk. The thrust of the present effort lies in the large-time, quasi-steady, periodic behavior. In accordance with the problem statement, the boundary conditions are

$$u = v = w = 0 \quad \text{at} \quad r = R \quad (6)$$

$$u = v = w = 0 \quad \text{at} \quad z = 0 \quad (7)$$

$$u = w = 0, v = r\Omega \cos \lambda t \quad \text{at} \quad z = H. \quad (8)$$

where $\Omega \equiv \epsilon\lambda$. To satisfy numerical stability requirements, the boundary conditions at the central axis are applied at a small, but finite, radius ($r = r_i$) (see Warn-Varnas et al., 1978):

$$u = 0, \quad \frac{\partial(v/r)}{\partial r} = 0, \quad \frac{\partial w}{\partial r} = 0 \quad \text{at} \quad r = r_i$$

The above system of equations is solved by using a well-established finite-difference numerical procedure. The numerical model selected is essentially a mark-and-cell scheme, and it has been validated in a number of rotating flow simulations (e.g., Warn-Varnas et al., 1978; Hyun et al., 1983). The specifics of the numerical schemes and algorithms have been documented (Williams, 1969; Warn-Varnas et al., 1978), and they are not

Nomenclature

A = aspect ratio of the cylinder $[=H/R]$
C_T = torque coefficient
H = cylindrical container height
R = cylindrical container radius
Re = rotational Reynolds number $[=R^2\Omega/\nu]$
S = Stokes layer thickness $[=(2\nu/\lambda)^{1/2}]$
T = torque on the disk
(r, θ, z) = cylindrical coordinates
(u, v, w) = velocity components
(u_f, w_f) = unsteady fluctuating parts of meridional flows
(u_s, w_s) = steady parts of meridional flows
ϵ = nondimensional amplitude of oscillation $[=\Omega/\lambda]$
δ_S = nondimensional Stokes layer thickness $[=(2\nu/\lambda)^{1/2}/H]$
δ_E = nondimensional Ekman layer thickness $[=(2\nu/\Omega)^{1/2}/H]$
η_S = axial coordinate scaled by the Stokes shear layer thickness $[=(H - z)/(2\nu/\lambda)^{1/2}]$
η_E = axial coordinate scaled by the Ekman layer thickness $[=(H - z)/(2\nu/\Omega)^{1/2}]$
λ = torsional-oscillating frequency
ν = kinematic viscosity
ρ = density
τ_t = spin-up time $[=\mathrm{E}^{-1/2}\Omega^{-1}$ for $\epsilon > O(1), (\mathrm{E}^{-1/2}\Omega^{-1}\epsilon^{-1}$ for $\epsilon \lesssim O(1))]$
Ω = amplitude of oscillation of the disk
ψ = meridional streamfunction.

reproduced here. The highlights of this numerical model are that the Poisson equation is solved by an ADI iterative approach and the differencing performed on a staggered mesh. Grid points were clustered near the solid boundaries, particularly near the oscillating upper endwall disk. Restrictions on the time step are subject to the Courant-Friedrichs-Lewy condition $\Delta t \leq \Delta s/u_{\max}$, where Δs is the smallest grid spacing and $u_{\max}$ is the largest velocity. Convergence was declared when the relative difference between two successive iterations fell below 10^{-5}. The time step Δt was taken to be sufficiently small to insure both numerical stability and resolution of the results. To determine the number of grid points necessary to obtain grid-independent solutions, a series of calculations with different space discretization have been conducted. Exemplary results of this test are shown in Fig. 2, which demonstrate the grid-convergence based on such comprehensive studies. For most computations, the mesh network was typically (52×62) in the (r-z) axial plane, and Δt was chosen such that one oscillating cycle consisted of 2048 ($=2^{11}$) time steps. In the case of a steady rotating disk, numerical results were in excellent agreement with the experimental data obtained by using the LDA technique [Sorensen & Loc, 1989].

Time-dependent solutions were produced by executing a time-marching integration of the governing equations. Guided by the preceding studies on spin-up [Greenspan & Howard, 1963; Wedemeyer, 1964], the transitory time τ_t to reach the quasi-steady periodic state is estimated as

$$\tau_t \sim \mathrm{E}^{-1/2}\Omega^{-1} \quad \epsilon > O(1)$$
$$\tau_t \sim \mathrm{E}^{-1/2}\Omega^{-1}\epsilon^{-1} \quad \epsilon \lesssim O(1) \qquad (9)$$

in which E ($\equiv \nu/\Omega H^2$) is the Ekman number. The estimate of τ_t for $\epsilon < O(1)$ is also consistent with the prediction by the theoretical analysis of Rosenblat (1959). In the present study, calculations continued up to a time level of nearly $2\tau_t$, at which the quasi-steady state was shown to have been established. Details of temporal evolutions of the numerical data are exemplified in Fig. 3. Typically, the transitory stage from $t = 0$ to the quasi-steady state encompasses less than ten cycles. In the present study, the quasi-steady state was thought to have been established when the nondimensional values of the flow variables differ less than 10^{-5} over the interval of one cycle.

Quantitative assessments of the numerical accuracy of the present calculations have made. The azimuthal velocity at mid-radius of the cylinder, obtained by using the (52×62) mesh, for values of ϵ smaller than 0.1, was in agreement with the analytical result of Rosenblat (1959) within one percent. Also, for several sample cases, comparisons were made between the present results and the results acquired by employing the numerical code based on the SIMPLE algorithm (Patankar, 1980).

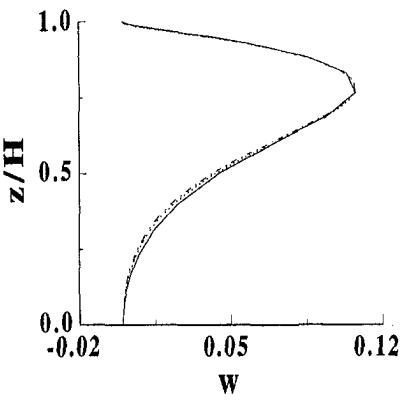

Fig. 2 Exemplary results of grid-convergence tests. Re = 500, A = 1.0, ϵ = 1.0, and at r/R = 0.5. Grid points are: ——, 22 × 22; . . ., 52 × 52; ——.——, 82 × 82.

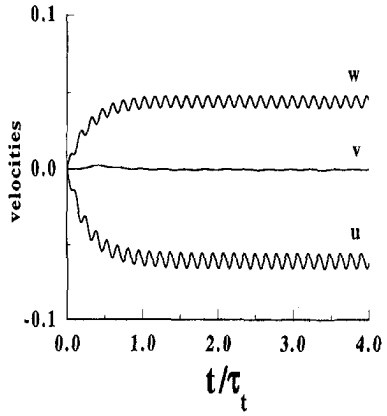

Fig. 3 Examplary plots of velocity evolutions. Re = 500, A = 1.0, and ϵ = 1.0. Position is at r/R = 0.5, z/H = 0.5.

These two sets of data were mutually consistent to a high degree of accuracy.

3 Results and Discussion

The numerical results for an aspect ratio $A = 1.0$ are to be scrutinized. No noticeable qualitative changes are observed as Re varies, from Re = 100 to 2000, thus in the ensuing discussions, the results at Re = 500 are exemplified. Also, as stated earlier, the flow structure in the central interior region is of interest. This is the region in which the direct effects of the sidewall are minimized, and, therefore, cross-comparisons of the numerical results with the theoretical predictions are meaningful in this central interior region.

First, the azimuthal velocity structure is examined. The analysis of Rosenblat gave a closed-form expression for v as

$$v = \epsilon\Omega r\{G_0 + \epsilon^2 G_2\}, \qquad (10)$$

in which

$$G_0 = e^{-\eta}\cos(\lambda t - \eta), \qquad (11)$$

and $\eta \equiv z/(2\nu/\lambda)^{1/2}$ denotes the axial coordinate scaled by the Stokes shear layer thickness $S \equiv (2\nu/\lambda)^{1/2}$. The first term in (10) indicates the classical Stokes shear-wave solution for an infinite flat plate executing a rectilinear torsional oscillation in its own plane in a fluid otherwise at rest (see, e.g., Schlichting, 1968). The G_2 term represents the second-order correction to v, and G_2 contains higher harmonics up to 3λ. The detailed expression for G_2 is very lengthy and complicated, and the reader is referred to Eqs. (44a)–(44b) of the original paper by Rosenblat. Notice again that the validity of the analytical approach of Rosenblat is restricted by the requirement that ϵ be small.

Figure 4 illustrates the axial profile of v in the central area ($r/R \approx 0.5$). Clearly, when ϵ is small, almost perfect agreement is seen between the numerical results and the analytical predictions. Much of the azimuthal velocities are confined to the Stokes layer, and v decays rapidly outside of the Stokes layer. As ϵ increases, the axial extent of non-vanishing v increases. The comprehensive data on v demonstrate that, when ϵ is small, the dominant behavior of v in the interior core is describable by the Stokes shear-wave solution at the primary harmonic. As seen in Fig. 4, as ϵ becomes finite, the contributions of higher harmonics are not negligible, and the v-profiles exhibit more complex patterns over a broader region into the fluid. It is important to observe that, even when ϵ is appreciable, the dominant parts of nonvanishing v-profiles are still concentrated to the Stokes layer thickness. In the figures, the nondimensional axial coordinate scaled by the Stokes shear layer thickness S is

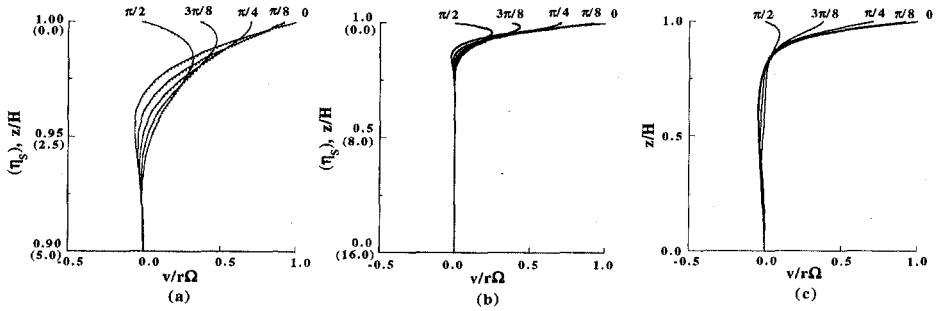

Fig. 4 Azimuthal velocity profile, $v/r\Omega$ versus z/H. In (a), ———, numerical results; . . ., analytical solutions. No analytical solutions are given in plots (b) and (c). Times for the curves are $\lambda t = 0$, $\lambda t = \pi/8$, $\lambda t = \pi/4$, $\lambda t = 3\pi/8$, $\lambda t = \pi/2$. (a) $\epsilon = 0.1$, (b) $\epsilon = 1.0$, (c) $\epsilon = 5.0$.

indicated in the parenthesis. Note the difference in scales used in the ordinates of Fig. 4.

One prominent distinction between the case of a rectilinearly oscillating flat plate and the case of a circularly oscillating disk lies in the meridional flow. It is well-known that, for the classical Stokes problem involving a rectilinearly oscillating infinite flat plate, meridional flows are identically zero. However, for the problem of a circularly oscillating disk, the presence of meridional flows (u, w) is a crucial element in the overall dynamics.

In conformity with the customary treatment, the meridional flows (u, w) are decomposed into time-averaged steady parts (u_s, w_s) and unsteady fluctuating parts (u_f, w_f), respectively. Rosenblat, by assuming $\epsilon \ll 1$, carried out regular expansion procedures up to the first order in ϵ. These manipulations produced closed-form solutions for (u_s, w_s) as well as (u_f, w_f), as stipulated in Eqs. (31) – (34) of Rosenblat (1959). For the sake of completeness, these analytical solutions are reproduced here:

$$u_f = \frac{r\Omega\epsilon}{4}\{e^{-\sqrt{2}\eta}\sin(2\tau - \sqrt{2}\eta) - e^{-2\eta}\sin(2\tau - 2\eta)\} \quad (12)$$

$$w_f = \frac{\Omega\epsilon}{8}\sqrt{\frac{2\nu}{\lambda}}\left\{(2-\sqrt{2})\cos\left(2\tau + \frac{1}{4}\pi\right) - 2e^{-\sqrt{2}\eta}\cos\left(2\tau - \sqrt{2}\eta + \frac{1}{4}\pi\right) + \sqrt{2}e^{-2\eta}\cos\left(2\tau - 2\eta + \frac{1}{4}\pi\right)\right\} \quad (13)$$

$$u_s = \frac{r\Omega\epsilon}{4}\{1 - e^{-2\eta}\} \quad (14)$$

$$w_s = \frac{\Omega\epsilon}{4}\sqrt{\frac{2\nu}{\lambda}}\{1 - 2\eta - e^{-2\eta}\} \quad (15)$$

However, in a later development in the same paper, Rosenblat asserted the inadequacy of such a straightforward expansion technique which led to Eqs. (12) – (15). This deficiency turned up in an unacceptable behavior of u_s and w_s at far fields from the disk. In an effort to rectify this shortcoming of the regular expansion approach, Rosenblat proposed an approximate Pohlhausen-type integral method to obtain an estimate of the axial extent of the region of non-vanishing steady radial flow. The particulars of this methodology are long and they are elaborated in Eqs. (58) – (62) of Rosenblat (1959), to which the interested reader is referred.

Figure 5 displays the axial profiles of u_f. Again, when ϵ is very small, nearly complete agreement is discernible between the numerical results and the analytical solutions [Eq. (12)]. The nonvanishing u_f is concentrated to the Stokes layer thickness $S \sim (2\nu/\lambda)^{1/2}$, and u_f is practically zero outside the Stokes layer. This implies that, in the interior region outside the Stokes layer thickness, the fluctuating part of radial velocity is negligibly small. When ϵ is appreciable, the dominant parts of nonvanishing u_f-profiles are still concentrated to the Stokes layer thickness. Note that, even when ϵ is finite, the principal parts of nonvanishing u_f are still largely confined to the Stokes layer thickness. In Fig. 5, for the sake of comparisons, the coordinates z based on the Stokes layer thickness, $\delta_s = (2\nu/\lambda)^{1/2}/H$, and the Ekman layer thickness, $\delta_E = (2\nu/\Omega)^{1/2}H$, are indicated in the parentheses.

The pattern of w_f is also revealing, as shown in Fig. 6. As portrayed in Eq. (13), the first term of w_f is not a function of z, and only the second and third terms decay exponentially outside the Stokes layer. Also, note that the overall magnitude of w_f is $O(S/r)$ of u_f. At moderate radii [e.g., see the curves at $r/R = 0.5$ in Fig. 6], the Stokes layer thickness S is much smaller than the radial distance r. Therefore, it is important to recognize that w_f is indeed orders of magnitude smaller than u_f for the parameter values of present concern. The profiles of w_f illustrate considerable discrepancies between the numerical

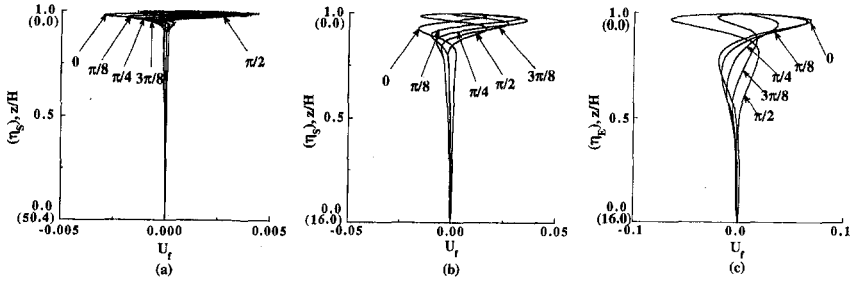

Fig. 5 Profile of the fluctuating part of radial velocity, $U_f[\equiv u_f/r\Omega]$ versus z/H. ———, numerical results; . . ., analytical solutions [Eq. (12)]. Times for the curves are $\lambda t = 0$, $\lambda t = \pi/8$, $\lambda t = \pi/4$, $\lambda t = 3\pi/8$, $\lambda t = \pi/2$. (a) $\epsilon = 0.1$, (b) $\epsilon = 1.0$, (c) $\epsilon = 5.0$.

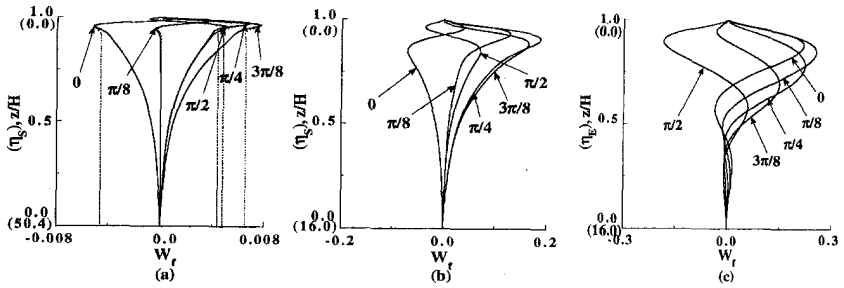

Fig. 6 Profile of the fluctuating part of axial velocity, W_f [$=w_f \mathrm{Re}^{1/2}/R\Omega$] versus z/H: ———, numerical results; . . . , analytical solutions [Eq. (13)]. Times for the curves are $\lambda t = 0$, $\lambda t = \pi/8$, $\lambda t = \pi/4$, $\lambda t = 3\pi/8$, $\lambda t = \pi/2$. (a) $\epsilon = 0.1$, (b) $\epsilon = 1.0$, (c) $\epsilon = 5.0$.

results and the predictions. It is noteworthy that the infinite-disk linearized analytical model of Rosenblat gives almost axially-uniform w_f outside of the Stokes layer. This is in contrast to the numerical results, which exhibit an appreciable z-dependence of w_f throughout much of the interior region. This is believed to be attributable to the general inadequacy of the straightforward regular series expansion technique adopted in Rosenblat.

A significant feature of the present investigation is the behavior of steady parts of meridional flows, i.e., (u_s, w_s). As stressed earlier, Eqs. (14) and (15) were acquired by Rosenblat in a series-expansion formalism. Of particular interest are the far-field patterns of (u_s, w_s) at large distances away from the oscillating disk. First, u_s-profiles are exemplified in Fig. 7. The numerical results show that, near the oscillating disk, a positive u_s is discernible, implying the existence of steady radially-outward flow. This has to be balanced by a negative u_s (radially-inward flow) at mid-height axial locations. In the bottom region of the cylinder, u_s approaches zero to satisfy the no-slip condition at the lower stationary disk. It is evident in Fig. 7 that Eq. (14), termed the potential-flow solution by Rosenblat, yields an inappropriate picture for u_s in much of the axial extent. As is apparent in Fig. 7, this potential-flow solution (shown by dots) gives a constant, finite value of u_s at the far fields, which begins at a small axial distance from the disk. In conjunction with this constant-u_s in the bulk of the interior, w_s of Eq. (15) (as shown by dots in Fig. 8) diverges almost linearly as z moves away from the disk. These far-field solutions of u_s and w_s, of Eqs. (14) and (15), which are the results of a straightforward series-expansion technique, are clearly unacceptable. This anomalous behavior was pointed out by Rosenblat himself, and he proposed an amended calculation procedure based on an approximate Pohlhausen-type method. The crux of this improved representation of u_s is that the convective inertia terms have to be properly included in the determination of flow character at large distances from the disk. The dashed lines of Figs. 7 and 8 are the results computed following the modified version of Rosenblat's analytical prediction. As illuminated in Fig. 7, the qualitative trends of this improved solution are consistent with the numerical results, although quantitative discrepancies are apparent. As is evident in Eqs. (14) and (15), the overall magnitude of w_s is $O(S/r)$ of u_s. This points to the overall smallness of w_s in comparison to u_s in realistic situations. The axial profiles of w_s, exhibited in Fig. 8, clearly demonstrate that a nonvanishing positive w_s is discernible up to moderate axial distances from the upper oscillating disk. This asserts that, in the bulk of the central interior region of the cylinder, a steady axial streaming toward the oscillating disk exists. As ϵ increases, the impact of this steady pumping effect is felt in a broader axial extent and its strength becomes more pronounced in the region father away from the oscillating disk.

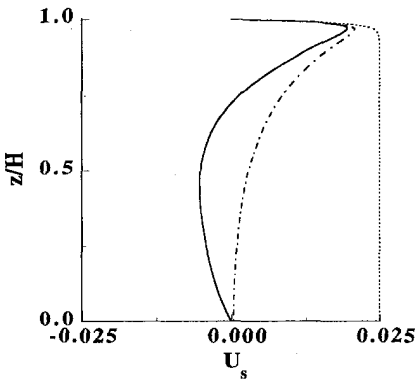

Fig. 7(a)

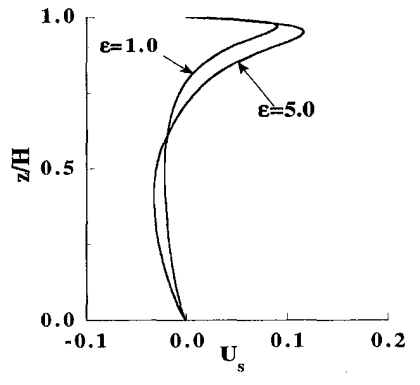

Fig. 7(b)

Fig. 7 Profile of the steady part of radial velocity, U_s [$=u_s/r\Omega$] versus z/H: ———, numerical results; ——.——, improved analytical solution [Eq. (59) of Rosenblat]; . . . , analytical solution [Eq. (14)]. (a) $\epsilon = 0.1$, (b) $\epsilon = 1.0$ and 5.0.

Utilizing the numerical solutions, depictions are made in Fig. 9 of the global pattern of clockwise-circulatory steady meridional streaming. In Fig. 9, plots of the meridional streamfunction ψ for u_s and w_s are given. Here, ψ is defined such that $u_s = (1/r)(\partial\Psi/\partial z)$, $w_s = -(1/r)(\partial\Psi/\partial r)$. The oscillation of the disk generates steady axial motions toward the oscillating disk at small and moderate radii. In the vicinity of the oscillating disk, the fluid is propelled radially outward. At large radii near the cylindrical sidewall, constrained by the finite geometry of the cylinder, the steady streaming turns away from the upper disk along the sidewall. This completes the overall circulatory path. The qualitative pattern of circulation remains largely unchanged as ϵ increases to a finite value; however, as anticipated, the flow intensifies as ϵ increases, as reflected in the maximum Ψ-values in Fig. 9. In summary, the present numerical solutions clearly demonstrate the existence of a small, but non-vanishing, steady meridional streaming, which is maintained by the disk oscillation. In the region near the hub, the meridional steady streaming is very weak, as demonstrated in Fig. 9.

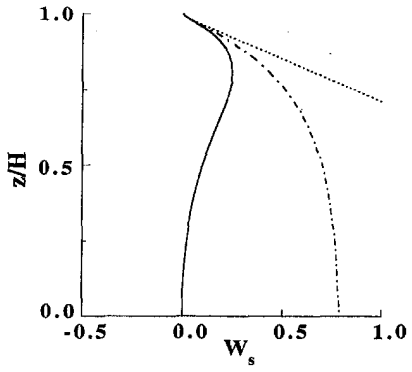

Fig. 8(*a*)

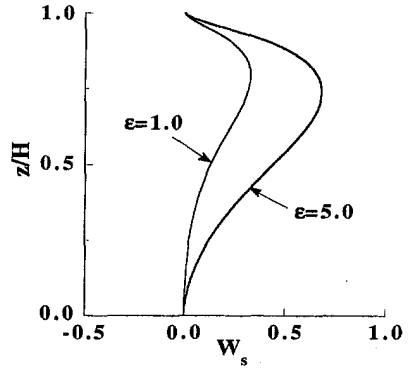

Fig. 8(*b*)

Fig. 8 Profile of the steady part of axial velocity, W_s [$=w_s \mathrm{Re}^{1/2}/R\Omega$] versus z/H: ——, numerical results; ——·——, improved analytical solution [Eq. (59) of Rosenblat]; . . . , analytical solution [Eq. (15)]. (a) $\epsilon = 0.1$, (b) $\epsilon = 1.0$ and 5.0

Companion laboratory flow visualizations were performed to portray the qualitative patterns of the meridional streaming. The experimental apparatus consisted of a closed cylindrical cavity ($R = 5.4$ cm, $H = 5.4$ cm) fabricated with plexiglass, together with an AC servo-motor unit which was controlled by a function generator, a slitbeam generator and photographic image-recording devices interfaced with a computer (see Choi et al., 1989, 1991; Lim et al., 1993). The time interval between successive photographic frames was chosen to be larger then the period of the oscillating disk. Typically, six consecutive frames were overlapped to produce images of steady streaming; an example is displayed in Fig. 10 (for Re = 496, $A = 1.0$, $\epsilon = 1.1$). The working fluid was a water-glycerine mixture. A number of such flow visualizations were made for varying values of Re, ϵ, and they show qualitative agreement with the numerically-constructed meridional steady streamings.

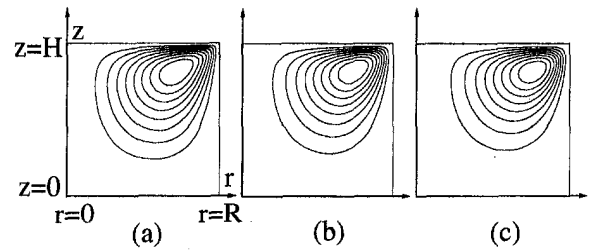

Fig. 9 Plots of meridional stream function Ψ for steady meridional flows (u_s, w_s), nondimensionalized by $\Omega R^3 \mathrm{Re}^{-1/2}$. $|\Psi|_{max}$ denotes the maximum value of ψ, and $\Delta\Psi$ the contour increment. (a) $\epsilon = 0.1$, $|\Psi|_{max} = 0.0689$, $\Delta\Psi = 0.00689$; (b) $\epsilon = 1.0$, $|\Psi|_{max} = 0.137$, $\Delta\Psi = 0.0137$; (c) $\epsilon = 5.0$, $|\Psi|_{max} = 0.162$, $\Delta\Psi = 0.0162$.

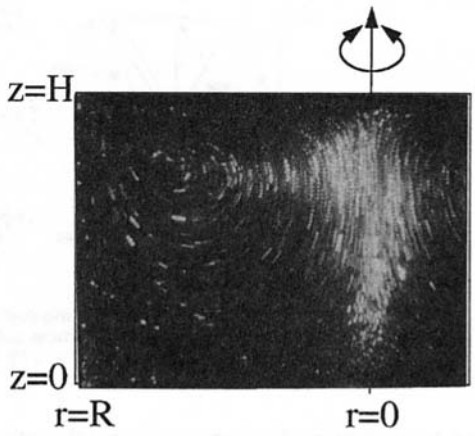

Fig. 10 Exemplary flow visualization of meridional steady streaming. Conditions are: Re = 496, $\epsilon = 1.1$, and $A = 1.0$. The uncertainty in measuring the location is estimated to be 8 percent.

The azimuthal flow data near the oscillating disk were processed to determine the torque T experienced by the disk:

$$T = 2\pi\rho\nu \int_0^R \left(\frac{\partial v(r, z = H, t)}{\partial z} \right) r^2 dr, \qquad (16)$$

from which the torque coefficient C_T is computed as

$$C_T = \frac{2T}{\rho R^5 \Omega^2} \qquad (17)$$

Typical time histories of C_T are displayed in Fig. 11. The application of the fast Fourier transform indicates that C_T, is dominated by the base harmonic for $\epsilon < O(1)$, and the magnitudes of the higher-harmonic terms are typically less then 1 percent of the base-harmonic term. In the case of $\epsilon = 5.0$, the magnitude of the third-harmonic (3λ) is about 5% of that of the base harmonic. Consequently, for the parameter values of present interest, C_T can be approximated as

$$C_T \cong |C_T| \cos(\lambda t + \delta). \qquad (18)$$

The variations of $|C_T|$ and δ with ϵ and Re are shown in Fig. 12. As anticipated, when ϵ is very small, the phase of C_T is $\pi/4$ ahead of the disk oscillation. These findings on $|C_T|$ and δ for $\epsilon \ll 1$ are in line with the theoretical prediction. The present results show that, as ϵ increases, δ decreases, implying that the phase lead is reduced. The amplitude $|C_T|$ decreases substantially as ϵ or Re increases.

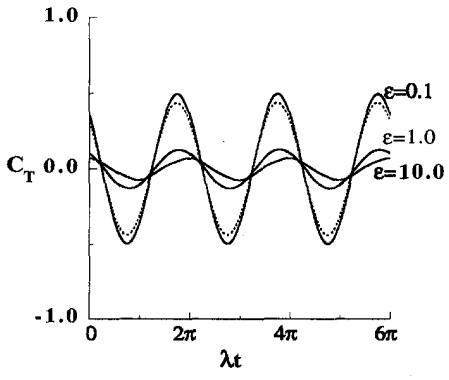

Fig. 11 Time history of torque coefficient, C_T. ——, numerical results for $\epsilon = 0.1$, 1.0, and 10.0; – – –, Rosenblat's solution for $\epsilon = 0.1$.

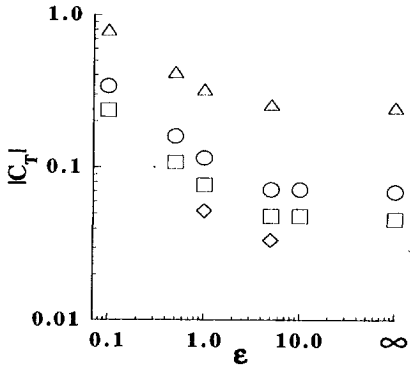

Fig. 12 (*a*)

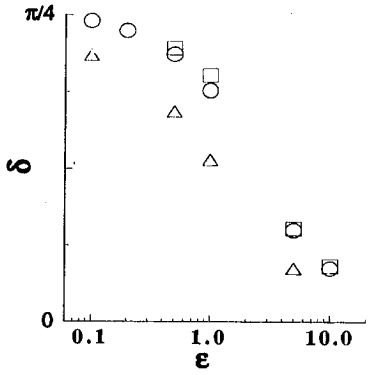

Fig. 12 (*b*)

Fig. 12 Behavior of $|C_T|$ and δ with ϵ and Re. △, Re = 100; ○, Re = 500; □, Re = 1000; ◇, Re = 2000. (a) $|C_T|$, (b) δ.

4 Conclusion

Much of the azimuthal velocities are confined to the Stokes layer. When ϵ is small, the analytical predictions of v are in excellent agreement with the numerical results. As ϵ increases, the effects of the higher harmonics are felt, and the v-profiles display more complex patterns in a broader axial extent.

The unsteady fluctuating part of the radial velocity, u_f, is largely confined to the Stokes layer thickness. The fluctuating part of the axial velocity, w_f, is much smaller than u_f for the parameter values of present concern. The analytical predictions for w_f, based on the straightforward regular expansion technique, show substantial variances with the numerical solutions.

The behavior of (u_s, w_s), the steady part of the meridional velocity, is analyzed in detail. Near the oscillating disk, a steady radially-outward flow is seen. At mid-height axial locations, a radially-inward flow is present. In the region near the stationary disk, u_s approaches zero. A nonvanishing w_s is discernible up to moderate axial distances from the oscillating disk. In the bulk of the central interior region, a steady axial streaming toward the oscillating disk exists. As ϵ increases, the steady streaming becomes more pronounced in a broader axial extent.

The torque coefficient is dominated by the base harmonic. The phase advance of $|C_T|$ over the disk oscillation decreases as ϵ increases or Re decreases. Also, $|C_T|$ is reduced substantially as ϵ increases to a value of $O(1)$ or Re increases. In the region of $\epsilon \gtrsim O(1)$, as ϵ increases, $|C_T|$ converges to the values of the steady rotating disk.

Acknowledgments

Appreciation is extended to the referees whose comments led to improvements in the revised manuscript. This work was supported in part by research grants from Tong Yang Machinery & Engineering Co. and from Tong Yang Magic Co., Korea.

References

Alonso, C. V., 1975, "Steady Laminar Flow in a Stationary Tank with a Spinning Bottom," ASME *Journal of Applied Mechanics,* Vol. 42, pp. 771–776.

Benney, D. J., 1964, "The Flow Induced by a Disk Oscillating in its Own Plane," *Journal of Fluid Mechanics,* pp. 385–391.

Choi, S., Kim, J. W., and Hyun, J. M., 1989, "Transient Free Surface Shape in an Abruptly-Rotating, Partially-Filled Cylinder," ASME JOURNAL OF FLUIDS ENGINEERING, Vol. 111, pp. 431–439.

Choi, S., Kim, J. W., and Hyun, J. M., 1991, "Experimental Investigation of the Flow with a Free Surface in an Impulsively Rotating Cylinder," ASME JOURNAL OF FLUIDS ENGINEERING, Vol. 113, pp. 245–249.

Greenspan, H. P., and Howard, L. N., 1963, "On a Time-Dependent Motion of a Rotating Fluid," *Journal of Fluid Mechanics,* Vol. 17, pp. 385–404.

Hyun, J. M., Leslie, F., Flowlis, W. W., and Warn-Varnas, A., 1983, "Numerical Solutions for Spin-Up from Rest in a Cylinder," *Journal of Fluid Mechanics,* Vol. 127, pp. 263–281.

Lang, E., Sridhar, K., and Wilson, N. W., 1994, "Computational Study of Disk Driven Rotating Flow in a Cylindrical Encloser," ASME JOURNAL OF FLUIDS ENGINEERING, Vol. 116, pp. 815–820.

Larrousse, M. F., 1987, "Transport Phenomena During Spin-Up/Spin-Down in the Bridgman-Stockbarger Technique," Ph.D. thesis, University of Clarkson.

Lim, T. G., Choi, S., and Hyun, J. M., 1993, "Transient Interface Shape of a Two-Layer Liquid in an Abruptly Rotating Cylinder," ASME JOURNAL OF FLUIDS ENGINEERING, Vol. 115, pp. 324–329.

Ottino, J. M., 1990, "Mixing, Chaotic Advection, and Turbulence," *Annual Review of Fluid Mechanics,* Vol. 22, pp. 207–253.

Pao, H-P., 1970, "A Numerical Computation of a Confined Rotating Flow," ASME *Journal of Applied Mechanics,* Vol. 37, pp. 480–487.

Patankar, S. V., 1980, *Numerical Heat Transfer and Fluid Flow,* McGraw-Hill, New York.

Rosenblat, S., 1959, "Torsional Oscillations of a Plane in a Viscous Fluid," *Journal of Fluid Mechanics,* Vol. 5, pp. 206–220.

Schlichting, H., 1968, *Boundary Layer Theory,* 7th Ed., McGraw-Hill, New York.

Singh, P., Radhakrichnan, V., and Narayan, K. A., 1988, "Fluctuating Flow Due to Unsteady Rotation of a Disk," *AIAA Journal,* Vol. 27, No. 2, pp. 150–154.

Sorensen, J. N., and Loc, T. P., 1989, "High-order Axisymmetric Navier-Stokes Code: Description and Evaluation of Boundary Conditions," *International Journal for Numerical Methods in Fluids,* Vol. 9, pp. 1517–1537.

Tomlan, P. F., and Hudson, J. L., 1971, "Flow Near an Enclosed Rotating Disk: Analysis," *Chemical Engineering Science,* Vol. 26, pp. 1591–1600.

Warn-Varnas, A., Fowlis, W. W., Piacsek, S., and Lee, S. M., 1978, "Numerical Solutions and Laser-Doppler Measurements," *Journal of Fluid Mechanics,* Vol. 85, pp. 609–639.

Wedemeyer, E. H., 1964, "The Unsteady Flow within a Spinning Cylinder," *Journal of Fluid Mechanics,* Vol. 20, pp. 383–399.

Williams, G. P., 1969, "Numerical Integration of the Three-Dimensional Navier-Stokes Equations for Incompressible Fluid," *Journal of Fluid Mechanics,* Vol. 37, pp. 727–750.

Flow Field Unsteadiness in the Tip Region of a Transonic Compressor Rotor

S. L. Puterbaugh
Aerospace Engineer.

W. W. Copenhaver
Research Aerospace Engineer.

Wright Laboratory,
Wright-Patterson Air Force Base, OH
45433-7251

An experimental investigation concerning tip flow field unsteadiness was performed for a high-performance, state-of-the-art transonic compressor rotor. Casing-mounted high frequency response pressure transducers were used to indicate both the ensemble averaged and time varying flow structure present in the tip region of the rotor at four different operating points at design speed. The ensemble averaged information revealed the shock structure as it evolved from a dual shock system at open throttle to an attached shock at peak efficiency to a detached orientation at near stall. Steady three-dimensional Navier Stokes analysis reveals the dominant flow structures in the tip region in support of the ensemble averaged measurements. A tip leakage vortex is evident at all operating points as regions of low static pressure and appears in the same location as the vortex found in the numerical solution. An unsteadiness parameter was calculated to quantify the unsteadiness in the tip cascade plane. In general, regions of peak unsteadiness appear near shocks and in the area interpreted as the shock-tip leakage vortex interaction. Local peaks of unsteadiness appear in mid-passage downstream of the shock-vortex interaction. Flow field features not evident in the ensemble averaged data are examined via a Navier-Stokes solution obtained at the near stall operating point.

Introduction

The state-of-the-art transonic compressor has evolved into a low-aspect-ratio, high-through-flow, highly loaded configuration where complex phenomena dominate the flow field. The tip flow field is particularly complex being made up of tip clearance flow, a shock system, and the casing and blade boundary layers as illustrated in Fig. 1. It is well known that the tip region contributes significantly to the overall loss generation within a rotor and virtually governs the rotor's operability. Therefore there is great interest in understanding the characteristic features of the flow mechanisms which exist in the tip flow field in order to improve performance and operability.

The tip flow field of the transonic rotor has been studied both experimentally and computationally by many authors. The experimental approaches involve three general methods. High frequency response pressure and temperature probes have been used by Alday (1993), Dunker and Hungenberg (1980), Gallus, et al. (1977), Weyer and Hungenberg (1975), and Ng and Epstein (1985). Optical and laser anemometry methods, which are quite difficult to apply in the tip region, have been employed by Nicholas and Freeman (1982), Rabe et al. (1988), and Suder and Celestina (1994). The computational approaches include efforts due to Adamczyk et al. (1993), Hah and Wennerstrom (1991), and Copenhaver et al. (1993). Each of these studies indicate that the tip vortex is a dominant flow structure in the tip region and suggest that the interaction between the tip vortex and the passage shock plays an important role in overall tip performance. Fundamental studies on shock vortex interaction by Kolkhoran (1993), Metwally et al. (1989), Cattafesta and Settles (1992), and Kolkhoran and Sfoza (1992) show that for strong shock vortex interactions, vortex breakdown can be expected with large levels of unsteadiness in both shock position and shock shape. It was also found that the intensity of the interaction was proportional to the shock system unsteadiness.

This paper investigates flow field unsteadiness in the tip region of the transonic rotor described by Wadia and Copenhaver (1994). The characteristics of the flow field as indicated by the ensemble averaged static pressure contours are also presented, though briefly, for completeness.

Little rotor-relative unsteady information concerning the tip flow field in the cascade plane of a transonic rotor can be found in the open literature. Most presentations of unsteadiness include rotor exit information such as Alday et al. (1993), Dunker and Hungenberg (1980), and Epstein et al. (1982). One possible reason for the lack of tip region data is that, since the time history of the signals must be simultaneously retained for multiple transducers, the data storage and handling requirements are imposing. Recent advances in computer mass storage and networking have made the current work tractable.

The test article used for the current work, denoted "Rotor 4," is a low-aspect-ratio, high-through-flow, highly loaded configuration. Rotor 4 has been the subject of a number of research papers such as Sellin et al. (1993), Copenhaver et al. (1993), Boyer et al. (1993), Hah and Puterbaugh (1992), Hah et al. (1993), and Wadia and Copenhaver (1994).

Test Apparatus

Test Rig. The experiment was performed at the Wright Laboratory Compressor Aero Research Lab. This facility is configured for closed-loop testing of high-speed, high-specific-flow fans and compressors with a maximum power requirement of 2000 horsepower. A schematic of the compressor test rig is shown in Fig. 2. Note that there are no IGV nor upstream struts in this test configuration.

Detailed design information concerning Rotor 4 was provided by Parker and Simonson (1982). The stator used in this study is a redesigned version using controlled diffusion airfoils based on the stator described by Wennerstrom (1984). The design point stage performance with Rotor 4 installed (operating point "A," test point ID srs930423010) along with some geometric information is given in Table 1.

Contributed by the Fluids Engineering Division for publication in the JOURNAL OF FLUIDS ENGINEERING. Manuscript received by the Fluids Engineering Division March 29, 1994; revised manuscript received June 7, 1996. Associate Technical Editor: Wing Ng.

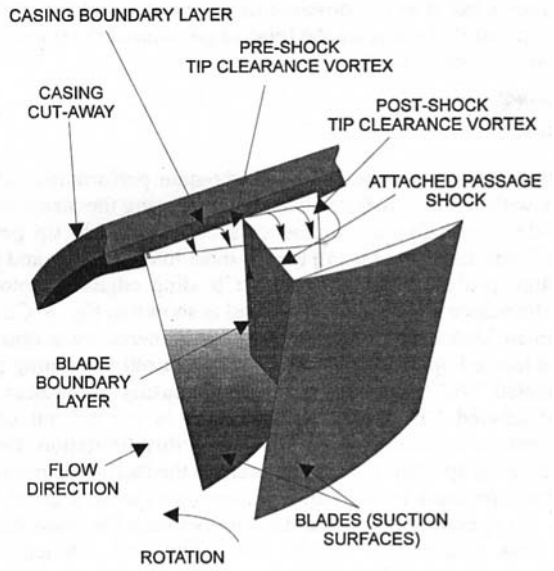

Fig. 1 Transonic compressor tip flow structures

Instrumentation. The test rig was instrumented to measure overall steady-state performance and time-resolved casing static pressures. Details of the rig and its steady-state instrumentation were reported by Law and Wadia (1992) and the details of the time-resolved static pressure measurements were reported by Sellin et al. (1993). Ten casing-mounted high-response transducers were used to measure the time resolved static pressure at the rotor tip. Sensing surface diameters were approximately 75 percent of the blade tip maximum thickness and 2.5 percent of a blade passage pitch. The mounting configuration is shown graphically in Fig. 3.

The ten transducers were evenly spaced in the region extending from 40 percent of the axial chord projection upstream of the leading edge to 80 percent downstream of the leading edge. Measurement density was limited due to physical space requirements for transducer installation. Although a higher measurement density would be desired the density is more than adequate to identify the dominant structures and quantify relative areas of high unsteadiness levels.

Data Acquisition and Reduction

Hardware and Methods. The sampling rate was set at four times the ninth harmonic of the blade pass frequency. This provided 40 samples to span one blade passage. The data were obtained at steady state operating points by recording on analog tape. The data were digitized from previously recorded analog tape and further processed by software. A "once-per-revolution" synchronization signal was used to phase lock the signals during processing. It was determined that an average of 125 time slice samples from each transducer output was required to obtain an adequate steady-state representation of the macroscopic tip flow structure. The averages were obtained for a discrete passage and do not contain any blade-to-blade variational information. Therefore the data presented in this study is from a single passage and is considered representative of all 20 individual passages. The data were ensemble averaged using:

$$\overline{p_x}(t) = \frac{1}{N}\sum_{k=1}^{N} p_x(t) \tag{1}$$

where x represents each axial location where measurements were obtained, N is the number of sample functions (125 in this case), and t is the time. Note that phase locking assured that the initial time for each sample function began at the same blade passage. Further details concerning the data processing can be found in Sellin et al. (1993).

Transducer Calibration and Measurement Uncertainty. The design of the test rig (Fig. 2) allowed the Kulite transducers to be calibrated in situ. With the rotor removed, known pressures were applied to each of the casing-mounted Kulites. Since the Kulite output is linear in the pressure range of interest, a two point calibration was performed, with pressures of atmospheric and 10 psig. The pressure measurement system provided for a frequency response of 63 kHz, nine times blade pass frequency with no amplitude attenuation. A discussion on the influence measurement frequency response on the results will be included in the Results section.

A measurement uncertainty analysis was performed for a representative discrete value of the unsteady pressure signal, which included the effect of all components involved in measurement and calibration. The bias error was estimated to be ±0.05 psi and the precision error was estimated to be ±0.07 psi. This gave an overall uncertainty of ±0.086 psi at a 95 percent confidence interval. The significance of the unsteadiness information could, of course, be compromised by excessive measurement uncertainty. In particular, the precision error component has a direct bearing if it is assumed that the bias error changes little over the recording period, which is a reasonable assumption. Therefore a worst case scenario was considered

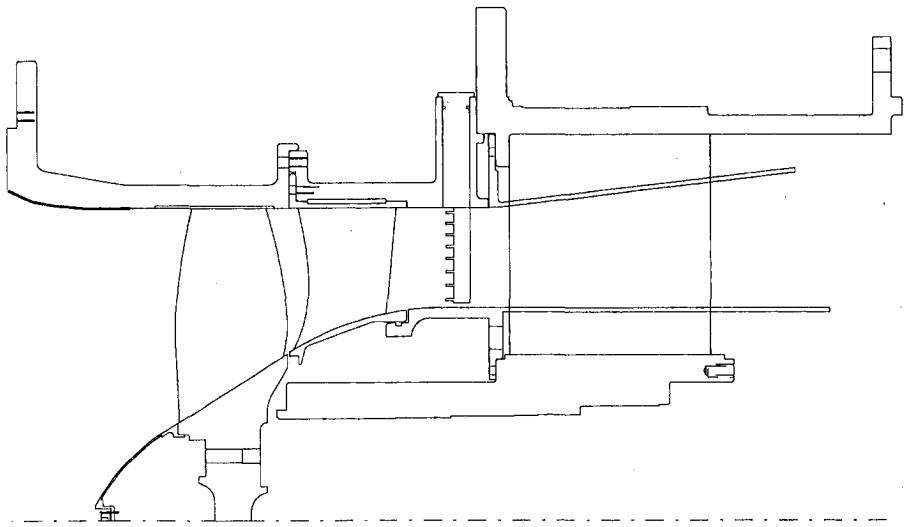

Fig. 2 Test rig cross section

Table 1 Stage performance and geometric specifications

Pressure ratio	1.953
Adiabatic efficiency	89.9%
Corrected specific flow	213.3 Kg/s/m^2 (43.70 lbm/s ft^2)
Corrected tip speed	457.2 m/s (1500 ft/s)
Approximate inlet tip relative Mach number	1.6
Mean rotor aspect ratio	1.320
Rotor inlet hub/tip ratio	0.312
Mean tip clearance	0.5% of tip chord

where the minimum steady state pressure and the full precision error was used to compute a threshold of the unsteadiness parameter (which is defined later) below which unsteadiness would be considered insignificant. The threshold resulting from the worst case scenario was 0.6 percent. Magnitudes of the unsteadiness parameter well over this value were seen in each case. This will become evident later in the fidelity of the unsteadiness plots.

Data Processing. An "unsteadiness parameter" was defined in order to quantitatively assess the randomness of the flow field within a discrete passage. The unsteadiness parameter was simply defined as the RMS value of a fluctuating quantity at a particular spatial location divided by its local time averaged value. This is analogous to the magnitude associated with turbulence level. For a quantity, Q, the unsteadiness parameter for a particular axial location i and circumferential location j is given by:

$$UP_{Q_{i,j}} \equiv \frac{1}{\bar{Q}_{i,j}} \sqrt{\frac{1}{N} \sum_{n=1}^{N} (Q_{i,j_n} - \bar{Q}_{i,j})^2} \qquad (2)$$

The analog pressure signals were processed in a manner which excluded passage-to-passage variation from the unsteadiness parameter calculation. This was accomplished by triggering the sampling process once per revolution using the synchronization pulse. The sampling process would then run for the time required for 3 blade passages to move past the transducers. Hence pressure signals from the same 3 passages were measured once per revolution. Therefore, the unsteadiness present in the plots which follow indicate actual variation of pressure within a given passage.

The nature of the laboratory frame fixed position of the casing mounted transducers limits the information which is obtainable. The unsteady information which is presented later will indicate the non-engine order variation in static pressure. Variations which are integral multiples of the once-per-revolution rotor frequency are not detected. The rotor potential field and the rotor/stator potential interaction will be included in the measurements but it is not possible to resolve the influence of the stator potential field since the relative position of the transducers and stator row is fixed.

Results

Rotor Performance. The steady-state performance of the stage with Rotor 4 installed was obtained using the instrumentation described above. For the present work, rotor tip performance was calculated using the tip-most total pressure and temperature probes mounted on stator leading edges. A rotor tip "performance map" at design speed is shown in Fig. 4. Casing-mounted high-response pressure measurements were obtained at the labeled operating points. The open throttle operating point is labeled "A," with back pressure increasing to the near stall point labeled "D." Note that point A is not a limit of the compressor operating range, but is a facility limitation. Due to closed-loop operation, losses inherent to the facility do not allow the back pressure to fall below a limiting value at a given flow rate. An operating point intermediate between the open throttle and peak efficiency is labeled "B." The peak efficiency operating point is labeled "C."

Tip Leakage Vortex. The trend of tip region shock position with back pressure variation in a transonic compressor rotor is currently fairly well understood. However, the interaction of the tip leakage vortex and the shock requires further study to fully understand. Many authors have described the formation of the tip leakage vortex that results from the fluid flow from the pressure side to the suction side of the blade through the clearance region (Inoue and Kuroumaru, 1989; Storer and Cumpsty, 1991; Stauter, 1993). Inoue and Kuroumaru (1989) and Storer and Cumpsty (1991) found that the core of the vortex is indicated by a low pressure "trough" which exists in measurements from casing mounted high frequency response pressure transducers. Suder and Celestina (1994) performed an extensive numerical and experimental study on tip clearance flow in transonic compressors. Their work has shed considerable light on the phenomena, indicating that high regions of blockage exist in the passage as a result of the interaction of the shock and vortex. The results presented in this study investigate the unsteadiness of this region. In a numerical experiment, Adamczyk et al. (1993) studied the tip leakage vortex and shock as they relate to compressor stall. It was deduced that the interaction between the vortex and the shock play a large part in high speed compressor stall. The geometric relationship between the vortex and the shock at higher back pressures is similar to that employed by Cattafesta and Settles (1992) in a study of vortex breakdown due to the interaction of a vortex and a normal shock.

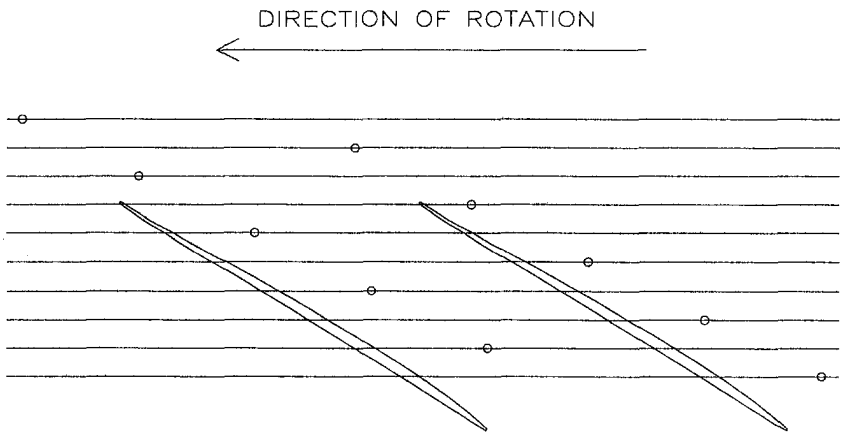

Fig. 3 Transducer mounting locations relative to rotor blade row

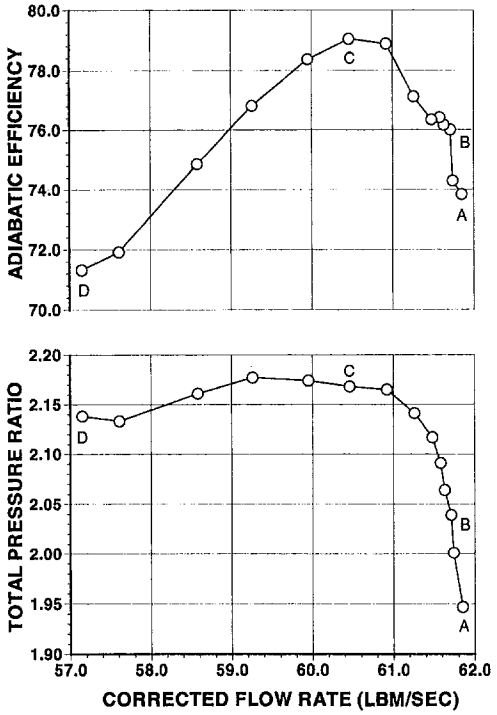

Fig. 4 Rotor tip section performance map at 100 percent N_c

Basic Flow Structure. The general nature of the steady shock structure in transonic rotors inboard of the blade tip has been reported by Pierzga and Wood (1985) and Wood et al. (1986). It is important here to describe the nature of the steady shock at the tip, as described by static pressure measurements, for comparison with the unsteadiness levels at each compressor operating point. The measured tip flow structure at each of the four operating points is presented in the form of a sequence of static pressure contour plots in Fig. 5(*a*)–5(*d*).

At operating point A (Fig. 5*a*) the leading edge shock is attached at the pressure surface leading edge, emanating toward the suction surface at an oblique angle with respect to the incoming flow. It is difficult to explain the exact nature of the shock at the suction surface due to the resolution of the pressure measurements. However, the measurement resolution is sufficient to establish the weakening of the shock near the suction surface termination point. A possible explanation for this was provided by Wood et al. (1986). Their measurements showed the shock to be leaned in the spanwise direction at the suction surface interface. The apparent shock weakening could be due to the oblique nature of the shock in the spanwise direction. However, the results reported in their work were for blade location inboard of the tip by 10 percent span. The work of Hah and Wennerstrom (1991) indicated that the shock becomes normal in the spanwise direction as it approaches the case. Since the measurements made in this study were at the case it is more likely that this weakening is due to the influence of the clearance flow on the shock than spanwise obliquity. Further study is required to completely establish the shock structure at the casing-blade suction surface interface. Downstream of the leading edge shock, the flow reaccelerates before encountering a secondary shock which is oriented approximately normal to the flow in this view. A high pressure region is present downstream of the leading edge shock near the pressure side leading edge.

As the back pressure is increased, the secondary shock moves forward in the passage until operating point B (Fig. 5*b*) where it appears to have coalesced with the leading edge shock and stands somewhat oblique to the incoming flow while still attached to the pressure side leading edge. At the rotor peak efficiency point, operating point C (Fig. 5*c*), the single shock remains attached but is oriented normal to the incoming flow. For operating points A, B, and C, a weak bow wave emanating from the leading edge and extending upstream can be seen. At the near stall point, operating point D (Fig. 5*d*), the shock has detached, standing ahead of the leading edge and extending over the adjacent passage entrance. In points B and C an area of low static pressure is present in mid-passage downstream of the shock. This region corresponds to the region of shock-vortex interaction as described by Suder and Celestina (1994) both computationally and experimentally on a rotor of similar loading level and tip clearance to chord ratios. These regions behind the shock where the vortex interacts with it will be explored further with the unsteadiness characteristics.

For comparison and to help identify the vortex, a steady 3D Navier Stokes computation using the method developed by Hah (1989) was performed for the rotor. The I-type grid used for the computation contained 152 nodes in the streamwise direction, 50 in the pitchwise direction, and 46 in the spanwise direction for a total of about 350,000 nodes. The clearance was spanned by 6 nodes and the blade chord was spanned by 95 nodes. The solutions for the rotor under study at operating points at 100 percent speed have been previously reported by Hah and Puterbaugh (1992). Excellent agreement was shown to exist between the experimental data and the numerical solution. Figure 6 shows the pressure distribution on the casing and the trajectory of the vortex given by the numerical solution. An

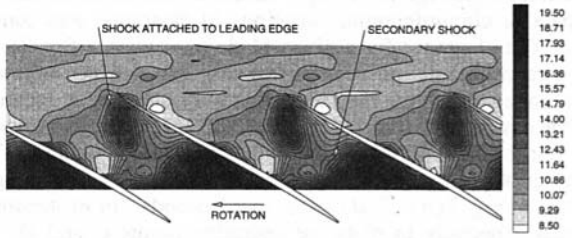

Fig. 5(*a*) Ensemble averaged static pressures-operating point A

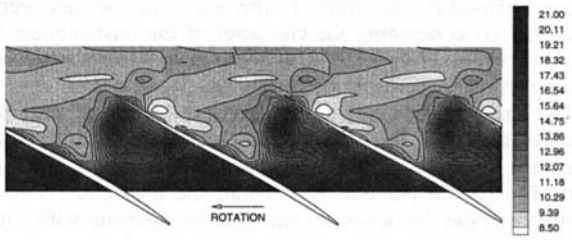

Fig. 5(*b*) Ensemble averaged static pressures-operating point B

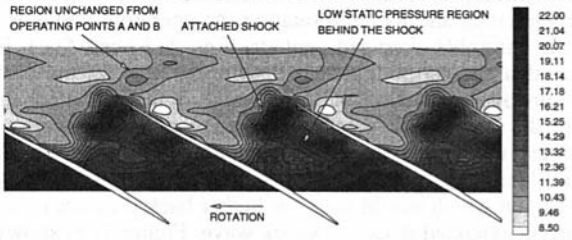

Fig. 5(*c*) Ensemble averaged static pressures-operating point C

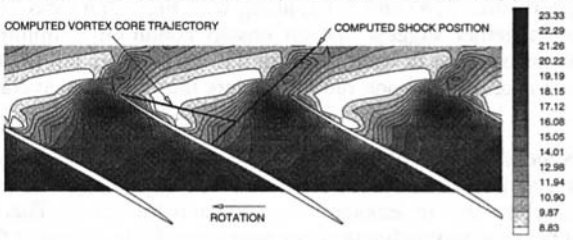

Fig. 5(*d*) Ensemble averaged static pressures-operating point D

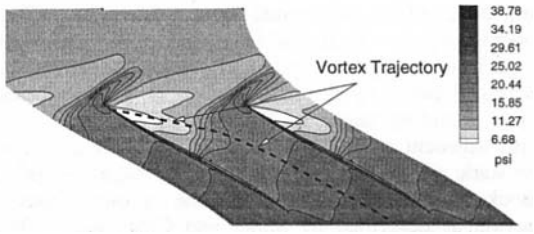

Fig. 6 Computed tip vortex trajectory and static pressure distribution

interaction clearly occurs between the vortex and the shock based on the change in the path of the vortex after intersecting the shock. The computed vortex core trajectory for the near stall operating condition is identified on the measured data (Fig. 5*d*) for comparison.

Unsteadiness Characteristics. This paper is intended to present the character of the unsteadiness as it relates to the cascade geometry and operating point. In order to do so, the pressure unsteadiness parameter for each of the discrete sample "positions" was computed for each of the operating points and plotted in a manner similar to that for the static pressure measurements. The result is a set of contours which indicate how much a discrete measurement varies from its ensemble averaged value with time. In addition to considering the need to exclude passage-to-passage variation discussed earlier, the impact of circumferential variations in clearance was considered. The clearance for a given blade passage is a function of the circumferential position on the case that the measurements were taken. Since the measurements were obtained at locations on the case within 10 degrees of each other, clearance variations are minimal and do not affect the unsteadiness parameters. The contour plots of pressure unsteadiness parameter values are presented in Fig. 7(*a*)–7(*d*). Note that "islands" of unsteadiness appear especially in plots for operating points C and D. The island like nature of the unsteadiness contours are due solely to the contouring algorithm. In the remainder of this section, observations concerning the character of the unsteadiness will be presented and related to other work in an attempt to describe its impact on compressor performance.

The maximum value of unsteadiness increases with back pressure and from inlet to exit. The maximum unsteadiness at operating point A is about 3.4 percent whereas at operating point D it is 9.8 percent. In general, the unsteadiness is low upstream of the shock system and high downstream with almost a step change upon encountering the shock.

An interesting observation can be made concerning ensemble averaged data and its interpretation. At operating points B and C, the ensemble averaged contour, Figs. 5(*b*) and 5(*c*), indicates that the shock is attached with the flow on the suction side-uncovered portion of the passage essentially unchanged from the lower back pressure operating points. However, the pressure unsteadiness parameter contours, Fig. 7(*c*), indicate that a local peak unsteadiness occurs on the suction side along the region which would soon (at higher back pressure) contain a strong extended detached shock wave. Figure 7(*b*) shows no evidence of local peaks in unsteadiness upstream of the leading edge. Figures 5(*b*) and 5(*c*), along with Figs. 7(*b*) and 7(*c*), taken together suggest that an unstart condition is imminent with an increase in back pressure. Of course, this information is not accessible if one only considers the ensemble averaged data.

Shock/Vortex Interaction. The maximum unsteadiness at any given operating point occurs either along a shock or in an area where the tip leakage vortex impacts the shock. The fact that peaks in unsteadiness occur near identifiable, coherent flow structures indicates that a process as simple as structure movement and/or as complex as an interaction of structures is occurring. This "deterministic" nature clearly dominates any "noncoherent" turbulence which may be present. The forcing function for this deterministic unsteadiness (in particular shock movement) may be attributed to processes described by 1) theories due to Ng and Epstein (1985) concerning wake shedding in a transonic rotor, to 2) Lee (1989) concerning disturbance propagation on a supercritical airfoil with flow separation, or to 3) vortex breakdown resulting from strong shock-vortex interaction as was seen by Metwally et al. (1989) and Cattafesta and Settles (1992). The results presented later in this study support the notion that in the tip region the unsteadiness is primarily driven by strong shock vortex interaction.

At peak efficiency, operating point: C (Fig. 7*c*), a local peak of unsteadiness occurs in about mid-passage downstream of the shock and then migrates to the pressure side of the adjacent blade. This feature grows and is more clearly defined at operating point D (Fig. 7*d*), where it can be seen to extend to the downstream edge of the area covered by the instrumentation. The location of this region of unsteadiness indicates that an interaction between the vortex and the shock may be its cause. The region of high unsteadiness behind the shock may be evidence of the vortex breakdown phenomena. Similar observations with somewhat stronger vortices have been made in fundamental flow studies by Metwally et al. (1989) and Cattafesta and Settles (1992). This flow structure probably contributes to

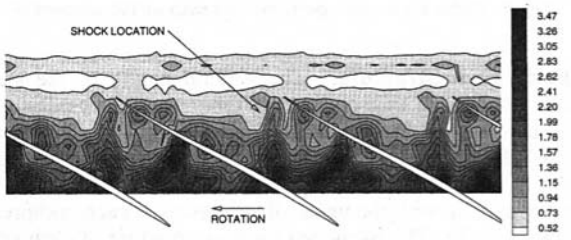

Fig. 7(*a*) Pressure unsteadiness parameter-operating point A

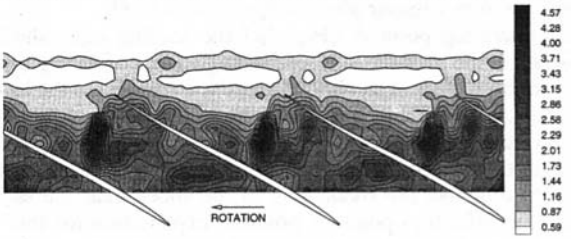

Fig. 7(*b*) Pressure unsteadiness parameter-operating point B

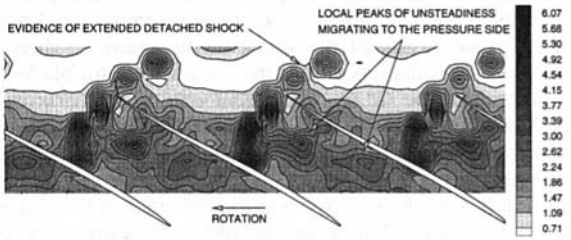

Fig. 7(*c*) Pressure unsteadiness parameter-operating point C

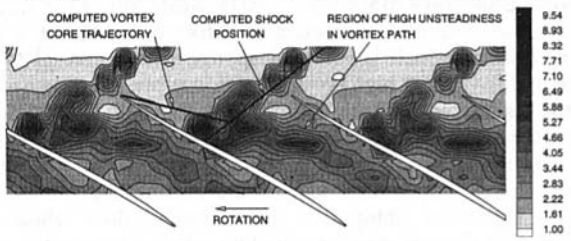

Fig. 7(*d*) Pressure unsteadiness parameter-operating point D

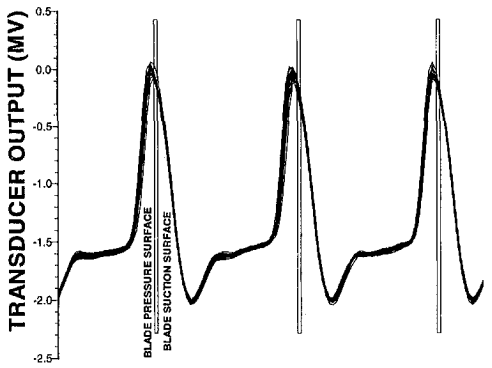

Fig. 8(*a*) 20 ensembles from transducer at 13 percent chord downstream of leading edge-operating point C

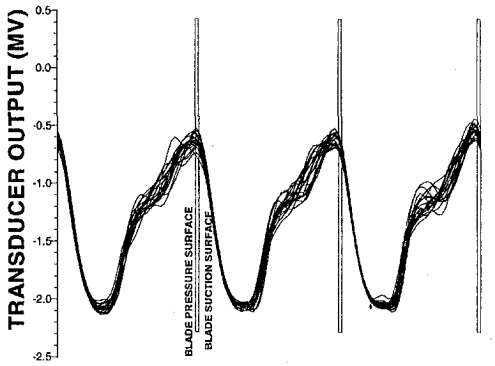

Fig. 8(*b*) 20 ensembles from transducer at 39 percent chord downstream of leading edge-operating point C

the increased randomness seen in rotor exit measurements toward the tip region by Alday et al. (1993) and Weyer and Hungenberg (1975). Furthermore, a link may also exist between unsteadiness from this source and tip losses. Kerrebrock (1980) observed that, in general, unsteadiness and inefficiency seem to increase together. Indeed, instantaneous efficiency contours at the rotor exit presented by Alday et al. showed a high loss region in the blade wakes and across the entire blade passage in the vicinity of the casing. Depending on the length scale of the resulting fluctuations at the rotor exit, efficiency can be negatively impacted by as much as 0.5 to 1.0 points based on estimates by Ng and Epstein (1985).

Examples of 20 sample functions for two different transducers at operating point C are shown in Figs. 8(a) and 8(b) in order to provide an indication of the signal character. Figure 8(a) shows the output of the transducer mounted 13 percent of rotor chord downstream of the leading edge and Fig. 8(b) shows the output of the transducer mounted 39 percent downstream of the leading edge.

The severity of the gradients seen in the pressure signals in Figs. 8(a) and 8(b) are directly influenced by the frequency response of the measurement/processing system and the transducer's sensing element size. The impact of each of these factors is to reduce, or "smear," high gradient regions that exist near blade surfaces and shocks. These effects cannot be avoided using this measurement technology. However, the fidelity of the ensemble averaged pressure contour plots presented here (Fig. 5) suggests that the flow fields were adequately represented.

Frequency response can also have an effect on unsteadiness measurements. Consider an ensemble of sample functions from a semi-periodic source similar to what is being considered in this paper. Assume that during the period when several of the sample functions were being recorded, a high frequency event occurred, such as a spike of finite amplitude. If a measurement system of infinite frequency response were used, the true amplitude of the spike would be measured. The difference between that instantaneous value (the peak) and the averaged value would then be incorporated into the unsteadiness calculation. Now if a measurement system of *finite* frequency response were used, the measured amplitude of the spike would be less than the true value. Therefore a smaller difference would exist between the instantaneous value and the averaged value. The resulting magnitude of unsteadiness would be less than that computed using the infinite frequency response system. Therefore, the unsteadiness calculations reported in this work must be considered conservative in magnitude, i.e., the actual unsteadiness could be greater, but not less. It is not felt that this factor should influence any of the interpretations or conclusions given here.

The ability of the signal processing system to phase lock the signals with rotor position is evident by the "ensemble-wise" periodicity of the signal at the highly negative sloped portion of the signal. This segment of the signal corresponds to the blade pass. The highly positive sloped portions of either signal correspond to the shock. Some shock movement is evident in each case in addition to some strength variation in Fig. 8(a). The signal in Fig. 8(b), being further downstream than 8(a), shows the highly unsteady nature of the flow field in mid-passage.

The extent of shock movement in the pitchwise direction was estimated from Fig. 8(a) to be approximately 20 percent of tip chord. This was done by examining the time history of the pressure signals at 13 percent chord, which indicates the mean shock position at about mid-passage. The shock is indicated by a sharp pressure rise whereas the blade is indicated by a sharp pressure drop. The range of shock positions was determined by calculating the time between a rise in the signal when crossing a threshold associated with the shock position and a drop in the signal when crossing a threshold associated with the blade position. This procedure was followed for each of the 125 sample functions that make up the ensemble. The change in these delta times, modified appropriately for geometry and time-space scaling, indicates the variation in shock position. Since the deltas were computed from shock-to-blade for each sample function, any influence of errors, in sample function-to-sample function blade position is eliminated. The measured shock motion (2.0 percent of chord) is somewhat greater but still within reasonable agreement with the chordwise shock movement of 0.2 to 0.6 percent estimated by Ng and Epstein (1985) based on work involving a rotor of similar design. In that work, an oscillating shock was postulated to be responsible for fluctuations in high response rotor exit measurements. A model based on assumed shock oscillation was developed to infer the shock movement in the chordwise direction from the measurements. It is possible that other phenomena, such as the tip clearance flow or various other interactions, which were not taken into account by the oscillating shock model were responsible for the difference in estimated shock motion. The shock motion computed in this study is on the order of magnitude of one third of the vortex diameter found by Metwally et al. (1989) in their shock vortex interaction study. These results further support the notion that the high level of unsteadiness in the tip region is a result of shock vortex interaction.

In view of the influence of unsteadiness on compressor performances described above, it is important to understand how rotor blade geometry, i.e., design parameters, affect unsteadiness. The two most significant sources of unsteadiness appear to be rotor-relative shock movement itself and the interaction between the tip leakage vortex and the moving shock. Therefore consideration must be given to the relationship between these phenomena and design parameters. It is well known that tip clearance plays a primary role in the strength of the tip leakage vortex. However, it is less clear how other design variables such as cascade parameters and loading levels influence shock

movement. Further study is required to establish the roles of these variables on shock movement and loss generation.

Conclusions

Casing-mounted high frequency response transducers have been used to obtain the time-resolved static pressure field at the tip of a state-of-the-art transonic compressor rotor. Both ensemble averaged and time history information has been processed and analyzed to support the following conclusions:

1) The tip shock structure appears as a dual shock system at open throttle, with the secondary shock moving forward and coalescing into one with the leading edge shock as back pressure is increased. The (tip) peak efficiency operating point coincides with a single attached shock, oriented normal to the flow in the cascade plane. Further increases in back pressure detach the shock and at the near stall operating point the shock is clearly detached and extends across the adjacent passage entrance. These findings add to those of Pierzra and Wood (1986) to include blade tip information.

2) There is evidence of a tip leakage vortex at each of the operating points. This is indicated by the presence of a local low pressure region upstream of the shock. These findings help to confirm the findings of Suder and Celestina (1994) among others.

3) The signal processing system successfully phase-locked the signals to the rotor position. This allows observation and analysis of features which can confidently be assigned to unsteadiness.

4) Local peaks of unsteadiness were observed extending from the leading edge away from the suction side of the blade at the tip peak efficiency operating point. The unsteadiness contours at this operating point resembled those at near stall. However, the ensemble averaged pressure plots revealed a structure in this region which remained similar to the lower back pressure condition. This, taken together with the other observations of coherent unsteadiness, indicates that much additional information is available from the signals' time history that is not available from the ensemble averaged data.

5) The shock was estimated to oscillate over a region of about 2.0 percent of blade chord. It was not possible to resolve an oscillation frequency greater than half of once-per-revolution due to the effective sampling rate of the laboratory-frame instrumentation.

6) Unsteadiness exists in clearly defined regions of the blade passage. In general, peaks appear near shocks and areas which are interpreted to include shock-tip leakage vortex interaction.

7) Local peaks of unsteadiness appear downstream of the impact of the tip leakage vortex against the shock. This is interpreted to be the unsteady interaction between the shock and the vortex.

Acknowledgments

Thanks are due to the Compressor Aero Research Lab staff at Wright-Patterson Air Force Base for their efforts in obtaining this data and to Derek Sellin in particular for help in processing and developing analysis tools.

References

Adamczyk, J. J., Celestina, M. L., and Greitzer, E. M., 1993, "The Role of Tip Clearance in High-Speed Fan Stall," ASME *Journal of Turbomachinery,* Vol. 115, pp. 28–39.

Alday, J., et al., 1993, "Flow Randomness and Tip Losses in Transonic Rotors," ASME Paper No. 93-GT-189.

Boyer, K. M., King, P. I., and Copenhaver, W. W., 1993, "Stall Inception in Single Stage, High-Speed Compressors with Straight and Swept Leading Edges," AIAA-93-1870.

Cattafesta, L. N., Settles, G. S., 1992, "Experiments on Shock/Vortex Interaction," AIAA-92-0315.

Copenhaver, W. W., Hah, C., and Puterbaugh, S. L., 1993, "Three-Dimensional Flow Phenomena in a Transonic, High-Through-Flow, Axial-Flow Compressor Stage," ASME *Journal of Turbomachinery,* Vol. 115, pp. 240–248.

Dunker, R. J., and Hungenberg, H. G., 1980, "Transonic Axial Compressor Using Laser Anemometry and Unsteady Pressure Measurements," *AIAA Journal,* Vol. 18, No. 8, pp. 973–979.

Epstein, A. H., et al., 1982, "Time-Resolved Measurements in a Low-Aspect-Ratio Transonic Compressor Stage," ASME Paper No. 82-GT-201.

Gallus, H. E., Bohn, D., and Broichhausen, K. D., 1977, "Measurements of Quasi-Steady and Unsteady Flow Effects in a Supersonic Compressor Stage," ASME *Journal of Engineering for Power,* Vol. 99, pp. 537–544.

Hah, C., and Puterbaugh, S. L., 1992, "A Critical Evaluation of a Three-Dimensional Navier-Stokes Method as a Tool to Calculate Transonic Flows Inside a Low-Aspect-Ratio Compressor," AGARD-CP-510.

Hah, C., Puterbaugh, S. L., and Copenhaver, W. W., 1993, "Unsteady Aerodynamic Flow Phenomena in a Transonic Compressor Stage," AIAA-93-1868.

Hah, C., and Wennerstrom, A. J., 1991, "Three-Dimensional Flowfields inside a Transonic Compressor with Swept Blades," ASME *Journal of Turbomachinery,* Vol. 113, pp. 241–251.

Inoue, M., and Kuroumaru, M., "Structure of Tip Clearance Flow in an Isolated Axial Compressor Rotor," ASME *Journal of Turbomachinery,* Vol. 111, No. 3, July, pp. 250–256.

Kerrebrock, J. L., 1980, "Flow in Transonic Compressors," *AIAA Journal,* Vol. 19, No. 4.

Kalkhoran, I. M., and Sforza, P. M., 1992, "Airfoil Pressure Measurements During Oblique Shock Wave-Vortex Interaction in a Mach 3 Stream," AIAA-92-2631-CP.

Kalkhoran, I. M., 1993, "Vortex Distortion During Vortex-Surface Interaction in a Mach 3 Stream," AIAA-93-0761.

Law, C. H., and Wadia, A. R., 1992, "Low Aspect Ratio Transonic Rotors: Part I-Baseline Design and Performance," ASME *Journal of Turbomachinery,* Vol. 115, pp. 218–225.

Lee, B. H. K., 1989, "Oscillatory Shock Motion Caused by Transonic Shock Boundary-Layer Interaction," *AIAA Journal,* Vol. 28, No. 5, pp. 942–944.

Metwally, O., Settles, G., and Horstman, C., 1989, "An Experimental Study of Shock Wave/Vortex Interaction," AIAA-89-0082.

Nicholas, D. J., and Freeman, C., 1982, "Recent Advances in the Performance of High Bypass Ratio Fans," presented at the 13th Congress of the International Council of Aeronautics (ICAS)/AIAA Aircraft System and Technology Conference, held in Seattle WA, Aug. 22–27.

Ng, W. F., and Epstein, A. H., 1985, "Unsteady Losses in Transonic Compressors," ASME *Journal of Engineering for Gas Turbines and Power,* Vol. 107, pp. 345–353.

Parker, D. E., and Simonson, M. R., 1982, "Transonic Fan/Compressor Rotor Design Study, Volume V," AFWAL-TR-82-2017, ADB-69405, Air Force Wright Aeronautical Laboratories, Wright-Patterson AFB, Ohio.

Pierzga, M. J., and Wood, J. R., 1985, "Investigation of the Three-Dimensional Flow Field Within a Transonic Fan Rotor: Experiment and Analysis," ASME *Journal of Engineering for Gas Turbines and Power,* Vol. 107, No. 2, pp. 427–435.

Rabe, D. C., Wennerstrom, A. J., and O'Brien, W. F., 1988, "Characterization of Shock Wave-Endwall Boundary Layer Interactions in a Transonic Compressor Rotor," ASME Paper No. 87-GT-166.

Sellin, M. D., Puterbaugh, S. L., and Copenhaver, W. W., 1993, "Tip Shock Structures in Transonic Compressor Rotors," AIAA-93-1869.

Stauter, R. C., 1993, "Measurement of the Three-Dimensional Tip Region Flow Field in an Axial Compressor," ASME *Journal of Turbomachinery,* Vol. 115, pp. 468–476.

Storer, J. A., and Cumpsty, N. A., 1991, "Tip Leakage Flow in Axial Compressors," ASME *Journal of Turbomachinery,* Vol. 113, Apr., pp. 252–259.

Suder, K. L., and Celestina, M. L., 1994, "Experimental and Computational Investigation of the Tip Clearance Flow in a Transonic Axial Compressor Rotor," ASME Paper No. 94-GT-365.

Wadia, A. R., and Copenhaver, W. W., 1994, "A Numerical and Experimental Investigation of the Effect of Throat Margin and Internal Contraction on Transonic Compressor Performance," ASME Paper No. 94-GT-286 (accepted for publication in the ASME *Journal of Turbomachinery*).

Wennerstrom, A. J., 1984, "Experimental Study of a High-Through-Flow Transonic Axial Compressor Stage," ASME *Journal of Engineering for Gas Turbine Power,* Vol. 106, No. 3, pp. 552–560.

Weyer, H. B., and Hungenberg, H. G., 1975, "Analysis of Unsteady Flow in a Transonic Compressor by Means of High-Response Measuring Techniques," AGARD-CP-177.

Wood, J. R., Strazisar, A. J., and Simony, S. P., 1986, "Shock Structure Measured in a Transonic Fan Using Laser Anemometry," AGARD-CP-401 Transonic and Supersonic Phenomena in Turbomachines.

Shigeru Sunada
Researcher,
Kawachi Millibioflight Project,
Exploratory Research for
Advanced Technology,
Research Development
Corporation of Japan,
4-7-6 Komaba Meguro-ku,
Tokyo 153, Japan

Akitoshi Sakaguchi
Researcher,
Fuji Heavy Industries LTD.,
1-1-11 Yonan Utsunomiya,
Tochigi 320, Japan

Keiji Kawachi
Professor,
Research Center for Advanced Science and
Technology, University of Tokyo,
4-6-5 Komaba Meguro-ku,
Tokyo 153, Japan

Airfoil Section Characteristics at a Low Reynolds Number

The aerodynamic characteristics of airfoils operating at $Re = 4 \times 10^3$ were examined, varying the parameters related to the airfoil shape such as thickness, camber, and roughness. Airfoils with good aerodynamic performance at this Re have the following shape characteristics: (1) they are thinner than airfoils for higher Re numbers, (2) they have a sharp leading edge, and (3) they have a camber of about five percent with its maximum camber at about mid-chord. The characteristics of airfoils are strongly affected by leading edge vortices. The measured two-dimensional airfoil characteristics indicate that the planform, which greatly affects the flight performance of the three-dimensional wing at high Reynolds numbers, has little effect on the flight performance at this Reynolds number.

Introduction

The dependence of airfoil performance on the chord Reynolds number (R_e) has been known for many years (Jacobs and Sherman, 1937) and the airfoil performance for Reynolds numbers above 10^6 has been investigated systematically (Abbott and Doenhoff, 1958).

Recently, the performance of airfoils operating at Reynolds numbers below 10^6 has been of interest for a variety of applications including remotely piloted vehicles, sailplanes, and human-powered vehicles (e.g., Gad-el-Hak, 1990). Much research has been performed for $Re \simeq 10^5$. The results of this research indicate that there is a large difference between airfoil characteristics for $Re > 10^6$ and those for $Re \simeq 10^5$. When the Reynolds number is below 10, the lift-drag ratio drops below 1 (Miyagi, 1964) and airfoils have no effect. The airfoil characteristics for $10 < Re < 10^5$ have not been investigated adequately.

Insect wings operate in this range and a few studies have been performed to determine their airfoil characteristics (e.g., Vogel, 1967). However, these studies were not systematic and more studies are required for the analysis of insect flight. In addition, airfoil characteristics in this range are becoming more important because the requirements for small-sized machinery are increasing (e.g., Kubo et al., 1993).

In the present study, the aerodynamic characteristics of selected airfoils were measured at $Re = 4 \times 10^3$. The results show that optimal gliding flight characteristics vary according to the Reynolds numbers.

Experimental Apparatus and Its Arrangement

The experimental apparatus is shown in Fig. 1. Fifteen wings, having the airfoils shown in Fig. 2, were towed through water in a tank (L_X = 1800 mm, L_Z = 700 mm, L_Y = 300 mm). The following variables related to airfoil section shape were investigated:

- Thickness (Airfoils (1), (2), (3) or Airfoils (4), (5)).
- Edge shape (Airfoils (5), (6), (7)).
- Camber (Airfoils (5), (8), (9), (10)).
- Position of maximum camber (Airfoils (8), (11), (12)).
- Corrugation (Airfoils (5), (13)).
- Roughness (Airfoils (5), (14), (15)).

The hydrodynamic forces in the x and z directions were measured by a load cell on which the wing was mounted. All wings used had a chord length, c, of 40 mm and a span length in water, b, of 270 mm. The ratio of the chord length to the span length in water, b/c, was 6.75. The wing velocity, V, reached a constant velocity, V_0 = 0.12 m/s, just after starting. The Reynolds number, $V_0 c/\nu$, is then 4×10^3.

The clearance between the wing and the bottom of the water tank, δ, is 25 mm. The value of δ/b is nearly equal to 0.1. This clearance introduces some three-dimensional effects, which are discussed in (A) below. The wave generated on the water surface causes wave drag, which is discussed in (B) below. As is explained, the resulting effects are so small that the coefficients obtained in these experiments are nearly equal to those of the two-dimensional airfoils.

(A) Effect of the Clearance on the Data Obtained. Two-dimensional lift curve slopes, $C_{l\alpha}$, are approximately equal to the three-dimensional lift curve slopes, $C_{L\alpha}$ (e.g., Anderson, 1991):

$$C_{l\alpha} = \frac{C_{L\alpha}}{1 - C_{L\alpha}/\pi AR_e} \simeq C_{L\alpha}. \tag{1}$$

The effective aspect ratio, AR_e, in this experiment is assumed to be $b/c = 6.75$ in the above equation.

The clearance also causes induced drag. However, this drag is much smaller than the variation in drag due to the angle of attack, as indicated by Eq. (5).

Therefore, the effect of the clearance between the wing and the bottom of the water tank on these measurements can be neglected.

(B) Effect of the Wave Drag. The wave drag is strongly affected by the Froude number, F_r. The Froude number, $F_r = V_0/\sqrt{gc}$, is 0.19 in this experiment. Wave drags of double-arc sections are shown by Havelock (1923) and Hoerner (1965).

Contributed by the Fluids Engineering Division for publication in the JOURNAL OF FLUIDS ENGINEERING. Manuscript received by the Fluids Engineering Division June 5, 1995; revised manuscript received July 22, 1996. Associate Technical Editor: D. P. Telionis.

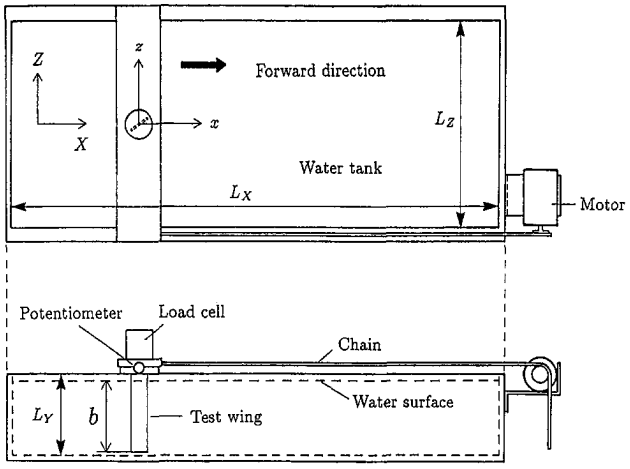

Fig. 1 Experimental apparatus and its arrangement

It can be expected from these data that the coefficients of the wave drag, $C_{DW} = D_W/1/2\rho V_0^2 bc$, are much smaller than the lift and drag coefficients, C_l and C_d. Therefore, the effect of the wave drag can also be neglected.

Analysis of Measurement Errors

The bias errors arise mainly from the load cell and strain amplifier. The maximum errors are about 10 percent. The precision error is mainly from the angle of attack measurement, the wing velocity measurement, and the disturbance resulting from the wing motion. The data of C_l and C_d have scatter and this results in an error of 15 percent.

The total measurement errors from these two sources in C_l or C_d are less than 18 percent $\sim \sqrt{15 \text{ percent}^2 + 10 \text{ percent}^2}$. These errors are small enough relative to (1) the effect of Reynolds number on airfoil and/or wing characteristics and (2) the differences in characteristics of the airfoils at $R_e = 4 \times 10^3$ that they can be ignored.

Results

Figures 3 and 4 show the α versus C_l and C_d versus C_l curves for Airfoils (1), (2), and (3) and those for Airfoils (4), (5), (6), and (7), respectively. Figures 3(b) and 4(b) indicate that the thinner wing has better performance. This is because $(C_l/C_d)_{max}$ becomes larger as the airfoil becomes thinner. The values of the characteristics of these airfoils, such as $(C_l/C_d)_{max}$, are

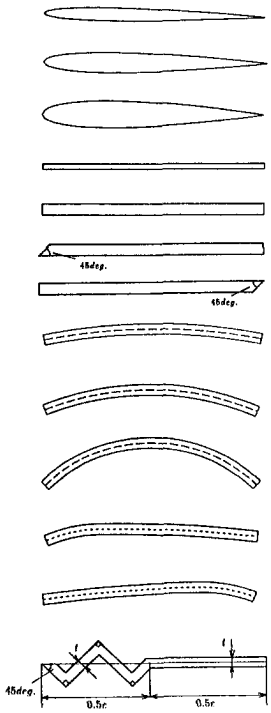

Airfoil(1):NACA0006
Airfoil(2):NACA0009
Airfoil(3):NACA0012
Airfoil(4):Flat plate
(Thickness ratio=2.5%)
Airfoil(5):Flat plate
(Thickness ratio=5%)
Airfoil(6):Flat plate
(Thickness ratio=5%, Sharp leading edge)
Airfoil(7):Flat plate
(Thickness ratio=5%, Sharp trailing edge)
Airfoil(8):Circular arc airfoil
(Thickness ratio=5%, Camber ratio=5%,
Location of the maximum camber=0.5c)
Airfoil(9):Circular arc airfoil
(Thickness ratio=5%, Camber ratio=10%,
Location of the maximum camber=0.5c)
Airfoil(10):Circular arc airfoil
(Thickness ratio=5%, Camber ratio=20%,
Location of the maximum camber=0.5c)
Airfoil(11):Circular arc airfoil
(Thickness ratio=5%, Camber ratio=5%,
Location of the maximum camber=0.25c)
Airfoil(12):Circular arc airfoil
(Thickness ratio=5%, Camber ratio=5%,
Location of the maximum camber=0.75c)
Airfoil(13):Corrugated airfoil
(Thickness ratio t/c = 5%)

Airfoil(14):Flat plate
(Thickness ratio=5%, Iron powder with mean diameter of 30μ on the surface)
Airfoil(15):Flat plate
(Thickness ratio=5%, Iron powder with mean diameter of 15μ on the surface)

Fig. 2 Test airfoils

included in Table 1. The values of lift curve slope, $C_{l\alpha}$, in Fig. 3(a) become larger as the airfoil becomes thinner. These results differ from those obtained for $Re > 10^6$ (Abbott and Doenhoff, 1958).

The cross-sectional area for the streamlined airfoil types, NACA 4-digit airfoil sections, is given by

$$S = 0.685 t_{max} c. \quad (2)$$

Airfoils (1), (2), and (3) have the same cross-sectional areas as the flat plates with thickness ratios of about 4, 6, and 8 percent, respectively. The lift slope of Airfoil (5), whose thickness ratio is 5 percent, is larger than those of Airfoils (1) and

Nomenclature

AR_e = effective aspect ratio
AR_e^* = modified effective aspect ratio given by Eq. (A.1)
b = span length in water
c = chord length
C_D, C_L = drag and lift coefficients of three-dimensional wing
C_{D0} = three-dimensional drag coefficient at $\alpha = 0$
C_{Di} = induced drag
C_{DW} = wave drag coefficient
C_d, C_l = drag and lift coefficients of two-dimensional airfoil
C_{d0} = two-dimensional drag coefficient at $\alpha = 0$
$C_{L\alpha}$ = three-dimensional lift curve slope
$C_{l\alpha}$ = two-dimensional lift curve slope
D_W = wave drag
F_r = Froude number
f = frequency of vortex shedding
g = gravitational acceleration, 9.8 m/s^2
L_X, L_Y, L_Z = size of water tank
Re = Reynolds number
S = area of airfoil
St = Strouhal number
t = thickness
U = forward velocity in a gliding flight
V = wing velocity
V_0 = terminal wing velocity
w = sinking speed
x, z = wing fixed coordinate systems
α = angle of attack
γ = flight path angle
δ = clearance between the wing and the bottom of the water tank
δ_n = coefficients of angle of attack given by Eq. (3)
ν = kinematic viscosity
ρ = density of fluid

Subscript

max = maximum value
min = minimum value

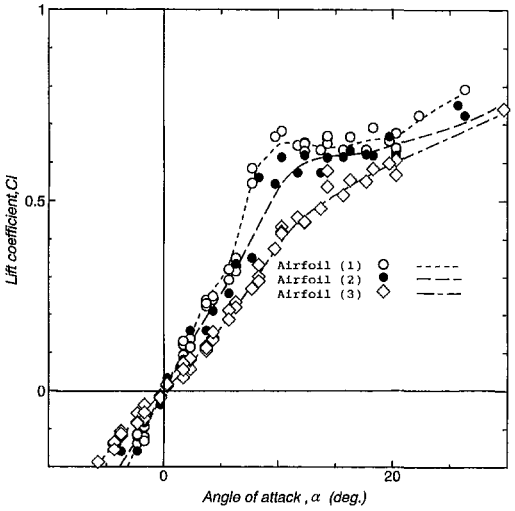

Fig. 3(*a*)

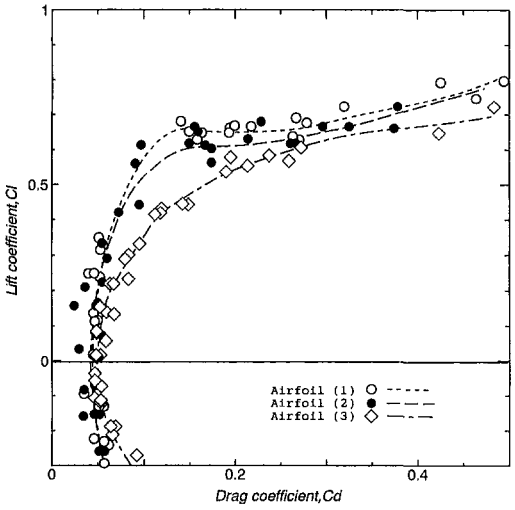

Fig. 3(*b*)

Fig. 3 Characteristics of streamlined airfoils. (*a*) $\alpha - C_l$, (*b*) $C_d - C_l$

(2). Thus, the flat plate has a larger lift slope than the streamlined airfoils of the same airfoil cross-sectional area (i.e., same airfoil weight).

Further, Fig. 4 also shows that the sharp leading edge airfoil has the best performance. The stall angle and $(C_l/C_d)_{max}$ of Airfoil (6) are larger than those of Airfoil (5), which has a simple flat plate shape and is considered the baseline. The above results agree with the performance obtained for airfoils at $10^5 < Re < 10^6$ (Schmitz, 1967). On the other hand, the performance of Airfoil (7) is nearly equal to that of Airfoil (5). The trailing edge shape was not observed to have any effect on airfoil characteristics.

The α versus C_l and C_d versus C_l curves for Airfoils (5), (8), (9), and (10) are shown in Figs. 5(*a*) and (*b*). The zero-lift angle changes with the camber, as is observed at high Reynolds numbers. The maximum lift-drag ratio $(C_l/C_d)_{max}$ is largest at a camber of about 5 percent. The lift-curve slope $C_{l\alpha}$ becomes larger with increasing camber.

Figures 6(*a*) and (*b*) show the α versus C_l and C_d versus C_l curves for Airfoils (8), (11), and (12). The zero-lift angle becomes smaller as the location of maximum camber becomes closer to the trailing edge. The $(C_l/C_d)_{max}$ of Airfoil (8) is a little larger than that of Airfoil (11) or (12). Airfoils with 5 percent camber have the best performance when the maximum camber position is about mid-chord.

The α versus C_l and C_d versus C_l curves of Airfoils (5) and (13) are shown in Figs. 7(*a*) and (*b*). This comparison was performed to examine the aerodynamic effect of corrugation of an insect wing. Airfoil (13) has poorer performance than Airfoil (5) as a result of corrugation. This result does not contradict the result obtained by Rees (1975) because his measurement indicated that the performance of the corrugated airfoil was nearly equal to that of the much thicker airfoil without corrugation. Based on the present finding that a thicker airfoil has poorer performance than a thinner one, the performance of the airfoil with corrugation in his work was poorer than that of an airfoil having the same thickness and no corrugation.

No difference was observed in the aerodynamic characteristics between Airfoils (5) and (14) or between Airfoils (5) and (15) in the present experiments. These results are different from the measurements for $Re > 10^5$ (McMasters and Henderson, 1979; Gadel-Hak, 1990). Two reasons can be postulated for why the variation of roughness of the surface of the airfoils does not affect the performance of the airfoils. One is that the Reynolds number in the present experiment, $R_e = 4 \times 10^3$, is far below the critical Reynolds number (Schmitz, 1967). The other is that the turbulence resulting from the wing motion is so large that the effect of roughness of the surface of the airfoils, which also causes turbulence, cannot be observed.

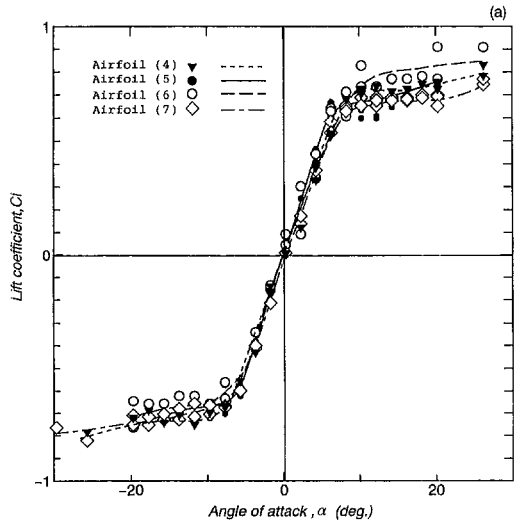

Fig. 4(*a*)

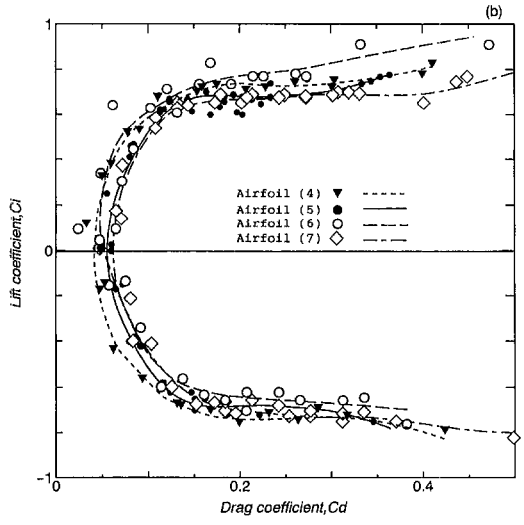

Fig. 4(*b*)

Fig. 4 Characteristics of flat plate airfoils. (*a*) $\alpha - C_l$, (*b*) $C_d - C_l$

Table 1 Parameters indicating characteristics of airfoils

	Lift slope Cl_α	Cl/Cd max (α deg)	$(Cl)^{3/2}/Cd$ max (α deg)	Cd at small angle of attack $C_d = C_{d0} + \delta_1\alpha + \delta_2\alpha^2$			$\delta_2 \Big/ \left(\frac{Cl_\alpha^2}{\pi}\right)$
				Cd_0	δ_1	δ_2	
Airfoil (1)							
Re = 4×10^3	3.7	6.4 (6)	4.6 (8)	$3.9*10^{-2}$	$-1.7*10^{-9}$	2.82	0.647
Re = $6 \times 10^{6[1]}$	5.9	90 (7)	78.0 (7.8)	$5.0*10^{-3}$	$-2.9*10^{-9}$	0.18	0.016
Airfoil (2)							
Re = 4×10^3	2.9	5.5 (6)	3.8 (8)	$3.6*10^{-2}$	$-5.1*10^{-9}$	2.42	0.889
Re = $4 \times 10^{4[2]}$	5.5	20 (6)	15 (5.9)	$1.6*10^{-2}$	$4.6*10^{-9}$	1.35	0.140
Re = $3 \times 10^{5[2]}$	5.5	51 (4.8)	35 (5.3)	$6.8*10^{-3}$	$-3.0*10^{-8}$	0.18	0.019
Re = $6 \times 10^{6[1]}$	6.1	125 (9.5)	104 (11.4)	$5.5*10^{-3}$	$-1.3*10^{-9}$	0.16	0.013
Airfoil (3)							
Re = 4×10^3	2.0	3.6 (12)	2.3 (10)	$4.8*10^{-2}$	$1.5*10^{-8}$	1.88	1.477
Re = $3 \times 10^{5[2]}$	5.7	46 (6)	37.8 (7.1)	$8.4*10^{-3}$	$-2.5*10^{-9}$	0.36	0.034
Re = $6 \times 10^{6[1]}$	6.3	95 (9)	***	$5.8*10^{-3}$	$-6.8*10^{-11}$	0.18	0.014
Airfoil (4)							
Re = 4×10^3	5.2	6.8 (5)	4.7 (5)	$4.2*10^{-2}$	$7.0*10^{-9}$	4.18	0.486
Airfoil (5)							
Re = 4×10^3	5.8	5.5 (5)	4.0 (6)	$5.7*10^{-2}$	$3.2*10^{-9}$	5.33	0.498
Airfoil (6)							
Re = 4×10^3	5.7	6.3 (4)	4.6 (7)	$5.6*10^{-2}$	$2.1*10^{-1}$	4.14	0.400
Airfoil (7)							
Re = 4×10^3	5.6	5.5 (5)	3.7 (7)	$6.1*10^{-2}$	$-1.5*10^{-1}$	5.16	0.535
Airfoil (8)							
Re = 4×10^3	5.9	8.6 (5)	7.6 (6)	$7.7*10^{-2}$	$-2.8*10^{-1}$	4.07	0.460
Airfoil (9)							
Re = 4×10^3	6.0	8.0 (10)	9.2 (10)	$1.0*10^{-1}$	$-2.6*10^{-1}$	3.04	0.265
Airfoil (10)							
Re = 4×10^3	6.7	3.6 (14)	4.1 (15)	$1.7*10^{-1}$	$6.9*10^{-2}$	3.11	0.218
Airfoil (11)							
Re = 4×10^3	5.7	7.3 (9)	6.7 (11)	$8.6*10^{-2}$	$-5.4*10^{-1}$	4.28	0.414
Airfoil (12)							
Re = 4×10^3	5.4	7.3 (3)	6.6 (6)	$6.9*10^{-2}$	$1.9*10^{-1}$	4.72	0.509
Airfoil (13)							
Re = 4×10^3	4.7	3.3 (11)	2.7 (11)	$1.6*10^{-1}$	$-4.3*10^{-1}$	1.98	0.282

[1] From Abbott and Doenhoff (1985), [2] from Jacobs and Sherman (1937).

The drag coefficient of an airfoil, C_d, is expanded to a power series as:

$$C_d = C_{d0} + \sum_{n=1} \delta_n \alpha^n \simeq C_{d0} + \delta_2 \alpha^2. \quad (3)$$

The total drag coefficient of a three-dimensional wing with a high aspect ratio, which has induced drag in addition to profile drag (e.g., Anderson, 1991) is, therefore, expressed as

$$\begin{aligned} C_D &\simeq C_{d0} + \delta_2\alpha^2 + C_L^2/\pi A\mathrm{R_e} \\ &\simeq C_{d0} + \delta_2\alpha^2 + (C_{l\alpha}\alpha)^2/\pi A\mathrm{R_e} \\ &\simeq C_{d0} + \left(\frac{C_{l\alpha}^2}{\pi A\ \mathrm{Re}}\right)\left\{1 + \frac{\delta_2}{C_{l\alpha}^2/\pi A\mathrm{R_e}}\right\}\alpha^2. \end{aligned} \quad (4)$$

The definition of drag component of a three-dimensional wing is discussed in the Appendix. The effective aspect ratio is in accordance with the geometrical aspect ratio when the spanwise lift distribution is elliptical. The parameter $\delta_2/(C_{l\alpha}^2/\pi A\mathrm{R_e})$, therefore, indicates the ratio between increase in profile drag due to increased angle of attack and induced drag. This parameter is much less than 1 for a wing with $A\mathrm{Re} = 10$ operating at a high Reynolds number. The induced drag is dominant and the profile drag is usually assumed to be constant at high Reynolds numbers (Johnson, 1980; Azuma, 1992). However, the quantity δ_2 drastically increases as the Reynolds number decreases, as shown in Table 1. It is now clear that the above commonly accepted assumption of constant profile drag is not applicable at low Reynolds numbers.

Referring to this parameter for a sample airfoil, NACA0009 (Airfoil(2) in Table 1), the drag coefficient for a three-dimensional wing should be approximated as follows:

$$C_D \simeq \begin{cases} C_{d0} + C_L^2/\pi A\mathrm{R_e}, & \text{for} \quad \mathrm{Re} > 10^5 \\ C_{d0} + \delta_2\alpha^2 + C_L^2/\pi A\mathrm{R_e}, & \text{for} \quad 10^4 < \mathrm{Re} < 10^5 \\ C_{d0} + \delta_2\alpha^2, & \text{for} \quad \mathrm{Re} < 10^4. \end{cases} \quad (5)$$

The above equations at $\mathrm{Re} > 10^4$ signify that the aspect ratio, $A\mathrm{R_e}$, that is the wing planform, is as important as the airfoil shape in determining C_{d0} and δ_2 for the three-dimensional wing characteristics. On the other hand, only the airfoil shape that determines δ_2 and C_{d0} is important at $\mathrm{Re} < 10^4$.

The effect of the aspect ratio on the three-dimensional wing characteristics becomes smaller as the Reynolds number decreases. The superiority of the high aspect ratio wing to the low aspect ratio wing is lost at low Reynolds numbers. This loss is further intensified when the structural problem of the bending moment at the wing root is taken into account.

Flow Visualization

Aluminum dust floating on the water surface was used to make the flow patterns around the airfoils visible. Flow visualization tests were performed using Airfoils (3), (5), (6), and (8). The angle of attack was set at 4, 6, 10, and 16 deg for Airfoil (5), and 6, 10, and 16 deg for the other airfoils. Pictures of the flow patterns around the airfoils were taken with a still camera moving with the wings. The shutter speed was $\frac{1}{15}$ s.

Figures 8(a) and (b) show the flow around Airfoils (5) and (6), respectively, at an angle of attack of 6 deg. A vortex was generated from the leading edge of these airfoils at all angles

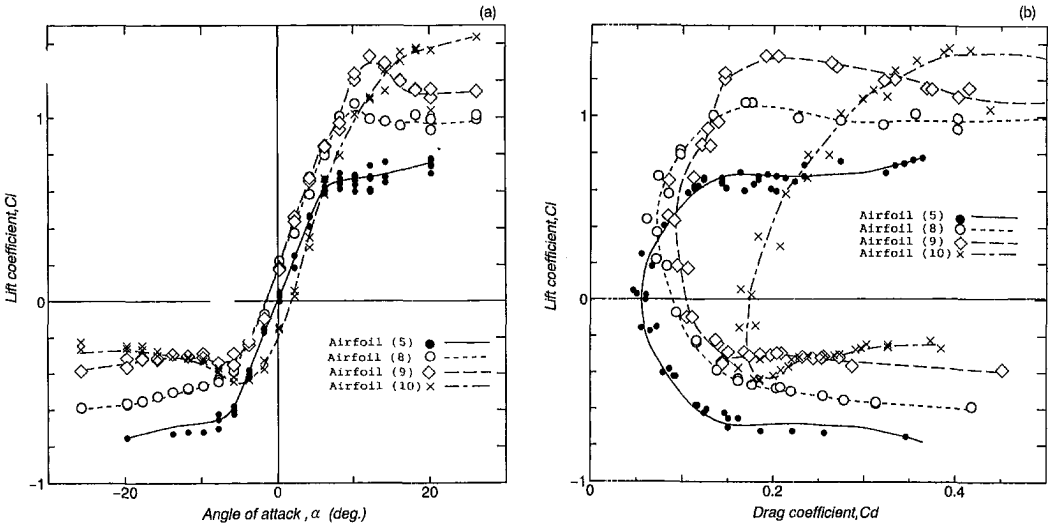

Fig. 5(*a*) Fig. 5(*b*)

Fig. 5 Characteristics of cambered airfoils. (*a*) $\alpha - C_l$, (*b*) $C_d - C_l$

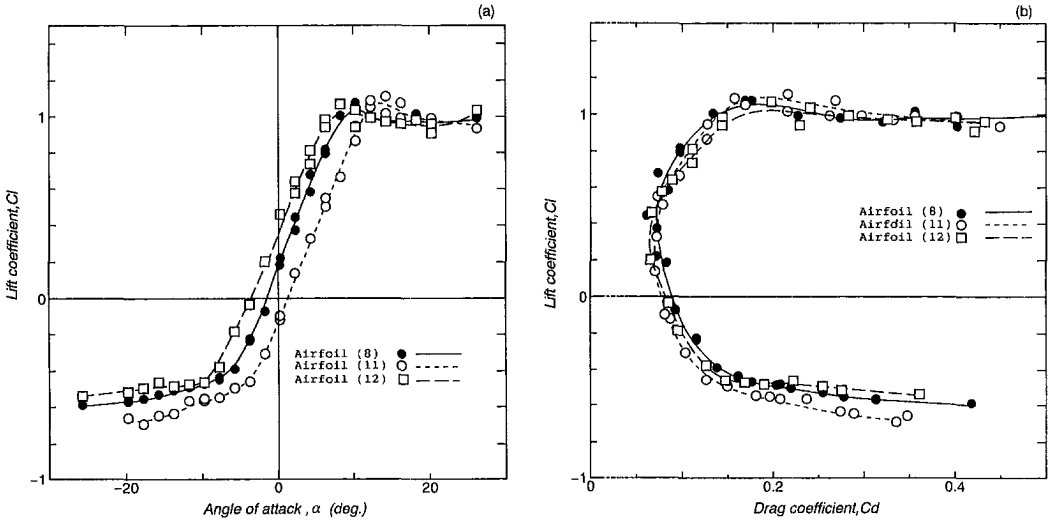

Fig. 6(*a*) Fig. 6(*b*)

Fig. 6 Effect of maximum camber position. (*a*) $\alpha - C_l$, (*b*) $C_d - C_l$

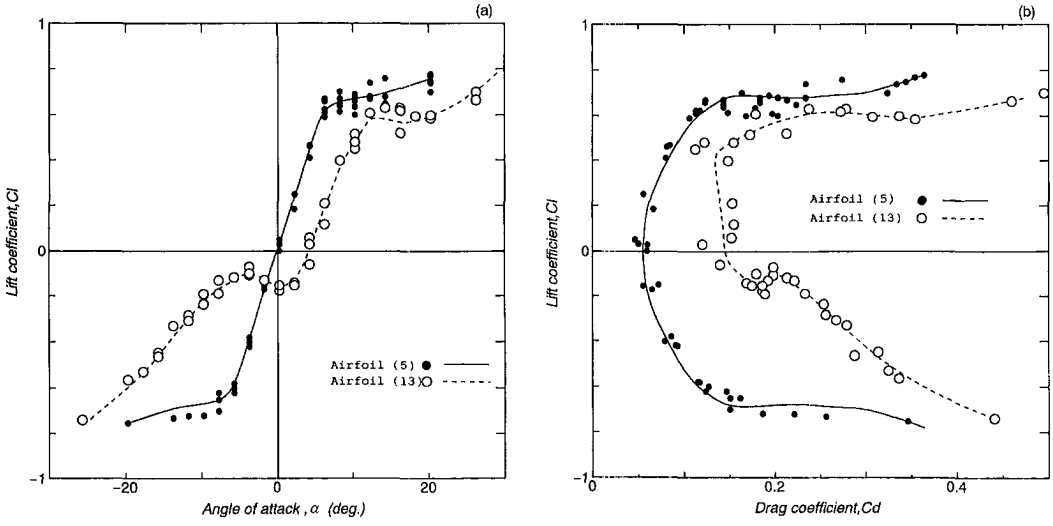

Fig. 7(*a*) Fig. 7(*b*)

Fig. 7 Characteristics of corrugated airfoil. (*a*) $\alpha - C_l$, (*b*) $C_d - C_l$

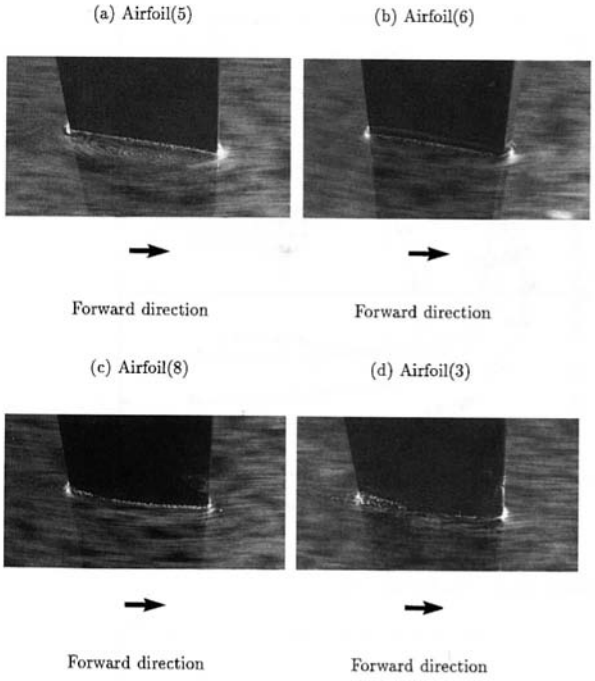

Fig. 8 Flow around airfoils (α = 6 deg). (*a*) Airfoil (5), (*b*) airfoil (6), (*c*) airfoil (8), (*d*) airfoil (3)

of attack. This vortex region became thicker as the angle of attack increased. The vortex region over the upper surface of Airfoil (5) was thicker than that of Airfoil (6). This can explain why the stall angle of Airfoil (6) was larger than that of Airfoil (5) in Fig. 4(*a*). The thinner vortex region over the upper surface of Airfoil (6) contributed to flow reattachment and the flow around the airfoil reattached to its upper surface at a larger angle of attack.

Figure 8(*c*) shows the flow around Airfoil (8) where the angle of attack was 6 deg. No vortex over its upper surface was observed and flow separation can be seen near the trailing edge. In contrast, at α = 10 deg and 16 deg the flow separated at the leading edge and a vortex was observed over the upper surface.

Figure 8(*d*) shows the flow around Airfoil (3). The angle of attack was 6 deg. No vortex was observed over the upper surface of the airfoil at α = 6 deg and 10 deg. The separation points were located at 0.5c and 0.2c at α = 6 deg and 10 deg, respectively. When the angle of attack was 16 deg, the flow separated at the leading edge and a vortex was seen only near the trailing edge. The absence of a vortex over the upper surface near the leading edge is responsible for the inferior aerodynamic characteristics of Airfoil (3).

Vortices in the wake were observed for all the airfoils at all angles of attack. The Strouhal number, St = $fc \sin \alpha/V_0$, is about 0.11 for Airfoil (5) at all angles of attack. The St for Airfoils (3), (6), and (8) is about 0.13 at $\alpha \leq 10$ deg. This number is about 0.17 for Airfoils (3) and (8) at α = 16 deg. For Airfoil (6) it is about 0.2. These values are close to the value of 0.16 for α = 16 deg at Re = $3 \times 10^4 \sim 2 \times 10^5$ reported by Fage and Johansen (1927, 1928). A flat, sharp-edged plate was used in their experiment.

Optimal Gliding Using a Wing Under Low Reynolds Number

The flight of a gliding wing is considered here. Conditions for the minimum gliding flight path angle (maximum flight range) and for the minimum sinking speed (maximum flight duration) are given by $(\partial/\partial C_L)\,(C_D/C_L) = 0$ and $(\partial/\partial C_L)\,(C_D/C_L^{3/2}) = 0$, respectively (e.g., Azuma, 1992). The well-known results for these conditions, C_L (maximum range) = $\sqrt{\pi AR_e C_{d0}}$ and C_L (maximum duration) = $\sqrt{3\pi AR_e C_{d0}}$, were obtained assuming constant profile drag. However, this is not applicable for low Reynolds number wings. The drag coefficient varies with the Reynolds number as indicated by Eq. (5). The lift and drag coefficients, C_L and C_D, and other parameters for maximum range and duration, therefore, vary with the Reynolds number, as shown in Table 2.

C_l/C_d and $C_l^{3/2}/C_d$ at low Reynolds numbers are much smaller than those at high Reynolds numbers (Table 1). The gliding flight performance (flight range or duration) of a low Reynolds

Table 2 (*a*) Optimal flight (minimum gliding angle)

Re	$C_{L,\gamma_{\min}}$	$(L/D)_{\max} \cong 1/\gamma_{\min}$	$C_{D,\gamma_{\min}}$	$U_{\gamma_{\min}}$
$10^5\sim$	$\sqrt{\pi AR_e\, C_{d0}}$	$\frac{1}{2}\sqrt{\pi AR_e/C_{d0}}$	$2C_{d0}$	$\sqrt{\left(\frac{2}{\rho}\right)\left(\frac{W}{S}\right)}\Big/\sqrt[4]{\pi AR_e\, C_{d0}}$
$10^4 \sim 10^5$	$\sqrt{C_{d0}\Big/\left(\frac{\delta_2}{Cl\alpha^2}+\frac{1}{\pi AR_e}\right)}$	$\frac{1}{2}\sqrt{1\Big/C_{d0}\left(\frac{\delta_2}{Cl\alpha^2}+\frac{1}{\pi AR_e}\right)}$	$2C_{d0}$	$\sqrt{\left(\frac{2}{\rho}\right)\left(\frac{W}{S}\right)}\sqrt[4]{\left(\frac{\delta_2}{Cl\alpha^2}+\frac{1}{\pi AR_e}\right)\Big/C_{d0}}$
$\sim 10^4$	$Cl\alpha\sqrt{C_{d0}/\delta_2}$	$\frac{Cl\alpha}{2}\sqrt{1/\delta_2 C_{d0}}$	$2C_{d0}$	$\sqrt{\left(\frac{2}{\rho}\right)\left(\frac{W}{S}\right)}\sqrt[4]{\delta_2/C_{d0}Cl\alpha^2}$

Table 2 (*b*) Optimal flight (minimum sinking speed)

Re	$C_{L,w_{\min}}$	$w_{\min}$	$C_{D,w_{\min}}$	$U_{w_{\min}}$
$10^5\sim$	$\sqrt{3\pi AR_e\, C_{d0}}$	$\sqrt[4]{\left(\frac{2}{\rho}\right)\left(\frac{W}{S}\right)}\sqrt{C_{d0}/(3\pi AR_e)^3}$	$4C_{d0}$	$\sqrt{\left(\frac{2}{\rho}\right)\left(\frac{W}{S}\right)}\Big/\sqrt[4]{16C_{d0}^2+3\pi AR_e\, C_{d0}}$
$10^4 \sim 10^5$	$\sqrt{3C_{d0}\Big/\left(\frac{\delta_2}{Cl\alpha^2}+\frac{1}{\pi AR_e}\right)}$	$\sqrt[4]{\left(\frac{2}{\rho}\right)\left(\frac{W}{S}\right)}\sqrt[4]{C_{d0}\Big/\left(\frac{\delta_2/Cl\alpha^2+1/\pi AR_e}{3}\right)^3}$	$4C_{d0}$	$\sqrt{\left(\frac{2}{\rho}\right)\left(\frac{W}{S}\right)}\Big/\sqrt{16C_{d0}^2+3C_{d0}\Big/\left(\frac{\delta_2}{Cl\alpha^2}+\frac{1}{\pi AR_e}\right)}$
$\sim 10^4$	$Cl\alpha\sqrt{3C_{d0}/\delta_2}$	$\sqrt[4]{\left(\frac{2}{\rho}\right)\left(\frac{W}{S}\right)}\sqrt[4]{C_{d0}\left(\frac{\delta_2}{3Cl\alpha^2}\right)^3}$	$4C_{d0}$	$\sqrt{\left(\frac{2}{\rho}\right)\left(\frac{W}{S}\right)}\Big/\sqrt[4]{16C_{d0}^2+3C_{d0}Cl\alpha^2/\delta_2}$

number wing is markedly inferior to a high Reynolds number wing.

Conclusions

An airfoil with good performance at Re = 4×10^3 has the following shape characteristics: (1) it is thinner than a higher Re airfoil, (2) it has a sharp leading edge, and (3) it has a camber of about 5 percent and its maximum camber position is about mid-chord. Airfoil performance at Re = 4×10^3 is strongly affected by leading edge vortices.

The induced drag is much smaller than the profile drag variation due to the angle of attack at Re = 4×10^3. Three-dimensional wing characteristics are determined by two-dimensional characteristics at low Reynolds numbers. The superiority of a high aspect ratio wing to a low aspect ratio wing diminishes as the Reynolds number decreases. This might be one reason why the aspect ratio of the wings of birds and insects decreases with the Reynolds number (Alexander, 1982). In addition, the popular assumption that profile drag is constant at high Reynolds numbers is not applicable at low Reynolds numbers.

References

Abbott, I. H., and Doenhoff, A. E. V., 1958, *Theory of Wing Sections,* Dover, New York.

Alexander, R. McN., 1982, "Size, Shape and Structure for Running and Flight," in *A Comparison to Animal Physiology,* Taylor, C. R., Johansen, K. and Bolis, L., eds., Cambridge: Cambridge University Press, pp. 309–324.

Anderson, Jr. J. D., 1991, "Fundamentals of Aerodynamics," McGraw-Hill, New York.

Azuma, A., 1992, "The Biokinetics of Flying and Swimming," Springer-Verlag, Tokyo.

Fage, A., and Johansen, F. C., 1927, "On the Flow of Air Behind an Inclined Flat Plate of Infinite Span," *Proceedings of The Royal Society,* London, England, Series A, Vol. 116, pp. 170–197.

Fage, A., and Johansen, F. C., 1928, "The Structure of the Vortex Sheet," *Philosophical Magazine,* Series 7, Vol. 5, pp. 417–441.

Gad-el-Hak, M., 1990, "Control of Low-Speed Airfoil Aerodynamics," *AIAA Journal,* Vol. 28, No. 9, pp. 1537–1552.

Havelock, T. H., 1923, "Studies in Wave Resistance: Influence of the Form of the Water-Plane Section of the Ship." *Proceedings of The Royal Society,* London, England, Series A, Vol. 103, pp. 571–585.

Hoerner, S. F., 1965, *Fluid-Dynamic Drag,* Published by the Author.

Jacobs, E. N., and Sherman, A., 1937, "Airfoil Section Characteristics as Affected by Variations of the Reynolds Number," NACA.TR-586.

Johnson, W., 1980, *Helicopter Theory,* Princeton University Press, Princeton, NJ.

Kubo, Y., Shimoyama, I., and Miura, H., 1993, "Study of Insect-Based Flying Microrobots," *IEEE International Conference on Robotics and Automation.*

McMasters, J. H., and Henderson, M. L., 1979, "Low-Speed Single-Element Airfoil Synthesis," NASA CP-2085.1-31.

Miyagi, T., 1964, "Ossen Flow Past a Flat Plate Inclined to the Uniform Stream," *Journal of the Physical Society of Japan,* Vol. 19, No. 6, pp. 1063–1073.

Perkins, C. D, and Hage, R. E., 1965, *Airplane Performance Stability and Control,* John Wiley & Sons, Inc., New York.

Rees, C. J.C., 1975, "Aerodynamics Properties of an Insect Wing Section and a Smooth Aerofoil Compared," *Nature,* Vol. 258, pp. 141–142.

Schmitz, F. W., 1967, "Aerodynamics of the Model Airplane. Part I. Airfoil Measurements," NACA-TM-X-60976.

Vogel, S., 1967, "Flight in Drosophila. III. Aerodynamic Characteristics of Fly Wings and Wing Models," *Journal of Experimental Biology,* Vol. 46, pp. 431–443.

APPENDIX

Definition of Three-Dimensional Wing Drag

Three-dimensional wing drag is composed of two components—profile drag and induced drag. The drag coefficient is expressed as

$$C_D = C_{D0} + C_L^2/\pi A R_e^* \qquad (A.1)$$

where the profile drag coefficient C_{D0} is constant.

The drag coefficient of three-dimensional wings is also expressed by using the drag components of two-dimensional wings as (refer to Eq. (4))

$$C_D = C_{d0} + \delta_2\alpha^2 + C_L^2/\pi A R_e. \qquad (A.2)$$

Two definitions of each drag component of three-dimensional wings have been widely used. The first, Definition A, states that any drag component proportional to the square of the angle of attack should be the induced drag. The remaining constant component should be the profile drag (Parkinson and Hage, 1965). The profile drag coefficient of three-dimensional wings is equal to the constant component of two-dimensional wings, $C_{D0} = C_{d0}$, by this definition. In Definition A, the induced drag coefficient $(C_{Di})_A$ is, then, given by Eqs. (A.1) and (A.2) as

$$(C_{Di})_A = \delta_2\alpha^2 + C_L^2/\pi A R_e = C_L^2/\pi A R_e^*. \qquad (A.3)$$

The induced drag coefficient in the above equation includes the component of the drag coefficient of the two-dimensional wing, $\delta_2\alpha^2$, which is proportional to the square of the angle of attack. The modified effective aspect ratio, AR_e^*, is smaller than the geometrical aspect ratio even for the elliptical wing.

The second, Definition B, states that the profile drag of three-dimensional wings should be equal to the drag of two-dimensional wings and this drag is assumed to be constant (Johnson, 1980). Thus,

$$(C_{D0})_B = C_{d0} + \overline{\delta_2\alpha^2}, \qquad (A.4)$$

where $\overline{\delta_2\alpha^2}$ is the mean value of $\delta_2\alpha^2$. In Definition B, the induced drag coefficient, $(C_{Di})_B$, is given as

$$(C_{Di})_B = C_L^2/\pi A R_e = C_L^2/\pi A R_e^*. \qquad (A.5)$$

By Definition B, the modified effective aspect ratio, AR_e^*, is equal to the effective aspect ratio, AR_e, and both are equal to the geometrical aspect ratio for the elliptical wing.

As a result, the difference in the definitions is caused by the classification of the drag component $\delta_2\alpha^2$. This component is classified as the induced drag (Definition A) or as the profile drag (Definition B). Both definitions give similar results at high Reynolds numbers because $\delta_2\alpha^2$ is much smaller than $C_L^2/\pi AR_e$. Research at only high Reynolds numbers has focused for long time on wing aerodynamics and this difference in definitions has not been addressed. Definition A has been used for practical purposes and Definition B has been used for theoretical purposes.

The present paper adopted Definition B and extended it because the modified effective aspect ratio, AR_e^* in Eq. (A.3) has no relation to the geometrical aspect ratio at low Reynolds numbers. In addition, at low Reynolds numbers the physical meaning of each component is clearer in Definition B than in Definition A.

P. R. Bandyopadhyay
Fellow ASME

J. M. Castano

J. Q. Rice

R. B. Philips

W. H. Nedderman

Naval Undersea Warfare Center,
Newport Division, Code 8233,
Newport RI 02841-1708

W. K. Macy
Graduate School of Oceanography,
University of Rhode Island, Kingston, RI

Low-Speed Maneuvering Hydrodynamics of Fish and Small Underwater Vehicles

The low-speed maneuvering by fish and small underwater vehicles is considered. The focus is on fluid engineering rather than on biology. An attempt is made to learn from aquatic animals and apply the distilled knowledge to build maneuvering devices. The work is described in three parts. In the first, the morphology of twenty eight species of fish is considered. They are classified into three categories: low speed highly maneuverable, high speed poorly maneuverable, and an overlapping category, viz., high speed highly maneuverable. The qualitative relationship between the length scales of their fins and maneuvering ability is examined. Next, an obstacle-filled aquarium is built and the maneuvering trajectories of two species of fish that are fast yet maneuverable, are video-taped and digitized. Their performance are compared with those of small underwater vehicles. In this manner, the maneuvering "gap" between nature and engineering which appears to be large, is quantified. Finally, based on their length scales in species of fish that are deft in maneuvering, a dorsal-fin based maneuvering device is built and its behavior is studied.

1 Introduction

Human interest in swimming and flight in nature is age-old. Such forms of locomotion have been perfected over millions of years of practice, and no wonder they have been the inspiration of many inventions that surround our life today. An aircraft in flight is the most vivid example. Since the historic flight of the Wright brothers, the biokinetics of swimming and flight has been studied in a systematic way, and some of the recent progress made has been summarized in Azuma (1992) and Wu, Brokaw, and Brennen (1975). Much has been learned about the biokinetics of basic locomotion like cruise swimming and flight. However, far less is known about the hydrodynamics of maneuvers like acceleration (burst of speed) or deceleration, or change in the direction of locomotion. There have been even fewer attempts to apply the knowledge gained from such studies to improve the maneuverability of engineering vehicles. Here, we report some of the progress made in this direction.

One approach to solving the practical needs of low-speed maneuvering hydrodynamics is to learn from aquatic locomotion and then apply that knowledge, after a pragmatic filtering, to engineering vehicles. A similar approach has been tried many times in the past, and, in fact, several examples can be cited where nature and engineering bear a remarkable morphological similarity (Azuma, 1992). The axial cross-sectional profile of a tuna is close to that of NACA profile 67-021, which offers maximum volume as well as a long laminar flow length (70 percent). Such a profile of trout is similar to NACA profile 63A016 and the laminar profile LB N-0016 given by Tani (1943) and Kármán (1954). The dolphin sectional axial profile is also very close to NACA profile 66018, which was invented artificially. The induced drag-reducing winglets of Gates Learjet 557, Fairchild 300, Canadair Challenger 601, and Boeing 777 are similar to the winglets of a condor. The leading edge flap in aircraft wings, developed by Handley Page, deployed during takeoff and landing, was originally inspired by feather configurations in bird wings. In the same vein, this present study assumes that much can be learned by studying fish families that are efficient in maneuvering. The study was motivated by a long-term effort to make a vehicle capable of undertaking a brisk or a small radius turn.

The study is described in three parts. As a starting point, to obtain an engineering clue to their superior maneuverability, the morphology of various fish families is examined to determine what makes some families more maneuverable than others. Three qualitative categories of fish are examined: (1) those that are maneuverable and are generally regarded as low-speed fish, (2) those that are known to cruise at a relatively high speed, and (3) those that can both cruise at high speed and are maneuverable. The length scales of the body and the fins are examined. The relationship between the fin morphology and the characteristics of locomotion is discussed, with emphasis placed upon maneuverability. Next, in an effort to partially quantify the gap in maneuverability in "nature" and man-made vehicles, we have first carried out maneuvering experiments on fish in captivity and compared the results with those of small underwater vehicles. Finally, in a bid to hasten the maneuverability of small underwater vehicles, a low-speed tow tank experiment has been carried out on a long and narrow dorsal fin mounted on a flow aligned cylinder to determine its performance when cambered, as a maneuvering device. The details of measurements and data analysis can be obtained from one of us (PRB) and only a brief summary will be presented here.

2 Relationship Between Fish Morphology and Locomotion

We first examine the control surfaces of a fish to gain insight into the origin of their impressive low-speed maneuverability. Morphology describes the shape and size of an animal. It has evolved in a way that allows an animal to lead a certain way of life, called ecology (the activities of feeding, reproduction etc.), in a certain environment, called habitat. Locomotion is the biomechanics of moving from point to point that makes the ecology possible. Due to interdependence, it is reasonable to assume that even the static morphology of a fish can provide clues to its locomotion, habitat, and ecology (Aleev, 1969). As a starting point, the morphology of various fish families is examined to determine what makes some families more maneuverable than others. The length scales of the body and fins are

Contributed by the Fluids Engineering Division for publication in the JOURNAL OF FLUIDS ENGINEERING. Manuscript received by the Fluids Engineering Division 16 May 1995; revised manuscript received Nov 26, 1996. Associate Technical Editor: R. L. Panton.

examined. The relationship between fin morphology and the characteristics of locomotion is discussed, with emphasis placed upon maneuverability.

2.1 Definition of Length Scales. The morphological length scales of a fish are shown schematically in Fig. 1. Three kinds of length scales are illustrated. The overall axial fork length of the main body is L, and the maximum height is T. The caudal fin is defined by width W_C and by axial length in the midplane L_C, measured from the middle of the caudal peduncle. The combined axial length of the first and second dorsal fins at the roots is defined by L_D, and its maximum span in the normal direction is given by S_D. The second dorsal fin is practically nonexistent in some families (for example, in salmon and dace). The axial distance of the leading edge of the second dorsal fin (also known as soft fin) at the root is given by L_2, while its axial length is given by D_2. Finally, the axial length of the anal fin at the root is given by A, and its leading edge is situated at an axial distance of L_A. Unlike the dorsal and anal fins, the ventral fin is hinged (or rooted) practically at a point, and not over its entire length. For this reason, the ventral fin is not compared with the dorsal and anal fins. The roughly elliptical cross section of the main body of the fish is also not considered.

The length scales shown in Fig. 1 were quantified from photographs of three categories of fish: (1) highly maneuverable but low-speed, (2) high-speed but not highly maneuverable, and (3) both highly maneuverable and high-speed. There is a factor of 2 to 10 between the absolute speeds of families of types (2) and (1). The low-speed maneuverable fish families tend to live in crowded areas like reefs, rocky shores, and at the bottom of the sea. On the other hand, those endowed with speed tend to live in swift streams or open seas. An attempt was made to carry out the classification objectively by comparing the relative proportion of the red and white muscles which would indicate the differences in their ability to maneuver and cruise, respectively. However, such data is rare (McLaughlin and Kramer 1991). The qualitative categorization then had to be based on the experience of Azuma (1992) and Wu (1994).

2.2 Caudal Fins. The results for the overall morphology are shown in Fig. 2. (The legends of Figs. 2–4 provide the common names of the fish families, followed by abbreviations of the Latin genus and species names, which are given in the appendixes A, B, and C.) It is interesting to see that the first and second categories indeed follow two different trends, while the third category falls in both of these clusters. For the same overall aspect ratio (L/T), the caudal fin is fuller (large L_C/W_C) in maneuverable, low-speed fish compared to those identified as fast swimmers.

2.3 Dorsal Fins. The results for the dorsal fins are shown in Fig. 3, which shows that those families that maneuver well have a high value of L_D/L ($0.4 < L_D/L < 0.6$), the mean being 0.5. Interestingly, the center of gravity is also located at this position. Figure 3 suggests that, in general, high-speed fish have short dorsal fins and maneuverable fish have long dorsal fins.

The aspect ratio of the dorsal fin is defined as S_D/L_D. The reciprocal of the aspect ratio of the dorsal fins is shown in Fig. 4. While all of the data generally fall between two radial lines (not shown) through the origin, the data for maneuverable fish are also bounded between two radial lines originating at $T/L = 0.2$ and $L_D/S_D = 3$. This "telescoping" of the data set of maneuverable fish families suggests an underlying closer scaling of their dorsal fins with their overall fish morphology. The

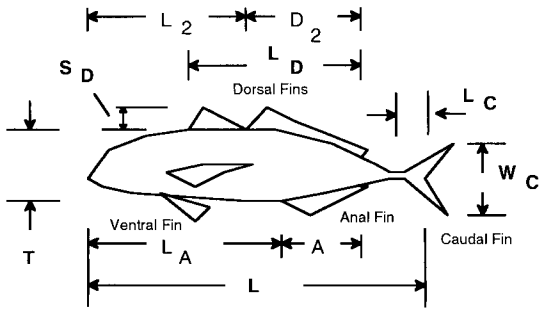

Fig. 1 Definition of length scales of a fish

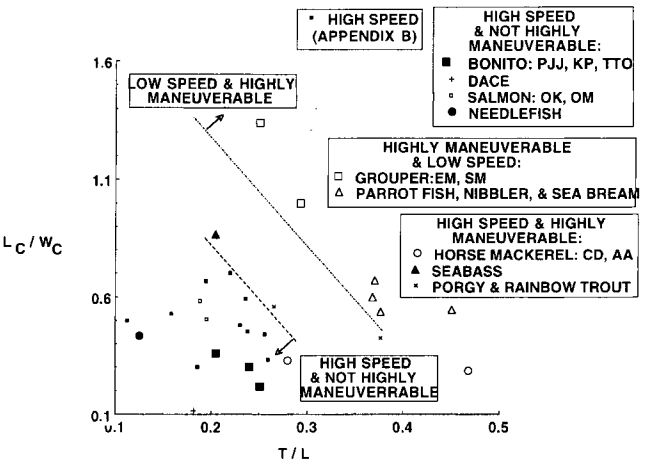

Fig. 2 Overall morphology and caudal fins of fish families

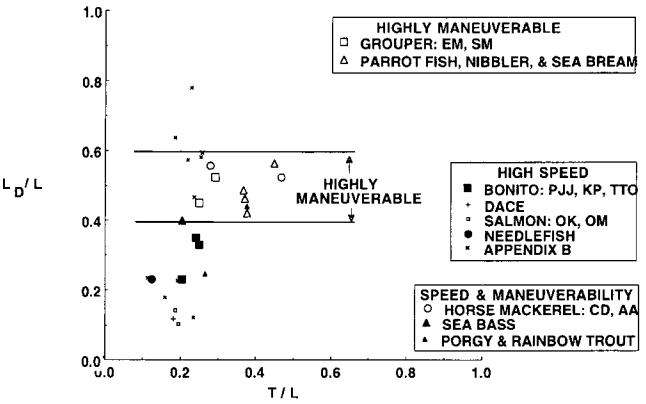

Fig. 3 Morphology of dorsal fins of fish families

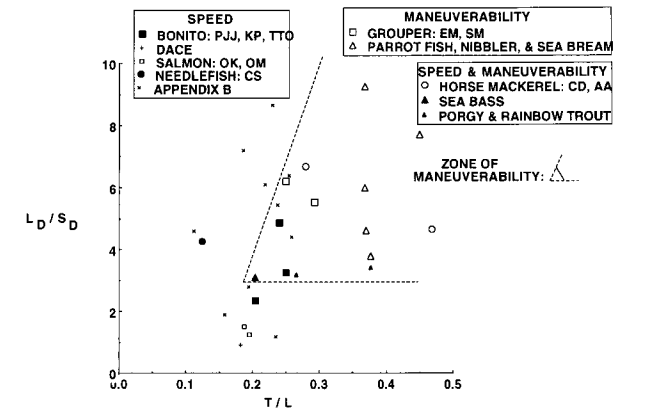

Fig. 4 Reciprocal of aspect ratio of dorsal fin

families having a low-aspect-ratio dorsal fin (higher values of L_D/S_D) and a low-aspect-ratio main body (large values of T/L) are highly maneuverable.

In Figs. 2 to 4, 28 species of fish have been considered. While the database is limited and some caution needs to be exercised, the trends are surprisingly clear. The slenderness ratio T/L represents the importance of side area (TL): a large side area will produce a large side thrust, but may be undesirable for fast cruise swimming due to frictional area. The dorsal fin adds to the side area and, therefore, improves maneuverability, which however, need to be retracted for cruise. (Both mackerel and bluefish do that, and this is utilized in the fluid engineering experiment described later.) The same area consideration is true for the caudal fin: a large side area helps maneuverability, while a small area allows high-speed cruising.

The examination of the relationship between morphology and locomotion was carried out to gain insight into low-speed maneuvering. The following conclusions can be drawn.

1. The dorsal fin versus overall aspect ratio plot indicates that maneuverable fish have low aspect ratio main body and dorsal fins, that is, low values of L/T and S_D/L_D, respectively.
2. The morphology of a highly maneuverable fish is characterized by long dorsal fins (L_D/L) whose span (S_D/L_D) is small, compared to those families that can cruise at high speed but are not highly maneuverable.
3. In highly maneuverable fish, the mean axial length of the dorsal fin is roughly $0.5L \pm 0.1L$.

3 Experiments Comparing Maneuverability of Fish and Small Underwater Vehicles

Mackerel and bluefish are abundantly available in the Narragansett Bay. They are oceanic fast swimmers not closely associated with the bottom. Bigelow and Schroeder (1953) describe bluefish as ". . . perhaps the most ferocious and bloodthirsty fish in the sea, leaving in its wake a trail of dead and mangled . . . fish on which it preys." The predatory lifestyle is reflected in their streamlined and morphologically similar shapes. Mackerel are slender fish with body length-to-depth ratios of 4.5 to 5.5:1. Their bodies are oval in cross section and taper to a thin caudal peduncle (base of the tail). Bluefish are more laterally compressed, having a length-to-depth ratio of approximately 4:1. Both have paired dorsal fins. In mackerel the two fins are about equal in length, the first dorsal being higher. In bluefish, the situation is reversed: the second dorsal is about twice as long and high as the first dorsal fin. Mackerel have five finlets dorsally and ventrally behind the second dorsal. In both species the anal fins are about equal in length and depth to the second dorsal fins. Both dorsal fins can be retracted into grooves in the dorsal surface of the body when swimming rapidly (Bigelow and Schroeder, 1953; Scott and Scott, 1988).

Due to their combined proficiency in speed and maneuverability, bluefish and mackerel were selected for an experimental investigation of their maneuvering trajectories. The distribution of their mass and fork length is shown in Fig. 5. A least-square powers law relationship is fitted to the data

$$m = 0.06L^{2.52}, \qquad (1)$$

where m is mass in grams and L is fork length in centimeters. Note that the exponent is less than 3, as expected. Both bluefish and mackerel appear to follow the same allametry trend. Note that they are both nearly neutrally buoyant in water (within $\pm 10\%$).

3.1 Acquisition and Analysis of Maneuvering Trajectories. The live fish maneuvering experiments were carried out in the Research Aquarium facility of the Graduate School of Oceanography, University of Rhode Island, Narragansett Bay Campus. The details relevant to hydrodynamics are given below. Although mackerel and bluefish are quite similar in morphology, habitat, and feeding habits, their behavior in captivity was surprisingly different. Mackerel were maintained in a circular fiberglass tank (2.44 m diameter) with a water depth of approximately 50 cm. The mackerel swam continually around the perimeter of the tank in a tight school. Their movements and behavior were recorded on videotape via a centrally-mounted overhead video camera (MTI-Dage M65) equipped with a 16 mm wide angle lens. Illumination was provided by four 75w VHO fluorescent lights (6200°K, intensity approximately 10^{-4} μE cm^{-2} s^{-1}). Mackerel were examined while cruising in their typical circumferential paths around the tank.

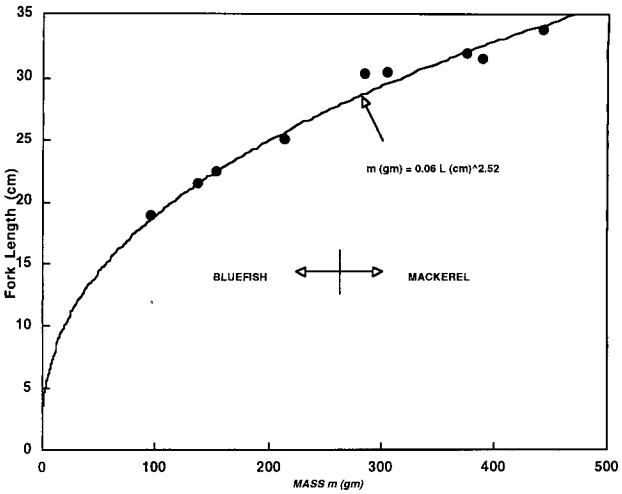

Fig. 5 Allametry of fish studied

Bluefish are generally less active under captive conditions. They were maintained in a rectangular fiberglass tank (Fig. 6). A CCD video camera (SONY SSC-S220) equipped with a 9-mm wide angle lens was mounted on an overhead rail, oriented over the center of the long axis of the tank. The camera mount could be positioned along the rail to view different sections of the tank. The bottom of the tank was painted white to improve contrast of the fish, and the water depth was maintained at 25 cm.

Several baffle (obstacle) designs were tested to attempt to force the bluefish to maneuver (turn). In the first case, an opaque plastic divider was installed, centered in the long axis of the tank, leaving a gap of 0.35 m at each end between the baffle and end wall of the tank. It was hoped that the fish would swim (or could be induced to swim) in a straight path down one side of the barrier, make a 180 deg turn through the gap, and then proceed down the opposite side. Since the semicircular fairings at the ends of the tank were made of flexible plastic, a moveable false tank side wall could then be employed to vary the width of the tank (moving the center baffle appropriately), and hence vary the radius of the 180 deg turn.

When it was learned that bluefish do not like to swim around opaque obstacles, a second method to induce maneuvering was attempted (Fig. 6). Vertical sections of plastic pipe were arrayed in a grid pattern in the center of the tank, providing multiple possible routes for the fish to swim through, making turns of varying radii. Bluefish were more willing to negotiate this more complex obstacle course than the former, simpler one. Both mackerel and bluefish maneuvering data are mostly at low speeds and for gentle curving trajectories. The problem of documenting their briskly maneuvering trajectories remains (that is lower radii swifter turns that are undertaken in response to the appearance of a predator or prey).

Swimming speeds and position of fish were determined from the video recordings. Fish position as a function of time was

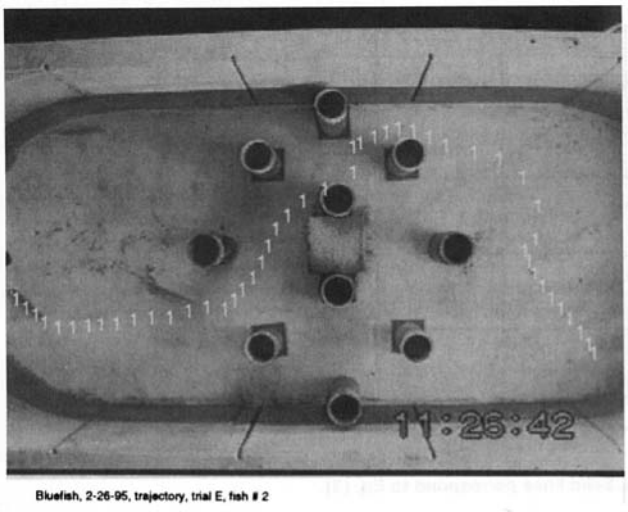

Fig. 6 The example of a digitized bluefish trajectory in the rectangular tank with pipe and cinder block maze. Fish motion marked is from right to left.

digitally extracted using the image processing and analysis program Optimas 4.1, using a motion analysis macro (Image Processing Solutions) to control the Sony S-VHS video recorder (SVO-9500 MD) via an RS 232 interface. This software package was run under Windows for Workgroups (Microsoft) on a DX-66 computer (Zeos Pantera DX-66) equipped with 16 MB of RAM, using a PC Vision Plus (Imaging Technology Inc.) frame grabber of 640 by 480 pixels of resolution. First, the image analysis program was calibrated for the particular camera and test conditions using a reference grid placed on the bottom of the test tank. Using this grid, spatial decalibration of the images for each test setup was performed to minimize geometric distortion caused by the wide angle video lenses needed to provide sufficient area coverage. Positions of individual fish were marked electronically on the video display by the operator, the computer then advanced the video the desired number of frames (3 to 30 frames per second (fps)) (NTSC standard is 30 fps), and the new positions were marked by the operator. Although the heads of both species are laterally displaced with each tailbeat, the location of minimum motion—just forward of the first dorsal fin—could not be reliably identified in the video recordings. Therefore for the sake of repeatability, the tips of the fishes' snouts were marked. (Mackerel and (to a lesser degree) bluefish swim carangiform style (Lindsey, 1978), with undulations generally confined to the rear one-third of the body. Therefore, the error due to a lack of discrimination between the nose and the fin tip is minimal.) The program then output x and y positions, distance traversed, elapsed time between samples, and the x and y speeds. From these parameters, normal acceleration was computed. The live weights and fork lengths of the fish were determined after anaesthetizing them with quinaldine.

The minimum theoretical resolution limit of the video analysis system was determined by the 640 by 480 pixel frame grabber. At the working distances employed in this study, this amounts to 0.39 cm. However, even the relatively high resolution V-VHS video format is limited to 400 horizontal video lines (vs. 240 for VHS), and thus the video format imposes a larger resolution limit. From repeated measurements of different cells of the calibration grid, composed of a section of fluorescent light egg-crate diffuser, the actual repeatable resolution was found to be about ± 1 cm.

In bluefish, during a turn, speed can routinely jump from 1 to 2 body length per second by a factor of 1.5 in 0.07 sec; this is a rate of a speed factor of 22/sec. On some occasions, speed can even jump by a factor of up to 3.5 in 0.07 s. Such large rates of change in low Reynolds numbers is generally unmatched in engineering. The unsteady hydrodynamics of such rapid changes has never been studied before. The hydrodynamic mechanism involved in such rapid maneuvers is intriguing. An Atlantic Mackerel 35 cm long cruising at 50 cm/s has a length Reynolds number of 1.8×10^5. The coefficient of friction of a similar dead fish is 5×10^{-3}, which lies between the calculated laminar and turbulent values of 3×10^{-3} and 6×10^{-3}, respectively (Bone in Hoar and Randall, 1978). The relevance of these steady state and dead fish data to maneuvering is unclear. The fins are smaller than the fork length, and they probably lie in a disturbed laminar environment at the upper end of maneuvering speeds. Because viscosity can amplify disturbances in the early stage of transition, one wonders how a fish handles a potentially rapid rise in friction drag with Reynolds number during maneuvering. These issues reappear in the experiment reported later.

In each test run of fish trajectory, three or four fish were tracked for a few seconds. A computer program was written to read the trajectory data, smooth it and compute maneuvering variables. Data smoothing was necessary to reduce possible errors introduced in the video capture and digitization process. Many smoothing methods were considered for the criss-crossing trajectories, including Lagrange polynomials, cubic splines and B-splines. The last method was found to fit the data the best. If the smoothing error is defined as the distance from the spline, then it was found to vary between 1 to 10 percent of the spacing of trajectory digitization, which is small. The Cartesian velocity and accelerations were from the interpolated B-spline points. The error due to discretization of the spline was between 2 to 6 percent of the total time for maneuver. The total error due to numerical analysis is between 5 to 16%. The trajectories near the beginning and ends of runs and also where the fish was not making a maneuver (very large turn radii) were excluded. The net result was smooth distributions in the processed variables. The same method of trajectory analysis was used for both fish and underwater vehicles. Literature survey indicates that, because of a higher degree of automation, our trajectory acquisition and analysis has produced a more accurate data set than what the common practice is with live biolocomotion studies on trajectory.

3.2 Comparison of Maneuvering Coefficients. The maneuvering performance of fish were compared with those of small underwater vehicles via three maneuvering coefficients; viz., coefficients of normal acceleration, turn, and work. The results for the first are given here. The coefficient of normal acceleration, C_g is nondimensionalized by g, the acceleration due to gravity: $C_g = (a_\perp/g)$, where the acceleration perpendicular to the path is given by $a_\perp = (v^2/r)$. Here v is total velocity and r is radius of curvature in trajectory that is given by Eq. (2), where x and y are Cartesian coordinates and t is time.

$$r = \frac{\left[\left(\frac{dx}{dt}\right)^2 + \left(\frac{dy}{dt}\right)^2\right]^{3/2}}{\left|\frac{dx}{dt}\frac{d^2y}{dt^2} - \frac{dy}{dt}\frac{d^2x}{dt^2}\right|} = \frac{v^3}{|v_x a_y - v_y a_x|} \qquad (2)$$

The coefficient of normal acceleration of bluefish and mackerel are compared in figure 7 with those of two small underwater vehicles called A and B here. They are approximately neutrally buoyant. The data pertain to a race track like maneuvering trajectory in open water that lie in a horizontal plane. The values of C_g are plotted against an ordinate of nondimensional turn radius r/L, where r is radius of turn and L is either the vehicle length or the fork length of a fish.

Figure 7 shows the following:

1. A large gap between the maneuvering capability of fish and that of the small underwater vehicles.

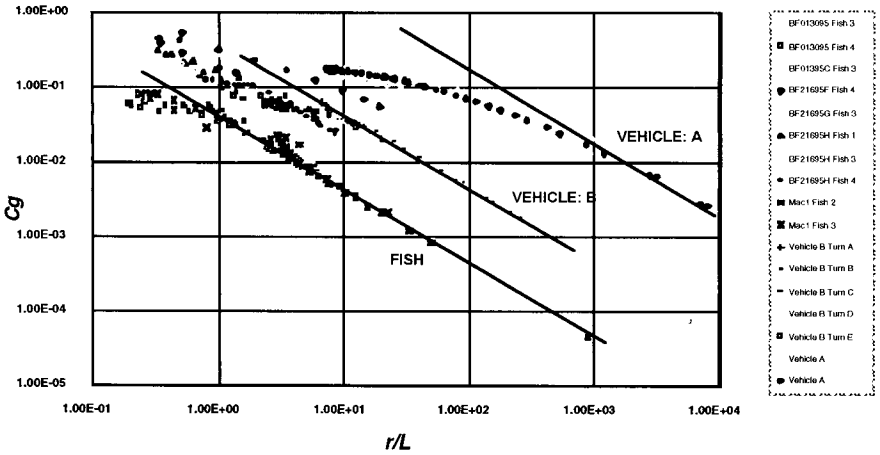

Fig. 7 Coefficient of normal acceleration. Solid lines correspond to Eq. (3).

2. There is a universal trend that is followed in large values of turn radii only.
3. At small values of turn radii, the trend departs from the universal.
4. Fish can carry out the shortest radii turns.
5. Compared to the underwater vehicles, fish can undertake the same radius turns (r/L) at a normal acceleration that is lower by a factor that can be as large as 10. One wonders, if fish also perform stealthier maneuvers. Presumably, they could do so by dint of lower speeds and laminar flow.

Figure 7 shows that, for large turn radii, there is a universal inverse power relationship:

$$C_g \sim \left(\frac{r}{L}\right)^{-1} \tag{3}$$

However, near their respective highest values of C_g (and lowest values of r/L), the data in both fish and vehicles, do not follow this trend. This behavior of departure at low radii of turns is intriguing. If speeds of vehicles and fish are expressed in terms of body length traveled per unit time, as commonly practiced in biology, it is possible to arrive at a scaling relationship of the coefficients of acceleration, turn and work that largely removes the low radii departures from the types shown in equation (3). This scaling requires us to propose the existence of an internal Froude number whose origin remains unclear at the present time. However, such scaling is useful because it allows us to achieve similarity over a very large range of Reynolds numbers covering both natural and man-made bodies in motion. This scaling is given below.

Propose that the coefficient of normal acceleration during a turn is a function of inertia forces, viscous forces and gravity force. Define Reynolds number, $\mathrm{Re} = VL/\nu$, and an Internal Froude number $\mathrm{Fr} = (V/\sqrt{gL})$, where V is the speed, L is the length and ν is the kinematic viscosity, and g is the acceleration due to gravity. These two ratios of forces can be combined as follows:

$$\frac{\mathrm{Fr}^4}{\mathrm{Re}} = \frac{V^3}{L^3}\frac{\nu}{g^2}$$

This combined parameter can be used to rescale the coefficient of normal acceleration shown in Fig. 7, and the result is shown in Fig. 8. The solid lines in Fig. 8 are of the type:

$$\frac{C_g}{\frac{\nu}{g^2}\left(\frac{V}{L}\right)^3} \sim \left(\frac{r}{L}\right)^{-1} \tag{4}$$

The rescaled coefficient now follows the inverse power trend over a greater range of radii in both the fish and vehicle data.

4 Experiments on a Brisk Maneuvering Device

While the propulsion mechanism in fish and underwater vehicles can be different, much can be learned by imbibing the maneuvering control surfaces of the former. We now describe an engineering experiment where the results of mounting a fish-like dorsal-fin device on a towed cylinder is investigated. This was motivated by the fact that, in some cases, the maneuvering of small underwater vehicles can be a slow process. Sometimes, small control surfaces ahead of the propulsor is first operated to provide an angle of attack to the vehicle which then leads to a large separation of the boundary layer on one side of the main cylindrical body. The resulting lift force then acts slowly to maneuver the body into a new trajectory. Because boundary layer separation having a large length scale is involved, the maneuvering process is slow and is not precisely controllable. Currently, a numerical simulation of the time delay is not feasible.

As mentioned earlier, in fast yet maneuverable species of fish like bluefish and mackerel, the dorsal fins (except the finlets of mackerel) are retracted flush with the dorsal surface of the body when swimming rapidly in a straight line. *When maneuvering or swimming slowly, the first and second dorsal fins are erect.* The section on fish morphology indicates that, a dorsal fin that is axially long but narrow along the span ($L_D > 0.4L$, but $S_D < L_D/4$), mounted closely (and deployed abruptly) on a flow aligned cylinder, and given an appropriate camber, could en-

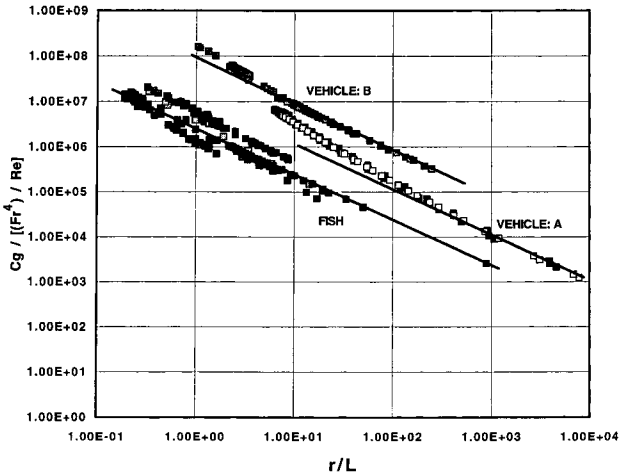

Fig. 8 Reduced coefficient of normal acceleration. Solid lines correspond to Eq. (4). Data as in Fig. 7.

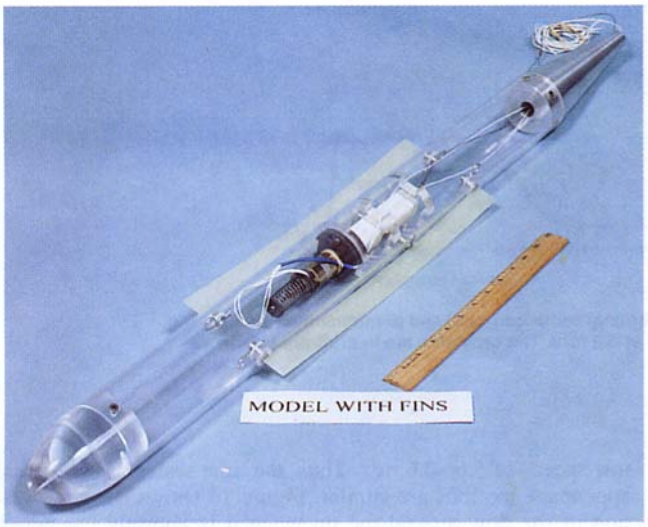

Fig. 9 Photograph of cylinder and dorsal fin assembly. The solenoid-cam arrangement inside the cylinder used to deploy the fins is also visible in the middle.

hance cylinder maneuverability. This strategy has been the subject of an experimental study reported below.

4.1 Model. A Plexiglas model, 76 mm in diameter (d) and 754 mm in length, was constructed. Figure 9 is a photograph of the model showing the pair of dorsal fins and the solenoid-cam mechanism used to deploy (that is, to camber) the fins when desired. The assembly of the model, balance and strut is shown in Fig. 10. The cylinder had an elliptic nose and the boundary layer was not tripped. A pair of dorsal fins was mounted on the cylinder diametrically opposite to each other. Both could be cambered simultaneously by the same mechanism and this prevented a roll of the model. The model was towed at constant speeds in the range 60–360 cm/s. The dorsal fin chord c was 38.3 cm and the dorsal fin span s was 2.54 cm. The Reynolds number based on the cylinder diameter Re_d varied in the range $4.73 \times 10^4 < \mathrm{Re}_d < 2.79 \times 10^5$ and the fin chord Reynolds number was in the range $2.38 \times 10^5 < \mathrm{Re}_c < 1.41 \times 10^6$.

The study of the morphology of the three categories of fish mentioned in Section 2 showed that the species which were maneuverable yet fast swimming, had a total fin length which was between 0.4 to 0.6 of the fork length of the fish. The fin length in the present experiment was chosen to be 0.508 times of the cylinder length. In the model, the dorsal fin has roughly the same aspect ratio (length/span = 15) as that of the cylinder (length/diameter = 11), which should help preserve the basic maneuvering characteristic of the cylinder. When cambered, the fin formed a circular arc of radius 1500 mm. The maximum camber was 12 mm. The fin was 1.5 mm thick, flexible and made of fiber reinforced plastic. Normally, the fin was aligned to the cylinder axis whereby it did not produce any side thrust. Inside the cylinder, a solenoid and cam mechanism was installed to camber the fin when a relay was tripped on the tow tank rails. Three dye ports were located to visualize the flow around the fin. They were located just upstream of the leading edge, near the point of maximum camber and just after the trailing edge. By means of a pipe, the cylinder was attached to a streamlined strut that was suspended from the carriage of the tow tank. A strain gage balance was housed internally at the cylinder strut joint to measure the moment due to side thrust to applied moments. The strain gage response was linear.

4.2 Tow Tank. The experiments were carried out in the Newport Low Speed Tow Tank which is 91 cm × 122 cm in cross-section and 18.3 m in length. The carriage is supported on ball bearings over machined circular rails. It carries the model that is mounted on a strut, pressurized dye tanks for flow visualization and instruments for balance and cam operation for fin cambering. Data acquisition is carried out using a Personal Computer. Flow visualization has been carried out using a 35 mm camera mounted on the carriage. An underwater color video camera is hung from the carriage. Relays are mounted on the rails to trigger the 35 mm camera and to camber the fin after tow speed reaches a steady state. When triggered, the camera takes a sequence of five still pictures. Three light sensors are located at known spacings to compute the carriage speed accurately. Tow speed is also measured by the carriage tow wire and pulley mechanism. At the highest speed, these two readings are within 5 percent of each other. A qualitative indication of when steady state has been reached is obtained from a Pitot-static tube. Diluted red food coloring dye is used for visualization. The top half of the model is painted white. Dim lighting is normally adequate for photography. Visualization of the flow around the dorsal fin has been carried out over the speed range 60–360 cm/s.

4.3 Results. Measurements of side thrust produced by the dorsal fins were carried out for the two cases of permanently cambered and abruptly cambered fins. Dye visualization of the viscous flow around the dorsal fin was then carried out using 35 mm and video cameras. The results are described below.

4.3.1 Balance Measurements. The cases of abrupt fin cambering were compared with those of permanently cambered fins. Figure 11 shows an example. The time traces of tow speed, side thrust and the triggering of fin cambering were recorded and they are highly repeatable. In the case of abrupt cambering, the cambering of the fin is carried out after steady state in tow speed is reached. A side thrust is produced immediately after cambering of the fin. The mean (damped) value of side thrust (L) is different in the two cases. The values are compared in Fig. 12. Each data point in Fig. 12 is an average of ten runs which are virtually indistinguishable. In Fig. 12, L^* represents the side thrust of a permanently cambered fin produced at an arbitrary tow speed of 4.34 m/s. Interestingly, in the permanently cambered case, side thrust moment, that is the lift force produced by the fins, is proportional closely to U_∞^2 as indeed it follows from irrotational airfoil theory (Batchelor, 1985). However, the exponent drops to 1.79 in case of the abruptly cambered fin. Because the index of 2 matches with irrotational theory, we think that the index of 1.79 is also reliable. This index of 1.79 indicates a slight loss of lifting performance in the unsteady case. The flow features observed in the visualization experiment described below, indicate that significant differences in the very low Reynolds number viscous flow around the fins exist between the two cases. Very low Reynolds number airfoils

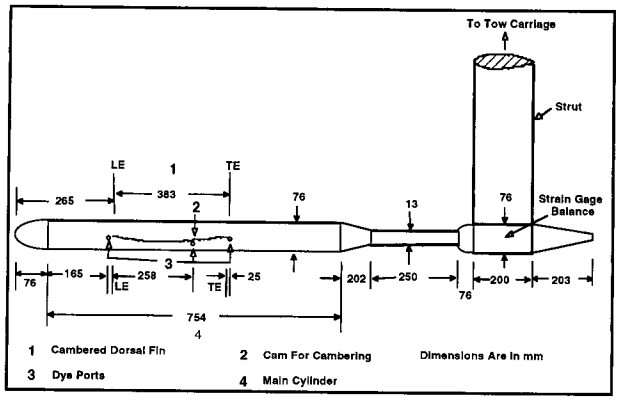

Fig. 10 Side view of assembly of cylinder with dorsal fin, balance and strut

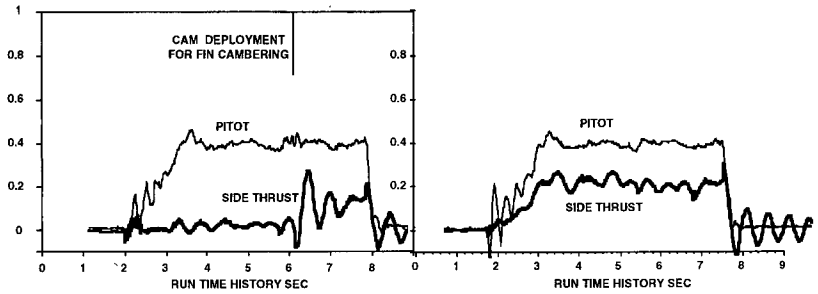

Fig. 11 Comparison of side thrust between abruptly cambered (left) and permanently cambered (right) fins at a steady state tow speed of 3.6 m/s. The ordinates are in arbitrary volt scale.

are known to exhibit similar history effects of changes in angles of attack.

The uncertainties in measurements were expressed as ([True − MeanCalibration/True] 1/FullSpan × 100)%. Side thrust measurements were within 3.2 percent of full span (reached at a tow speed of 4 m/s when fully cambered) at 99 percent confidence level. Pressure transducer measurements were within 0.8 percent of full span (1.3 psi) at 99 percent confidence level.

4.3.2 Flow Visualization. Dye flow visualization was carried out for both the abruptly cambered and the permanently cambered fins. Flow visualization and measurements of the straight fin case were also carried out; the results indicated a non-separating and non-expanding wake. In the Re_d range of the present experiments, cylinders and spheres have a constant value of coefficient of drag (Figs. 1.4 and 1.5 in Schlichting 1979). The viscous flow features described below were independent of the Reynolds number range tested probably because, therein also, the fin drag coefficient remains a constant. The pictures in Figs. 13 and 14 were taken at a tow speed of 60 cm/s. In both Figs. 13 and 14, the pictures (a) to (e) were taken at intervals of roughly 150 ms. Flow direction is from right to left. The pictures were taken with the camera looking down on the model and upstream at the leading edge of the fin. This distorted the pictures—at the upstream end, the cylinder and flow features there look narrower in the cross-stream direction. At the downstream end, the cylinder diameter of 76 mm can be taken as the reference length scale. The time taken to camber the fin is roughly 0.2–0.4 s. The time taken by a fluid particle to traverse the length of the fin chord is 0.1–0.6 s for tow speeds of 3.6–0.6 m/s. Thus, the time scales of the fin and appendage motions are similar. Figure 13 shows the visualization of the flow around the fin when it is abruptly cambered. This figure can be contrasted with the visualization of the permanently cambered case shown in Fig. 14. Figures 13 and 14 show the entire fin and its wake.

Several flow features can be observed when the fin is abruptly cambered. When the fin is first cambered (Fig. 13(*a*)), the flow near the leading edge remains symmetrical. The wake also remains aligned to the cylinder axis. With increasing time, the flow features begin to be influenced by the cambering: the leading edge flow becomes skewed and the fin wake starts to follow the trailing edge slope. The lower (pressure) side of the leading edge develops a bulge, presumably a separation bubble, which has an unsteady character. In Fig. 13(*b*)–(*e*), it alternates between a large and a small bubble. A similar unsteady behavior can be observed on the upper surface near the leading edge also.

On the other hand, when the fin is permanently cambered, the flow around the leading edge is always skewed, the separation bubble in the under-side of the leading edge is stable and the wake follows the trailing edge slope. Furthermore, the wake is *narrower* than that in the abruptly cambered case.

The flow visualization appears to corroborate the side thrust measurements shown in Fig. 12. The axially aligned cylinder tends to generate a zero pressure gradient except near the nose

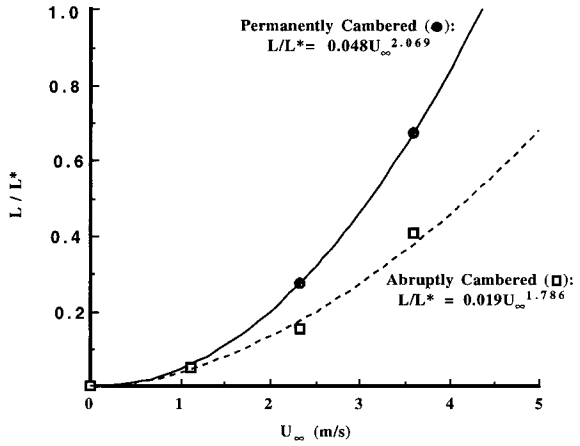

Fig. 12 Relationships of side thrust due to fin cambering with tow speed

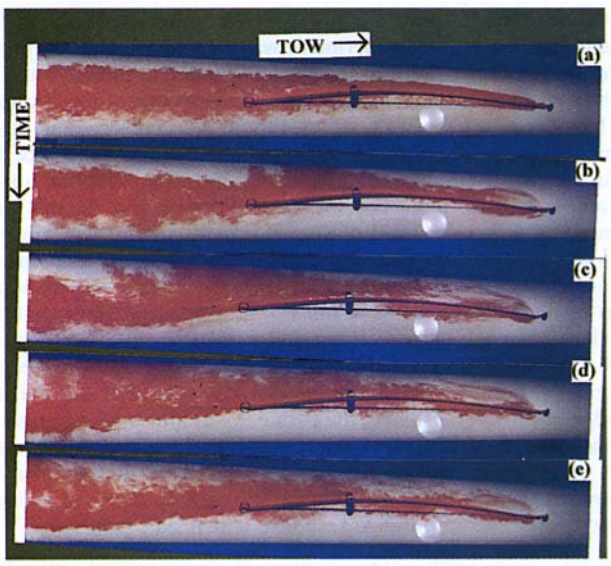

Fig. 13 Dye picture of flow around the abruptly cambered fin. U_∞ = 60 cm/s.

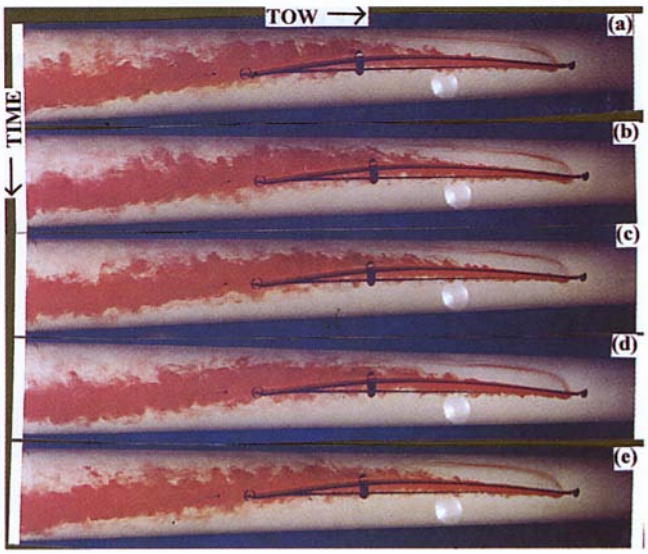

Fig. 14 Dye picture of flow around the permanently cambered fin. U_∞ = 60 cm/s.

and the tail cone. However, the cambered fin tends to produce a pressure difference across itself in the circumferential plane of the cylinder. Because the cylinder diameter is larger than the fin blockage, the effect of the former dominates and the flow near the trailing edge of the fin tends to remain attached. The slightly higher force generated by the permanently cambered fin can also be attributed to the fact that the fin wake is narrower in that case (lift and drag in a hydrofoil tend to be directly related). The ratio of the fin span to cylinder radius, as well as the locations of the leading and trailing edges of the fin with respect to the locations of the nose and tail cone may be critical to the detailed pressure distributions, the viscous flows and the exponents of side thrust produced. In this work, we have experimented with nondimensional values observed in, generally speaking, bluefish and mackerel.

5 Conclusions

Because life forms have evolved in water, forms of locomotion is much more varied and complex in water than in air. Most investigations on swimming have been on cruise and not much is known about low speed maneuvering. The morphology of fins of fish families was studied in an effort to understand the origin of their superiority in maneuverability. No matter what their speed capabilities are, maneuverable species of fish share several common trends in the length scales of their fins. Here, an attempt has also been made to quantify the maneuvering gap between species of fish that are relatively fast swimming yet highly maneuverable, and small underwater vehicles. Finally, a fish-like dorsal fin device is developed that is cambered abruptly for immediate production of side thrust without any separation of the main cylinder. The bulk of this side thrust is irrotational in origin as in a lifting airfoil. However, some complex unsteady viscous interactions are also present between the dynamic leading edge of the fin and the cylinder boundary layer. The latter requires further investigation.

Acknowledgments

This research was funded by ONR (Manager: J. Fein), ONR LPP (Manager: Dr. S. Dickinson), NUWC IR (Manager: Dr. K. Lima) and by the NUWC Director of Science & Technology (Dr. R. H. Nadolink). Their support is gratefully acknowledged. The results were presented at the ARPA-ONR Review Meeting on Biolocomotion, held at the Johns Hopkins Univ., Mar. 20–22, 1995 and ASME Summer Meeting at San Diego, Ca, July 7–11, 1996. The first author is thankful to Dr. Richard H. Nadolink of NUWC for interesting him in the subject.

References

Aleev, Yu. G., 1969, "Function and Gross Morphology in Fish," *Israel Program for Scientific Translations,* Jerusalem, U. S. Dept. of Commerce, Washington, DC.

Azuma, A., 1992, *The Bio-Kinetics of Flying and Swimming,* Springer-Verlag, New York.

Batchelor, G. K., 1985, *An Introduction to Fluid Dynamics,* Cambridge Univ. Press.

Bigelow, H. B., and W. C. Schroeder, 1953, "Fish of the Gulf of Maine," *Fish. Bull.* Vol. 53(74), pp. 1–577.

Hoar, W. S., and D. J. Randall, eds., 1978, *Fish Physiology,* Vol. VII Locomotion, Academic Press, New York.

Kármán, T. V., 1954, *Aerodynamics: Selected Topics in the Light of Their Historical Development,* Cornell University Press, Ithaca.

Lindsey, C. C., 1978, "Form, Function, and Locomotory Habits in Fish," W. S. Hoar and D. J. Randall, eds., *Locomotion Fish Physiology,* Vol. 7, Academic Press, New York, pp. 1–100.

McLaughlin, R. L., and D. L. Kramer, 1991, "The Association Between Amount of Red Muscle and Mobility in Fishes: A Statistical Evaluation," *Environmental Biology of Fishes,* Vol. 30, pp. 369–378.

Schlichting, H., 1979, *Boundary-Layer Theory,* McGraw-Hill.

Scott, W. B., and M. G. Scott, 1988, "Atlantic Fish of Canada," *Canadian Bulletin of Fisheries and Aquatic Sciences,* 219, p. 731.

Tani, I., 1943, "On the Design of Airfoils in Which the Transition of the Boundary Layer is Delayed," (in Japanese), *Report of the Aeronautical Research Institute,* Tokyo Imperial University, Vol. XIX, No. 250.

Wu, T. Y., 1994, "Biohydrodynamics of Aquatic Locomotion," *Proceedings of the NUWC-NPT Seminar Series on Swimming and Flight in Nature,* P. R. Bandyopadhyay (compiler), NUWC-NPT Technical Memorandum 942080 Naval Undersea Warfare Center, Newport, RI, 11 Aug.

Wu, T. Y. T., C. J. Brokaw, and C. Brennen, eds., 1975, *Swimming and Flying in Nature, vols. 1 and 2,* Plenum Press, New York.

Appendix A

Genus and Species of Fish Families Studied[1]

1. Families that are highly maneuverable (including burst of speed) are listed below:

Family	Abbreviations: Genus and Species
Grouper:	EM: *Epinephelus moara*
	SM: *Sebasticus marmoratus*
Parrot Fish:	OF: *Oplegnathus fasciatus*
Nibbler:	GP: *Girella punctata*
Sea Bream:	MM: *Mylio macrocephalus*
	CM: *Chrysophrys major*

2. Families that have high speed are identified below:

Family	Abbreviations: Genus and Species
Bonito:	PJJ: *Pneumatophorus japonicus japonicus*
	KP: *Katsuwonus pelamis*
	TTO: *Thunnus thynnus orientalis*
Dace:	THH: *Tribolodon hakonensis hakonensis*
Salmon:	OK: *Oncorhynchus keta*
	OM: *Oncorhynchus masou*
Needlefish:	CS: *Cololabis saira*

3. Families that have both speed and maneuverability are listed below:

Family	Abbreviations: Genus and Species
Horse Mackerel:	CD: *Caranx delicatissimus*
	AA: *Atropus atropus*
Pisces:	Sea Bass

[1] From Azuma (1992).

Appendix B

Genus and Species of High-Speed Fish Families[2]

Family	Genus and Species
Dolphin	*Coryphaena hippurus*
Yellowtail	*Seriola quanqueradiata*
Atka Mackerel	*Pleurogrammaus monopterygius*
Gray Mullet	*Mugil cephalus*
Barracuda	*Sphyraena pinguis*
Sockeye Salmon	*Oncorhynchus nerka*
Bluefin Tuna	*Thunnus thynnus*
Skipjack	*Katsuwonus pelamis*
Spanish Mackerel	*Scomberomorus niphonius*
Pacific Slury	*Cololabis saira*

[2] From Wu (1994).

Appendix C

Genus and Species of High-Speed, Highly-Maneuverable Fish Families[2]

Family	Genus and Species
Porgy	*Pagrus pagrus*
Rainbow Trout	*Salmo gairdnerii*

Computation of Unsteady Viscous Marine-Propulsor Blade Flows—Part 1: Validation and Analysis

E. G. Paterson
Hunter Rouse Graduate Fellow,
Currently, Assistant Research Scientist.
Assoc. Mem. ASME

F. Stern
Professor. Mem. ASME

Iowa Institute of Hydraulic Research and
Department of Mechanical Engineering,
The University of Iowa, Iowa City, IA
52242-1585

In this two-part paper, time-accurate solutions of the Reynolds-averaged Navier-Stokes equations are presented, which address through model problems, the response of turbulent propeller-blade boundary layers, and wakes to external-flow traveling waves. In Part 1, the Massachusetts Institute of Technology flapping-foil experiment is simulated and the results validated through comparisons with data. The physics of unsteady blade flows are shown to be complex with analogy to Stokes layers and are explicated through visualization and Fourier analysis. It is shown that convection induced steady/unsteady interaction causes deformation of the external-flow waves and is responsible for the upstream- and downstream-traveling pressure-gradient waves over the foil and in the wake, respectively. The nature of the unsteady displacement thickness suggests viscous-inviscid interaction as the mechanism for the response. In Part 2, a parametric study is undertaken to quantify the effects of frequency, foil geometry, and waveform.

Introduction

In comparison to other rotating machinery, marine propulsors are unique in that they are susceptible to cavitation and, more importantly for the work herein, operate in the thick hull boundary layer and/or appendage wakes. This creates a flow which, at design conditions, is inherently interactive and unsteady. Moreover, at off-design conditions (e.g., maneuvering) complex natural (i.e., vortex shedding from the hull) and forced (i.e., propulsor) unsteady interactions occur. Computational fluid dynamics (CFD) methods have been applied extensively to the steady-flow approximation of propeller/hull interaction. These methods typically use an interactive approach, i.e., a body-force propeller representation in a Reynolds-averaged Navier-Stokes (RANS) method obtained interactively using a vortex-lattice propeller-performance method for specified inflow (e.g., Stern et al., 1994a). CFD methods have also been applied to the steady-flow problem of open-water (i.e., uniform inflow) propeller-blade and wake flows both for idealized (Kim and Stern, 1990) and practical turboprop and marine propulsors (Stern et al., 1994b). Despite the advances made by these methods, the unsteady complete-configuration flow, whose understanding is critical for issues such as cavitation, vibration, and acoustics, remains as a computational Grand Challenge and requires both further CFD development and experimental fluid dynamics (EFD) validation data. Recent efforts, including those reported here, have been directed toward meeting this challenge by addressing issues of time-accurate RANS for fixed- and moving-boundary problems (Paterson, 1994), practical marine propulsors with simplified periodic inflows (Chen et al., 1994), and self-propelled maneuvering underwater vehicles (McDonald and Whitfield, 1996).

Historically, the rational approach for analysis of unsteady propulsor hydrodynamics has been through the use of two-dimensional models of propeller blade and wake flow, i.e., a foil embedded in vertical and horizontal traveling waves (gusts) at the dominant frequencies (i.e., up to reduced frequency of 10) of the ships nominal wake. As such, the model problem is directly related to the classical and fundamental work on unsteady boundary layers and unsteady lifting flows. However, both bodies of work have been approached with differing perspectives, i.e., as viscous- and inviscid-flow problems, respectively, thus creating a need for more comprehensive study. Nevertheless, the previous work provides a framework for understanding unsteady, viscous, lifting blade flows.

Nearly all work on unsteady boundary layers is for a flat plate subject to a uniform stream with superimposed temporal, spatial, or traveling horizontal-wave outer-flow oscillation. Most information, however, is for laminar and turbulent boundary layers with temporal-wave outer flow (e.g., Telionis, 1981; Spalart and Baldwin, 1989; Shima, 1993) where it is known that the response is characterized by small-amplitude Stokes-layer overshoots, phase leads, and streaming and, in addition, limited interaction between mean and turbulent motions. Spatial-wave outer flows, on the other hand, which are related to ship hydrodynamics problems involving free-surface piercing bodies with gravity waves, have only recently been put in context of Stokes layers (Choi et al., 1996). Choi et al. (1996) showed that Stokes-layer behavior is observed, but is significantly larger in amplitude than the temporal wave, and that nonlinear interaction between the zeroth- and first-harmonic velocity components result in an asymmetric wake response. Of most interest for the work here is the traveling-wave outer flow. However, as in the case of spatial waves, very limited information is available (Choi et al., 1996; Patel 1975, 1977). Choi et al. (1996) did show that for laminar flow, the boundary layer response to traveling waves was extreme, i.e., very large overshoots and large phase lags, for certain combinations of wave speeds and frequencies. Unfortunately, virtually no work exists for turbulent boundary layers subject to traveling waves, particularly at the level of resolution required to validate RANS methods and turbulence models and explicate the interaction between mean and turbulent motions.

The situation for unsteady lifting flows is similarly incomplete: the results are limited in range, most notably frequency, and contradictory since they resolve differing levels of physics.

Contributed by the Fluids Engineering Division for publication in the JOURNAL OF FLUIDS ENGINEERING. Manuscript received by the Fluids Engineering Division July 20, 1995; revised manuscript received September 23, 1996. Associate Technical Editor: G. Em Karniadakis.

For example, the pioneering linear potential flow theories for foils embedded in traveling vertical waves (Sears, 1941) and traveling waves with both vertical and horizontal components (Horlock, 1968) neglect interaction of the outer unsteady flow with the mean flow field and suffer frequency restrictions due to use of the steady Kutta condition. Nonlinear potential flow methods (Goldstein and Atassi, 1976) show that steady/unsteady interaction significantly accelerates and distorts the waves resulting in a much different lift response. As further shown by Basu and Hancock (1978), this interaction additionally creates a complex unsteady foil wake which is a combination of its shed vorticity due to lift and the deformed gust. Use of the steady Kutta condition in potential flow theories has been shown to be invalid (Poling and Telionis, 1986) for reduced frequencies $k = \omega L/2U_0$ above 2 due to nonzero loading at the trailing edge. More importantly, Poling and Telionis (1986) postulated, through visualization of strong curvature of the near-wake streamlines, that viscous-inviscid interaction may be an important feature of high-frequency gust flows. Finally, the wave characteristics of the pressure field, which are particularly important for acoustics and cavitation, differ significantly between theory and EFD and CFD. While the classical theories predict constant phase angle along the foil (i.e., a temporal-wave response), EFD (e.g., Commerford and Carta, 1974) and compressible Euler-equation CFD (Atassi et al., 1993; Adamcyzk and Brand, 1972) show upstream- and downstream-traveling pressure waves. No definitive explanation for this response has been advanced since most studies are either focused on other aspects (e.g., acoustic energy as opposed to purely hydro or aerodynamic sources) or limited in scope and/or range of parameters.

Obviously, there are many issues to be addressed and much work is required in understanding their relative importance, parametric dependencies, and relationship to practical applications. Therefore, the objectives of the present work are twofold. First, in Part 1, unsteady-flow calculations and validation through comparisons with the Massachusetts Institute of Technology (MIT) Marine Hydrodynamics Laboratory flapping-foil experiment (FFX) are presented. The results are discussed for steady and unsteady flow, including comparisons with the data, and an analysis provided to explicate the observed response. Second, in Part 2, a parametric study of frequency, waveform, and foil geometry is presented to relate the observations made in Part 1 to the classical and fundamental work, to further explicate the response, and to determine implications with regard to practical applications.

MIT Flapping-Foil Experiment

The FFX consists of a foil embedded in traveling vertical and horizontal waves generated by upstream pitching foils (Fig. 1) and was designed to provide detailed measurements for validation of unsteady CFD methods and determination of appropriate Kutta conditions for unsteady potential-flow methods. Details of the experimental objectives, apparatus, procedures, and uncertainty are documented by Rice (1991), Delpero (1992), and Horwich-Lurie (1993). Associated with FFX was the 29–30 March 1993 Office of Naval Research (ONR)/MIT Unsteady-Flow Workshop in which various groups of researchers submitted blind computations (i.e., with only the experimental conditions and boundary data) and met at the workshop for the comparisons with the data and discussion. Paterson and Stern (1993) provide a discussion of the Workshop results.

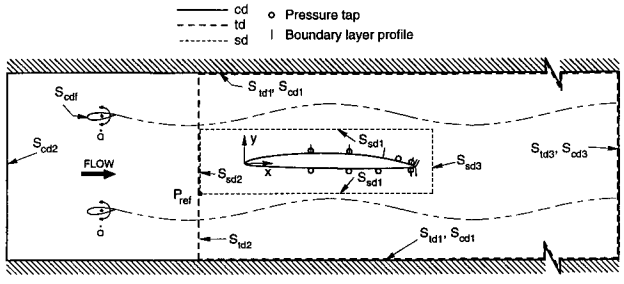

Fig. 1 Flapping-foil experiment geometry and solution domain boundaries

The experiments were performed in the closed-loop MIT Variable-Pressure Water Tunnel which has a 53 in long and 20 inches square test section and a freestream turbulence level of about 1 percent. The foil is a modified NACA 66 fixed at an angle of attack of 1.18–1.34 deg with transition set at $x = 0.105$ on both sides. Modifications were made to the foil geometry to account for blockage such that the foil in the tunnel produced the same steady pressure distribution as the unmodified foil in open-water conditions. The flappers are NACA 0025 and are driven by a variable-speed motor with an amplitude of 6 deg and a frequency of 16 Hz. The corresponding Re based on the foil chord length is 3.78×10^6 and the frequency parameter is $\xi = 3.6$.

Velocity and surface-pressure measurements were made using a two-component laser Doppler velocimeter and miniature pressure transducers, respectively. For the unsteady measurements, the value at each time step is the ensemble, or phase, average over 250 periods and had a temporal discretization of 180 points over the period.

Prior to the workshop, steady and unsteady (U, V) data was provided on the small domain boundaries and 60 percent of the tunnel domain inlet along with steady boundary-layer profiles. After the workshop, unsteady boundary-layer profiles and pressure data was provided at the locations shown in Fig. 1. In general, comparisons are made to the data whenever possible.

Computational Method

In the following, the method is briefly described, an overview is given of the solution domains, boundary conditions, and grid generation, and numerical uncertainty is discussed.

Description. The Reynolds-averaged Navier-Stokes (RANS) equations are written in the physical domain using Cartesian coordinates with x positive downstream, y normal to x, and the origin at the foil leading edge (Fig. 1) and are partially transformed (i.e., coordinates only) into nonorthogonal curvilinear coordinates such that the computational domain forms a simple rectangular parallelepiped with equal grid spacing. The transformed equations are reduced to algebraic form using finite-analytic (FA) spatial discretization (Chen and Chen, 1984), where the FA coefficients are obtained from a local analytical solution to the linearized momentum equations, and second-order accurate backward finite-difference temporal discretization. This results in a computational stencil that includes all eight neighboring nodal values and the values at the two previous time-steps. The overall solution procedure is based upon the two-step pressure-implicit split-operator (PISO) algorithm (ISSA, 1985) and a pressure equation derived from the discrete continuity equation. In step 1 of the algorithm, the implicit momentum equations are solved iteratively using line-ADI with under-relaxation and the pressure from the previous time step. Step 2 consists of iterations between line-ADI solution of the implicit pressure equation and an explicit velocity correction. In both steps of the algorithm, iterative convergence is required to ensure time accuracy and is measured using residuals based upon the difference between iterates. Also, the FA coefficients, which are dependent upon the local velocity, are updated at each step thus retaining the nonlinearity of the equations. Closure is attained through a quasi-steady application of the Baldwin-Lomax turbulence model with modifications to account both for the effects of wake asymmetry (Rodi and

Srinivas, 1989) and axial pressure gradients (Granville, 1987). Note that complete details of the methods used are presented in Paterson (1994).

Solution Domains and Boundary Conditions. The FFX was conducted such that calculations could be performed for a small domain with given boundary data, for a tunnel domain with a specified inflow, or for the complete domain, including the upstream flappers. At the workshop, the authors submitted blind computations using the small domain. Subsequent calculations included all three domains, including a complete-domain calculation using unsteady Chimera domain decomposition. All three domains (small, tunnel, and complete) are shown in Fig. 1. Referring to the notation in Fig. 1, the boundary conditions for the small domain are:

(1) On the top and bottom (S_{sd1}), U is from data, V is from continuity, and p is from an integrated form of the Euler equation.
(2) On the inlet (S_{sd2}), U, V are from data and p is from the axial Euler equation.
(3) On the exit (S_{sd3}), zero-diffusion and zero-pressure-gradient conditions are applied.

For the tunnel domain:

(1) On the tunnel walls (S_{td1}), slip boundary conditions are used, that is, $\partial U/\partial y = 0$, $V = 0$, and $\nabla p \cdot \mathbf{n} = 0$.
(2) On the inlet (S_{td2}), U, V is from a combination of data and an inviscid model and p is from the axial Euler equation.
(3) On the exit (S_{td3}), zero-diffusion and zero-pressure-gradient conditions are applied.

For the complete domain, the boundary conditions are the same as the tunnel domain except for:

1) On the inlet (S_{cd2}), uniform flow and zero-pressure-gradient conditions are used.
2) On the flapping-foils (S_{cdf}), the no-slip condition is used, that is, $U = -\alpha\xi \cos(\xi\tau)(y - y_r)$, $V = -\alpha\xi \cos(\xi\tau)(x - x_r)$, and $\nabla p \cdot \mathbf{n} = 0$ where α is the flapper amplitude, (x_r, y_r) is the center of rotation, τ is the nondimensional time, and ξ $(=\omega L/U)$ is the frequency parameter.

Grid Generation. Two grid-generation techniques were used depending on the domain and grid topology. EAGLE (Thompson, 1987) was used to generate C-grids for the foil in the small domain and the flappers in the complete domain. Algebraic H-grids were generated for both the tunnel and complete domains with hyperbolic tangent stretching functions and transfinite interpolation such that the grid spacing was controlled along the foil surface, leading and trailing edges, and the flapper wakes. For the complete domain, Chimera domain decomposition (Suhs and Tramel, 1991) was used to resolve the oscillating flappers by decomposing the domain into three separate, but coupled domains.

Numerical Uncertainty. The recent publication of ASME Standards and Guidelines for numerical uncertainty (Freitas, 1993) are important in signaling a new era in CFD development and application. Recently, Stern et al. (1996) critically reviewed the standards and guidelines, grouped them into documentation

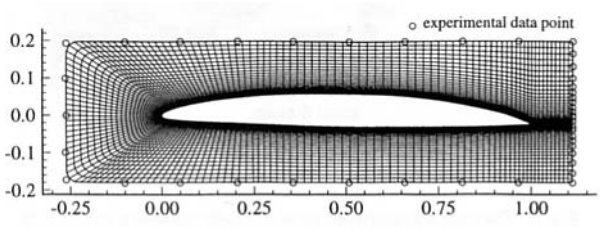

Fig. 2 Small-domain grid with data locations

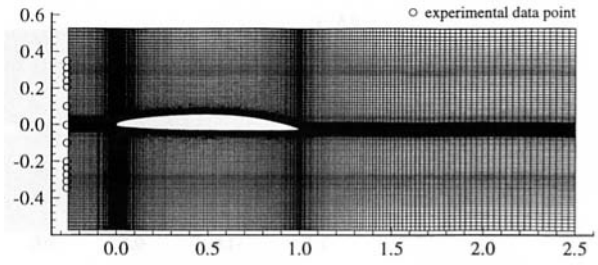

Fig. 3 Tunnel-domain grid with data locations

(1, 7, 8), verification (2–6), and validation (9, 10), and provided implementation recommendations.

Documentation of the unsteady algorithm is provided in Paterson (1994). In addition, the core CFD method has been applied to many steady-flow applications and is well documented (e.g., Stern et al., 1996).

Verification analysis consists of evaluating iterative and grid convergence, minimization of phase (i.e., time-step convergence) and dissipation errors, and determination of order-of-accuracy. Iterative convergence typically required 25 and 50 iterations for the implicit momentum and pressure/velocity-correction steps, respectively. Residuals less than 0.0001 and/or a drop of three orders of magnitude were used as the stopping criterion.

Grid convergence was studied for both steady and unsteady flow. For steady flow, the number of points in the boundary-layer and near-wall grid spacing were increased and decreased, respectively, until the change of velocity profiles and wall-shear stress between grids was approximately 1 percent. For unsteady flow, effect of axial resolution and, therefore, inherent artificial dissipation upon the wave amplitude was studied in the tunnel domain without the foil. Approximately 40 points/wavelength were required to maintain 90 percent of the amplitude at the exit of the domain. The number of points across the flapper wakes for both tunnel and complete domains was not studied.

Time-step convergence and phase error was assessed by varying the time step and comparing solution and data Fourier-series phase angles. For both small and tunnel domains, the difference in phase response, in both inviscid and viscous regions, between 50 and 64 time steps/period was approximately 0.5 percent.

Due to solution dependent FA coefficients, the order of the method is a function of cell Re and aspect ratio and, as such, the discretization does not lend itself to the typical term-by-term order-of-accuracy analysis that is common to finite-difference methods. However, using a grid-doubling scheme and Richardson extrapolation, order-or-accuracy of the core viscous-flow solver has been calculated for a variety of problems. For simple (i.e., laminar flat-plate boundary-layer and fully-developed annular-pipe flows) and complex (i.e., high Re flat plate, axisymmetric bodies, surface-piercing foils) flows (Dolphin, 1996; Zhang and Stern, 1996) with high Re (i.e., up to 10^9) and very highly stretched grids (i.e., aspect ratio up to 10^6), order-of-accuracy has been shown to range from 1.5 to 2.5. Note that this level of order-or-accuracy is comparable to, and in some cases better than, second-order finite-difference discretizations on stretched, non-orthogonal grids.

Validation, which is the purpose of this paper, is provided through detailed comparison with the MIT FFX data and is presented in the following sections.

Computational Grids and Conditions

The grids used are shown in Figs. 2–4. The small- and tunnel-domain grids have 181×80 and 180×179 points, respectively. In comparison, the complete domain has 240×179 and 71×40 points for the foil and flappers, respectively, for a total of 48,640. For each domain, approximately 40 points span the

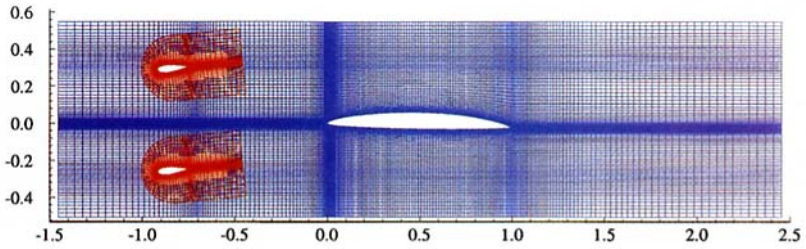

Fig. 4 Complete-domain overset-grid system

boundary-layer and the near-wall grid spacing was set such that the first grid point was located at $y^+ \approx 0.1$.

The calculations were performed at the experimental values of Re and ξ and at an angle of attack of 1.34 deg. The small-domain solution submitted for the workshop used the data for boundary conditions as previously described. Since the data did not correspond to the boundary-point locations, the data was smoothed using a cubic spline and interpolated both in time and space using a biquadratic polynomial. However, the coarseness of the data lead to erroneous results, especially for pressure. To validate the boundary condition formulation, a revised calculation was made with high resolution boundary data interpolated from the tunnel-domain solution. For tunnel-domain inlet boundary S_{td2}, smoothed and interpolated data provided approximately 60 percent of the tunnel inflow area and, as previously mentioned, the remaining 40 percent was specified by matching a potential-flow approximation to the data [see Paterson (1994) for details]. Figure 5 shows the tunnel-domain and data inlet profiles in terms of zeroth- and first-order harmonics. Also shown are second-harmonic amplitudes (U_2, V_2), which are large, particularly near the flapper wakes, and which were attributed to an excited mode of tunnel vibration (Horwich-Lurie, 1993). For the complete domain, the boundary-conditions were well-posed and required no special treatment. However, use of the Baldwin-Lomax turbulence model with overset grids presented difficulties. Because of these difficulties and the low flapper $\mathrm{Re}_L = 6.3 \times 10^5$, it was assumed that the flapper flow was laminar. Lastly, transition was fixed by forcing the eddy viscosity upstream of the boundary-layer trip to zero.

The steady-flow solution was used as the starting point for each calculation and typically 2 periods for the small domain and 4 periods for the tunnel and complete domains were required to attain a periodic solution. For the small and tunnel domains, the time step was $\frac{1}{50}$ of a period ($\Delta t = 0.01745$) and for the complete domain, the time step was $\frac{1}{64}$ of the period ($\Delta t = 0.01364$). CPU time per period and memory required on a CRAY YMP was 15 minutes/4MW, 45 minutes/6MW, and 120 minutes/8MW for the small, tunnel, and complete domains, respectively.

Discussion of Results and Comparison to Data

In the following, a brief description of the similarities and differences between the solutions on the different domains is provided. Then, using only the tunnel-domain solution, the results are compared to data and discussed in terms of the zeroth (steady) and first- and second-order (unsteady) Fourier harmonic amplitudes and phases which are defined as

$$\phi(t) = \phi_0 + \sum_{n=1}^{2} \phi_n \sin(n\xi t + \gamma_{\phi,n})$$

$$\phi_n = \sqrt{a_n^2 + b_n^2}$$

$$\gamma_{\phi,n} = \tan^{-1}(a_n/b_n)$$

$$a_n = \frac{2}{T}\int_{\tau=0}^{T} \phi(\tau)\cos(n\xi\tau)d\tau$$

$$b_n = \frac{2}{T}\int_{\tau=0}^{T} \phi(\tau)\sin(n\xi\tau)d\tau \qquad (1)$$

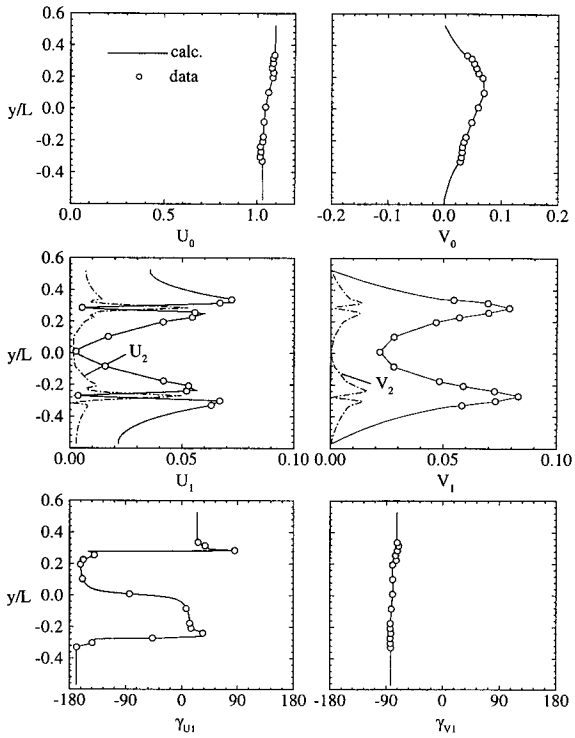

Fig. 5 Comparison of boundary data and tunnel-domain inlet conditions

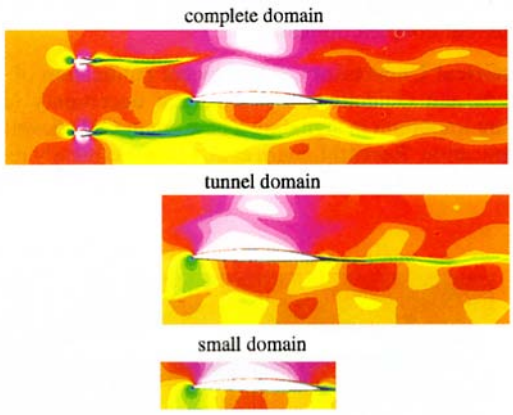

Fig. 6 Domain comparison: axial-velocity contours at $t/T = 0$

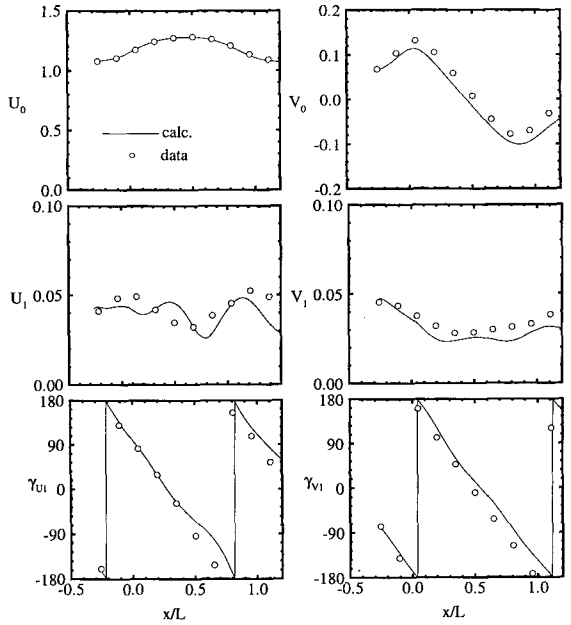

Fig. 7(*a*)

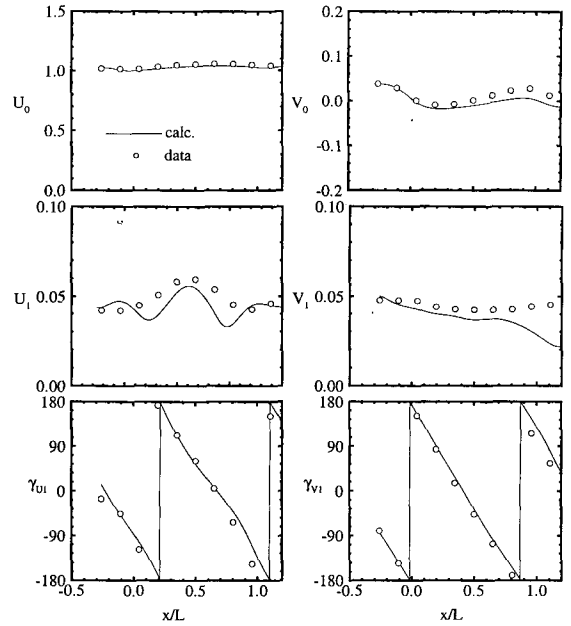

Fig. 7(*b*)

Fig. 7 Comparison of data and calculation on small-domain boundaries. (*a*) Small-domain top boundary; (*b*) small-domain bottom boundary

where ϕ represents one of the flow variables. Note that Eq. (1) was evaluated for every point in the domain by using the last period of simulation.

Comparison of Solution Domains. In Paterson and Stern (1993), it was shown that the solutions gave similar overall agreement with the data, except for the small domain with data-prescribed boundary conditions, for both steady and unsteady flow. This demonstrated that, despite differences in boundary conditions, grid generation, and CPU-time and memory requirements, complex problems could be handled with a variety of formulations. There were, however, some differences. It was shown, as previously mentioned, that the small domain with data-prescribed boundary conditions introduced erroneous higher harmonics which were attributed to the coarseness of the data. The small-domain formulation, however, was validated

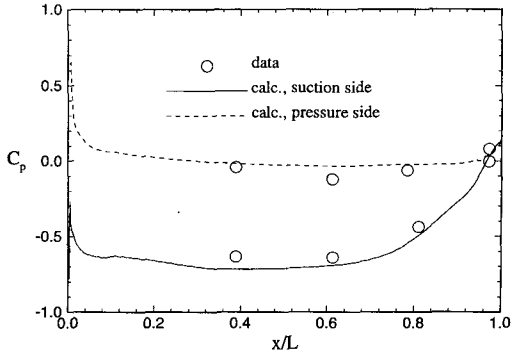

Fig. 8 Surface-pressure distribution: zeroth harmonic

by using boundary conditions prescribed by interpolating from the tunnel-domain solution. This showed nearly identical results as the tunnel domain. The inclusion of pressure-gradient effects in the turbulence model for one tunnel-domain calculation significantly improved the solution. The complete-domain solution was similar to the others, but had some small differences due to the laminar-flow treatment of the flappers, the lack of tunnel-induced vibration (i.e., response was almost purely first harmonic), and the definition of the non-dimensional velocity.

As an overall comparison, Fig. 6 shows axial-velocity contours for each of the domains at $t/T = 0$. The difference in the domain size, consistency between the solutions, and wavy nature of the flow are evident. The small- and tunnel-domain solutions are nearly identical. The complete domain shows continuity across the overlaid-grid region and flapper wakes, due to their laminar treatment, that are wider than tunnel domain and data.

Given the above discussion, the tunnel-domain solution with pressure gradient modifications will be used for discussion of the results and analysis of the response.

Steady Flow (Zeroth Harmonic). The zeroth harmonic is the same as a steady-flow solution and displays typical foil flow. Figure 7, which is a comparison in the inviscid region of the flow field on the small-domain boundaries, shows (U_0, V_0) on S_{sd1} top and bottom. U_0 and data agree and show acceleration on the suction side, whereas V_0 is similar in shape, but shows a small underprediction in comparison to the data. Surface pressure and wall-shear stress is shown in Figs 8 and 9, respectively. The pressure shows agreement with the data and the stress displays the fixed transition along with a small region of separation over the last 5 percent on the suction side. Velocity profiles, at selected stations, are shown in the left column of Fig. 10 and show good agreement with the data. This level of agreement, which required pressure-gradient modifications to the turbu-

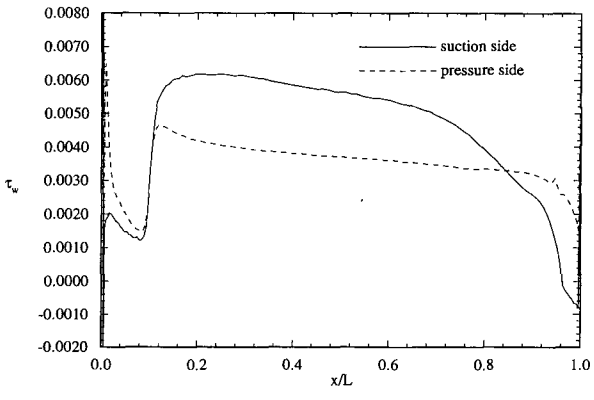

Fig. 9 Wall-shear stress distribution: zeroth harmonic

lence model, appears to be a general assessment of the current capabilities of isotropic turbulence models since it is consistent with the other participants in the FFX workshop and overall results found in the literature.

Unsteady Flow. Figure 7 includes first-harmonic amplitude (U_1, V_1) and phase (γ_{U1}, γ_{V1}). On S_{sd1} top, U_1 and data agree in magnitude and display spatial sinusoidal oscillations of nearly the same form and V_1 agrees in magnitude and shape with the data. On S_{sd1} bottom, U_1 shows agreement in both the magnitude and shape and V_1 shows an axial decay in comparison to the data. The phases are in agreement with the data on both top and bottom and show a downstream-traveling wave [in the Fourier analysis, the argument of the trigonometric functions ($\xi t + \gamma$) is equivalent to characteristic lines $\xi(t \pm x/c)$, which corresponds to downstream ($\gamma = -\xi x/c$) or upstream ($\gamma = +\xi x/c$) traveling waves].

Figure 11 shows the lift and drag time histories over one period. The lift shows a large second harmonic which is consistent with the inflow. The drag is also second harmonic and indicates a small phase lead in comparison to the lift. Figure 12 shows the surface-pressure first-harmonic amplitude and phase, the former of which has similar amplitude in comparison to the data. The shapes and zero values at certain x/L are different and unconfirmed by the limited data. A large second harmonic (figure not shown) is consistent with the lift and drag and inlet profiles. On both sides, the streamwise increasing phase indicates upstream-traveling waves which are unconfirmed by the data of nearly constant phase. It should be noted that the uncertainty of the pressure data was much debated at the ONR workshop and that, unfortunately, no estimate was provided.

Figure 13 shows the wall-shear stress first-harmonic amplitude and phase. There is no data for validation of the amplitudes, however, the phase indicates the influence of the pressure gradient: on the pressure side, decreasing values (i.e., downstream-traveling wave) on the forebody and upstream-traveling wave on the afterbody; and on the suction side, an upstream-traveling wave which leads the pressure by about 80 deg. This implies that the direction of the near-wall flow is opposite of the external-flow traveling wave.

The velocity first-harmonic amplitude and phase profiles indicate, for $x \leq 0.784$ (pressure side) and $x \leq .9$ (suction side), amplitudes with small overshoots and phases with increasing lags with x and smooth transition across the boundary layer. In contrast, for x greater than these values, a two-layer structure is displayed with relatively constant amplitude of different magnitude for the inner and outer flows with a zero amplitude and phase shift (180 deg/130 deg on suction/pressure sides) at the inner/outer boundary which is at approximately the boundary-layer edge. Figure 10 shows this at two selected stations on both sides of the foil. In the wake, where there is no data, the amplitude shows large overshoots and the phase initially shows a continuation of the boundary-layer response and then by $x = 1.1$, leads on both the pressure and suction sides. The unsteady boundary-layer response is also depicted in Fig. 14 which shows perturbation-velocity (i.e., difference between steady and unsteady) time-history contours which vividly exhibit the features previously described.

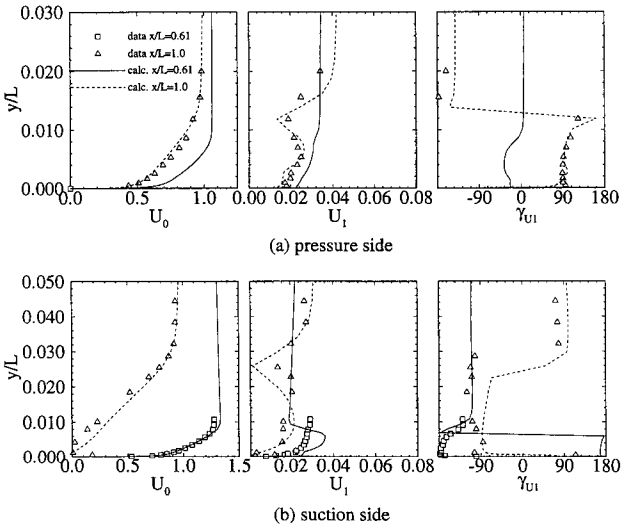

Fig. 10 Velocity profiles

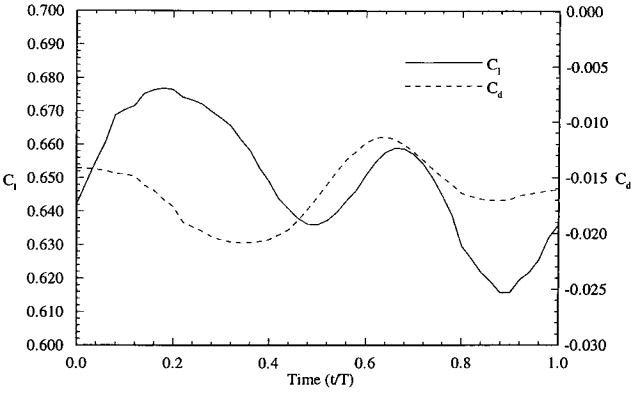

Fig. 11 Lift and drag time histories

Figure 15 shows the perturbation velocity vectors and particle traces at $t/T = 0.8$. The interaction between the flapper-wake vortices and foil is complex: distortion and increased speed on the suction (wavespeed, $c \approx 1.26$) versus the pressure ($c \approx 1.05$) side such that the flapper-wake vortices are out of phase by the time they reach the foil trailing edge; and secondary counter-rotating vortices near the trailing edge and in the wake. The latter directly correlate with and explain the region where the first-harmonic velocity profiles displayed the two-layer structure. Also, the distortion and wake complexity has similarity to that shown by Basu and Hancock (1978) and is a result of the unsteady wake sheet interacting with the distorted gust.

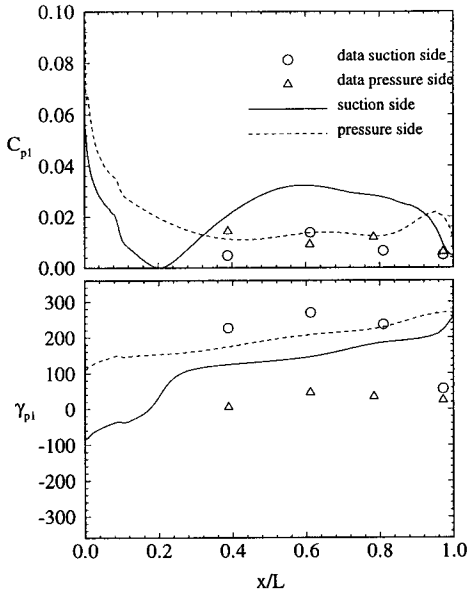

Fig. 12 Surface-pressure distribution: first harmonic amplitude and phase

Figure 15 also shows the perturbation axial pressure-gradient contours. This figure (and others in the time series which are not shown) indicates the direct correspondence between the flow pattern and axial pressure gradient, i.e., the perturbation flow directions are consistent with the regions of favorable and adverse gradients. The wake is complex, including higher harmonics and upstream- and downstream-traveling waves over the foil and in the near wake and in the intermediate wake, respectively. The upstream-traveling waves are consistent with the surface-pressure first-harmonic phase.

Analysis of Unsteady Response. To explain the unsteady response and, in particular, the nature of the correspondence between pressure gradient and external flow waves, an analysis of the pressure gradient is presented. Substituting the first three terms of the velocity Fourier series into the axial Euler equation gives

$$-\frac{\partial p}{\partial x} = p_{x_0} + \sum_{n=1}^{2} p_{x_n} \sin\left(n\xi t + \gamma_{U_n} + \hat{\gamma}_{p_{x_n}}\right) \qquad (2)$$

where p_{x_n} is the amplitude and $\hat{\gamma}_{p_{x_n}}$ is the phase shift of the pressure gradient with respect to $\gamma_{U_n} \approx -n\xi x/c$. The thirty-two terms which comprise p_{x_n} were evaluated along lines outside the boundary layer at $y^+ \approx 10^4$ (Fig. 16(a)) and it was determined that three terms, for each order, are dominant such that

$$p_{x_n} = \sqrt{\left(nU_n\xi + U_0U_n\frac{\partial\gamma_{U_n}}{\partial x}\right)^2 + \left(U_0\frac{\partial U_n}{\partial x}\right)^2}$$

$$\hat{\gamma}_{p_{x_n}} = \tan^{-1}\left(\frac{nU_n\xi + U_0U_n\dfrac{\partial\gamma_{U_n}}{\partial x}}{U_0\dfrac{\partial U_n}{\partial x}}\right) = \tan^{-1}(A) \qquad (3)$$

The first term in p_{x_n} is from the temporal derivative and the second and third, which represent steady/unsteady interaction, are from the convective term. Three cases are of particular interest:

(1) $U_n \neq U_n(x)$ (i.e., $U_{x,n} = 0$) such that $A = \pm\infty$ and $\hat{\gamma}_{p_{x_n}} = \pm\pi/2$, where + corresponds to a lead (i.e., temporal wave with $c \to \infty$) and − to a lag (i.e., spatial wave with $c \to 0$)

(2) $U_n \approx ax$ (i.e., $U_{x,n} = a$) such that A and $\hat{\gamma}_{p_{x_n}} = 0$. This corresponds to a downstream-traveling wave in phase with the velocity wave.

(3) $U_n \approx \sin(n\xi xB/c)$ (i.e., $U_{x_n} \approx \cos(n\xi xB/c)$) such that $A \approx \tan(n\xi xB/c)$ and $\hat{\gamma}_{P_{x_n}} \approx n\xi xB/c$, where

(A) $B < 1$ corresponds to a downstream-traveling wave

(B) $B = 1$ corresponds to a temporal, or stationary, wave

(C) $B > 1$ corresponds to an upstream-traveling wave.

For reference, note that a simple flat-plate boundary layer subject to a horizontal traveling waves is case (1), i.e., $U_0 = 1$, $\partial U_1/\partial x = 0$, $p_{x_1} = U_1\xi(1 - \xi/c)$, and $\hat{\gamma}_{p_{x_1}} = \pi/2$.

Figure 16(b) shows U_1 amplitudes along the evaluation lines. It is harmonic over the foil (i.e., case 3), which is consistent with the spatial oscillations shown for both EFD and CFD in Fig. 7, and linearly decreasing in the wake (i.e., case 2). Figure 16(c) is a plot of $U_1\xi + U_0U_1(\partial\gamma_{U,1}/\partial x)/U_0(\partial U_1/\partial x)$ and indicates a tangent-function behavior over the foil with $B = 1.2$ and 1.8 on the pressure and suction sides, respectively. This corresponds to upstream-traveling waves, which are consistent with Fig. 12, traveling at a wave speed of 0.2 and 0.8. In the wake, similarly strong conclusions are difficult due to departure from case 2 behavior (i.e., oscillations and singularities in A at each point where $\partial U_1/\partial x$ is zero), however, in subsequent

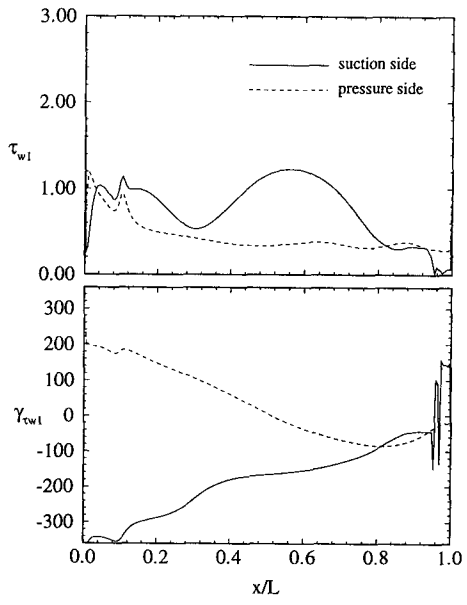

Fig. 13 Wall-shear stress distribution: first harmonic amplitude and phase

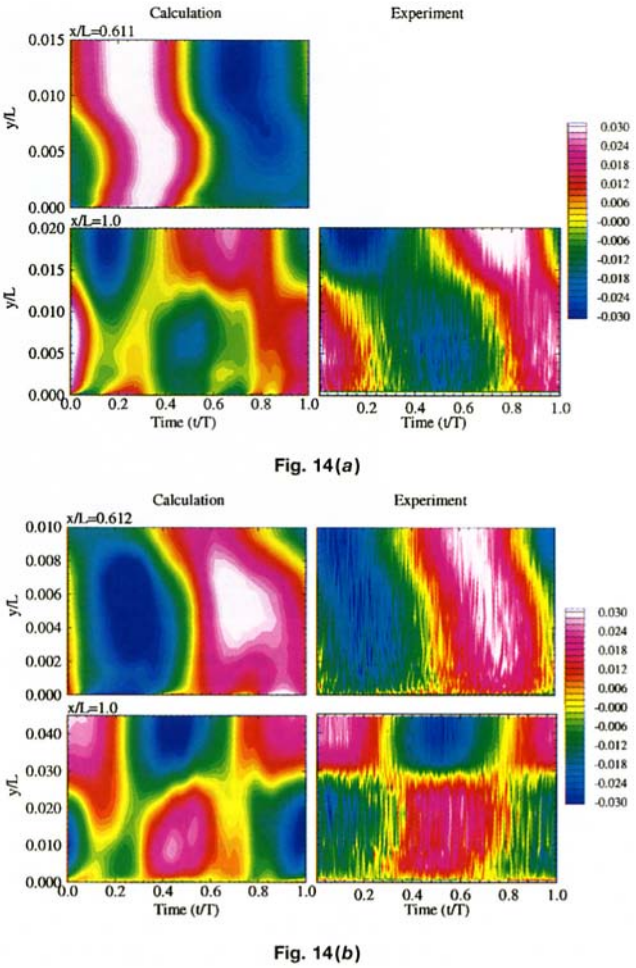

Fig. 14(a)

Fig. 14(b)

Fig. 14 Perturbation-velocity time-history contours. (a) Pressure side; (b) suction side

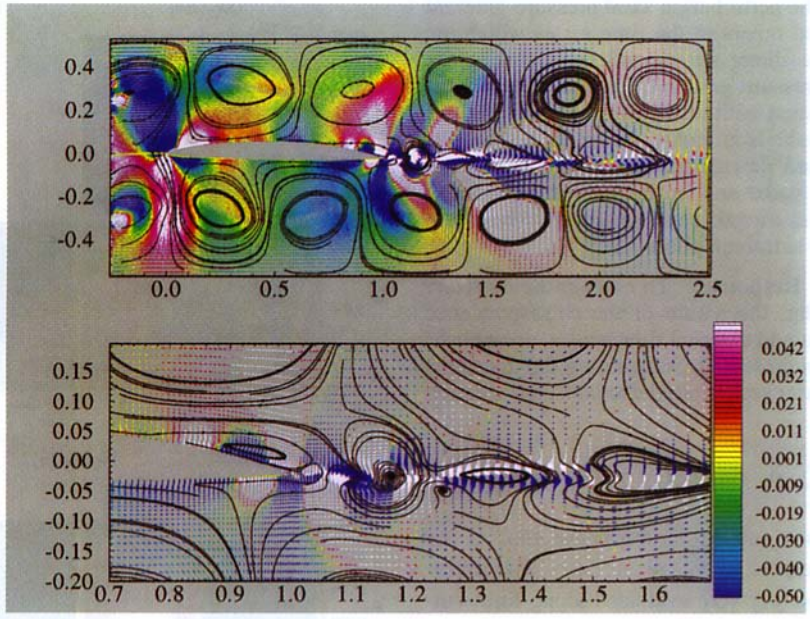

Fig. 15 Overall and detailed views of perturbation axial-pressure-gradient contours and instantaneous particle traces at $t/T = 0.8$

discussion, it is shown that the pressure-gradient exhibits downstream-traveling waves in the intermediate wake.

Figure 16(d) shows the displacement-thickness first-harmonic amplitude. Similar spatial oscillations as U_1 are observed, but with relatively larger values in the near wake. The maximum value coincides with the location where U_1 changes from oscillatory to linear behavior. This suggests viscous-inviscid interaction in the form of a pulsating near-wake displacement thickness as the source for the pressure-gradient response.

The relationship between velocity and pressure first-harmonic phases is shown in Fig. 17 for the outer ($y^+ \approx 10^4$), overlap ($y^+ \approx 200$), and sub-layer ($y^+ \approx 0.1$) regions. Also, for the outer region, the pressure-gradient phase was obtained both by differentiation of the pressure Fourier series and from the Euler-equation-derived pressure gradient Eq. (3). The pressure indicates upstream-traveling waves over the foil and a temporal, or stationary, wave in the wake downstream of the displacement-thickness peak. Also, it is nearly constant across the boundary layer. On the foil in the outer and overlap regions, the velocity shows a downstream-traveling wave, whereas in the sub-layer region it follows the pressure gradient, which is consistent with the wall-shear stress. In the wake, the velocity shows a downstream-traveling wave. The pressure gradient indicates upstream- and downstream-traveling waves over the foil and in the wake, respectively. Over the foil and in the near wake, close agreement is shown between the two pressure gradients, which validates the Euler-equation analysis.

The velocity first harmonic amplitude and phase in wall coordinates (figure not shown) shows that the largest overshoots occur near $y^+ \approx 1000$, which also corresponds to where the phase abruptly changes from the outer to inner values. The amplitudes display a double peak across the boundary layer and the phase is constant in the sublayer and the lags shown in the velocity profiles (Fig. 10) occur in the overlap region. The role of the turbulence model vs. physics for the sub-layer region is unknown, as no data is available.

Summary and Conclusions

Time-accurate RANS solutions of unsteady viscous lifting blade flows were presented and validated through comparisons with MIT FFX data. Solutions were obtained on three different domains, one of which used dynamic overset meshes, and, despite differences in boundary conditions, gave similar overall agreement. The zeroth harmonic, which was the same as steady-flow calculations, displayed typical foil response and showed that turbulence model corrections for pressure gradient were necessary for accurate solution. Despite using a quasi-steady application of the Baldwin-Lomax turbulence model, the unsteady velocity profiles showed remarkably close agreement with the data and displayed a Stokes layer response but with additional complexities such as two-layer profiles due to trailing-edge counter-rotating vortices. Unfortunately, lift and drag data were not obtained and agreement between CFD and data unsteady pressure response was poor. The CFD indicated upstream- and downstream-traveling pressure and pressure-gradient waves over the foil and in the wake, respectively. Detailed analysis showed that distortion of the external flow waves, particularly on the suction side, is significant and may be partially responsible for the complex wake structure. Also, Fourier series analysis of the velocity and axial Euler equation showed that the upstream traveling pressure waves were due to convection-induced interaction between the zeroth and first harmonics and require sinusoidal variation, as was shown by both the CFD and FFX data, of the velocity first-harmonic amplitude. The nature of the unsteady displacement thickness suggests viscous-inviscid interaction as the source of this response.

Clearly, the FFX flow is complex and requires more work to understand the variety of flow features and their implication with regard to propulsor hydrodynamics. Therefore, a parametric study is justified. In Part 2, a parametric study of frequency, waveform, and foil geometry is presented to relate the observations made in Part 1 to the classical and fundamental work on unsteady boundary layers and lifting flows, to further explicate the response observed in the FFX, and to determine implications with regard to practical applications.

Acknowledgments

This research was sponsored by ONR under Contracts N00014-92-J-1118 and N00014-91-J-1203 under the administration of Mr. Jim Fein and Dr. Ed Rood whose support is greatly appreciated. Computer funds were provided by the NASA Numerical Aerodynamic Simulation Program, the Navy

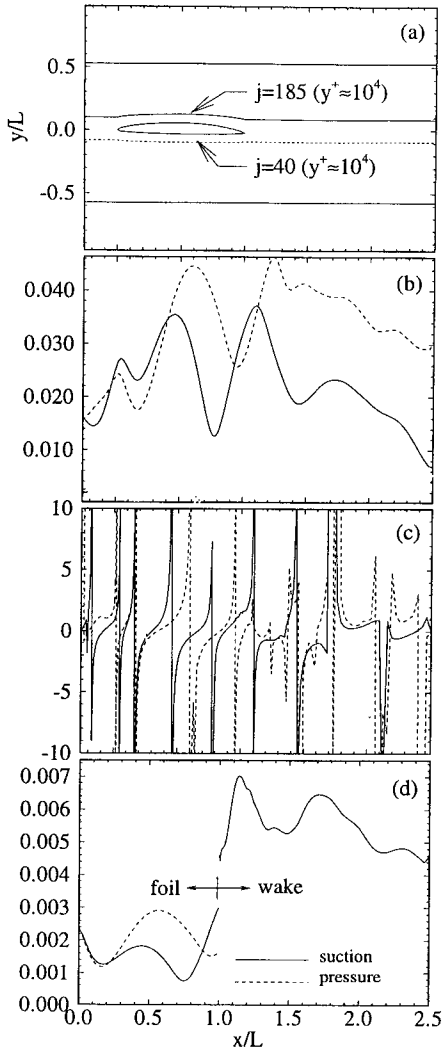

Fig. 16 Euler equation analysis. (*a*) Locations; (*b*) U_1; (*c*) $\tan(\hat{\gamma}_{p_{x_1}})$; (*d*) δ^* first-harmonic amplitude

Oceanographic Office Primary Oceanographic Prediction System, and the Army Corps of Engineers Waterways Experiment Station. The first author is grateful for the support provided by the IIHR Hunter Rouse Graduate Fellowship.

References

Attassi, H. M., Fang, J., and Patrick, S., 1993, "Direct Calculation of Sound Radiated From Bodies in Nonuniform Flows," ASME JOURNAL OF FLUIDS ENGINEERING, Vol. 115.

Basu, B. C., and Hancock, G. J., 1978, "The Unsteady Motion of a Two-Dimensional Aerofoil in Incompressible Inviscid Flow," *Journal of Fluid Mechanics,* Vol. 87.

Chen, B., Stern, F., and Kim, W. J., 1994, "Computation of Unsteady Viscous Marine Propulsor Blade and Wake Flow," *Proceedings of the 20th Symposium on Naval Hydrodynamics,* Santa Barbara, CA.

Chen, C. J., and Chen, H. C., 1984, "Finite-Analytic Numerical Method for Unsteady Two-Dimensional Navier-Stokes Equations," *Journal of Computational Physics,* Vol. 53, pp. 210–226.

Choi, J. E., Sreedhar, M., Stern, F., 1996, "Stokes Layers in Horizontal-Wave Outer Flows," ASME JOURNAL OF FLUIDS ENGINEERING, Vol. 118, No. 3.

Commerford, G. L., and Carta, F. O., 1974, "Unsteady Aerodynamic Response of a Two-Dimensional Airfoil at High Reduced Frequency," *AIAA Journal,* Vol. 12, No. 1.

Delpero, P. M., 1992, "Investigation of Flows around a Two-Dimensional Hydrofoil Subject to a High Reduced Frequency Gust Loading," M.S. thesis, Massachusetts Institute of Technology.

Dolphin, G., 1996, "Evaluation of CFD for Flat Plate, Axisymmetric, and Ship Geometries from Model to Full-Scale Reynolds Numbers," M.S. thesis, The University of Iowa.

Frietas, C. J., 1993, "Editorial," ASME JOURNAL OF FLUIDS ENGINEERING, Vol. 115, No. 3, pp. 399–400.

Goldstein, M. E., and Attasi, H. A., 1976, "A Complete Second-Order Theory for the Unsteady Flow About an Airfoil Due to a Periodic Gust," *Journal of Fluid Mechanics,* Vol. 74.

Granville, P. S., "Baldwin-Lomax Factors for Turbulent Boundary-Layers in Pressure Gradients," *AIAA Journal,* Vol. 25, No. 12, 1987, pp. 1624–1627.

Horlock, J., 1968, "Fluctuating Lift Forces on Aerofoils Moving Through Transverse and Chordwise Gusts," ASME *Journal of Basic Engineering,* pp. 494–500.

Horwich Lurie, B. 1993, "Unsteady Response of a Two-Dimensional Hydrofoil Subject to High Reduced Frequency Gust Loading," M.S. thesis, Massachusetts Institute of Technology.

Issa, R. I., 1985, "Solution of the Implicitly Discretised Fluid Flow Equations by Operator-Splitting," *Journal of Computational Physics,* Vol. 62, pp. 40–65.

Kim, H. T., and Stern, F., 1990, "Viscous Flow around a Propeller-Shaft Configuration with Infinite-Pitch Rectangular Blades," *Journal of Propulsion,* Vol. 6, No. 4, pp. 434–444.

McDonald, H., and Whitfield, D., 1996, "Self-Propelled Maneuvering Underwater Vehicles," *Proceedings of the 21st Symposium on Naval Hydrodynamics,* Trondheim, Norway.

Patel, M. H., 1975, "On Laminar Boundary Layers in Oscillatory Flow," *Proceedings of the Royal Society of London A.,* Vol. 347, pp. 99–123.

Patel, M. H., 1975, "On Turbulent Boundary Layers in Oscillatory Flow," *Proceedings of the Royal Society of London A,* Vol. 353, pp. 121–143.

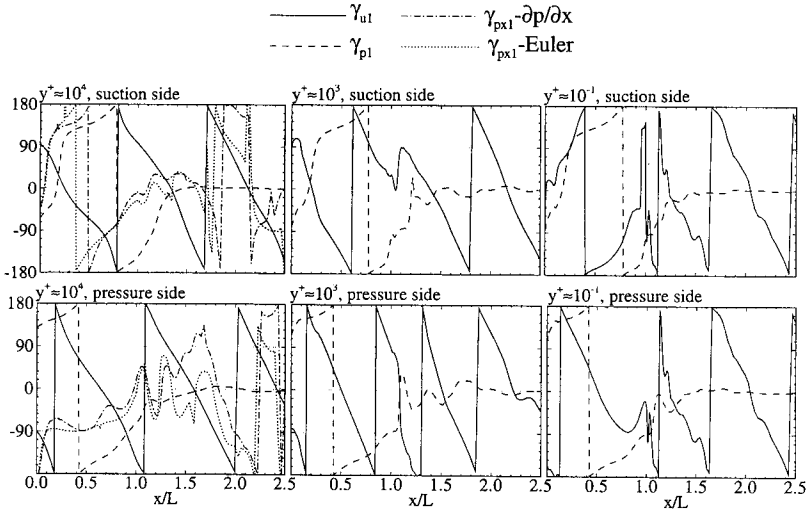

Fig. 17 Velocity, pressure, and pressure-gradient first-harmonic phase for outer, logarithmic, and sub-layer regions

Paterson, E. G., 1994, "Computation of Natural and Forced Unsteady Viscous Flow with Application to Marine Propulsors," Ph.D. thesis, The University of Iowa.

Paterson, E. G., and Stern, F., 1993, "Computation of Unsteady Viscous Flow with Application to the MIT Flapping-Foil Experiment," *Proceedings of the 6th International Conference on Numerical Ship Hydrodynamics,* Iowa City, Iowa.

Poling, D. R., and Telionis, D. P., 1986, "The Response of Airfoils to Periodic Disturbances—The Unsteady Kutta Condition," *AIAA Journal,* Vol. 24, No. 2.

Rice, J. Q., 1991, "Investigation of a Two-Dimensional Hydrofoil in Steady and Unsteady Flows," M.S. thesis, Massachusetts Institute of Technology.

Rodi, W., and Srinivas, K., 1989, "Computation of Flow and Losses in Transonic Turbine Cascades," *Z. Flugwiss. Weltraumforsch,* Vol. 13, pp. 101–119.

Sears, W. R., 1941, "Some Aspects of Non-Stationary Airfoil Theory and Its Practical Application," *Journal of Aeronautical Sciences,* Vol. 8.

Shima, N., 1993, "Prediction of Turbulent Boundary Layers with Second-Moment Closure: Part 1—Effects of Periodic Pressure Gradient, Wall Transpiration, and Free-Stream Turbulence," ASME JOURNAL OF FLUIDS ENGINEERING, Vol. 115, No. 1.

Spalart, P. R., and Baldwin, B. S., 1989, "Direct Simulation of a Turbulent Oscillating boundary Layer," *Turbulent Shear Flows 6,* J. C. Andre et al., eds., Spring-Verlag.

Stern, F., Paterson, E. G., and Tahara, Y., 1996, "CFDSHIP-IOWA: Computational Fluid Dynamics Method for Surface-Ship Boundary Layers, Wakes, and Wave Fields," IIHR Report 381, Institute of Hydraulic Research, The University of Iowa.

Stern, F., Kim, H. T., Zhang, D. H., Toda, Y., Kerwin, J., and Jessup, S., 1994a, "Computation of Viscous Flow around Propeller-Body Configurations: Series 60 C_B = .6 Ship Model," *Journal of Ship Research,* Vol. 38, No. 2, pp. 137–157.

Stern, F., Zhang, D. H., Chen, B., Kim, H. T., and S. D. Jessup, 1994b, "Computation of Viscous Flow around Propeller-Shaft Configurations," *Proceedings of the 20th Symposium on Naval Hydrodynamics,* Santa Barbara, CA.

Suhs, N. E., and Tramel, R. W., 1991, "PEGSUS 4.0 User's Manual," Arnold Engineering Development Center, AEDC-TR-91-8.

Telionis, D. P., 1981, *Unsteady Viscous Flow,* New York, Springer-Verlag.

Thompson, J. F., 1987, "A Composite Grid Generation Code for General 3-D Regions," *AIAA 25th Aerospace Sciences Meeting,* Reno, NV.

Zhang, Z., and Stern, F., 1996, "Wave-Induced Separation," ASME JOURNAL OF FLUIDS ENGINEERING, Vol. 118, No. 3.

S. Ceccio
Associate Professor,
Mechanical Engineering and
Applied Mechanics,
University of Michigan,
Ann Arbor, MI 48109-2121

S. Gowing
Mechanical Engineer.

Y. T. Shen
Naval Architect.

David Taylor Model Basin,
Naval Surface Warfare
Center-Carderock Division,
Carderock, MD 20084-5000

The Effects of Salt Water on Bubble Cavitation

Experiments were performed to examine differences in bubble cavitation inception, form, and acoustic emission in fresh and salt water. The tests were conducted on an axisymmetric headform known as the ITTC body, and acoustic emission, cavitation bubble size, and cavitation event rates were measured for a variety of cavitation numbers and dissolved air contents at a fixed dynamic head for both fresh and salt water. Differences were detected in the cavitation inception index, cavitation bubble size distribution, and the resulting overall acoustic emission. These differences may be attributed to variations in the freestream nuclei population, and it is hypothesized that the solution of salt reduced the number and size of freestream nuclei. Differences in the overall acoustic emission were attributed to variation in the bubble event rate and average maximum bubble size between the fresh and salt water cavitation.

Introduction

Model cavitation tests are typically conducted in fresh water while full scale ships operate in sea water, yet sea water is different from fresh water in ways that could affect the cavitation. In has been known for some time that sea water foams and stabilizes bubbles more readily than fresh water. Blanchard (1957) found that bubbles coalesce much more rapidly in tap water than in sea water and that bubbles produced in sea water are much smaller and persist longer than in fresh water. The experiments of Abe (1962) show that sea water foams and produces white-caps more readily than fresh water, and Miyake and Abe (1948) compared natural sea water with artificial sea water made from inorganic salts and found both to have much greater foaming ability for making white-caps than fresh water. A recent review of bubble formation and foaming processes in sea water is provided by Peltzer and Griffin (1987). This effect is illustrated in Fig. 1, which shows the difference between bubble formation in salt and fresh water through the impingement of a water jet. In the container filled with fresh water, many large bubbles appeared and disappeared in a relatively short time. In the salt water, no individual large bubbles occurred. Instead, an enormous amount of smaller bubbles were generated and persisted in the container for a very long time. Thus, noticeable differences in bubble sizes may exist between salt water and fresh water even if the bubble generation mechanism is the same, and these processes could affect the small bubbles or nuclei which play such an important role in cavitation inception. Moreover, the volumetric solubilities of oxygen and nitrogen in sea water are also lower than in fresh water (Gowing, 1987). Crump (1949) determined that air-saturated seawater cavitation in a venturi was best represented in fresh water testing by super-saturating the fresh water 30 percent. This reduced the tension of the fresh water to zero which matched the tension measured with the venturi tests of the seawater.

In the present study, we will examine the effect of dissolved salts on the inception, form, and acoustics of bubble cavitation. This research is intended to explore differences in cavitation inception and cavitation noise between fresh and sea water which could cause potential deficiencies in the scaling of model cavitation data to full scale ship propellers and appendages. Of course, sea water also contains organic compounds which can alter its rheology (Jenkinson 1993), and the presence of organic compounds may change the effective nuclei distribution of sea water. However, we presently limit our investigation to the effect of inorganic additives.

Experimental Setup

Test Model and Facility. The 12 in. water tunnel of the Naval Surface Warfare Center-Carderock Division (CDNSWC) was used for the cavitation tests. The tunnel has a semi-rectangular closed-jet test section made of Plexiglass which is 15.2 cm wide, 30.4 cm tall, and 68.6 cm long. With the test model in place, the maximum variation of dynamic pressure, $(1/2)\rho U_O^2$, was 2 percent in the horizontal plane and 1 percent in the vertical plane in the core of flow that impinges on the model. The density, ρ, is that of the water, and U_O is the average freestream velocity. The static pressure variation along the top of the test section was measured, and the pressure closest to the location of minimum pressure on the model, P_O, was used to determine the cavitation index, $\sigma = P_O - P_V/(1/2)\rho U_O^2$, where P_V is the vapor pressure of the water at the test temperature. Note that the vapor pressure of salt and fresh water are slightly different.

The model blockage of the test section area was 5.9 percent. Because the test section is twice as high as it is wide, the linear blockage of the headform was 37 percent in the horizontal plane but only 18 percent in the vertical plane. This should have caused more flow acceleration along the side of the headform than the top, causing the lowest pressure to occur on the side of the headform. But because the reference pressure could only be measured along the test section top, the cavitation inception index, σ_i, values are high compared to values measured in larger tunnels. But this should not significantly affect the differences between salt and fresh water cavitation which were the objectives of this study.

An axisymmetric headform was used as the test body for the experiments. The headform is a modified ellipsoidal shape with a diameter of 5.59 cm known as the ITTC headform (Lindgren and Johnsson, 1966). The freestream surface pressure distribution for this headform may be found in Hoyt (1966), and the cavitation pattern on the headform have been examined by Arakeri and Acosta (1973) and more recently Ceccio (1990). The headform was fabricated of Lucite and was highly polished.

Instrumentation. The ITTC headform was instrumented with three circumferential, flush-mounted electrodes which were used to detect and measure individual traveling cavitation

Contributed by the Fluids Engineering Division for publication in the JOURNAL OF FLUIDS ENGINEERING. Manuscript received by the Fluids Engineering Division September 21, 1995; revised manuscript received June 7, 1996. Associate Technical Editor: Jong H. Kim.

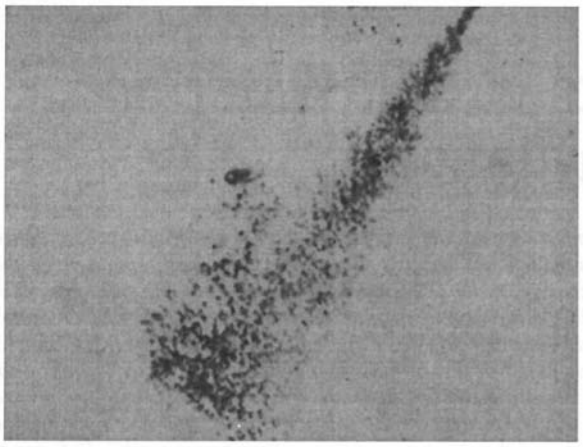

Fig. 1(*a*) Fresh water

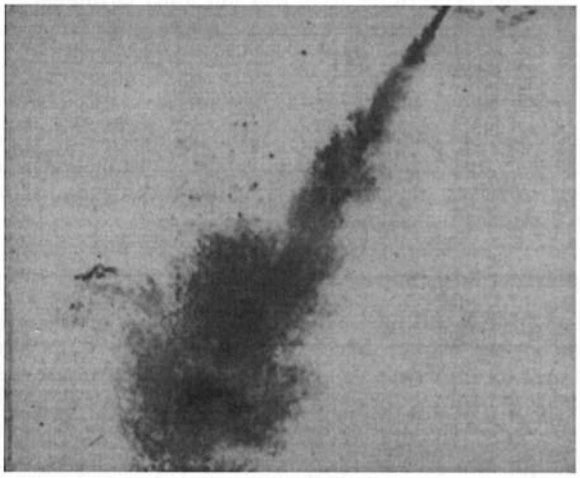

Fig. 1(*b*) Salt water

Fig. 1 Bubble formation by identical water jets in fresh and salt water. Notice that the bubbles formed in the salt water are much smaller compared to those in the fresh water.

bubbles. They were located downstream of the minimum pressure point on the headform surface (Fig. 2). The electrodes measure the local electrical impedance of the water near the surface. As a cavitation bubble passes over the electrodes, the local impedance between the electrodes changes, and the magnitude of this impedance change correlates with the size of the cavitation bubble (Ceccio, 1990). The peak of the electrode signal is proportional to the major diameter of the bubble base, and the relationship between the major diameter and the electrode signal was calibrated photographically. Furthermore, the volume of the bubble can be related to the major diameter through a relationship derived from a photographic study of many bubbles (Ceccio, 1990). The electrode geometry detects

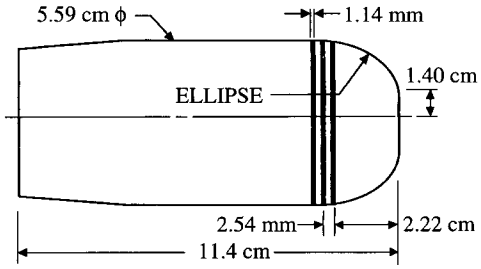

Fig. 2 Schematic diagram of the ITTC headform showing its dimensions and the location of the three circumferential electrodes

every cavitation bubble at a particular streamwise location on the headform. The position of the center electrode was chosen to be near the position of maximum bubble volume for this headform, and for moderate event rates, only one bubble would pass over the electrode at any given time.

With the circular electrode system, two types of measurements were made. First, the bubble event rate and maximum size distribution were measured. Second, the maximum size was compared with the acoustic emission of the detected bubble. The pulses from the electrodes were recorded on tape and played back through a pulse height analyzer for size spectra and number density measurements. Because the electrical impedance of fresh and salt water differ significantly, bridge zeroing and calibration were performed separately for each type of water.

An ITC model 1042 spherical piezoelectric hydrophone (resonant frequency of 80 kHz) was placed inside the headform in a cavity filled with degassed water and vented to atmospheric pressure. Because of the good acoustic impedance match between Lucite and water, the interior of the cavity allows the noise generated by the bubble cavitation to reach the hydrophone relatively undisturbed. Although this geometry placed the hydrophone in the near-field of the collapsing bubbles, this setup isolated the hydrophone from the test section, preventing extraneous effects on the data such as changes in transmission quality of the water or bubbles attaching to the hydrophone under vacuum conditions. These effects often make acoustic comparisons difficult for low pressure cavitation tests. The hydrophone signal was amplified, high-pass filtered at 1 kHz and recorded on analog tape, then played back for narrow band and $\frac{1}{3}$ octave analysis up to 200 kHz. Because no attempt was made to correct for reverberation of sound in the tunnel test section, the spectra present a relative comparison between cases. Images of the cavitation were recorded with open shutter flash photography and with SVHS video.

Fresh and Salt Water Preparation. The fresh water used in the tunnel came from the laboratory drinking water supply, and the salt water was created by adding artificial sea salt (''40 Fathoms'' from Marine Enterprises) to the fresh water after the fresh water tests were finished. The sea salt that was used is a blend of pure inorganic salts that recreates the average mixture found in the ocean. Hence it would not have trace organic

Nomenclature

A_C = percent saturation of dissolved air at atmospheric pressure, %
f = frequency, Hz
I = acoustic impulse, Pa·s
N = bubbles/second, 1/s
P_A = acoustic pressure produced by a collapsing bubble, kPa
P_O = freestream pressure, kPa
P_V = liquid vapor pressure, kPa
$\overline{P_S^2}$ = mean square acoustic pressure, $(\text{kPa})^2$
r = acoustic range, m
R_M = bubble maximum base diameter, m
$S_B(f)$ = acoustic spectrum of an individual bubble, $(\text{kPa})^2 \cdot \text{s}^2$
$S(f)$ = overall acoustic spectrum, $(\text{kPa})^2 \cdot \text{s}^2$
U_O = freestream velocity, m/s
γ = bubble total lifetime/bubble collapse time
Δf = bandwidth, Hz
ρ = liquid density, kg/m^3
σ = cavitation number
σ_i = inception cavitation number
τ = bubble collapse time, s

materials that might contribute surfactant effects as might be found in salts made from dried sea water. The salt was added to the fresh water until the specific gravity of the mixture was 1.023 times the specific gravity of the fresh water at the same temperature. This density ratio is in the middle of the range found for open ocean water, 1.020–1.027 (Smith, 1974). The dissolved air content of the salt and fresh water were measured using a Van Slyke Gas Apparatus.

Uncertainties. The dynamic head within the test section was fixed for both salt water and fresh water runs. This quantity was determined to an accuracy of ±2 percent. The test section static pressure and vapor pressure was determined to within ±2 percent. Thus, the uncertainty in σ is ±3.5 percent which is approximately ±0.025. The uncertainty in $(\sigma_i - \sigma)/\sigma_i$ becomes ±0.035.

The uncertainty in the event rate is ±5 percent, and a bias error resulted from baseline noise of the electrode system which resulted in the undercounting of bubbles with size less than 0.2 mm. The uncertainty in the maximum bubble size is ±0.2 mm. Uncertainties in the acoustic spectra are <5 percent, and the processes were taken to be stationary. Uncertainty in measurement of the acoustic impulse is ±0.005 Pa·s, and this includes the uncertainty due to the selection of integration limits.

The surface tension and viscosity of salt water will differ from that of fresh water. The dynamic viscosity of salt water may increase by as much as 10 percent (Jenkinson 1993), and this will result reduction in test Reynolds number on approximately eight percent. The tests were conducted at a sufficiently high Reynolds number (approximately 5×10^5 based on headform diameter) such that this variation will not significantly effect the results. Variation in surface tension may result in modification to the critical nuclei population, but we do not expect it to effect the dynamics of the macroscopic cavitation.

Results

Test Parameters for Comparison. To compare cavitation in fresh and salt water at similar conditions, the tests were conducted with the same test section dynamic pressure (31.2 kPa) as measured by the pressure drop through the upstream tunnel contraction. This required a slight adjustment of the tunnel velocity to account for the difference in densities of fresh and salt water.

The tests were repeated at two air contents as measured by the saturation level of each mixture relative to atmospheric pressure. Because the ability of salt water to dissolve air is less than that of fresh water by roughly 27 percent, the actual amounts of dissolved air in the salt water tests were less than that of the fresh water tests. But by keeping the saturation levels the same, the mechanisms that create the bubble spectra in the tunnel would have the same potential for out-gassing or absorption, and this would, hopefully, create similar bubble spectra for the two types of water. The air contents, A_C, are presented as percent saturation at atmospheric pressure. The salt water sigma values were calculated with the vapor pressure of seawater which is depressed about two percent from fresh water pressures.

The frequency of cavitation events was monitored by watching the electrode pulse data on an oscilloscope screen and data were collected at 4–6 frequencies of event rates. Post analysis then showed the development of the cavitation on the headform. The size of the cavitation bubbles reported here is the maximum bubble base diameter on the headform surface. The uncertainty associated with the measurement of the bubble base diameter is estimated to be 15 percent based on the uncertainty associated with the calibration. The event rate measurement has a maximum uncertainty of approximately 10 percent due to the intermittent occurrence of patch cavitation and the threshold level of signal noise.

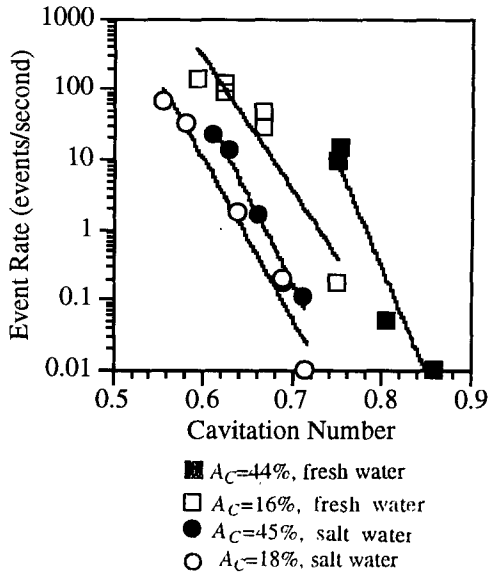

Fig. 3 Bubble cavitation event rates dependence on cavitation number. Only bubbles with base diameter greater than 1.2 mm are counted. (Uncertainty in Cavitation Number is ±0.025 and uncertainty in event rate is ±5 percent).

Bubble Cavitation Inception. Cavitation inception for these tests was defined as the event rate of 1 bubble per second for bubble sizes greater than 1 mm. This condition is representative of that which an observer might "call" inception. Because the test conditions that were recorded did not always include a condition exactly at inception as defined, the bubble event rates were plotted as a function of the cavitation index, and the value of σ at inception was determined by interpolation of those data at the 1 event per second value. These plots are shown in Fig. 3. For both values of air content, inception in the salt water occurred at a lower value of sigma than in the fresh water. The ratio of the salt to fresh water cavitation inception index was about 0.85–0.89 for both air contents. Previous bubble cavitation experiments on headforms in this same tunnel showed variations in σ, similar to those in Fig. 3, to be caused by nuclei density variations in the order of 20 to 25 (Ling et al., 1982). This difference in nuclei populations could have occurred in these tests given the difference in the waters and the test section pressures at inception, and more discussion about this possibility will be presented below. The increase in the bubble event rate with decreasing cavitation number was approximately logarithmic for both the salt and fresh water tests.

Developed Cavitation. The size distributions of the bubble cavities were different between fresh and salt water in the low air content case. Figure 4 shows the relative size distributions at different developed cavitation conditions as noted by the parameter $(\sigma_i - \sigma)/\sigma_i$. For similar values of this parameter, the salt water cavities were smaller than the fresh water ones. Because the sizes of the salt cavities were mostly less than 1.3 mm, the definition used for visual cavitation inception (size 1 mm) biased the inception values to a lower number since many small bubbles were not counted in the salt water case. If the data in Fig. 3 are replotted to include all size bubbles, then the inception values between fresh and salt water are closer together as shown in Fig. 5. Although the small salt water bubbles would not be detected visually for inception, they may contribute significantly to the acoustic data. For the high air content case, the relative size distributions of the fresh and salt water cavities were more similar, as shown in Fig. 6 with most of the cavities being less than 1.2 to 1.3 mm in size. At very low pressures,

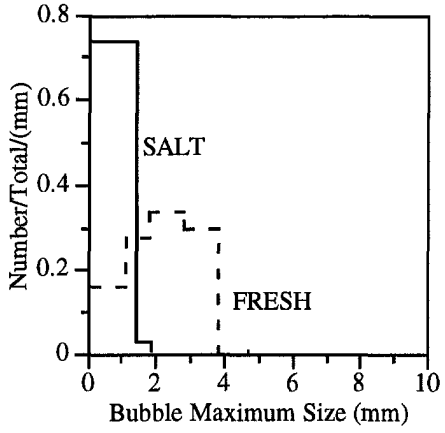

	$(\sigma_i - \sigma)/\sigma_i$	Events/second
FRESH	-0.04	0.21
SALT	+0.07	4.4

Fig. 4(*a*)

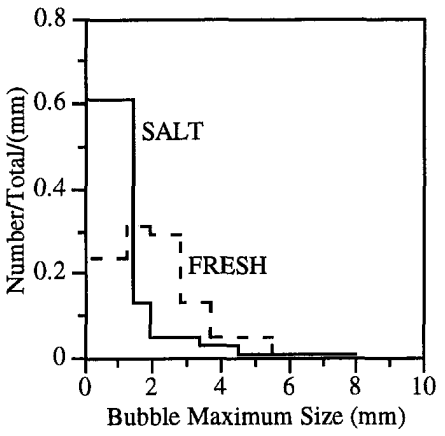

	$(\sigma_i - \sigma)/\sigma_i$	Events/second
FRESH	+0.08	37
SALT	+0.10	160

Fig. 4(*b*)

partial attached cavities appeared for all test conditions. The overall appearance of bubble cavitation is shown in Fig. 7.

Acoustic Results-Emission From Individual Bubbles. The acoustic emission from individual cavitation bubbles were recorded simultaneously with the maximum bubble base diameter. The acoustic impulse, I, defined as

$$I = \int_{t_1}^{t_2} P_A \, dt$$

was determined for each individual acoustic emission. P_A is the acoustic pressure produced by the bubble, and the time interval of the integral is chosen to capture the initial pressure pulse produced by the bubble (Ceccio and Brennen, 1991). Figure 8 shows a plot of acoustic impulse versus maximum bubble size for individual cavitation bubbles produced in both salt and fresh water at low air content, and the error associated with the calculation of the impulse is approximately +/− 10 percent. For bubbles smaller than approximately 5 mm maximum base diameter, the acoustic impulses produced by both fresh and salt water bubbles are similar, with the emission from the salt water bubbles being only slightly higher. For larger bubbles the acoustic emissions of the bubbles are widely scattered, and are often

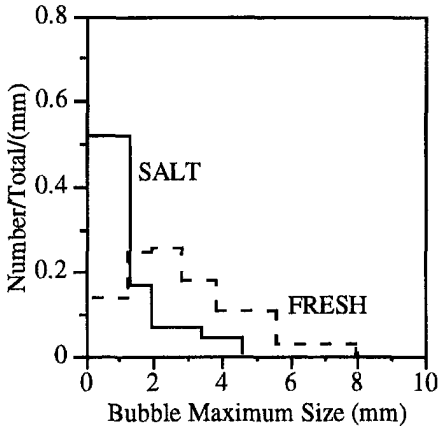

	$(\sigma_i - \sigma)/\sigma_i$	Events/second
FRESH	+0.14	110
SALT	+0.14	190

Fig. 4(*c*)

Fig. 4 Bubble cavity size distributions in low air content tests at three equivalent cavitation conditions $(\sigma_i - \sigma)/\sigma_i$. The size plotted is the maximum base diameter. Dashed lines are for the fresh water data and solid lines are for the saltwater data. (Uncertainty in $(\sigma_i - \sigma)/\sigma_i$ is ±0.035, uncertainty in maximum bubble size is ±0.2 mm, and uncertainty in the event rate is ±5 percent.)

muted when compared with the smaller bubbles. These data are consistent with those of Ceccio and Brennen (1991), who determined that larger bubbles on the ITTC headform often collapsed without producing an appreciable acoustic impulse due to their interaction with the viscous flow near the headform.

Acoustic Results-Spectra. The overall acoustic emission from bubble cavitation on the headforms were examined. Typical high pass filtered narrow band and $\frac{1}{3}$ octave band data are shown in Figs. 9 and 10, respectively. No distinct spectral characteristics appear, but overall sound pressure levels do increase with higher cavitation event rates and decreasing values of σ, and the spectra shapes remain similar. Data are presented here only in the 10 kHz–100 kHz frequency range, but analysis of the tapes showed increased noise levels during cavitation up to

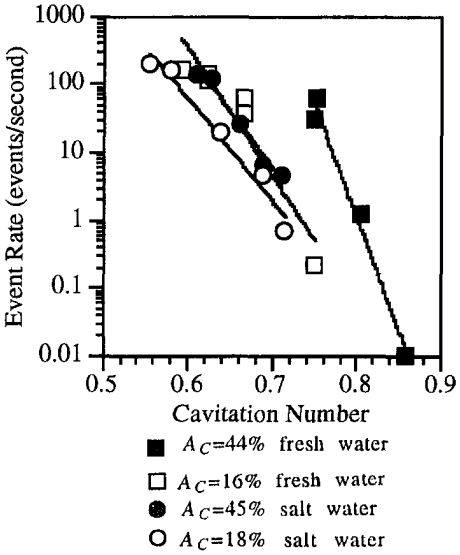

Fig. 5 Bubble cavitation event rates dependence on cavitation number. All detected bubbles are counted. (Uncertainty in the Cavitation Number is ±0.025, and uncertainty in the event rate is ±5 percent.)

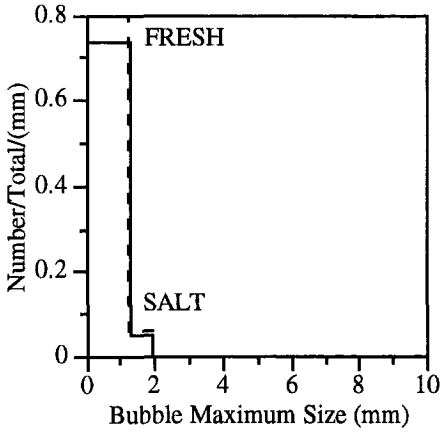

	$(\sigma_i - \sigma) / \sigma_i$	Events/second
FRESH	+0.04	1.2
SALT	+0.03	6.3

Fig. 6(*a*)

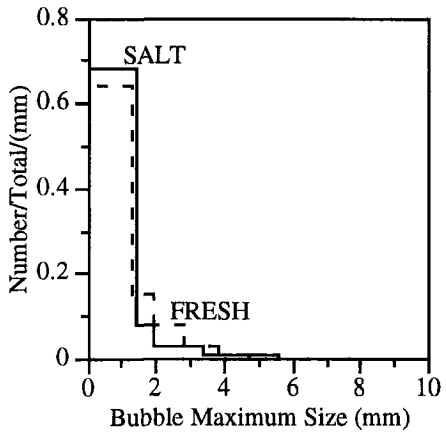

	$(\sigma_i - \sigma) / \sigma_i$	Events/second
FRESH	+0.03	61
SALT	+0.05	120

Fig. 6(*b*)

Fig. 6 Bubble cavity size distributions for cavitation in high air content tests or two equivalent cavitation conditions ($(\sigma_i - \sigma)/\sigma_i$). The size plotted is the maximum base diameter. (Uncertainty in $(\sigma_i - \sigma)/\sigma_i$ is ±0.035, uncertainty in maximum bubble size is ±0.2 mm, and uncertainty in the event rate is ±5 percent.)

about 150 kHz. The appearance of attached cavities caused increased noise levels from 100 Hz–1 kHz. The increased noise levels of the attached cavities were present despite the 1 kHz high-pass filtering, and these data were not the result of aliasing in the instruments.

Figure 11 shows the sound pressure level in the $\frac{1}{3}$ octave bands centered on 10 kHz, 25 kHz, and 50 kHz plotted against cavitation event rates for the fresh and salt water data. The tests with the lowest event rates are not shown because their sound pressures did not increase above background levels. The sound pressure levels increase logarithmically with event rate, and the sound pressure levels increase at a greater rate than the square root of the event rate which would be predicted for an assimilation of identical random events. These trends are highlighted with the solid lines in Fig. 11. Notice that the salt water sound pressure levels are generally higher than that of the fresh water for equivalent event rates. Moreover, the sound pressure levels of the salt water increase at a slower rate with increases in event rate, but the increases are still logarithmic. The levels are 10 kHz and 25 kHz are higher than at the 50 kHz frequency. At high event rates, the differences between salt and fresh water disappear, and this is where patch cavitation begins to appear.

Discussion

Two significant differences were found between the cavitating flows of fresh and salt water. First, for similar conditions, the event rate of traveling bubble cavitation was lower in salt than in fresh water. Moreover, the average maximum size of the cavitation bubbles was smaller in salt water compared to fresh water. Second, the overall acoustic emission of the cavitation in salt water was stronger than that in fresh water for equivalent conditions. As the event rate increased, the overall acoustic emission increased for both cases, with that of the fresh water increasing more rapidly. For very high event rates at lower cavitation numbers, the emission from bubble cavitation in salt and fresh water converged.

The first observation may be explained by differences in the stabilized freestream nuclei distribution in salt and fresh water. Lower inception pressures and event rates for the salt water case suggests that there are fewer active nuclei (Ling et al., 1982). Also, the preponderance of smaller traveling bubbles in the salt water cases suggest that nuclei which are present in the salt water have a smaller effective critical radius. The constant asymptotic growth rate of cavitating nuclei implies that the maximum size of traveling bubbles will be found in a narrow range, and this is observed here. Nuclei sizes typically range over two orders of magnitude, while maximum bubble sizes range over less than one order of magnitude. However, smaller nuclei will lead to smaller traveling bubbles, since there may be a delay in their inception, and they will only grow under the influence of the strongest tensions found in narrow regions close to the point of minimum pressure (Ceccio and Brennen, 1991; Meyer, Billet, and Holl, 1992; Liu and Brennen, 1995). It can be therefore be inferred that the nuclei population in the salt water was suppressed, with relatively fewer and smaller nuclei compared to that of the fresh water. One might think that nuclei would be more numerous in salt versus fresh water for the same relative saturation level, but perhaps the greater overall quantity of air in the fresh water results in a greater nuclei density.

The observation about the overall acoustic emission of the salt water cavitation seems paradoxical. With lower event rates and smaller bubbles, it is expected that the emission from the salt water cavitation would be proportionally less than that of the fresh water. However, the reverse was observed. Even after the data was normalized by the bubble event rate, the salt water cavitation is observed to produce more noise that fresh water cavitation at comparable cavitation numbers. This difference only disappears at very high bubble event rates. Moreover, it was found that the emission from individual bubbles of similar maximum size was not appreciably different when formed in salt and fresh water.

These apparently contradictory results can be explained by recognizing that the acoustic emission from a traveling bubble is not linearly proportional to its maximum size. We can explore this idea by examining the noise scaling rules of Fitzpatrick and Strasberg (1956) who showed that the noise spectra produced by bubble cavitation can be scaled by basic bubble parameters such as the bubble maximum volume and the collapse time of the bubble. Blake et al. (1977) examined the scaling of bubble cavitation noise showing that acoustic spectra of sound produced by the growth and collapse of an individual cavitation bubble, $S_B(f)$, can be scaled with the bubble maximum size, R_M, the bubble collapse time, τ, the freestream static pressure, P_O, and the distance between the bubble and the hydrophone, r:

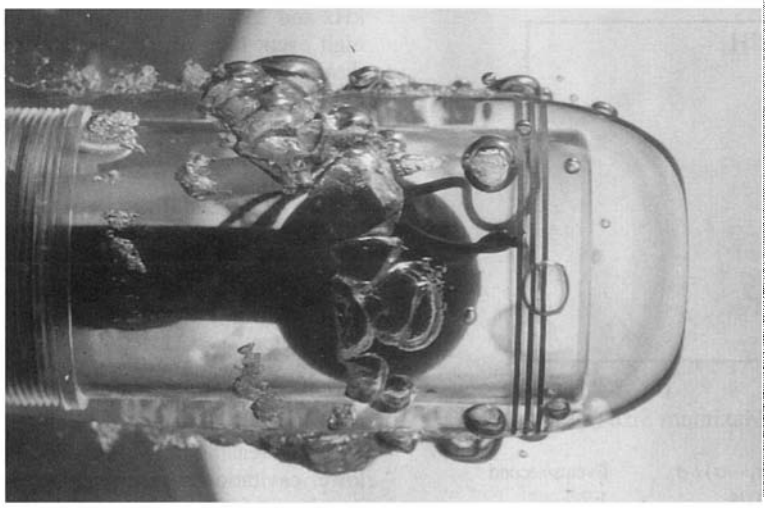

Fig. 7(*a*)

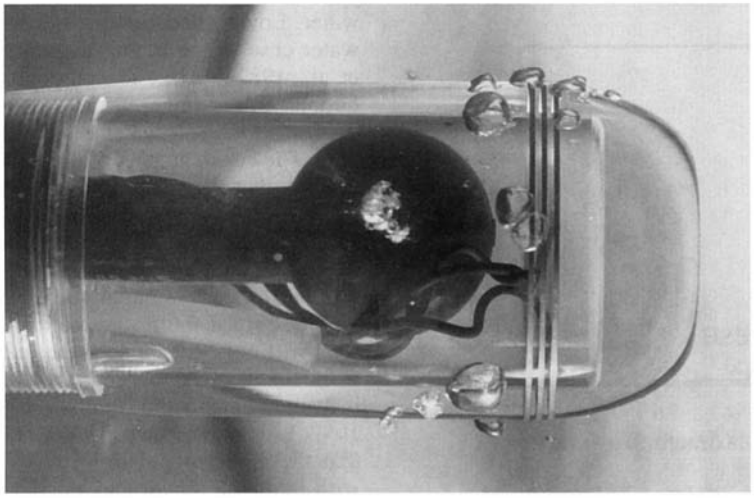

Fig. 7(*b*)

Fig. 7 Comparison of bubble cavitation appearance for both the fresh and salt water cases with $\sigma = 0.63$ for the fresh water case $((\sigma_i - \sigma)/\sigma_i = 0.14)$, and $\sigma = 0.58$ for the salt water case $((\sigma_i - \sigma)/\sigma_i = 0.10)$. Both are at the lower air content. (Uncertainty in the Cavitation Number is ±0.025 and in $(\sigma_i - \sigma)/\sigma_i$ is ±0.035.)

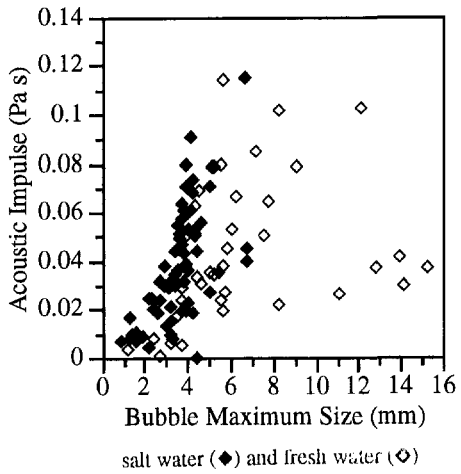

Fig. 8 Acoustic impulse from individual traveling bubbles plotted against the bubble maximum base diameter for salt water and fresh water. Note that the larger bubbles often do not produce a significant acoustic emission. (Uncertainty in the Acoustic Impulse is ±0.005 Pa s, and uncertainty in maximum bubble size is ±0.2 mm.)

$$\frac{S_B(f)r^2}{\rho P_O R_M^4} = S_B(f\tau)$$

The value of r will vary somewhat depending on the bubble size, and an average value was used in the scaling. The bubble collapse time is proportional to its maximum size and the freestream condition, following Rayleigh's formula for the collapse of an unbounded spherical bubble:

$$\tau = \epsilon \frac{R_M}{U_O}\left(\frac{2}{\sigma}\right)^{1/2}$$

where ϵ is a scaling factor which is 0.915 for the case of an unbounded spherical bubble. Blake et al. (1977) found that ϵ was approximately 15 percent less for traveling cavitation. Lastly, the spectrum from an individual bubble can be related to the sound pressure level produced by the bubble:

$$\int_0^\infty S_B(f)df = \int_0^\infty P_A^2(t)dt = \gamma\tau\overline{P_A^2}$$

where $\gamma\tau$ is the lifetime of the bubble. A measured narrow

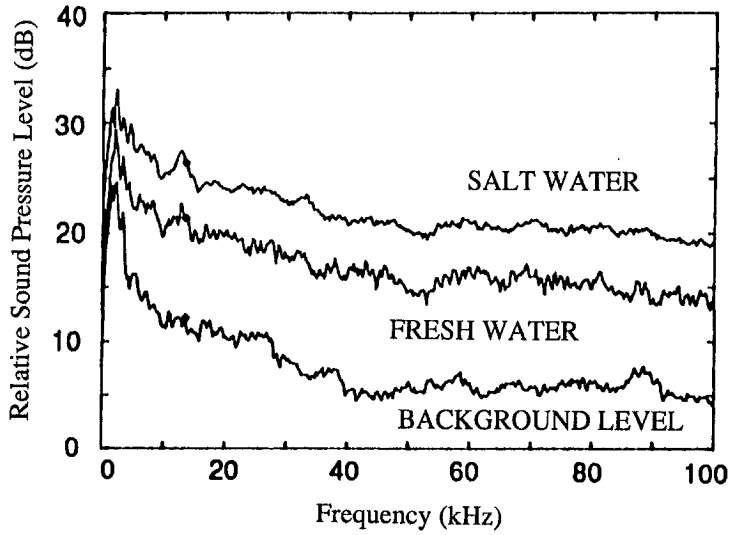

Fig. 9 Typical narrow band spectra for bubble cavitation on the ITTC headform. Note that the signal was conditioned with a 1kHz high pass filter. $(\sigma_i - \sigma)/\sigma_i = +0.14 \pm 0.035$ for both data sets. (Uncertainty in SPL is >5 percent.)

band sound spectrum $S(f)$ in the frequency interval Δf can then be interpreted as

$$S(f) = \gamma\tau\overline{P_S^2}(f, \Delta f)/\Delta f$$

where $\overline{P_S^2}$ is the measured mean square pressure. Thus, the normalized narrow band spectrum becomes

$$\frac{r^2\gamma\tau}{\rho P_O R_M^4}\frac{\overline{P_S^2}(f, \Delta f)}{\Delta f} = S(f\tau)$$

The sound contributed by many cavitating bubbles is expected to be linearly additive until their density on the headform is sufficiently large to produce interference between the individual cavitating bubbles (Arakeri and Shanmuganathan, 1985). If the bubble event rate is N events per second, the overall measured spectrum, $S(f\tau)$, is given by

$$S(f\tau) = N\gamma\tau S_B(f\tau)$$

Therefore, the normalized bubble spectrum is given by

$$\frac{r^2}{N\rho P_O R_M^4}\frac{\overline{P_S^2}(f, \Delta f)}{\Delta f} = S_B(f\tau)$$

In summary, this scaling of the sound pressure level should collapse the data onto a single curve if the spectrum of sound emitted by a collapsing bubble scales proportionally with the bubble maximum volume and collapse time, if the bubbles do not interfere with one another, and if their emitted noise is linearly additive. The $\frac{1}{3}$ octave sound pressure levels presented in Figure 11 can then be normalized with the scaling

$$\frac{r^2}{N\rho P_O R_M^4}\frac{\overline{P_S^2}(f, \Delta f)}{\Delta f} = \left(\frac{\overline{P_S^2}(f, \Delta f)}{\Delta f}\right)_{\text{NORM}}$$

The event rate can be normalized with the overall bubble lifetime.

Figure 12 shows the normalized sound pressure levels plotted against normalized event rate for both the high and low air content $\frac{1}{3}$ octave sound pressure level data. Employed in the normalization are the measured maximum bubble size and event rates, and the mean bubble lifetime is calculated using the theoretical collapse time based on the bubble maximum size and a

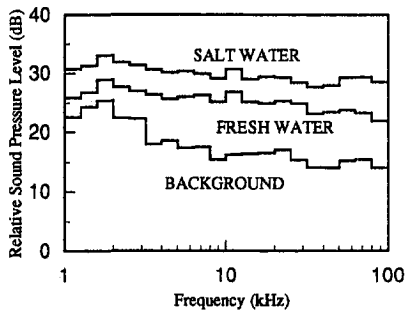

Fig. 10 Typical $\frac{1}{3}$ octave spectra for bubble cavitation on the ITTC headform. Note that the signal was conditioned with a 1 kHz high pass filter. $(\sigma_i - \sigma)/\sigma_i = +0.14 \pm 0.035$ for both data sets. (Uncertainty in SPL is <5 percent.)

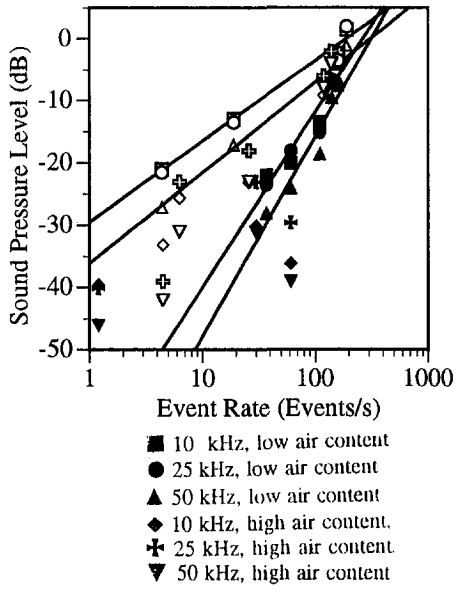

Fig. 11 $\frac{1}{3}$ octave sound pressure level plotted against total event rate for fresh and salt water bubble cavitation. Open symbols denote salt water, and filled symbols denote fresh water. (Uncertainty in the event rate is ±5 percent, and the uncertainty in SPL is <5 percent). The SPL scale differs from that in Figure 9 and 10. The solid lines present the average envelope in SPL defined by the 10 kHz and the 50 Khz SPL data for fresh and salt water.

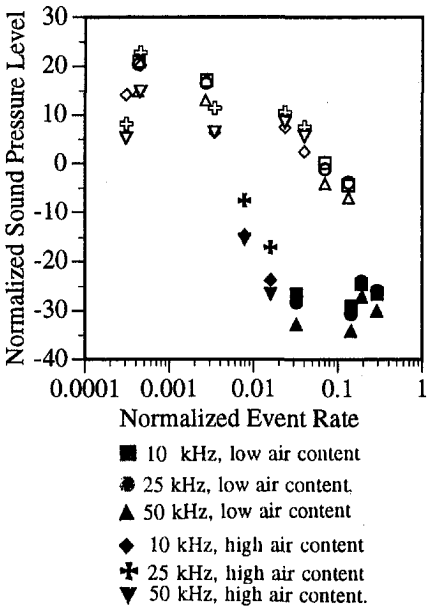

Fig. 12 Normalized sound pressure level plotted against normalized event rate for salt and fresh water bubble cavitation. Open symbols denote salt water, and filled symbols denote fresh water. (Uncertainty in the event rate is ±5 percent, and the uncertainty in SPL is <5 percent.)

scaling value of $\gamma \approx 3$ derived from examination of spherical bubble dynamics (Blake et al., 1977). The event rate is normalized with the mean bubble lifetime. The sound pressure levels of the salt and fresh water cases do not coincide, and the normalized sound pressure level of the salt water bubble cavitation is consistently higher than that of the fresh water cavitation. As the normalized event rate increases for the salt water, the normalized sound pressure level decreases, while the opposite is true for the fresh water case.

The normalization does not collapse the data. Indeed, one of the key assumptions of the scaling may not hold true: the emitted sound from the bubbles is not proportional to the bubble maximum size since larger cavitation bubbles do not necessarily produce a stronger acoustic emission upon collapse. As indicated in Fig. 8, the acoustic impulse generated by larger bubbles in the fresh water is often much lower that than produced by smaller bubbles, and this is consistent with the observations of Ceccio and Brennen (1991) who found that larger bubbles may be sheared by the surrounding viscous flow to such an extent that they may collapse without the strong volume accelerations necessary for significant acoustic emission. The average maximum size of the bubbles occurring in the fresh water were generally 2 to 3 times the size of those in the salt water, and the larger fresh water bubbles do not produce as strong an acoustic emission, on average, compared with the smaller salt water bubbles. The trends in Fig. 12 also support this hypothesis. As the event rate increases for the salt water cavitation, the normalized sound pressure level goes down, and at these higher event rates the average bubble size has increased. Moreover, as the event rate is reduced for the fresh water case, the normalized sound pressure level increases, and for these lower event rates the bubble size has decreased. It is important to note that the sound pressure levels presented are for frequencies above 1 kHz, and these trends may not be present in the low frequency noise.

Conclusions

For nominally identical flow conditions, there can be significant differences between bubble cavitation in fresh and salt water. The maximum size and event rate of bubble cavitation in salt water was reduced compared to that of fresh water. Conversely, the acoustic emission of the bubble cavitation in salt water was larger than the sound produced by fresh water bubble cavitation. These observations may be explained by the hypothesis that the nuclei distribution in the salt water is suppressed compared to those in fresh water for the same relative saturation of air. With fewer and smaller free stream nuclei in the salt water, both the size and number of macroscopic cavitation bubbles are reduced. The acoustic results can be explained by the fact that larger cavitation bubbles do not necessarily produce a larger acoustic emission. Indeed, the smaller cavitation bubbles in the salt water flow produced, on average, more sound than the larger bubbles which occurred in the fresh water flow. This result is consistent with the examination of the sound emitted by individual bubbles which indicated that larger bubbles produce, on average, a smaller acoustic emission compared to smaller bubbles. Because bubbles of similar size produced similar acoustic emission whether in salt water or fresh water, the chemical differences of the waters do not appear to directly influence the acoustics. Rather, the differences in the overall acoustic emission between salt and fresh water bubble cavitation is largely a function of the event rate and average bubble size, and these last two factors are principally determined by the freestream nuclei distribution.

While the addition of inorganic salts is shown to influence the process of bubble cavitation, additional organic materials in seawater may also effect the inception and form of cavitation via free stream nuclei effects. The changes in seawater rheology may potentially influence both the inception and development of limited cavitation. More study is necessary to determine what influence organic materials in seawater may have on cavitation.

Acknowledgments

This project was supported by the David Taylor Model Basin Independent Research Program. Prof. Ceccio received support under the Navy/ASEE Summer Faculty Fellowship Program and ONR contract N-00014-93-1-0029, Dr. E. P. Rood, monitor. The editorial comments of Dr. Murray Strasberg are also appreciated.

References

Abe, T., 1962, "On the Stable Formation of Sea Water in Seas," *Journal of the Oceanographical Society of Japan,* 20th Anniversary Volume, pp. 242–250.

Arakeri, V. J., and Acosta, A. J., 1973, "Viscous Effects in the Inception of Cavitation on Axisymmetric Bodies," ASME JOURNAL OF FLUIDS ENGINEERING, Vol. 95, pp. 519–527.

Arakeri, V. J., and Shanmuganathan, V., 1985, "On the Evidence for the Effect of Bubble Interference on Cavitation Noise," *Journal of Fluid Mechanics,* Vol. 159, pp. 131–150.

Blake, W. K., Wolpert, M. J., and Geib, F. E., 1977, "Cavitation Noise and Inception as Influenced by the Boundary Layer Development on a Hydrofoil," *Journal of Fluid Mechanics,* Vol. 80, pp. 617–640.

Blanchard, D. C., and Woodcock, A. H., 1957, "Bubble Formation and Modification in the Sea and its Meteorological Significance," *Tellus,* Vol. 9, No. 2, pp. 145–158.

Ceccio, S. L., 1990, "Observations of the Dynamics and Acoustics of Traveling Bubble Cavitation," Report E249.11, California Institute of Technology, Division of Engineering and Applied Science.

Ceccio, S. L., and Brennen, C. E., 1991, "Observations of the dynamics and Acoustics of Traveling Bubble Cavitation," *Journal of Fluid Mechanics,* Vol. 233, pp. 633–660.

Crump, S. F., 1949, "Determination of Critical Pressures for the Inception of Cavitation in Fresh and Sea Water as Influenced by Air Content of Water," DTMB Report. No. 575, NS 713–065.

Fitzpatrick, H. M., and Strasberg, M., 1956, "Hydrodynamic Sources of Sound," *Proc. 1st Symposium on Naval Hydrodynamics,* Washington, D. C., pp. 241–280.

Gowing, S., 1987, "Dissolving of Bubbles in a Liquid," DTNSRDC Report 87/006.

Hoyt, J., 1966, "Wall Effect on ITTC Standard Head Shape Pressure Distribution," *Proc. 11th International Towing Tank Conference,* Tokyo, 1966.

Jenkinson, I. R., 1993, "Bulk-Phase Viscoelastic Properties of Seawater," *Oceanologica Acta,* Vol. 16, pp. 317–334.

Lindgren, H., and Johnsson, C., 1966, "Cavitation Inception on Headforms: ITTC Comparative Experiments," *Proc. 11th International Towing Tank Conference,* Tokyo.

Ling, S. C., Gowing, S., and Shen, Y. T., 1982, "The Role of Microbubbles on Cavitation Inception on Headforms," *Proc. 14th Naval Hydrodynamic Symposium,* Ann Arbor, Michigan.

Liu, Z., and Brennen, C. E., 1995, "Models of Cavitation Event Rates," *Proc. International Symp. on Cavitation,* Deauville, France, pp. 321–328.

Meyer, R. S., Billet, M. L., and Holl, J. W., 1992, "Freestream Nuclei and Traveling Bubble Cavitation," ASME JOURNAL OF FLUIDS ENGINEERING, Vol. 114, pp. 672–679.

Miyake, Y., and Abe, T., 1948, "A Study on the Foaming of Sea Water. Part 1," *Journal of Marine Research,* Vol 7, 1948, pp. 67–73.

Peltzer, R. D., and Griffin, O. M., 1987, "Stability and Decay Properties of Foam in Seawater," NRL Memorandum Report 5949.

Smith, F. G., 1974, *Handbook of Marine Science,* Vol. 1, CRC Press.

A Capacitance Sensor for Two-Phase Liquid Film Thickness Measurements in a Square Duct

G. E. Thorncroft
Graduate Research Assistant.

J. F. Klausner
Associate Professor.

Department of Mechanical Engineering,
University of Florida,
Gainesville, FL

The use of capacitance sensors for measuring liquid film thickness or phase concentration in two-phase flow has gained popularity in recent years. In designing such sensors, there are many issues which must be considered in order to optimize performance: desired temporal and spatial resolution, two-phase flow regime, permittivity of the phases, duct geometry, electrical shielding, and temperature variation in the flow field. These issues are discussed, and the design of a 12.7 mm square cross section capacitance sensor which measures liquid film thickness in either stratified or annular two-phase flow is presented. Using a composite material analysis and an effective permittivity ratio, predictive relations for capacitance as a function of liquid film thickness have been derived for stratified and annular film patterns. The analysis eliminates the need for calibrating the sensor for stratified and annular flow regimes. Optical measurements of liquid film thickness using a high resolution CCD camera are compared against those using the capacitance sensor in conjunction with the predictive relations. The sensor was tested on a bench top for a stratified film pattern with no flow and two different electrode configurations (upward and side configurations) using FC-87, a low-permittivity (ϵ_r = 1.72) dielectric fluid. The standard deviations between the film thicknesses measured optically and those predicted using the capacitance sensor and analysis are 0.014 and 0.019 mm for the respective upward and side electrode configurations. The sensor was also implemented in a vertical flow boiling facility, which uses FC-72 (ϵ_r = 1.75) as the working fluid. Time-averaged film thicknesses measured using the capacitance sensor are compared against ensemble-averaged measurements using the CCD camera for annular vertical upflow and downflow. The upflow and downflow standard deviations are 0.17 and 0.093 mm, respectively. As expected, the agreement for vertical flow is not as good as that for the horizontal no-flow case, because large fluctuations in film thickness are characteristic of annular two-phase flow, and the uncertainty of the photographic measurement is increased.

Introduction

Capacitance sensors have recently gained popularity for measuring vapor volume fraction in two-phase flows. Their popularity is primarily due to the fact that they are noninvasive and are simple to operate. However, the design of capacitance sensors can vary greatly depending on the desired temporal and spatial resolution, signal-to-noise ratio, two-phase flow pattern, and temperature variations, among others. For this reason, prior investigators have put forth great effort in (i) understanding those factors which dictate the performance of capacitance sensors, and (ii) improving the performance of those sensors. Most prior work has been carried out for two-phase flows through circular tubes, but many of the results can be generalized to other geometries. The focus of previous work may be categorized as described below.

1 Sensor Geometry. The sensitivity of the capacitance sensor to changes in liquid film thickness or vapor volume fraction strongly depends on the geometry of the sensing electrodes, and various investigators have examined the performance of different electrode configurations. Irons and Chang (1983) and Chun and Sung (1986) tested strip and ring type electrodes for gas/powder and liquid/vapor flows, respectively. Gregory and Mattar (1973) and Abouelwafa and Kendall (1980) tested many different electrode configurations for liquid/vapor flows, including helical, strip, parallel plate, and concave plate. Ozgu and Chen (1973) considered ring type and parallel-strip type electrodes and discussed the required spacing between electrodes to achieve the optimum sensitivity. These studies revealed, among other things, that the calibration of a capacitance sensor is flow regime dependant. Therefore the anticipated flow regime should be considered in choosing the electrode configuration.

2 Analytical/Numerical Modeling. Analytical attempts have been made to estimate the sensor output for various flows. Abouelwafa and Kendall (1979a, 1979b) estimated the output of helical and concave-plate type sensors for homogeneous, slug, annular, and stratified flows by assuming a uniform charge distribution on diametrically opposed electrodes as well as uniform flux lines between them. Chun and Sung (1986) used a similar approach for ring type electrodes. Geraets and Borst (1988) solved for the three-dimensional potential field between helical electrodes and developed a closed form expression for the capacitance associated with annular and dispersed flows. Gupta et al. (1994) used a finite-difference technique to solve for the potential field between concave plates with stratified flow. Although they used this solution to compute the impedance, it may also be used to compute the capacitance.

3 Spatial Sensitivity. Xie et al. (1990) conducted a detailed investigation on the effect of electrode size, wall thickness, and the proximity of electrical shielding on the spatial sensitivity of a concave plate capacitance sensor. Based on their

Contributed by the Fluids Engineering Division for publication in the JOURNAL OF FLUIDS ENGINEERING. Manuscript received by the Fluids Engineering Division October 9, 1995; revised manuscript received July 22, 1996. Associate Technical Editor: O. C. Jones.

analysis, they attempted to optimize the electrode design so that the sensor output is approximately linear and independent of flow regime. However, due to nonuniformities in the electric field with changes in flow regime, such a sensor is not attainable. Klug and Mayinger (1994) used an eight-electrode sensor to measure impedance in horizontal gas/liquid flows. Capacitance was also considered for nonconducting fluids. The impedance was measured between various pairs of electrodes, each sensitive to a different region of the flow. The impedances measured from these pairs was compared to those produced by known flow patterns in order to identify flow regime and volume fraction.

4 Temporal Resolution for Dynamic Measurements. Various authors have used the time history of the capacitance signal output as a way of discerning information about the flow structure. Geraets and Borst (1988) used the signal time history as a way of characterizing the flow pattern in horizontal gas liquid flows. Klausner et al. (1992) examined the power spectral density function for the capacitance signal to study the low frequency fluctuations of film thickness in horizontal stratified and annular liquid vapor flows. Keska et al. (1994) also studied frequency and power spectral density distributions, from time traces of concentration, film thickness, and pressure, in horizontal air water flow.

5 The Effect of Temperature Variations. Klausner et al. (1992) discussed the effect of temperature variations on both the permittivity of the phases and the surrounding sensor body and devised a temperature-correction scheme to account for the effect.

In this work, an experimental investigation and analysis are presented for predicting the output of a capacitance sensor consisting of parallel-plate electrodes mounted inside a square duct (12.7 × 12.7 mm) as a function of liquid film thickness. Both stratified and annular flow patterns are considered. Since the fluids considered have a low relative permittivity (FC-87, ϵ_r = 1.72; FC-72, ϵ_r = 1.75), the analysis was very useful in designing a sensor with satisfactory resolution. Furthermore, the analysis eliminates the need for sensor calibration when measuring horizontal stratified flow or annular flow film thickness. The analysis is validated by well-controlled isothermal stratified film thickness measurements made on a bench top. The sensor is then installed in a vertical two-phase flow facility, where annular flow film thickness measurements are obtained via a digital imaging facility and compared against those measured using the capacitance sensor in conjunction with the analysis. The temperature range over which the flow boiling facility operates is 20 to 80°C, and thus it is necessary to account for nonisothermal conditions, which is inherent in the analysis.

Sensor Design and Instrumentation

An exploded view of the square cross section capacitance sensor is illustrated in Fig. 1. The sensor is constructed from four 12.7 mm thick Lexan walls, chemically welded with acrylic resin. The square channel cross section is 12.7 × 12.7 mm. The length of the channel is 40 cm. Lexan was chosen for its strength, and because its optical clarity allows for visual inspection of the flow pattern and liquid film. Two sets of parallel brass plates, 12.7 × 60 mm in size, span the width of the channel and are attached to the inside surfaces of the walls. The two sensor pairs are mounted 90 degrees apart from one another to account for asymmetries in the film thickness if present. Two Lexan flanges welded at each end of the sensor allow for connection to a vertical section of the flow boiling facility, which consists of 12.7 × 12.7 mm ID square brass tubing.

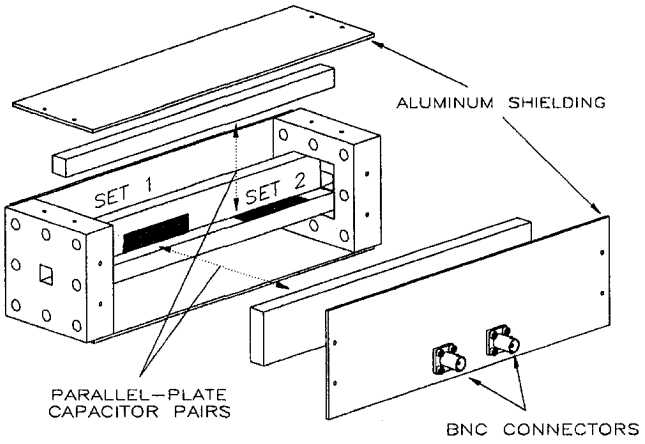

Fig. 1 Exploded view of capacitance meter used in this work (wiring omitted for clarify)

Surrounding the sensor are 4 aluminum plates, mounted to the sides of the flanges, each grounded to shield the electrodes from external electromagnetic fields. The two sensor pairs are connected together (in parallel for the current configuration) with shielded cable, then connected to BNC fittings mounted on the aluminum plate. The wiring of the sensor has been omitted in the figure for clarity. The sensor is connected via BNC fittings and shielded cable to a Keithley 590 digital CV analyzer. The instrument measures capacitance with a resolution of 0.1 fF and is accurate to 0.1 percent of full scale.

In order to test the adequacy of the capacitance sensor analysis, a Videk Megaplus CCD digital camera is used to photograph the liquid film through a visual section. The liquid film thicknesses measured using the capacitance sensor are compared with CCD camera film thickness measurements. The camera provides digital images with 1320 × 1100 pixel resolution, using a Vivitar 50 mm macrolens for high resolution and low distortion. The images are captured with an Epix 4 megabyte frame grabber installed in an AT style personal computer. The image is then analyzed using Pixfolio, a PC-based image processing software, where measurements of film thickness are made from the image with an estimated resolution of 0.01 mm.

Methodology of Sensor Analysis

An analysis is performed on two parallel plates of area A, separated by a distance d, with a homogeneous material of relative permittivity ϵ_r in between. For the ideal case where

Nomenclature

A = area of capacitance sensor, m^2
C = capacitance, pf
C^* = relative capacitance, $(C - C_v)/(C_L - C_v)$
d = distance between parallel plates, also square channel width, m or mm
α = vapor volume fraction
δ = film thickness, mm
ϵ_r = relative permittivity, $C^2/(N \cdot m^2)$

Subscripts

a = annular flow
L = liquid
s = side configuration
u = upward configuration
v = vapor

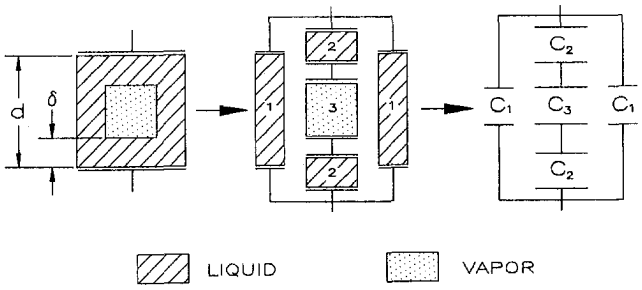

Fig. 2 Reduction of square vapor core flow geometry into composites

$\sqrt{A} \gg d$, the electric field is constant throughout the material, and the capacitance is given by

$$C = \frac{\epsilon_o \epsilon_r A}{d}, \tag{1}$$

where $\epsilon_o = 8.85 \times 10^{-12}\ C^2/(N \cdot m^2) = 8.85$ pf/m is the permittivity of free space. Due to the linearity of the Laplace equation which governs the potential field within the sensor, the capacitance of a composite material in the space between the plates can be analyzed by constructing an equivalent circuit of series and parallel capacitances. For example, the composite material shown in Fig. 2 has a capacitance

$$C = C_1 + \left[\frac{1}{C_2} + \frac{1}{C_3} + \frac{1}{C_2}\right]^{-1} + C_1 \tag{2}$$

where C_1, C_2, and C_3 are computed using Eq. (1) applied to the equivalent geometry shown.

The composite structure depicted in Fig. 2 is equivalent to a steady two-phase annular flow where the vapor core has a square cross section. Of course, in a real flow, the annular core is never completely square in cross section. When the vapor volume fraction is small the annular core approaches a circular shape, but for small vapor volume fractions annular flow is not likely to occur. And as the volume fraction approaches unity the core shape approaches a square with rounded corners. Given this reasoning, the calibration procedure assumes that the annular core cross section will be square.

Nevertheless, it is of interest to determine the degree of error introduced in the vapor volume fraction measurement when the shape of the core is circular. To address this concern, the method of composites, described above, is repeated for the case of a round vapor core geometry. The capacitance sensor is divided into very small composites, as demonstrated in Fig. 3. For the same vapor volume fraction, the computed capacitance for the

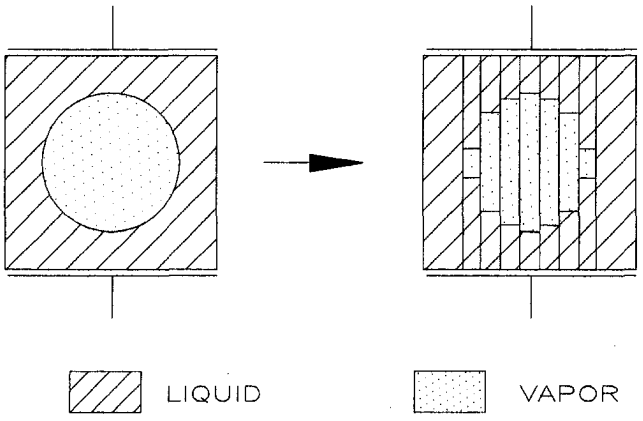

Fig. 3 Reduction of round vapor core capacitance into composites

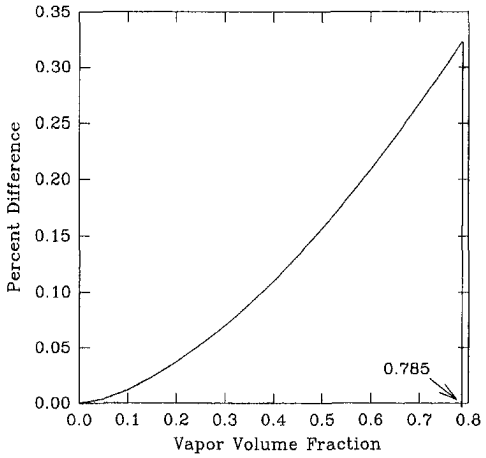

Fig. 4 Percent difference in capacitance between annular flow with a square and round vapor core

round vapor core may be compared against that of a square core. The percent difference between the computed capacitance for the two geometries is depicted in Fig. 4. The comparison is made up to a vapor volume fraction of 0.785, which corresponds to the largest circular vapor core that can exist in a square cross section. It is seen is that, when the vapor volume fraction is small, the error in approximating the round vapor core as square becomes vanishingly small. As the vapor volume fraction increases, the error increases. However, two points are worth noting. First, as the vapor volume fraction increases, the shape of the core will begin to conform to the shape of the square channel. Indeed, for annular flow conditions achievable in the current two-phase flow facility ($\alpha > .80$), the vapor core appears to be a square with rounded corners. Second, the maximum error in Fig. 4 is less than 0.30 percent, which is within the accuracy of the measuring technique. It is noted, however, that the small error is partially due to the fact that the ratio of the liquid to vapor permittivity is small, $\epsilon_L/\epsilon_v = 1.75$. Therefore for this work, the vapor core geometry can be effectively approximated as square without the introduction of any significant error.

Stratified Film Results

It is desirable to test the capacitance film thickness sensor on a bench top where the liquid film can be precisely controlled and measured. For liquid/vapor mixtures it is not possible to do so for the annular flow regime. So instead, the sensor was tested on the bench top using FC-87 ($\epsilon_r = 1.72$) for a stratified liquid layer. These tests validate the composite material analysis, which will subsequently be used to evaluate the liquid film thickness for annular flow. The usefulness of this methodology for evaluating the annular flow film thickness will be demonstrated in the proceeding section.

The square channel may be placed in two different orientations: the upward orientation and the side orientation, as shown in Fig. 5. C_u and C_s denote the capacitances measured for a stratified liquid layer in the respective upward and side orientations. Assuming that (1) is valid, the ratio of the liquid to vapor permittivity can be expressed as

$$\frac{\epsilon_L}{\epsilon_v} = \frac{C_L}{C_v}, \tag{3}$$

where C_L is the measured capacitance when the sensor is filled with pure liquid and C_v is the measured capacitance when the sensor is filled with pure vapor. The ratio of C_L to C_v is referred to here as the effective permittivity ratio. Using Eqs. (1) and (3) and the composite material analysis, the dimensionless ca-

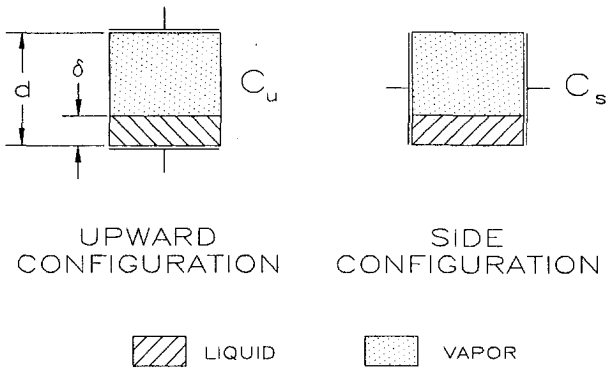

Fig. 5 Upward and side configurations of a parallel-plate capacitor in stratified flow

pacitances for a stratified liquid layer in the upward and side orientations as shown in Fig. 5, may be expressed as

$$C_u^* = \frac{C_u - C_v}{C_L - C_v} = \frac{1}{\frac{C_L}{C_v} - 1}\left(\frac{\frac{C_L}{C_v}}{\frac{\delta}{d} + \frac{C_L}{C_v}\left(1 - \frac{\delta}{d}\right)} - 1\right) \quad (4)$$

and

$$C_s^* = \frac{C_s - C_v}{C_L - C_v} = \frac{\delta}{d} \quad (5)$$

where δ is the liquid film thickness and d is the channel width.

Figures 6 and 7 show the predicted film thickness as a function of capacitance for the upward and side orientations respectively. Also shown are the measured film thicknesses using the CCD camera associated with the measured capacitances using the parallel plate sensor. The capacitances were measured for only one set of parallel plates. The estimated uncertainty of the CCD camera measurements is ±.01 mm. This does not include possible error due to a capillary rise at the three-phase contact line (liquid/vapor/solid). However, it is seen that there is good agreement between the analysis and the experimental measurements, and it is concluded that the capillary rise is small. The standard deviations for the measured and predicted film thickness for the upward and side orientations are 0.014 and 0.019 mm, respectively, which validates the composite material analysis. Also, 0.02 mm, the largest standard deviation, may be taken

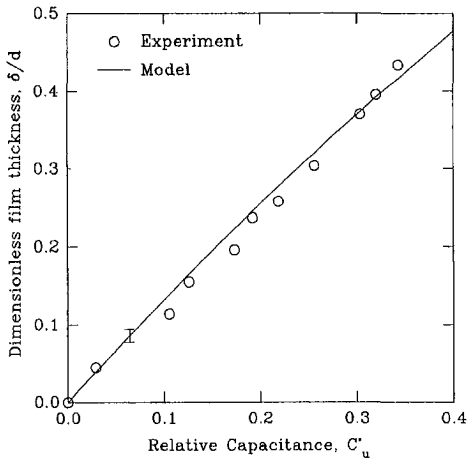

Fig. 6 Comparison between predicted and measured film thickness for the upward orientation; capacitance is measured using the sensor, and film thickness is measured by the CCD camera

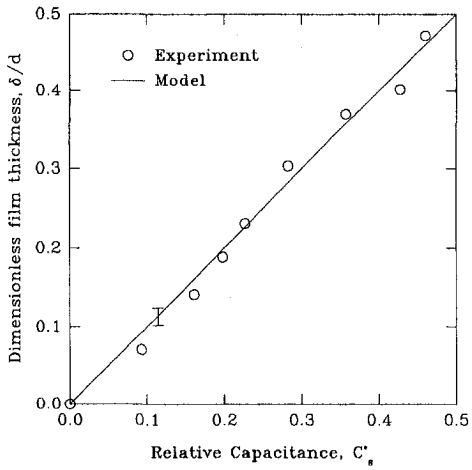

Fig. 7 Comparison between predicted and measured film thickness for the side orientation; capacitance is measured using the sensor, and film thickness is measured using the CCD camera

as the smallest liquid film thickness which can be resolved using the sensor. C_u and C_s may be computed using Eqs. (4) and (5) for a given film thickness at any system temperature provided C_L and C_v are known as a function of temperature.

Annular Flow Results

For the sensor design considered herein using one set of parallel plates and FC-72 as the working fluid, the calibration curves for C_L and C_v as a function of temperature are shown in Fig. 8. Over the temperature range considered, 23–60°C, C_L and C_v are approximately linear functions of temperature. The objective in this work is to measure the liquid film thickness for annular two-phase vertical upflow or downflow using the capacitance sensor without having to calibrate it for annular flow conditions. Utilizing the composite material analysis shown in Fig. 2 in conjunction with Eq. (2), the capacitance, C_a^*, for annular flow with a square cross section and uniform film thickness may be expressed as

$$C_a^* = \frac{C_a - C_v}{C_L - C_v} = \frac{2\left(\frac{\delta}{d}\right)}{\left(\frac{C_L}{C_v} - 1\right)} \times \left[\frac{C_L}{C_v} - \frac{1}{2\left(\frac{\delta}{d}\right) + \frac{C_L}{C_v}\left(1 - 2\left(\frac{\delta}{d}\right)\right)}\right]. \quad (6)$$

Thus, Eq. (6) and the calibration curves for C_L and C_v are used to evaluate the liquid film thickness, δ, for a measured annular flow capacitance, C_a.

The capacitance sensor was placed in-line in a vertical flow boiling facility charged with FC-72. For a given system pressure, two-phase flow was established by evaporating liquid FC-72 in a preheater section. There are approximately 120 diameters of adiabatic developing length for the liquid/vapor mixture prior to entering the capacitance sensor. The flow boiling facility is configured such that either vertical upflow or downflow may be established in the capacitance sensor. Both sets of electrodes were used for the annular flow tests. Directly adjacent to the capacitance sensor is a visual test section, through which the liquid film can be observed. The system mass flux and vapor quality are adjusted to obtain annular two-phase flow. The liquid film in two-phase flow is inherently unstable and thus the film

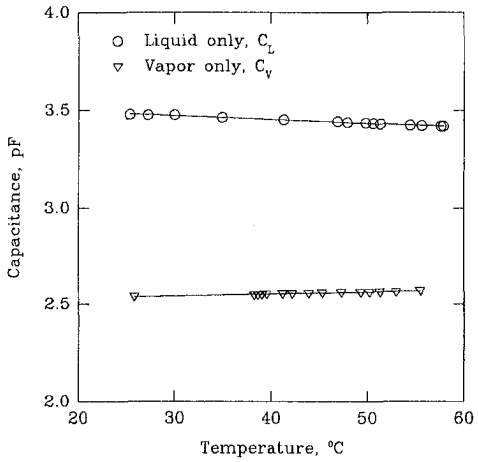

Fig. 8 Temperature calibration of C_L and C_v

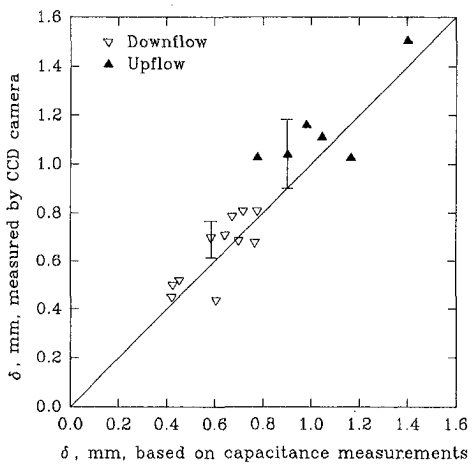

Fig. 10 Comparison of annular two-phase flow liquid film thickness measured with capacitance sensor and CCD camera

displays large temporal and spatial variations. Typical CCD photographs of the annular flow liquid film for vertical upflow and downflow are shown in Figs. 9(*a*) and 9(*b*), respectively. An ensemble of ten photographs were used to evaluate the liquid film thickness in vertical downflow using the CCD camera; twenty photographs were used for upflow due to the highly variable nature of the film. A comparison between the film thickness measured from photographs and a time-averaged measurement using the capacitance sensor is shown in Fig. 10. There are several factors which add to the uncertainty of the photographic film thickness measurement. These include: finite resolution of the camera, 0.01 mm; large temporal and spatial variations in the film, which result in statistical error due to finite sampling; and uncertainty in clearly identifying the liquid/vapor interface. A conservative estimate for the uncertainty of measuring the liquid film thickness using the photographic technique is ±0.25 mm for downflow and ±0.53 mm for upflow. Considering the large temporal and spatial variations in film thickness, the comparison is satisfactory. It is seen that the largest deviation is for vertical upflow. This is because the liquid film for upflow is considerably more variable than that for downflow. The standard deviation for the downflow comparison is 0.093 mm and that for upflow is 0.173 mm, which is within the uncertainty of the photographic measurements.

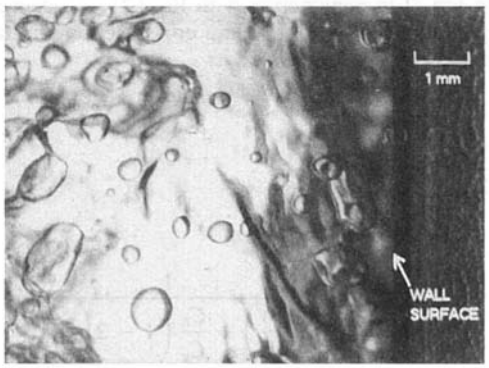

Fig. 9(*a*) Typical photograph of annular upflow liquid film

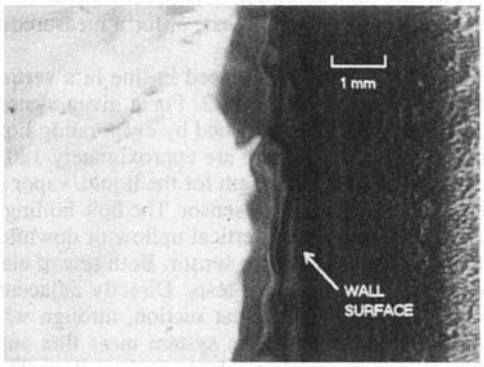

Fig. 9(*b*) Typical photograph of annular downflow liquid film

Conclusions

A parallel-plate capacitance sensor has been designed and tested to measure liquid film thickness in horizontal stratified flow and vertical annular upflow and downflow. A simplified model has been presented for predicting the capacitance output as a function of film thickness. The capacitance sensor resolution is satisfactory and the model compares well with experimental data. Thus in order to use the parallel plate capacitance sensor design to measure liquid film thickness in either horizontal stratified or vertical annular flow, the only calibration required is the determination of C_L and C_v over a temperature range. Because the stratified film tests were carefully controlled on a bench top, the film thicknesses obtained using the capacitance measurements and analysis deviate from those using the CCD camera significantly less than for the annular flow tests. The deviation for vertical annular flow is greater than that of stratified flow because of the difficulty in measuring film thickness with the camera. The deviation in upflow is larger than that of downflow due to the greater variability of the film. It is believed that the values of film thickness based on capacitance measurements are more reliable than those obtained from CCD camera photographs.

Acknowledgments

This work was performed while the lead author was supported as a Florida Space Grant Fellow. The authors also wish to thank 3M Corporation for donating the perfluorocarbon fluids used in this work.

References

Albouelwafa, M. S. A., and Kendall, E. J. M., 1979a, "Analysis and Design of Helical Capacitance Sensors for Volume Fraction Measurement," *Review of Scientific Instruments,* Vol. 50, No. 7, pp. 872–878.

Albouelwafa, M. S. A., and Kendall, E. J. M., 1979b, "Determination of the Theoretical Capacitance of a Concave Capacitance Sensor," *Review of Scientific Instruments,* Vol. 50, No. 9, pp. 1158–1159.

Albouelwafa, M. S. A., and Kendall, E. J. M., 1980, "The Use of Capacitance Sensors for Phase Percentage Determination in Multiphase Pipelines," *IEEE Transactions Instrumentation and Measurement,* Vol. IM-29, No. 1, pp. 24–27.

Chun, M. H., and Sung, C. K., 1986, "Parametric Effects on the Void Fraction Measurement," *International Journal of Multiphase Flow,* Vol. 12, pp. 627–640.

Geraets, J. J. M., and Borst, J. C., 1988, "A Capacitance Sensor for Two-Phase Void Fraction Measurement and Flow Pattern Identification," *International Journal of Multiphase Flow,* Vol. 14, No. 3, pp. 305–320.

Gregory, G. A., and Mattar, L., 1973, "An In-Situ Volume Fraction Sensor for Two-Dimensional Flows of Non-Electrolytes," *Journal of Canadian Petroleum Technology,* Vol. 12, pp. 48–52.

Gupta, D., Sen, S., and Das, P. K., 1994, "Finite-Difference Resistance Modelling for Liquid Level Measurement in Stratified Gas-Liquid Systems," *Measurement Science and Technology,* Vol. 5, pp. 574–579.

Irons, G. A., and Chang, J. S., 1983, "Particle Fraction and Velocity Measurement in Gas-Powder Systems by Capacitance Transducers," *International Journal of Multiphase Flow,* Vol. 9, No. 3, pp. 289–297.

Keska, J. K., 1994, "Experimental Investigation of Spatial Concentration Spectra of a Solid in a Slurry in Horizontal Pipeline Flow," *Flow Measurement Instrumentation,* Vol. 5, No. 3, pp. 155–163.

Klausner, J. F., Zeng, L. Z., and Bernhard, D. M., 1992, "Development of a Film Thickness Probe Using Capacitance for Asymmetrical Two-Phase Flow with Heat Addition," *Review of Scientific Instruments,* Vol. 63, No. 5, pp. 3147–3152.

Klug, F., and Mayinger, F., 1994, "Impedance Based Flow Reconstruction-A Novel Flow Composition Measuring Technique for Multi-Phase-Flows," *Nuclear Engineering and Design,* Vol. 146, pp. 35–42.

Ozgu, M. R., and Chen, J. C., 1973, "A Capacitance Method for Measurement of Film Thickness in Two-Phase Flow," *Review of Scientific Instruments,* Vol. 44, No. 12, pp. 1714–1716.

Xie, C. G., Stott, A. L., Plaskowski, A., and Beck, M. S., 1990, "Design of Capacitance Electrodes for Concentration Measurement of Two-Phase Flow," *Measurement Science and Technology,* Vol. 1, pp. 65–78.

Renwei Mei
Department of Aerospace Engineering, Mechanics & Engineering Science, University of Florida, Gainesville, FL 32611

R. J. Adrian
Department of Theoretical and Applied Mechanics, University of Illinois at Urbana-Champaign, Urbana, IL 61801

T. J. Hanratty
Department of Chemical Engineering, University of Illinois at Urbana-Champaign, Urbana, IL 61801

Turbulent Dispersion of Heavy Particles With Nonlinear Drag

The analysis of Reeks (1977) for particle dispersion in isotropic turbulence is extended so as to include a nonlinear drag law. The principal issue is the evaluation of the inertial time constants, β_α^{-1}, and the mean slip. Unlike what is found for the Stokesian drag, the time constants are functions of the slip velocity and are anisotropic. For settling velocity, V_T, much larger than root-mean-square of the fluid velocity fluctuations, u_0, the mean slip is given by V_T. For $V_T \to 0$, the mean slip is related to turbulent velocity fluctuation by assuming that fluctuations in β_α are small compared to the mean value. An interpolation formula is used to evaluate β_α and V_T in regions intermediate between conditions of $V_T \to 0$ and $V_T \gg u_0$. The limitations of the analysis are explored by carrying out a Monte-Carlo simulation for particle motion in a pseudo turbulence described by a Gaussian distribution and Kraichnan's (1970) energy spectrum.

Introduction

Small particles, drops or bubbles in a turbulent environment assume a turbulent behavior because of their response to the fluid velocity fluctuations. The principal problem in predicting the dispersion of particles is that the statistics of the fluid fluctuations must be specified along the paths of the particles, which are not known a priori. Considerable progress has been made in calculating the turbulence properties by solving the equation of motion for a prescribed fluid turbulence since Tchen's (1947) work. Satisfactory solutions have been presented by Reeks (1977), Pismen and Nir (1978), and Nir and Pismen (1979). The common feature of these analyses is that Corrsin's (1959) independence approximation is used and the fluid turbulence is assumed to be isotropic and Gaussian. A simplified version of Tchen's equation was used that includes only Stokes drag and gravitational force. In many applications, however, the particle Reynolds number exceeds unity. This paper examines the dispersion of particles and the mean-square of the particle velocity fluctuations when the drag does not obey Stokesian law.

The equation of motion for a heavy particle is

$$\frac{4}{3}\pi a^3 \rho_p \frac{d\mathbf{V}}{dt} = \frac{4}{3}\pi a^3 \rho_p \mathbf{g} + \phi 6\pi \rho_f \nu a(\mathbf{u}(\mathbf{Y}, t) - \mathbf{V}) \quad (1)$$

with

$$\frac{d\mathbf{Y}}{dt} = \mathbf{V} \quad (2)$$

and

$$\phi = C_D \, \mathrm{Re}_p/24. \quad (3)$$

In the above, $\mathbf{Y}(t)$ and $\mathbf{V}(t)$ are the trajectory and velocity of the particle, $\mathbf{u}(\mathbf{Y}, t) = \mathbf{u}(\mathbf{x}, t)|_{x=Y}$ and $\mathbf{u}(\mathbf{x}, t)$ is the fluid velocity in a frame moving with a mean uniform velocity. Therefore $\mathbf{u}(\mathbf{Y}, t)$ is the fluid fluctuating velocity seen on the particle trajectory. Term $\mathbf{g} = g\mathbf{e}_1$ is the gravitational acceleration, ρ_p and ρ_f are particle and fluid density, ν is the kinematic viscosity of the fluid, C_D is the standard drag coefficient, and the instantaneous Reynolds number is defined as

$$\mathrm{Re}_p = |\mathbf{u} - \mathbf{V}| 2a/\nu. \quad (4)$$

Contributed by the Fluids Engineering Division for publication in the JOURNAL OF FLUIDS ENGINEERING. Manuscript received by the Fluids Engineering Division December 18, 1994; revised manuscript received July 24, 1996. Associate Technical Editor: M. W. Reeks.

Equation (1) is a simplified version of Tchen's (1947) formulation with the Stokesian drag ($\phi = 1$) replaced by a nonlinear drag ($\phi \geq 1$) and the unsteady forces such as the Basset history force and added-mass force are neglected. For $\mathrm{Re}_p \ll 1$, the effect of the Basset history force on the dispersion of particles in an isotropic turbulence has been shown to be negligible (Mei et al., 1991). It has also been demonstrated (Mei et al., 1991; Mei and Adrian, 1992; Mei, 1994b) that, as Re_p increases, the unsteady force associated with acceleration becomes less important compared to the nonlinear quasi-steady drag at low frequencies. Therefore, Eq. (1) is a valid approximation for studying particle dispersion in turbulence with a finite particle Reynolds number.

Reeks (1980) considered particle-dispersion in phase space, without the effect of a settling velocity, by using the Eulerian direct interaction theory to close Liouville's equation of particle motion. Within that framework, it is difficult to handle more general nonlinear drag laws in three dimensions (as Reeks pointed out). Lumley (1978) considered the effect of large settling velocity, V_T, on the particle time constants in the nonlinear drag range and indicated that the response time associated with the longitudinal component is smaller than that with the lateral component. He suggested that the particle fluctuating velocity can be characterized by a linear equation using two time constants. However, when the settling velocity is comparable with the turbulence velocity, the expansion for large V_T used by Lumley fails since the effects of turbulence on V_T and on the time constants are not determined.

In the nonlinear drag range, Kada and Hanratty (1960), Tunstall and Houghton (1968), Murray (1970), Hwang (1983, 1985), and Ikeda and Yamasaka (1989) found a reduction in V_T for a particle in a turbulent flow or in an oscillating flow due to the nonlinearity of the drag. Maxey (1987) studied the gravitational settling of aerosol particles in a pseudo Gaussian turbulence by using a random Fourier series representation (Kraichnan, 1970). In the Stokesian drag range, he found that turbulence increases the particle settling velocity since particles with finite inertia tend to accumulate in regions of high strain rate and low vorticity. Wang and Maxey (1993) used a direct numerical simulation (DNS) of forced isotropic turbulence and found that the enhancement in settling velocity is even stronger than in a pseudo-Gaussian turbulence when a linear drag law is used.

This paper focuses on the stationary behavior (V_T = constant) of particles in isotropic, Gaussian turbulence subjected only to nonlinear (i.e., non-Stokesian) drag and a gravitational force. The central questions are as follows:

(i) How does the nonlinearity of the drag affect the dispersion and the root-mean-square of the particle velocity fluctuation?

(ii) How do the nonlinearity of the drag and turbulence affect the inertial time constants and the settling velocity of the particle?

To address these issues analytically, two limiting cases are considered: (i) large V_T for which the critical assumption is Taylor's frozen field hypothesis and (ii) zero V_T for which the critical approximation is that the randomly varying particle time constant is replaced by the time averaged value. These limits are used to develop an approximate formulation that spans the full range of particle settling velocity for the case where the fluctuations of β are small compared to the mean value. In this way, Reeks' (1977) analysis is extended to describe particle turbulence.

The complete derivation of the theory outlined above is lengthy and can be found in Mei (1990) and in a report by Mei et al. (1993). This paper outlines the analysis and presents final results. The approximate theory is validated by performing a Monte-Carlo simulation of particle motion in turbulence with a fully nonlinear drag law and arbitrary body force. Subsequently, the approximate theory is used to explore parametrically particle turbulence, including the effects of an anisotropic particle time constant and the effect of turbulence on the settling velocity.

Analyses for Particle Turbulence

Asymptotic Behavior of Particle Motion With Large Settling Velocity. For finite Re_p, the following relation from Clift et al. (1978) is used for the steady-state drag,

$$\phi = (1 + b\ \mathrm{Re}_p^n), \tag{5}$$

with $b = 0.15$ and $n = 0.687$. Equation (1) with the above ϕ creates a difficulty because $\mathrm{Re}_p C_D$ is nonlinear in $(\mathbf{u} - \mathbf{V})$. In the limit of $V_T \gg u_0$, or

$$\lambda = V_T/u_0 \gg 1 \tag{6}$$

this can be handled by expanding ϕ near an average particle Reynolds number,

$$\mathrm{Re}_1 = V_T 2a/\nu, \tag{7}$$

in a Taylor series valid for small $(\mathrm{Re}_p - \mathrm{Re}_1)$. By using binomial expansions for ϕ, $|\mathbf{u} - \mathbf{V}|$, and $\phi 6\pi\rho_f\nu a(\mathbf{u} - \mathbf{V})$, taking an ensemble average or a time average of (1), utilizing the symmetry relation $\langle(v_2 - u_2)^2\rangle = \langle(v_3 - u_3)^2\rangle$, and neglecting triple correlations of the turbulent fluctuations of $O(\lambda^{-3})$, the following equation is obtained for the ensemble averaged particle velocity:

$$V_T = V_{TS}\left\{1 + b\ \mathrm{Re}_1^n + bn\ \mathrm{Re}_1^n \frac{\frac{n+1}{2}\langle(v_1 - u_1)^2\rangle + \langle(v_2 - u_2)^2\rangle}{V_T^2}\right\}^{-1} \tag{8}$$

where

$$V_{TS} = \frac{2}{9}\frac{\rho a^2 g}{\nu} = \frac{g}{\beta_S}, \quad \beta_S = \frac{9}{2}\frac{\nu}{\rho a^2}, \tag{9}$$

are the settling velocity and the inertial parameter of the particle in the Stokes regime, respectively, and $\rho = \rho_p/\rho_f$ is the density ratio. In (8),

$$\mathbf{v} = \mathbf{V} - V_T\mathbf{e}_1 \tag{10}$$

is the turbulent particle velocity and $\langle(u_\alpha - v_\alpha)^2\rangle$ can be evaluated by recognizing that for a linear system

$$\langle u_\alpha v_\alpha\rangle = \langle v_\alpha^2\rangle \tag{11}$$

(see Appendix A in Mei et al., 1993). Equation (8) indicates that turbulent fluctuations reduce V_T.

Nomenclature

a = radius of spherical particles
$D(\tau)$ = Eulerian auto-correlation function
D_f = fluid turbulent diffusivity
D_{ij} = particle turbulent diffusivity tensor
$E(k)$ = energy spectrum in the wavenumber space
$E_{11}(k_1)$ = longitudinal energy spectrum
Fg = Froude number based on typical wave number, k_0, of fluid turbulence and u_0
g = gravitational acceleration
k = wave number
L_{11} = integral length scale of the fluid turbulence
p = probability density function
Re_0 = particle Reynolds number based on the average slip velocity
$\mathrm{Re}p_S$ = particle Reynolds number based on settling velocity in the Stokes drag range
$\mathrm{Re}u_0$ = $= u_0 2a/\nu$, particle turbulence Reynolds number
Re_1 = $= V_T 2a/\nu$, particle settling Reynolds number
$R^p_{u_iu_j}(\tau)$ = fluid Lagrangian correlation tensor evaluated on the particle trajectory
$R^p_{v_\alpha v_\alpha}(\tau)$ = particle velocity correlation
$S^p_{u_\alpha u_\alpha}(\omega)$ = power spectrum of the fluid velocity seen by an observer moving on the particle trajectory
$S_{V_\alpha V_\alpha}(\omega)$ = power spectrum of the particle velocity
T_f and T_i = final and initial instants of the time averaging process
T_0 = Eulerian integral time scale of turbulence
$\mathbf{u}$ = fluid turbulence
u_0 = rms turbulent velocity
$\mathbf{v}$ = particle turbulent velocity
v_d = $= |\mathbf{u} - \mathbf{V}|$, particle slip velocity
$\langle v_1^2\rangle$ and $\langle v_2^2\rangle$ = particle turbulence intensity
V_d = mean particle slip velocity
V_T = particle settling velocity
V_{TS} = particle settling velocity in the Stokes drag range
$\Phi_{ij}(\mathbf{k}, \tau)$ = turbulence energy spectrum tensor
$\mathbf{Y}$ = particle displacement vector
β = reciprocal of time constants or inertial parameter of the particle
β_S = β in the Stokesian drag range
ϕ = correction for Stokesian drag
λ = particle settling rate = V_T/u_0
ρ_f and ρ_p = fluid and particle material densities
ρ = $= \rho_p/\rho_f$, particle-to-fluid density ratio
τ = time delay
ω = frequency
ν = fluid kinematic viscosity

Overhead

$\sim$ = denote the normalization using $1/k_0$ and u_0

A differential equation for the components of the fluctuating velocity is obtained by subtracting (8) from (1) and neglecting terms of order λ^{-2}:

$$\frac{dv_\alpha}{dt} = \beta_\alpha(u_\alpha - v_\alpha), \quad \alpha = 1 \text{ or } 2. \tag{12}$$

The particle inertial parameters β_α are

$$\beta_1/\beta_S = 1 + b(1 + n)\,\mathrm{Re}_1^n, \tag{13a}$$

$$\beta_2/\beta_S = 1 + b\,\mathrm{Re}_1^n. \tag{13b}$$

Lumley (1978) developed an approximation for the drag at large λ and also found that $\beta_1 > \beta_2$. The above can be shown to be equivalent to the result of Lumley. The particle turbulence $\langle v_\alpha^2 \rangle$ can be calculated for a given energy spectrum of the fluid turbulence by solving (12).

Extension of Reeks' Analysis for Particles With Arbitrary λ And Anisotropic Response. In Reeks' (1977) analysis, the assumption of Stokes drag resulted in the use of an isotropic reciprocal time constant for heavy particles $\beta_1 = \beta_2 = \beta_S = 9\nu/(2\rho a^2)$. Mei (1990) modified Reeks' theory to calculate the turbulence properties for particles with anisotropic response $\beta_1 \geq \beta_2$ by solving (12). Corrsin's (1959) independence approximation was used and the turbulence was assumed to be isotropic and Gaussian. Following Kraichnan (1970) and Maxey (1987), the energy spectral density function of the Eulerian fluid velocity, $\Phi_{ij}(\mathbf{k}, \tau)$, was assumed separable in $\mathbf{k}$ and τ:

$$\Phi_{ij}(\mathbf{k}, \boldsymbol{\tau}) = D(\tau)\,\frac{1}{4\pi}\,\frac{E(k)}{k^2}\left(\delta_{ij} - \frac{k_i k_j}{k^2}\right) \tag{14}$$

where $D(\tau)$, the auto-correlation function of the fluid velocity fluctuations in a frame moving with a mean velocity, characterizes the self-decay of the turbulent eddies and $E(k)$ is the distribution of energy in wave number space. The auto-correlation function is taken as

$$D(\tau) = \exp(-\omega_0^2\tau^2/2), \tag{15}$$

and $E(k)$ is taken as

$$E(k) = \frac{32u_0^2}{\sqrt{2\pi}}\,\frac{k^4}{k_0^5}\exp(-2k^2/k_0^2). \tag{16}$$

Equation (15) implies that the Eulerian integral time scale is given by $T_0 = \sqrt{\pi/2}/\omega_0$. The value of k_0 in (16) is related to the longitudinal integral length scale, $L_{11} = \pi E_{11}(0)$, as

$$k_0 = \sqrt{2\pi}/L_{11}. \tag{17}$$

In this study, $\omega_0 = k_0u_0$ or $\gamma = \omega_0/(k_0u_0) = 1$ is chosen. Other values of γ have been explored in a discussion of the effects of turbulence structure on the particle settling velocity (Mei, 1994a). To relate the turbulence properties of the particles to known physical quantities, the following dimensionless variables and parameters are introduced:

$$\tilde{t} = tk_0u_0, \quad \tilde{Y} = Yk_0, \quad \tilde{\mathbf{V}} = \mathbf{V}/u_0, \quad \tilde{D}_{\alpha\alpha} = D_{\alpha\alpha}k_0/u_0, \tag{18}$$

$$\mathrm{Fg} = u_0^2k_0/g, \quad \tilde{\beta}_\alpha = \beta_\alpha/(k_0u_0), \tag{19}$$

where Fg is the Froude number defined in Reeks (1977) to characterize the effect of the gravitational force on particle dispersion.

Mei (1990) obtained the following results for the dimensionless correlation functions $\tilde{R}^p_{u_iu_j}(\tilde{\tau})$ of the velocity fluctuations of the fluid that are seen by the particle:

$$\tilde{R}^p_{u_1u_1}(\tilde{\tau}) = \frac{D(\tilde{\tau})}{\mu_{22}^2(\tilde{\beta}_2, \tilde{\tau})\mu_{11}^{1/2}(\tilde{\beta}_1, \tilde{\tau})}\exp\left[-\frac{\lambda^2\tilde{\tau}^2}{8\mu_{11}(\tilde{\beta}_1, \tilde{\tau})}\right] \tag{20}$$

and

$$\tilde{R}^p_{u_2u_2}(\tilde{\tau}) = \frac{1}{2}\left\{1 + \frac{\mu_{22}(\tilde{\beta}_2, \tilde{\tau})}{\mu_{11}(\tilde{\beta}_1, \tilde{\tau})}\left[1 - \frac{\lambda^2\tilde{\tau}^2}{4\mu_{11}(\tilde{\beta}_2, \tilde{\tau})}\right]\tilde{R}^p_{u_1u_1}(\tilde{\beta}_2, \tilde{\tau})\right\}, \tag{21}$$

where

$$\sigma^2 = \gamma^2 + \frac{\lambda^2}{4}, \tag{22}$$

$$f(\tilde{\beta}_\alpha, \tilde{\tau}) = \frac{\sqrt{\pi/2}}{2\sigma\tilde{\beta}_\alpha}\exp\left(\frac{1}{2}\tilde{\beta}_\alpha^2/\sigma^2 + \tilde{\beta}_\alpha\tilde{\tau}\right)\mathrm{erfc}\left(\frac{1}{\sqrt{2}}(\sigma\tilde{\tau} + \tilde{\beta}_\alpha/\sigma)\right) \tag{23}$$

$$h(\tilde{\beta}_\alpha, \tilde{\tau}) = f(\tilde{\beta}_\alpha, \tilde{\tau}) + f(\tilde{\beta}_\alpha, -\tilde{\tau}) - 2f(\tilde{\beta}_\alpha, 0) \tag{24}$$

$$\mu_{11}(\tilde{\beta}_\alpha, \tilde{\tau}) = 1 + \frac{1}{2}\left\{h(\tilde{\beta}_\alpha, \tilde{\tau}) + \frac{1}{\sigma^2}\left[\exp(-\sigma^2\tilde{\tau}^2/2) - 1\right] + \sqrt{\pi/2}\,\frac{\tilde{\tau}}{\sigma}\,\mathrm{erf}\left(\frac{\sigma\tilde{\tau}}{\sqrt{2}}\right)\right\} \tag{25}$$

$$\mu_{22}(\tilde{\beta}_2, \tilde{\tau}) = 1 + \left(1 - \frac{\lambda^2}{8\sigma^2}\right)[\mu_{11}(\tilde{\beta}_2, \tilde{\tau}) - 1] - \lambda^2\tilde{\beta}_2^2/(16\sigma^4)h(\tilde{\beta}_2, \tilde{\tau}). \tag{26}$$

The Lagrangian correlation function for the particles, the turbulent intensities of the particles, and the long-time diffusivities of the particles are related to the correlation function $\tilde{R}^p_{u_\alpha u_\alpha}(\tilde{\tau})$ for $\tilde{\tau} > 0$ by the following equations:

$$\tilde{R}^p_{v_\alpha v_\alpha}(\tilde{\tau}) = \tfrac{1}{2}\int_0^\infty \tilde{R}^p_{u_\alpha u_\alpha}(z)[\exp(-\tilde{\beta}_\alpha(z + \tilde{\tau})) + \exp(-\tilde{\beta}_\alpha|z - \tilde{\tau}|)]dz, \tag{27}$$

$$\langle \tilde{v}_\alpha^2 \rangle = \tilde{\beta}_\alpha\int_0^\infty \tilde{R}^p_{u_\alpha u_\alpha}(z)\exp(-\tilde{\beta}_\alpha z)dz, \tag{28}$$

$$\tilde{D}_{\alpha\alpha} = \int_0^\infty \tilde{R}^p_{u_\alpha u_\alpha}(z)dz. \tag{29}$$

These results contain the effects of two sources of non-linearity: the essential nonlinearity associated with Lagrangian motion and the nonlinearity associated with the drag law. However, in order to use (20)–(29), $\tilde{\beta}_1$, $\tilde{\beta}_2$, and λ (or V_T) need to be specified. This is accomplished by developing an interpolation formula between the asymptotic cases of $\lambda \to 0$ and $\lambda \to \infty$.

Turbulence Characteristics of Particles For $\lambda \to \infty$. The calculation of the turbulence characteristics of the particles with (6) for $\lambda \to \infty$ is done by using Csanady's (1963) approximations that the trajectory of a particle, relative to a frame moving with the mean fluid flow, is nearly a straight line $\mathbf{Y} = (V_T t, 0, 0)$, and that Taylor's frozen field hypothesis is a valid approximation. For the asymptotic case of $\lambda \to \infty$, the influence of fluid turbulence on the settling velocity is small and can be neglected in (8). The following approximation for V_T is obtained:

$$V_T = g/\beta_2(1 + O(\lambda^{-2})) \approx g/\beta_2 \quad \text{and} \quad \lambda = 1/(\mathrm{Fg}\,\tilde{\beta}_2). \tag{30}$$

It can be shown that the dimensionless diffusivities are

$$\tilde{D}_{11} = \sqrt{2\pi}/\lambda = \sqrt{2\pi}\ \mathrm{Fg}\ \tilde{\beta}_2, \quad \tilde{D}_{22} = \tfrac{1}{2}\sqrt{2\pi}\ \mathrm{Fg}\ \tilde{\beta}_2 \quad (31a, b)$$

and the intensities are

$$\langle \tilde{v}_1^2 \rangle \sim \sqrt{2\pi}\ \mathrm{Fg}\ \tilde{\beta}_1\tilde{\beta}_2, \quad \langle \tilde{v}_2^2 \rangle \sim \tfrac{1}{2}\sqrt{2\pi}\ \mathrm{Fg}\ \tilde{\beta}_2. \quad (32a, b)$$

Lumley (1978) recognized that $\tilde{\beta}_1 > \tilde{\beta}_2$ but the dependence of $\langle \tilde{v}_\alpha^2 \rangle$ on $\tilde{\beta}_1$ and $\tilde{\beta}_2$ was not clear at the time. It is seen from (13) that $\tilde{\beta}_1$ is always greater than $\tilde{\beta}_2$. If the anisotropy in the time constants is not taken into account, the prediction of $\langle \tilde{v}_1^2 \rangle$ can be in error by 30 percent at $\mathrm{Re}_1 \sim 10$.

Particle Motion With Zero Settling Velocity. In the absence of body forces, the equation governing the particle motion,

$$\frac{d\mathbf{V}}{dt} = \beta_S(1 + b\ \mathrm{Re}_p^n)(\mathbf{u} - \mathbf{V}) = \beta(\mathbf{u} - \mathbf{V}) \quad (33)$$

is different from (12) in that β in (33) varies with time.

Let

$$v_d = |\mathbf{u} - \mathbf{V}|, \quad V_d = \langle v_d \rangle = \langle |\mathbf{u} - \mathbf{V}| \rangle, \quad (34)$$

$$\mathrm{Re}_0 = V_d 2a/\nu, \quad (35)$$

where v_d and V_d are the instantaneous and the average magnitude of the slip velocity between fluid and particle. The average particle Reynolds number, Re_0, is based on V_d. In equation (33), the time varying β can be decomposed into a mean, $\langle\beta\rangle$, and a fluctuation, β',

$$\beta = \langle\beta\rangle + \beta' \quad (36)$$

so that

$$\frac{d\mathbf{V}}{dt} = \langle\beta\rangle(\mathbf{u} - \mathbf{V}) + \beta'(\mathbf{u} - \mathbf{V}). \quad (37)$$

Define

$$r = \langle\beta'^2\rangle^{1/2}/\langle\beta\rangle \quad (38)$$

as the ratio of the rms value of β' to the mean value $\langle\beta\rangle$. If $r \ll 1$, the second term in (37), which is very difficult to handle analytically, may be neglected. The mean value $\langle\beta\rangle$ is approximated as

$$\langle\beta\rangle \approx \beta_S(1 + b\ \langle \mathrm{Re}_p \rangle^n) = \beta_S(1 + b\ \mathrm{Re}_0^n) \quad (39)$$

where $\langle v_d^n \rangle$ has been approximated by V_d^n with less than 2 percent error (Mei, Adrian and Hanratty, 1993). After neglecting the nonlinear fluctuating term, Eq. (37) can be expressed in dimensionless form as

$$\frac{d\tilde{\mathbf{V}}}{d\tilde{t}} \approx \langle\tilde{\beta}\rangle(\tilde{\mathbf{u}} - \tilde{\mathbf{V}}). \quad (40)$$

The mean slip velocity, V_d, is yet to be determined. For $V_T = 0$, the statistics of $(u_\alpha - v_\alpha)$ are identical for $\alpha = 1, 2$ and 3. A Gaussian distribution in $\mathbf{u}(\mathbf{x}, t)$ implies that $\mathbf{V}(t)$ is also Gaussian for a strictly linear system. For the present nonlinear system with $\langle\beta\rangle$ depending on $(\mathbf{u} - \mathbf{V})$, this is a good approximation and its validity will be confirmed by the results from the Monte-Carlo simulation. Hence the probability distribution of $v_d = [(v_1 - u_1)^2 + (v_2 - u_2)^2 + (v_3 - u_3)^2]^{1/2}$ is approximately Maxwellian, with a probability density function (pdf) given by

$$p(v_d) = \sqrt{2/\pi}\ v_d^2/\sigma_v^3\ \exp(-\tfrac{1}{2}v_d^2/\sigma_v^2) \quad (41)$$

where, using Eq. (11),

$$\sigma_v^2 = \langle (v_\alpha - u_\alpha)^2 \rangle = u_0^2 - \langle v_\alpha^2 \rangle. \quad (42)$$

The mean value of v_d is, after integration,

$$V_d = \sqrt{8/\pi}\ \sigma_v, \quad (43)$$

or

$$V_d = \left[\frac{8}{3\pi}\,(3u_0^2 - \langle v_1^2 \rangle - \langle v_2^2 \rangle - \langle v_3^2 \rangle)\right]^{1/2}. \quad (44)$$

Equations (20), (28), (39), and (44) are closed. They can be solved iteratively for $\tilde{R}^n_{u_\alpha u_\alpha}(\tilde{\tau})$, $\langle \tilde{v}_\alpha^2 \rangle$, $\langle \tilde{\beta}_\alpha \rangle$ and $\tilde{V}_d$; the diffusivity $\tilde{D}_{\alpha\alpha}$ is obtained from (29) after the solution converges.

It should be noted that as Re_0 increases the nonlinearity in the drag law becomes stronger, and the neglect of β' in (37) introduces larger errors. Therefore, the present analysis for zero settling velocity may fail to predict, accurately, the intensity of particle turbulence at very high particle Reynolds numbers. This issue will be further discussed when comparisons are made with results from the Monte-Carlo simulation.

Particle Motion for the Case of Arbitrary λ. The predictions for particle dispersion with a nonlinear drag law have been presented for two extreme cases, i.e., $\lambda = 0$. and $\lambda \to \infty$. An interpolation scheme based on the results for $\lambda = 0$ and $\lambda \to \infty$ (Mei et al., 1993) is used to carry out calculations for $\lambda \sim O(1)$. The average slip velocity $\tilde{V}_d$ is approximated as

$$\tilde{V}_d = \left[\lambda^2 + \frac{8}{3\pi}\,(3 - \langle \tilde{v}_1^2 \rangle - \langle \tilde{v}_2^2 \rangle - \langle \tilde{v}_3^2 \rangle)\right]^{1/2}. \quad (45)$$

The time-averaged particle Reynolds number is then given by

$$\mathrm{Re}_0 = V_d 2a/\nu = \tilde{V}_d\ \mathrm{Re}u_0 \quad (46)$$

where

$$\mathrm{Re}u_0 = u_0 2a/\nu \quad (47)$$

is a turbulence particle Reynolds number, which characterizes the influence of the turbulence velocity u_0 on the drag.

For a finite λ, β_α can again be decomposed into mean and fluctuating parts and β'_α may be neglected to the leading order. The following interpolation incorporates the anisotropy of β_α at finite λ,

$$\beta_1/\beta_S \approx 1 + b(1 - n)\ \mathrm{Re}_0^n + bn\ \mathrm{Re}_0^{n-1}\ \mathrm{Re}u_0\left[(2\lambda)^2 + \frac{8}{3\pi}\,(3 - \langle \tilde{v}_1^2 \rangle - 2\langle \tilde{v}_2^2 \rangle)\right]^{1/2} \quad (48a)$$

$$\beta_2/\beta_S \approx 1 + b\ \mathrm{Re}_0^n. \quad (48b)$$

The above representation is not exact, but it is satisfactory in that it recovers (13) and (39) in the small and large λ limits. Hereafter, $\langle\ \rangle$ will be omitted for the averaged values of particle inertial parameters.

The particle settling velocity may be approximated as

$$V_T = g/\beta_2, \quad \text{or} \quad \lambda = 1/(\mathrm{Fg}\ \tilde{\beta}_2). \quad (49a, b)$$

This recovers (30) to $O(\lambda^{-1})$ for the case of $\lambda \to \infty$, and is exact when the drag is in the Stokes range for all values of λ.

Equations (20)–(21), (28), (45), and (48)–(49) constitute a closed system. The solution is obtained iteratively. The numerical integration (28) requires most of the computation but it is straightforward to implement it. The validity of the interpolation formula will be confirmed by comparing with the results from a Monte-Carlo simulation. The influence of turbulent velocity fluctuations on $\tilde{\beta}_\alpha$ and λ and on the particle turbulence in the nonlinear drag range can be examined parametrically.

In subsequent sections, "~" will be dropped and the results will be presented in dimensionless form, unless otherwise mentioned.

Monte-Carlo Simulation for Particle Motion in Isotropic Gaussian Turbulence. The analyses presented above involve several assumptions: Corrsin's independence approximation, the replacement of the instantaneous particle inertial parameters by averaged values (as in (40)), the neglect of the contribution from the fluctuating particle time constant, the use of a Gaussian distribution for particle velocity in the nonlinear drag range, and interpolation formulae for V_d, β_α, and λ. To validate the analyses and to gain an understanding of the characteristics of particle motion in the nonlinear drag range, Monte-Carlo simulations of random particle motions were performed in an isotropic, Gaussian pseudo-turbulence with $D(\tau)$ and $E(k)$ given by (15–16) for $\gamma = 1$. The method of generating the pseudo-turbulence $u_i(\mathbf{x}, t)$ follows exactly that of Kraichnan (1970) and Maxey (1987). The number of Fourier modes used in each realization is $N = 64$. Ensemble averages over a large number of particles (N_p) are compared with the above analysis.

In Reeks' (1977) analysis, two parameters, β_2 and Fg, are sufficient to describe the particle dispersion in the Stokes drag range. For nonlinear drag, three independent dimensionless parameters are needed: $\beta_S = 9\nu/(2\rho a^2 k_0 u_0)$, $\mathrm{Fg} = u_0^2 k_0/g$ and $\mathrm{Re}u_0 = u_0 2a/\nu$ if $\gamma = \omega_0/(k_0 u_0)$ is fixed. These three parameters are chosen because they can be calculated directly from the physical properties of the particle and the fluid and a knowledge of the turbulence; quantities such as β_α and λ are not known a priori. Alternatively, one can define a Stokes particle Reynolds number

$$\mathrm{Re}p_s = V_{TS} 2a/\nu = \frac{4}{9}\frac{\rho a^3 g}{\nu^2} \tag{50}$$

which is related to β_s, Fg and $\mathrm{Re}u_0$ as

$$\mathrm{Re}p_s = \mathrm{Re}u_0/\beta_s\ \mathrm{Fg}. \tag{51}$$

The dependence of the solution on β_s, $\mathrm{Re}u_0$, and Fg can be seen explicitly from the following particle dynamic equation that is solved numerically,

$$d\mathbf{V}/dt = \beta_s[1 + b\ \mathrm{Re}u_0^n|\mathbf{u} - \mathbf{V}|^n](\mathbf{u} - \mathbf{V}) + 1/\mathrm{Fg}, \tag{52}$$

$$d\mathbf{Y}/dt = \mathbf{V}, \tag{53}$$

which are dimensionless forms of Eqs. (1)–(2).

Equations (52)–(53) were solved using a multi-step fourth-order predictor (Adams-Bashforth)-corrector (Adams-Moulton) method. It is accurate up to $O(\Delta t^4)$. The integrations for all particle trajectories start from $\mathbf{Y} = 0$ at $t = 0$ with an initial velocity $(V_1, V_2, V_3) = (\lambda', 0, 0)$ where λ' is the settling velocity estimated from the nonlinear analysis.

The statistical quantities of interest are obtained by averaging over N_p independent particles and over a time period of $(T_f - T_i)$ in which T_i is a time after which the particle reaches a dynamic equilibrium with the surrounding turbulence and the particle diffusivities reach stationary, long time values, and T_f is the time at which the computation stops. The lateral quantities are further averaged over $\alpha = 2$ and $\alpha = 3$ to improve the statistical accuracy. The details are given in Mei et al. (1993) and in Mei (1990).

Results and Discussions

Verification of the Nonlinear Analysis

Comparisons With The Monte-Carlo Simulation. A study of the convergence characteristics of the Monte-Carlo simulation for averaged quantities, such as β_2, λ, V_d, $\langle v_\alpha^2\rangle$, and $D_{\alpha\alpha}$, indicates that at least $N_p = 2000$ particle trajectories are needed to obtain accurate values of particle diffusivities with a reasonable computation time for each particle; $N_p \geq 4000$ is used for the results to be reported. For $\mathrm{Re}u_0 = 4$, $\beta_S = 0.6667$, and $\mathrm{Fg} = 1$ (which give $\mathrm{Re}_0 = 5.6232$ and $\lambda = 0.9975$), the "errors" in the 4000-particle average are at most 1 percent for $\langle v_\alpha^2\rangle$ and 3 percent for $D_{\alpha\alpha}$ in comparison to a 13,000-particle average.

Table 1 compares, in detail, the dispersion results obtained with a 5000-particle average to the nonlinear analysis for six cases, for which $\mathrm{Re}u_0$ ranges from 1.3289 to 13.289, Fg ranges from 0.2 to ∞, and the settling rate, λ, ranges from 0 to 8.1. At $\mathrm{Re}u_0 = 1.3289$, the differences in $\langle v_\alpha^2\rangle$ and $D_{\alpha\alpha}$ predicted by the simulation and by the analysis are less than 3.5 percent. The largest "error" of 3.27 percent for λ occurs at $\lambda \approx 1$ because this case is not close to either of the two limiting cases.

It is worth mentioning here that previous investigators (Reeks, 1977; and Pisman and Nir, 1978) found that, if gravitational effects are neglected ($\mathrm{Fg} \gg 1$), the particle diffusivity can exceed dimensionless fluid diffusivity $D_f = 0.8926$ for the Gaussian spectrum considered here. (Pisman and Nir's analysis gave a more accurate value of $D_f = 0.903$.) Both the nonlinear analysis and the Monte-Carlo simulation show that this is also the case when a nonlinear drag law is used.

Usually, the particle Reynolds number is taken as an indication of the nonlinearity of the dynamic equation. The average particle Reynolds number based on the average slip velocity, Re_0, increases with increasing turbulence intensity, characterized by $\mathrm{Re}u_0 = u_0 2a/\nu$, or with increasing particle settling velocity, λ. However, the true measure of the nonlinearity of the system should be $r = \langle\beta'^2_2\rangle^{1/2}/\beta_2$ because the fluctuating component of the viscous drag, $\beta'_\alpha(u_\alpha - v_\alpha)$, is the nonlinear term that cannot be handled analytically and is neglected by assuming $r \ll 1$. This causes an under-prediction of the intensity of particle turbulence which is illustrated in the comparison between the analysis and the Monte-Carlo simulation in Table 1 for M.C.5 and M.C.6. However, note that the particle diffusivities do not show such a trend.

Consider the first four cases in Table 1. The first three have about the same values of r and the differences between the prediction and the simulation are about the same. The fourth has a larger Re_0 ($\approx$11) and larger λ ($\approx$8.1) but smaller r. Overall errors of $\langle v_\alpha^2\rangle$ and $D_{\alpha\alpha}$ are smaller. The last two cases are for higher $\mathrm{Re}u_0$, much larger particle inertia and relatively small or zero gravity. The value of r is 2–3 times larger than in the previous four cases. The larger $\mathrm{Re}u_0$ are associated with larger r and larger errors in predicting β_α, λ, Re_0, $\langle v_\alpha^2\rangle$, and $D_{\alpha\alpha}$. However, it should be pointed out that the last two cases are very extreme. These particles have very large inertia ($\beta_2 < 0.05$) and small settling rates. Though the relative errors in predicting the intensities are as large as 11 percent for the lateral component, the particles have little energy associated with the random motion in such cases. If the gravitational force increases, the value of r will decrease and the prediction will then be improved. In many practical cases of particle dispersion in turbulence, the region of interest in the (β_2, λ) parameter space is where the particle response time is comparable with the local turbulence time scale, say $\beta \sim O(1)$. Under these circumstances, the present nonlinear analysis is adequate to predict β_α, λ, Re_0, $\langle v_\alpha^2\rangle$, and the particle diffusivity.

Figure 1 compares the pdf's of the particle velocity and the particle-fluid slip velocity, predicted by the Monte Carlo simulation, to that from the nonlinear analysis. This is for a case with zero settling rate and very large inertia ($\beta_2 = 0.0473$) at relatively high average particle Reynolds number ($\mathrm{Re}_0 = 10.3$). Even in such a nonlinear situation ($r = 0.126$), the particle velocity follows the Gaussian distribution very well. For a very large settling rate ($\lambda \approx 8.12$), better agreement (not shown here) is observed for both the lateral and longitudinal component. Figure 1 shows that the slip velocity, $v_d = |\mathbf{u} - \mathbf{V}|$, in a three-dimensional space follows the Maxwellian distribution. Thus, it can be concluded that the particle velocity can be approxi-

Table 1 Comparison between the analysis and the simulation of 5000 particles

$u_0 2a/\nu$, $\frac{\beta_S}{k_0 u_0}$, $\frac{u_0^2 k_0}{g}$		$\frac{\beta_2}{k_0 u_0}$	$\lambda = \frac{V_T}{u_0}$	$\frac{\langle u - v \rangle 2a}{v}$	$\frac{\langle v_1^2 \rangle}{u_0^2}$	$\frac{\langle v_2^2 \rangle}{u_0^2}$	$\frac{D_{11}}{k_0 u_0}$	$\frac{D_{22}}{k_0 u_0}$	$\frac{\langle \beta_2'^2 \rangle^{1/2}}{\beta_2}$
1.3289	M.C.1	0.5026	0.0030	1.6423	0.3965		1.0542		0.0511
0.4165	Anal.	0.5052	0	1.6650	0.3835		1.0305		
∞	%	0.52		1.38	3.28		2.25		
1.3289	M.C.2	0.5168	0.9295	2.0433	0.3906	0.3690	0.9815	0.9181	0.0544
0.4165	Anal.	0.5209	0.9599	2.1105	0.3945	0.3599	0.9802	0.9169	
2	%	0.79	3.27	3.29	1.00	2.47	0.13	0.13	
1.3289	M.C.3	0.5445	1.7965	2.8900	0.3936	0.3108	0.8858	0.6830	0.540
0.4165	Anal.	0.5487	1.8226	2.9760	0.3885	0.3084	0.8636	0.7049	
1	%	0.77	1.44	3.13	1.30	0.77	2.51	3.21	
1.3289	M.C.4	0.6011	8.1182	10.9418	0.1999	0.0933	0.2945	0.1561	0.0320
0.3386	Anal.	0.6022	8.1358	10.9912	0.2021	0.0936	0.2992	0.1586	
0.2041	%	0.02	0.22	0.45	1.10	0.32	1.60	1.60	
6.6445	M.C.5	0.0468	0.001	10.280	0.0595		1.1898		0.126
0.0271	Anal.	0.0473	0.0	10.306	0.0553		1.2119		
∞	%	1.07		0.25	7.06		1.86		
13.289	M.C.6	0.0221	1.0291	24.578	0.0298	0.0243	1.1749	1.0104	0.165
0.0095	Anal.	0.0227	1.1011	25.556	0.0282	0.0216	1.0880	0.9650	
40	%	2.71	7.00	3.98	5.37	11.11	7.40	4.49	

M.C.: Monte-Carlo simulation.
Anal. Nonlinear analysis.
%: Percentage difference between M.C. and nonlinear analysis.

mated as Gaussian in the nonlinear drag range provided that the fluid turbulence is Gaussian.

The behavior of the ensemble averaged particle diffusivities (using 4000 particles) is shown in Fig. 2 for the case at zero settling with strong nonlinearity, $\mathrm{Re}_0 = 10.3$. The long time values of the diffusivities, $D_{\alpha\alpha}(\tau)$, obtained from the nonlinear analysis and from the time average of the simulation are also included. Good agreement is observed. The fluctuation of $D_{\alpha\alpha}(\tau)$ at large time is typical for an ensemble of this size. Similar agreement for $D_{\alpha\alpha}$ is obtained for a large settling rate ($\lambda \approx 8.12$).

Figure 3 compares the normalized particle velocity correlation functions, $C_{\alpha\alpha}(\tau) = R_{v_\alpha v_\alpha}(\tau)/\langle v_\alpha^2 \rangle$, found from the Monte-Carlo simulation and predicted by using the nonlinear analysis for three cases. The first case is for $C_{11}(\tau)$ at $\lambda \approx 1$. The analytical prediction needs an interpolation in order to obtain λ and β_α. As shown, the results from the simulations and the nonlinear analysis are in very good agreement. The second case corresponds to a very large settling rate, $\lambda \approx 8.12$. The analytical results, based on the interpolation, are very close to the asymptotic result that uses Taylor's frozen field hypothesis, and to the results from the Monte-Carlo simulation.

Comparisons of the correlation function of the fluid velocity fluctuations seen by the particle, $R^p_{u_\alpha u_\alpha}(\tau)$, obtained by the simulation and by the nonlinear analysis, are shown in Fig. 4 for particles with $\lambda \approx 8.12$. Good agreement is observed. Figure 4 indicates that the statistics of the fluid turbulence seen by the particle is approximated quite well by the analysis, even with two sources of nonlinearity. From the comparisons of both $R^p_{u_\alpha u_\alpha}(\tau)$ (input) and $C_{11}(\tau)$ (output) obtained with the simulation and the nonlinear analysis, it is concluded that the nonlinear behavior of the particle motion is accurately approximated by the quasi-linear equation (12).

Comparison With the Experimental Data Of Wells and Stock (1983). Figure 5 compares predicted particle diffusivities with the measurements of Wells and Stock (1983) in decaying grid turbulence. The particle diameter is 57 μm and the material density, $\rho_p = 2420$ kg/m^3. The fluid rms velocity is taken as $u_0 = 14.6$ cm/s in the prediction. The fluid diffusivity is approximated by that of 5 μm particles, $D_f \sim 4.9$ cm^2/s. Since the fluid diffusivity is $D_f \sim 0.903 u_0/k_0$, this gives $k_0 \sim 2.69$ cm^{-1} or $\omega_0 \sim 39.3$ s^{-1}. Thus $v_f \sim 0.1505$ cm^2/s, $\mathrm{Re} u_0 \sim 0.553$ and $\beta_S \sim 1.079$. The particle Reynolds number exceeds one at large set-

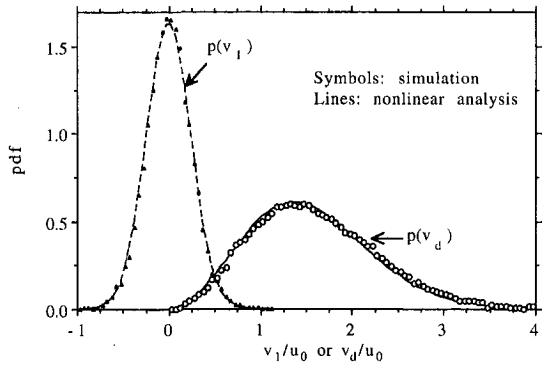

Fig. 1 Comparison of pdf's of particle velocities between Monte-Carlo simulation and nonlinear analysis. $\mathrm{Re} u_0 = (u_0 2a)/\nu = 6.6445$, $\beta_S/(k_0 u_0) = 0.0271$, $V_T = 0$; Fg $= (u_0^2 k_0)/g = \infty$, $N_p = 1000$ for $p(v_1)$ and $N_p = 2000$ for $p(v_d)$.

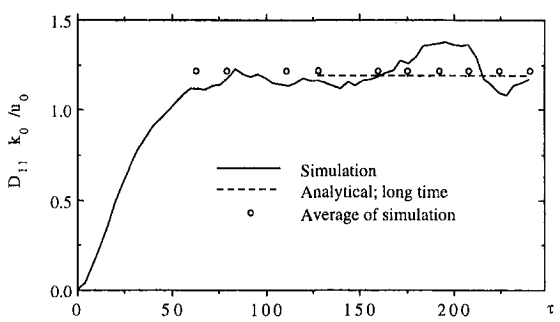

Fig. 2 Ensemble averaged ($N_p = 4000$) particle diffusivity D as a function of time at: $(u_0 2a)/\nu = 6.6445$, $\beta_S/(k_0 u_0) = 0.0271$, $(u_0^2 k_0)/g = \infty$, $V_T = 0$

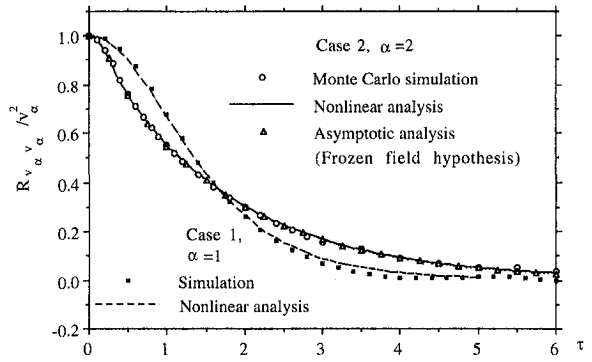

Fig. 3 Comparison of normalized correlation functions of particle velocity between simulation (N_p = 4000) and analyses.
Case 1 (α = 1): $(u_0 2a)/\nu$ = 4, $\beta_S/(k_0 u_0)$ = 0.6667, $(u_0^2 k_0)/g$ = 1; $\lambda = V_T/u_0 \approx$ 0.98, $Re_0 = \langle(|u - V|2a)/\nu\rangle \approx$ 5.623.
Case 2 (α = 2): $(u_0 2a)/\nu$ = 1.3289, $\beta_S/(k_0 u_0)$ = 0.3386, $(u_0^2 k_0)/g$ = 0.204; $\lambda = V_T/u_0 \approx$ 8.12, $Re_0 = \langle(|u - V|2a)/\nu\rangle \approx$ 11.

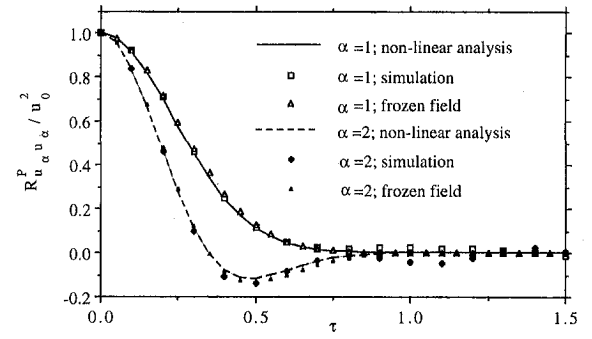

Fig. 4 Comparison of fluid velocity correlation functions seen by the particle between the simulation (N_p = 4000) and analysis.
$(u_0 2a)/\nu$ = 1.3289, $\beta_S/(k_0 u_0)$ = 0.3386, $(u_0^2 k_0)/g$ = 0.204; $V_T/u_0 \approx$ 8.12, $\langle(|u - V|2a)/\nu\rangle \approx$ 11.

tling velocity. In the experiment, the transverse component of the particle diffusivity was obtained by measuring the mean square displacement in the normal direction. As can be seen, the comparison is quite satisfactory in view of the difficulties in measuring the diffusivity and in using a low Reynolds number energy spectrum in the analysis.

Results of the Nonlinear Analyses

Particle Turbulence. The primary results of the nonlinear analyses are the root-mean square of the turbulent velocity and

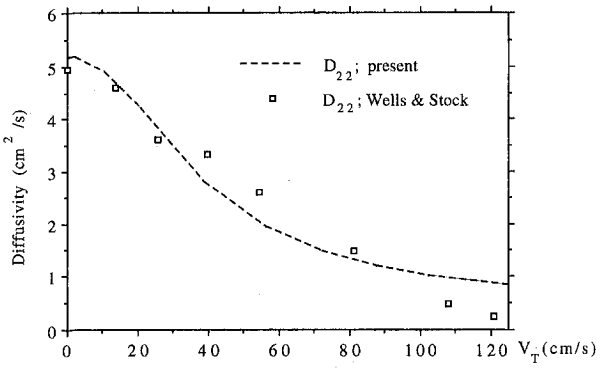

Fig. 5 Comparison of the particle diffusivities with experimental data of Wells and Stock (1983)

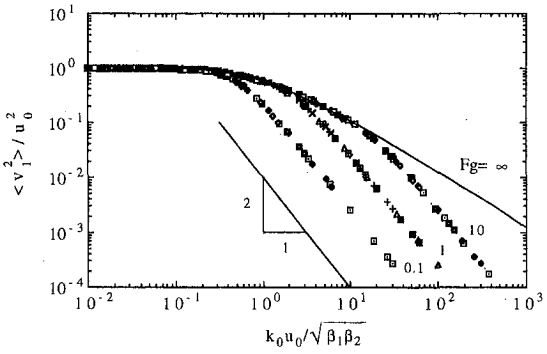

Fig. 6(*a*)

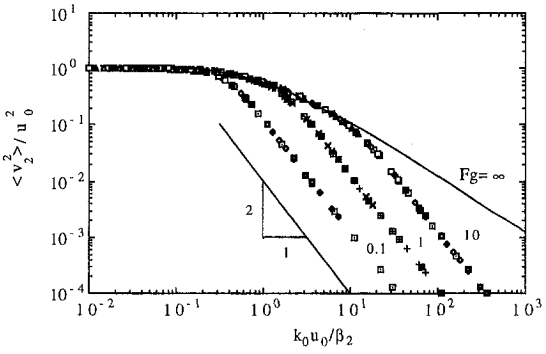

Fig. 6(*b*)

Fig. 6 Dependence of particle intensities on $\sqrt{\beta_1\beta_2}/k_0u_0$ and $\beta_2/(k_0u_0)$ at Fg = $(u_0^2k_0)/g$ = 0.1, 1, 10 and ∞. For each Fg, data correspond to Re_{u_0} = $(u_0 2a)/\nu$ = 0.1, 0.5, 1, 5, 10, and 25. (*a*) longitudinal; (*b*) lateral.

the turbulent diffusivity in directions parallel ($\langle v_1^2\rangle$, D_{11}) and perpendicular ($\langle v_2^2\rangle$, D_{22}) to the direction of gravity. These are obtained from the extension of Reek's analysis to the case of anisotropic time constants (equations (4–29)). The dimensionless groups that enter into the analysis are Fg, β_α, Re_{u_0}, and γ.

Figures 6(*a*) and 6(*b*) can be used to estimate $\langle v_1^2\rangle$, $\langle v_2^2\rangle$ and D_{11}, D_{22}, if k_0, u_0, β_α, and λ are known. It is noted that Re_{u_0} and λ do not enter into the correlation since they affect only the estimate of β_α. The longitudinal intensity of the particle turbulence depends on Fg, β_1, and β_2; in the linear range it depends only on Fg and β_2. Note that $\langle v_1^2\rangle$ is proportional to $\beta_1\beta_2$ at $\lambda \to \infty$, as shown by (32*a*), and that β_1 and β_2 are close in value when $\lambda \to 0$. Therefore $(\beta_1\beta_2)^{-1/2}$ is used as the abscissa in Fig. 6(*a*). Calculations from the nonlinear theory, given in

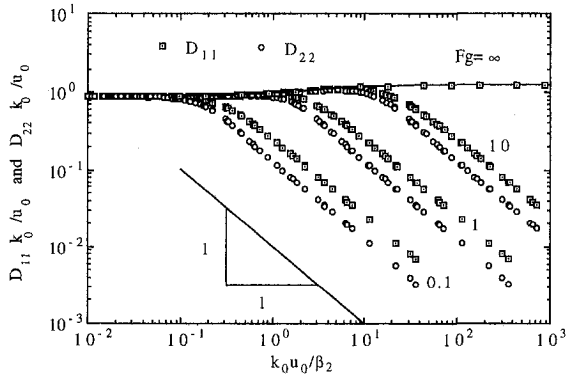

Fig. 7 Dependence of particle dppiffusivities on β_2/k_0u_0 at Fg = $(u_0^2k_0)/g$ = 0.1, 1, 10 and ∞. For each Fg, data correspond to Re_{u_0} = $(u_0 2a)/\nu$ = 0.1, 0.5, 1, 5, 10, and 25.

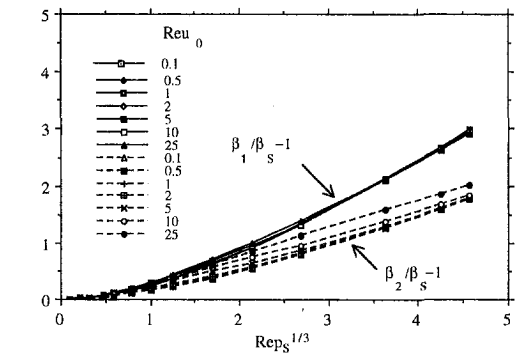

Fig. 8(a)

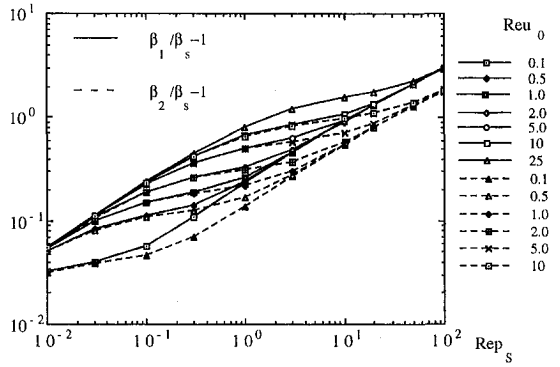

Fig. 8(b)

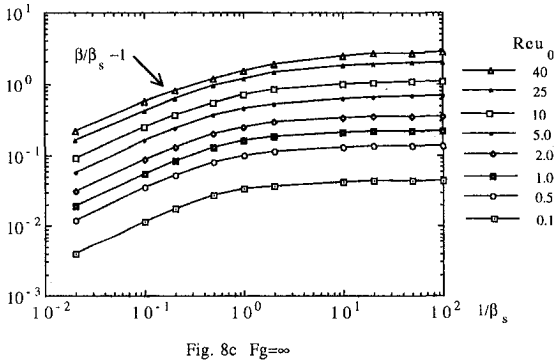

Fig. 8c Fg=∞

Fig. 8(c)

Fig. 8 Particle inertial parameters as functions of Rep_S = (4/9) ($(\rho a^3 g)/\nu^2$) or $\beta_S/(k_0 u_0)$ at different values of Fg = $(u_0^2 k_0)/g$ and Reu_0 = $(u_0 2a)/\nu$ (ranging from 0.1 to 100). (a) Fg = 1.0; (b) Fg = 10; (c) Fg = ∞.

Fig. 6(*a*), shows that $\langle v_1^2 \rangle$ is correlated very well by Fg and $(\beta_1\beta_2)^{1/2}$. The lateral component is related only to Fg and β_2 regardless of the values of the turbulence particle Reynolds number Reu_0.

Calculated values of the particle diffusivities D_{11} and D_{22} can also be characterized by Fg and β_2, as shown in Fig. 7. Thus, both the intensities and the diffusivities can be described by two parameters, instead of three, in the nonlinear drag range. It is interesting to note that the particle diffusivity is larger than that of the fluid diffusivity in the nonlinear drag range if Fg is large and β_2 is finite, as shown in Fig. 7. This is consistent with the result of Reeks obtained for the linear drag case.

Particle Inertial Parameter. The particle inertial parameter, β_α, needs to be estimated in order to use Figs. 6 and 7. Figure 8 shows that the calculated value of β_α, normalized by the value for Stokesian drag, β_S, depends on Fg, Rep_S, and Reu_0. The inertial parameters are seen to be strongly anisotropic at large Rep_S. For Fg $\leq$ 0.1, the effect of turbulence on β_α, is small because the effect of gravitational settling is strong. For Reu_0 varying from 0.1 to 100, β_α/β_S remains almost unchanged. Thus, the values of β_α/β_S, can be easily computed by assuming Reu_0 = 0 for Fg $\leq$ 0.1.

Figure 8(*a*) shows the behavior of β_α/β_S for Fg = 1. When particle size (or $Rep_S^{1/3}$) increases, β_S increases, as does the anisotropy of β_α. It can be seen that the turbulence has little effect on β_1 at Fg = 1. However, the effect of Reu_0 on β_2 is very clear. As Reu_0 increases, the nonlinearity becomes stronger. Consequently, the effective particle inertia in the lateral direction decreases due to an increase in the instantaneous drag and the strong nonlinearity. This effect is more pronounced at higher values of Fg, as shown in Fig. 8(*b*) for Fg = 10. At Fg $\geq$ 10, the gravitational effect is relatively weak and the anisotropy in β_α is not so strong as for smaller Fg. Asymptotic values exist for β_1 and β_2 as $Rep_S \to \infty$ for all values of Reu_0 at finite Fg; they are given by (13).

The effect of turbulence on β_α, that arises because of the nonlinearity of the drag, is seen most clearly in Fig. 8(*c*) for Fg $\to \infty$. In the absence of body forces, it is very difficult to obtain the effective particle inertial parameter β in the nonlinear drag range because the only velocity known a priori to define the particle Reynolds number is the turbulence rms velocity u_0, which gives Reu_0. However, Reu_0 is not the particle Reynolds number $Re_0 = \langle |\mathbf{u} - \mathbf{V}| \rangle 2a/\nu$. If Stokes drag law is used, a 10 percent error would exist in the calculation of Re_0 at $Reu_0 \geq$ 0.5 when $\beta_S \leq 1$. A 100 percent error would result from the use of the Stokes drag law for $Reu_0 \geq 10$ and $\beta_S \leq 0.1$. The results in Fig. 8 are thus useful when Fg is large. This can occur at large flow rates when the fluid turbulence is large.

The Settling Rate. The role of fluid turbulence or fluid oscillation in the direction of gravity in decreasing particle settling velocity V_T has been known for years (Tunstall and Houghton, 1968; Murray 1970; Schöneborn, 1975; Hwang, 1985; Ikeda and Yamasaka, 1989; Mei, 1990). The mechanism for the decrease in V_T is the increase in the average drag caused by the fluid turbulence or unsteadiness when the drag law is nonlinear. An increase in the particle settling velocity has also been recently discovered (Maxey, 1987) and thoroughly examined using a direct numerical simulation (Wang and Maxey, 1993). The mechanism for the increase in V_T is a preferential concentration (or trajectory bias) of particles in regions of larger strain rate and lower vorticity. The preferential concentration was found to have a profound effect on increasing the settling velocity when the particle response time is close to the Kolmogorov time scale and when the particle Reynolds number is small. Wang and Maxey (1993) also reported that V_T can be reduced from that observed in a still fluid when the particle Reynolds number exceeds one and the drag law is in the nonlinear range.

By using Monte-Carlo simulations with linear and nonlinear drag laws, the effects of these competing mechanisms on the particle settling velocity were investigated in Mei (1994a) using the low Reynolds number energy spectrum given by equation (16). The parameter γ was varied from 0 (frozen turbulence limit) to 3. Maxey's (1987) finding was reproduced in the linear drag range. For non-frozen turbulence the effect of trajectory bias on the settling was found to be small in comparison with the effect of the nonlinear drag associated with the turbulence when the particle Reynolds number is of order one. It is noted that both the energy spectrum and the small scale turbulence structure in the DNS are more realistic than that in the random Fourier modes representation of the pseudo turbulence used in the Monte-Carlo simulation. Thus it is not possible to draw a precise boundary in a multi-parameter space (particle inertia, settling velocity, particle Reynolds number) to separate regions of settling velocity enhancement and settling velocity reduction based on the Monte Carlo simulation (Mei, 1994a). In this paper, the interpolation formula for the settling velocity does not take into account the effect of preferential concentration on reducing V_T; hence the present analysis is mostly applicable

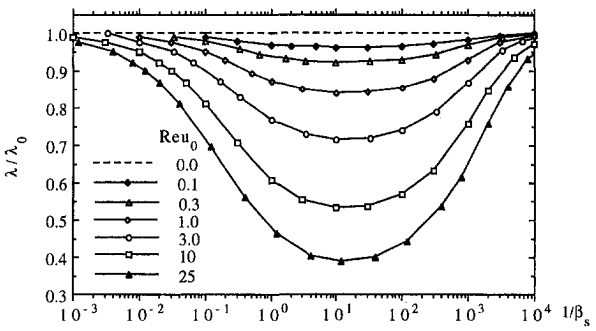

Fig. 9 Effect of turbulence on the particle settling velocity. $\lambda_0 = V_T/u_0$ is the settling rate of particle in a still fluid at $Reu_0 = (u_0 2a)/\nu \to 0$ and $Fg = (u_0^2 k_0)/g = 1000$.

when the drag law is in the fully nonlinear range and the particle response time is larger than the Kolmogorov time scale. Some error due to the neglect of preferential concentration is expected when a linear drag law is applicable.

Define λ_0 as the particle settling rate for the case of zero turbulence, i.e., in a still fluid. It approaches $V_{TS}/u_0 = 1/(\mathrm{Fg}\,\beta_S)$ if the particle Reynolds number is much less than one, where Fg is defined by (19). A common practice among hydrologists in studying the sedimentation of sand particles in rivers is to include the part of the added mass force related to the particle acceleration and to neglect terms containing fluid acceleration, such as $(2/3)\pi a^3 \rho_f (d\mathbf{u}/dt)$ and $(2/3)\tau a^3 \rho_f (D\mathbf{u}/Dt)$ (Mei, 1994b), and the history force term in the particle equation of motion. Such a procedure gives

$$\beta_s \to \beta_s \Big/ \left(1 + \frac{1}{2\rho}\right). \tag{54}$$

A modified Froude number

$$\mathrm{Fg}' = \mathrm{Fg}\ (\rho + 1/2)/(\rho - 1) \tag{55}$$

which can be used instead of Fg. It is noted that Fg′ is exactly the quantity xf used by Ikeda and Yamasaka (1989) where χ is $\rho' = (\rho - 1)/(\rho + 1/2)$.

The influences of Fg, β_s, and Reu_0 on λ/λ_0 is illustrated in Fig. 9 for Fg or Fg′ = 1000 and $\gamma = 1$. As $\beta_s \to 0$ or ∞, $\lambda/\lambda_0 \to 1$ regardless the values of Reu_0 and Fg. This can be explained as follows: for $\beta_s \to \infty$, the particle inertia is very small and the particle closely follows the fluid turbulence. Thus the slip velocity between the particle and the fluid is effectively given by the settling velocity and is not affected by the turbulence. For $\beta_s \to 0$, the particle inertia is very large so that the particle fluctuating velocity is much smaller than the particle settling velocity. Then the particle settles in an effectively still fluid. For particles with β_s of order one, the effect of the fluid turbulence is the strongest: This is because the particle follows the motion of the fluid to some extent, but still retains some velocity difference from the fluid. If the settling rate is not high, the fluid turbulence becomes a more important factor in determining the average slip velocity. At Fg = 1 and 10 (not shown here), there are 17 and 30 percent decrease in the settling velocity as Reu_0 increases from 0 to 25 at $\beta_s \sim O(1)$. At Fg = 1000, which implies a very small gravitational force compared to the inertial force of the fluid turbulence, the reduction in λ is more than 60 percent at $\beta_s = 10$.

Summary and Conclusions

The analysis of Reeks (1977) for the stationary behavior of particles in a Gaussian, isotropic turbulence has had an important impact because it provides a means to estimate particle turbulence as a function of the inertial time constant, β_S^{-1}, and the terminal velocity of the particle, V_T. The representation of the drag by Stokes drag simplifies the problem because β_s is independent of the slip velocity.

This paper extends Reek's analysis by using a nonlinear drag law. The results have the same limitations as Reeks' analysis in that the fluid turbulence is assumed to be isotropic and Gaussian. The principal contributions are the extension of Reeks' analysis to the case of anisotropic time constants (Eqs. (14)–29) and the development of approximate relation for the anisotropic particle time constants β_α^{-1}, and the average slip velocity.

In the limit of large V_T, $(u_0/V_T)^2 \ll 1$, the turbulence terms in (8), (45), and (48) can be ignored. Therefore, the average effective slip velocity, V_d, is given by V_T and β_α by (13a, b). It is noted that the inertial time constant in the direction of gravity, β_1^{-1}, is smaller than that in the direction perpendicular to the gravity, β_2^{-1}. A consequence of this is that the particle follows turbulent velocity fluctuations in the direction of gravity better than in the directions perpendicular to the gravity.

For the case of $V_T = 0$, slip occurs because of turbulent velocity fluctuations of the particles and the fluid. By assuming a Gaussian distribution for the particle velocity, Eq. (44) is derived for an average magnitude of the slip velocity v_d. Because there is no preferred direction, β_α is isotropic. A mean value, $\langle\beta\rangle$, is related to V_d. In order to utilize Reeks' analysis the equation of motion of the particle is linearized. This requires the assumption that the fluctuations in β are small comparing with $\langle\beta\rangle$ and limits the applicability of the nonlinear analysis.

Interpolation formulae are used to evaluate β_α, settling velocity V_T, and the slip velocity, V_d, for the situations when $V_T/u_0 = O(1)$. See Eqs. (45), (48a, b), and (49a, b).

The primary results are the prediction of root-mean-square turbulent velocity fluctuations and the turbulent diffusivity in directions parallel ($\langle v_1^2\rangle$, D_{11}) and perpendicular ($\langle v_2^2\rangle$, D_{22}) to the direction of gravity given in Fig. 6 and Fig. 7. The inertial time constants in these figures are calculated from the interpolation formulas (48a, b). These interpolation formulae contain a Reynolds number, Re_0, based on effective slip velocity that is approximated by (45). Quantities u_0 and k_0 are specified by the magnitude of the fluid velocity fluctuation and the length scale of the fluid turbulence.

One of the concerns when a nonlinear drag law is used is the estimation of the effects of the turbulence on the settling velocity, the mean slip velocity, and the inertial time constants. The analyses presented in this paper predicts that fluid turbulence decreases V_T. This is consistent with a body of previous work cited in the Introduction. While both mechanisms (reduction and enhancement of settling velocity V_T) can be in force, the analysis presented in this paper pertains to the case when the drag nonlinearity is strong.

Acknowledgment

This work was partly supported by NSF through CBT 88-00980 and ATM 89-20605.

References

Basset, A. B., 1888, *A Treatise On Hydrodynamics,* Vol. 2, Dover Publications Inc.

Chao, B. T., 1964, "Turbulent Behavior of Small Particles in Dilute Suspension," *Osterreichisches Ingenieur-Archiv,* Vol. 18, pp. 7–21.

Clift, R., Grace, J. R., and Weber, M. E., 1978, *Bubbles, Drops and Particles,* Academic Press.

Corrsin, S., 1959, "Progress Report on Some Turbulent Diffusion Research," *Advances in Geophysics 6, Academic Press, 161–184.*

Corrsin, S., and Lumley, J. L., 1956, "On the Equation of Motion for a Particle in a Turbulent Fluid," *Applied Scientific Research,* Vol. A6, pp. 114–116.

Csanady, G. T., 1963, "Turbulent Diffusion of Heavy Particles in the Atmosphere." *Journal of Atmospheric Science,* Vol. 20, pp. 201–208.

Hinze, J. O., 1975, *Turbulence.* McGraw-Hill.

Hwang, P. A., 1985, "Fall Velocity of Particles in Oscillating Flow," *Journal of Hydraulic Engineering,* Vol. 111, pp. 485–502.

Ikeda, S., and Yamasaka, M., 1989, "Fall Velocity of Single Spheres in Vertically Oscillating Fluids," *Fluid Dynamics Research,* Vol. 5, pp. 203–216.

Kada, H., and Hanratty, T. J., 1960, "Effects of Solids on Turbulence in a Fluid," *AIChE Journal,* Vol. 6, pp. 624–630.

Kraichnan, R. H., 1970, "Diffusion by a Random Velocity Field," *Physics of Fluids,* Vol. 13, pp. 22–31.

Lumley, J. L., 1957, "Some Problems Connected with the Motion of Small Particles in Turbulent Fluid," Ph.D thesis, The John Hopkins University, Baltimore, Md.

Lumley, J. L., 1978, "Two-Phase and Non-Newtonian Flows," Chapter 7 in *Turbulence,* P. Bradshaw, ed., Springer-Verlag.

Lundgren, T. S., and Pointin, Y. B., 1976, "Turbulent Self-Diffusion," *Physics of Fluids,* Vol. 19, pp. 355–358.

Maxey, M. R., 1987, "The Gravitational Settling of Aerosol Particles in Homogeneous Turbulence and Random Flow Fields," *Journal of Fluid Mechanics,* Vol. 174, pp. 441–465.

Mei, R., 1990, "Particle Dispersion in isotropic Turbulence and Unsteady Particle Dynamics at Finite Reynolds Number," Ph.D thesis, University of Illinois at Urbana-Champaign, Urbana, IL.

Mei, R., 1994*a*, "Effect of Turbulence on the Gravitational Settling Velocity in Non-Linear Drag Range," *International Journal of Multiphase Flow,* Vol. 20(2), pp. 273–284.

Mei, R., 1994*b*, "Flow Due to an Oscillating Sphere and an Expression for Unsteady Drag on the Sphere at Finite Reynolds Number," *Journal of Fluid Mechanics,* Vol. 270, pp. 133–174.

Mei, R., and Adrian, R. J., 1992, "Flow Past a Sphere with an Oscillation in the Free-Stream and Unsteady Drag at Finite Reynolds Number," *Journal of Fluid Mechanics,* Vol. 237, pp. 323–341.

Mei, R., Adrian, R. J., and Hanratty, T. J., 1991, "Particle Dispersion in Isotropic Turbulence Under Stokes Drag and Basset Force with Gravitational Settling," *Journal of Fluid Mechanics,* Vol. 225, pp. 481–495.

Mei, R., Adrian, R. J., and Hanratty, T. J., 1993, "Particle Dispersion in Isotropic Turbulence Under Non-Stokesian Drag with Gravitational Settling," TAM Report No. 735, UILU-ENG-93-6033.

Mei, R., Lawrence, C. J., and Adrian, R. J., 1991, "Unsteady Drag on a Sphere at Finite Reynolds Number With Small Fluctuations in the Free-Stream Velocity," *Journal of Fluid Mechanics,* Vol. 233, pp. 613–628.

Murray, S. P., 1970, "Settling Velocities and Vertical Diffusion of Particles in Turbulent Water," *Journal of Geophysical Research,* Vol. 75, pp. 1647–1654.

Nielsen, P., 1984, "On the Motion of Suspended Sand Particles," *Journal of Geophysical Research,* Vol. 89, pp. 616–626.

Nir, A., and Pismen, L. M., 1979, "The Effect of a Steady Drift on the Dispersion of a Particle in Turbulent Fluid," *Journal of Fluid Mechanics,* Vol. 94, pp. 369–381.

Phythian, R., 1975, "Dispersion of Random Velocity Fields," *Journal of Fluid Mechanics,* Vol. 67, pp. 145–153.

Pismen, L. M., and Nir, A., 1978, "On the Motion of Suspended Particles in a Stationary Homogeneous Turbulence," *Journal of Fluid Mechanics,* Vol. 84, pp. 193–206.

Reeks, M. W., 1977, "On the Dispersion of Small Particles Suspended in an Isotropic Turbulent Fluid," *Journal of Fluid Mechanics,* Vol. 83, pp. 529–546.

Reeks, M. W., 1980, "Eulerian Direct Interaction Applied to the Statistical Motion of Particles in Turbulent Field," *Journal of Fluid Mechanics,* Vol. 97, pp. 569–590.

Schöneborn, P.-R., 1975, "The Interaction Between a Single Particle and Oscillating Fluid," *International Journal of Multiphase Flow,* Vol. 2, pp. 307–317.

Stokes, G. G., 1851, "On the Effect of Internal Friction of Fluids on the Motion of Pendulum," *Trans. Camb. Phil. Soc.,* Vol. 9, p. 8. Reprinted in *Math. and Physics Papers III,* Cambridge University Press, 1922.

Tunstall, E. B., and Houghton, G., 1968, "Retardation of Falling Spheres by Hydraulic Oscillations," *Chemical Engineering Science,* Vol. 23, pp. 1067–1081.

Tchen, C. M., 1947, "Mean Value and Correlation Problems Connected With the Motion of Small Particles Suspended in a Turbulent Fluid," Ph.D thesis, Delft University, Netherlands.

Wang, L. P., and Maxey, M. R., 1993, "Settling Velocity and Concentration Distribution of Heavy Particles in Homogeneous Isotropic Turbulence," *Journal of Fluid Mechanics,* Vol. 256, pp. 27–68.

Wells, M. R., and Stock, D. E., 1983, "The Effects of Crossing-Trajectories on the Dispersion of Particles in a Turbulence Flow," *Journal of Fluid Mechanics,* Vol. 136, pp. 31–62.

Yudine, M. I., 1959, "Physical Consideration on Heavy Particle Diffusion," *Advances in Geophysics,* Vol. 6, New York, Academic Press, pp. 185–191.

Contaminant Transport Through Single Fracture With Porous Obstructions

J. L. Lage
J. Lindsay Embrey Associate Professor,
Mechanical Engineering Department,
Southern Methodist University,
Dallas, TX, 75275-0337
Mem. ASME

Transport of contaminant through a single fracture, modeled as a closely spaced parallel plates aperture, is analyzed theoretically and numerically. Permeable contact regions between the plates are modeled as fixed packs of homogeneous, isotropic, and inert porous material. A nondimensional theoretical expression for estimating the equivalent global permeability of the aperture is presented in terms of the relative volume occupied by the contact regions. Transient transport of contaminant (solute) through this heterogeneous system is analyzed considering injection of fluid with uniform concentration at the inlet of the fracture. For natural systems, it is verified that relative volume and distribution of contact regions affect clean-up time, defined as the time necessary for the complete removal of contaminant, only indirectly by varying the equivalent permeability of the system, otherwise their effect is negligible. The clean-up time of a clear (of contact regions) fracture, is correlated with the Peclet number for $10^{-1} \leq Pe \leq 10^{6}$.

Introduction

The areas of groundwater flow of contaminants, geothermal energy extraction, geological disposal of nuclear waste, and enhanced oil recovery, emerged in recent years as areas of increased research activity. These areas have in common the very irregular medium in which the transport processes take place. One example is the medium composed of fluid flowing through small apertures (fractures) within rocks. In recent years, such irregular geological formations have been considered as good candidates for radioactive waste isolation (Buddemeier and Hunt, 1988; Thoma et al., 1992). To the hydrogeologist, they represent conduits for the movement of contaminants in clay acquitards, clay liners, rock acquitards, and acquifers (Mackay and Cherry, 1989).

The understanding of fluid flow through small apertures is fundamental for the macroscopic characterization of transport processes through geological faults (Montazer and Wilson, 1984) and fractured rocks (Pyrak-Nolte et al., 1987). Three main flow regimes are known to exist within a fracture: Darcy flow (Darcy, 1856), cubic law flow (Snow, 1968), and capillary flow (Wang and Narasimhan, 1985). Proposed flow models include: fractures in porous media (Sudicky and Frind, 1982), channel flow (Rasmuson and Neretnieks, 1986), and variable aperture fractures (Tsang and Tsang, 1987). More complex fractals and network models were reviewed by Sahimi (1993).

There are numerous conceptual models for flow and transport in single fracture (for an extensive review see Novakowski and Lapcevic, 1994). Tsang and Tsang (1989), for instance, showed that the bulk of the flow tends to coalesce into preferred flow paths or channels that offer least resistance to the flow. Muralidhar (1990) presented a very interesting study of flow and transport in single rock fracture modeled as parallel plates with impermeable contact areas. His mathematical approach was based on Stokes flow where the convective inertia term of the momentum equation is neglected. This model is known to be valid for small fluid velocity (Schlichting, 1979) as in the case of fluid flowing *naturally* through rock fractures with small apertures. His results showed, among other things, that the equivalent permeability is a weak function of the shape of the contact areas as long as the average aperture is small.

The present study considers steady flow through a fully saturated fracture with *permeable* contact areas where additional viscous and form drag effects have to be accounted for. These permeable contact areas simulate, for instance, fracture-filling material accumulated near contact regions between two rough-walled fracture surfaces (Eaton and Bixler, 1987; Festoy and Van Golf-Racht, 1989), or poorly characterized secondary minerals formed by weathering reactions that can partially or completely clog fractures (Thoma et al., 1992). It is also a simplified model of colloids, characterized as porous material, known to deposit and partially clog a fracture (Kessler and Hunt, 1993).

The present model includes multidirectional convective and diffusive effects, with the convective inertia term included in the momentum equation leading to a more general mathematical model of the momentum transport within a fracture. This extended momentum transport model is believed to be essential for simulating the transport of contaminant by injection of high speed fluid during clean-up, a situation in which inertia effects can not be neglected. For simplicity, the permeable contact areas are assumed as homogeneous, isotropic, and inert, and the solid surfaces of the fracture are assumed impermeable to contaminant (solute) diffusion. The model extends the works of Tsang and Tsang (1989) and Muralidhar (1990).

Formulation

Consider an incompressible Newtonian fluid with constant properties saturating a single rock fracture. The rock fracture is modeled as a thin rectangular channel with equivalent aperture h, formed by two parallel plates, having contact regions composed of rigid, homogeneous and isotropic porous material, Fig. 1. The three dimensional balance equations of mass, momentum and species concentration are, respectively,

$$\nabla \cdot \mathbf{W} = 0 \tag{1}$$

$$(\mathbf{W}\nabla)\cdot \mathbf{W} = -\frac{1}{\rho}\nabla p + \nu\nabla^2\mathbf{W} - \frac{\nu\phi}{K}\mathbf{W} - \frac{c_F\phi^2}{K^{1/2}}|\mathbf{W}|\mathbf{W} \tag{2}$$

$$\frac{\partial C}{\partial t} + \mathbf{W}\cdot\nabla C = D\nabla^2 C \tag{3}$$

Contributed by the Fluids Engineering Division for publication in the JOURNAL OF FLUIDS ENGINEERING. Manuscript received by the Fluids Engineering Division July 27, 1995; revised manuscript received April 2, 1996. Associate Technical Editor: F. Giralt.

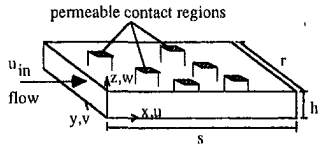

Fig. 1 Single rock fracture: rectangular channel with permeable contact regions

where $\mathbf{W}$ is the local fluid intrinsic velocity, $\mathbf{W} = u\mathbf{i} + v\mathbf{j} + w\mathbf{k}$, p is the fluid pressure, t is the time, C is the species concentration, ρ, ν, and D are the fluid density, kinematic viscosity, and mass diffusivity, and ϕ, K, and c_F are the porosity, permeability, and Forchheimer inertia coefficient of the porous medium, respectively. Other parameters of interest are the equivalent width, h, depth, r, and length, s, of the fracture (see Fig. 1).

The momentum transport Eq. (2) is somewhat uncommon when dealing with underground hydrologic clear fluid or saturated porous systems. A concise derivation of it can be found in Hsu and Cheng (1990). The physical meaning of most terms can be found in detail in Nield and Bejan (1992). Notice that the equivalent porous medium viscosity is assumed as equal to the fluid viscosity in Eq. (2).

Equations (1)–(3) model the transient transport of species with a steady flow. That the flow through a fully saturated single rock fracture reaches steady state almost instantaneously was showed by Muralidhar (1990). The same is generally true also for flow through fully saturated porous medium, as noted by Nield (1991).

Boundary and initial conditions are impermeable and nonslip at the solid surfaces ($u = v = w = 0$, at $y = 0$ and r, and at $z = 0$ and h), steady fully developed inlet flow ($u = u(y, z)$, $v = w = 0$ at $x = 0$) with averaged velocity equal to u_{in}, uniform inlet concentration ($C = C_{in}$ at $x = 0$), nondiffusing solid surfaces ($\partial C/\partial y = 0$ at $y = 0$ and r, and $\partial C/\partial z = 0$ at $z = 0$ and h) and uniform initial concentration ($C = C_0$ at $t = 0$). A nondiffusion condition is imposed at the outlet of the fracture ($\partial C/\partial x = 0$ at $x = s$).

The two rightmost terms, respectively Darcy and Forchheimer terms, of the general momentum equation for fluid flow through saturated porous medium (Hsu and Cheng, 1990), Eq. (2), model the impeding effect (viscous drag and form drag) imposed on the fluid flow by the porous contact regions. These two terms are absent within a clear fluid region where $\phi = 1.0$ and $K \to \infty$.

Secondary transversal dispersion effects within the fracture, not accounted for in Eq. (3), are negligible (Hsu and Cheng, 1990) if fluid molecular diffusion (D) is much larger than the dispersion diffusion ($\sim u_{in}h$). Notice that with no mass transfer through the solid surfaces of the fracture, the species transport by convection and diffusion is essentially longitudinal (along the x axis) in the present configuration.

Considering a fracture with slender geometry, $h \ll (r, s)$, the vertical (z) variation of pressure can be neglected. The velocity field is then assumed to be fully developed in z within both, clear fluid and porous, regions. The horizontal velocity components can be written as the product of the h-averaged horizontal velocity components, u' and v', with a shape function that determines the velocity profile in the z direction, $g(z)$:

$$p(x, y, z) = p'(x, y) \tag{4}$$

$$u(x, y, z) = u'(x, y)g_{f,s}(z) \tag{5}$$

$$v(x, y, z) = v'(x, y)g_{f,s}(z) \tag{6}$$

$$w(x, y, z) = 0 \tag{7}$$

The double subscript in shape function g (f for fluid and s for porous region) anticipates different velocity profiles for flow within a clear fluid region and for flow within a porous region. The concentration is also considered to have negligible variation in the z-direction, so

$$C(x, y, z) = C'(x, y) \tag{8}$$

With Eqs. (4)–(8), the three dimensional balance Eqs. (1)–(3) valid for a slender fracture, become,

$$\nabla \cdot \mathbf{W}' = 0 \tag{9}$$

$$g_{f,s}^2(\mathbf{W}'\nabla)\cdot\mathbf{W}' = -\frac{1}{\rho}\nabla p' + g_{f,s}\nu\nabla^2\mathbf{W}' - \left(-\frac{d^2 g_{f,s}}{dz^2} + g_s\frac{\phi}{K}\right)\nu\mathbf{W}' - g_s^2\frac{c_F\phi^2}{K^{1/2}}|\mathbf{W}'|\mathbf{W}' \tag{10}$$

$$\frac{\partial C'}{\partial t} + g_{f,s}\mathbf{W}'\cdot\nabla C' = D\nabla^2 C' \tag{11}$$

where now $\mathbf{W}' = u'\mathbf{i} + v'\mathbf{j}$. Notice that the shape function of the Darcy and Forchheimer terms do not carry the subscript f since these two terms are identically zero within a clear fluid

Nomenclature

c_F = Forchheimer coefficient
C = species concentration, kg/m^3
D = mass diffusivity, m^2/s
Da = Darcy number, Eq. (18)
f, F, $F^{(2)}$ = shape factors, Eqs. (15)–(17)
g = shape function
h = fracture width, m
p = pressure, Pa
P = nondimensional pressure, Eq. (18)
Pe = Peclet number, Pe = Re Sc
K = permeability, m^2
r = fracture depth, m
R = nondimensional fracture depth
Re = Reynolds number, Eq. (18)
s = fracture length, m
S = nondimensional fracture length
Sc = Schmidt number, Eq. (18)
t = time, s
u, v, w = Cartesian fluid intrinsic velocity components, m/s
U, V = nondimensional velocity components, Eq. (18)
x, y, z = Cartesian coordinates, m
X, Y = nondimensional Cartesian coordinates, Eq. (18)
ϵ = relative contact region volume
ϕ = porosity
η = displacement efficiency, Eq. (43)
ν = kinematic viscosity, m^2/s
χ = nondimensional concentration, Eq. (18)
Γ = auxiliary parameters
ρ = density, kg/m^3
τ = nondimensional time, Eq. (18)

Superscripts

( )^0 = zero contact region volume
( )$'$ = two dimensional
( )* = effective
$\overline{\ }$ = space averaged

Subscripts

eg = equivalent global
f = clear fluid region
m = clean-up
r = replacement
s = fluid saturated porous region
in = inlet
out = outlet
0 = initial

region. The next step consists of averaging Eqs. (9)–(11) in z, by integrating them from $z = 0$ to $z = h$:

$$\nabla \cdot \mathbf{W}' = 0 \tag{12}$$

$$(\mathbf{W}'\nabla)\cdot \mathbf{W}' = -\frac{1}{F_{f,s}^{(2)}\rho}\nabla p' + \frac{F_{f,s}}{F_{f,s}^{(2)}}\nu\nabla^2\mathbf{W}' - \left(-\frac{2f_{f,s}}{h^2F_{f,s}^{(2)}} + \frac{F_s}{F_s^{(2)}}\frac{\phi}{K}\right)\nu\mathbf{W}' - \frac{c_F\phi^2}{K^{1/2}}|\mathbf{W}'|\mathbf{W}' \tag{13}$$

$$\frac{1}{F_{f,s}}\frac{\partial C'}{\partial t} + \mathbf{W}'\cdot\nabla C' = \frac{1}{F_{f,s}}D\nabla^2 C' \tag{14}$$

where,

$$F_{f,s} = \frac{1}{h}\int_0^h g_{f,s}\,dz \tag{15}$$

$$F_{f,s}^{(2)} = \frac{1}{h}\int_0^h g_{f,s}^2\,dz \tag{16}$$

$$f_{f,s} = h\left.\frac{dg_{f,s}}{dz}\right|_h \tag{17}$$

Notice that $F_{f,s}$ is identically equal to one since $\mathbf{W}'$ is the z-averaged velocity. Once the shape functions for clear fluid and porous regions are known and the nondimensional shape factors, $F_{f,s}^{(2)}$ and $f_{f,s}$, computed, Eqs. (12)–(14) will form a system of two-dimensional nonlinear partial differential equations. The nonlinearity is due to the inclusion of inertia terms in the momentum transport equation (Eq. (13)): the left-most term, $(\mathbf{W}'\nabla)\mathbf{W}'$, represents the convective inertia effect; the right-most term, $(c_F\phi^2/K^{1/2})|\mathbf{W}'|\mathbf{W}'$, represents the macroscopic inertia term or microscopic form drag imposed to the flow by the porous medium. The simplification from three-dimensional system to bidimensional system, although straightforward, requires the additional effort of determining the nondimensional shape factors listed in Eqs. (15)–(17).

The system of equations is nondimensionalized using the following nondimensional parameters:

$$(X, Y) = \frac{(x, y)}{h},\quad \mathbf{V} = \frac{1}{u_{\text{in}}}\mathbf{W}',\quad P = \frac{p'}{\rho u_{\text{in}}^2},\quad \tau = \frac{u_{\text{in}}}{h}t,$$

$$\text{Re} = \frac{u_{\text{in}}h}{\nu},\quad \text{Da} = \frac{K}{h^2},\quad \chi = \frac{C' - C_0}{C_{\text{in}} - C_0},\quad \text{Sc} = \frac{\nu}{D} \tag{18}$$

where (X, Y), $\mathbf{V}$, P, τ, and χ are, respectively, the nondimensional horizontal coordinates, fluid velocity, pressure, time, and species concentration. Additional nondimensional groups are the Reynolds number, Re, the Darcy number, Da, and the Schmidt number, Sc. Notice that u_{in} is the average incoming fluid velocity, C_0 is the initial species concentration within the fracture, assumed to be uniform at $t = 0$, and C_{in} is the uniform species concentration of the incoming fluid.

The nondimensional system of equations is

$$\nabla \cdot \mathbf{V} = 0 \tag{19}$$

$$(\mathbf{V}\nabla)\cdot\mathbf{V} = -\frac{1}{F_{f,s}^{(2)}}\nabla P + \frac{1}{F_{f,s}^{(2)}\text{Re}}\nabla^2\mathbf{V} - \left(-\frac{2f_{f,s}}{F_{f,s}^{(2)}} + \frac{1}{F_s^{(2)}}\frac{\phi}{\text{Da}}\right)\frac{1}{\text{Re}}\mathbf{V} - \frac{c_F\phi^2}{\text{Da}^{1/2}}|\mathbf{V}|\mathbf{V} \tag{20}$$

$$\frac{\partial\chi}{\partial\tau} + \mathbf{V}\cdot\nabla\chi = \frac{1}{\text{Sc Re}}\nabla^2\chi \tag{21}$$

Nondimensional conditions, with $R = r/h$ and $S = s/h$, are: $U = 6Y(R - Y)/R^2$ and $V = 0$, at $X = 0$; $U = V = 0$, at $Y = 0$ and R; $\chi = 1.0$ at $X = 0$; $\partial\chi/\partial Y = 0$ at $Y = 0$ and R; $\chi = 0$ at $\tau = 0$; $\partial\chi/\partial X = 0$ at $X = S$.

Theoretical Analysis

The redimensionalization (reduction to a two-dimensional problem) procedure, from Eq. (2) to Eq. (10), transforms the term expressing the z-wise diffusion of horizontal velocity into Darcy-like terms, linear in fluid velocity,

$$\nu\frac{\partial^2(u, v)}{\partial z^2} = \nu(u', v')\frac{d^2g_{f,s}}{dz^2} \tag{22}$$

Considering the coefficient multiplying the linear velocity term of Eq. (20), an effective Darcy number, Da*, can be expressed as

$$\frac{\phi}{\text{Da}^*} = \left(-\frac{2f_{f,s}}{F_{f,s}^{(2)}} + \frac{1}{F_s^{(2)}}\frac{\phi}{\text{Da}}\right) \tag{23}$$

where the groups within parentheses are the horizontal viscous diffusion coefficient and the original (porous medium) Darcy term coefficient, respectively. So, the boundary (viscous) effect of top and bottom surfaces, when closely spaced, is translated into a *volumetric viscous drag effect* within both, clear fluid and porous, regions. Noting that $f_{f,s}$ is always negative, the redimensionalization affects the flow as to decrease the effective Darcy number (or to decrease the effective permeability) of a porous region.

Also noteworthy from Eq. (23) is that the original Darcy term coefficient within a porous region becomes negligible compared with the surface viscous drag coefficient when

$$\text{Da} \gg \frac{\phi}{-2f_s} \tag{24}$$

Furthermore, from scaling Eq. (20), the form drag effect (Forchheimer term) is smaller than the viscous effect (Darcy term) within a porous region when

$$\text{Da} < \left(\frac{1}{F_s^{(2)}\phi c_F\,\text{Re}}\right)^2 \tag{25}$$

Equations (24) and (25) reveal a very interesting and useful result: whenever they are satisfied, the existence of permeable (porous) contact regions can be neglected so the entire fracture can be modeled as a region saturated with clear fluid with no contact regions, simplifying the analysis considerably.

Equivalent Global Permeability

From a hydrological point of view, it is interesting to predict the impeding effect imposed by contact regions to the flow. This effect is translated into a total pressure drop experienced by the fluid. This pressure drop is related to an equivalent global permeability of the medium, in nondimensional form Da_{eg}. By Darcy's law, in a scaling form:

$$\text{Da}_{\text{eg}} \sim \frac{1}{\text{Re}\left(\dfrac{\Delta P}{S}\right)} \tag{26}$$

where the total flow pressure drop through the fracture length, S, is defined as $\Delta P = P_{\text{in}} - P_{\text{out}}$.

An upper bound estimate of Da_{eg} can be obtained considering the relative contact volume ϵ of the rock fracture, defined as the ratio between the volume occupied by the contact regions and the fracture total volume. Assuming S_s and R_s as the equivalent length and depth of the contact region, then

$$\epsilon = \frac{S_s R_s}{SR} \tag{27}$$

Consider now the contact area as a rectangular strip covering the entire depth of the fracture, from $Y = 0$ to $Y = R$. In this case, $R_s = R_f = R$. For a certain volume of contact region, this is certainly the configuration that leads to the maximum impeding effect (maximum pressure gradient) through the fracture. That is why the following analysis offers only an upper bound estimate of Da_{eg}.

The total pressure drop $\Delta P/S$ necessary for determining Da_{eg} (Eq. (26)) is a function of the pressure drop through the clear fluid region, $\Delta P_f/S_f$, and the pressure drop through the porous contact region, $\Delta P_s/S_s$:

$$\mathrm{Da}_{eg} \sim \frac{1}{\mathrm{Re}} \frac{1}{\left[\left(\frac{\Delta P_f}{S_f}\right)(1-\epsilon) + \left(\frac{\Delta P_s}{S_s}\right)\epsilon\right]} \tag{28}$$

Clear fluid and porous saturated pressure drops are obtained from scaling the continuity and momentum Eqs. (19) and (20), considering each region separately (for basic scaling rules, see Bejan, 1994, ch. 1). Within the clear fluid region, the scaled continuity and momentum equations are:

$$\frac{1}{S_f} \sim \frac{V_f}{R} \tag{29}$$

$$\left(\frac{1}{S_f} + \frac{V_f}{R}\right) \sim \frac{\Delta P_f}{F_f^{(2)} S_f} - \frac{1}{F_f^{(2)}\,\mathrm{Re}\,S_f^2} + 2f_{f,s}\frac{1}{F_f^{(2)}\,\mathrm{Re}} \tag{30}$$

Combining both, Eqs. (29) and (30),

$$\frac{\Delta P_f}{S_f} \sim \frac{F_f^{(2)}}{S_f} + \frac{1}{\mathrm{Re}}\left(\frac{1}{S_f^2} - 2f_f\right) \tag{31}$$

The last three terms of Eq. (31) are, respectively, the convective inertia, the viscous diffusion and the surface viscous drag scales.

Within the fluid saturated porous contact region, the scaled continuity and momentum equations, and the corresponding pressure drop scale equation, are, respectively,

$$\frac{1}{S_s} \sim \frac{V_s}{R} \tag{32}$$

$$\left(\frac{1}{S_s} + \frac{V_s}{R}\right) \sim \frac{1}{F_s^{(2)}}\frac{\Delta P_s}{S_s} - \frac{1}{F_s^{(2)}\,\mathrm{Re}\,S_s^2} - \left(-\frac{2f_{f,s}}{F_s^{(2)}} + \frac{1}{F_s^{(2)}}\frac{\phi}{\mathrm{Da}}\right)\frac{1}{\mathrm{Re}} - \frac{c_F\phi^2}{\mathrm{Da}^{1/2}} \tag{33}$$

$$\frac{\Delta P_s}{S_s} \sim \frac{F_s^{(2)}}{S_s} + \frac{1}{\mathrm{Re}}\left(\frac{1}{S_s^2} - 2f_s + \frac{\phi}{\mathrm{Da}}\right) + \frac{c_F\phi^2}{\mathrm{Da}^{1/2}}F_s^{(2)} \tag{34}$$

where the last two terms of Eq. (34) are the scales of the Darcy and the Forchheimer terms.

Now, the equivalent Darcy number can be obtained by combining Eqs. (31) and (34) with Eq. (28),

$$\mathrm{Da}_{eg} \sim \frac{1}{\mathrm{Re}} \frac{1}{\left[\left(\frac{F_f^{(2)}}{S_f} + \frac{1}{\mathrm{Re}}\left(\frac{1}{S_f^2} - 2f_f\right)\right)(1-\epsilon) + \left(\frac{F_s^{(2)}}{S_s} + \frac{1}{\mathrm{Re}}\left(\frac{1}{S_s^2} - 2f_s + \frac{\phi}{\mathrm{Da}}\right) + \frac{c_F\phi^2}{\mathrm{Da}^{1/2}}F_s^{(2)}\right)\epsilon\right]} \tag{35}$$

Equation (35) is useful in practical situations in two distinct ways. When enough information about the system is available (average flow speed through the fracture, fluid properties, type of porous obstruction, etc.) Da_{eg} can be estimated from Eq. (35) and its value used in Eq. (26) to predict the global pressure drop through the fracture.

Evidently, there will be situations in the field where detailed information is not available. In this case, obtaining pressure drop measurements for a certain mass flow rate is enough to estimate Da_{eg} from Eq. (26). Equation (35) can be used then in an inverse way to estimate some of the unknown parameters. For instance, if the fluid properties, flow averaged speed, and the porous obstruction material are known, an estimate of the relative contact volume, ϵ, within the fracture can be obtained from Eq. (35).

Convective Inertia Limit

Natural fluid flow through geological formations, as fractured rocks, is generally very slow due to the relatively small pressure gradient (hydrostatic pressure) combined with the large viscous impeding effect caused by the closely spaced plates. That is why the neglect of convective inertia is a standard procedure when writing the momentum equation. However, there are situations when high speed flow might occur through a rock fracture, for instance during the clean-up of underground contaminated areas by injection of a high speed fluid. It is useful to appreciate the circumstances under which the convective inertia effect is indeed negligible.

It is easy to verify from Eq. (35) that the convective inertia effect becomes relevant only when

$$\mathrm{Re} > \frac{1}{F_f^{(2)}}\left(\frac{1}{S_f} - 2f_f S_f\right) \tag{36}$$

within the clear fluid region of a single rock fracture, and when

$$\mathrm{Re} > \frac{1}{F_s^{(2)}}\left(\frac{1}{S_s} - 2f_s S_s + \frac{\phi}{\mathrm{Da}}S_s\right) \quad \text{and} \quad S_s < \frac{\mathrm{Da}^{1/2}}{\phi^2 c_F} \tag{37}$$

within the permeable contact regions. Notice that the Reynolds number constraint of Eq. (37) predominates over the porous region length (S_s) constraint as long as the Darcy effect overcomes the Forchheimer effect, or in other words, whenever Eq. (25) is satisfied.

Shape Factors

The attention is now turned into evaluating the shape factor terms, $F_{f,s}^{(2)}$ and $f_{f,s}$. Within a clear fluid region, the fully developed velocity profile is shaped by

$$g_f(z) = \frac{6z(h-z)}{h^2} \tag{38}$$

There follows

$$F_f^{(2)} = \tfrac{6}{5} \quad \text{and} \quad f_f = -6 \tag{39}$$

The effective permeability within a clear fluid region, obtained from Eq. (23) with Eq. (39), is slightly different (smaller) than the one indicated in Muralidhar (1990). The

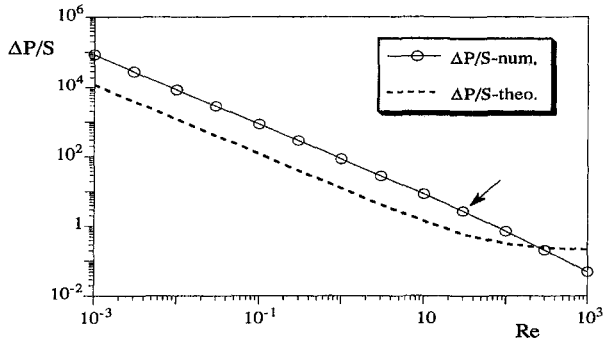

Fig. 2 Comparison between theoretically predicted pressure drop, Eq. (31), and pressure drop results from numerical simulations. ($\epsilon = 0$)

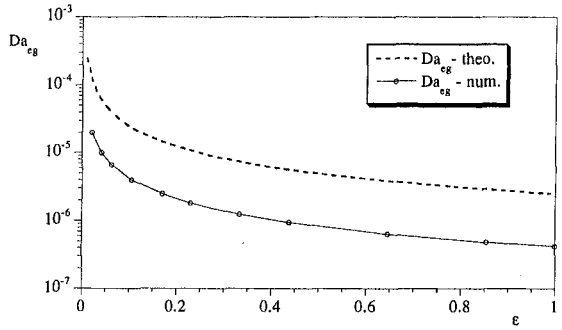

Fig. 3 Comparison between equivalent global Darcy number predicted theoretically by Eq. (35) and results from numerical simulations. ($Re = 10^{-3}$, $R_S = R$)

reason being the inclusion, in the present analysis, of the convective inertia term in the momentum Eq. (2). The neglect of this term is consistent with setting $F_f^{(2)} = 1.0$ in Eq. (39). (Notice that $F_f^{(2)}$ is the only contribution of the convective inertia term to Eq. (23)).

Considering the flow within a low permeability porous medium contact region, low enough to validate a Brinkman-extended Darcy model (in a scaling form, $Da \ll 1/(\phi c_F\, Re)^{1/2}$), the fully developed velocity profile is shaped by (Kaviany, 1985)

$$g_s(z) = \Gamma_1 - \Gamma_2(e^{\alpha[(z/h)-1]} + e^{-\alpha(z/h)}) \qquad (40)$$

where

$$\Gamma_1 = \frac{(1 - e^{-2\alpha})}{[1 - e^{-2\alpha} - 2(1 - e^{-\alpha})^2\alpha^{-1}]},$$

$$\Gamma_2 = \frac{(1 - e^{-\alpha})}{[1 - e^{-2\alpha} - 2(1 - e^{-\alpha})^2\alpha^{-1}]}$$

and

$$\alpha = \left(\frac{\phi}{Da}\right)^{1/2}$$

So, the shape factor terms for porous region can be written as

$$F_s^{(2)} = \Gamma_1 + \Gamma_2^2\left[2e^{-\alpha} - \frac{(1 - e^{-2\alpha})}{\alpha}\right] \quad \text{and}$$

$$f_s = \alpha\Gamma_2(e^{-\alpha} - 1). \qquad (41)$$

Numerical Simulations

Equations (19)–(21), and shape parameters listed in Eqs. (39) and (41), are solved using the control volume method with SIMPLE algorithm (Patankar, 1980) and QUICK scheme (Leonard, 1979), a second-order method. Discretized equations are solved with the efficient Tri-Diagonal-Matrix algorithm using an implicit alternating-direction Gauss-Seidel iterative method. The present code is a modified version (upgraded) of the one used by Lage et al. (1991) and validated against experimental results for simulating indoor pollutant transport through a ventilated enclosure.

Convergence criteria are: relative norm of pressure gradient being smaller than 10^{-6} for flow convergence, and relative norm of volume averaged concentration being smaller than 10^{-5} for species concentration convergence. After performing extensive grid accuracy tests, it is observed that a 80 by 50 grid is sufficient to guarantee a three percent or smaller discrepancy with results obtained using a 120 by 75 grid.

Results

The parameter space to be considered includes: fracture geometry (S, R), contact region relative volume (ϵ), Re, Sc, Da, ϕ, c_F. Results are obtained considering the *hypothetical* case of hydrochloric acid or ammonia being transported by water through a fracture with contact regions formed by the deposition of soil or sand. Physical parameter values considered here are: $S = 2R = 6$, $Da = 10^{-6}$ and $\phi = 0.4$ (typical of soil and sand, Nield and Bejan, 1992), $c_F = 1.75/(150\phi^3)^{1/2} = 0.56$ (from Ergun, 1952, model), and porous medium shape factors from Eq. (41): $F_s^{(2)} = 1.001582$ and $f_s = -634.5$.

Figure 2 compares the pressure drop per unit of fracture length, $\Delta P/S$, obtained from Eq. (31) with pressure drop obtained numerically, considering no contact regions ($\epsilon = 0$). The qualitative agreement between theory and numerical simulations is noteworthy. Not so evident from this figure is a breaking point (see arrow) in the slope of the curve for the numerical results at Reynolds number approximately equal to 30 indicating the increased importance of the convective inertia. Recall from Eq. (36) that convective inertia becomes predominant, theoretically, at Reynolds 87. An increased discrepancy between theoretical and numerical results is expected when convective inertia predominates because scale analysis essentially linearizes the momentum equation.

In Fig. 3, the theoretical equivalent global Darcy results are compared with numerical results. This illustrates the case of contact regions with variable relative volume, ϵ, and occupying the entire depth of the fracture, $R_s = R$. Typical Reynolds number for natural geological flow of water through fractured rock, $Re = 10^{-3}$, is considered in this case.

For $\epsilon > 0.1$, the equivalent global Darcy number is controlled by the Darcy term, $Da_{eg} \sim 10^{-6}/\epsilon$, according with Eq. (35). The agreement between theoretical and numerical results is within a factor of order O(1), consistent with the analytical method of scale analysis (Bejan, 1994).

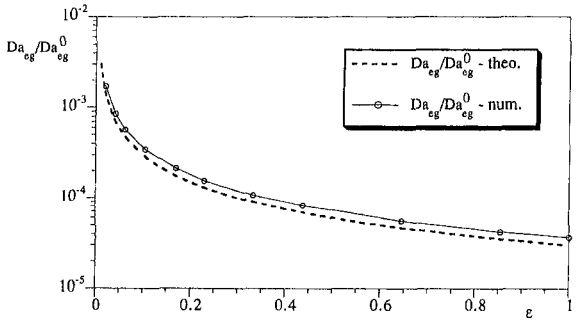

Fig. 4 Normalized equivalent global permeability predicted by Eq. (42) compared with numerical results. ($Re = 10^{-3}$, $R_S = R$)

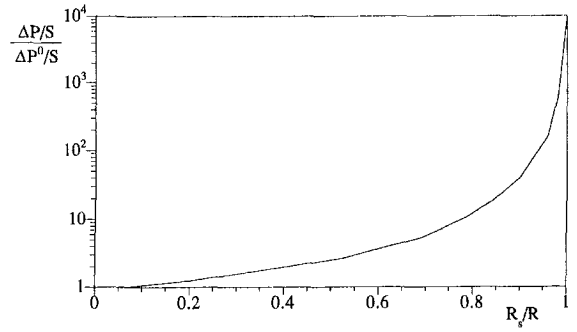

Fig. 5 Effect of contact region maximum depth (R_S/R) on relative total pressure drop. (Re = 10^{-3}, S/S_S = 43.75 percent)

The theoretical and numerical equivalent global permeability results of Fig. 3 are presented in Fig. 4 in a normalized form. The normalization parameters are, respectively, the theoretical equivalent global Darcy number of unobstructed rock fracture,

$$\mathrm{Da}^0_{\mathrm{eg}}\,|_{\mathrm{theo.}} \sim \frac{1}{\dfrac{\mathrm{Re}}{5} + 12.03} = 8.312 \times 10^{-2} \qquad (42)$$

and the numerical equivalent global Darcy number of unobstructed rock fracture, $\mathrm{Da}^0_{\mathrm{eg}}\,|_{\mathrm{num.}} = 1.161 \times 10^{-2}$. Although using different normalization values, the excellent agreement between theoretical and numerical normalized results indicates the coherence of the analytical predictions.

In the case of contact regions partially covering the entire depth of the fracture, $R_s < R$, the total pressure drop is expected to lie in between the pressure drop with no contact region ($\Delta P^0/S = 8.618 \times 10^4$) and the pressure drop with contact region from $Y = 0$ to R. The fluid is expected to flow preferentially through the clear fluid passage until the pressure loss becomes comparable with the pressure loss of flowing through the permeable contact region. This becomes evident considering some numerical results presented in Fig. 5. In this case, the length of the contact region is maintained constant, equal to 43.75 percent of the total fracture length ($S = 6$) and the pressure drop for $R_s/R = 1.0$ is $\Delta P/S = 1.053 \times 10^9$. It is seen from Fig. 5 that the pressure drop through the contact region affects the total pressure drop predominantly at $R_s/R > 80$ percent.

The species transport process is studied with a displacement efficiency defined as:

$$\eta(\tau) = \frac{\bar{C}' - C'_0}{C'_{\mathrm{in}} - C'_0} = \bar{\chi}(\tau) \qquad (43)$$

where $\bar{\chi}$ is the volume averaged nondimensional concentration.

Figure 6, for Re = 10^{-3} and Sc = 10^3 (typical of HCl and NH_3 diffusing in water, Eckert and Drake, 1987), presents the time evolution of displacement (clean-up) efficiency, η, for four different configurations. The abscissa of Fig. 6 is written in terms of volume replacement time, $\tau_r = \tau/S$, or the time it takes for replenishing one entire fracture volume base on inlet fluid velocity.

The basic configuration is the clean fracture configuration ($\epsilon = 0$). Three other configurations are shown schematically at the bottom of the figure (the fluid flows from left to right, as the arrow indicates). Notice that the porous obstruction configuration one ($\epsilon_1 = 31$ percent) has relative volume similar to that of configuration two ($\epsilon_2 = 34$ percent) but different distribution. Configuration three has a porous obstruction distribution similar to configuration one, but almost twice its relative volume ($\epsilon_3 = 56$ percent). Also plotted is the time evolution of the surface averaged concentration at the outlet of the fracture,

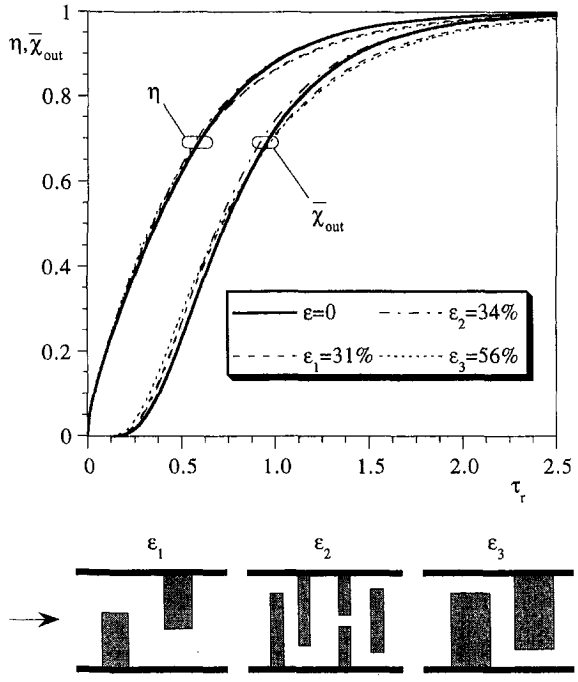

Fig. 6 Effect of contact region distribution and relative volume on displacement efficiency and averaged outlet concentration. (Re = 10^{-3}, Sc = 10^3)

$$\bar{\chi}_{\mathrm{out}} = \frac{1}{R}\int_0^R \chi\,|_{X=S}\,dY \qquad (44)$$

Notice from Fig. 6 that the time evolution of displacement efficiency for different ϵ, with various contact area distributions, is essentially the same as the one for $\epsilon = 0$. The same is true for the averaged outlet concentration. Therefore, for natural systems, as long as the flow pressure is sufficient for achieving the required Reynolds number, the presence of fracture obstructions has a negligible effect on the global transport of contaminants. It is then conclusive that the amount of contaminant trapped within the porous regions would not be significant.

Figure 7 presents, for $\epsilon = 0$, the time evolution of displacement efficiency for several cases. Dotted lines are for several Schmidt number values and fixed Re = 10^{-3}. Notice the change in behavior as Schmidt number increases: for Sc = 10^2 (Pe = Re Sc = 0.1) the efficiency evolves in a exponential-like fashion as it is the case of a perfectly mixed (diffusion dominated) regime, one in which the outlet concentration is the same as the concentration at any point inside the fracture. As Sc increases to 10^4 (Pe = 10), a piston-like regime (when η evolves linearly with time) develops at the beginning of the process, indicating

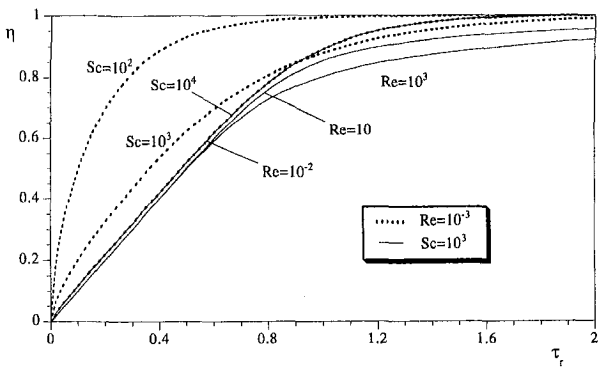

Fig. 7 Time evolution of displacement efficiency. ($\epsilon = 0$)

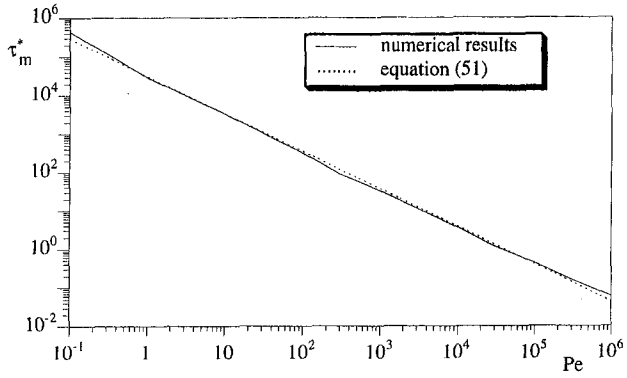

Fig. 8 Clean-up final time versus Peclet number. (ϵ = 0)

the increased importance of convection. This convection effect is responsible also for the crossing of Sc = 10^3 and Sc = 10^4 curves at $\tau_r \sim 0.9$.

Continuous lines are for several Reynolds number values and fixed Sc = 10^3. Observe that results for Sc = 10^4 and Re = 10^{-3} (Pe = 10) and Sc = 10^3 and Re = 10^{-2} (Pe = 10) are indistinguishable, confirming that the Peclet number controls the contaminant transport process evolution with time. Notice also that increasing Re extends the time duration of the piston-like regime.

Of interest is the time it takes for the flow to clean up the fracture space entirely, τ_m, from $\bar{\chi}$ = 0 to 1.0 (numerically $\bar{\chi} \geq 0.9999$). In this context, it is more practical to redefine the nondimensional time using the Reynolds number, $\tau^*_m = \tau_m/\mathrm{Re}$. Notice that as long as the factor (h^2/ν) is kept constant,

$$\frac{\tau^*_m(\mathrm{Pe}_1)}{\tau^*_m(\mathrm{Pe}_2)} = \frac{t_m(\mathrm{Pe}_1)}{t_m(\mathrm{Pe}_2)} \tag{45}$$

where Pe_1 and Pe_2 are two distinct Peclet numbers and t_m is the physical (in seconds) clean up time. This time scaling helps eliminate the apparent contradiction displayed in Fig. 7 where higher Reynolds number seems to imply in longer clean-up time. Figure 8 presents the clean-up time for various Peclet numbers. Notice that for clean-up of HCl or NH_3 with natural flow, Re = 10^{-3}, the Peclet number is equal to one. So for most practical purposes, the contaminant transport process with high speed fluid injection, Re > 10^{-3}, in a clear fracture is convection dominated. From the numerical results, an expression for the final clean-up time is obtained as

$$\tau^*_m = 31646.4\ \mathrm{Pe}^{-0.977} \tag{46}$$

and plotted in Fig. 8 (dotted line) for comparison. Equation (46) is accurate to within one percent.

Limitations

The separation of variables, as, for example, $u = u'(x, y)g(z)$, when the flow region is a sequence of clear fluid – porous – clear fluid – porous regions requires the assumption that all hydrodynamic development lengths are negligibly small.

For transition from clear fluid to porous region, the assumption is accurate as long as the Darcy number is small: the developing length in a low permeability porous region is predicted as $x_s \sim h\ \mathrm{Da}^{1/2}$ (Nield and Bejan, 1992).

The transition from porous to clear region is more subtle. For clear fluid flow through parallel plates, with uniform incoming flow, the entrance length is predicted as $x_f = 0.0065h$ Re (Sparrow, 1955), where Re is based on h as defined in Eq. (18). So, for Re = 10^{-3} (typical of natural flow within a fracture), the developing length is of the order of 6.5×10^{-6}h which is about 10^6 times smaller than the fracture length assumed here (S = 6). Since the flow coming out of a low permeability porous region is not uniform (distorted due to Brinkman effect) the development length is expected to be even shorter (this effect might become negligible if porosity variation near the surface is included in the analysis). Results for Re > 10 should be taken cautiously. The total pressure drop through the fracture, $\Delta P/S$, is underestimated when the developing length within a clear fluid region following a porous region is not accounted for. Notice, however, that the analytical results showed that whenever a reasonable fracture volume (more than 10 percent) is clogged with low permeability porous material the Darcy friction effect is expected to prevail, so the developing length effect (although existent) should have only a minor influence on the $\Delta P/S$ value.

The correctness of imposing nondiffusion species concentration boundary condition at the outlet of the fracture is now discussed. For Peclet number smaller than one (e.g., Pe = 0.1, the lowest value used here) diffusion is expected to predominate. In this case, the assumption of a nondiffusive outlet boundary condition is conservative when it comes to determine the total clean-up time. Notice that as the concentration inside the fracture increases with time, diffusion through the outlet boundary (with the downstream fluid) would induce a faster change in the concentration inside the fracture, accelerating the cleaning process. For increasing Peclet number, when convection is enhanced, the diffusive outlet boundary condition effect becomes less pronounced. For Pe = 1.0, for instance, the maximum difference between displacement efficiency obtained with nondiffusive outlet boundary and displacement efficiency with diffusive boundary and constant concentration $\chi_{\mathrm{out}} = 0$, is less than six percent.

Summary and Conclusions

A theoretical and numerical study is performed considering the transport of contaminant through a fully saturated single rock fracture. The fracture is modeled as a rectangular channel, with permeable contact regions.

A two dimensional flow model valid for slender fractures, considering the convective inertia effects, the viscous (Brinkman) effects, and the additional drag effects (viscous and form) within permeable contact regions, is obtained by integrating the three dimensional equation along the width of the fracture. Theoretical analysis (Eqs. (24) and (25)) indicates that the presence of permeable contact regions within the fracture can be neglected provided that the associated viscous and form drags are negligible compared with the viscous drag imposed by the closely spaced plates.

A theoretical general expression for calculating the equivalent global permeability of the fracture is presented. This expression provides a powerful engineering tool for predicting the predominant flow regime within a fracture. For instance, it allows obtaining a parametric range within which convective inertia effects can be neglected.

Good agreement between numerical and theoretical results confirms the consistency of the analytical predictions. Transient transport of contaminant, involving a clean-up procedure with fluid injection, is monitored in terms of a displacement efficiency and the surface averaged concentration at the outlet of the fracture. Results with physical parameters within practical range indicate that the clean-up process is insensitive to the distribution of contact regions throughout the fracture and its relative volume. For a clean fracture (no contact region) the clean-up time is a function of Peclet number only.

Acknowledgments

The financial support provided by the J. L. Embrey Professorship in Mechanical Engineering is greatly appreciated. Part of this work was performed on a DEC Alpha/AXP 3000/600,

running OSF 1.2, provided by Digital Equipment Corporation to the School of Engineering and Applied Science of SMU, under a seed grant program agreement.

References

Bejan, A., 1994, *Convection Heat Transfer,* Wiley, New York.

Buddemeier, R. W., and Hunt, J. R., 1988, "Transport of Colloidal Contaminants in Ground Water: Radionuclide Migration at the Nevada Test Site," *Applied Geochemistry,* Vol. 3, pp. 535–548.

Darcy, H., 1856, *Les Fontaines Publiques de la Ville de Dijon,* Victor Dalmond.

Eaton, R. R., and Bixler, N. E., 1987, "Analysis of a Multiphase, Porous Flow Imbibition Experiment in Fractured Volcanic Tuff," *Geophysics Monograph Series,* Vol. 42, pp. 91–93.

Eckert, E. R. G., and Drake, R. M., 1987, *Analysis of Heat and Mass Transfer,* Hemisphere, Washington D.C.

Ergun, S., 1952, "Fluid Flow Through Packed Columns," *Chemical Engineering Progress,* Vol. 48, pp. 89–94.

Festoy, S., and Van Golf-Racht, T. D., 1989, "Gas Gravity Drainage in Fractured Reservoirs Through New Dual-Continuum Approach," *SPE Reservoir Engineering,* Vol. 4, pp. 271–278.

Hsu, C. T., and Cheng, P., 1990, "Thermal Dispersion in a Porous Medium," *International Journal of Heat and Mass Transfer,* Vol. 33, pp. 1587–1597.

Kaviany, M., 1985, "Laminar Flow Through a Porous Channel Bounded by Isothermal Parallel Plates," *International Journal of Heat and Mass Transfer,* Vol. 28, pp. 851–858.

Kessler, J. H., and Hunt, J. R., 1993, "Open Channels in Fractures Maintained by Deposition and Erosion of Colloids," *1993 Int. High Level Rad. Waste Mgnt. Conf.,* Las Vegas, pp. 26–30.

Lage, J. L., Bejan, A., and Anderson, R., 1991, "Efficiency of Transient Contaminant Removal From a Slot Ventilated Enclosure," *International Journal of Heat and Mass Transfer,* Vol. 34, pp. 2603–2615.

Leonard, B. P., 1979, "A Stable and Accurate Convective Modeling Procedure Based on Quadratic Upstream Interpolation," *Computational Methods Applied Mechanical Engineering,* Vol. 19, pp. 59–98.

Mackay, D. M., and Cherry, J. R., 1989, "Groundwater Contamination: Pump-and-Treat Remediation," *Environmental Science Technology,* Vol. 23, pp. 630–636.

Montazer, P., and Wilson, W. E., 1984, "Conceptual Hydrologic Model of Flow in the Unsaturated Zone, Yucca Mountain, Nevada—US Geological Survey," *Water Resource Investigation Report,* Vol. 84-4345.

Sahimi, M., 1993, "Flow Phenomena in Rocks: from Continuum Models to Fractals, Percolation, Cellular Automata, and Simulated Annealing," *Reviews of Modern Physics,* Vol. 65, pp. 1393–1534.

Muralidhar, K., 1990, "Flow and Transport in Single Rock Fractures," *Journal of Fluid Mechanics,* Vol. 215, pp. 481–502.

Nield, D. A., 1990, "The Limitations of the Brinkman-Forchheimer Equation in Modeling Flow in a Saturated Porous Medium and at an Interface," *International Journal of Heat and Fluid Flow,* Vol. 12, pp. 269–272.

Nield, D. A., and Bejan, A., 1992, *Convection in Porous Media,* Springer, New York.

Novakowksi, K. S., and Lepcevic, P. A., 1994, "Field Measurement of Radial Solute Transport in Fractured Rock," *Water Resources Research,* Vol. 30, pp. 37–44.

Patankar, S. V., 1980, *Numerical Heat Transfer and Fluid Flow,* Hemisphere, Washington D.C..

Pyrak-Nolte, L. J., Myer, L., Cook, N. G. W., and Witherspoon, P. A., 1987, "Hydraulic and Mechanical Properties of Natural Fractures in Low Permeability Rock," *Proceedings International Society for Rock Mechanics,* 6th Int. Congr. on Rock Mechanics, Montreal, Canada, Vol. 1, pp. 225–231.

Rasmuson, A., and Neretnieks, I., 1986, "Radionuclide Transport in Fast Channels in Crystalline Rock," *Water Resources Research,* Vol. 22, pp. 1247–1256.

Schlichting, H., 1979, *Boundary Layer Theory* (7th Edn.), McGraw-Hill, New York.

Snow, D. T., 1968, "Rock Fracture Spacings, Openings and Porosities," *Journal of Soil Mechanics Foundation Division Proceedings ASCE,* Vol. 94, pp. 73–91.

Sparrow, E. M., 1955, "Analysis of Laminar Forced Convection Heat Transfer in the Entrance Region of Flat Rectangular Ducts," NACA TN-3331.

Sudicky, E. A., and Frind, E. O., 1982, "Contaminant Transport in Fractured Porous Media: Analytical Solutions for a System of Parallel Fractures," *Water Resources Research,* Vol. 18, pp. 1634–1642.

Thoma, S. G., Gallegos, D. P., and Smith, D. M., 1992, "Impact of Fracture Coatings on Fracture/Matrix Flow Interactions in Unsaturated, Porous Media," *Water Resources Research,* Vol. 28, pp. 1357–1367.

Tsang, Y. W., and Tsang, C. F., 1987, "Channel Model of Flow Through Fractured Media," *Water Resources Research,* Vol. 23, pp. 467–479.

Tsang, Y. W., and Tsang, C. F., 1989, "Flow Channeling in a Single Fracture as a Two-Dimensional Strongly Heterogeneous Permeable Medium," *Water Resources Research,* Vol. 25, pp. 2076–2080.

Wang, J. S. Y., and Narasimhan, T. N., 1985, "Hydrologic Mechanisms Governing Fluid Flow in Partially Saturated, Fractured Porous Tuff at Yucca Mountain," *Water Resources Research,* Vol. 21, pp. 1861–1874.

O. Rahli
Researcher.

L. Tadrist
Researcher.

M. Miscevic
Ph.D Student.

R. Santini
Researcher.

Laboratoire de l'Institut Universitaire des Systèmes Thermiques Industriels (IUSTI), U.M.R. 139 Université de Provence-Centre de St Jérôme-Case 162, Avenue Escadrille Normandie Niemen, 13397 Marseille, Cedex 20, France

Fluid Flow Through Randomly Packed Monodisperse Fibers: The Kozeny-Carman Parameter Analysis

Experimental studies have been carried out on fluid flow through porous media made up of randomly packed monodisperse fibers. The permeability and the Kozeny-Carman parameter k_k are deduced from experimental results. The variations of the permeability increase exponentially with the porosity. The parameter k_k is a decreasing function of the porosity ϵ and tends asymptotically to a value close to that deduced from a modified Ergun relation. The important decrease, observed for small aspect ratios, is certainly an effect of the cut sections of fibers. The results in terms of parameter k_k are systematically compared to those deduced from various theoretical models. The variation laws of the parameter k_k, deduced from different models, present important discrepancies with our experimental results.

I Introduction

Fibrous porous media, with their considerable diversity terms in structural and physico-chemical properties, play an important role in a number of industrial applications. These media generally present high porosity values and are often composed of fibers or of fiber-like particles (e.g., fiberglass, filters, insulating materials . . .).

Rahli et al. (1993) and Milewski (1986) determined the relationship between porosity and fiber aspect ratio for random packing of monodispersed fibers under dry conditions. Compared to a random packing of spherical particles for which the porosity is comprised between 0.36 and 0.40, the fibrous medium porosity ranges from 0.35 to 0.90 for an aspect ratio of 4 to 70.

Studies have been carried out on fluid flow through a fibrous medium. There have been relatively few such studies and little information is available. This complex flow model does not easily allow accurate analytical solutions to be developed.

Previous works give numerous experimental values for permeability at different porosity values (Carman, 1938; Wiggins, 1939; Jackson and James, 1986). The wide range of media used, however, does not allow any specific relationship to be deduced. These values are actually quite specific to each experiment since the geometry of medium is not clearly defined (filter, fiberglass etc.).

Flow parallel and perpendicular to a set of cylinders is generally analyzed using a single-cell model. In the parallel flow analysis developed by Happel and Brenner (1986), a closed-form solution is found for the one-dimensional flow in an annulus, bounded on the inside by a solid cylinder (diameter d) and on the outside by a shear-free surface (diameter $d + \delta$). This outer cylinder is assumed to represent the extent of the interaction between the solid cylinder and its surrounding environment.

To determine k_k for a random arrangement of cylinders, Happel and Brenner (1986) have proposed a linear combination of the Kozeny Carman parameters, calculated for parallel and perpendicular flows. Some experimental studies have been carried out on media with high porosity values and in which the geometrical shape of the fibers is not clearly defined. The fiber aspect ratio is generally assumed to be large enough for the diameter to be considered the only relevant dimension of the particle.

The present work consisted in determining the Kozeny-Carman k_k parameter for porous medium composed of identical fibers randomly packed. Experimental analysis of this parameter in an unconsolidated porous medium was conducted. A variation law for k_k versus porosity ϵ and aspect ratio r is proposed. The results are systematically compared to different experimental and theoretical models found in literature.

II Experimental Results and Analysis

II(a) Experimental Setup and Method. The aim was to analyze the behavior of a fluid flow crossing a fibrous medium. A self-acting device was specially built to produce identical fibers. Spools of copper and bronze wire (150 μm in diameter) are fed into this device. The system is fitted with an electronically-controlled pulse motor and a locking-type wire cutter, which allows wire to be cut to a predetermined length (Fig. 1(*a*)). Moreover, several wires may be cut simultaneously. The cutter produces a beveled fiber extremity (rather than a 90 deg cross section). The bezel dimensions are negligible, regardless of the fiber length (Fig. 1(*b*)). For aspect ratios greater than 30, the copper fibers tend to bend and thus produce significant distortion during random packing. The bronze wire, however, is considerably more rigid and resistant to bending for aspect ratios up to 80. For fiber aspect ratios greater than 100, there is considerable bending for all types of fibers. These predimensioned fibers are then randomly stacked in a measuring cell by progressively packing and vibrating the cell. The porosity is then determined by weighing the fibers. For a given fiber aspect ratio r_1, we have a corresponding porosity ϵ_1. The other media are obtained according to the same operating procedure. The only parameter which differs from one porous medium to another is the length of the fibers which make up the packing. This causes the modification of the porosity of the packing. The medium m_2 made up of fibers with a given aspect ratio r_2 leads a porosity ϵ_2 which differs from ϵ_1.

Figure 1(*c*) illustrates a view from above of the porous medium studied, that is randomly packed monodisperse fibers of identical length (3.8 mm) and of constant diameter (150 μm)

Contributed by the Fluids Engineering Division for publication in the JOURNAL OF FLUIDS ENGINEERING. Manuscript received by the Fluids Engineering Division July 11, 1995; revised manuscript received May 22, 1996. Associate Technical Editor: Jong H. Kim.

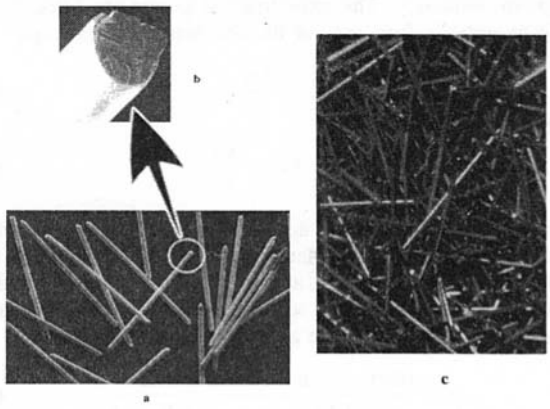

Fig. 1(*a*) Photograph of a fiber sample. Fig. 1(*b*) Photograph of a fiber ending. Fig. 1(*c*) Photograph of the structure of a medium made up of randomly packed fibers (diameter = 150 μm and $r \approx 25$)

for all the fibers which make up the packing. Observation of the packing may be described qualitatively as being made up of criss-crossed fibers, thus corresponding to randomly packed rigid monodisperse fibers.

An experimental device was used to determine the flow law for a fluid moving through a fibrous medium in an upward direction. The enclosure (Fig. 2) holding the fibers is placed between two identical and interconnected reservoirs. Two overflow outlets ensure that the level of the liquid remains constant in these reservoirs. The operating principle consists in imposing a fixed height difference between the level of the liquids in the two reservoirs. The liquid then flows through the porous medium. The variation in pressure drop ΔH is determined systematically between the inlet and the outlet of the fibrous medium according to the superficial velocity. The experimental procedure involved measuring both the flow rate Q through a medium with a predetermined section A (thus $U = Q/A$) and the corresponding pressure drop $\Delta P = \rho g \Delta H$ at a predetermined distance H.

Bear (1988) states that there are two equations describing the flow mechanism in porous media:

$$\text{Darcy's law (1856)} \quad \frac{\Delta P}{H} = \frac{\mu}{K} U \tag{1}$$

$$\text{Forchheimer's law (1901)} \quad \frac{\Delta P}{H} = \alpha U + \beta U^2 \tag{2}$$

where U is the superficial velocity and H is the length of the particle bed.

In such an expression, the parameters αU and βU^2 will vary with viscous and inertia effects respectively, as has been shown by a number of other authors (Ahmed-Sunada, 1969; Ergun, 1952; MacDonald, 1979, etc.). For a very low U value (e.g., Darcy flow) the βU^2 portion can be considered negligible, in which case the following expression can be used to determine the permeability:

$$K = \frac{\mu}{\alpha} \tag{3}$$

The experimental points were then approximated using a first-

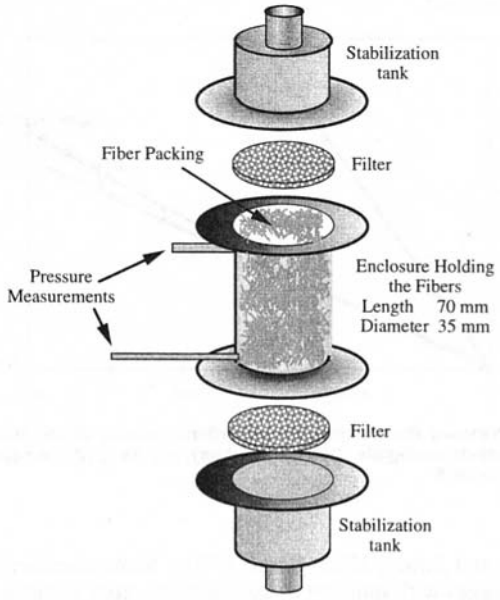

Fig. 2 Schematic diagram of experimental cell used to determine the flow laws for each type of fiber aspect ratio. Fibers (diameter = 150 μm and $4.5 \leq r \leq 66.7$)

or a second-degree polynomial. The coefficients of the first-degree polynomial were initially determined using the least-square method. Before introducing a second-degree term into the regression polynomial, the statistical Snedcor test was applied. This approach is used to test whether the improvement associated with the introduction of a second term is meaningful (Neuilly, 1993). If the improvement is found to be meaningful, second-degree polynomial regression is used. The coefficients of this polynomial are then determined using the least-square method. The error of these coefficients is defined by their standard deviation (Neuilly, 1993).

Figure 3 shows two examples of variations in pressure drop relative to superficial velocity. The first example corresponds to a situation in which the inertia effects are negligible compared to the viscous effects (Darcean flow). In the second example, the inertia effects cannot be neglected beyond a certain velocity. In this latter case, the deduced linear portion of the regression polynomial is drawn on the same graph.

This was the procedure we adopted for determine the flow laws and we considered only the velocity ranges where the flow remains Darcean.

II(b) Results. The permeability values vary in relation to the porosity of the medium $\epsilon(L/d)$ (Fig. 4). This variation increases in proportion to the porosity value. The permeability varies from 20 to 20,000 Darcy, for a porosity between 0.35 and 0.90. The experimental results are given in Table 1. The porosities and corresponding permeability values are given for different aspect ratios. The permeability was found to vary according to the porosity, especially for high ϵ values. This variation follows an exponential law.

Many approaches based on simplified geometrical shapes are developed by different authors (Dullien, 1992; Kozeny, 1927;

Nomenclature

a_p = specific area of the fiber (m^{-1})
d = fixed fiber diameter = 150 10^{-6} m
H = height of the fibrous medium (m)
K = permeability of the fibrous medium (m^2)
k_k = Kozeny-Carman parameter
L = fiber length (m)
N_e = the effective pore number
ΔP = pressure drop of fluid flow through a medium (Pa)
r = aspect ratio of fibers (L/d)
U = superficial fluid velocity (m/s)
α = parameter defined in eq. (2 & 3)
β = parameter defined in eq. (2)
γ = the fiber-extremity surface/total fiber surface
ϵ = porosity of the medium
μ = dynamic viscosity of the fluid (Pa.s)

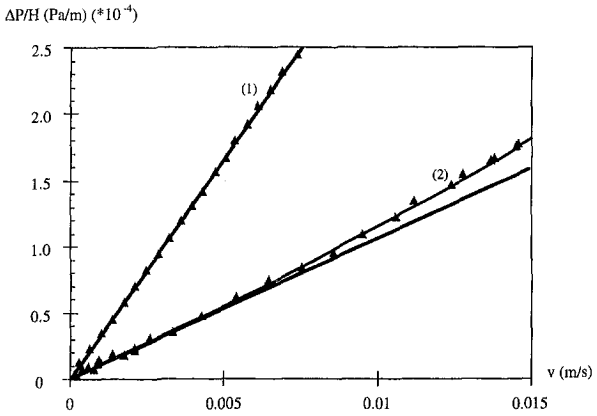

Fig. 3 Pressure drop versus the superficial velocity of the liquid; (1) Inertial effects negligible (Darcean regime), r = 14.7; (2) Non-Darcean regime, r = 20.2

Jackson and James, 1986; Kyan, 1970). Some consider capillary passages with uniform or non-uniform cross sections. Others assume that the flow passes through serial or parallel (or a combination of both) networks. These authors generally associate their results (both numerical and experimental) with the porosity of the medium and with the specific area of the particle using the Kozeny-Carman relation. The constant k_k which appears in this equation is then determined for the media under study. This parameter characterizes the ability of a fluid to move through the porous structure.

In the present work, this method was applied to the case of monodispersed randomly-packed fibers. The variations in the Kozeny-Carman k_k parameter is deduced from experimental permeability values, and the following relationships are studied.

$$K = \frac{\epsilon^3}{k_k(1-\epsilon)^2 a_p^2} \tag{4}$$

where k_k is the Kozeny-Carman constant, a_p the specific area of the particle and ϵ the porosity of the medium. It was assumed that the porous medium presents the properties of a capillary pathway, with the hydraulic radius and cross-sectional perpendicular to the pore axes. The path taken by the liquid passing through the pores is extremely complex, with an average capillary length greater than the reference value. For the fibers used in this study, the specific area is determined using the following relation:

$$a_p = \frac{2(2r+1)}{rd} \tag{5}$$

where r is the fiber aspect ratio (L/d).

The parameter k_k of the porous medium is then determined:

$$k_k = \frac{\epsilon^3 r^2 d^2}{4K(1-\epsilon)^2(2r+1)^2} \tag{6}$$

From the experimental results obtained for randomly stacked fibers and from relation (6), the variations of the k_k parameter were deduced as a function of porosity and of aspect-ratio values. These values are given in Table 1. The error in porosity values is due essentially to the inaccuracy in measuring the bed height, estimated at ±0.5 mm. The error in fiber length is equal to 2.5 percent, taking into account the errors introduced by the fiber extremities and the inaccuracy in measuring these lengths.

The variations in the k_k parameter are shown in Fig. 5 for porosity and Fig. 6 for the aspect ratio of fibers, respectively. A specific error value is attributed to each experimental point. It can be seen that the variations of this parameter in relation to r and ϵ are similar. They decrease continuously and show an asymptotic tendency. The experimental points are fitted using simple hyperbolic functions of the following expressions:

$$k_k = \frac{3.6}{\epsilon} \tag{7}$$

$$k_k = 3.6 + \frac{30}{r} \tag{8}$$

The asymptotic value of k_k approaches 3.6 and r tends toward infinity ($\epsilon = 1$). This is similar to the result obtained using the modified Ergun equation (k_k approaches 4.17). This variation law for k_k parameter is used to assess the combined influence of the fiber-extremity surface and the total fiber surface:

$$\gamma = \frac{\text{fiber-extremity area}}{\text{total fiber area}} = \frac{1}{2r+1} \tag{9}$$

This variation law follows a hyperbolic curve for k_k. The contribution of the fiber-extremity surface falls below 2 percent for r values greater than 25. The value of k_k remains constant beyond this r value (Fig. 6). It seems therefore that the fiber-extremity surface plays a non-negligible role in the variation of k_k for low aspect ratio ($r < 25$).

III Discussion

There are relatively few works focusing on the permeability of a porous fibrous media. Moreover, fibrous media actually include a wide range of porous media presenting different textures (filter, fiberglass, material, etc.). To our knowledge, no works have been published for media comprised of randomly-packed monodispersed rigid fibers. In this section we attempt to compare the experimental results to those suggested by different authors for fibrous media (in their broadest definition).

The different models presented in these works consider different pile-type geometric shapes. The fibers are aligned either parallel or perpendicular to the direction of the flow. For fibers randomly packed, the proposed model is deduced from a combination of previous arrangements.

Jackson and James (1986) conducted a bibliographic study of this field, including experimental results and theoretical models for the evaluation of permeability. Experimental results are available for 25 different fibrous media with fiber diameters varying from 10 Å to 10 mm. In all cases, it is assumed that the fiber aspect ratio is large enough for the diameter to be considered the only relevant dimension for the particle.

To predict the permeability of randomly-packed fibers, these authors have proposed a model based on a cubic network. By summing the friction losses in parallel and perpendicular flows, and by evaluating the individual resistance values (using the

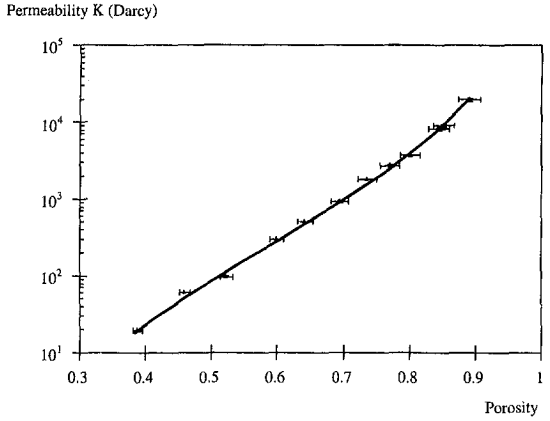

Fig. 4 Variation in the permeability in relation to the fibrous medium's porosity ϵ. Fibers (diameter = 150 μm and 4.5 ≤ r ≤ 66.7)

Table 1 Experimental values for K and k_k parameters with different fiber aspect ratios and different porosity values

Aspect ratio r	Porosity ϵ	Permeability K (Darcy)	Relative error $\Delta K/K$ (%)	Parameter k_k	Relative error $\Delta k_k/k_k$ (%)
4.5	0.39	19	1.7	9.3	19
7.3	0.46	60	0.5	6.8	19
10.7	0.52	99	0.1	8.2	19
14.7	0.60	302	0.4	5.8	21
18.0	0.64	502	1.0	5.5	23
20.2	0.70	938	2.6	5.1	26
25.2	0.74	1807	1.2	4.3	27
31.2	0.77	2716	2.2	4.3	30
33.3	0.80	3654	1.8	4.9	32
42.7	0.84	8134	4.2	4.2	40
50.0	0.85	9156	3.0	4.2	40
66.7	0.89	19728	6.2	4.2	52

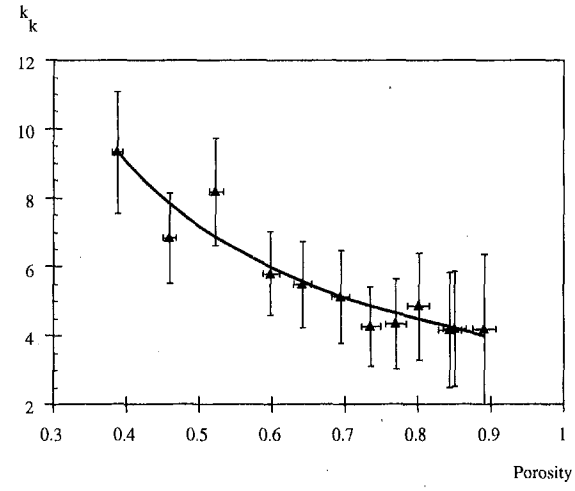

Fig. 5 Variation in the k_k parameter in relation to the fibrous medium's porosity. Fibers (diameter = 150 μm and $4.5 \leq r \leq 66.7$)

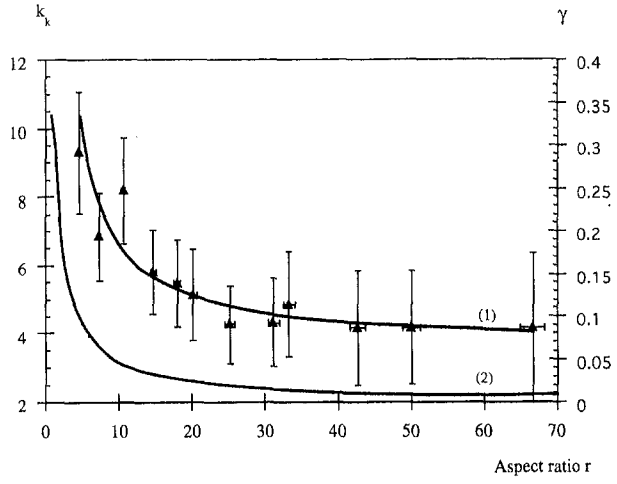

Fig. 6 Variation in the k_k parameter (1) and of the γ contribution of the fiber-extremity surface (relation 9) (2) in relation to the aspect ratio

Drummond and Tahir formula, 1984), the following relationship has been deduced:

$$\frac{K}{d^2} = \frac{3}{5}\left(-\mathrm{Ln}\,(1-\epsilon) - 0.931 + O(\mathrm{Ln}\,(1-\epsilon))^{-1}\right) \quad (10)$$

These authors point out that this law is only valid for high porosity values ($\epsilon > 0.7$).

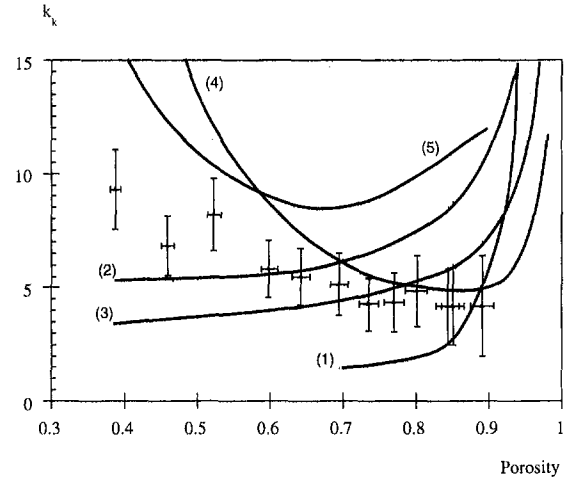

Fig. 7 Variation in the permeability in relation to the fibrous medium's porosity ϵ: ▲ our experimental results. (1) Jackson and James model (1986); (2) Happel and Brenner model (perpendicular) (1986); (3) Happel and Brenner model (parallel) (1986); (4) Kyan et al. model (1970); (5) Sahraoui and Kaviany model (1992)

Numerical solutions of the Navier-Stokes equation have been studied by Sahraoui and Kaviany (1992) for two-dimensional flow across arrays of cylinders using a finite-difference method. The variation law for permeability versus the porosity deduced from this approach is as follows:

$$K = 0.0606\,\frac{\pi}{4}\,\frac{\epsilon^{5.1}}{(1-\epsilon)}\,d^2 \quad 0.4 \leq \epsilon \leq 0.8 \quad (11)$$

From relations (10) and (4), and (11) and (4) the variations of k_k parameters from these models are deduced (respectively, Fig. 7 curves (1) and (5)).

Kyan et al. (1970), have noted the existence of a surprisingly large friction loss, despite the porosity of the layer. Using a geometric model of the fibrous bed, they assumed that the fluid was not flowing through a significant portion of the pore space. They postulated that the total pressure drop across the bed is equal to the sum of the pressure drop values associated with viscous loss, drag, and fiber deflection. They propose a correlation to determine the k_k parameter in relation to the porosity of the medium and to the effective pore number N_e defined by the following relation:

$$N_e = \sqrt{\frac{\pi}{(1-\epsilon)\sin\alpha}} - 2.5 \quad (12)$$

where α is the angle between two adjacent fibers. The author suggests a value equal to 30 deg. The k_k parameter then takes the following expression:

$$k_k = \frac{[62.3N_e^2(1-\epsilon) + 107.4]\epsilon^3}{16N_e^6(1-\epsilon)^4} \quad (13)$$

The variation of k_k versus the porosity is represented in Fig. 7 (curve 4).

Kaviany (1991) deduced the Kozeny-Carman parameter from the works of Happel and Brenner (1986) for a flow parallel or perpendicular to the cylinder axis. The k_k parameter is expressed in relation to the porosity. The Kozeny-Carman "constant" k_k was found to be for parallel flow (Fig. 7 (curve 3)):

$$k_k = \frac{2\epsilon^3}{(1-\epsilon)\left[2\,\mathrm{Ln}\,\frac{1}{1-\epsilon} - 3 + 4(1-\epsilon) - (1-\epsilon)^2\right]} \quad (14)$$

For a flow perpendicular to the cylinder, the Kozeny-Carman "constant" k_k becomes (Fig. 7 (curve 2)):

$$k_k = \frac{\frac{2\epsilon^3}{(1-\epsilon)}}{\mathrm{Ln}\,\frac{1}{1-\epsilon} - \frac{1-(1-\epsilon)^2}{1+(1-\epsilon)^2}} \quad (15)$$

The values of the k_k parameter deduced from various models and from our experimental results are then compared (Fig. 7). The patterns can be divided into two distinct behavior types:

An increasing tendency with large variations when the porosity value is greater than 0.85 (Happel and Brenner as reported by Kaviany (1991), and Jackson and James (1986)). Our experimental results showed precisely the opposite tendency,

A parabolic tendency presenting a minimum. This value is obtained for a porosity of 0.7 (Sahraoui and Kaviany, 1991) and of 0.85 (Kyan et al., 1970). In all cases, the experimental results were found to decrease when the porosity increases.

The variation of k_k in relation to porosity proposed in literature are difficult to interpret. The curves showing an increase in k_k with porosity are obtained by summing the friction losses for each particle. The curves presenting minimum values are obtained by directly assessing the friction losses within an ordered network of cylinders.

The decrease in k_k in relation to porosity for monodispersed randomly-packed fibers crossed by a liquid, may be due to the fact that the fluid trajectories become less tortuous as the porosity increases.

In fact the expression of the Kozeny-Carman parameter is: $k_k = 2\gamma\tau^2$ where τ is the tortuosity, γ the particle form factor.

It is generally admitted that the tortuosity translates the path covered by the fluid through the porous medium. From this consideration the trajectories become rectilinear when porosity increases. The borderline corresponds to the virtual absence of particles which leads to a rectilinear trajectory of the fluid, in other words a tortuosity which is equal to unity. This leads us to observe that the Kozeny-Carman parameter decreases when the porosity tends to unity.

When the fiber-extremity surface of the fibers is large, the k_k values are quite high. The size of this surface has a non-negligible influence on the porosity and on the path of the fluid. These comparisons indicate that the models based on the fibers arranged in simple ordered networks, do not accurately predict the permeability of the randomly-packed monodispersed rigid fibers.

IV Conclusion

In this work, experimental studies were carried out on fluid flowing through porous media made of randomly-packed monodispersed fibers. A systematic study was conducted for different porosity values ϵ. The variations of the permeability values plotted against the porosity of the medium are determined using experimental flow laws and Darcy's law. The permeability varies from 20 to 20,000 Darcy when the porosity varies from 0.38 to 0.90.

By extending the Kozeny-Carman relation to cylindrical particle stackings, the evolution of the k_k parameter was determined in relation to the porosity ϵ and the aspect ratio r of a fiber. The k_k parameter decreases continuously with an asymptotic tendency toward the value of 3.6 for porosity tending to 1. These experimental results show that the fiber-extremity surface plays a non-negligible role in the k_k value for low aspect ratio ($r < 25$). The experimental results compared to the models existing in literature present different behavior. The theoretical models, established for regular arrays of fibers do not correctly describe the behavior of randomly packed fibers.

It therefore seems that new approaches must be developed. These models must take into account the aspect ratio of the randomly-stacked fibers.

References

Ahmed, N., and Sunada, D. K., 1969, "Non Linear Flow in Porous Media," *Journal of the Hydraulics Division,* Proceedings of the American Society of Civil Engineers, Vol. 6, pp. 1847–1857.

Bear, J., 1988, *Dynamics of Fluids in Porous Media,* Dover Publications.

Carman, P. C., 1938, "The Determination of the Specific Surface of Powders. I," *Society Chemical Industry (Transactions and Communications),* Vol. 57, pp. 225–234.

Darcy, H., 1856, *Les Fontaines Publiques de la Ville de Dijon,* Dalmont, Paris.

Forchheimer, P. H., 1901, "Wasserbewegun Durch Boden," *Zeitschrift des Vereines Deutscher Ingenieur,* Vol. 49, pp. 1736–1749, Vol. 50, pp. 1781–1788.

Drummond, J. E., and Tahir, M. I., 1984, "Laminar Viscous Flow Through Regular Arrays of Parallel Solid Cylinders," *International Journal of Multiphase Flow,* Vol. 10, pp. 515–540.

Dullien, F. A. L., 1992, *Porous Media: Fluid Transport and Pore Structure,* Academic Press, Second Edition.

Ergun, S., 1952, "Fluid Flow Through Packed Columns," *Chemical Engineering Progress,* Vol. 48, pp. 89–94.

Happel, J., and Brenner, H., 1986, *Low Reynolds Number Hydrodynamics,* Martinus Nijhoff Publishers.

Jackson, G. W., and James, D. F., 1986, "The Permeability of Fibrous Porous Media," *Canadian Journal of Chemical Engineering,* Vol. 64, pp. 364–374.

Kaviany, M., 1991, "Principles of Heat Transfer in Porous Media," *Mechanical Engineering Series,* Springer-Verlag.

Kozeny, J., 1927, "Über Kapillare Leitung des Wassers im Boden," *Sitzungsberichte Akademie der Wissenschaften,* Wien, Vol. 136, pp. 271–306.

Kyan, C. P., Wasan, D. T., and Kintner, R. C., 1970, "Flow of Single-Phase Fluids Through Fibrous Beds," *Industrial and Engineering Chemistry Fundamentals,* Vol. 9, pp. 596–603.

Macdonald, I. F., El-Sayed, M. S., Mow, K., and Dullien, F. A. L., 1979, "Flow Through Porous-Media—The Ergun Equation Revisited," *Industrial and Engineering Chemistry Fundamentals,* Vol. 18, No. 3, pp. 199–207.

Milewski, J. V., 1986, "Efficient Use of Whiskers in the Reinforcement of Ceramics," *Advanced Ceramic Materials,* Vol. 1, pp. 36–41.

Neuilly, M., 1993, "Modélisation et Estimation des Erreurs de Mesure," *Technique et Documentation,* Lavoisier.

Rahli, O., Tadrist, L., Santini, R., and Pantaloni, J., 1993, "Fluid Flow and Heat Transfer Analysis in Fibrous Porous Media," *3rd World Conference on Experimental Fluid Mechanics and Heat Transfer, Honolulu-USA,* Vol. 2, pp. 1577–1582.

Sahraoui, M., and Kaviany, M., 1992, "Slip and No-slip Boundary Condition at Interface of Porous, Plain Media," *International Journal of Heat and Mass Transfer,* Vol. 35, No. 4, pp. 927–943.

Wiggins, E. J., Campbell, W. B., and Maass, O., 1939, "Determination of the Specific Surface of Fibrous Materials," *Canadian Journal of Research,* Vol. 17, Section B, pp. 318–324.

The Axisymmetric Sudden Expansion Flow of a Non-Newtonian Viscoplastic Fluid

G. C. Vradis
Associate Professor
of Mechanical Engineering.
Mem. ASME

M. V. Ötügen
Associate Professor
of Aerospace Engineering.

Department of Mechanical, Aerospace, and Manufacturing Engineering,
Polytechnic University,
Six Metro Tech Center,
Brooklyn, NY 11201

The flow of a non-Newtonian viscoplastic Bingham fluid over an axisymmetric sudden expansion is studied by numerically solving the governing fully-elliptic continuity and momentum equations. Solutions are obtained for a wide range of Reynolds and yield numbers in the laminar flow regime with constant fluid properties. The present work demonstrates that the finite-difference technique can successfully be employed to obtain solutions to separating/reattaching internal flows of Bingham plastics. The results demonstrate the strong effects of the yield and Reynolds numbers on both the integral and the local structure of the separating and reattaching flow. Higher yield numbers result in larger overall effective viscosities and thus faster flow recovery downstream of the sudden expansion. The reattachment length decreases with increasing yield numbers, eventually reaching an asymptotic nonzero value which, in turn, is dependent on the Reynolds number. The strength of the recirculating flow also decreases with increasing yield numbers.

Introduction

Many fluids encountered in a large number of industrial applications are fluids that require a certain minimum stress level before they are able to sustain a velocity gradient, and thus, flow. This minimum shear stress is termed the "yield stress," and is a property of the specific fluid. Since a velocity gradient cannot be sustained for shear stress levels below the yield stress value, "core flow regions" result. Within the core flow region, the fluid moves as a solid body with no velocity gradients. Fluids behaving in this manner include paints, food products, plastics, aqueous foams, slurries, pharmaceutical products, polymeric solutions, and paper pulp. Some of these fluids exhibit an elastic behavior. However, many are purely viscous fluids, and while some of these fluids are yield-power law fluids with nonlinear stress-strain rate relationships, the rheological behavior of a large number of them can nevertheless be described by the constitutive equation for a Bingham fluid as given by Bird et al. (1960).

Although these fluids are of importance in many industries, the literature on the internal flow and thermal behavior of Bingham plastics is surprisingly limited. In an early study, Chen et al. (1970) employed an integral boundary-layer formulation to calculate the laminar flow of a Bingham fluid in the entrance region of a straight circular pipe. Soto and Shah (1976) followed with a numerical solution to the same flow problem for a yield-power law fluid, employing the boundary layer equations. The corresponding Graetz problem for Bingham fluids was solved by Wissler and Schecter (1959) and Blackwell (1985). These are the first results to demonstrate the strong influence of the yield number on the hydrodynamic problem and its weak effect on the thermal entrance problem. Lipscomb and Denn (1984) reported on the properties of numerical solutions to Bingham fluid flows in complex geometries and concluded that yielding and flow must occur throughout the flow domain. Recently, Vradis et al. (1993) numerically investigated the simultaneously developing velocity and thermal fields of a Bingham fluid in the entrance region of circular pipes employing the fully elliptic governing equations. The work demonstrated the viability of finite difference-based numerical techniques in solving non-separating internal flows of Bingham fluids. The results confirmed the earlier suggestions that the yield number does not have a strong effect on the heat transfer problem. Instead, it is the Brinkman number which has a strong influence on the thermal field. The study of Vradis et al. also indicated a stronger dependence of the velocity field on the yield number than previously predicted through reduced forms of the governing equations. A number of studies, both experimental and analytical/computational, have concentrated on the flow of Casson fluids, another class of viscous-yield stress fluids. Casson fluids accurately describe the rheological behavior of blood, as established by Merrill et al. (1964). The works by Aroesty and Gross (1972) and Nakamura and Sawada (1990) concentrated on the pulsatile flow of such fluids through straight tubes and through an axisymmetric stenosis respectively.

The number and extent of reports on the turbulent flows of viscous-yield stress fluids are also limited. Most of the previous studies are experimental investigations and turbulent models that accurately predict flow behavior are yet to be developed. Wilson and Thomas (1985) reported on the structure of the near wall velocity field in the case of pipe flows of Bingham fluids, while Park et al. (1989) and Wildman et al. (1992) reported on mean and turbulent velocity distributions obtained using laser Doppler velocimetry in flows of yield-power law fluids through a circular pipe, and in an axisymmetric gradual contraction respectively.

At the present, the knowledge base on internal flows of Bingham fluids is quite limited. There are no numerical studies reported in the literature that involve separated internal flows of Bingham fluids. Such flows are common in industrial applications. Thus, an improved understanding of the effects of the pertinent physical and geometrical parameters on the flow field can result in better product quality as well as improved process efficiency. The flow over a sudden expansion in a circular pipe is frequently encountered in practice exhibiting all the complexities of a separated flow while at the same time affording a geometry that is simple enough to formulate a numerical scheme in the cylindrical coordinate system.

In the present, the internally separating flow of a Bingham fluid through an axisymmetric sudden expansion is studied for a downstream-to-upstream diameter ratio of two. The Reynolds number was varied in the range between 2 and 100 while the

Contributed by the Fluids Engineering Division for publication in the JOURNAL OF FLUIDS ENGINEERING. Manuscript received by the Fluids Engineering Division May 19, 1994; revised manuscript received July 23, 1996. Associate Technical Editor: R. L. Panton.

yield number varied from zero (Newtonian fluid) to 10. The fluid properties, namely the density and plastic viscosity are assumed constant. A finite-difference formulation of the governing elliptic equations for mass conservation and momentum balance is used along with a coupled-variables technique to solve the resulting system of nonlinear equations which are linearized by employing an iterative marching solution procedure.

The Governing Equations

The nondimensionalized governing elliptic equations for the steady, laminar, incompressible flow of a non-Newtonian fluid in cylindrical coordinates are:

$$\frac{\partial u}{\partial x} + \frac{1}{r}\frac{\partial rv}{\partial r} = 0 \tag{1}$$

$$u\frac{\partial u}{\partial x} + v\frac{\partial u}{\partial r} = -\frac{\partial p}{\partial x} + \frac{1}{\mathrm{Re}}\left[\frac{\partial}{\partial x}\left[2\mu_{\mathrm{eff}}\frac{\partial u}{\partial x}\right] + \frac{1}{r}\frac{\partial}{\partial r}\left[\mu_{\mathrm{eff}} r\left[\frac{\partial u}{\partial r} + \frac{\partial v}{\partial x}\right]\right]\right] \tag{2}$$

$$u\frac{\partial v}{\partial x} + v\frac{\partial v}{\partial r} = -\frac{\partial p}{\partial r} + \frac{1}{\mathrm{Re}}\left[\frac{1}{r}\frac{\partial}{\partial r}\left[r2\mu_{\mathrm{eff}}\frac{\partial v}{\partial r}\right] + \frac{\partial}{\partial x}\left[\mu_{\mathrm{eff}}\left[\frac{\partial u}{\partial r} + \frac{\partial v}{\partial x}\right]\right] - 2\mu_{\mathrm{eff}}\frac{v}{r^2}\right], \tag{3}$$

In the case of a Bingham fluid the relationship between the stress tensor τ and the rate of deformation tensor Δ is given by the following formula (Bird et al., 1960):

$$\tau = \left\{\eta + \frac{\tau_0}{\sqrt{\frac{1}{2}(\Delta:\Delta)}}\right\}\Delta \quad \text{for} \quad \tfrac{1}{2}(\tau:\tau) > \tau_0^2, \tag{4a}$$

$$\Delta = 0 \quad \text{for} \quad \tfrac{1}{2}(\tau:\tau) \le \tau_0^2 \tag{4b}$$

Here $\Delta_{ij} = \partial u_i/\partial x_j + \partial u_j/\partial x_i$ and $\Delta:\Delta = \sum_i \sum_j \Delta_{ij}\Delta_{ji}$ is the second invariant of Δ. In cylindrical coordinates the function $\frac{1}{2}(\Delta:\Delta)$ is given by:

$$\tfrac{1}{2}(\Delta:\Delta) = 2\left[\left[\frac{\partial v}{\partial r}\right]^2 + \left[\frac{v}{r}\right]^2 + \left[\frac{\partial u}{\partial x}\right]^2\right] + \left[\frac{\partial v}{\partial x} + \frac{\partial u}{\partial r}\right]^2 \tag{4c}$$

As a result, the nondimensional effective viscosity is defined as:

$$\mu_{\mathrm{eff}} = \left\{1 + \frac{Y}{\sqrt{\frac{1}{2}(\Delta:\Delta)}}\right\} \quad \text{for} \quad \tfrac{1}{2}(\tau:\tau) \ge \tau_0^2, \tag{5a}$$

and

$$\mu_{\mathrm{eff}} = \infty \quad \text{for} \quad \tfrac{1}{2}(\tau:\tau) \le \tau_0^2, \tag{5b}$$

where $Y = \tau_0 R_w/\eta U_i$ is the yield number for Bingham fluids and serves as a nondimensional yield stress.

The constitutive equation for the Bingham fluid (Eqs. (5*a*) and (5*b*)) is independent of time thus, the characterization of such fluids as "purely viscous." It should be emphasized here that for fluids that exhibit thixotropy the results of the present work are not valid. Such fluids are characterized by a time-delay period within which the fluid transitions from its previous rheological state to a new one imposed by the changing shearing environment. Given that typically such time-delay periods are greater than the characteristic time scale of the flow, any predictions of flow characteristics for a thixotropic fluid using the present work is invalid.

Solution Technique

The numerical technique used in the present study is described in detail by Bentson and Vradis (1987), and Vradis and Van Nostrand (1992). The method will be discussed here only briefly and the reader is referred to these papers for further details. The system of the mass conservation and momentum equations is discretized by employing the staggered grid proposed by Weltch et al. (1966) for the Marker and Cell (MAC) method. Fully second order accurate finite-difference approximations are used for the derivatives appearing in the governing equations. The convective streamwise derivatives are upwinded using second order approximations to ensure stability. Centered, second-order accurate differences are used for all other terms. The resulting system of algebraic equations for mass conservation and momentum is solved by employing an iterative marching technique. In this technique, the linearized equations are solved simultaneously along lines in the radial direction using an efficient block-tridiagonal matrix inversion technique. The convergence parameter employed in the present analysis is the magnitude of the maximum residual in the difference equations. The discretization is made in such a way that the continuity equation is always satisfied to "machine accuracy" at any stage of the solution procedure. Therefore, convergence is checked for the two momentum equations and the iterative procedure is terminated when the residual becomes less than 10^{-4}.

In the core regions of the flow the effective viscosity, μ_{eff}, attains an infinite value since $\Delta = 0$. Large values of μ_{eff} create convergence problems since the coefficient matrix becomes

Nomenclature

C_f = friction coefficient, $\tau_w/\rho U_i^2$
D = diameter of upstream pipe
L_R = reattachment length
p = nondimensional pressure, $P/\rho U_i^2$
P = pressure
r = nondimensional radial distance, R/R_w
r_o = nondimensional "core" radius, R_0/R_w
R = radial distance
R_o = radius of the "core"
R_w = radius of the upstream pipe
Re = Reynolds number, $\rho U_i D/\eta$
u = nondimensional streamwise velocity, U/U_i
u_{cl} = nondimensional centerline velocity
U = streamwise velocity
U_i = streamwise bulk velocity at inlet
v = nondimensional radial velocity, V/U_i
V = radial velocity
x = nondimensional streamwise distance, X/D
X = streamwise distance
Y = yield number, $\tau_o R_w/\eta U_i$
γ = strain rate
Δ = rate of deformation tensor
η = plastic viscosity
μ = effective viscosity
μ_{eff} = nondimensional effective viscosity, μ/η
ρ = density
τ = stress tensor
τ_o = yield stress

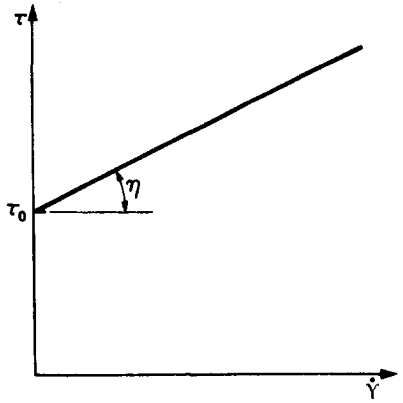

(a)

Fig. 1(a)

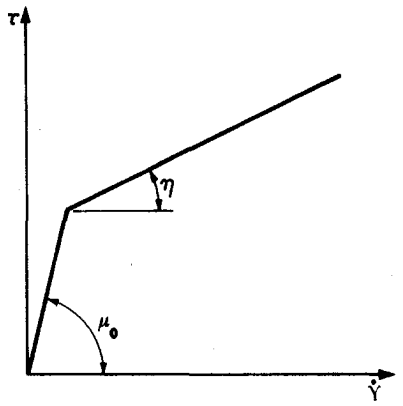

(b)

Fig. 1(b)

Fig. 1 Rheological description of; (*a*) Bingham fluid, (*b*) present approximation

very "stiff" due to large differences in the magnitude of its elements. In order to avoid such problems, μ_{eff} is "frozen" at a relatively high value of μ_o when the value of $\Delta{:}\Delta$ drops below a certain preset level, thus guaranteeing convergence. The same approach was adopted by other researchers in the past (O'Donovan and Tanner, 1984 and Lipscomb and Denn, 1984). The result of such an approximation is that the rheological behavior of the fluid is altered from that of an actual Bingham fluid shown in Fig. 1(*a*) to the biviscosity fluid shown in Fig. 1(*b*). An investigation was performed to study the effect of μ_o on the accuracy and computational efficiency of the solution procedure. It is established that the results become insensitive to this high cutoff value, once it exceeds $\mu_o = 1000\eta$. The same value for μ_o was adopted by O'Donovan and Tanner (1984) and Beverly and Tanner (1992) after extensive numerical experimentation. Due to the sharp variations in the values of effective viscosity, in order to obtain convergence, very strong under-relaxation of the effective viscosity is necessary from one iteration level to the next, especially in the earlier stages of the iterative procedure.

Results and Discussion

The geometry and the boundary conditions of the problem are shown in Fig. 2. The flow at the inlet ($x = 0$) is assumed to be fully developed, steady, laminar, incompressible flow of a Bingham fluid in a circular pipe, has been presented earlier by Skelland (1948) and is given here in its nondimensional form by the following expression (Vradis et al., 1993;);

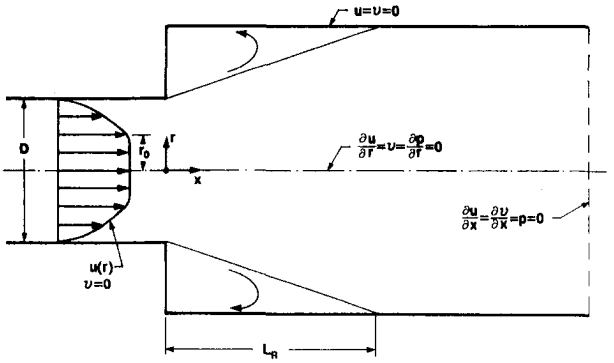

Fig. 2 Geometry and boundary conditions

$$u(r) = \frac{1}{2}\frac{Y}{r_0}(1 - r^2) - Y(1 - r) \quad \text{for} \quad r_0 \le r \le 1 \quad (6a)$$

$$u(r) = \frac{1}{2}\frac{Y}{r_0}(1 - r_0^2) - Y(1 - r_0) \quad \text{for} \quad 0 \le r \le r_0 \quad (6b)$$

At the exit plane of the computational domain the flow is assumed fully developed. Thus, the streamwise derivatives of the velocity components are zero while the pressure is uniform. The length of the computational domain depends on the Reynolds and yield numbers and is not known *a priori*. For each case, it has to be adjusted individually, sometimes through multiple trial runs. After each computational run, it is always verified that the downstream boundary is located far enough to allow a completely fully developed flow at the exit. This is accomplished by verifying that the friction coefficient has reached its analytically obtained asymptotic value for a pipe flow (Vradis et al., 1993). Along the solid walls, the velocity satisfies the no-slip condition ($u = v = 0$). The grid used for obtaining the results presented is a variable, 78 × 80 grid in the streamwise and transverse directions, respectively. It is finer close to the step and the pipe wall. The large number of points selected for the radial direction is due to the anticipated large gradients in flows of Bingham fluids. Extensive numerical experimentation established the grid-independent nature of the results obtained with the above defined grid.

The convergence rate of the numerical scheme strongly depends on the yield number as demonstrated in Fig. 3. For a fixed grid size and Reynolds number, the higher the yield number is, the higher the number of iterations required for convergence to a given accuracy level. This is due to the increased stiffness of the coefficient matrix for larger yield numbers. For the higher yield numbers, convergence is obtained only after using a very

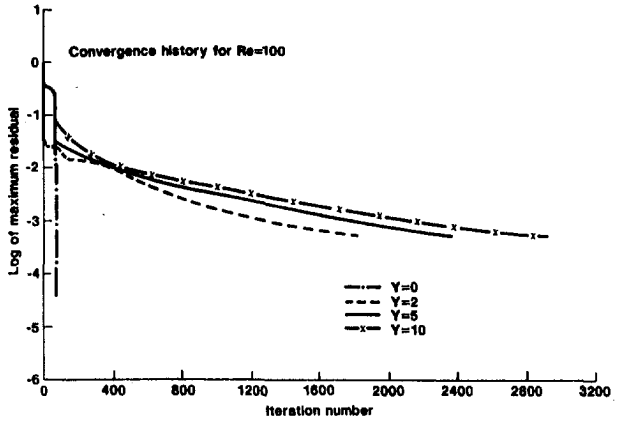

Fig. 3 Convergence history for the numerical scheme

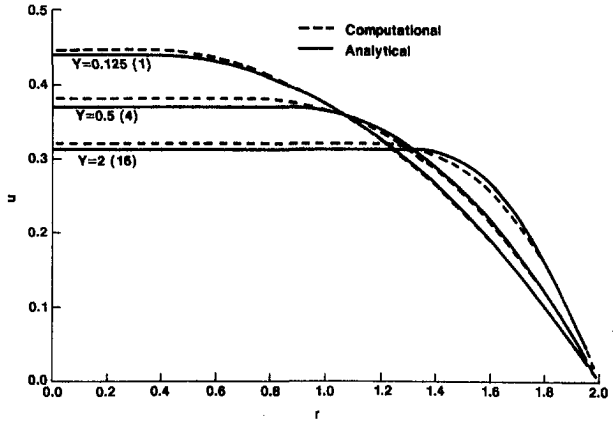

Fig. 4 Fully developed velocity profiles at pipe exit

strong under-relaxation of the effective viscosity (of the order of 90 to 99 percent). In these cases, the number of iterations required to reach the prescribed residual level of 10^{-4} was of the order of 5000 to 7000. A particular difficulty with convergence was experienced for yield numbers of 0.25 and 0.5. Relatively coarse grids had to be used in the streamwise direction for these two cases in order to obtain convergence. No such problems were encountered for the rest of the yield numbers studied.

The accuracy of the solution procedure is established by comparing the numerical results obtained in the fully developed flow region with those given by the exact analytical solution of the governing equations in this region (Eqs. (6*a*) and (6*b*)), and by comparing the reattachment length in the Newtonian fluid ($Y = 0$) case with the available experimental and numerical solutions. Figure 4 shows the fully developed velocity profiles at the exit of the pipe for different yield numbers (the number in parenthesis is the corresponding yield number based on the conditions downstream of the step, which is eight times of that based on the upstream pipe conditions). The computationally obtained profiles are very close to the exact analytical profiles with the maximum difference less than 3 percent. It is interesting to note that the discrepancy between the analytical and the computational solutions is larger in the central portion of the pipe and it vanishes near the wall. This is a desirable outcome since, typically, the near wall flow characteristics are the ones that are of engineering importance.

Figure 5(*a*) shows the predicted reattachment length as a function of the Reynolds number, for both Newtonian and non-Newtonian fluids. Also shown is the reattachment length for a power-law fluid with an index of $n = 0.65$ as given by Halmos et al. (1975). The predicted values for a Newtonian fluid ($Y = 0$) are in excellent agreement with the experimental results of Macagno and Hung (1967). For a Newtonian flow, the reattachment length increases approximately linearly with the Reynolds number. In a laminar flow, the diffusion of momentum is due only to molecular viscosity and thus, it can be said that for each fluid the growth of the separated shear layer has a fixed time constant. As the Reynolds numbers is increased, the shear layer is convected faster and therefore, grows thick enough to reach the downstream wall at a further distance from the expansion step. It is observed that L_R has a linear dependence on Re also for the Bingham fluids. For the power-law fluid in the range of $0 < \mathrm{Re} < 20$ the dependence of the reattachment length on Reynolds number is approximately linear, with L_R values comparable to those for a Newtonian fluid flow. On the other hand, for $\mathrm{Re} > 20$ the dependence of L_R on the Reynolds number is nonlinear and the values clearly diverge from that of the Newtonian fluid.

In the case of a Bingham fluid, as the yield number increases the rate of increase of the reattachment length with the Reynolds number decreases substantially. This point is further demonstrated in Fig. 5(*b*) which shows the variation of the reattachment length with the yield number for Re = 10 and 100. Higher yield numbers result in larger effective viscosities which in turn reduce the reattachment length. As the effective viscosity becomes large and the reattachment length is significantly reduced, the relative influence of the Reynolds number becomes less significant. The extrapolation of the constant Y lines to Re = 0, yields a fixed value of about 0.3, which compares well with the experimental range given by Macagno and Hung (1967). For small yield numbers, the dependence of the reattachment length on the yield number is strong. However, on the high end of the yield number range studied, the dependence of the reattachment length on this number becomes weak as indicated by Fig. 5(*b*). The effect of the yield stress, in essence, is similar to that of fluid elasticity, which has been shown to induce shorter separated flow regions in sudden expansion geometries (Pak et al., 1990; Perera and Walters, 1977).

Figure 6 shows the developing profiles of the streamwise velocity downstream of the expansion for two pairs of Reynolds and yield numbers. At the edge of the step, the inlet flow is fully developed exhibiting a plug flow region at the center. Downstream of the sudden expansion, a recirculating flow zone is observed for both flow cases. The magnitude of the negative velocity in the recirculating zone is two orders of magnitude smaller than the bulk velocity. The extent of the negative velocity region decreases with increasing streamwise distance and eventually the flow reattaches. At this point, all flow is forward with positive streamwise velocity throughout. Further downstream the flow becomes fully developed, again exhibiting a plug flow region about the centerline and a shear flow region

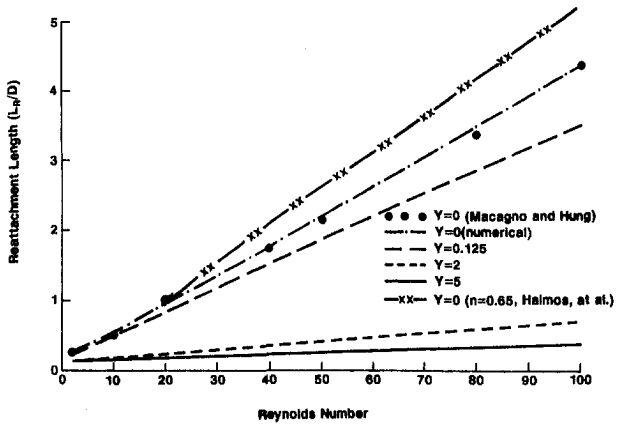

Fig. 5(*a*)

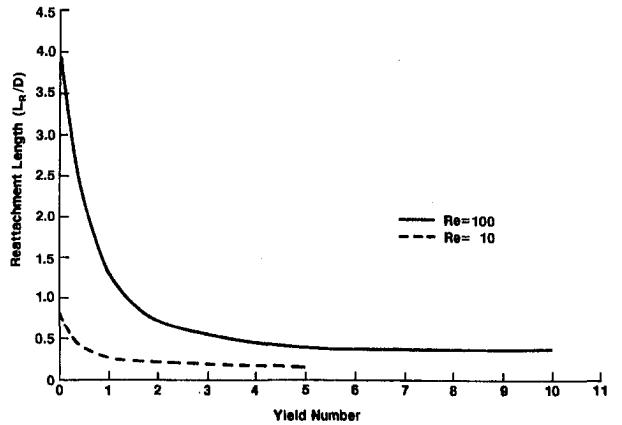

Fig. 5(*b*)

Fig. 5 Dependence of reattachment length on; (*a*) Reynolds number, (*b*) yield number

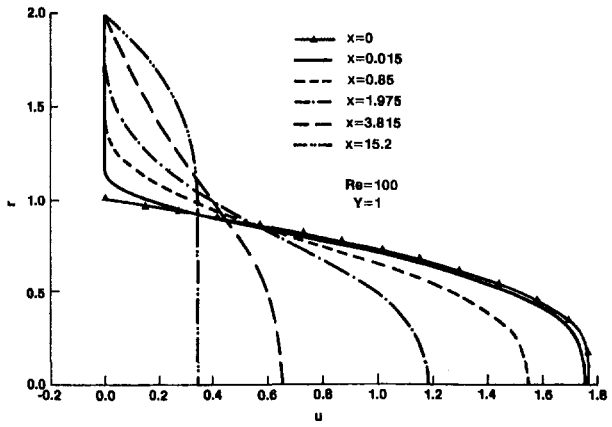

Fig. 6(*a*)

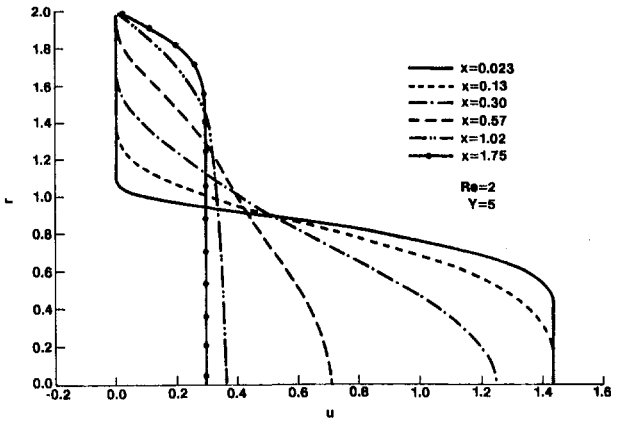

Fig. 6(*b*)

Fig. 6 Evolution of the streamwise velocity profiles downstream of the step

near the wall. Comparing Figs. 6(a) and 6(b), the effect of larger yield numbers and smaller Reynolds numbers on the flow development becomes obvious. The flow shown in Fig. 6(b) becomes fully developed downstream of the expansion much faster than its counterpart in Fig. 6(a). This is mainly due to the reduced reattachment length and the increased effective viscosity that is brought on by the larger yield number. An interesting feature of the flow is the disappearance of the initial plug flow region through the expansion. For both sets of Reynolds and yield numbers, the initial plug flow region at the inlet is quickly destroyed downstream of the expansion as the new mixing layer grows rapidly. The cause for this behavior is the deceleration of the flow imposed by the sudden expansion, which in turn generates a radial gradient of v in the plug flow region, hence a finite μ_{eff}.

The effect of the yield number on flow development is further investigated in Fig. 7(a) which shows the centerline velocity distributions for a range of yield numbers and Re = 100. Increasing yield numbers result in higher slopes of the centerline streamwise velocity immediately downstream of the step. This is mainly due to the reduced development lengths for larger yield number flows. Based on the centerline velocity, the flow development is completed by approximately $x = 5$ for $Y = 5$, while the corresponding for a Newtonian fluid is about $x = 25$. The opposite trend is observed when the Reynolds number is increased for a fixed yield number (Fig. 7(b)). Higher Reynolds numbers lead to larger reattachment lengths and thus longer flow development regions downstream of the expansion. It is also noted that both the inlet and the fully developed downstream centerline velocities are uniform for all different Reynolds numbers in Fig. 7(b). This is not the case in Fig. 7(a), where larger Y values result in larger plug flow regions and thus smaller fully developed centerline streamwise velocities.

The evolution of the radial velocity, v, is presented in Fig. 8(a). THe radial velocity is zero at the inlet due to the fully developed flow conditions. It again reaches the value of zero asymptotically at the exit as fully developed flow conditions are re-established. In between, v is positive throughout with the exception of a small region within the recirculation zone adjacent to the step wall where the flow is moving away from the wall and towards the pipe centerline. Downstream of the step, the velocity magnitude increases rapidly as the flow adjusts to the expansion and a new shear layer develops. In all cases the maximum of v is obtained around a streamwise location where reattachment occurs. As the Reynolds number increases and the yield number decreases, the length of the recirculating flow region increases. This results in a shift of the streamwise location and a decrease in the value of maximum v. The breakup of the core region immediately downstream of the sudden expansion due to the severe deceleration along the centerline results in the relatively high positive values of the radial velocity. This velocity maximizes at a radial location of about $r = 0.8$ for Re = 100 and $Y = 1$ (Fig. 8(b)). Further away from the centerline, it rapidly drops assuming a negative value at about $r = 1.1$, indicating the existence of the recirculating flow region. Further downstream beyond the separated flow region, the radial velocity is everywhere positive, with its maximum value diminishing as fully developed flow conditions are approached.

The distribution of the friction coefficient along the wall is shown in Fig. 9(a) for a Reynolds number 100 and for a range of yield numbers. In Newtonian flows, a small counter-rotating

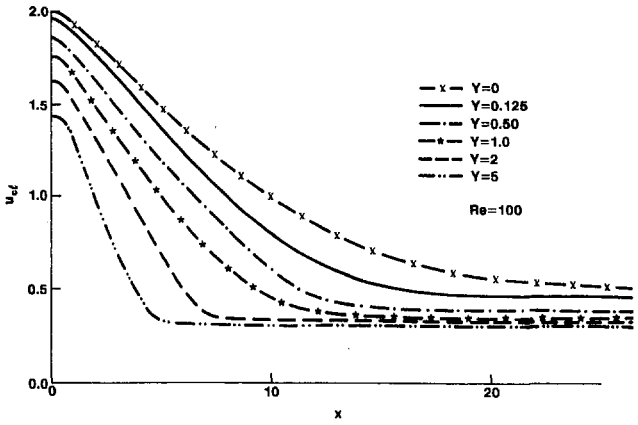

Fig. 7(*a*)

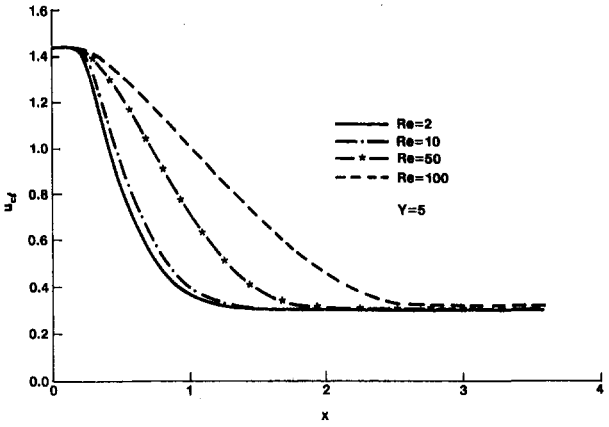

Fig. 7(*b*)

Fig. 7 Streamwise distribution of the centerline velocity

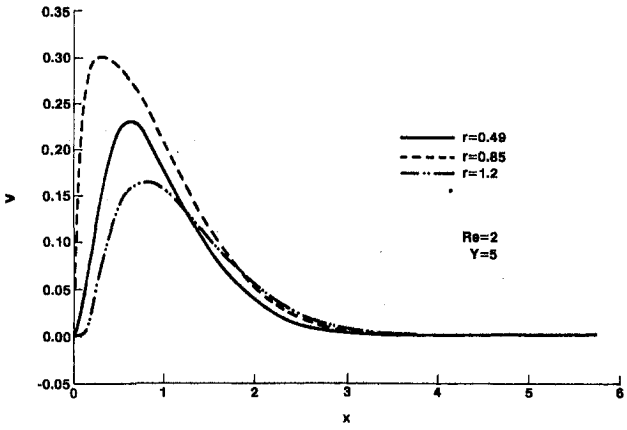

Fig. 8(*a*)

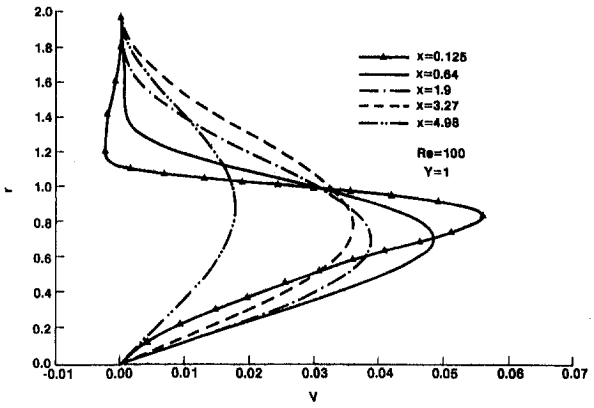

Fig. 8(*b*)

Fig. 8 Evolution of the radial velocity downstream of the step

vortex is observed at the corner of the expansion step and the downstream pipe wall. From the inset in Fig. 9(*a*) it is evident that this corner vortex exists also for a Bingham fluid. Immediately downstream of the step, a small region of negative friction coefficient is observed characterizing a counter-rotating flow. However, the computations indicate that the strength and extent of this vortex diminishes with increasing yield numbers. This small zone of negative C_f is followed by a positive C_f region which characterizes the larger recirculating bubble. The extent of this positive C_f region decreases with increasing yield numbers indicating the shrinking size of the recirculating bubble. The variation of C_f with the Reynolds number is shown in Fig. 9(*b*) for a yield number of 5. The extent of the recirculating flow region increases with increasing Reynolds numbers as the zero-crossing of the friction coefficient is shifted further downstream.

Figure 10 shows the vorticity distributions in the separating and reattaching flow region for yield numbers ranging between $Y = 0.125$ and 2. The Reynolds number is fixed at 100. The vorticity distribution for a Newtonian fluid has also been calculated (not shown here) and compared with the experimental data of Macagno and Hung (1967) for Re = 100. The agreement was found to be very good giving further credence to the present computations. As the yield number increases, the zero vorticity line within the recirculating flow region is shifted upstream indicating the shrinking of this region. The reduction of recirculation length is manifested also by the upstream-shifting of all constant vorticity contours. As mentioned earlier, this shrinkage is the result of the increase in the value of the effective viscosity as the yield number increases. This effect is found to be more pronounced at higher Reynolds numbers. The maximum value of the vorticity within the recirculation bubble decreases sharply as the yield number increases. This indicates a reduced strength of the recirculation bubble for large yield numbers. The region of positive vorticity in the recirculation bubble, showing the near-wall reverse flow, also shrinks with increasing yield numbers as does its magnitude. This also can be attributed to the diminishing strength of the recirculation at larger Y values. For $Y = 2$ (Fig. 10(*d*)) an additional zero vorticity contour appears downstream at about $x = 3.5$, which indicates the re-formation of the core region in the fully developed flow.

The distribution of the effective viscosity μ_{eff} in the initial expansion region is shown in Fig. 11 for the flow with Re = 100 and $Y = 1$. (Note that the figure does not include reattachment; flow reattachment occurs at $x/R_w \approx 8$ for this flow). The shear layer developing from the step edge is associated with small values of effective viscosity, caused by the large rates of deformation. Even on the centerline, the drop in the effective viscosity immediately downstream of the step is quite dramatic showing the very rapid destruction of the initial core flow region. Downstream of this initial destruction process is a region of moderate viscosity. Between $x/D = 0.33$ and 2, the centerline effective viscosity remains nearly constant. Further downstream, μ_{eff} starts increasing again as the conditions for a new core flow region start developing. The recirculating bubble is associated with high values of the effective viscosity. This is due to the relatively small rates of deformation in that region.

A question of considerable interest is, are there regions in the recirculation bubble where the actual value of μ_{eff} reaches infinity? This relates to the fundamental question of whether or not a stagnant fluid region exists within the recirculation bubble for sufficiently large yield numbers. For an actual Bingham fluid with the rheology defined by Eqs. (5*a*) and (5*b*) (Fig. 1(*a*)), in flow regions where the yield criterion $(\tau.\tau) > \tau_0^2$ is not satisfied, the only permissible motion is that of a solid body. Therefore, assuming that the no-slip condition at the wall is still valid, the fluid has to be stagnant in the near-corner region.

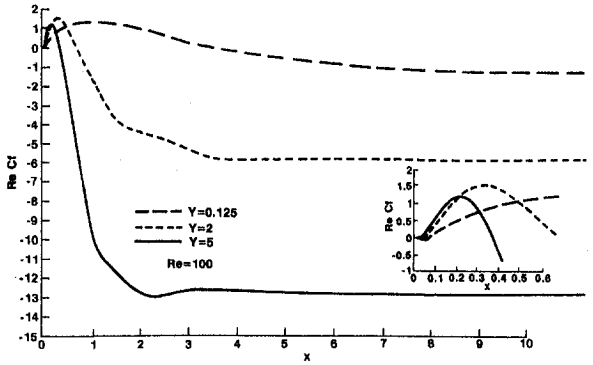

Fig. 9(*a*)

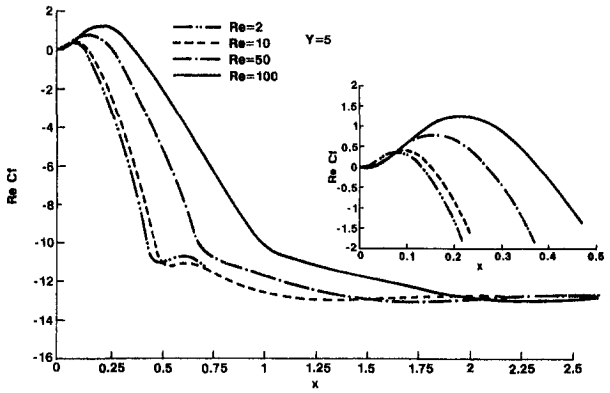

Fig. 9(*b*)

Fig. 9 The distribution of friction coefficient

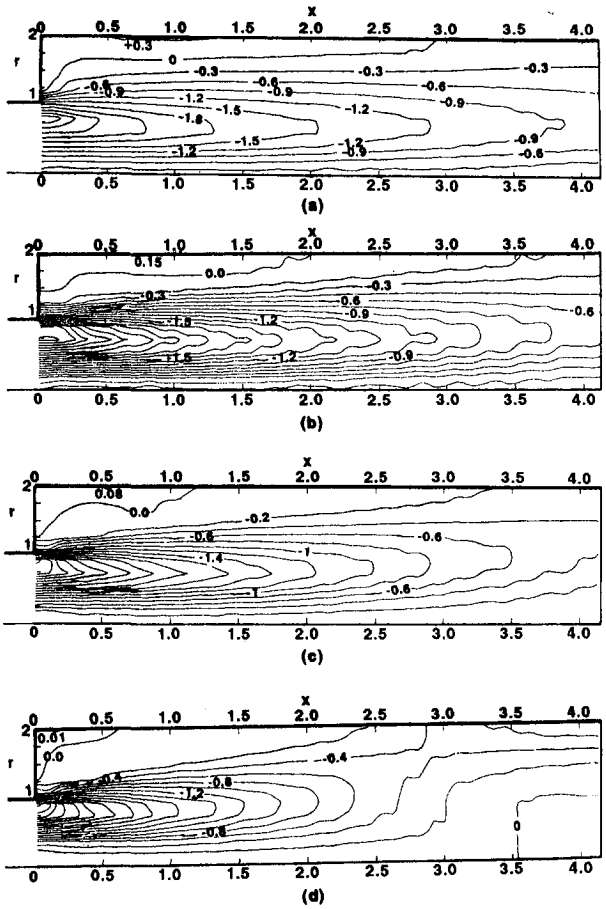

Fig. 10 Vorticity contours for Re = 100; (*a*) Y = 0.125, (*b*) Y = 0.5, (*c*) Y = 2, (*d*) Y = 2

The experiments of Ma et al. (1985) seem to confirm the existence of a stagnant flow zone. However, it is questionable that the measurement system employed would be able to distinguish very slow motion from no motion. The existence of a near-wall positive vorticity region (shown if Fig. 10) also seems to contradict the notion of a stagnant fluid zone in the recirculation bubble. Furthermore, the slope of the reattachment length versus the yield number line in Fig. 5(b) clearly indicates a tendency toward a nonzero asymptotic value for large Y values. This is consistent with the theoretical results of Lipscomb and Denn (1984) who argue that once a flow field is established, the existence of stagnant regions is not possible. Unfortunately, due to the inherent nature of the computational study with its requirement for the modification of the fluid rheology as indicated in Fig. 1(b), no definite conclusions can be drawn.

Conclusions

A finite-difference based, second-order accurate scheme has been successfully employed to predict the flow of a Bingham fluid over an axisymmetric sudden expansion. In order to avoid convergence problems due to a highly stiff coefficient matrix, the effective viscosity is limited to a maximum value of $\mu_{\text{eff}} = 1000\,\eta$. The results indicate a strong dependence of the separating and reattaching flow field on both the Reynolds number and the yield number. For all yield number cases studied, higher Reynolds number lead to longer reattachment lengths. On the other hand, increasing yield numbers result in shorter reattachment lengths and smaller recirculating flow regions. Higher yield numbers also result in smaller vorticity levels in the separated flow indicating reduced strengths of recirculation. This is caused by the increased levels of effective viscosity at higher yield number flows. The inlet plug flow region is not sustained through the sudden expansion. This zone of zero velocity gradient is completely destroyed within a short distance from the expansion step. The fully developed pipe flow conditions are obtained at shorter streamwise distances from the step for larger yield numbers. Once the flow is fully developed, a plug flow region again appears around the pipe axis. The recirculating flow region for the Bingham fluid has the same general features as with those of the Newtonian fluid. This is confirmed by the wall shear stress results which show the existence of a counter rotating vortex near the step corner, similar to the one observed in laminar Newtonian flows.

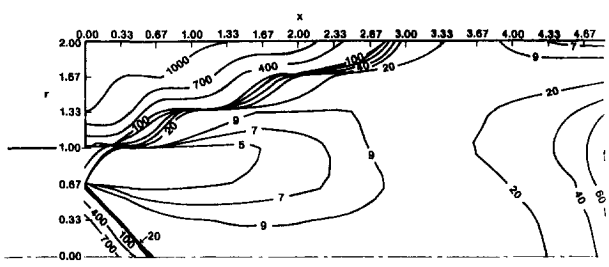

Fig. 11 Effective viscosity contours for Re = 100 and Y = 1

Acknowledgments

The authors gratefully acknowledge the Exxon Education Foundation for funding this project. The computer time provided by the Pittsburgh Supercomputer Center under grant MSM890007P is also acknowledged.

References

Aroesty, J., and Gross, J. F., 1972, "Pulsatile Flow in Small Blood Vessels—I," *Biorheology,* Vol. 9, pp. 34–43.

Bentson, J., and Vradis, G., 1987, "A Two-Stage Pressure Correction Technique for the Incompressible Navier-Stokes Equations," *AIAA paper 87-0545,* 25th Aerospace Sciences Meeting, January 12–15, Reno, NV.

Beverly, C. R., and Tanner, R. I., 1992, "Numerical Analysis of Three-Dimensional Bingham Plastic Flow," *Journal of Non-Newtonian Fluid Mechanics,* Vol. 42, pp. 85–115.

Bird, R. B., Stewart, W. E., and Lightfoot, E. N., 1960, *Transport Phenomena,* Wiley, New York, pp. 101–104.

Blackwell, B. F., 1985, "Numerical Solution of the Graetz Problem for a Bingham Plastic in Laminar Tube Flow With Constant Wall Temperature," ASME *Journal of Heat Transfer,* Vol. 107, pp. 466–468.

Chen, S. S., Fan, L. T., and Hwang, C. L., 1970, "Entrance Region Flow of the Bingham Fluid in a Circular Pipe," *AIChE Journal,* Vol. 16, No. 2, pp. 293–299.

Halmos, A. L., Boger, D. V., and Cabelli, A., 1975, "The Behavior of a Power-Law Fluid Flowing Through a Sudden Expansion: Part I. A Numerical Solution," *AIChE Journal,* Vol. 21, No. 3, pp. 540–549.

Lipscomb, G. G., and Denn, M. M., 1984, "Flow of Bingham Fluids in Complex Geometries," *Journal of Non-Newtonian Fluid Mechanics,* Vol. 14, pp. 337–346.

Ma, C-Y., White, J. L., Wessert, F. C., and Min, K., 1985, "Flow Patterns in Carbon Black Filled Polyethylene at the Entrance to the Die," *Journal of Non-Newtonian Fluid Mechanics,* Vol. 17, pp. 275–287.

Macagno, E. O., and Hung, T. K., 1967, "Computational and Experimental Study of a Captive Annular Eddy," *Journal of Fluid Mechanics,* Vol. 28, Part I, pp. 43–64.

Merrill, E. W., Benis, A. M., Gilliland, E. R., and Salzman, E. W., 1965, "Pressure-flow Relations of Human Blood in Hollow Fibers at Low Flow Rates," *Journal of Applied Physiology,* Vol. 20, pp. 954–967.

Nakamura, M., and Sawada, T., 1990, "Numerical Study on the Unsteady Flow of Non-Newtonian Fluid," ASME *Journal of Biomechanical Engineering,* Vol. 112, pp. 100–103.

O'Donovan, E. J., and Tanner, R. I., 1984, "Numerical Study of the Bingham Squeeze Film Problem," *Journal of Non-Newtonian Fluid Mechanics,* Vol. 15, pp. 75–83.

Pak, B., Cho, Y. I., and Choi, S. U. S., 1990, "Separation and Reattachment of Non Newtonian Fluid Flows In a Sudden Expansion Pipe," *Journal of Non-Newtonian Fluid Mechanics,* Vol. 37, pp. 175–199.

Park, J. T., Mannheimer, R. J., Grimley, T. A., and Morrow, T. B., 1989, "Pipe Flow Measurements of a Transparent Non-Newtonian Slurry," ASME JOURNAL OF FLUIDS ENGINEERING, Vol. 111, Sept., pp. 331–336.

Perera, M. G. N., and Walters, K., 1977, "Long Range Memory Effects in Flows Involving Abrupt Changes in Geometry. Part 2: The Expansion/Contrac-

tion/Expansion Problem," *Journal of Non-Newtonian Fluid Mechanics,* Vol. 2, pp. 191–204.

Skelland, A. H. P., 1948, *Non-Newtonian Flow and Heat Transfer,* Wiley, New York.

Soto, R. J., and Shah, V. L., 1976, "Entrance Flow of a Yield-Power Law Fluid," *Applied Science Research,* Vol. 32, pp. 73–85.

Vradis, G., Dougher, J., and Kumar, S., 1993, "Entrance Pipe and Heat Transfer for a Bingham Plastic," *International Journal of Heat and Mass Transfer,* Vol. 36, No. 3, pp. 543–552.

Vradis, G., and VanNostrand, L., 1992, "Laminar Coupled Flow Downstream of an Asymmetric Sudden Expansion," *AIAA Journal of Thermophysics and Heat Transfer,* Vol. 6, No. 2, Apr–June.

Welch, J. E., Harlow, F. H., Shannon, J. P., and Daly, B. J., 1966, "The MAC Method," Los Alamos Scientific Lab, Rept. LA-3425.

Wildman, D. J., Ekmann, J. M., Kadambi, J. R., and Chen, R. C., 1992, "Study of the Flow Properties of Slurries Using the Refractive Index Matching Technique and LDV," *Powder Technology,* Vol. 73, pp. 211–218.

Wilson, K. C., and Thomas, A. D., 1985, "A New Analysis of the Turbulent Flow of Non-Newtonian Fluids," *The Canadian Journal of Chemical Engineering,* Vol. 63, Aug. 1985 pp.

Wissler, E. H., and Schechter, R. S., 1959, "The Graetz-Nusselt Problem (with extension) for a Bingham Plastic," *Chemical Engineering Progress Symposium Series 29,* Vol. 55, pp. 203–208.

Journal of Fluids Engineering

Technical Briefs

On End-Wall Corner Vortices in a Lid-Driven Cavity

T. P. Chiang,[1] Robert R. Hwang,[1] and W. H. Sheu[1]

We conducted a flow simulation to study the laminar flow in a three-dimensional rectangular cavity. The ratio of cavity depth to width is 1:1, and the span to width aspect ratio (SAR) is 3:1. The governing equations defined on staggered grids were solved in a transient context by using a finite volume method, in conjunction with a segregated solution algorithm. Of the most apparent manifestation of three-dimensional characteristics, we addressed in this study the formation of corner vortices and its role in aiding the transport of fluid flows in the primary eddy and the secondary eddies.

1 Introduction

Recirculating flow is commonplace in many engineering fields. Conducting analyses to gain insight into the evolution of vortical flows is, thus, critical for developmental engineers. We considered in this study an extensively studied lid-driven flow in a rectangular cavity with the depth to width ratio, 1:1, and the span to width ratio, 3:1 (see Fig. 1). Geometric simplicity of this problem facilitates both experimental calibrations and numerical predictions.

Experimentally, the lid-driven cavity problem was first investigated by Pan and Acrivos (1967), followed by numerous visualization studies (Koseff and Street, 1984; Aidun et al., 1991). These measurement data suffice to depict a salient flow pattern. The pioneer numerical work was due to Burggraf (1966), who conducted only two-dimensional analysis. With the advent of high-speed computers and ever-increasing large disk space, three-dimensional simulations (Freitas et al., 1985; Ku et al., 1987; Freitas and Street, 1988; Cortes and Miller, 1994) have become feasible and are a great aid in acquiring additional details. Notable, among others, is the numerical confirmation of the laboratory observed corner vortices (Koseff et al., 1983).

From knowledge gained from the previous studies, it is now a generally recognized fact that the cavity of interest is filled with a primary eddy, downstream and upstream secondary eddies, and possibly meandering Taylor-Görtler longitudinal vortices as the Reynolds number is sufficiently high (see Fig. 1(*a*)). Previous investigations, however, did not focus much on the end-wall corner vortices other than noting their existence. This motivated us to conduct the present study with an aim to improve our understanding of corner vortices present near the end wall of the lid-driven cavity.

2 Governing Equations and Numerical Procedures

We considered in this study the following dimensionless velocity-pressure formulation for an incompressible Navier-Stokes fluid flow:

$$\frac{\partial u_i}{\partial x_i} = 0, \tag{1}$$

$$\frac{\partial u_i}{\partial t} + \frac{\partial}{\partial x_m}(u_m u_i) = -\frac{\partial p}{\partial x_i} + \frac{1}{\mathrm{Re}}\frac{\partial^2 u_i}{\partial x_m \partial x_m}, \tag{2}$$

where $i = 1 \sim 3$. Hereinafter, we denote u_i and p as the velocity components and the modified pressure, respectively. In Eq. (2), $\mathrm{Re} = (U_c B/\nu)$ is referred to as the Reynolds number, where ν stands for the kinematic viscosity, B the width of the cavity, and U_c the lid velocity.

To avoid oscillatory solutions in the pressure field, the present analysis is formulated for staggered grids (Patankar, 1980). Use of grid staggering demands velocity nodes to be stored only at the control faces. This grid arrangement facilitates conducting a finite volume integration of working equations in their representative control volume. In modeling the equations of motion, a higher-order QUICK scheme of Leonard (1979) has been the choice for discretizating the non-linear advective fluxes. Among the possible solution algorithms to solve for primitive variables, we adopted the segregated approach, known as the SIMPLE (Patankar, 1980) solution algorithm. The readers are referred to the work of Patankar (1980) for additional details.

3 Code Validation

Prior to predicting the flow physics in the rectangular cavity, we conducted a validation study by solving a problem which is amenable to analytic Navier-Stokes solutions. In a cubical cavity of unit length, we carried out the analysis on a $31 \times 31 \times 31$ uniform grid system. Subject to the boundary velocities given by $(u, v, w) = (\frac{1}{2}(y^2 + z^2), -z, y)$ the exact pressure solution takes the following form:

$$p = \tfrac{1}{2}(y^2 + z^2) + \frac{2}{\mathrm{Re}}x.$$

According to the computed errors cast in an L_2-norm form for primitive variables, namely (0.55×10^{-6}, 0.19×10^{-6}, 0.13

[1] Associate Professor, Professor, and Professor, respectively, Department of Naval Architecture and Ocean Engineering, National Taiwan University, 73 Chou-Shan Rd., Taipei, Taiwan.

Contributed by the Fluids Engineering Division of THE AMERICAN SOCIETY OF MECHANICAL ENGINEERS. Manuscript received by the Fluids Engineering Division May 24, 1996; revised manuscript received September 18, 1996. Associate Technical Editor: S. A. Jordan.

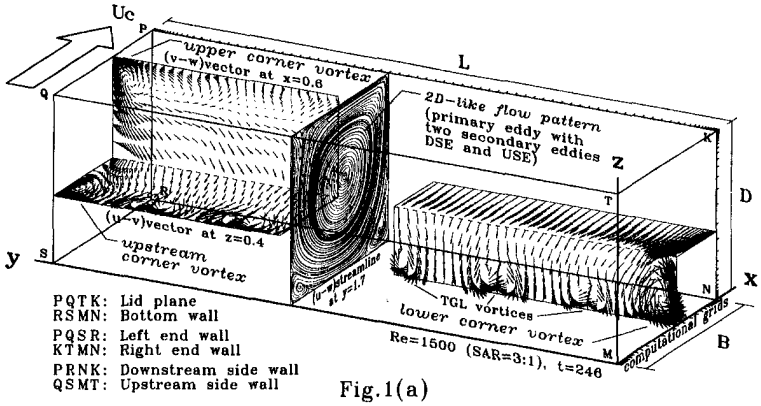

Fig.1(a)

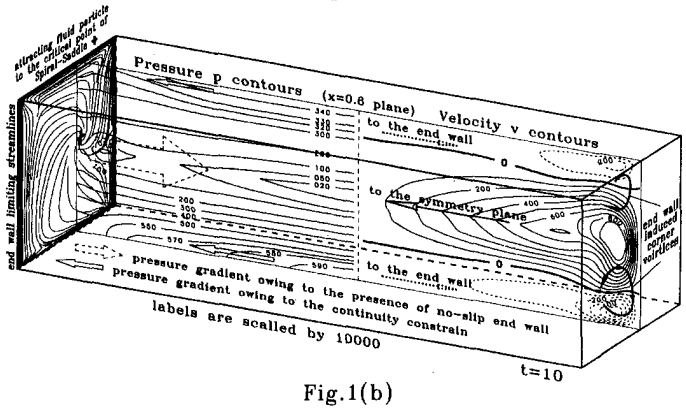

Fig.1(b)

Fig. 1 Problem definition and the description of the end wall effects. (*a*) Global flow structure; (*b*) the end wall induced pressure contours and spanwise velocity contours.

$\times 10^{-6}$, 0.23×10^{-4}) for (u, v, w, p) respectively, together with the maximum relative errors, (0.1×10^{-2}, 0.11×10^{-4}, 0.12×10^{-4}, 0.12×10^{-2}), we confirmed the validity of the proposed discretization method.

Having successfully completed an analytic validation test, we conducted also a grid refinement test for further confirmation of the computer code being developed. The target problem was that of the lid-driven cavity problem of the present interest. Here, we considered Re = 1000 and spanwise aspect ratio SAR = 1:1 for comparison purposes. With good agreement with other predicted velocities u ($x = 0.5$, $y = 0.5$, z) and w (x, $y = 0.5$, $z = 0.5$), as shown in Fig. 2, and the success of grid refinement test, it is concluded that the proposed analysis tool is well-suited for solving incompressible Navier-Stokes equations.

4 Results and Discussions

In Fig. 1(a), the configuration of the present interest is defined by two ratios, namely, depth to width (D/B = 1:1) and span to width (L/B = 3:1). In this study the mesh, with a grid of resolution of $34 \times 91 \times 34$, was stretched in regions where the boundary layers may develop. For this study, we considered Re = 1500. The emphasis was placed on the formation of the corner vortices, as shown in Fig. 1(a), in the vortical flow development.

4.1 End Wall Effect. A manifestation of this three-dimensional flow is the spanwise component generated by the two end walls. As shown in Fig. 1(b), the decelerating fluid particles adjacent to the end walls induce a negative pressure gradient. This, in turn, causes an inward spanwise flow motion inside the primary cell. Under these circumstances, a positive spanwise pressure gradient in the regions near the lid plane and the floor of the cavity is established. Mass continuity demands that the particles proceed toward the two end-walls. This conceptually amounts to placing a suction pump in the core region so that the fluid particles near the junctures of the floor, lid plane, and the upstream and downstream side walls of the cavity are entrained to both end-walls. It is also important to note that a less apparent outward-running spiral motion is visible near the lid plane. These spiraling particles will be finally engulfed into the primary core via corner vortices present near the two end walls.

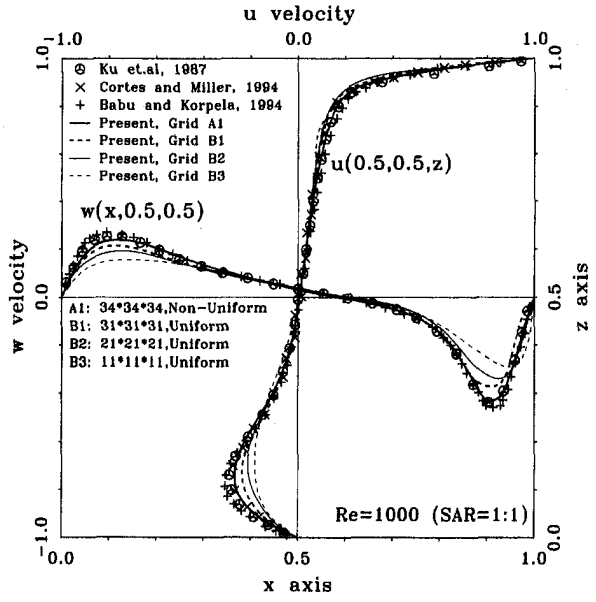

Fig. 2 Comparison studies with other numerical solutions for velocity profiles $u(0.5, 0, 5, z)$ and $w(x, 0.5, 0.5)$, together the grid convergence test for Re = 1000

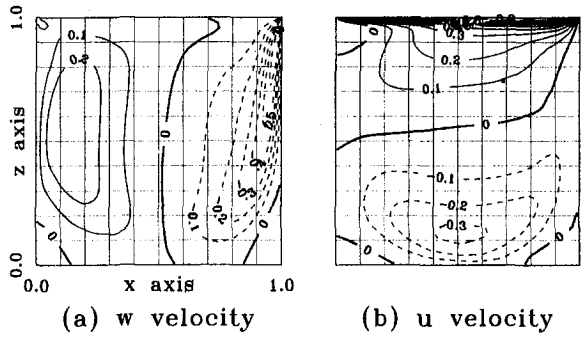

Fig. 3 The velocity contours at the $y = 2.0$ plane at $t = 24$. (*a*) *w* velocity; (*b*) *u* velocity

4.2 *x*-Plane Corner Vortices. The end-wall corner vortices are not necessarily present at the upper and lower corners of the x planes. Their presence is rather dependent on the spanwise and the primary circulating flow motions. As indicated in Fig. 3(a), in the upper cavity fluid particles which are characterized as possessing $w > 0$, as a direct result of the character of primary flow, can facilitate the formation of the upper corner vortices. On the other hand, the downward velocity $w < 0$ aids in forming a lower corner vortex. According to Fig. 4(a), lower corner vortices under no circumstances can be found in regions of $x < 0.5$, where $w > 0$. As the $x = 0.7$ plane is approached, descending fluids, as shown in Fig. 4(b), cause the upper corner vortex to disappear. Whether or not corner vortices at x planes will be finally established depends on the sign of the w velocity component in the primary vortex motion (see Fig. 3). Simply stated, $w > 0$ in the upper cavity while $w < 0$ in the lower cavity allow the formation of corner vortices at every account.

Corner eddies are believed to be the result of a mutual adjustment of the shear and the pressure forces to the no-slip condition applied at the two end walls. These stress-induced vortices cause a rotational flow (see Fig. 5). Vortices of this kind are prone to depart from the two end walls and aid the nearby particles being engulfed into the primary flow. Also notable is that the centroids of corner vortices are not necessarily close to the corner. Once the upper corner vortex forms, it is situated at the corner. In contrast, the center of the lower corner vortex is comparatively distant away from the intersection of the floor and the two end walls. This phenomenon is shown at the $x = 0.8$ plane in Fig. 6. To provide us with useful guidance for examining whether or not these corner vortices will form, we have plotted contour lines of $w = 0$ and $v = 0$ in Figs. 4–6. So long as a line of $w = 0$ intersects the line of $v = 0$, corner vortices are expected to form.

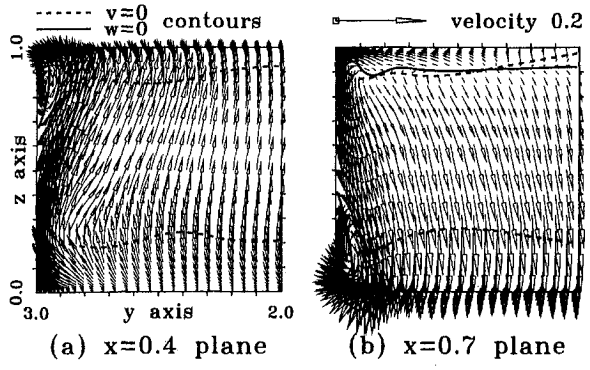

Fig. 4 Flow structures at two x planes at $t = 24$. (*a*) $x = 0.4$ plane; (*b*) $x = 0.7$ plane.

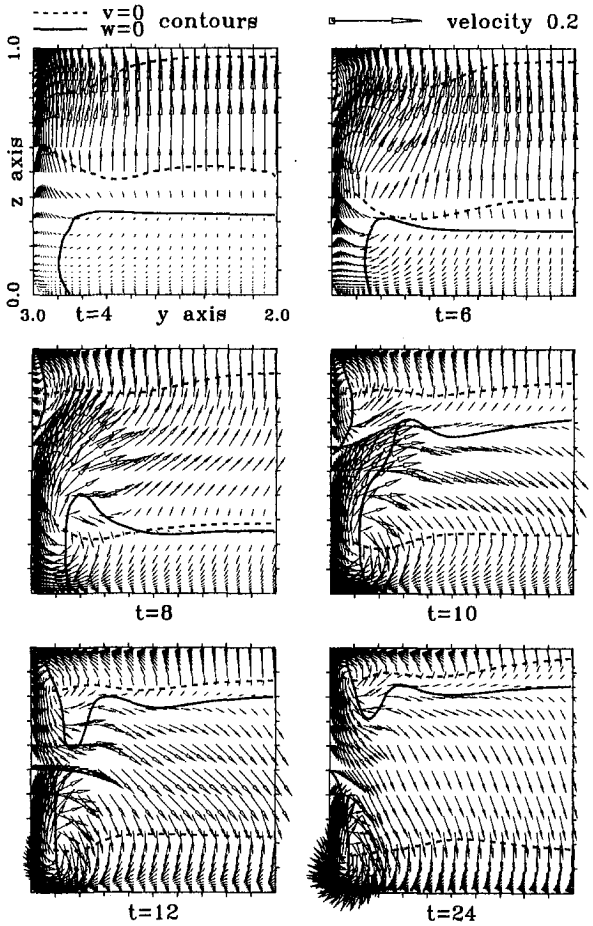

Fig. 5 Development of corner vortices at the $x = 0.6$ plane at $t = 4$, 6, 8, 10, 12, and 24

4.3 *z*-Plane Corner Vortices. In the z-plane, flow patterns in Fig. 7 bear strong resemblance to those computed at the x planes. Like the streamwise location of x plotted in Fig. 3(a) for which $w = 0$, the location of z that demands $u = 0$ in

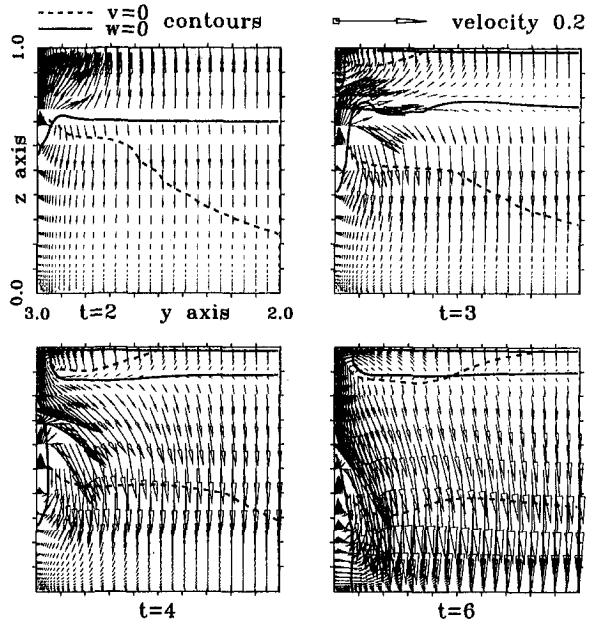

Fig. 6 Flow structures at the $x = 0.8$ plane at $t = 2$, 3, 4, and 6

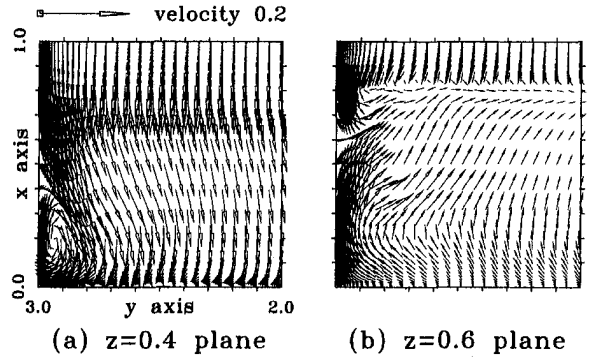

Fig. 7 Flow structure at two z planes at $t = 24$. (a) at $z = 0.4$ plane; (b) at $z = 0.6$ plane

Fig. 3(b) plays an essential role in judging whether the upstream corner vortex can be formed at the z planes. In Fig. 3(b), zero contour profiles of $u = 0$ closely resemble those of $w = 0$ in Fig. 3(a), except in the region fairly near the lid plane where $w = 0$ and $u = 1$. In view of the degree of physical complications, flow patterns at different z planes are regarded as much simpler than those at x planes. Unlike the upper and lower corner vortices at the x planes, the downstream corner vortices are hardly visible at the z planes. Except at the lid plane where $u = 1$, the value of u is less than zero in regions close to $x = 1$. Such a negative velocity gives rise to a strongly rotational downstream corner eddy in regions fairly close to $z = 1$.

4.4 The Role of Corner Vortices. As Fig. 1(a) reveals, there exist corner vortices in the cavity. The formation of such corner vortices constitutes the global transport structure in that fluid particles near the two end walls are engulfed into the primary core with the aid of corner vortices. Corner vortices, as a consequence, aid the exchange of fluid flows in the cavity. Conceptually, this amounts to placing a suction pump near the end wall, to which the nearby particles are attracted. In support of this statement, we plotted in Fig. 8 the particle tracers. Particles are clearly sucked into the attracting spiral saddle point via the corner vortices.

5 Conclusions

In the present analysis, we considered the incompressible fluid flow inside the investigated 3:1:1 cavity. Of three dimensional spiraling features, we have addressed under what conditions corner vortices will form. Through this study, it is concluded that the presence of corner vortices in the vicinity of two end-walls aids flow transport. Fluid particles coming across corner vortices will be lifted up and then drawn in the spiral-saddle point and then spiral towards the symmetry plane in the primary core.

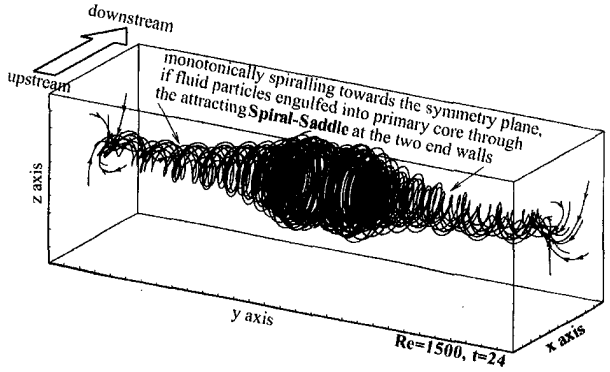

Fig. 8 Particle tracers for illustration of the attraction of fluids to the saddle point with the aid of corner vortices

Acknowledgment

The authors would like to express their thanks for financial support from the National Science Council under contract number NSC 80-0410-E002-51.

References

Aidun, C. K., Triantafillopoulos, N. G., and Benson, J. D., 1991, "Global Stability of a Lid-Driven Cavity with Throughflow: Flow Visualization Studies," *Phys. Fluids,* Vol. A3, pp. 2081–2091.

Babu, V. and Korpela, S. A., 1994, "Numerical Solutions of the Incompressible, Three-Dimensional Navier-Stokes Equations," *Computer Fluids,* Vol. 23, No. 5, pp. 675–691.

Burggraf, O. R., 1966, "Analytical and Numerical Studies of the Structure of Steady Separated Flows," *Journal of Fluid Mechanics,* Vol. 24, No. 1, pp. 113–151.

Cortes, A. B., and Miller, J. D., 1994, "Numerical Experiments With the Lid-Driven Cavity Flow Problem," *Computer Fluids,* Vol. 23, No. 8, pp. 1005–1027.

Freitas, C. J., Street, R. L., Findikakis, A. N., and Koseff, J. R., 1985, "Numerical Simulation of Three-Dimensional Flow in a Cavity," *Int. J. Numer. Methods Fluids,* Vol. 5, pp. 561–575.

Freitas, C. J., and Street, R. L., 1988, "Non-Linear Transport Phenomena in a Complex Recirculating Flow: A Numerical Investigation," *Int. J. Numer. Meths. in Fluids,* Vol. 8, pp. 769–802.

Koseff, C. J., Street, R. L., Gresho, C. D., Upson, J. A., Humphrey, J. A. C., and To, W. H., 1983, "A Three-Dimensional Lid-Driven Cavity Flow: Experiment and Simulation," *Proc. 3rd Int. Conf. Num. Meth. Lam. and Turb. Flow, Seattle,* Aug.

Koseff, J. R., and Street, R. L., 1984a, "Visualization Studies of a Shear Driven Three-Dimensional Recirculating Flow," ASME JOURNAL OF FLUIDS ENGINEERING, Vol. 106, No. 1, pp. 21–29.

Koseff, J. R. and Street, R. L., 1984b, "On End Wall Effects in a Lid-Driven Cavity Flow," ASME JOURNAL OF FLUIDS ENGINEERING, Vol. 106, pp. 385–389.

Koseff, J. R. and Street, R. L., 1984c, "The Lid-Driven Cavity Flow: A Synthesis of Qualitative and Quantitative Observations," ASME JOURNAL OF FLUIDS ENGINEERING, Vol. 106, pp. 390–398.

Ku, H. C., Hirsh, R. S., and Taylor, T. D., 1987, "A Pseudospectral Method for Solution of the Three-Dimensional Incompressible Navier-Stokes Equations," *J. Comput. Phys.,* Vol. 70, pp. 439–462.

Leonard, B. P., 1979, "A Stable and Accurate Convective Modeling Procedure Based on Quadratic Upstream Interpolation," *Comput. Methods Appl. Mech. Engrg.,* Vol. 19, pp. 59–98.

Pan, F., and Acrivos, A., 1967, "Steady Flows in Rectangular Cavities," *Journal of Fluid Mechanics,* Vol. 28, pp. 643–655.

Patankar, S. V., 1980, *Numerical Heat Transfer and Fluid Flow,* Hemisphere.

Effects of N^+ Ion Implantation on Surface Modification of Cavitation Damage for 0Cr13Ni9Ti SS of Turbine Materials

Jian Hua Wu and Gong Chun Chai

In this paper, six technologies have been used to implant N^+ into 0Cr13Ni9Ti SS, which is a kind of general turbine material in China, and their comparative experiments have been done to get a much better technology of modification of cavitation damage. The results show that the ability of cavitation resistance for 0Cr13Ni9Ti SS by N^+ ion implantation can reach

[1] Senior Engineer and Professor, Senior Engineer, respectively, Nanjing Hydraulic Research Institute, 225 Guangzhou Road, Nanjing, 210029, People's Republic of China.

Contributed by the Fluids Engineering Division of THE AMERICAN SOCIETY OF MECHANICAL ENGINEERS. Manuscript received by the Fluids Engineering Division August 31, 1995; revised manuscript received August 12, 1996. Associate Technical Editor: J. Katz.

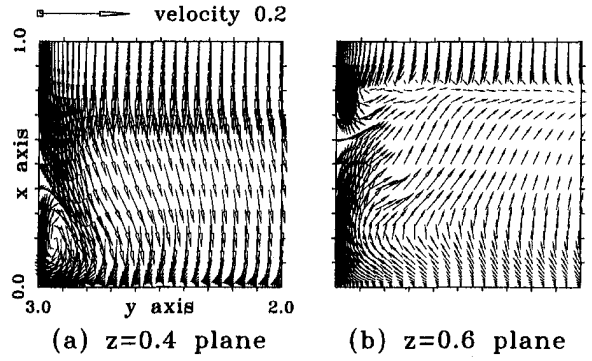

Fig. 7 Flow structure at two z planes at $t = 24$. (a) at $z = 0.4$ plane; (b) at $z = 0.6$ plane

Fig. 3(b) plays an essential role in judging whether the upstream corner vortex can be formed at the z planes. In Fig. 3(b), zero contour profiles of $u = 0$ closely resemble those of $w = 0$ in Fig. 3(a), except in the region fairly near the lid plane where $w = 0$ and $u = 1$. In view of the degree of physical complications, flow patterns at different z planes are regarded as much simpler than those at x planes. Unlike the upper and lower corner vortices at the x planes, the downstream corner vortices are hardly visible at the z planes. Except at the lid plane where $u = 1$, the value of u is less than zero in regions close to $x = 1$. Such a negative velocity gives rise to a strongly rotational downstream corner eddy in regions fairly close to $z = 1$.

4.4 The Role of Corner Vortices. As Fig. 1(a) reveals, there exist corner vortices in the cavity. The formation of such corner vortices constitutes the global transport structure in that fluid particles near the two end walls are engulfed into the primary core with the aid of corner vortices. Corner vortices, as a consequence, aid the exchange of fluid flows in the cavity. Conceptually, this amounts to placing a suction pump near the end wall, to which the nearby particles are attracted. In support of this statement, we plotted in Fig. 8 the particle tracers. Particles are clearly sucked into the attracting spiral saddle point via the corner vortices.

5 Conclusions

In the present analysis, we considered the incompressible fluid flow inside the investigated 3:1:1 cavity. Of three dimensional spiraling features, we have addressed under what conditions corner vortices will form. Through this study, it is concluded that the presence of corner vortices in the vicinity of two end-walls aids flow transport. Fluid particles coming across corner vortices will be lifted up and then drawn in the spiral-saddle point and then spiral towards the symmetry plane in the primary core.

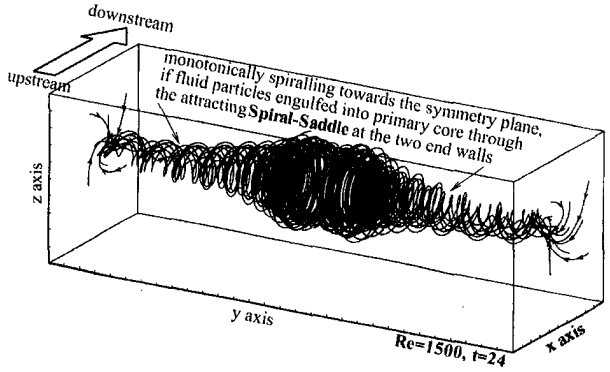

Fig. 8 Particle tracers for illustration of the attraction of fluids to the saddle point with the aid of corner vortices

Acknowledgment

The authors would like to express their thanks for financial support from the National Science Council under contract number NSC 80-0410-E002-51.

References

Aidun, C. K., Triantafillopoulos, N. G., and Benson, J. D., 1991, "Global Stability of a Lid-Driven Cavity with Throughflow: Flow Visualization Studies," *Phys. Fluids,* Vol. A3, pp. 2081–2091.

Babu, V. and Korpela, S. A., 1994, "Numerical Solutions of the Incompressible, Three-Dimensional Navier-Stokes Equations," *Computer Fluids,* Vol. 23, No. 5, pp. 675–691.

Burggraf, O. R., 1966, "Analytical and Numerical Studies of the Structure of Steady Separated Flows," *Journal of Fluid Mechanics,* Vol. 24, No. 1, pp. 113–151.

Cortes, A. B., and Miller, J. D., 1994, "Numerical Experiments With the Lid-Driven Cavity Flow Problem," *Computer Fluids,* Vol. 23, No. 8, pp. 1005–1027.

Freitas, C. J., Street, R. L., Findikakis, A. N., and Koseff, J. R., 1985, "Numerical Simulation of Three-Dimensional Flow in a Cavity," *Int. J. Numer. Methods Fluids,* Vol. 5, pp. 561–575.

Freitas, C. J., and Street, R. L., 1988, "Non-Linear Transport Phenomena in a Complex Recirculating Flow: A Numerical Investigation," *Int. J. Numer. Meths. in Fluids,* Vol. 8, pp. 769–802.

Koseff, C. J., Street, R. L., Gresho, C. D., Upson, J. A., Humphrey, J. A. C., and To, W. H., 1983, "A Three-Dimensional Lid-Driven Cavity Flow: Experiment and Simulation," *Proc. 3rd Int. Conf. Num. Meth. Lam. and Turb. Flow, Seattle,* Aug.

Koseff, J. R., and Street, R. L., 1984a, "Visualization Studies of a Shear Driven Three-Dimensional Recirculating Flow," ASME JOURNAL OF FLUIDS ENGINEERING, Vol. 106, No. 1, pp. 21–29.

Koseff, J. R. and Street, R. L., 1984b, "On End Wall Effects in a Lid-Driven Cavity Flow," ASME JOURNAL OF FLUIDS ENGINEERING, Vol. 106, pp. 385–389.

Koseff, J. R. and Street, R. L., 1984c, "The Lid-Driven Cavity Flow: A Synthesis of Qualitative and Quantitative Observations," ASME JOURNAL OF FLUIDS ENGINEERING, Vol. 106, pp. 390–398.

Ku, H. C., Hirsh, R. S., and Taylor, T. D., 1987, "A Pseudospectral Method for Solution of the Three-Dimensional Incompressible Navier-Stokes Equations," *J. Comput. Phys.,* Vol. 70, pp. 439–462.

Leonard, B. P., 1979, "A Stable and Accurate Convective Modeling Procedure Based on Quadratic Upstream Interpolation," *Comput. Methods Appl. Mech. Engrg.,* Vol. 19, pp. 59–98.

Pan, F., and Acrivos, A., 1967, "Steady Flows in Rectangular Cavities," *Journal of Fluid Mechanics,* Vol. 28, pp. 643–655.

Patankar, S. V., 1980, *Numerical Heat Transfer and Fluid Flow,* Hemisphere.

Effects of N^+ Ion Implantation on Surface Modification of Cavitation Damage for 0Cr13Ni9Ti SS of Turbine Materials

Jian Hua Wu and Gong Chun Chai

In this paper, six technologies have been used to implant N^+ into 0Cr13Ni9Ti SS, which is a kind of general turbine material in China, and their comparative experiments have been done to get a much better technology of modification of cavitation damage. The results show that the ability of cavitation resistance for 0Cr13Ni9Ti SS by N^+ ion implantation can reach

[1] Senior Engineer and Professor, Senior Engineer, respectively, Nanjing Hydraulic Research Institute, 225 Guangzhou Road, Nanjing, 210029, People's Republic of China.

Contributed by the Fluids Engineering Division of THE AMERICAN SOCIETY OF MECHANICAL ENGINEERS. Manuscript received by the Fluids Engineering Division August 31, 1995; revised manuscript received August 12, 1996. Associate Technical Editor: J. Katz.

Table 1 N^+ implanted technologies for 0Cr 13Ni9Ti SS

No.	Dose ($\times 10^{17}$) (ion/cm^2)	Beam current (μA/cm^2)	Energy (kev)	Temperature (°C)
1	1	33	80	230
2	4	33	80	230
3	10	33	80	230
4	1	35	80	400
5	4	35	80	400
6	10	35	80	400

more than 2 times of that before treatment. Meanwhile, for various technologies of N^+ ion implantation the changes of the surface compounds and their organizations are analysed by X-ray diffraction (XRD).

Nomenclature

a = amplitude of a sample (μm)
f = frequency of a sample (kHz)
t = water temperature of experiment (°C)
t' = surface temperature when ion implanted (°C)
T = time subjected to cavitation damage (hr)
WL = weight loss (mg)
WLR = WL/T = weight loss rate (mg/hr)
WTi = WL_0/WL_i = ratio of WL_0 of sample No. 0 to WL_i of No. i

1 Introduction

Cavitation damage of turbines has been one of general but very difficult problems. In order to reverse this kind of damage, a large amount of money has been spent yearly on the research to correct it. Second, stopping operation for mending has had an influence on the production of generating electricity. Therefore, it is necessary to develop and present new kinds of cavitation resistant materials for turbines.

Ion implantation technique, which has been developed since the 70's, has better effects on surface modification of metals, i.e., on friction, wear, hardness, fatigue, and so on, but few of papers on modification of cavitation damage have been published. Because cavitation damage can be explained as effects of cavitation bubbles to solid wall, and of combinations of hardness, fatigue, wear and other factors, it is believable that ion implantation technique has excellent effects on modification of cavitation damage for turbines and other possible cavitation components (Wu and Chai, 1994).

In this paper, six technologies have been used to implant N^+ into 0Cr13Ni9Ti SS, and their comparative experiments have been performed to reach a much better technology of modification of cavitation damage. The present results show that the ability of cavitation resistance for 0Cr13Ni9Ti SS by N^+ ion implantation can reach more than 2 times of that before treatment.

2 Ion Implantation Technique and Its Technologies

Ion implantation technique is that a surface of a solid is bombarded by some kind of ions with large energy, and their atoms are introduced into the surface or its special locations so that the properties of the surface or itself of the solid can be modified.

Effects of ion implantation technique on surface modification for metal materials are closely related to its technologies. Where the recent technique and our research are concerned, these technological parameters include kind of ion, dose and energy and temperature of implanted ions, and etc (Wang, 1991; Williamson, 1990). In this paper, the technologies of N^+ ion implantaion into 0Cr13Ni9Ti SS are shown in Table 1.

3 Experimental Apparatus and Methods

3.1 Experimental Apparatus. The experimental apparatus is shown in Fig. 1. Cavitation damage of the sample in the experimental liquid is brought about by high frequency vibration of the amplitude variation shaft, the vibration frequency of the sample is measured by a frequency meter, the amplitude is controlled by a millivoltmeter through a piezoelectric crystal plate.

Weight variations among all samples are less than 0.5 g. The samples are weighed before and after every experiment by a precise balance which has a accuracy of 0.05 mg.

3.2 Experimental Methods. Comparative experiments have been done to compare the effects of modification of N^+ implanted 0Cr13Ni9Ti SS with that of no implantation and to get the best technology of N^+ ion implantation for this material.

Experimental liquid is distilled water. Temperature of experimental liquid t = 23–27°C, frequency f = 17.05–17.25 kHz, amplitude a = 30 μm. In addition to the period of 2 hours, the experimental periods of 4, 6 and 8 hours are added.

Before every experiment, the sample is weighed after cleaning of it with acetone, alcohol, and dry of it. And after finishing the experiment, it is weighed according to the same procedure.

For various technologies of N^+ ion implantation the changes of surface compounds and their organizations for 0Cr13Ni9Ti SS are analysed by X-ray diffraction (XRD) to study the mechanisms of modification.

4 Results and Discussions

4.1 Indices of Cavitation Damage. In the past, weight loss rate (WLR) is one of the most frequently used indices on cavitation damage. It can be defined as weight loss of a workpiece in unit time due to cavitation damage, expressed by

$$\mathrm{WLR} = \frac{\mathrm{WL}}{T} \tag{1}$$

where WL is weight loss of a workpiece due to cavitation damage, T is time subjected to cavitation damage.

4.2 Analyses of Effects on Modification of Cavitation Damage in WLR. The sample in which N^+ is not implanted is numbered No. 0, No. 1–No. 3 is a group of lower temperature implantation when t' = 230°C, and No. 4–No. 6 is a group when t' = 400°C.

Table 2 is the result of lower temperature group No. 1–No. 3 and No. 0, and Table 3 is the result of No. 4–No. 6 and No. 0. In these two tables WT is a ratio of weight loss WL_0 of sample No. 0 to weight loss WL_i of No. 1–No. 6, and WL is given by

$$\mathrm{WL} = \frac{1}{4}\sum_{j=1}^{4} \mathrm{WL}j \tag{2}$$

It is a mean value of weight losses of four samples which are treated by a same technology. DWL is given by

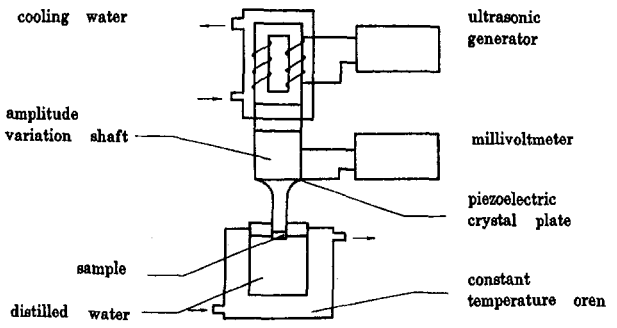

Fig. 1 Experimental apparatus

Table 2 Results of cavitation damage on N^+ implantation at $t' = 230°C$

	T = 2.0 (hr)				T = 4.0 (hr)				T = 6.0 (hr)				T = 8.0 (hr)			
No.	WLR	WL	DWL	WT	WLR	WL	DWL	WT	WLR	WL	DWL	WT	WLR	WL	DWL	WT
0	2.18	4.36	0.19	1.00	4.30	17.19	2.41	1.00	4.15	24.89	0.64	1.00	4.63	37.04	1.35	1.00
1	0.96	1.93	0.02	2.26	2.76	11.04	0.27	1.56	3.18	19.05	0.50	1.31	3.69	29.55	0.45	1.25
2	0.94	1.87	0.01	2.37	1.78	7.13	0.24	2.41	3.01	18.04	1.37	1.38	3.19	25.52	0.56	1.45
3	0.87	1.74	0.03	2.50	1.69	6.75	0.29	2.54	2.34	14.02	0.39	1.78	2.66	21.28	0.42	1.74

Table 3 Results of cavitation damage on N^+ implantation at $t' = 400°C$

	T = 2.0 (hr)				T = 4.0 (hr)				T = 6.0 (hr)				T = 8.0 (hr)			
No.	WLR	WL	DWL	WT	WLR	WL	DWL	WT	WLR	WL	DWL	WT	WLR	WL	DWL	WT
0	2.18	4.36	0.19	1.00	4.30	17.19	2.41	1.00	4.15	24.89	0.64	1.00	4.63	37.04	1.35	1.00
4	0.78	1.56	0.06	2.79	1.56	6.25	0.12	2.75	2.08	12.50	0.15	1.99	2.51	20.05	0.32	1.85
5	0.48	0.95	0.05	4.59	0.98	3.90	0.11	4.40	1.63	9.76	0.19	2.55	2.20	17.64	0.29	2.10
6	0.42	0.83	0.04	5.25	0.93	3.73	0.10	4.64	1.46	8.79	0.21	2.83	1.80	14.44	0.22	2.56

$$\mathrm{DWL} = \frac{1}{4}\sum_{j=1}^{4}(\mathrm{WL}j - \mathrm{WL})^2 \qquad (3)$$

It is a variance of weight losses which indicates the discrepancy among the four samples. WLR is calculated in Eq. (1).

From Table 2 or Fig. 2, at $t' = 230°C$, the properties of cavitation resistance for 0Cr13Ni9Ti SS have been greatly modified after N^+ ion implantation. And the effects of modification increase when N^+ implaninted doses increase. These results can be explained that the modifying layer gets thicker and that the N^+ concentration is bigger when doses increase. Meanwhile, changes of surface microstructure are benefit to modification of cavitation damage so that a new protective coating of cavitation resistance is formed.

In addition, with the incrcase of experimental time WLR_0 of sample No. 0 ranges from 4.30 to 4.63 when $T > 2.0$ hours, while WLR_3 of No. 3 which is implanted by higher doses is from 1.69 to 2.66. These results indicate not only larger weight loss of No. 0 than that of No. 3, but also much more severe cavitation damage of the former than that of the latter.

From the results of a higher temperature group at $t' = 400°C$ (shown in Table 3 or Fig. 3), on the one hand, the effects on modification increase when doses increase, on the other hand, under the conditions of same doses, the effects on modificaion of a higher temperature group are greatly superior to that of a lower temperature group. For the sample No. 6 and No. 3 of dose $1 \times 10^{18} N^+/cm^2$, for example, their WT are 5.25, 2.50 respectively when $T = 2.0$ hours. Though $T = 8.0$ hours, we have that $WT_6 = 2.56$ and $WT_3 = 1.74$. That is to say, N^+ implanted temperatures have greatly effects on modification of cavitation damage for 0Cr13Ni9Ti SS. These results may be analyzed from two aspects. First, N^+ ion implantation at a higher temperature forms a thicker protective coating to cavitation damage, which may be explained in Fig. 4 (Williamson, 1990, and Wang, 1991). Second, it produces some kinds of new compounds which are not contained in 0Cr13Ni9Ti SS

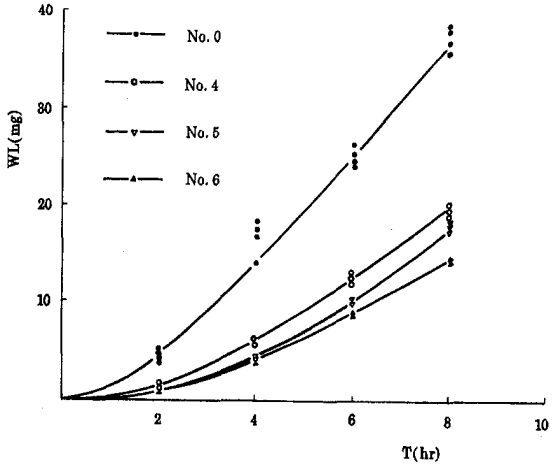

Fig. 3 Results of cavitation damage on N^+ implantation at $t' = 400°C$

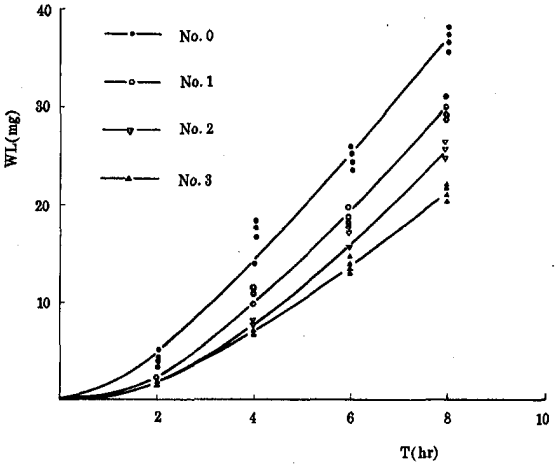

Fig. 2 Results of cavitation damage on N^+ implantation at $t' = 230°C$

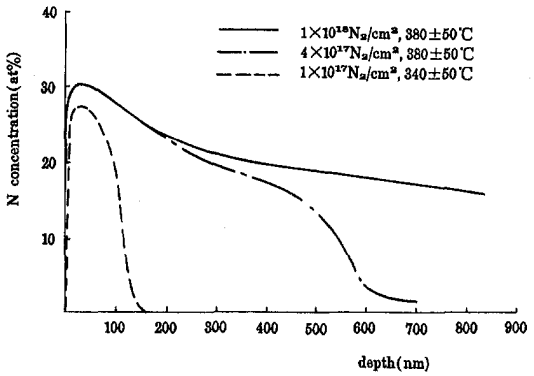

Fig. 4 N^+ concentration distributions in depth at various temperatures

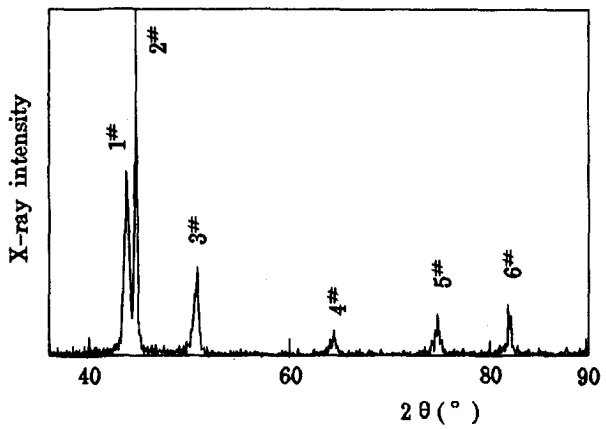

Fig. 5 XRD analyses of sample No. 0

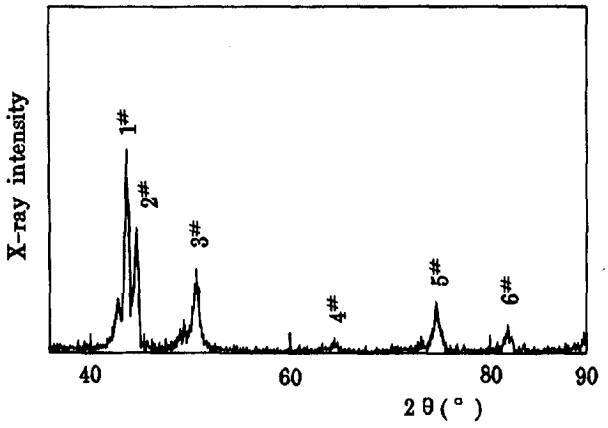

Fig. 7 XRD analyses of sample No. 4

of no N^+ ion implantation or of lower temperature N^+ ion implantation. These kinds of new compounds have better effects on modification of cavitation damage, which could be proved by XRD analyses as followings.

4.3 XRD Analyses for N^+ Implanted 0Cr13Ni9Ti SS. XRD analyses of samples No. 0, No. 1, No. 4 and No. 6 are shown in Fig. 5 to Fig. 8. For sample No. 0 of no N^+ implantation, from Fig. 5, there are six characteristic peaks at the range of 36 deg $\leq 2\theta \leq$ 90 deg. Peak 1 (2θ = 43.52 deg), 3 (50.60 deg) and 5 (74.50 deg) are characteristic peaks of metal compound CrFeNi, and their solid solubility is limited in a narrow range. Peak 2 (2θ = 44.50 deg), 4 (67.90 deg) and 6 (82.40 deg) are solid solution Fe—Cr and αFe with a wide solid solubility.

From Fig. 6–Fig. 8, peak 1, 3 and 5 do not greatly change, while peak 2, 4 and 6 get smaller. These results indicate that N^+ ion implantation has smaller effects on metal compounds than solid solutions. And a series of peaks in the lefts of peak 1, 3 and 5 represent many kinds of new nitrogen compounds.

In Fig. 6, new nitrogen compounds are

Fe_3N, 2θ = 41.18 deg
$Cr_2(C, N)$, 2θ = 42.40 deg
Fe_4N, 2θ = 47.83 deg
Fe_3NiN, 2θ = 48.10 deg

In Fig. 7, we can get

$Cr_2(C, N)$, 2θ = 42.40 deg
$\beta - Cr_2N$, 2θ = 42.60 deg
$(Cr_2Fe)_2N_{1-x}$, 2θ = 42.80 deg
FeNiN, 2θ = 45.31 deg and 48.93 deg.

From Fig. 8, when doses increase, peak intensities are greatly strengthened though the locations of the peaks are similar to Fig. 7, that is to say, at higher dose implantation, the concentrations of new nitrogen compounds get bigger.

In addition, comparing No. 1 of the lower temperature group with No. 4 of the higher temperature group, temperatures of N^+ ion implantation have great effects on surface organizations though their doses are same. Moreover, lower temperature forms some nitrogen compounds of Fe, while higher temperature, nitrogen compounds of Cr. These may be metallurgical mechanisms that N^+ ion implantation at higher temperature has better effects on modification of cavitation damage than that at lower temperature.

5 Conclusions

For 0Cr13Ni9Ti SS of turbine materials, at N^+ ion implantation of higher temperature and higher dose, the properties of cavitation resistance have greatly been modified. The effects on the modification increase when N^+ doses increase, and implantation at t' = 400°C has better effects than that at t' = 230°C. The ability of modification by N^+ ion implantation can reach more than 2 times of that before treatment.

Cavitation damage experiments and XRD analyses show that Fe and N compounds are formed at N^+ ion implantation of lower temperature, and Cr and N compounds are formed at higer temperature, that is to say, Cr and N compounds have better effects on modification of cavitation damage for 0Cr13Ni9Ti SS.

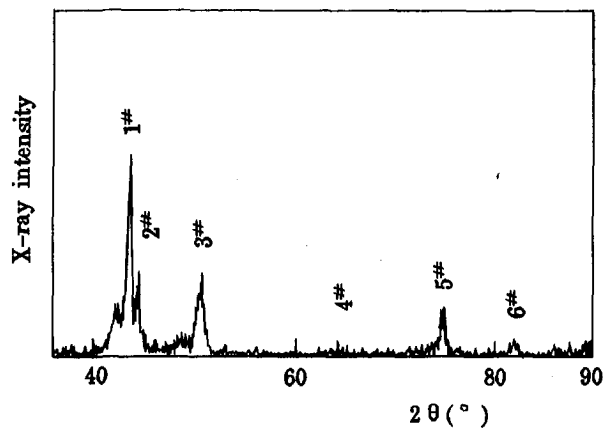

Fig. 6 XRD analyses of sample No. 1

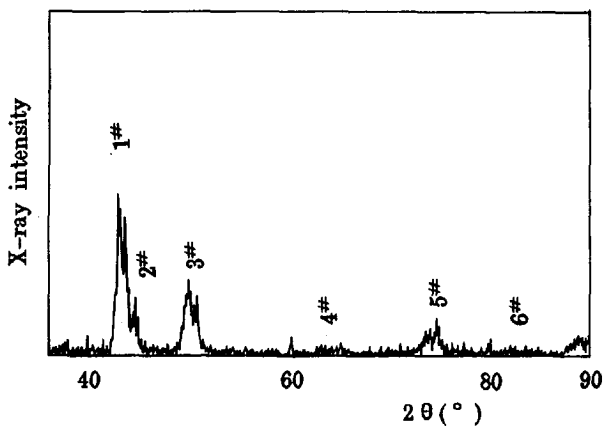

Fig. 8 XRD analyses of sample No. 6

Acknowledgments

The authors are very grateful to the consultation and assistance of Prof. Wang, G. H. in the Dept. of Physics, Nanjing University.

References

Wang, G. H., 1991, *Physics of Particle—Solid Interaction,* Chinese Science Press.

Williamson, D. L., et al., 1990, "Solid Solution Strengthening of Stainless Steel Surface Layers by Rapid, High—Dose, Elevated Temperature Nitrogen Ion Implantation," *Materials Letters,* Vol. 9, No. 9, May.

Wu, J. H., and Chai, G. C., 1994, "Applications of Ion Implantation Technique to Modification of Cavitation Damage for Turbines," *J. of Nanjing Hydraulic Research Institute,* No. 4, (in Chinese).

Laminar Pulsatile Flow Through an Axisymmetric Sudden Expansion

R. Budwig,[1] C. J. Egelhoff,[1] and S. Tavoularis[2]

Introduction

Internal flows through sudden expansions have been of considerable interest because they involve dramatic changes in the flow pattern which affects mixing, local wall shear stress, overall pressure drop and wall heat and mass transfer. For example, it is well known that sites in the arterial tree where there are sudden area increases are prone to vascular diseases, such as atherosclerosis (Nerem, 1992). Sudden expansion flows are also attractive as relatively simple paradigms of recirculating flows, inviting fruitful theoretical analyses and serving as benchmark cases for the testing of CFD codes and turbulence models.

Most of the previous work on axisymmetric sudden expansion (ASE) flows has been on steady laminar (e.g., Back and Roschke, 1972) or stationary turbulent (e.g., Devenport and Sutton, 1993) cases. These studies have demonstrated that the extent of the recirculation zone increases with Reynolds number increasing up to a critical value at which transition to turbulence occurs.

The only available study of pulsatile flows in ASE is the computational work by Ma et al. (1994), which, however, focuses on wall heat and mass transfer. On the other hand, several studies have dealt with pulsatile internal flows of relevance to the human circulatory system, such as in stenoses (e.g., Ohja et al., 1989) and aneurysms (e.g., Elger et al., 1995).

In the present investigation, we report detailed measurements of strongly pulsatile, laminar flow through an ASE. Steady flow measurements through the same ASE, along with some preliminary pulsatile flow results, were reported earlier by Budwig and Tavoularis (1995). These authors observed a strong asymmetry of the recirculating region, which can be attributed to secondary flows driven by slight temperature differences between the circulating fluid and the fluid in the viewing tank (see Fig. 1). Secondary flows have been observed in laminar pipe flows (Mori and Futagami, 1967) even at a fluid-wall temperature difference as small as 0.2 K (Grolman, 1988). In any case, the steady flow results reported by Budwig and Tavoularis (1995) corresponded to nearly axisymmetric recirculation patterns, obtained by slight fluid injection into the test section, immediately downstream of the expansion.

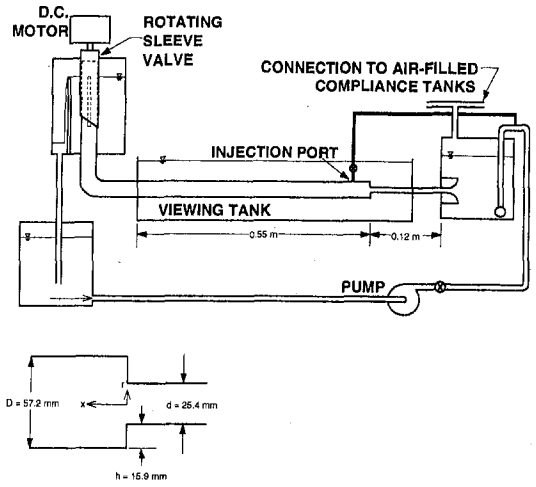

Fig. 1 Schematic of the ASE apparatus

The steady flow recirculation zone lengths at Reynolds numbers (based on the bulk velocity and the upstream tube diameter) Re = 131 and 253 were, respectively, 14.4 h and 24.8 h (h is the step height), comparable to those in previous studies. An attempt to produce a steady flow at Re = 409 failed, as the flow became unstable, with the core jet flapping around at irregular time intervals.

The issues of instability and transition in an ASE have not yet been resolved, as Back and Roschke (1972) report transition at Re = 350, while Feuerstein et al. (1975) indicated the much higher value Re = 1090; it is clear, however, that instability in an ASE depends strongly on the upstream flow conditions.

Unsteady laminar flows in relatively simple systems appear to be solvable by existing computational methods. It is clear, however, that the validity of such solutions must be confirmed experimentally, due to their sensitivity to many extraneous factors, such as geometrical asymmetries, asymmetries in the entrance and outlet conditions and undesirable temperature differences and flow disturbances. Moreover, the prediction of instability and transition is well beyond the current capacity of unsteady viscous codes. The present study was meant to be the basis for establishing an extensive computational and experimental program on internal pulsatile flows, which will address a variety of issues beyond those discussed herein.

Experimental Setup and Measuring Procedures

The experiments were conducted at the University of Ottawa in a closed-loop flow facility shown schematically in Fig. 1. Steady and pulsatile flows of a refractive index matching fluid (a combination of water, ammonium thiocyanate, and glycerin, see Budwig, 1994) were produced with the use of a centrifugal pump and a rotating sleeve valve. The test section consisted of two circular cast acrylic tubes, with dimensions shown in Fig. 1 and forming an axisymmetric sudden expansion with a diameter ratio of 2.25. The tolerance on the diameter of the cast acrylic tubing was ±0.3 mm. The two acrylic tubes were bonded together on a 19 mm thick coupling ring that held the tubes concentric to ±0.05 mm. The test section was immersed in a rectangular viewing tank, filled with the same refractive matching fluid, whose kinematic viscosity was 12.5×10^{-6} m^2/s.

[1] Associate Professor and Graduate Student, respectively, Department of Mechanical Engineering, University of Idaho, Moscow, ID 83844.

[2] Professor, Department of Mechanical Engineering, University of Ottawa, Ottawa, Ontario, Canada K1N6N5.

Contributed by the Fluids Engineering Division of THE AMERICAN SOCIETY OF MECHANICAL ENGINEERS. Manuscript received by the Fluids Engineering Division February 20, 1996; revised manuscript received September 23, 1996. Associate Technical Editor: P. R. Bandyapahyay.

Acknowledgments

The authors are very grateful to the consultation and assistance of Prof. Wang, G. H. in the Dept. of Physics, Nanjing University.

References

Wang, G. H., 1991, *Physics of Particle—Solid Interaction,* Chinese Science Press.

Williamson, D. L., et al., 1990, "Solid Solution Strengthening of Stainless Steel Surface Layers by Rapid, High—Dose, Elevated Temperature Nitrogen Ion Implantation," *Materials Letters,* Vol. 9, No. 9, May.

Wu, J. H., and Chai, G. C., 1994, "Applications of Ion Implantation Technique to Modification of Cavitation Damage for Turbines," *J. of Nanjing Hydraulic Research Institute,* No. 4, (in Chinese).

Laminar Pulsatile Flow Through an Axisymmetric Sudden Expansion

R. Budwig,[1] C. J. Egelhoff,[1] and S. Tavoularis[2]

Introduction

Internal flows through sudden expansions have been of considerable interest because they involve dramatic changes in the flow pattern which affects mixing, local wall shear stress, overall pressure drop and wall heat and mass transfer. For example, it is well known that sites in the arterial tree where there are sudden area increases are prone to vascular diseases, such as atherosclerosis (Nerem, 1992). Sudden expansion flows are also attractive as relatively simple paradigms of recirculating flows, inviting fruitful theoretical analyses and serving as benchmark cases for the testing of CFD codes and turbulence models.

Most of the previous work on axisymmetric sudden expansion (ASE) flows has been on steady laminar (e.g., Back and Roschke, 1972) or stationary turbulent (e.g., Devenport and Sutton, 1993) cases. These studies have demonstrated that the extent of the recirculation zone increases with Reynolds number increasing up to a critical value at which transition to turbulence occurs.

The only available study of pulsatile flows in ASE is the computational work by Ma et al. (1994), which, however, focuses on wall heat and mass transfer. On the other hand, several studies have dealt with pulsatile internal flows of relevance to the human circulatory system, such as in stenoses (e.g., Ohja et al., 1989) and aneurysms (e.g., Elger et al., 1995).

In the present investigation, we report detailed measurements of strongly pulsatile, laminar flow through an ASE. Steady flow measurements through the same ASE, along with some preliminary pulsatile flow results, were reported earlier by Budwig and Tavoularis (1995). These authors observed a strong asymmetry of the recirculating region, which can be attributed to secondary flows driven by slight temperature differences between the circulating fluid and the fluid in the viewing tank (see Fig. 1). Secondary flows have been observed in laminar pipe flows (Mori and Futagami, 1967) even at a fluid-wall temperature difference as small as 0.2 K (Grolman, 1988). In any case, the steady flow results reported by Budwig and Tavoularis (1995) corresponded to nearly axisymmetric recirculation patterns, obtained by slight fluid injection into the test section, immediately downstream of the expansion.

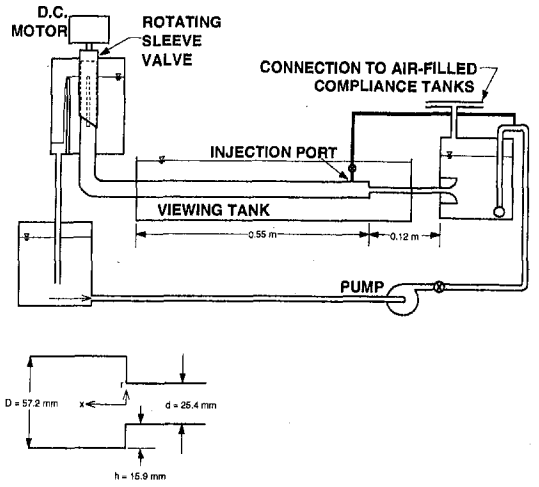

Fig. 1 Schematic of the ASE apparatus

The steady flow recirculation zone lengths at Reynolds numbers (based on the bulk velocity and the upstream tube diameter) Re = 131 and 253 were, respectively, 14.4 h and 24.8 h (h is the step height), comparable to those in previous studies. An attempt to produce a steady flow at Re = 409 failed, as the flow became unstable, with the core jet flapping around at irregular time intervals.

The issues of instability and transition in an ASE have not yet been resolved, as Back and Roschke (1972) report transition at Re = 350, while Feuerstein et al. (1975) indicated the much higher value Re = 1090; it is clear, however, that instability in an ASE depends strongly on the upstream flow conditions.

Unsteady laminar flows in relatively simple systems appear to be solvable by existing computational methods. It is clear, however, that the validity of such solutions must be confirmed experimentally, due to their sensitivity to many extraneous factors, such as geometrical asymmetries, asymmetries in the entrance and outlet conditions and undesirable temperature differences and flow disturbances. Moreover, the prediction of instability and transition is well beyond the current capacity of unsteady viscous codes. The present study was meant to be the basis for establishing an extensive computational and experimental program on internal pulsatile flows, which will address a variety of issues beyond those discussed herein.

Experimental Setup and Measuring Procedures

The experiments were conducted at the University of Ottawa in a closed-loop flow facility shown schematically in Fig. 1. Steady and pulsatile flows of a refractive index matching fluid (a combination of water, ammonium thiocyanate, and glycerin, see Budwig, 1994) were produced with the use of a centrifugal pump and a rotating sleeve valve. The test section consisted of two circular cast acrylic tubes, with dimensions shown in Fig. 1 and forming an axisymmetric sudden expansion with a diameter ratio of 2.25. The tolerance on the diameter of the cast acrylic tubing was ±0.3 mm. The two acrylic tubes were bonded together on a 19 mm thick coupling ring that held the tubes concentric to ±0.05 mm. The test section was immersed in a rectangular viewing tank, filled with the same refractive matching fluid, whose kinematic viscosity was 12.5×10^{-6} m^2/s.

[1] Associate Professor and Graduate Student, respectively, Department of Mechanical Engineering, University of Idaho, Moscow, ID 83844.

[2] Professor, Department of Mechanical Engineering, University of Ottawa, Ottawa, Ontario, Canada K1N6N5.

Contributed by the Fluids Engineering Division of THE AMERICAN SOCIETY OF MECHANICAL ENGINEERS. Manuscript received by the Fluids Engineering Division February 20, 1996; revised manuscript received September 23, 1996. Associate Technical Editor: P. R. Bandyapahyay.

The fluid was seeded with silicon dioxide particles having a diameter of 1 μm and measurements were conducted using a two-component, fiberoptic, laser-Doppler velocimeter. The LDV used a 160 mm focal length lens with 26.5 mm beam separation yielding a measuring volume with a diameter of about 0.075 mm and a length of 1.2 mm. The LDV lens assembly was traversed manually with an uncertainty of 0.2 mm. The measurements over different cycles were synchronized using the signal of an optical sensor mounted on the rotating sleeve valve. The results were phase averaged over seven consecutive cycles, with typically 100 samples taken during each cycle. The cycle-to-cycle variation for the reported cases was found to be negligible. The typical uncertainty of the LDV results was 1.5 mm/s. The uncertainty of the experimentally determined recirculation zone length was 0.8 h.

As discussed in the Introduction, nearly axisymmetric flow was obtained by steadily injecting a small quantity of fluid into the recirculation zone, through an injection port at the top of the large tube at about $x/h = 0.63$. For the pulsatile flow the injection rate was adjusted so that time averaged vertical velocity profile became symmetric at $x/h = 4.8$.

An Analytical Expression

Although an analytical expression for pulsatile flow through a sudden expansion is not available, it is useful to consider an expression for the velocity profiles far downstream of the expansion, based on the analysis of Atabek and Chang (1961). In the far field, the velocity profile is independent of the distance from the entrance, but depends only on radial position r, the time, t, in the pulsatile flow cycle, and the shape of the pulsatile waveform. The relationship for the velocity profile is given as follows:

$$\frac{u(r,t)}{U_{b,\text{ave}}} = 2\left(1 - \frac{r^2}{a^2}\right) + \text{Real}\left\{\sum_{k=1}^{n}(a_k - ib_k) \times \left[\frac{J_o\left(i^{(3/2)}\sqrt{k}\alpha\,\frac{r}{a}\right) - J_o\left(i^{(3/2)}\sqrt{k}\alpha\right)}{J_2(i^{(3/2)}\sqrt{k}\alpha)}\right] e^{i2\pi k(t/\tau)}\right\} \quad (1)$$

where $U_{b,\text{ave}}$ is the time-averaged bulk velocity, $U_{b,\text{ave}} = Q_{\text{ave}}/\pi a^2$ (Q_{ave} is the time-averaged volume flow rate and a is the tube radius), τ is the period of pulsation, $\alpha = a(2\pi/\tau\nu)^{1/2}$ is the Womersley number (ν is the kinematic viscosity), i is $\sqrt{-1}$, J_0 and J_2 are the zeroth and second-order Bessel functions with complex arguments, and a_k and b_k are the Fourier coefficients of the periodic flow rate waveform. The Bessel functions were written in terms of the Kelvin functions ber and bei, which were calculated from series expansions as outlined by Elger (1992).

Results and Discussion

The measured, pulsatile, flow rate waveform, shown in Fig. 2(a), and, with more detail, in Fig. 2(b) was approximately sinusoidal, although exhibiting a measurable asymmetry. The pulsatile component was quite strong, with the peak-to-average flow rate ratio being 1.56. The mean Reynolds number was $\text{Re}_m = 121$ and the Womersley number was $\alpha = 5.0$, both based on the smaller tube diameter. The measured upstream centerline velocity waveform and the corresponding theoretical (Eq. (1)) waveform for fully developed pulsatile flow, shown in Fig. 2(b), differed, in root mean square, by less than 5 percent $U_{\text{cl,ave}}$, which indicates that the flow entering the sudden expansion was essentially fully developed pulsatile flow. A few far-field velocity profiles, obtained by substituting Fourier coefficients calculated from the measured flow rate waveform into Eq. (1), are shown in Fig. 2(c). Five Fourier coefficients were found sufficient for this purpose. It can be seen that, for the present experimental conditions, reverse flow near the wall could be expected over part of the cycle (e.g., at $t/\tau = 0.00$ and 0.875). Further computation has shown that the near wall reverse flow in the far-field would occur for $0 \le t/\tau \le 0.093$ and $0.83 \le t/\tau \le 1.00$, namely over 26.3 percent of the cycle. This reversal is associated with the pulsatile character of the flow and not with separation at the sudden expansion.

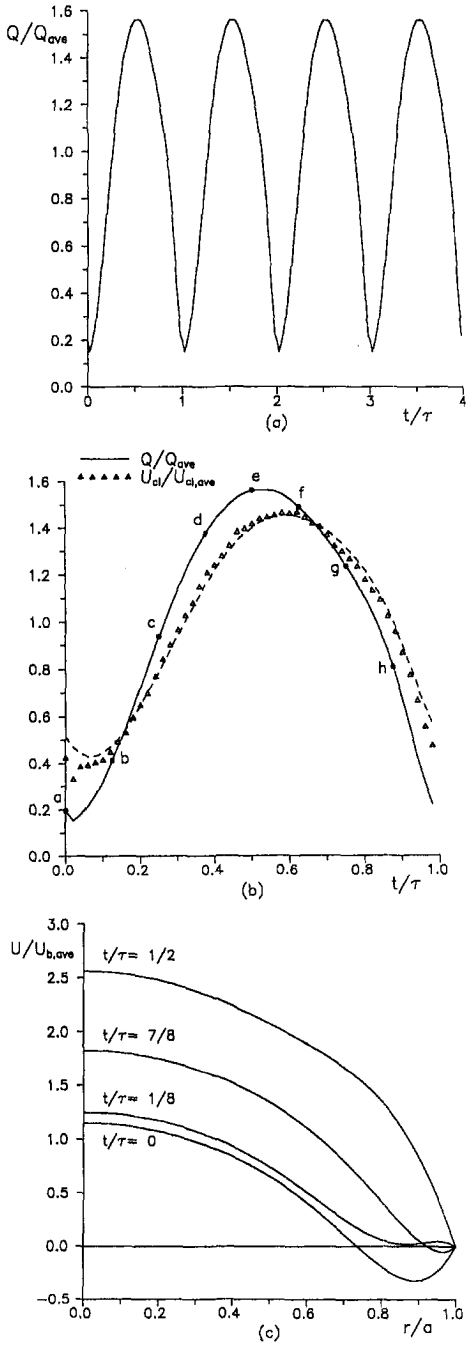

Fig. 2 (a) and (b) The pulsatile flow waveform: $Q_{\text{ave}} = 1.82$ lpm, $U_{\text{cl,ave}} = 0.113$ m/s (entrance tube); △ measurements, - - - fully developed pulsatile flow (equation 1); letters (a) through (h) on Fig. 2(b) denote times of vector plots in Fig. 3. (c) Far-field velocity profiles based on Eq. (1); $U_{b,\text{ave}} = 0.0118$ m/s.

Figure 3 shows vector plots of the velocity on the vertical centerplane. Figures 3(b) to (g) ($0.125 \le t/\tau \le 0.75$) show a recirculation region of limited length, while Figs. 3(a) and (h) show near wall reverse flow over the entire measurement

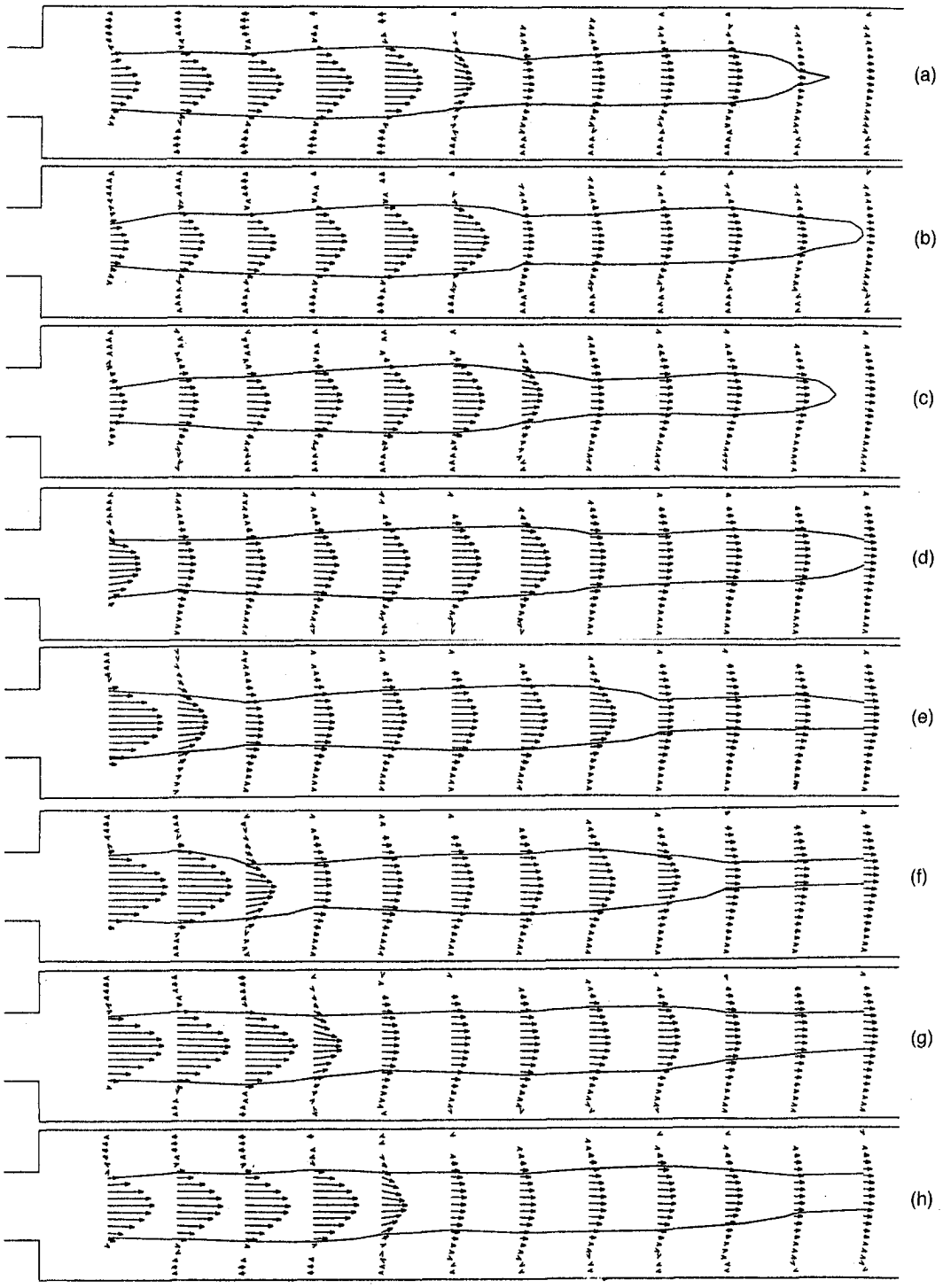

Fig. 3 Vector plots of the pulsatile flow (see Fig. 2b for phase times). — axial velocity isotachs with $U_{iso}/U_{b,ave}$ = 1.69 (a, b), 2.54 (c, d, g), 3.14 (e), 2.37 (h); $U_{b,ave}$ = 0.0118 m/s.

range, in conformity with the far-field predictions. The recirculation zone length, for the cases to which it applies, was measured by examining the vector plots for the location of near wall flow reversal. Figure 4 shows the measured recirculation zone lengths together with its quasi-steady (i.e., corresponding to the instantaneous bulk Reynolds number) estimate, based on the Back and Roschke (1972) measurements. The trends shown by the two sets of results are entirely opposite with the instantaneous recirculation zone length correlating with bulk acceleration rather than the Reynolds number. Quasi-steady predictions are, of course, entirely inadequate in describing flow reversal in this pulsatile ASE flow.

An inspection of Fig. 3 reveals the presence of alternating inward and outward-facing patterns of the velocity vectors, which are consistent with the presence of traveling waves in the larger tube. To assist in the characterization of these waves, we have plotted one axial isotach on each vector plot and then estimated the speed of these waves from the distances between corresponding wave crests from one vector plot to the next, over the range $3.2 < x/h < 16$. The wave speed was found to

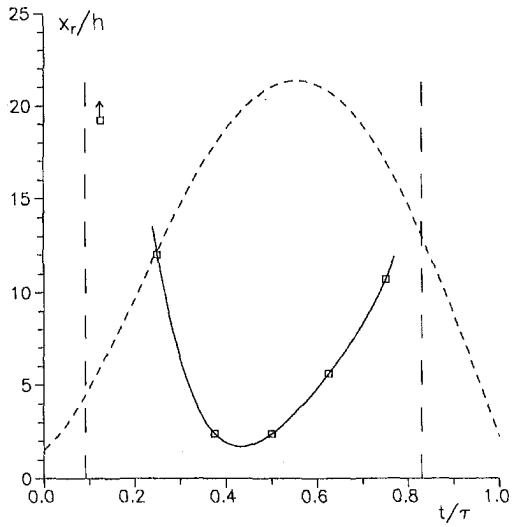

Fig. 4 Recirculation zone length for pulsatile ASE flow measurements; □ measurements, - - - quasi-steady prediction. The vertical dashed lines enclose the region in which the far-field flow was not reversed near the wall. The arrow indicates near-wall reverse flow in the entire measurement domain ($x/h < 19.2$).

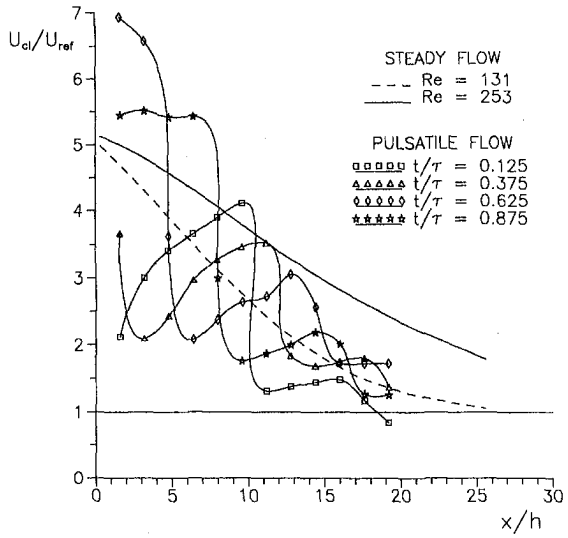

Fig. 5 Axial development of centerline velocity. U_{ref} is the time averaged centerline velocity in the far field. Steady flow: U_{ref} = 0.0246 m/s for Re = 131 and U_{ref} = 0.0424 m/s for Re = 253. Pulsatile flow: Re_m = 121 and U_{ref} = 0.0224 m/s.

be essentially constant throughout the cycle and equal to 0.68 times the time averaged bulk velocity in the smaller tube (or 3.4 times that in the larger tube). Measurements in the same setup and with the same mean and peak bulk flow rates, but at approximately twice the frequency of pulsation (α = 7.0), found the wave speed to increase to 1.08 times the average bulk velocity in the smaller tube, thus indicating that the relative wave speed increases with increasing Womersley number. The present results conform qualitatively with the small-amplitude, inviscid wave analysis of Tutty and Pedley (1994), which predicted the formation of traveling wave packets in pulsatile flow past a backward facing step.

Finally, the variation of the instantaneous velocity along the centerline is plotted in Fig. 5, together with steady flow measurements in the same setup. The existence of traveling waves is clearly indicated by the phase shifting in the velocity maxima and minima along the cycle. One may also note that the average velocity decay curve for a pulsatile flow with Re_m = 121 is close to the decay curve for steady flow with Re = 131, while the curve for steady flow with Re = 253 indicates a substantially longer development length.

Conclusions

The main conclusion of the present study is that flow patterns for a strongly pulsating flow in an ASE differ dramatically from steady flow patterns. Waves forming in pulsatile flows propagate with a speed that increases with increasing Womersley number.

Acknowledgment

Financial support for this work was provided by the Natural Sciences and Engineering Research Council of Canada and by the Development Fund of the Faculty of Engineering of the University of Ottawa.

References

Atabek, J. B., and Chang, C. C., 1961, "Oscillatory Flow Near the Entry of a Circular Tube," *Zeitschrift fuer Angewandte Mathematik und Physik,* Vol. 12, pp. 185–201.

Back, L. H., and Roschke, E. J., 1972, "Shear-Layer Flow Regimes and Wave Instabilities and Reattachment Lengths Downstream of an Abrupt Circular Channel Expansion," ASME *Journal of Applied Mechanics,* Vol. 39, pp. 677–681.

Budwig, R., 1994, "Refractive Index Matching Methods for Liquid Flow Investigations," *Experiments in Fluids,* Vol. 17, pp. 350–355.

Budwig, R., and Tavoularis, S., 1995, "Steady and Pulsatile Flows Through an Axisymmetric Sudden Expansion," *Proceedings of the Forum on Unsteady Flows,* ASME FED-Vol. 216, pp. 55–60.

Devenport, W. J., and Sutton, E. P., 1993, "An Experimental Study of Two Flows Through an Axisymmetric Sudden Expansion," *Experiments in Fluids,* Vol. 14, pp. 423–432.

Elger, D., 1992, "The Validity of the Linear Orifice Impedance Model for Predicting the Impedance of a Tube," *Journal of the Acoustical Society of America,* Vol. 91, pp. 3136–3143.

Elger, D., Slippy, J., and Budwig, R., 1995, "A Numerical Study of the Hemodynamics in an Abdominal Aortic Aneurysm," *Proceedings of the 1995 Biomedical Fluids Engineering Symposium,* ASME FED-Vol. 212, pp. 15–22.

Feuerstein, I. A., Pike, G. K., and Rounds, G. F., 1975, "Flow in an Abrupt Expansion as a Model for Biological Mass Transfer Experiments," *Journal of Biomechanics,* Vol. 8, pp. 41–51.

Grolman, E., 1988, "Laser Doppler Anemometry in a Single Phase Turbulent Pipe Flow," University of Amsterdam Masters Thesis.

Ma, P., Li, X., and Ku, D. N., 1994, "Heat and Mass Transfer in a Separated Flow Region for High Prandtl and Schmidt Numbers Under Pulsatile Conditions," *International Journal of Heat and Mass Transfer,* Vol. 37, No. 17, pp. 2723–2736.

Mori, Y., and Futagami, K., 1967, "Forced Convective Heat Transfer in Uniformly Heated Horizontal Tubes (2nd report)," *Int. Journal of Heat and Mass Transfer,* Vol. 10, pp. 1801–1813.

Nerem, R. M., 1992, "Vascular Fluid Mechanics, the Arterial Wall, and Atherosclerosis," ASME *Journal of Biomechanical Engineering,* Vol. 114, pp. 274–282.

Ojha, M., Cobbold, R. S., Johnston, K. W., and Hummel, R. L., 1989, "Pulsatile Flow Through Constricted Tubes: an Experimental Investigation using Photochromic Tracer Methods," *Journal of Fluid Mechanics,* Vol. 203, pp. 173–197.

Tutty, O. R., and Pedley, T. J., 1994, "Unsteady Flow in a Nonuniform Channel: A Model for Wave Generation," *Physics of Fluids,* Vol. 6, No. 1, pp. 199–208.